Experimental study of Pluto's atmosphere and aerosols

Lora Jovanovic

université PARIS-SACLAY

Experimental Study of Pluto's Atmosphere and Aerosols

Étude Expérimentale de l'Atmosphère et des Aérosols de Pluton

Thèse de doctorat de l'université Paris-Saclay

École doctorale n° 579 – Sciences Mécaniques et Énergétiques, Matériaux et Géosciences (SMEMaG)
Spécialité de doctorat : Structure et Évolution de la Terre et des Autres Planètes
Unité de recherche : Université Paris-Saclay, UVSQ, CNRS, LATMOS, 78280, Guyancourt, France
Référent : Université de Versailles Saint-Quentin-en-Yvelines (UVSQ)

Thèse présentée et soutenue à Paris-Saclay, le 10 Septembre 2021, par

Lora JOVANOVIC

Composition du Jury

Cyril SZOPA Professeur des Universités, UVSQ/LATMOS	Président
Emmanuel LELLOUCH Astronome, SU/LESIA	Rapporteur & Examinateur
Ella SCIAMMA-O'BRIEN Research Scientist, NASA Ames	Rapportrice & Examinatrice
François FORGET Directeur de Recherche, SU/LMD	Examinateur
Sandrine VINATIER Chargée de Recherche, SU/LESIA	Examinatrice
Vassilissa VINOGRADOFF Chargée de Recherche, AMU/PIIM	Examinatrice

Direction de la thèse

Nathalie CARRASCO Professeure des Universités, UVSQ/LATMOS	Directrice de thèse
Thomas GAUTIER Chargé de Recherche, UVSQ/LATMOS	Co-encadrant de thèse

Thèse de doctorat

NNT : 2021UPASJ011

À *mes parents, Magdalena et Nova, et à ma sœur, Lidia…*

À *ma famille, ici ou là-bas…*

“Znanje, to su zlatne lestvice koje nas vode u nebesa; znanje je svetlost koja osvetljava naš put kroz ovaj svet i vodi nas u život budućnosti, pun neuvele slave...”

Mihajlo Idvorski Pupin

Remerciements

Et après quelques mois, que dis-je ! 3 années de durs labeurs, je n'aurais jamais pensé que ces quelques lignes seraient les plus difficiles à écrire… J'aimerais remercier tous ceux qui ont contribué de près ou de loin à cette fantastique aventure, sans pour autant froisser les éventuelles personnes que j'aurais pu oublier lors de mon remue-méninge en solo.

Je tiens avant tout à exprimer ma profonde gratitude à mes deux directeurs de thèse, Nathalie Carrasco et Thomas Gautier. Je ne saurais vous remercier assez de m'avoir fait confiance, de m'avoir accueillie dans votre équipe, de m'avoir offert un cadre de travail plus qu'idéal durant ces trois années de thèse. Je vous remercie également pour votre disponibilité, votre grande gentillesse et bienveillance, votre soutien, tous les encouragements que vous m'avez apportés quand j'en avais besoin, vos remarques pertinentes et conseils avisés. Tant scientifiquement qu'humainement, vous m'avez beaucoup apporté… Du fond du cœur, MERCI infiniment !

Que serait cette thèse sans l'aide précieuse de Ludovic Vettier et Guy Cernogora ?! Merci d'avoir été à mes côtés pour dévoiler presque tous les mystères des plasmas type Pluton et Triton, mais aussi pour tous ces bons moments de franche rigolade passés autour d'un café plus ou moins fort et derrière un QMS et des CMOS « Pimousse » plus que capricieux !

Au sein de l'équipe ATMOSIM, j'aimerais également remercier mes collègues et ami(e)s Jérémy Bourgalais, Audrey Chatain, Thomas Drant, David Dubois, Julien Maillard, Zoé Perrin, Laura Selliez et Sarah Tigrine. Mentions spéciales pour mon bro' Jérémy, mon coach de Vie et modèle en Science, et pour Zoé à qui je lègue de bon cœur l'institut de Beauté ZoRa ! Sans oublier les stagiaires – petits et grands – que j'ai eu l'immense plaisir d'encadrer : Nour B., César Feniou, Nans G., Nicolas Jaisle et Eyléa P.

Mes remerciements vont également aux autres collègues et ami(e)s du LATMOS avec qui j'ai eu le plaisir d'échanger durant ces trois années, que ce soit en réunions Jeunes Planétos, en pauses café/thé ou autour d'un de mes cinq bons repas me définissant* : Léa Bonnefoy, Caroline Freissinet, Pierre Gilbert, Edith Hadamcik, Yann Hervé, Christophe Mathé, Ophélie McIntosh, Valentin Moulay, Nicolas Oudart, Loïc Rossi, Aurélien Stcherbinine, Cyril Szopa, Margaux Vals… (Désolée si j'ai oublié quelqu'un !)

* *Lora en 5 repas* : Sodebo Salade Roma /// McDonald's Menu Maxi Best Of Big Mac (avec Coca Zéro pour le régime) /// Burger King Double Whopper (avec Coca Zéro pour le régime) /// Menu Picard à 5€ (Gnocchis, Crumble Mangue-Passion, Limonade Pulco) /// Menu Midi au Restaurant Chinois (3 Nems, Bœuf aux Oignons avec des Pommes de Terre, Perle de Coco)

Que serait cette thèse (bis !) sans la contribution inestimable de mes collègues hors-LATMOS : Carlos Afonso, Basile Augé, Tanguy Bertrand, Philippe Boduch, Laurent Broch, Arnaud Buch, Aotmane En Naciri, Marie Fayolle, Laurène Flandinet, Luc Johann, François-Régis Orthous-Daunay, Van Phan, Olivier Poch, Silvia Protopapa, Eric Quirico, Pascal Rannou, Hermann Rothard, Bernard Schmitt, Isabelle Schmitz-Afonso, Véronique Vuitton et Cédric Wolters. Merci à vous tous pour nos manip's et nos échanges !

Que serait mon monde sans mes ami(e)s, rencontré(e)s sur les bancs du collège ou de la fac, dans un autocar direction la Serbie, ou en soirées bien arrosées en boissons soft ?! Merci

ainsi à Océane B., Jules B. de M., Lorenzo C., Naila C., Barnabé C., Isis C., Viktoria Đ., Nicodème D., Anastasios G., Chloé H., Yassin J., Amal M., Marina M., Alice P., Robin S., Jeffrey T., Dajana V. et Kévin W. K.

Un immense MERCI à Emmanuel Lellouch et Ella Sciamma-O'Brien d'avoir accepté de rapporter mon manuscrit de thèse, ainsi qu'à Cyril Szopa, François Forget, Sandrine Vinatier et Vassilissa Vinogradoff pour leur participation à mon jury de thèse !

Не могу да завршим а да не изразим сву своју захвалност и љубав својој породици, а посебно родитељима Магдалени и Нови, и сестри Лидии. Хвала вам на безусловној подршци! Хвала вам за све!

Моје последње мисли лете мојим анђелима Јованком-Вана и Десанком-Деса. Тамо где сте отишле, надам се да сте поносне на мене...

LORA JOVANOVIC

Résumé

Le 14 Juillet 2015, la sonde *New Horizons* de la NASA a survolé Pluton, révélant une atmosphère et une surface complexes observées nulle part ailleurs dans le Système Solaire. La surface de Pluton est composée de glaces de diazote N_2, de méthane CH_4, et de monoxyde de carbone CO. Au cours de l'orbite elliptique de Pluton, ces glaces subissent un cycle de sublimation/condensation à l'origine d'une atmosphère ténue (~11 µbar à la surface). Cette atmosphère est majoritairement composée de N_2 et CH_4, avec ~500 ppm de CO. Soumise au rayonnement ultraviolet extrême et aux photons Lyman-α, elle est le siège de la production d'aérosols photochimiques, des particules solides en suspension dans l'atmosphère. Les processus exacts de formation de ces aérosols ne sont toutefois pas encore bien définis. Ces particules solides, dont la composition chimique et les propriétés optiques sont inconnues, sont observées jusqu'à plus de 350 km d'altitude dans l'atmosphère de Pluton. Des modèles numériques ont montré que la présence de ces aérosols dans l'atmosphère pouvait avoir un impact sur la chimie atmosphérique et le climat de Pluton. De plus, il a été suggéré que ces aérosols sédimentent et constituent une source de matière organique à la surface de Pluton.

Dans le cadre de ma thèse, j'ai utilisé une approche expérimentale afin d'étudier les aérosols de Pluton, de leur formation dans la haute atmosphère à leur devenir en surface, en passant par leurs interactions avec l'atmosphère. La formation des aérosols de Pluton par photochimie et leur composition chimique sont les sujets de la première et de la deuxième partie de cette thèse de Doctorat (Chapitre III et Chapitre IV). L'interaction des aérosols de Pluton avec le rayonnement solaire et la contribution des aérosols photochimiques en tant qu'agent colorant à la surface de Pluton sont les sujets de la troisième et de la quatrième partie de cette thèse de Doctorat (Chapitre V et Chapitre VI).
Le dispositif expérimental PAMPRE (Production d'Aérosols en Microgravité par Plasma REactif), situé au LATMOS, a été utilisé afin de simuler la chimie atmosphérique de Pluton et synthétiser des analogues d'aérosols photochimiques, communément appelés "tholins". Des expériences ont également été réalisées au GANIL, en utilisant le dispositif expérimental IGLIAS (Irradiation de GLaces d'Intérêt Astrophysique). En irradiant les tholins avec des ions lourds, l'objectif était de simuler le vieillissement de la matière organique à la surface de Pluton dû aux particules chargées constituant le rayonnement cosmique galactique.

Grâce aux analyses physico-chimiques effectuées, tant pour caractériser la composition chimique de l'atmosphère simulée de Pluton que celle des analogues d'aérosols synthétisés, j'ai pu conclure à l'importance de la réactivité de N_2 et CO dans la chimie atmosphérique de Pluton. L'azote contenu dans les molécules produites en phase gazeuse et incorporées ultimement dans les particules solides est inclus non seulement sous la forme de fonctions chimiques terminales (amine, nitrile, isonitrile), mais aussi sous la forme d'hétérocycles azotés (triazine, pyrazole, pyrazine, pyrrole). Quant à l'oxygène, seules des fonctions chimiques oxygénées terminales (alcool, acide carboxylique, carbonyle) ont été détectées. Ces molécules organiques azotées et/ou oxygénées sont responsables d'une forte absorption dans le domaine spectral ultraviolet par les analogues d'aérosols de Pluton et une absorption plus modérée dans le visible et l'infrarouge proche. Ces résultats sont cohérents avec les observations spectrales faites de la surface et de l'atmosphère de Pluton par les instruments à bord de la sonde *New Horizons*. Enfin, grâce aux expériences d'irradiation des analogues d'aérosols de Pluton par des ions lourds, j'ai pu conclure au vieillissement de la surface de Pluton par irradiation par le rayonnement cosmique galactique, expliquant probablement les spectres caractéristiques de la région Cthulhu.

Abstract

On July 14th, 2015, the NASA's *New Horizons* spacecraft flew by Pluto, revealing a complex atmosphere and surface seen nowhere else in the Solar System. Pluto's surface ices are composed of molecular nitrogen N_2, methane CH_4, and carbon monoxide CO. During Pluto's elliptical orbit, these ices undergo a sublimation/condensation cycle resulting in a tenuous atmosphere (~11 μbar at the surface). This atmosphere is mostly composed of N_2 and CH_4, with ~500 ppm of CO. Subjected to extreme ultraviolet radiation and Lyman-α photons, it is the place of photochemical aerosol production, aerosols being solid particles in suspension in the atmosphere. The exact processes of formation of these aerosols are however not well constrained yet. These solid particles, whose chemical composition and optical properties are unknown, are observed up to more than 350 km of altitude in the atmosphere of Pluto. Numerical models have shown that the presence of these aerosols in the atmosphere could have an impact on the atmospheric chemistry and climate of Pluto. Moreover, it has been suggested that these aerosols sediment and constitute a source of organic matter on the surface of Pluto.

During my Ph.D., I used an experimental approach to study the aerosols of Pluto, from their formation in the upper atmosphere to their evolution on the surface, through their interactions with the atmosphere. The formation of Pluto's aerosols by photochemistry and their chemical composition are the subjects of the first and second part of this Ph.D. thesis (Chapter III and Chapter IV). The interaction of Pluto's aerosols with solar radiation and the contribution of photochemical aerosols as a coloring agent on the surface of Pluto are the subjects of the third and fourth part of this Ph.D. thesis (Chapter V and Chapter VI).
The experimental setup PAMPRE (Production of Aerosols in Microgravity by Reactive Plasma), located at LATMOS, has been used to simulate the atmospheric chemistry of Pluto and to synthesize analogues of photochemical aerosols, usually called "tholins". Experiments have also been performed at GANIL, using the IGLIAS (Irradiation of Astrophysical Ices) experimental setup. By irradiating tholins with heavy ions, the objective was to simulate the ageing of organic matter on the surface of Pluto due to the charged particles constituting the galactic cosmic rays.

Thanks to the physicochemical analyses carried out to characterize the chemical composition of Pluto-simulated atmosphere as well as that of the synthesized aerosol analogues, I was able to conclude to the importance of N_2 and CO reactivity in the atmospheric chemistry of Pluto. The nitrogen contained in the molecules produced in the gas phase and ultimately incorporated in the solid particles is included not only in the form of terminal functional groups (amine, nitrile, isocyanide), but also in the form of nitrogen heterocycles (triazine, pyrazole, pyrazine, pyrrole). Regarding oxygen, only terminal oxygenated chemical functions (alcohol, carboxylic acid, carbonyl) were detected. These nitrogenous and/or oxygenated organic molecules are responsible for a strong absorption in the ultraviolet spectral range by Pluto aerosol analogues and a more moderate absorption in the visible and near-infrared. These results are consistent with spectral observations of Pluto's surface and atmosphere by instruments onboard *New Horizons*. Finally, thanks to the experiments of irradiation of Pluto aerosol analogues by heavy ions, I was able to conclude that the surface of Pluto is processed by galactic cosmic ray irradiation, probably explaining the characteristic featureless spectra of the Cthulhu region.

TABLE OF CONTENTS

Résumé

I. Introduction

Pluton a été découverte le 18 Février 1930 par Clyde W. Tombaugh, un astronome américain amateur à la recherche de la « Planète X » prédite par Percival Lowell et supposée perturber les orbites d'Uranus et de Neptune (Leonard, 1930). Elle possède 5 satellites naturels : Charon (découverte en 1978, avec qui elle forme un système binaire, Christy and Harrington (1978, 1980)), Nix et Hydre (découverte en 2005, Weaver *et al.* (2006)), Kerbéros (découverte en 2011, Showalter *et al.* (2011)) et Styx (découverte en 2012, Showalter *et al.* (2012)). Initialement considérée comme la neuvième planète du Système Solaire, elle a été reclassée en 2006 en tant que planète naine, faisant partie d'un vaste ensemble d'objets trans-neptuniens (International Astronomical Union, 2006).

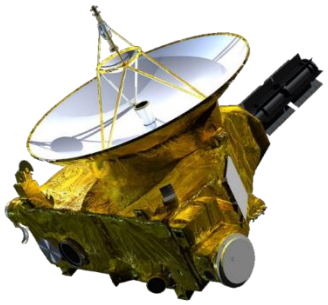

Figure A : La sonde *New Horizons*. *Crédit* : NASA/JHU-APL/SwRI.

À ce jour, seule la sonde *New Horizons* (NASA) (Figure A) a survolé le système plutonien, le 14 Juillet 2015, donnant ainsi un aperçu des caractéristiques surfaciques (composition de la surface, structures géologiques, *etc.*), et physiques et chimiques de l'atmosphère (profils de température et de pression de l'atmosphère, composition de l'atmosphère accompagnée de profils de densité, *etc.*). Ces données ont été obtenues grâce aux sept instruments portés par la sonde, à savoir le spectrographe imageur dans l'ultraviolet Alice, l'imageur panchromatique haute-résolution LORRI, le spectromètre d'ions et d'électrons PEPSSI, l'imageur dans le visible et l'infrarouge Ralph (composé des instruments MVIC et LEISA), le radiomètre REX, le détecteur de poussières interplanétaires SDC, et l'instrument électro-optique SWAP.

Pluton présente à sa surface des glaces, dont la composition chimique a initialement été déterminée à partir d'observations télescopiques au sol, par spectroscopie infrarouge, puis confirmée lors du survol de Pluton par la sonde *New Horizons*. Il est essentiellement question de glaces de diazote (N_2), de méthane (CH_4), et de monoxyde de carbone (CO), reposant sur un socle constitué de glace d'eau (Figure B) (Owen *et al.*, 1993; Grundy *et al.*, 2016; Protopapa *et al.*, 2017; Schmitt *et al.*, 2017). À ~45 K (température à la surface de Pluton, Gladstone *et al.* (2016),

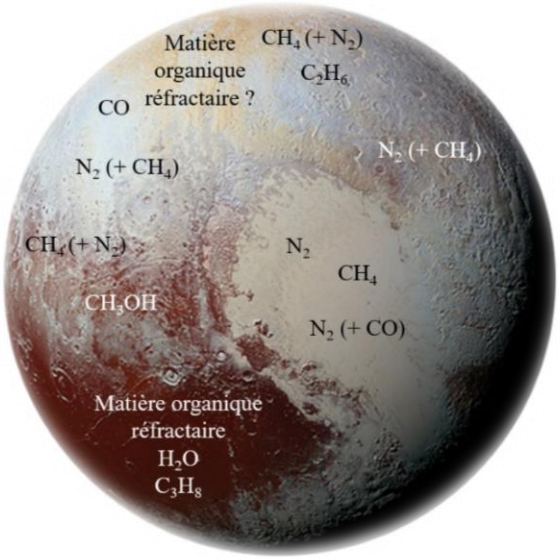

Figure B : Vue simplifiée de la composition de la surface de Pluton, d'après les études menées par Grundy *et al.* (2016), Protopapa *et al.* (2017), Schmitt *et al.* (2017), et Cook *et al.* (2019). *Crédit* : NASA/JHU-APL/SwRI.

Hinson *et al.* (2017)), ces glaces volatiles[1] N_2, CH_4 et CO sont en équilibre avec leur pression de vapeur saturante et subissent un cycle saisonnier de sublimation/condensation alimentant l'atmosphère ténue de Pluton (*e.g.*, Owen *et al.*, 1993; Stern *et al.*, 2015; Grundy *et al.*, 2016; Forget *et al.*, 2017). Des glaces d'éthane (C_2H_6), de méthanol (CH_3OH) et de propane (C_3H_8) ont également été détectées à la surface (Cook *et al.*, 2019), ainsi qu'une contribution significative d'un matériau organique réfractaire sombre non glacé, en particulier dans la région Cthulhu (Figure B) (Grundy *et al.*, 2016; Protopapa *et al.*, 2017; Schmitt *et al.*, 2017). L'origine de cette matière organique réfractaire est encore débattue (Cruikshank *et al.*, 2015; Sekine *et al.*, 2017; Grundy *et al.*, 2018; Protopapa *et al.*, 2020).

La présence d'une atmosphère autour de Pluton a été confirmée par occultation stellaire le 9 Juin 1988 (Hubbard *et al.*, 1988; Elliot *et al.*, 1989). La pression à la surface de Pluton a été estimée par Gladstone *et al.* (2016) et Hinson *et al.* (2017) respectivement à 10,2 ± 0,7 et 12,8 ± 0,7 µbar, tandis que la température proche de la surface varie entre 38,9 ± 2,1 et 51,6 ± 3,8 K. Cette atmosphère, qui s'étend jusqu'à environ 1600 km au-dessus de la surface de Pluton, est essentiellement composée de N_2 et de CH_4 ; le rapport de mélange de CH_4 variant de ~0.28-0.35 % à la surface de Pluton à 50 % à environ 1450 km d'altitude (Young *et al.*, 2018). En plus de ces deux composés majoritaires, 515 ± 40 ppm de CO, quelques dizaines de ppm de cyanure d'hydrogène (HCN) (Lellouch *et al.*, 2017), et des hydrocarbures (C_xH_y) en plus faibles proportions ont également été détectés. Parmi ces hydrocarbures, nous pouvons citer la présence effective d'acétylène (C_2H_2), d'éthylène (C_2H_4), d'éthane (C_2H_6) et de propyne (C_3H_4) (Gladstone *et al.*, 2016; Young *et al.*, 2018; Steffl *et al.*, 2020).

Figure C : Les aérosols de Pluton, mis en évidence par l'imageur LORRI de la sonde *New Horizons*. *Crédit* : NASA/JHU-APL/SwRI.

En raison de la composition chimique de l'atmosphère de Pluton semblable à celle de Titan (le plus gros satellite de Saturne), le profil thermique particulier de son atmosphère, et la présence d'un point d'inflexion dans la courbe de lumière de l'occultation stellaire ayant confirmé la présence d'une atmosphère autour de Pluton, la présence d'aérosols solides a été débattue dès les années 1990's (Stansberry, Lunine and Tomasko, 1989; Lellouch, 1994; Lara, Ip and Rodrigo, 1997; Krasnopolsky and Cruikshank, 1999). Ces aérosols ont finalement été mis en évidence par la mission *New Horizons*, comme en témoigne le halo bleuté observé sur la Figure C (Stern *et al.*, 2015; Gladstone *et al.*, 2016; Cheng *et al.*, 2017; Young *et al.*, 2018).

[1] Pour les objets trans-neptuniens et les petits corps de la ceinture de Kuiper, les glaces volatiles sont traditionnellement définies comme des glaces dont la pression de vapeur saturante est supérieure à celle de la glace d'eau pure.

Les aérosols de Pluton, représentant 0,05 à 0,1 ppm_V du volume de l'atmosphère, s'étendent jusqu'à plus de 350 km d'altitude et se décomposent en une vingtaine de couches superposées de quelques km d'épaisseur.

Des processus de formation similaires à ceux des aérosols de Titan ont été proposés pour ces aérosols de Pluton (Gladstone *et al.*, 2016; Luspay-Kuti *et al.*, 2017; Cheng *et al.*, 2017; Wong *et al.*, 2017; Young *et al.*, 2018; Lavvas *et al.*, 2020). Les aérosols de Pluton seraient ainsi formés par une photochimie complexe se déroulant dans la haute atmosphère, de 300 à 900 km d'altitude (Stern *et al.*, 2018; Young *et al.*, 2018).

Cette photochimie serait initiée par le rayonnement ultraviolet extrême (EUV) et les photons Lyman-α solaires. Le rayonnement EUV est suffisamment énergétique pour casser les liaisons triples de N_2 et de CO dans la haute atmosphère, tandis que les photons Lyman-α – provenant directement du Soleil ou diffusés par le milieu interplanétaire – cassent les liaisons C–H du méthane à des altitudes plus basses (Gladstone, Pryor and Stern, 2015; Gladstone *et al.*, 2016; Grundy *et al.*, 2018; et références citées). Bien que les voies réactionnelles exactes de formation de ces aérosols ne soient pas encore bien contraintes, il est supposé que la photochimie de Pluton implique des molécules neutres et ioniques formées à partir de l'ionisation et de la dissociation du diazote N_2, du méthane CH_4 et du monoxyde de carbone CO, majeurs constituants de l'atmosphère de Pluton (Gladstone *et al.*, 2016; Lellouch *et al.*, 2017; Young *et al.*, 2018). Cette chimie formerait des hydrocarbures complexes, des nitriles et des molécules oxygénées. Ces molécules polymériseraient ensuite pour former les aérosols solides (Figure D) (Gladstone *et al.*, 2016; Wong *et al.*, 2017; Young *et al.*, 2018; Gladstone and Young, 2019; Krasnopolsky, 2020).

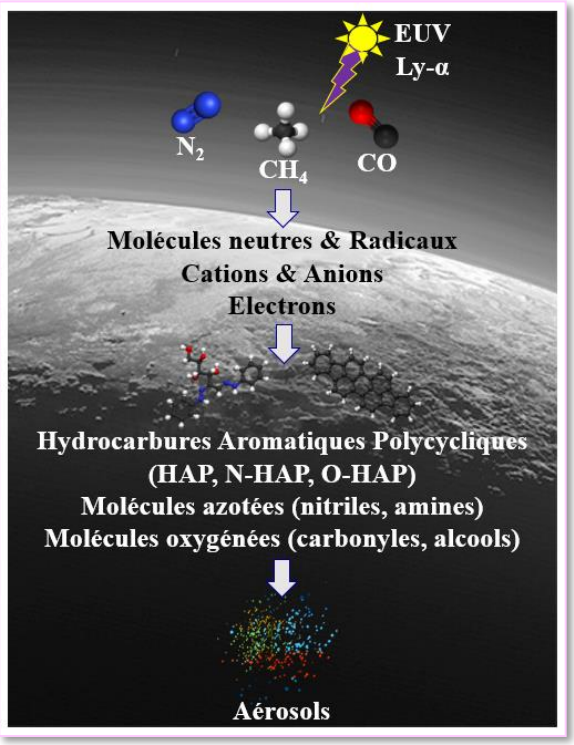

Figure D : Schéma simplifié de la formation des aérosols de Pluton. *Crédit* : NASA/JHU-APL/SwRI.

La formation des aérosols de Pluton par photochimie et leur composition chimique sont les sujets de la première et de la deuxième partie de cette thèse de Doctorat (Chapitre III et Chapitre IV).

Ensuite, à plus basses altitudes, entre 200 et 400 km où la température est de ~70 K, interviendraient des processus de condensation de molécules gazeuses photochimiques sur les aérosols solides (Luspay-Kuti *et al.*, 2017; Mandt *et al.*, 2017; Wong *et al.*, 2017; Lavvas *et al.*, 2020). Cette condensation impliquerait les espèces suivantes : C_2H_2, C_2H_4, C_2H_6, HCN, CH_2NH, C_3H_4, C_3H_6, CH_3CN, C_4H_2, HC_3N, C_2H_3CN, C_2N_2, CH_3C_2CN et C_6H_6 (Lara, Ip and Rodrigo, 1997; Krasnopolsky and Cruikshank, 1999; Luspay-Kuti *et al.*, 2017; Gao *et al.*, 2017; Mandt *et al.*, 2017; Wong *et al.*, 2017; Lavvas *et al.*, 2020).

À hautes altitudes, les monomères constitutifs de ces brumes mesureraient environ 10 nm de rayon et s'agrègeraient en particules fractales de 0,15 µm de rayon. Lors de leur sédimentation, ces agrégats fractals croîtraient ensuite en particules sphériques de 0,5 µm de rayon, par ces processus de condensation des hydrocarbures photochimiques présents dans l'atmosphère (Stern *et al.*, 2015; Gladstone *et al.*, 2016; Cheng *et al.*, 2017; Gao *et al.*, 2017; Young *et al.*, 2018; Lavvas *et al.*, 2020).

Des modèles numériques récents ont montré que ces aérosols pouvaient affecter profondément la chimie atmosphérique de Pluton, en déplétant par exemple l'atmosphère de ses hydrocarbures de type C_2 qui adhèrent aux aérosols chargés négativement, entraînant ensuite la formation d'hydrocarbures plus complexes (Luspay-Kuti *et al.*, 2017; Wong *et al.*, 2017; Krasnopolsky, 2020). Le climat de Pluton peut également être affecté par ces aérosols, qui peuvent servir de noyaux de condensation (Lavvas *et al.*, 2016; Luspay-Kuti *et al.*, 2017; Gao *et al.*, 2017; Wong *et al.*, 2017; Lavvas *et al.*, 2020) ou par un refroidissement radiatif direct de l'atmosphère par l'absorption des radiations solaires (Zhang, Strobel and Imanaka, 2017). En effet, la température de l'atmosphère de Pluton à ~400 km d'altitude est environ 30 à 40 K plus froide que les prédictions des modèles pour une atmosphère sans aérosols en équilibre thermique (Zhu, Strobel and Erwin, 2014; Gladstone *et al.*, 2016; Zhang, Strobel and Imanaka, 2017). Ce refroidissement de l'atmosphère est difficile à expliquer en ne prenant en compte que des espèces gazeuses (*e.g.*, Krasnopolsky, 2018), telles que HCN (Lellouch *et al.*, 2017) ou des molécules d'eau provenant de l'afflux de grains de poussière de la ceinture de Kuiper (Strobel and Zhu, 2017). Bien que l'hypothèse d'agents de refroidissement gazeux ne soit pas complètement écartée, Zhang, Strobel and Imanaka (2017) ont suggéré que ce refroidissement pouvait être dû aux particules de brume et à leurs propriétés optiques. En effet, les aérosols de Pluton absorberaient dans les domaines spectraux de l'UV-Visible et de l'infrarouge lointain, ce qui affecterait considérablement le bilan thermique de l'atmosphère de Pluton compte tenu de la température de surface (et donc, de la fonction d'émission de Planck de Pluton), mais ils seraient moins absorbants dans l'IR proche et moyen (Zhang, Strobel and Imanaka, 2017; Grundy *et al.*, 2018; et références citées). Les taux de chauffage et de refroidissement calculés par Zhang, Strobel and Imanaka (2017) pour les aérosols semblent être 100 fois plus importants que ceux des espèces gazeuses. Il semblerait ainsi que les particules de brume dominent l'équilibre thermique de l'atmosphère de Pluton depuis la surface jusqu'à ~700 km d'altitude. Par ailleurs, ces aérosols photochimiques pourraient également constituer une source de matière organique à la surface de Pluton, expliquant ainsi toutes les couleurs observées dans la Figure B, du rouge foncé des régions Cthulhu et Krun au doré du pôle nord de Pluton (Lowell Regio) (Protopapa *et al.*, 2017, 2020; Grundy *et al.*, 2018).

L'interaction des aérosols de Pluton avec le rayonnement solaire et la contribution des aérosols photochimiques en tant qu'agent colorant à la surface de Pluton sont les sujets de la troisième et de la quatrième partie de cette thèse de Doctorat (Chapitre V et Chapitre VI).

Compte tenu de tous ces effets mentionnés ci-dessus, l'étude des processus de formation et des propriétés physiques et chimiques des aérosols de Pluton est essentielle pour une meilleure compréhension non seulement de la chimie atmosphérique de Pluton, mais aussi de son climat (modulé par les interactions entre le rayonnement, les constituants de son atmosphère et ses

aérosols), et de sa surface hétérogène. En plus des observations directes de Pluton, depuis le sol ou avec les instruments embarqués à bord de la sonde *New Horizons*, il existe différentes approches pour étudier la chimie atmosphérique et la formation des aérosols de Pluton, ainsi que leurs propriétés physiques et chimiques. Par exemple, grâce à la modélisation numérique, des mécanismes théoriques sont confrontés aux observations. Quant à la simulation expérimentale en laboratoire – approche que j'ai utilisée dans le cadre de mon Doctorat – son objectif est de reproduire la chimie atmosphérique de Pluton, à l'aide d'un mélange gazeux représentatif soumis à une source d'énergie, et de former des analogues d'aérosols, soumis ensuite à diverses analyses physico-chimiques à l'aide d'instruments analytiques de pointe.

Dans le cadre de mon Doctorat, j'ai utilisé une approche expérimentale afin d'étudier les aérosols de Pluton, de leur formation dans la haute atmosphère à leur devenir en surface, en passant par leurs interactions avec l'atmosphère.

II. Matériel et Méthodes

Le dispositif expérimental PAMPRE (Production d'Aérosols en Microgravité par Plasma REactif, Szopa, Cernogora *et al.* (2006), Alcouffe *et al.* (2010)), situé au LATMOS (*Laboratoire Atmosphères, Observations Spatiales*, Guyancourt, France) (Figure E), a été utilisé afin de simuler la chimie atmosphérique de Pluton et synthétiser des analogues d'aérosols photochimiques, communément appelés « tholins » (Figure F).

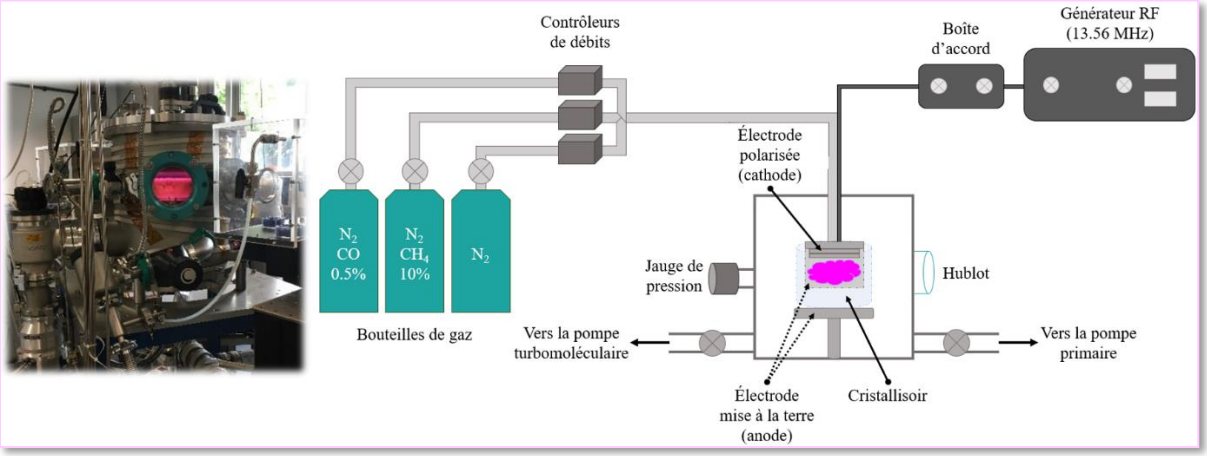

Figure E : Photographie (*à gauche*) et schéma (*à droite*) du dispositif expérimental PAMPRE utilisé pour simuler la chimie atmosphérique de Pluton et synthétiser des analogues d'aérosols photochimiques.

PAMPRE est un réacteur permettant d'obtenir un plasma en appliquant une décharge radio-fréquence (RF) dans un mélange gazeux N_2:CH_4:CO représentatif des composants majoritaires de l'atmosphère de Pluton. La décharge RF simule les photons solaires arrivant au voisinage de Pluton et initiant la formation des aérosols par photochimie, tandis que le plasma reproduit les couches atmosphériques réactives où se forment les aérosols de Pluton.

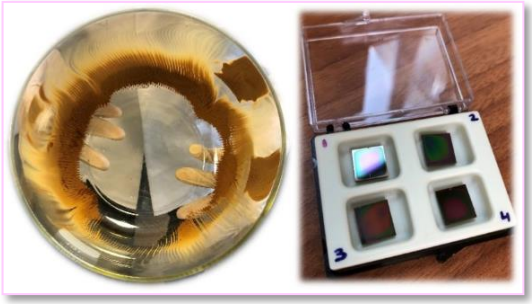

Figure F : Les tholins de Pluton synthétisés à l'aide du dispositif expérimental PAMPRE, sous forme de poudre (*à gauche*) ou de film mince (*à droite*).

Des expériences ont été réalisées au GANIL (*Grand Accélérateur National d'Ions Lourds*, Caen, France), en utilisant le dispositif expérimental IGLIAS (Irradiation de GLaces d'Intérêt Astrophysique, Augé *et al.* (2018)) (Figure G). En irradiant les tholins avec des ions lourds, l'objectif était de simuler le vieillissement de la matière organique à la surface de Pluton dû aux particules chargées constituant le rayonnement cosmique galactique (GCR).

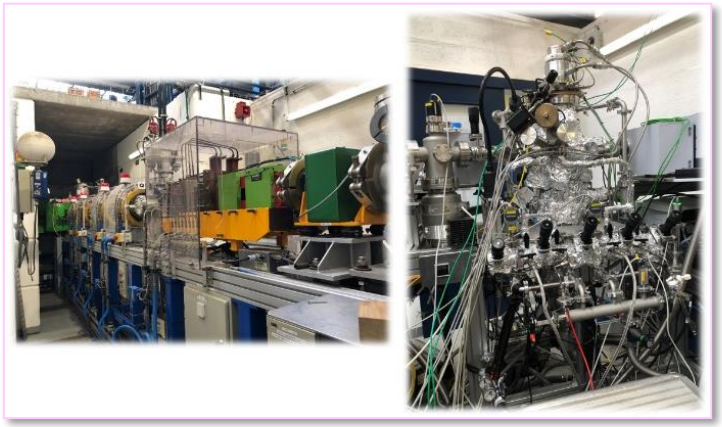

Figure G : Faisceau d'ions lourds IRRSUD (IRRadiation SUD) au GANIL (*à gauche*) et dispositif expérimental IGLIAS (*à droite*), utilisés pour simuler le vieillissement de la matière organique à la surface de Pluton dû aux particules chargées constituant le rayonnement cosmique galactique.

Différentes techniques analytiques ont été utilisées au cours de ce Doctorat afin de caractériser l'atmosphère simulée de Pluton et les tholins de Pluton (Tableau A).

Tableau A : Techniques d'analyse employées au cours de ce Doctorat.

Technique d'analyse	Objectifs
ANALYSE EN PHASE GAZEUSE	
Spectrométrie de masse quadripolaire (QMS), avec ionisation électronique (EI)	• Comprendre la composition et la chimie de l'atmosphère de Pluton
ANALYSE EN PHASE SOLIDE : COMPOSITION CHIMIQUE	
Spectrométrie de masse à haute résolution (HRMS) Technique Orbitrap™, avec ionisation par électronébulisation (ESI) ou photo-ionisation à pression atmosphérique (APPI)	• Comprendre la composition chimique des aérosols de Pluton • Évaluer les implications prébiotiques des aérosols de Pluton
HRMS Spectrométrie de masse à résonance cyclotronique ionique (FT-ICR), avec désorption-ionisation laser (LDI)	• Comprendre l'évolution moléculaire de la matière organique à la surface de Pluton soumise à une irradiation par GCR
Analyse de la composition élémentaire	• Comprendre la chimie atmosphérique et la composition chimique des aérosols de Pluton
Chromatographie en phase gazeuse couplée à la spectrométrie de masse (GC-MS)	• Évaluer les implications prébiotiques des aérosols de Pluton, en déterminant les structures des molécules constituant les analogues d'aérosols de Pluton
ANALYSE EN PHASE SOLIDE : MORPHOLOGIE	
Microscopie électronique à balayage (MEB)	• Comprendre l'évolution morphologique de la matière organique à la surface de Pluton soumise à une irradiation par GCR

ANALYSE EN PHASE SOLIDE : PROPRIÉTÉS SPECTRALES	
Spectroscopie infrarouge (IR) Technique de réflectance totale atténuée (ATR)	Comprendre la composition chimique des aérosols atmosphériques de Pluton
Spectroscopie infrarouge à transformée de Fourier (FTIR)	Comprendre l'évolution compositionnelle de la matière organique à la surface de Pluton soumise à une irradiation par GCR
Spectroscopie ultraviolet-visible (UV-Vis)	Comprendre l'évolution des propriétés optiques de la matière organique à la surface de Pluton soumise à une irradiation par GCR
Ellipsométrie spectroscopique	Comprendre le transfert radiatif des aérosols de Pluton en déterminant les indices optiques [*n*, *k*] des analogues d'aérosols de Pluton

III. Résumé des résultats et implications pour Pluton

III.1. Concernant la composition chimique de l'atmosphère de Pluton

Dans la première partie de ma thèse de Doctorat (Chapitre III), en utilisant le dispositif expérimental PAMPRE, j'ai reproduit la chimie atmosphérique de Pluton conduisant à la formation des aérosols photochimiques. Deux mélanges gazeux caractérisés par différentes proportions N_2:CH_4:CO ont été étudiés, afin de tenir compte de la variabilité en termes de composition chimique de l'atmosphère de Pluton à différentes altitudes, comme cela a été observé en 2015 lors du survol de Pluton par *New Horizons*. Le mélange gazeux A_{400} (N_2:CH_4:CO = 99%:1%:500ppm) est représentatif des principaux composants présents dans l'atmosphère de Pluton à ~400 km d'altitude, tandis que le mélange gazeux A_{650} (N_2:CH_4:CO = 95%:5%:500ppm) reproduit l'atmosphère de Pluton entre 600 et 700 km d'altitude (Young *et al.*, 2018). Pour étudier la composition chimique de l'atmosphère simulée de Pluton, j'ai utilisé un spectromètre de masse quadripolaire (QMS). Les molécules neutres et les cations formés *in situ* dans l'atmosphère simulée de Pluton ont été analysés, afin de donner un aperçu de la diversité des molécules formées par photochimie dans l'atmosphère de Pluton et déterminer les espèces précurseurs et les voies réactionnelles à l'origine des aérosols de Pluton. Pour identifier les espèces neutres formées dans l'atmosphère de Pluton simulée par PAMPRE, les spectres de masse acquis ont été déconvolués à l'aide d'une méthode Monte-Carlo (Gautier *et al.*, 2020). Les cations formés dans le mélange réactionnel A_{400} ont été comparés à ceux formés dans l'atmosphère simulée de Titan, étudiée par Dubois, Carrasco, Jovanovic *et al.* (2020), afin d'évaluer l'effet du CO sur la chimie des ions positifs d'un mélange N_2:CH_4.

Les résultats obtenus par QMS concernant les molécules neutres formées dans l'atmosphère simulée de Pluton ont montré la formation significative de molécules organiques azotées et/ou oxygénées, jusqu'à *m/z* 91. Les composés azotés détectés correspondent à des molécules comportant des groupes fonctionnels amine –NH et $–NH_2$, ou nitrile –C≡N. Nous avons également détecté des hétérocycles azotés, tels que des structures de type triazine, pyrazole et pyrrole. Les composés porteurs d'oxygène correspondent essentiellement à des molécules avec

un groupe fonctionnel oxygéné terminal, incluant des alcools –OH, des acides carboxyliques –COOH et des carbonyles –C=O (Figure H).

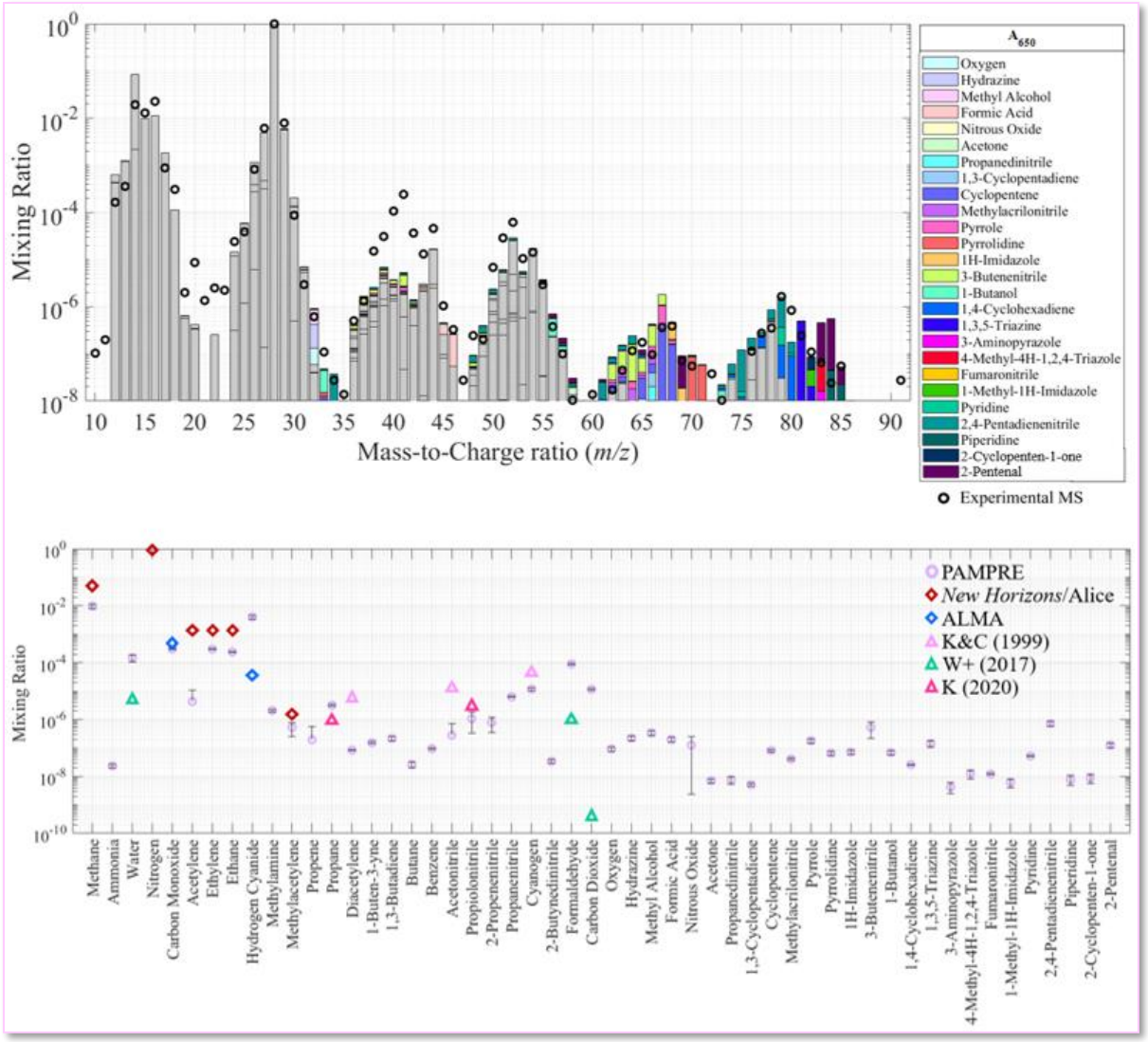

Figure H : Résultats de la déconvolution du spectre de masse des molécules neutres formées dans l'atmosphère simulée de Pluton A_{650}. *En haut* : Top 5 % des résultats de la déconvolution du spectre de masse. Les cercles noirs correspondent au spectre de masse expérimental, tandis que les barres colorées correspondent à la contribution calculée par le code de déconvolution pour les différentes molécules. *En bas* : Comparaison des résultats expérimentaux avec les observations de Pluton et les prédictions issues de modèles photochimiques.

Mes simulations en laboratoire de l'atmosphère de Pluton ont confirmé la formation de dioxyde de carbone (CO_2) et de formaldéhyde (H_2CO) en phase gazeuse prédite par Wong *et al.* (2017). Néanmoins, je n'ai pu conclure ni sur la formation d'eau (H_2O) prédite par Wong *et al.* (2017), ni sur la formation de dioxygène (O_2) questionnée par Kammer *et al.* (2017).

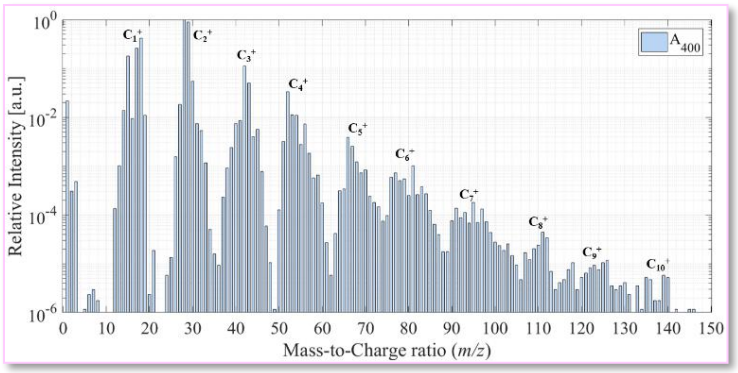

Figure I : Cations formés dans l'atmosphère simulée de Pluton A_{400}.

Concernant les cations formés dans l'atmosphère simulée de Pluton, j'ai observé la production d'une grande variété d'ions positifs, jusqu'à *m/z* 150 (Figure I), malgré l'absence de détection d'une ionosphère autour de Pluton (Hinson *et al.*, 2018). Parmi ces cations, nous comptons non seulement des ions organiques azotés, mais aussi des ions oxygénés.

L'analyse conjointe des molécules neutres et des cations formés dans l'atmosphère simulée de Pluton a mis en évidence l'importance des réactions ion-molécule en chaîne dans les mécanismes de formation d'espèces de plus en plus lourdes et la formation ultime d'aérosols solides. Parmi les différents mécanismes proposés pour expliquer la croissance moléculaire et la formation d'aérosols dans l'atmosphère de Titan, l'hypothèse que je privilégie dans le cas de Pluton, au vu de mes résultats, concerne la croissance moléculaire par copolymérisation de nitriles, et incorporation de cyanure d'hydrogène HCN dans les molécules. De telles structures hautement insaturées et riches en azote, en constituant le squelette des macromolécules à l'origine des aérosols solides, sont suspectées être responsables d'une forte absorption des radiations, en particulier dans le domaine spectral UV (Rao, 1975), comme discuté dans la troisième partie de ma thèse de Doctorat (Chapitre V).

Ces analyses QMS de l'atmosphère simulée de Pluton ont également mis en évidence l'incomplétude des modèles photochimiques actuels de Pluton (Lara, Ip and Rodrigo, 1997; Krasnopolsky and Cruikshank, 1999; Luspay-Kuti *et al.*, 2017; Wong *et al.*, 2017; Krasnopolsky, 2020), et donc la nécessité d'inclure dans les futurs modèles des voies réactionnelles étendues de la chimie de l'azote, avec un accent particulier sur les nitriles, ainsi que des voies incluant la chimie du CO.

III.2. Concernant la composition chimique des aérosols de Pluton

Dans la deuxième partie de ma thèse de Doctorat (Chapitre IV), j'ai synthétisé des analogues d'aérosols de Pluton sous forme de grains sphériques solides (poudre), en utilisant le dispositif expérimental PAMPRE, à partir de mélanges gazeux comportant différentes proportions de N_2:CH_4:CO, afin de reproduire les aérosols formés à différentes altitudes dans l'atmosphère de Pluton, telle qu'observée en 2015 (Young *et al.*, 2018). L'échantillon P_{400} est représentatif des aérosols se formant à ~400 km d'altitude dans l'atmosphère de Pluton. L'échantillon P_{650} est un analogue des aérosols se formant entre 600 et 700 km d'altitude. Pour déterminer la composition chimique de ces tholins de Pluton, j'ai effectué des analyses par spectroscopie infrarouge (IR) et de la composition élémentaire. Les échantillons ont également été analysés par spectrométrie de masse à haute résolution (HRMS), avec les techniques ESI+/Orbitrap et APPI±/Orbitrap. Afin d'obtenir des informations sur la structure des molécules constituant les tholins, et d'évaluer les implications prébiotiques des aérosols de Pluton, l'échantillon P_{400} a

également été analysé par chromatographie en phase gazeuse couplée à la spectrométrie de masse (GC-MS), après dérivatisation par du DMF-DMA, un agent d'alkylation et de formylation augmentant la volatilité et la stabilité thermique des molécules à analyser.

Les analyses de la composition élémentaire ont montré une incorporation substantielle d'atomes d'azote dans les analogues d'aérosols de Pluton. L'azote représente environ 36 et 45 % en masse des tholins de Pluton P_{650} et P_{400}, respectivement. Grâce au diagnostic dans l'IR moyen, j'ai conclu que les fonctions chimiques porteuses d'azote correspondent essentiellement aux amines primaires et secondaires $–NH_2$ et –NH, aux doubles liaisons C=N de cycles aromatiques et hétéroaromatiques, aux nitriles –C≡N, aux isonitriles –N≡C et aux carbodiimides –N=C=N– (Imanaka *et al.*, 2004; Socrates, 2004; Gautier *et al.*, 2012) (Figure J). Les tholins de Pluton sont également très riches en hétérocycles azotés, tels que des structures de type triazine, pyrazole et pyrazine, détectées par GC-MS (Figure K). De tels hétérocycles azotés ont également été identifiés par QMS parmi les molécules en phase gazeuse produites dans l'atmosphère simulée de Pluton étudiée dans le Chapitre III.

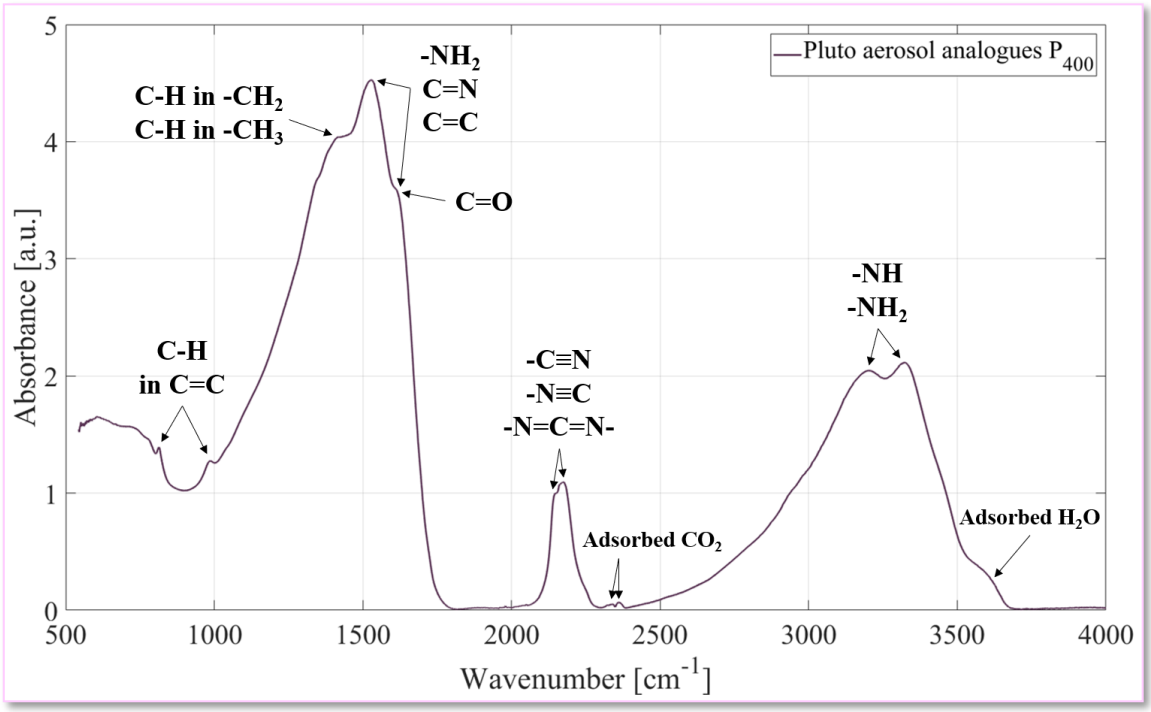

Figure J : Spectre infrarouge des analogues d'aérosols de Pluton P_{400} (échantillon sous forme de poudre).

Les analyses de la composition élémentaire ont également montré une proportion significative de molécules porteuses d'oxygène, formées entre autres par la chimie du CO, avec environ 1,9 et 1,7 % d'oxygène en masse dans les échantillons P_{400} et P_{650}, respectivement. Ainsi, les tholins de Pluton diffèrent des tholins de Titan par l'incorporation d'atomes d'oxygène dans les molécules constituant le matériau solide, via la chimie du CO. Grâce à l'analyse GC-MS, j'ai conclu que les fonctions chimiques porteuses d'oxygène correspondent essentiellement à des groupes fonctionnels carbonyles –C=O, alcools –OH, éthers *R*–O–*R'*, et carboxyles –COOH terminaux. Cependant, aucun hétérocycle oxygéné, tel que des structures de type furane, pyrane ou pyrone, n'a été détecté (Figure K).

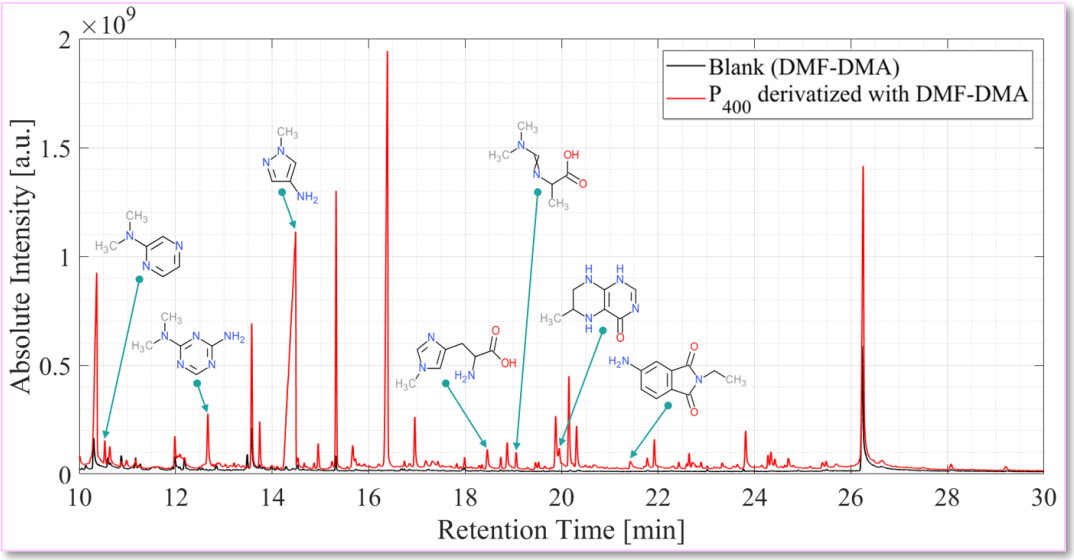

Figure K : Chromatogramme des analogues d'aérosols de Pluton P_{400} (échantillon sous forme de poudre), dérivatisés par du DMF-DMA.

J'ai noté une influence du pourcentage de méthane – et donc de l'altitude de formation des aérosols sur Pluton – sur la composition chimique des aérosols. Des proportions N_2:CH_4:CO différentes affectent fortement les teneurs en azote et en oxygène des aérosols. En particulier, j'ai montré que les aérosols produits à basses altitudes (échantillon P_{400}) contiennent plus d'azote et d'oxygène que les aérosols produits à hautes altitudes (échantillon P_{650}).

En combinant tous mes résultats obtenus par HRMS, spectroscopie IR, analyse de la composition élémentaire, et GC-MS, j'ai conclu que la réactivité de N_2 et CO est importante dans la formation et la croissance des aérosols de Pluton. Comme indiqué précédemment, les analogues des aérosols de Pluton sont riches en molécules organiques insaturées portant de l'azote et/ou de l'oxygène. Ces espèces, probablement très réactives, peuvent ainsi faciliter la formation d'autres molécules plus complexes constituant les aérosols. Mes résultats soulignent également ici la nécessité d'inclure des voies réactionnelles étendues impliquant l'azote et l'oxygène dans les futurs modèles photochimiques de Pluton.

III.3. Concernant les indices optiques des aérosols de Pluton

Dans la troisième partie de ma thèse de Doctorat (Chapitre V), j'ai déterminé les indices optiques (indices *n* et *k*, parties réelle et imaginaire de l'indice de réfraction complexe) des tholins de Pluton déposés sous forme de films minces sur des substrats de silicium, et j'ai étudié l'effet de ces propriétés sur l'atmosphère et la surface de Pluton. Trois types d'analogues ont été synthétisés à partir de mélanges gazeux présentant différentes proportions N_2:CH_4:CO, afin de reproduire les aérosols formés à différentes altitudes dans l'atmosphère actuelle de Pluton. En plus des échantillons F_{400} et F_{650}, j'ai également synthétisé un échantillon dans un mélange gazeux réactif N_2:CH_4:CO = 99,5%:0,5%:500ppm. Cet échantillon nommé F_H est représentatif des aérosols formés en-dessous de 350 km d'altitude au-dessus de la surface de Pluton (Young *et al.*, 2018). Ces trois mélanges gazeux qui diffèrent par leur rapport de mélange du méthane peuvent également être considérés comme des analogues de l'atmosphère de Pluton à différentes saisons ou époques (Bertrand and Forget, 2016; Stern, Binzel, *et al.*, 2017; Bertrand

et al., 2019). Les indices optiques des tholins de Pluton ont été déterminés de l'UV au proche IR par ellipsométrie spectroscopique, avec deux méthodes d'inversion, un modèle de Tauc-Lorentz modifié et une inversion numérique « longueur d'onde par longueur d'onde ».

La caractérisation des indices *n* et *k* a montré une forte absorption des radiations dans l'UV et le visible par les tholins de Pluton (Figure L), attribuée à leurs molécules organiques porteuses d'azote et d'oxygène, qui ont été détectées et sont discutées dans le Chapitre IV. L'absorption dans le domaine spectral proche-IR par les tholins de Pluton s'est avérée plus modérée, avec des indices *k* de quelques 10^{-3} (Figure L).

J'ai noté une dépendance des indices *n* et *k* au rapport de mélange du méthane, et donc à l'altitude de formation des aérosols dans l'atmosphère de Pluton (Figure L). La teneur en azote et en oxygène dans les aérosols de Pluton formés à basses altitudes étant augmentée (comme discuté dans le Chapitre IV), cela conduit à une augmentation des valeurs de *n* et de *k*. Cette dépendance des indices optiques au rapport de mélange de CH_4 a également des implications dans le transfert radiatif atmosphérique saisonnier et le paléoclimat de Pluton.

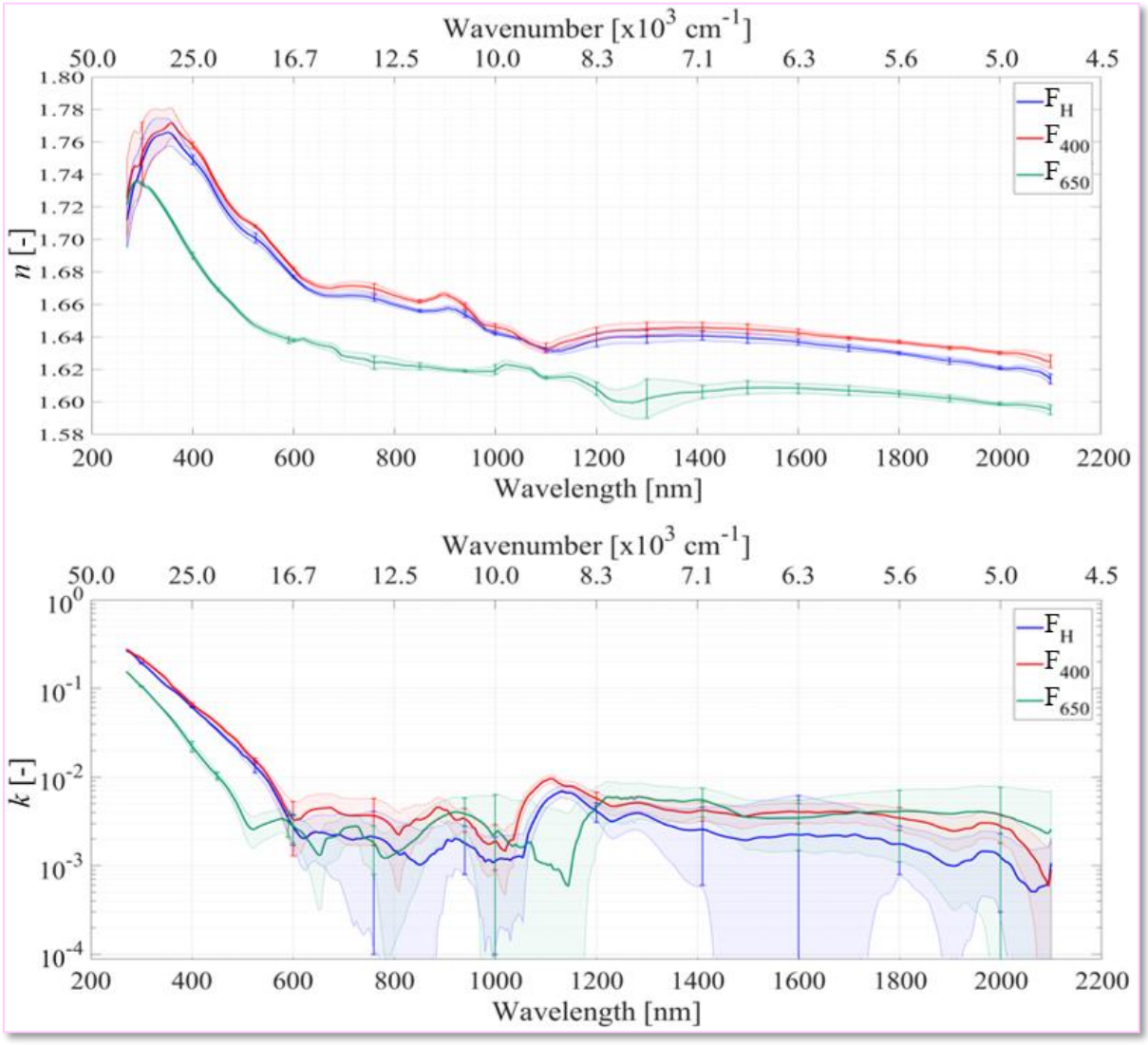

Figure L : Parties réelle *n* (*en haut*) et imaginaire *k* (*en bas*) de l'indice de réfraction complexe des tholins de Pluton F_H (en bleu), F_{400} (en rouge) et F_{650} (en vert) (échantillons sous forme de films minces).

La comparaison de mes données Pluton avec les indices optiques déterminés pour les tholins de Titan par Khare *et al.* (1984) a montré que les tholins de Pluton présentent des indices *n* globalement similaires à ceux de Titan. Cependant, des différences ont été observées quant aux indices *k*. En particulier, les indices *k* des tholins de Pluton sont d'un ordre de grandeur plus élevés que ceux de Titan dans le proche IR. Dans le domaine spectral UV, les indices *k* des tholins de Pluton sont également plus élevés, ce qui est probablement dû à la réactivité du diazote et du monoxyde de carbone dans le mélange gazeux réactionnel produisant les aérosols de Pluton.

Les propriétés optiques des tholins dépendent de leur composition chimique, et en particulier de leur contenu en azote et en oxygène. Comme les tholins de Pluton ont une composition différente de celle des tholins de Titan (comme discuté dans le Chapitre IV), j'ai proposé les indices optiques déterminés pendant mon Doctorat comme nouveaux paramètres d'entrée entre 270 et 2100 nm pour modéliser l'atmosphère et les propriétés de surface de Pluton.

Mes indices optiques des tholins de Pluton ont été utilisés par Silvia Protopapa comme paramètres d'entrée dans son modèle de surface de Pluton. Les résultats de la modélisation ont montré l'adéquation de ces indices optiques pour reproduire les observations de la composition de la surface de Pluton par les instruments MVIC et LEISA, au moins dans les domaines spectraux UV et visible (Figure M). Ces indices optiques ont également été implémentés par Tanguy Bertrand et Pascal Rannou dans un modèle de diffusion atmosphérique de la lumière. Ces résultats ont montré que les tholins de Pluton absorbent 5 à 10 fois moins que les tholins de Titan à 500 nm, cette absorption plus faible étant cohérente avec les observations de la brume de Pluton faites par l'instrument Alice (Figure M).

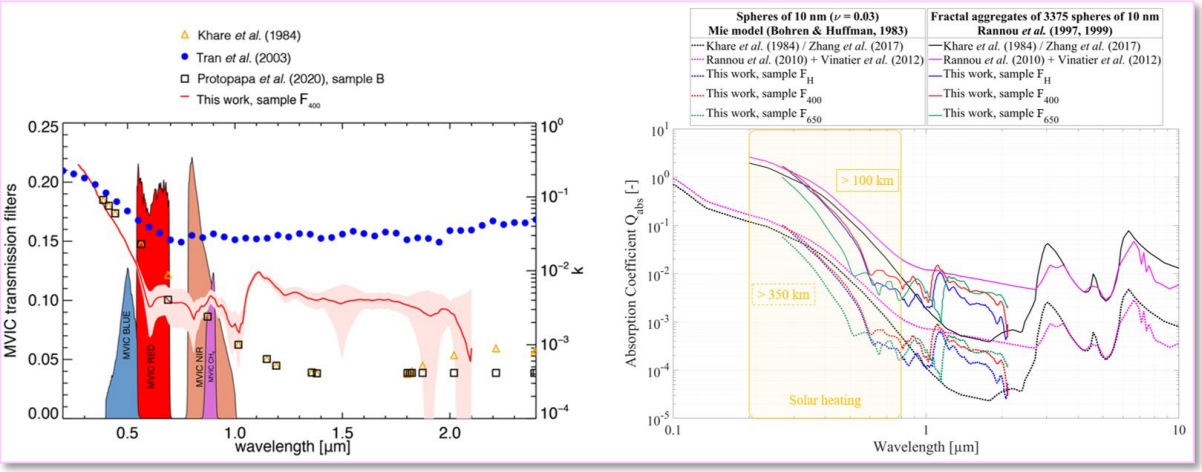

Figure M : Modélisation de la surface (*à gauche*) et de l'atmosphère (*à droite*) de Pluton, en utilisant les indices optiques présentés dans cette thèse de Doctorat.

III.4. Concernant la matière organique à la surface de Pluton

Enfin, dans la quatrième partie de ma thèse de Doctorat (Chapitre VI), j'ai d'abord discuté de l'aptitude des tholins de Pluton à reproduire les observations de la région équatoriale sombre de Pluton, appelée Cthulhu, et ensuite, j'ai étudié l'effet de l'irradiation par les rayons cosmiques galactiques (GCR) sur la matière organique à la surface de Pluton.

J'ai été impliquée dans une étude dont l'objectif était d'expliquer l'origine et la composition de la région Cthulhu : Fayolle, Quirico, Schmitt, Jovanovic *et al.* (2021). Dans cette étude, des mesures en réflectance ont été effectuées en laboratoire pour tester l'aptitude de mes tholins de Pluton P_{400} et P_{650} à reproduire les spectres en réflectance de la région Cthulhu, collectés par *New Horizons* à la fois dans le domaine spectral visible et dans le proche IR par les instruments MVIC et LEISA. À partir des spectres en réflectance obtenus en laboratoire et de la comparaison directe avec les données de *New Horizons*, nous avons conclu que les tholins de Pluton, et en particulier l'échantillon P_{400}, reproduisent assez bien le niveau photométrique de la surface de Pluton dans le proche IR, mais que la pente dans la gamme spectrale rouge des tholins de Pluton ne correspond pas à celle de la surface de Pluton. De plus, les tholins de Pluton fraîchement synthétisés sont caractérisés par de fortes bandes d'absorption qui ne sont pas retrouvées dans les spectres de *New Horizons*. Pour expliquer ces divergences, nous avons proposé plusieurs hypothèses, les deux plus probables étant une forte porosité des terrains sombres de la région Cthulhu, et l'irradiation par les rayons cosmiques galactiques (GCR) de la matière organique déposée en surface.

Pour soutenir l'hypothèse de l'irradiation par les GCR à la surface de Pluton, j'ai synthétisé des tholins de Pluton sous forme de grains solides sphériques (échantillon P_P) et de films minces (échantillon F_P) à partir d'un mélange gazeux N_2:CH_4:CO = 99%:1%:500ppm. Ces tholins ont été soumis à une irradiation par des ions lourds ^{136}Xe à 75 MeV au GANIL/IRRSUD et plusieurs analyses *in situ* et *ex situ* ont été effectuées. De telles énergies correspondent à la partie haute énergie du flux de GCR atteignant la surface de Pluton. Des analyses *ex situ* par microscopie électronique à balayage (MEB) ont été réalisées pour étudier l'évolution morphologique des tholins de Pluton soumis à une irradiation par des ions lourds. Des analyses spectroscopiques *in situ* dans les domaines spectraux du visible et de l'infrarouge moyen ont été réalisées pour étudier l'évolution des propriétés optiques et de la composition chimique des tholins de Pluton sous irradiation par des ions lourds. Des analyses *ex situ* par spectrométrie de masse à résonance cyclotronique ionique et à transformée de Fourier (FT-ICR) ont été effectuées pour mieux comprendre l'évolution de la composition moléculaire des tholins de Pluton après irradiation par des ions lourds. Enfin, des mesures *in situ* par QMS ont fourni un aperçu des molécules gazeuses relarguées par les tholins de Pluton sous irradiation par des ions lourds.

Les observations MEB ont mis en évidence un changement micro-structurel des tholins de Pluton P_P soumis à une irradiation par des ions lourds (Figure N, images A, B, et C), affectant l'aspect macro-morphologique observé à l'œil nu. Par effet de pulvérisation, les tholins de Pluton irradiés présentent des zones hétérogènes, avec des agrégats compacts entourés de zones dépourvues de tholins (Figure N, image D). J'ai suggéré que l'irradiation GCR pourrait affecter la porosité de la matière organique déposée à la surface, dans la région Cthulhu.

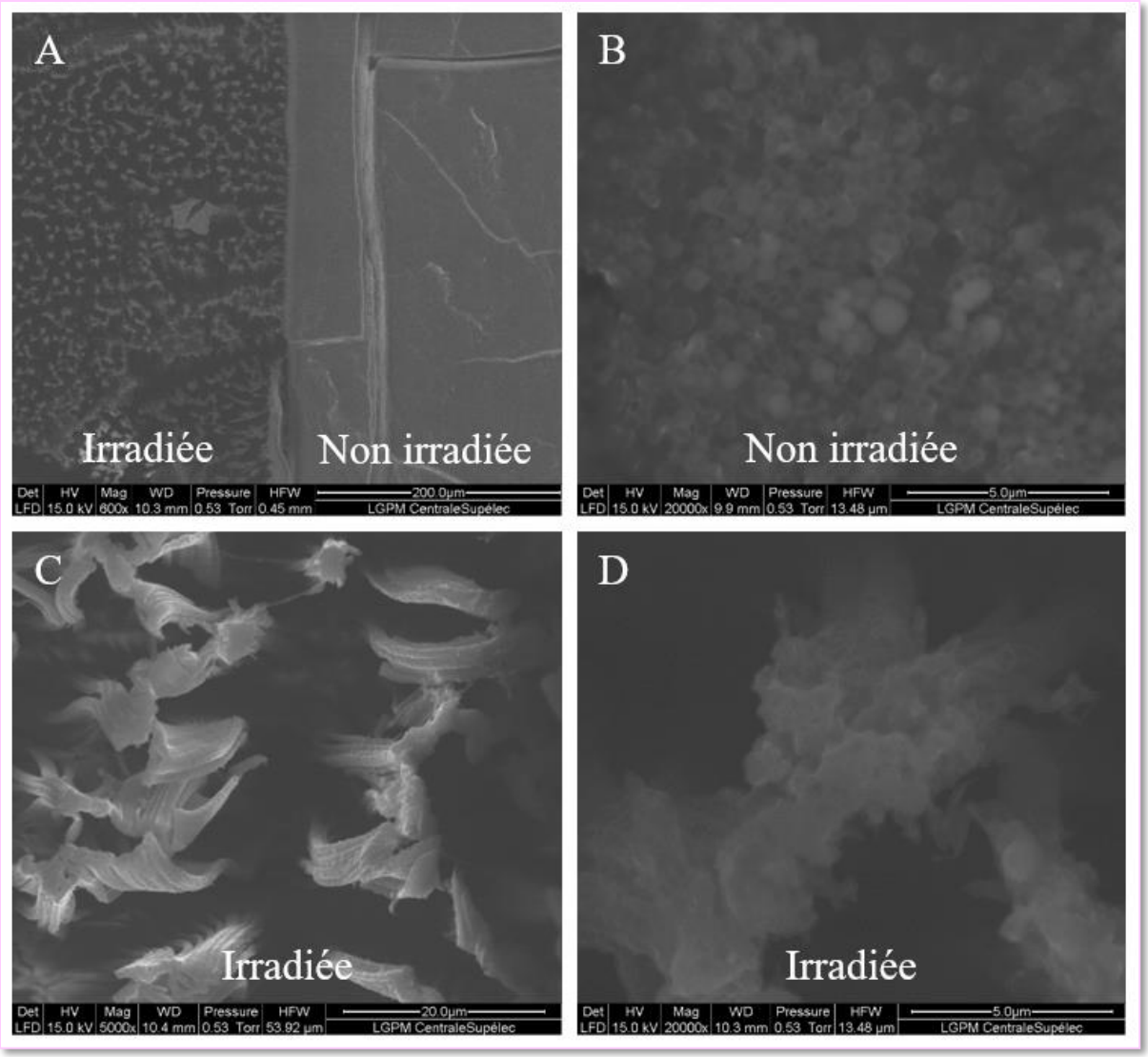

Figure N : Images MEB des parties non irradiée et irradiée d'une pastille réalisée à partir de tholins de Pluton P_P sous forme de poudre, dont la moitié de la surface a été soumise à l'irradiation par des ions lourds ^{136}Xe.

Dans le domaine des longueurs d'onde visibles, les mesures spectroscopiques ont montré que l'irradiation par des ions lourds entraîne une diminution de l'absorbance des tholins de Pluton F_P, et un probable rougissement du matériau (Figure O, spectre du haut). En ce qui concerne le domaine spectral de l'infrarouge moyen, nous avons remarqué après une irradiation par des ions lourds une diminution globale de l'intensité de toutes les bandes d'absorption fondamentales caractéristiques des tholins de Pluton F_P (Figure O, spectre du bas), affectant également probablement les harmoniques situées dans le proche infrarouge. Cette diminution est due à la fois aux effets de la pulvérisation et de la radiolyse.

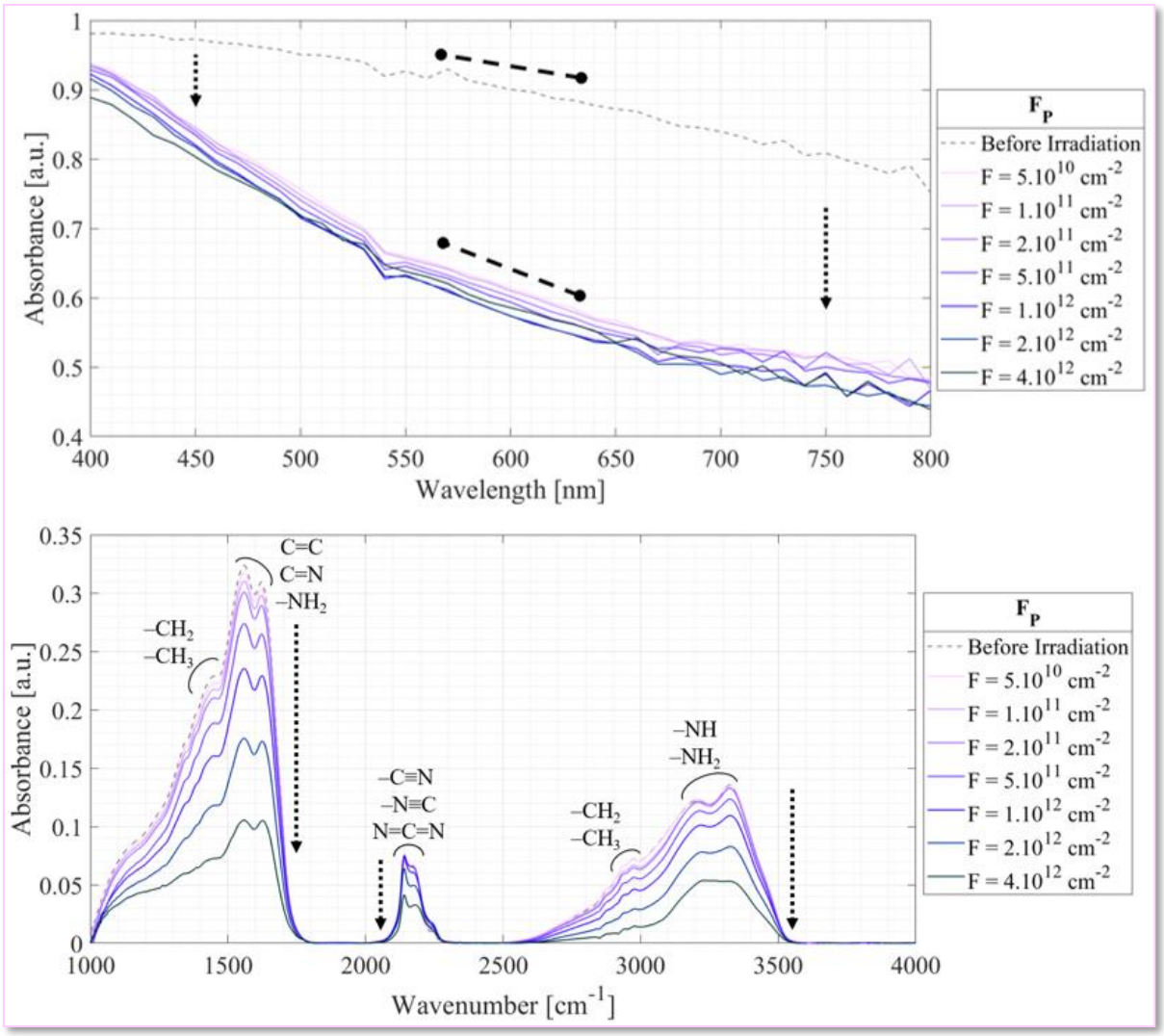

Figure O : Évolution spectrale des tholins de Pluton F_P (échantillon sous forme de film mince) soumis à l'irradiation par des ions lourds ^{136}Xe, à différentes fluences F. *En haut* : Dans le visible. *En bas* : Dans l'infrarouge moyen.

Ces observations – diminution de l'absorbance dans le visible, rougissement de la matière, et diminution des bandes d'absorption dans l'infrarouge moyen – confortent l'hypothèse que l'irradiation de la matière organique à la surface de Pluton par les GCR pourrait expliquer les différences entre les spectres de la surface de Pluton et les spectres en réflectance des tholins de Pluton fraîchement synthétisés.

La formation de nouvelles molécules après l'irradiation des tholins de Pluton P_P par des ions lourds a été mise en évidence par les analyses FT-ICR. Ces molécules filles sont caractérisées par des rapports H/C et N/C inférieurs à 0,5, et le calcul de leur nombre d'insaturation est cohérent avec des hydrocarbures poly-aromatiques insaturés et des hydrocarbures poly-aromatiques porteurs d'azote. Ces molécules sont également riches en atomes d'oxygène, suggérant la formation d'hydrocarbures poly-aromatiques contenant de l'oxygène après irradiation par des ions lourds.

L'analyse QMS a révélé que les tholins de Pluton F_P soumis à une irradiation par des ions lourds relarguent des molécules en phase gazeuse jusqu'à *m/z* 52. Ces molécules correspondent notamment à des hydrocarbures insaturés, et des molécules portant des groupes fonctionnels nitrile, isonitrile ou carbodiimide. Parmi les molécules insaturées relarguées, les plus abondantes sont l'acétylène C_2H_2 et le cyanure d'hydrogène HCN (Figure P).

Ces résultats suggèrent que l'irradiation de la surface de Pluton par les GCR pourrait éjecter des molécules supplémentaires depuis la surface, et ces molécules pourraient être retenues dans l'atmosphère de Pluton et participer à la formation d'aérosols photochimiques plus complexes.

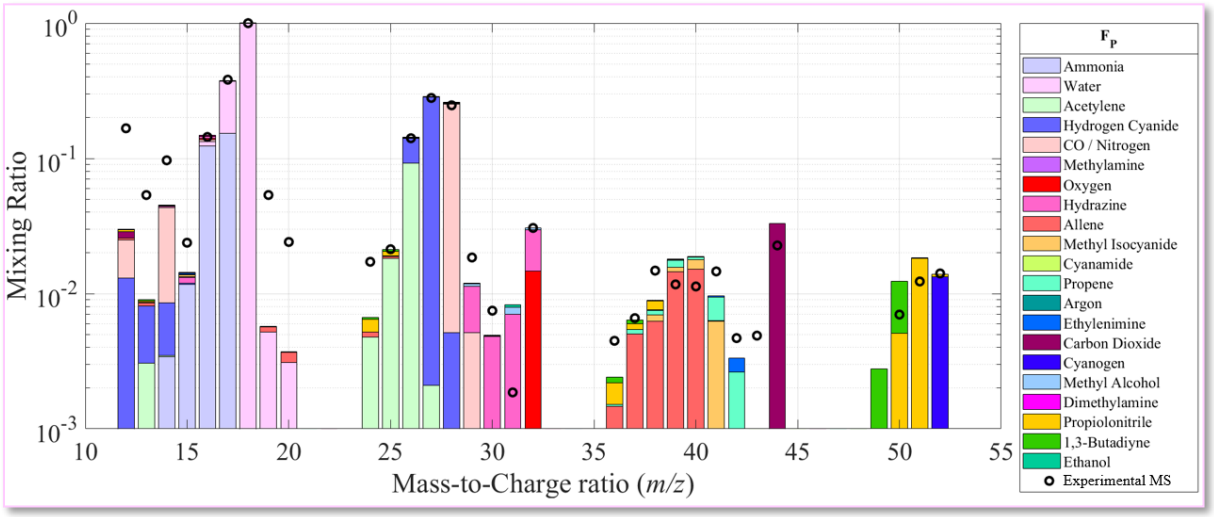

Figure P *:* Résultats de la déconvolution du spectre de masse des molécules relarguées par les tholins de Pluton F_P soumis à l'irradiation par des ions lourds ^{136}Xe. Les cercles noirs correspondent au spectre de masse expérimental, tandis que les barres colorées correspondent à la contribution calculée par le code de déconvolution pour les différentes molécules.

Références bibliographiques

Alcouffe, G. *et al.* (2010) 'Capacitively coupled plasma used to simulate Titan's atmospheric chemistry', *Plasma Sources Science and Technology*, 19(1), p. 15008. doi: 10.1088/0963-0252/19/1/015008.

Augé, B. *et al.* (2018) 'IGLIAS: A new experimental set-up for low temperature irradiation studies at large irradiation facilities', *Review of Scientific Instruments*. American Institute of Physics, 89(7), p. 75105. doi: 10.1063/1.5028056.

Bertrand, T. *et al.* (2019) 'The CH4 cycles on Pluto over seasonal and astronomical timescales', *Icarus*, 329, pp. 148–165. doi: https://doi.org/10.1016/j.icarus.2019.02.007.

Bertrand, T. and Forget, F. (2016) 'Observed glacier and volatile distribution on Pluto from atmosphere–topography processes', *Nature*, 540, p. 86. Available at: https://doi.org/10.1038/nature19337.

Cheng, A. F. *et al.* (2017) 'Haze in Pluto's atmosphere', *Icarus*, 290, pp. 112–133. doi: https://doi.org/10.1016/j.icarus.2017.02.024.

Christy, J. W. and Harrington, R. S. (1978) 'The Satellite of Pluto', *The Astronomical Journal*, 83(8), pp. 1005–1008.

Christy, J. W. and Harrington, R. S. (1980) 'The Discovery and Orbit of Charon', *Icarus*, 44(1), pp. 38–40. doi: 10.1016/0019-1035(80)90051-2.

Cook, J. C. *et al.* (2019) 'The distribution of H2O, CH3OH, and hydrocarbon-ices on Pluto: Analysis of New Horizons spectral images', *Icarus*, 331, pp. 148–169. doi: 10.1016/j.icarus.2018.09.012.

Cruikshank, D. P. *et al.* (2015) 'The surface compositions of Pluto and Charon', *Icarus*, 246, pp. 82–92. doi: https://doi.org/10.1016/j.icarus.2014.05.023.

Dubois, D. *et al.* (2020) 'Positive ion chemistry in an N2-CH4 plasma discharge: Key precursors to the growth of Titan tholins', *Icarus*, 338, p. 113437. doi: https://doi.org/10.1016/j.icarus.2019.113437.

Elliot, J. L. *et al.* (1989) 'Pluto's atmosphere', *Icarus*, 77(1), pp. 148–170. doi: https://doi.org/10.1016/0019-1035(89)90014-6.

Fayolle, M. *et al.* (2021) 'Testing tholins as analogues of the dark reddish material covering Pluto's Cthulhu region', *Icarus*.

Forget, F. *et al.* (2017) 'A post-New Horizons global climate model of Pluto including the N2, CH4 and CO cycles', *Icarus*, 287, pp. 54–71. doi: https://doi.org/10.1016/j.icarus.2016.11.038.

Gao, P. *et al.* (2017) 'Constraints on the microphysics of Pluto's photochemical haze from New Horizons observations', *Icarus*, 287, pp. 116–123. doi: https://doi.org/10.1016/j.icarus.2016.09.030.

Gautier, T. *et al.* (2012) 'Mid- and far-infrared absorption spectroscopy of Titan's aerosols analogues', *Icarus*, 221(1), pp. 320–327. doi: https://doi.org/10.1016/j.icarus.2012.07.025.

Gautier, T. *et al.* (2020) 'Decomposition of electron ionization mass spectra for space application using a Monte-Carlo approach', *Rapid Communications in Mass Spectrometry*, 34(8), p. e8684. doi: 10.1002/rcm.8684.

Gladstone, G. R. *et al.* (2016) 'The atmosphere of Pluto as observed by New Horizons', *Science*, 351(6279). Available at: http://science.sciencemag.org/content/351/6279/aad8866.abstract.

Gladstone, G. R., Pryor, W. R. and Stern, S. A. (2015) 'Lyα@Pluto', *Icarus*, 246, pp. 279–284. doi: https://doi.org/10.1016/j.icarus.2014.04.016.

Gladstone, G. R. and Young, L. A. (2019) 'New Horizons Observations of the Atmosphere of Pluto', *Annual Review of Earth and Planetary Sciences*, 47(1), pp. 119–140. doi: 10.1146/annurev-earth-053018-060128.

Grundy, W. M. *et al.* (2016) 'Surface compositions across Pluto and Charon', *Science*, 351(6279). Available at: http://science.sciencemag.org/content/351/6279/aad9189.abstract.

Grundy, W. M. *et al.* (2018) 'Pluto's haze as a surface material', *Icarus*, 314, pp. 232–245. doi: https://doi.org/10.1016/j.icarus.2018.05.019.

Hinson, D. P. *et al.* (2017) 'Radio occultation measurements of Pluto's neutral atmosphere with New Horizons', *Icarus*, 290, pp. 96–111. doi: https://doi.org/10.1016/j.icarus.2017.02.031.

Hinson, D. P. *et al.* (2018) 'An upper limit on Pluto's ionosphere from radio occultation measurements with New Horizons', *Icarus*, 307, pp. 17–24. doi: https://doi.org/10.1016/j.icarus.2018.02.011.

Hubbard, W. B. *et al.* (1988) 'Occultation evidence for an atmosphere on Pluto', *Nature*, 336, p. 452. Available at: http://dx.doi.org/10.1038/336452a0.

Imanaka, H. *et al.* (2004) 'Laboratory experiments of Titan tholin formed in cold plasma at various pressures: Implications for nitrogen-containing polycyclic aromatic compounds in Titan haze', *Icarus*, 168(2), pp. 344–366. doi: https://doi.org/10.1016/j.icarus.2003.12.014.

International Astronomical Union (2006) '(134340) Pluto, (136199) Eris, and (136199) Eris I (Dysnomia)', *International Astronomical Union*, 8747.

Kammer, J. A. *et al.* (2017) 'New Horizons Upper Limits on O2 in Pluto's Present Day Atmosphere', *The Astronomical Journal*, 154(2), p. 55. doi: 10.3847/1538-3881/aa78a7.

Khare, B. N. *et al.* (1984) 'Optical constants of organic tholins produced in a simulated Titanian atmosphere: From soft X-ray to microwave frequencies', *Icarus*, 60(1), pp. 127–137. doi: https://doi.org/10.1016/0019-1035(84)90142-8.

Krasnopolsky, V. A. (2018) 'Some problems in interpretation of the New Horizons observations of Pluto's atmosphere', *Icarus*, 301, pp. 152–154. doi: https://doi.org/10.1016/j.icarus.2017.08.021.

Krasnopolsky, V. A. (2020) 'A photochemical model of Pluto's atmosphere and ionosphere', *Icarus*, 335, p. 113374. doi: https://doi.org/10.1016/j.icarus.2019.07.008.

Krasnopolsky, V. A. and Cruikshank, D. P. (1999) 'Photochemistry of Pluto's atmosphere and ionosphere near perihelion', *Journal of Geophysical Research: Planets*, 104(E9), pp. 21979–21996. doi: 10.1029/1999JE001038.

Lara, L. M., Ip, W. and Rodrigo, R. (1997) 'Photochemical Models of Pluto's Atmosphere', *Icarus*, 130(1), pp. 16–35. doi: https://doi.org/10.1006/icar.1997.5798.

Lavvas, P. *et al.* (2016) 'Photochemical aerosol formation in planetary atmospheres: A comparison between Pluto and Titan', in *AAS/Division for Planetary Sciences Meeting Abstracts #48*, p. 224.06. Available at: https://ui.adsabs.harvard.edu/abs/2016DPS....4822406L.

Lavvas, P. *et al.* (2020) 'A major ice component in Pluto's haze', *Nature Astronomy*. doi: 10.1038/s41550-020-01270-3.

Lellouch, E. (1994) 'The Thermal Structure of Pluto's Atmosphere: Clear vs. Hazy Models', *Icarus*, 108(2), pp. 255–264. doi: https://doi.org/10.1006/icar.1994.1060.

Lellouch, E. *et al.* (2017) 'Detection of CO and HCN in Pluto's atmosphere with ALMA', *Icarus*, 286, pp. 289–307. doi: https://doi.org/10.1016/j.icarus.2016.10.013.

Leonard, F. C. (1930) 'The New Planet Pluto', *Leaflet of the Astronomical Society of the Pacific*, 1, pp. 121–124.

Luspay-Kuti, A. *et al.* (2017) 'Photochemistry on Pluto: Part I. Hydrocarbons and aerosols', *Monthly Notices of the Royal Astronomical Society*, 472(1), pp. 104–117. doi: 10.1093/mnras/stx1362.

Mandt, K. E. *et al.* (2017) 'Photochemistry on Pluto: Part II. HCN and nitrogen isotope fractionation',

Monthly Notices of the Royal Astronomical Society, 472(1), pp. 118–128. doi: 10.1093/mnras/stx1587.

Owen, T. C. *et al.* (1993) 'Surface Ices and the Atmospheric Composition of Pluto', *Science*, 261(5122), pp. 745 LP – 748. Available at: http://science.sciencemag.org/content/261/5122/745.abstract.

Protopapa, S. *et al.* (2017) 'Pluto's global surface composition through pixel-by-pixel Hapke modeling of New Horizons Ralph/LEISA data', *Icarus*, 287, pp. 218–228. doi: https://doi.org/10.1016/j.icarus.2016.11.028.

Protopapa, S. *et al.* (2020) 'Disk-resolved Photometric Properties of Pluto and the Coloring Materials across its Surface', *The Astronomical Journal*, 159(2), p. 74. doi: 10.3847/1538-3881/ab5e82.

Rao, C. N. R. (1975) 'Ultra-violet and visible spectroscopy'. Butterworth.

Schmitt, B. *et al.* (2017) 'Physical state and distribution of materials at the surface of Pluto from New Horizons LEISA imaging spectrometer', *Icarus*, 287, pp. 229–260. doi: https://doi.org/10.1016/j.icarus.2016.12.025.

Sekine, Y. *et al.* (2017) 'The Charon-forming giant impact as a source of Pluto's dark equatorial regions', *Nature Astronomy*, 1(0031), pp. 1–6. doi: 10.1038/s41550-016-0031.

Showalter, M. R. *et al.* (2011) 'New Satellite of (134340) Pluto: S/2011 (134340) 1', *International Astronomical Union*, 2769(1), p. 1.

Showalter, M. R. *et al.* (2012) 'New Satellite of (134340) Pluto: S/2012 (134340) 1', *International Astronomical Union*, 9253(1), p. 1.

Socrates, G. (2004) *Infrared and Raman Characteristic Group Frequencies: Tables and Charts*. John Wiley & Sons, Ltd. doi: 10.1016/0003-2670(94)80274-2.

Stansberry, J. A., Lunine, J. I. and Tomasko, M. G. (1989) 'Upper limits on possible photochemical hazes on Pluto', *Geophysical Research Letters*, 16(11), pp. 1221–1224. doi: 10.1029/GL016i011p01221.

Steffl, A. J. *et al.* (2020) 'Pluto's Ultraviolet Spectrum, Surface Reflectance, and Airglow Emissions', *Astrophysical Journal*.

Stern, S. A. *et al.* (2015) 'The Pluto system: Initial results from its exploration by New Horizons', *Science*, 350(6258). Available at: http://science.sciencemag.org/content/350/6258/aad1815.abstract.

Stern, S. A. *et al.* (2017) 'Past epochs of significantly higher pressure atmospheres on Pluto', *Icarus*, 287, pp. 47–53. doi: https://doi.org/10.1016/j.icarus.2016.11.022.

Stern, S. A. *et al.* (2018) 'The Pluto System After New Horizons', *Annual Review of Astronomy and Astrophysics*, 56(1), pp. 357–392. doi: 10.1146/annurev-astro-081817-051935.

Strobel, D. F. and Zhu, X. (2017) 'Comparative planetary nitrogen atmospheres: Density and thermal structures of Pluto and Triton', *Icarus*, 291, pp. 55–64. doi: https://doi.org/10.1016/j.icarus.2017.03.013.

Szopa, C. *et al.* (2006) 'PAMPRE: A dusty plasma experiment for Titan's tholins production and study', *Planetary and Space Science*, 54(4), pp. 394–404. doi: https://doi.org/10.1016/j.pss.2005.12.012.

Weaver, H. A. *et al.* (2006) 'Discovery of two new satellites of Pluto', *Nature*, 439(7079), pp. 943–945. doi: 10.1038/nature04547.

Wong, M. L. *et al.* (2017) 'The photochemistry of Pluto's atmosphere as illuminated by New Horizons', *Icarus*, 287, pp. 110–115. doi: https://doi.org/10.1016/j.icarus.2016.09.028.

Young, L. A. *et al.* (2018) 'Structure and composition of Pluto's atmosphere from the New Horizons solar ultraviolet occultation', *Icarus*, 300, pp. 174–199. doi: https://doi.org/10.1016/j.icarus.2017.09.006.

Zhang, X., Strobel, D. F. and Imanaka, H. (2017) ‘Haze heats Pluto’s atmosphere yet explains its cold temperature’, *Nature*, 551, p. 352. Available at: https://doi.org/10.1038/nature24465.

Zhu, X., Strobel, D. F. and Erwin, J. T. (2014) ‘The density and thermal structure of Pluto’s atmosphere and associated escape processes and rates’, *Icarus*, 228, pp. 301–314. doi: https://doi.org/10.1016/j.icarus.2013.10.011.

I. Pluto and laboratory simulations of planetary atmospheres

I.1. Historical background

I.1.1. Discovery of the Pluto system

Pluto was discovered on February 18th, 1930 by Clyde William Tombaugh (1906-1997), an American amateur astronomer (Figure I.1) searching for the "Planet X" predicted by Percival Lowell (1855-1916) and supposed to disturb the orbits of Uranus and Neptune (Leonard, 1930).

Figure I.1: Clyde W. Tombaugh, the amateur astronomer who discovered Pluto in 1930 at the Lowell Observatory. *Credit*: Lowell Observatory.

At the Lowell Observatory (Flagstaff, Arizona, USA, founded by Lowell in 1894), on the nights of January 23rd and 29th, 1930, Tombaugh photographed the sky in the direction of the Gemini constellation, using a 33cm-diameter telescope. On the night of February 18th, these 2 cm^2 photographic plates were compared using a blink comparator. The stars being fixed in the sky, the luminous point which moved by 3 mm on the photographs (see Figure I.2) could only correspond for Tombaugh to the ninth planet of the Solar System, whose discovery was so much awaited. Note that this point was located at 5° from the position predicted by Lowell for "Planet X" (*e.g.*, Stern, 1992, 2014; Stern and Mitton, 1998; Doressoundiram and Lellouch, 2008; Elkins-Tanton, 2011).

The discovery was announced on March 13th, 1930, after the capture of other photographs confirming the existence of the planet. The name Pluto, suggested by Venetia Burney (an 11-year-old girl), was adopted on March 24th, 1930 for its mythological reference to the Roman God of the Underworld (and not in reference to the dog Pluto from Disney, in fact, the opposite is true) and as a tribute to Percival Lowell whose initials correspond to the first two letters of Pluto (♇ is the astronomical symbol for Pluto) (*e.g.*, Stern, 1992, 2014; Stern and Mitton, 1998; Doressoundiram and Lellouch, 2008; Elkins-Tanton, 2011).

Figure I.2: Discovery of Pluto by comparing two pictures of the sky in direction of the Gemini constellation, taken by Clyde W. Tombaugh on January 23rd (*left*) and 29th (*right*), 1930 at the Lowell Observatory. The white arrows indicate Pluto having moved by 3 mm on the photographic plates measuring 2 cm^2. *Credit*: Lowell Observatory.

It should be noted that much later, in 1993, following the fly-by of Neptune by the *Voyager 2* spacecraft, it was demonstrated that the residual irregularities of the motions of Uranus and Neptune were based on observational errors (Standish, 1993). Less than two years after the serendipitous discovery of penicillin by Alexander Fleming, the fortuitous discovery of Pluto was therefore based on an erroneous hypothesis, and Pluto was not the "Planet X".

On June 22nd, 1978, James Walter Christy examined enlarged images of Pluto acquired during three nights in April and May 1978 with a 155 cm astrometric reflector at the U.S. Naval Observatory (Flagstaff, Arizona, USA). On the pictures of Pluto, Christy noted a protuberance (see the red circle in Figure I.3) appearing periodically, suggesting the presence of a large satellite. The discovery was announced on July 7th, 1978 by the International Astronomical Union (IAU), and the name Charon was adopted, in reference to the Ferryman of the Dead in Greek mythology, and in honor of Christy's wife, Charlene (Christy and Harrington, 1978, 1980).

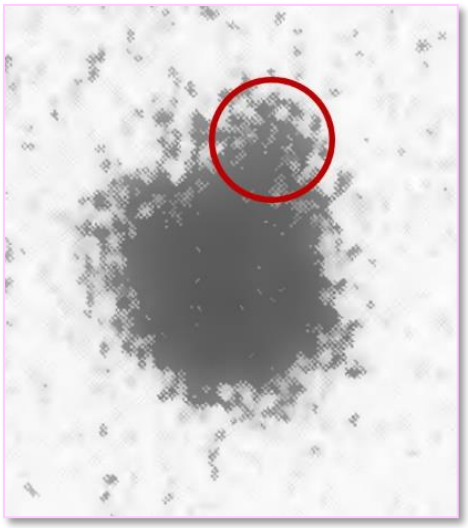

Figure I.3: Magnified picture of Pluto taken by James W. Christy on July 2nd, 1978 at the U.S. Naval Observatory. The red circle corresponds to the periodic protuberance that led to the discovery of Charon. *Credit*: The image is adapted from Christy and Harrington (1978).

Pluto and Charon are in synchronous rotation, with a period of 6.387 Earth days (Andersson and Fix, 1973). In addition, both bodies take the same time to make a circular revolution around a common center of mass, *i.e.*, synchronous revolution of 6.387 Earth days (Christy and Harrington, 1978, 1980; Buie, Tholen and Grundy, 2012). Charon thus always presents the same hemisphere to Pluto, and *vice versa*. Note that, due to Charon's significant mass, the barycenter of their masses lies outside Pluto (and is external to Charon as well). Therefore, we refer to a "binary system", the first one discovered in the Solar System (McKinnon, 1989; Stern, 1992, 2014; Stern and Mitton, 1998; Doressoundiram and Lellouch, 2008; Elkins-Tanton, 2011).

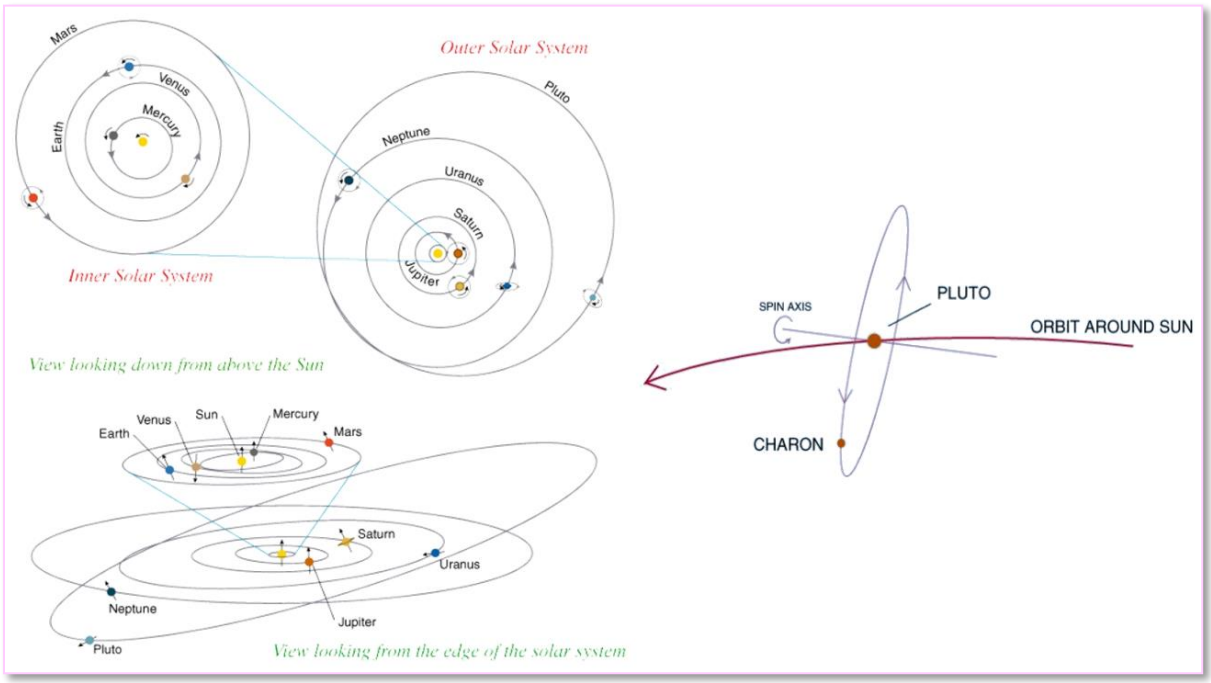

Figure I.4: On the *left*, the elliptical (e_P = 0.2488) and inclined (i_P = 17.16°) orbit of Pluto around the Sun. On the *right*, inclination of the Pluto-Charon binary system with respect to the plane of its orbit around the Sun ($i_{P\text{-}C}$ = 119.59°). *Credit*: The *left* figure is from https://atmos.nmsu.edu/~nchanove/A105S04/lecture_38.html and the *right* figure is from http://abyss.uoregon.edu/~js/ast121/lectures/lec21.html.

The binary system is inclined at 119.59° with respect to the plane of its orbit around the Sun (see Figure I.4.right). Between 1985 and 1990, the plane of the orbit of Charon and Pluto around their common barycenter was aligned with the Earth, allowing astronomers to observe mutual events, or mutual eclipses, *i.e.*, light curves obtained after several passages of Pluto in front and behind Charon (Binzel, 1989; Stern, 1992, 2014; Doressoundiram and Lellouch, 2008). By comparing these light curves, the first accurate radii and densities of the two bodies could be determined, reflectance maps could be drawn, and spectra could be acquired for both bodies to retrieve their surface compositions (*e.g.*, Binzel, 1989).

The other satellites of Pluto (see Figure I.5), smaller and irregularly shaped, were discovered much later, during sessions of *Hubble Space Telescope* (HST) observations. Nix and Hydra were both discovered in 2005 (Weaver *et al.*, 2006), Kerberos in 2011 (Showalter *et al.*, 2011), and Styx in 2012 (Showalter *et al.*, 2012). Their quasi-circular orbits around the Pluto-Charon system barycenter are coplanar, with periods which are approximately integer multiples of Charon's orbital period. For Charon, Styx, Nix, Kerberos, and Hydra respectively, the ratios of their orbital periods are close to 1:3:4:5:6 (Brozović *et al.*, 2015; Showalter and Hamilton, 2015). Styx, Nix, and Hydra are tied together by a three-body resonance (Showalter and Hamilton, 2015).

In total, Pluto has five natural satellites: Charon, Styx, Nix, Kerberos, and Hydra shown in Figure I.5 from the left to the right (not to scale).

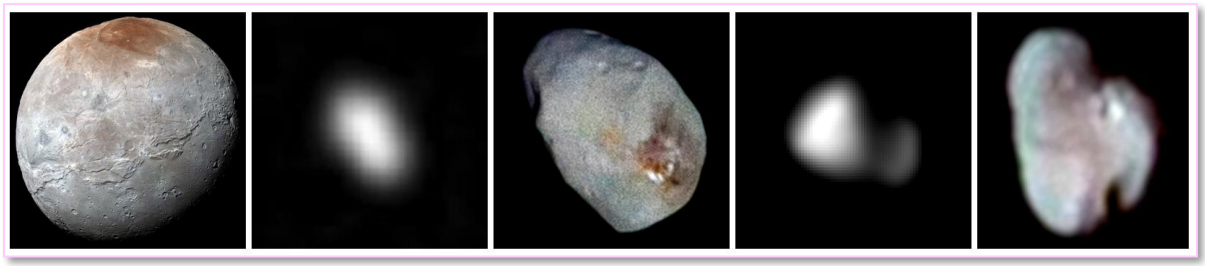

Figure I.5: The five satellites of Pluto, imaged by *New Horizons* during the fly-by of the Pluto system on July 2015. From the *left* to the *right*: Charon, Styx, Nix, Kerberos, and Hydra (not to scale). *Credit*: NASA/JHU-APL/SwRI.

Neither the HST observations, nor those of *New Horizons* allowed to conclude to the presence of an additional satellite or a ring around Pluto (Steffl *et al.*, 2006; Steffl and Stern, 2007; Stern *et al.*, 2015; Lauer *et al.*, 2018).

I.1.2. Orbital and physical parameters of Pluto

The principal orbital and physical parameters of Pluto are reported in Table I.1.

Table I.1: Orbital and physical parameters of Pluto.

Orbital parameters	Pluto
Semi-major axis (a)	39.48 AU (5.91×10^9 km)
Perihelion	29.66 AU (4.44×10^9 km)
Aphelion	49.31 AU (7.38×10^9 km)
Eccentricity (e)	0.2488
Inclination to the ecliptic (i)	17.16°
Obliquity	119.59°
Orbital period	247.688 terrestrial years
Rotation period	6.3872 terrestrial days (retrograde)
Average orbital speed	4.743 $km.s^{-1}$
Physical parameters	**Pluto**
Mean radius	1,188.3 ± 1.6 km
Mass	(1.303 ± 0.003) $\times10^{22}$ kg
Mean density	1,854 ± 11 $kg.m^{-3}$
Surface gravity	0.62 $m.s^{-2}$
Escape velocity	1.2 $km.s^{-1}$
Percent rock by mass	65.5 ± 0.5 %
Oblateness	< 0.6%
Geometric albedo	0.08 to 1
Surface temperature	38.9 ± 2.1 to 51.6 ± 3.8 K
Surface pressure	10.2 ± 0.7 to 12.8 ± 0.7 µbar

Pluto is located more than 30 AU (Astronomical Unit) from the Sun and makes a revolution around the Sun in 247.688 Earth years. Being beyond the orbit of Neptune, it is therefore a Trans-Neptunian Object (TNO), as is the case for all the small bodies of the Kuiper belt (KBO, Kuiper Belt Object). With the discovery of Eris in 2005 (Brown and Schaller, 2005), the IAU decided in 2006 to redefine the notion of “planet”. Pluto being part of a large population of small bodies of smaller or similar sizes, it lost its status of “planet” in favor of that of “dwarf planet” (International Astronomical Union, 2006).

Pluto being inclined at 119.59° with respect to the plane of its orbit (see Figure I.4.right), the rotation around its pole axis is thus done in a retrograde way (*i.e.*, clockwise), in 6.387 Earth days. Also, because of this important obliquity, Pluto presents unusual climate zones characterized by strong seasonal variations in solar illumination *versus* latitude (Earle and

Binzel, 2015), and thus an overlap of tropical and arctic zones (Binzel *et al.*, 2017). On Pluto, the seasons are very marked, with polar nights several Earth-decades long (Binzel *et al.*, 2017). In addition, the strong eccentricity of Pluto's orbit (e = 0.2488, see Figure I.4.left) causes an asymmetry of the seasons, with a northern summer more intense and shorter than the southern summer. At aphelion (49.31 AU), the energy available from sunlight is only ~40% of that available when Pluto is at perihelion (29.66 AU) (Earle and Binzel, 2015). Pluto's obliquity oscillates between ~103° and ~128° and Pluto's eccentricity between 0.222 and 0.266 on million-year timescales (Binzel *et al.*, 2017; Earle *et al.*, 2017), creating Milanković-type insolation cycles influencing Pluto's past climate.

With its radius of 1,188.3 ± 1.6 km (Nimmo *et al.*, 2017), Pluto is smaller than Mercury as well as seven satellites in the Solar System: Ganymede, Titan, Callisto, Io, the Moon, Europa, and Triton. Pluto is nearly spherical with an oblateness of less than 0.6% (Nimmo *et al.*, 2017).

I.1.3. Origin of the Pluto system

The formation of the Pluto-Charon binary system, as well as that of the small satellites is still widely debated (*e.g.*, Stern *et al.*, 2018; Canup, Kratter and Neveu, 2021; McKinnon *et al.*, 2021). Among the different mechanisms proposed to explain the formation of the Pluto system, the one for which there are the most favorable arguments relates to the formation of the Pluto-Charon binary system from a massive collision between two precursors of similar size (radius $\approx 10^3$ km), which would have occurred rather early in the history of the Solar System (McKinnon, 1989; Canup, 2005, 2011; McKinnon *et al.*, 2017, 2021; Sekine *et al.*, 2017; Arakawa, Hyodo and Genda, 2019; Canup, Kratter and Neveu, 2021). Indeed, the large masses of Pluto and Charon, the large specific angular momentum of the pair, and the coplanar orbits of Pluto's small satellites argue in favor of a giant-impact origin, like the giant collision which created our Moon. This impact should have occurred at low velocity (McKinnon *et al.*, 2017, 2021), between partially differentiated precursors (Canup, 2011; Desch, 2015; Arakawa, Hyodo and Genda, 2019). After the giant impact, Pluto and Charon could have accreted some of the debris, the rest being ejected at high velocity. During this ejection, high-velocity collisions among the debris particles could have occurred, leading either to the ejection of the debris out of the Pluto-Charon binary system, or to the retention of the debris in stable orbits around the binary system (Kenyon and Bromley, 2014; Bromley and Kenyon, 2020).

I.1.4. The *New Horizons* mission

At the end of the 1980s, with the detection of an atmosphere surrounding Pluto (discussed in more details below), the idea of a spacecraft reconnaissance of the Pluto system emerged. This idea was reinforced with the discovery of Pluto's evolving surface and atmosphere, the presence of small satellites, and the discovery of the Kuiper Belt (for more details about the genesis of the *New Horizons* mission, see *e.g.*, Stern (1993, 2008) Guo and Farquhar (2008), Weaver and Stern (2008), and Neufeld (2016)).

The highest priority objectives set out by the *National Aeronautics and Space Administration* (NASA) for this mission were (Young *et al.*, 2008):

- Characterization of the global geology and morphology of Pluto and Charon by obtaining hemispheric panchromatic maps and color maps, acquired at moderate and high phase angles, with sufficient dynamic range and signal/noise ratio.
- Mapping of the surface composition of Pluto and Charon by obtaining hemispheric infrared spectroscopic maps with sufficient spectral resolution, to determine the spatial distribution of the volatile ices on Pluto's and Charon's surfaces.
- Characterization of the neutral atmosphere of Pluto and its escape rate, by determining the precise composition of Pluto's atmosphere, its thermal structure, and the properties of Pluto's aerosols.

Secondary and tertiary objectives included (Young *et al.*, 2008):

- Characterization of the time variability of Pluto's surface and atmosphere, Pluto's ionosphere and solar wind interaction, and the energetic particle environment of Pluto and Charon.
- Imaging of Pluto and Charon in stereo.
- Mapping of the terminators of Pluto and Charon and of the surface composition of selected areas on Pluto and Charon with high resolution, and of the surface temperature of Pluto and Charon.
- Searching for neutral species including H, H_2, HCN, C_xH_y, and other hydrocarbons and nitriles in Pluto's upper atmosphere, for an atmosphere around Charon, for magnetic fields of Pluto and Charon, and for additional satellites and rings.
- Determination of the bolometric Bond albedos for Pluto and Charon.
- Refining of the bulk parameters (radii, masses, densities) and orbits of Pluto and Charon.

To meet these objectives, the payload of scientific instruments was composed of seven advanced instruments, whose objectives are reported in Table I.2:

- **Alice**: an ultraviolet imaging spectrograph (52 to 187 nm) (Stern *et al.*, 2008)
- **LOng-Range Reconnaissance Imager (LORRI)**: a high-resolution panchromatic imaging instrument (350 to 850 nm) (Cheng *et al.*, 2008)
- **Pluto Energetic Particle Spectrometer Science Investigation (PEPPSI)**: a spectrometer measuring ions and electrons from tens of keV to ~1 MeV (McNutt *et al.*, 2008)
- **Ralph**: a visible/infrared imager, which is the combination of two instruments, **Multi-spectral Visible Imaging Camera (MVIC)** and **Linear Etalon Imaging Spectral Array (LEISA)** (Reuter *et al.*, 2008)
  - **Ralph/MVIC**: a visible and near-infrared panchromatic and color imager, comprising four filters (*blue* from 400 to 550 nm, *red* from 540 to 700 nm, *near-infrared* from 780 to 975 nm, and a *narrow methane absorption band filter* from 860 to 910 nm)
  - **Ralph/LEISA**: a short-wavelength, infrared imaging spectrometer (1.25 to 2.5 µm)
- **Radio science EXperiment (REX)**: an instrument designed for uplink and radiometry measurements (Tyler *et al.*, 2008)
- **Student Dust Counter (SDC)**: an impact dust detector designed by students from University of Colorado Boulder (Horányi *et al.*, 2008)
- **Solar Wind Around Pluto (SWAP)**: an instrument designed to study the interaction between the solar wind and Pluto's atmosphere (McComas *et al.*, 2008)

Table I.2: Main scientific objectives of the instruments onboard the *New Horizons* spacecraft (non-exhaustive list).

Instrument	Main objectives
Alice	• Determination of the principal constituents of Pluto's atmosphere and its escape rate and escape regime • Characterization of the vertical profiles (pressure, temperature) of Pluto's atmosphere and density profiles of the constituents of Pluto's atmosphere • Characterization of atmospheric haze optical depth • Searching for an atmosphere around Charon
LORRI	• Characterization of the global geology and morphology of Pluto and Charon through panchromatic mapping at high resolution • Searching for atmospheric haze at a vertical resolution < 5 km

	• Mapping of the terminators of Pluto and Charon • Refining of the bulk parameters (radii, masses, densities) of Pluto and Charon • Searching for additional satellites and rings
PEPPSI	• Characterization of Pluto's neutral atmosphere and its escape rate • Characterization of Pluto's ionosphere and interaction with the solar wind
Ralph (MVIC & LEISA)	• Characterization of the global geology and morphology of Pluto and Charon through panchromatic imaging • Mapping of the surface composition of Pluto and Charon through color and spectral imaging
REX	• Characterization of the vertical profiles (pressure, temperature, density) of Pluto's atmosphere • Studying emission temperature of Pluto's and Charon's surfaces • Refining of the bulk parameters (radii, masses, densities) of Pluto and Charon
SDC	• Quantification and analysis of interplanetary dust
SWAP	• Characterization of the composition and density of the plasma escaping from Pluto's atmosphere • Determination of the interaction between the solar wind and Pluto's ionosphere

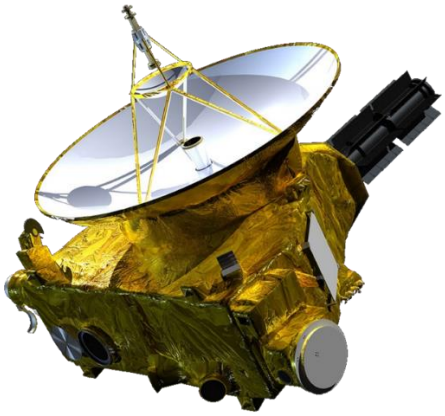

Figure I.6: The *New Horizons* spacecraft. *Credit*: NASA/JHU-APL/SwRI.

The *New Horizons* spacecraft (shown in Figure I.6) was launched by an Atlas V 551 rocket on January 19th, 2006 onto a direct trajectory to Jupiter. There, *New Horizons* spacecraft executed a Jupiter gravity assist on February 28th, 2007, to target Pluto. The spacecraft flew by Pluto at closest approach, at a distance of 13,700 km, and at a speed of ~13.8 km.s^{-1}, on July 14th, 2015, probing the Pluto system with its suite of instruments (*e.g.*, Stern *et al.*, 2018).

I.2. Pluto's interior and geology

The mean density of 1,854 ± 11 kg.m^{-3} (Nimmo *et al.*, 2017) (see Table I.1) suggests that Pluto is a differentiated body (Stern, 1989). ⅔ of the internal structure (*i.e.*, ~66%) would correspond to a rocky core on which probably lies a 100km-thick layer of liquid water (H_2O), above which would lie a ~300km-thick water-ice-dominated mantle bedrock (Barr and Collins, 2015; Johnson *et al.*, 2016; Nimmo *et al.*, 2016; McKinnon *et al.*, 2017; Bierson, Nimmo and McKinnon, 2018; Kamata *et al.*, 2019; Kimura and Kamata, 2020). Recent modeling studies supported the hypothesis of a subsurface ocean composed of water with probably a small amount of ammonia (Nimmo *et al.*, 2016; Kimura and Kamata, 2020). The presence of ammonia in this water ocean (1-5%wt relative to H_2O) can significantly depress its melting temperature and thus increase the possibility of existence of this subsurface ocean (Lewis, 1971; Desch *et al.*, 2009). To prevent this ocean from completely freezing, methane clathrates were also proposed as thermal insulator (Kamata *et al.*, 2019).

Pluto's interaction with the solar wind is consistent with an unmagnetized body. The magnetic field measured at the surface of Pluto by the SWAP instrument is lower than 30 nT (McComas *et al.*, 2016).

New Horizons revealed that Pluto's surface exhibits a spectacular geological diversity (see Figure I.7).

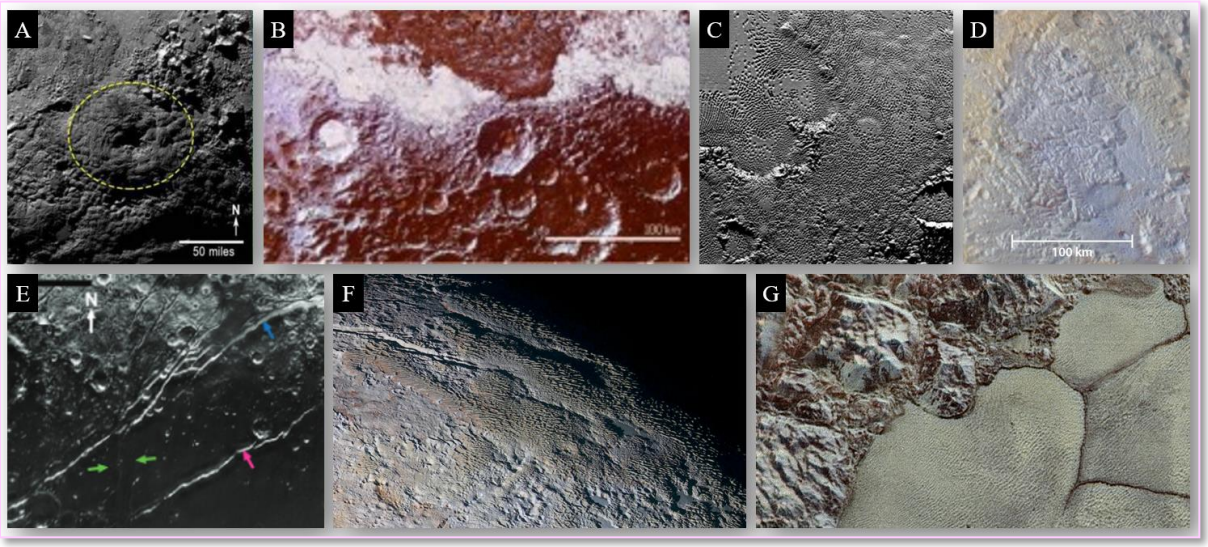

Figure I.7: The geology of Pluto through the eyes of *New Horizons*. **(A)** Wright Mons at 22°S, 173°E. **(B)** Impact craters at Viking Terra. **(C)** Pits formed by sublimation processes. **(D)** Dendritic valley networks at Pioneer Terra. **(E)** Extensive tectonic features at Cthulhu Regio. **(F)** Bladed Terrain of Tartarus Dorsa. **(G)** Water ice mountains at Al-Idrisi Montes and dunes on the surface of convection

cells at Sputnik Planitia. *Credit*: The images are from Moore *et al.* (2016, 2017, 2018), White *et al.* (2017), Stern *et al.* (2018), and Telfer *et al.* (2018).

Indeed, mountains with depressions in their center at Wright Mons and Piccard Mons (see Figure I.7.A) and evidence for cryovolcanism at Virgil Fossae and Viking Terra were observed (see the locations of these places in Figure I.8). This evidence for cryovolcanism supports the hypothesis of an ocean world (Grundy *et al.*, 2016; Moore *et al.*, 2016; Protopapa *et al.*, 2017; Schmitt *et al.*, 2017; Cruikshank *et al.*, 2019, 2021; Martin and Binzel, 2021). Pluto's hemisphere encountered by *New Horizons* also presents ~5,000 impact craters (see Figure I.7.B) of various morphologies (*i.e.*, simple bowl-shaped craters, craters with central piton, eroded craters) whose diameters vary from 0.5 to 300 km. Their distribution in a non-uniform way on Pluto suggests a resurfacing of the surface (for instance, this resurfacing would be ≤ 10 million years old at Sputnik Planitia) (Moore *et al.*, 2016; Robbins *et al.*, 2017; Singer *et al.*, 2021). At eastern Tombaugh Regio, elongated ripples, dimples and pits of a few hundred meters to 25 km wide and about 1 km deep were observed as well (see Figure I.7.C). These structures would be formed by the sublimation of the volatile ices on the surface of Pluto (Moore *et al.*, 2016; Howard, Moore, White, *et al.*, 2017; White *et al.*, 2017). Diverse channels and valley networks were also observed, for instance at Pioneer Terra (see Figure I.7.D). Such channels and valley networks could be witnesses of liquid flow in the past of Pluto (Moore *et al.*, 2016; Howard, Moore, Umurhan, *et al.*, 2017; Stern *et al.*, 2018). Hundreds of km long faults were observed in different regions of Pluto as well (see Figure I.7.E), and in particular normal faults, evidence of extensive tectonic activity (Moore *et al.*, 2016). Bladed terrains were observed at Tartarus Dorsa (see Figure I.7.F). These are deposits of methane ice subjected to sublimation processes forming reliefs up to a few hundred meters high, marked by ridges oriented North/South (Moore *et al.*, 2017, 2018; Moores *et al.*, 2017). Finally, in the vicinity of the water ice mountains located at Al-Idrisi Montes and rising up to 3 km in elevation (Moore *et al.*, 2016), convection cells of 10 to 40 km across (*i.e.*, the polygonal structures observed in Figure I.7.G) were observed at Sputnik Planitia, a gigantic nitrogen glacier (McKinnon *et al.*, 2016; Trowbridge *et al.*, 2016; Vilella and Deschamps, 2017). On the surface of these convection cells, dunes were observed (see Figure I.7.G). These dunes could be formed by winds blowing on ~200 to ~300 µm particles of methane ice at less than 10 $m.s^{-1}$ (Telfer *et al.*, 2018).

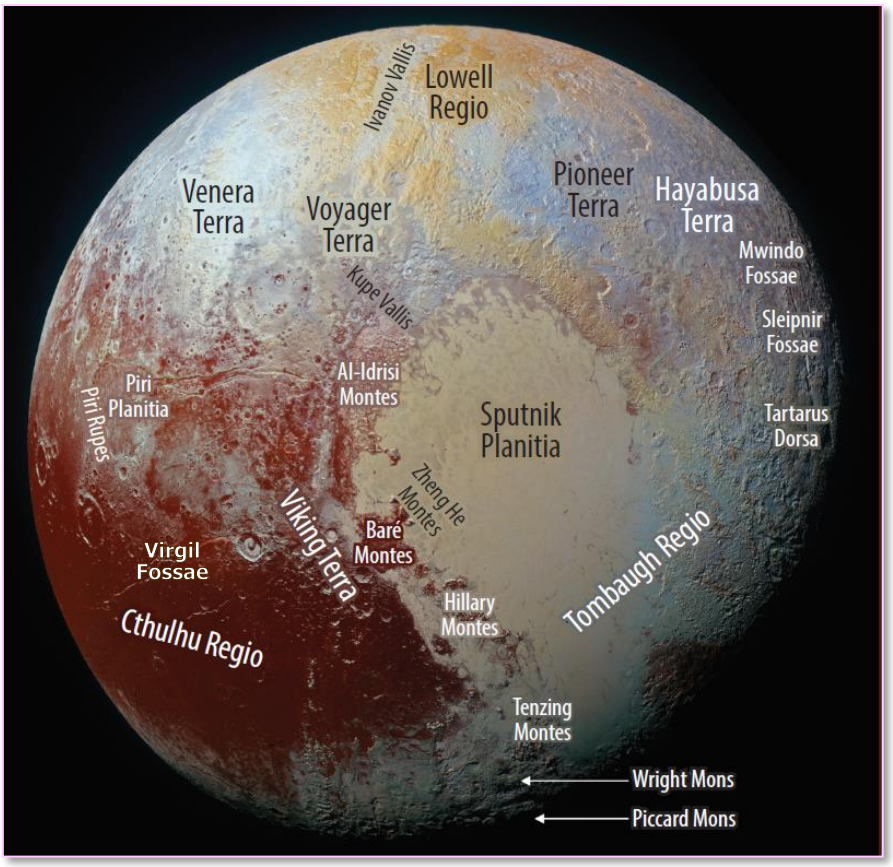

Figure I.8: Pluto's encounter hemisphere as imaged by *New Horizons* during the fly-by that took place on July 14th, 2015. This image is a composite of high-resolution panchromatic images taken by the LORRI instrument and low-resolution color images from the Ralph instrument. The colors were enhanced to show the diversity of surface units on Pluto. Place names, both formal and informal, are shown. Note that Pluto's North Pole (Lowell Regio) is oriented up and slightly towards the reader, whereas the dark reddish Cthulhu Regio straddles the equator. *Credit*: The image is from Stern *et al.* (2018).

The reader is referred to *e.g.*, Moore *et al.* (2016), White *et al.* (2017) and Stern *et al.* (2018) for exhaustive reviews about the different geological features on Pluto's surface.

I.3. Pluto's surface ices, atmosphere and aerosols

I.3.1. Volatile ices on Pluto's surface

As early as the 1970s, astronomers wondered about the possible presence of an atmosphere around Pluto (*e.g.*, Hart, 1974; Golitsyn, 1975; Benner, Fink and Cromwell, 1978), due to the detection of methane CH_4 ice on the surface of Pluto by infrared (IR) spectroscopy measurements conducted by Cruikshank, Pilcher and Morrison (1976). Pluto's tenuous

atmosphere was definitely evidenced by stellar occultations[2] simultaneously observed by eight independent ground-based teams on June 9th, 1988 (Hubbard *et al.*, 1988; Elliot *et al.*, 1989).

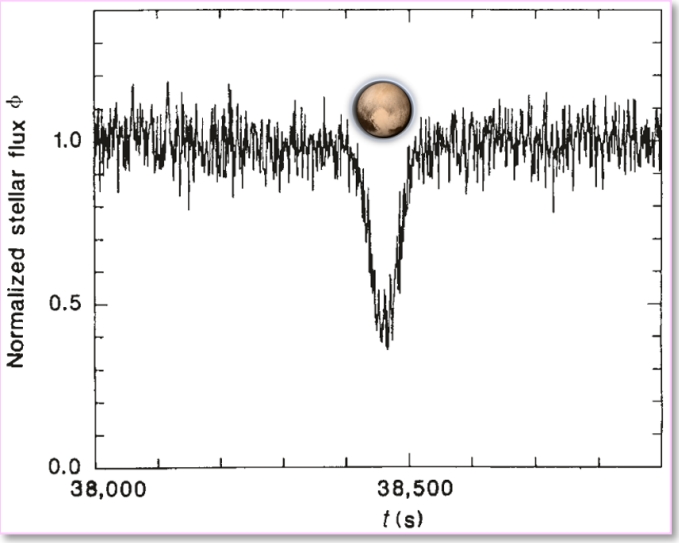

Figure I.9: Light curve observed on June 9th, 1988, evidencing the presence of an atmosphere surrounding Pluto. *Credit*: The figure is adapted from Hubbard *et al.* (1988).

Indeed, by observing the light curve of the distant star in front of which Pluto passed (*i.e.*, stellar occultation), it was observed that the signal received decreased (*i.e.*, immersion) and then increased (*i.e.*, emersion) gradually, suggesting the presence of an atmosphere around Pluto, whose pressure is higher than the nanobar level (see Figure I.9). In contrast, when the planetary body has no atmosphere, the signal decreases and reappears sharply.

At that time, however, the chemical composition of this atmosphere was uncertain. Later, based on the identification by IR spectroscopy of ices composed of molecular nitrogen N_2 (at 2.15 µm) and carbon monoxide CO (at 1.58 and 2.35 µm), and the confirmation of the presence of CH_4 ice on Pluto's surface (Figure I.10), Pluto's atmosphere was supposed to be composed of N_2, CH_4 and CO (Owen *et al.*, 1993). Indeed, during Pluto's elliptic orbit (see Figure I.4.left), these volatile ices[3] in vapor-pressure equilibrium at Pluto's surface temperature (~45 K) undergo a seasonal sublimation and condensation cycle that supplies the atmosphere (*e.g.*, Owen *et al.*, 1993; Stern *et al.*, 2015; Grundy *et al.*, 2016; Forget *et al.*, 2017).

Several further spectroscopic analyses contributed to a better characterization of the surface of Pluto (*i.e.*, distribution and evolution of the volatile ices), in the ultraviolet (UV), visible, and near-IR spectral ranges (*e.g.*, Cruikshank *et al.*, 1997; Douté *et al.*, 1999; Grundy and Buie,

[2] Stellar occultation: The word "occultation" comes from the Latin word *occultare* meaning "to hide". When a planet, a satellite, or an asteroid passes in front of a bright star and occults it, the starlight received by the observer decreases (phenomenon called immersion) and then increases again (phenomenon called emersion). In particular, when a planetary body has an atmosphere, the starlight dims because light rays are spreading through refraction by the atmosphere and because of extinction by the atmosphere. Through stellar occultations, astronomers can thus determine temperature, pressure and number density profiles of the upper atmosphere of the planetary body of interest, and infer information about the composition and the extinction of this atmosphere (*e.g.*, Elliot, 1979; Elliot and Olkin, 1996).

[3] For Trans-Neptunian Objects (TNO) and small bodies of the Kuiper belt (KBO), volatile ices are traditionally defined as ices whose saturated vapor-pressure is higher than the one of pure water ice.

2001; Grundy, Buie and Spencer, 2002; Protopapa *et al.*, 2008; Buie *et al.*, 2010; Merlin *et al.*, 2010; Grundy *et al.*, 2013, 2014).

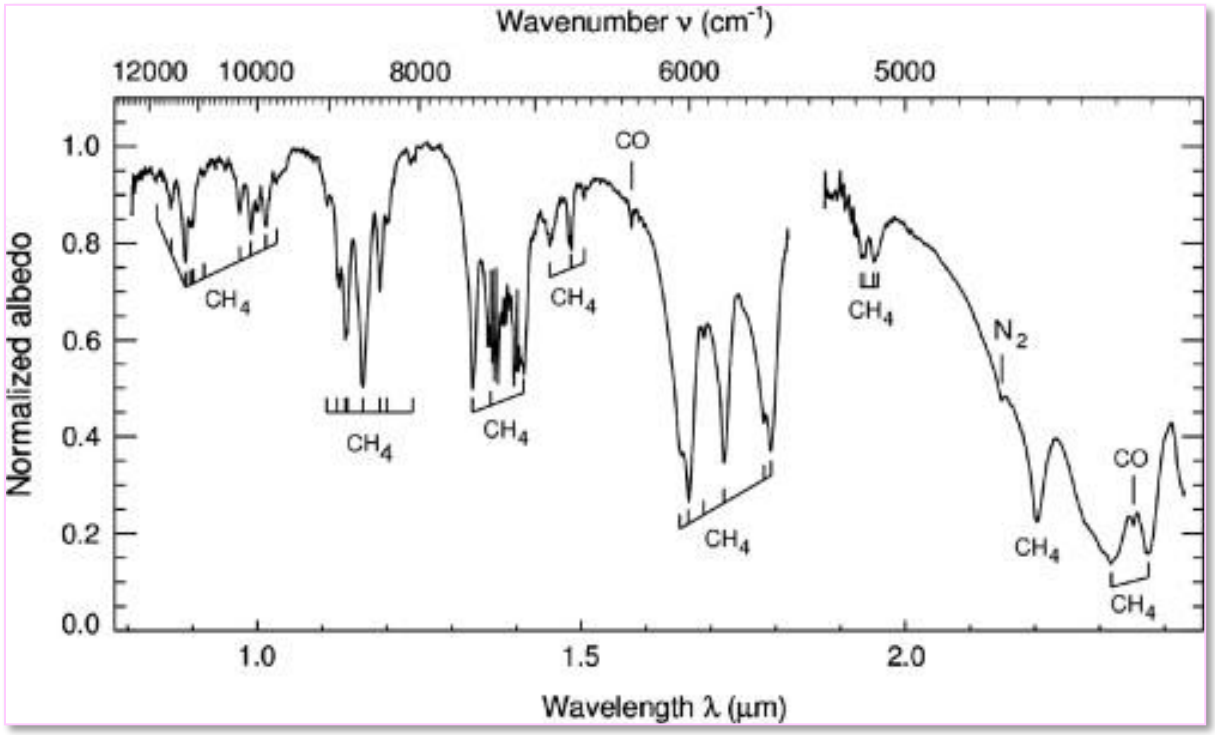

Figure I.10: Volatile ices of molecular nitrogen N_2, methane CH_4, and carbon monoxide CO detected by infrared spectroscopy on Pluto's surface. These ices in vapor-pressure equilibrium undergo a seasonal sublimation/condensation cycle supplying Pluto's tenuous atmosphere. *Credit*: The figure is from Grundy *et al.* (2013).

The latitudinal distribution of these different ices on the surface of Pluto is very complex (see Figure I.11) (Grundy *et al.*, 2016; Protopapa *et al.*, 2017; Schmitt *et al.*, 2017) and seems to evolve over time (Grundy *et al.*, 2014). Indeed, spectroscopic measurements acquired with the LEISA instrument during *New Horizons* fly-by showed that on Pluto, N_2 (Figure I.11.A), CH_4 (Figure I.11.B), and CO (Figure I.11.C) ices mix on a molecular scale, resulting in properties different than those for pure ice (Grundy *et al.*, 2016; Protopapa *et al.*, 2017; Schmitt *et al.*, 2017). These intimate mixtures were highlighted by the slight shifts in the methane spectral bands, depending on the proportion of methane in the solid N_2:CH_4 mixture. Measurements by the LEISA instrument also confirmed that these volatile ices lie on a water ice bedrock particularly visible at Cthulhu Regio (Figure I.11.D), strong enough to support the high reliefs observed for instance at Al-Idrisi Montes (see Figure I.7.G, discussed above) (Cruikshank *et al.*, 2015; Grundy *et al.*, 2016; Moore *et al.*, 2016; Protopapa *et al.*, 2017; Schmitt *et al.*, 2017).

A significant contribution of organic matter was also observed on the surface of Pluto (Figure I.11.E) (Grundy *et al.*, 2016; Protopapa *et al.*, 2017; Schmitt *et al.*, 2017).

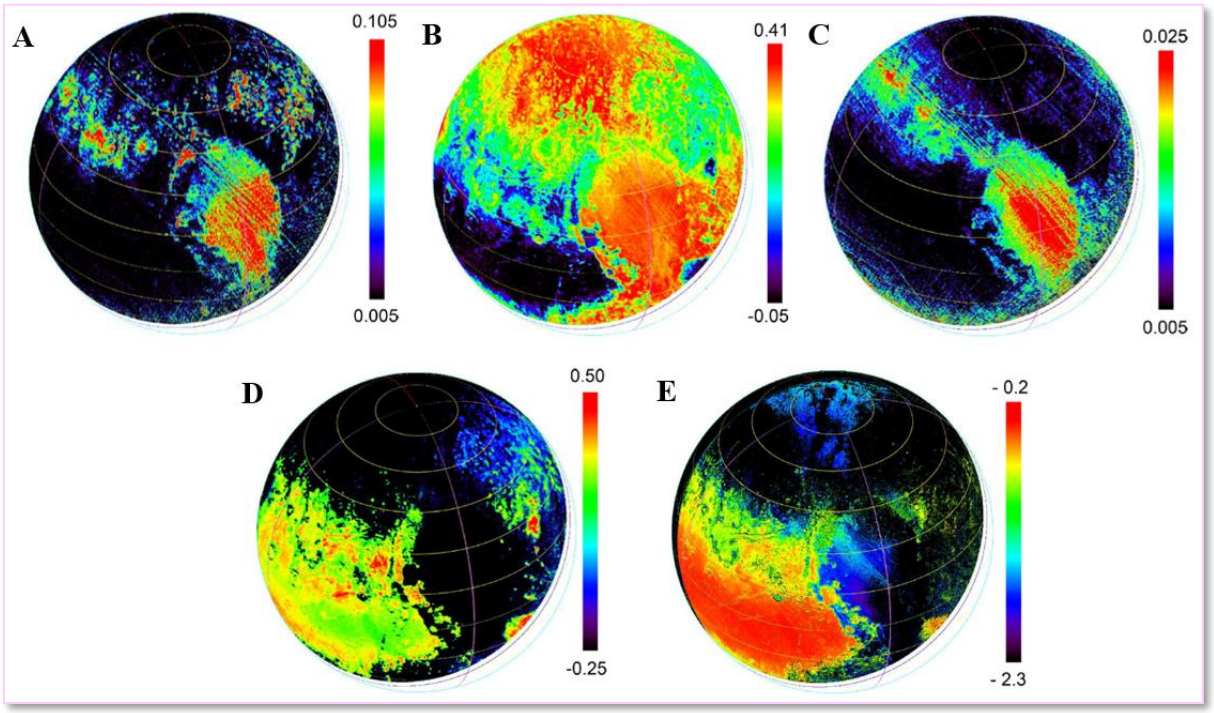

Figure I.11: Distribution of ices and organic matter on the surface of Pluto. **(A)** N_2 map (2.15 µm band). **(B)** CH_4 map (integration of the 1.58-1.83 µm band). **(C)** CO map (1.58 µm band). **(D)** H_2O map (2 µm band). **(E)** Organic material map. The color bars from black to red indicate increasing proportions of the material considered. For maps (B), (D) and (E), the negative values are due to the integration of a considered band depth over a wavelength continuum. *Credit*: The maps are from Schmitt *et al.* (2017).

The reader is referred to *e.g.*, Grundy *et al.* (2016), Protopapa *et al.* (2017) and Schmitt *et al.* (2017) for a detailed description on the distribution of the volatile ices N_2, CH_4, and CO, water ice, and organic material on Pluto's surface.

LEISA measurements also confirmed the presence of ethane C_2H_6 ice on Pluto's surface (DeMeo *et al.*, 2010; Cook *et al.*, 2019), whose distribution presents a longitudinal variability (Holler *et al.*, 2014). Ices composed of methanol CH_3OH and propane C_3H_8 were detected on Pluto's surface as well (Cook *et al.*, 2019).

To date, three hypotheses have been proposed for the origin of this dark red organic matter spreading on the surface of Pluto especially along the equator. The first hypothesis proposes the formation of this organic material at the time of the formation of the planet itself, during the giant impact at the origin of the Pluto-Charon binary system. During this giant collision, the extremely high energy delivered could have caused the melting of a significant part of the surface and the icy water bedrock of the proto-Pluto, forming an ocean of warm liquid water.

In this ocean, simple organic molecules, such as formaldehyde, could have polymerized to form more complex macromolecules constituting the red material currently present on Pluto's surface (Sekine *et al.*, 2017). However, this hypothesis cannot explain the spatial distribution of organic terrains at Pluto, nor their apparent age, younger than Charon. The second hypothesis proposes that these organics are formed by irradiation of the volatile ices on the surface of Pluto, mainly by solar UV radiation and Galactic Cosmic Rays (GCR)[4], with also a small contribution from charged solar wind particles (Cruikshank *et al.*, 2015). This hypothesis has been quite well documented through laboratory experiments, which showed that irradiation both with UV photons (*e.g.*, Materese *et al.*, 2014) or electrons (*e.g.*, Materese *et al.*, 2015) and swift heavy ions analogous to GCR (*e.g.*, Augé *et al.*, 2016) of different ices relevant to Pluto's surface (N_2, CH_4, CO, C_2H_6) can trigger a rich and complex chemistry, forming a complex refractory residue which might account for the dark red, non-icy material on Pluto's surface. This process would be similar to the processing of ices on cometary surfaces. However, here again, the spatial distribution of organics on Pluto's surface remains to be fully explained by this hypothesis. Finally, the third hypothesis suggests that photochemical aerosols produced in the atmosphere and then deposited on Pluto's surface (discussed in more details below) could account for Pluto's colors at large scales, from the dark red color of Cthulhu Regio and Krun Macula to the gold hue on Pluto's North Pole (Lowell Regio) (Protopapa *et al.*, 2017, 2020; Grundy *et al.*, 2018).

This third hypothesis is investigated in the fourth part of this Ph.D. thesis (Chapter VI).

Note that these three hypotheses are not mutually exclusive and that Pluto's colors could be due to successive processing of the surface material. However, Protopapa *et al.* (2020) demonstrated that only one kind of organic material was needed to reproduce MVIC and LEISA observations of Pluto's dark terrains, which would exclude different origins for different organic terrains.

[4] Galactic Cosmic Rays (GCR) are energetic particles propagating in the InterStellar Medium (ISM). These energetic particles encompass essentially charged, but also neutral particles. Charged particles include 88% protons (H nuclei), 9% helium (He) nuclei, the rest being electrons, various heavy ions (*e.g.*, C, O, Mg, Si, Fe), and trace amounts of antiprotons and positrons. The neutral particles consist of gamma (γ) rays and neutrinos. The density of GCR in the ISM is not negligible: one particle per 10^3 m^3. The energies of these particles range from 10^8 to 10^{21} eV. Although still debated, the standard model for the origin of GCR specifies that the charged particles and the neutrinos originate from violent supernovae explosions and shock waves in the ISM. In particular, low-energy particles (10^8 to 10^{10} eV) are accelerated in magnetized sites, such as white dwarfs, neutron stars, supernovae, whereas high-energy particles (> 10^{10} eV) are accelerated in shock waves linked to jets from active galactic nuclei containing a supermassive black hole. During their travel through the ISM, the charged particles of the GCR collide with the interstellar atoms and molecules, producing γ rays (*e.g.*, Blasi, 2013; Grenier, Black and Strong, 2015; Amato and Blasi, 2018).

I.3.2. Pluto's atmosphere

Ground-based spectroscopic observations conducted in 1992 allowed to strictly identify gaseous methane from Pluto's atmosphere (Young *et al.*, 1997), and its average mixing ratio was estimated to be ~0.5% between 2010 and 2015 (Lellouch *et al.*, 2009, 2011, 2015). Carbon monoxide was detected in 2010 through ground-based high-resolution spectroscopic measurements (Lellouch *et al.*, 2011) and the CO mixing ratio was quantified in 2015 at 515 ± 40 ppm by submillimeter observations with the Atacama Large Millimeter/submillimeter Array (ALMA) interferometer (Lellouch *et al.*, 2017). ALMA observations also showed that hydrogen cyanide HCN is present in Pluto's atmosphere. HCN mixing ratio is higher than 1.5×10^{-5} above 450 km of altitude, and equal to 4×10^{-5} near 800 km of altitude above the surface (Lellouch *et al.*, 2017).

New Horizons studied Pluto's atmosphere with radio, solar, and stellar occultations, airglow observations and imaging (Gladstone *et al.*, 2016; Cheng *et al.*, 2017; Hinson *et al.*, 2017; Young *et al.*, 2018; Steffl *et al.*, 2020). The plasma environment and Pluto's interaction with solar wind were studied as well (Bagenal *et al.*, 2016; McComas *et al.*, 2016).

The structure of Pluto's atmosphere was determined from radio occultation data measured by the REX instrument and solar ultraviolet occultation data recorded by the Alice spectrograph (Gladstone *et al.*, 2016; Hinson *et al.*, 2017; Young *et al.*, 2018). The pressure at the surface of Pluto was estimated by Gladstone *et al.* (2016) and Hinson *et al.* (2017) to be 10.2 ± 0.7 and 12.8 ± 0.7 µbar, respectively, whereas the near-surface temperature ranges from 38.9 ± 2.1 K (at ingress) to 51.6 ± 3.8 K (at egress) (see Table I.1). Note that earlier ground-based observations showed a significant increase in pressure on the surface of Pluto by a factor of 3 between 1988 and 2015 (*e.g.*, Elliot *et al.*, 1989; Lellouch *et al.*, 2011; Dias-Oliveira *et al.*, 2015; Sicardy *et al.*, 2016). Regarding the temperature profile on Pluto (shown in Figure I.12), a strong temperature inversion was observed for both ingress and egress REX measurements, at altitudes lower than 20 km (Gladstone *et al.*, 2016). This strong temperature inversion is qualitatively consistent with profiles retrieved from ground-based stellar occultation measurements (*e.g.*, Sicardy *et al.*, 2003; Elliot *et al.*, 2007; Dias-Oliveira *et al.*, 2015). However, two notable differences were observed between the REX profiles obtained at ingress and egress. First, the temperature inversion inferred from REX measurements at ingress (6.4 ± 0.9 $K.km^{-1}$) is much stronger than at egress (3.4 ± 0.9 $K.km^{-1}$). Second, the temperature inversion at ingress ends abruptly at an altitude of ~4 km, marking the top of a distinctive boundary layer, whereas the temperature inversion at egress appears to extend to the surface,

indicating the absence of this boundary layer. These notable differences between ingress and egress retrievals indicate the presence of horizontal variations in temperature (Gladstone *et al.*, 2016).

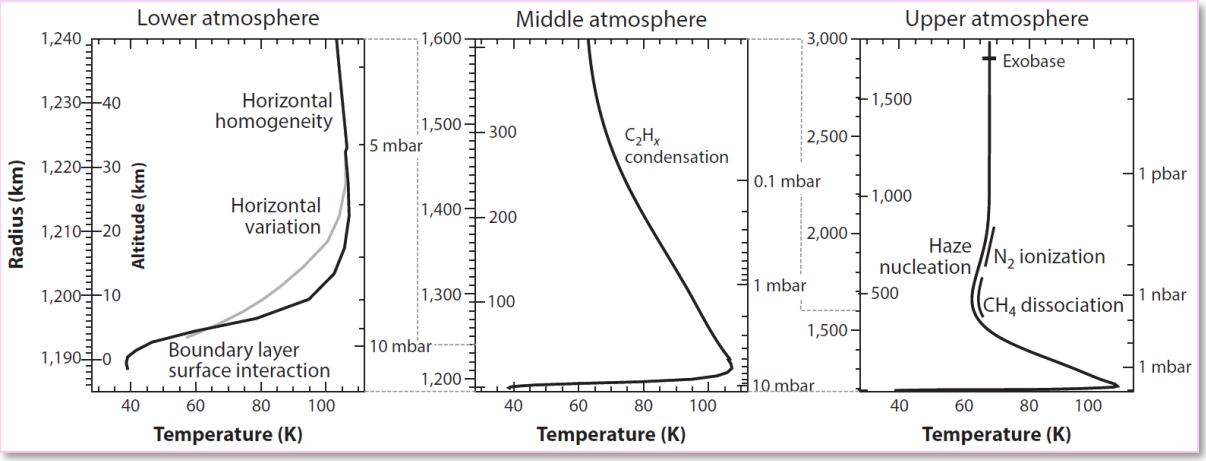

Figure I.12: Pressure-temperature profile for Pluto's atmosphere at the time of the *New Horizons* fly-by. In all panels, the black curves correspond to the REX retrieval at ingress. In the "lower atmosphere" panel (*left panel*), the grey curve corresponds to the REX retrieval at egress. *Credit*: The figure is from Stern *et al.* (2018).

The precise composition of Pluto's atmosphere (*i.e.*, vertical profiles for different components of Pluto's atmosphere, shown in Figure I.13) was inferred from Alice UV measurements. Pluto's atmosphere, which extends to about 1,600 km above the surface of Pluto, is mainly composed of N_2 and CH_4. The CH_4 mixing ratio varies from ~0.28-0.35% at the surface of Pluto (maintained by warm CH_4-rich ice (Forget *et al.*, 2017)) to 50% at about 1,450 km of altitude (Young *et al.*, 2018). The CH_4 mixing ratio shows a transition from eddy mixing (with eddy diffusion coefficient between 550 and 4,000 $cm^2.s^{-1}$) near the surface to diffusive separation at altitude, modulated by an upward CH_4 flux of $\sim 7\times10^8$ molecules.$cm^{-1}.s^{-1}$ (Young *et al.*, 2018). The homopause (*i.e.*, the altitude where eddy diffusion is equal to molecular diffusion) was constrained to be at most 12 km above the surface (Young *et al.*, 2018). The mean CH_4 atmospheric mixing ratio is also predicted to vary from 0.01% to 5% over annual or astronomical timescales (Bertrand and Forget, 2016; Stern, Binzel, *et al.*, 2017; Bertrand *et al.*, 2019).

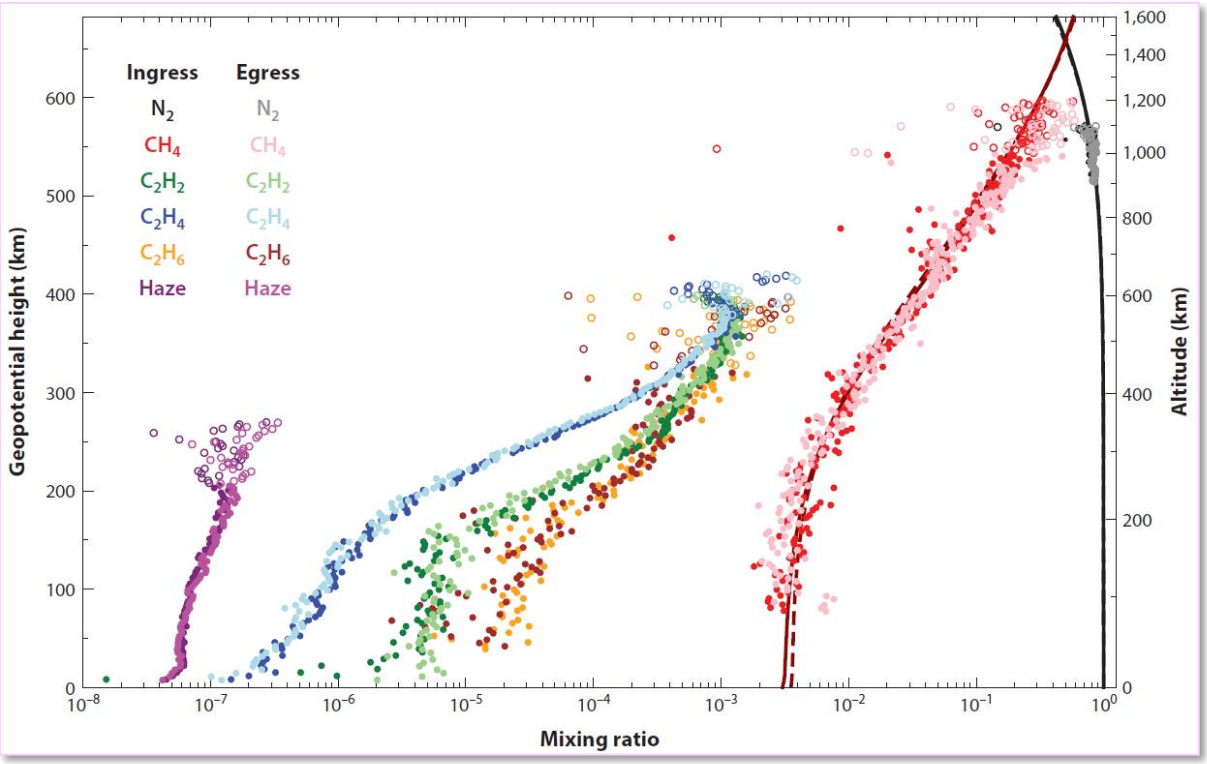

Figure I.13: Mixing ratio as a function of geopotential height (*left y*-axis) and altitude above the surface (*right y*-axis), derived from UV solar occultations obtained with the Alice instrument at ingress and egress. The black and grey data points correspond to N_2 mixing ratio, the red and salmon dots to CH_4, the dark and light green dots to C_2H_2, the dark and light blue dots to C_2H_4, the yellow and brown dots to C_2H_6, and the purple and pink data points to Pluto's photochemical haze. *Credit*: The figure is from Stern *et al.* (2018).

In addition to N_2, CH_4, CO, and HCN, C_2 hydrocarbons – acetylene C_2H_2, ethylene C_2H_4, and ethane C_2H_6 –, as well as propyne C_3H_4 are also present in the atmosphere as trace species (Gladstone *et al.*, 2016; Lellouch *et al.*, 2017; Young *et al.*, 2018; Steffl *et al.*, 2020).

Regarding the profile of the C_2 hydrocarbons in Pluto's atmosphere, we notice that their concentrations do not increase monotonically when approaching the surface. On the contrary, these concentration profiles exhibit inversions between 200 and 400 km of altitude, in particular for C_2H_2 and C_2H_4. Because of the low temperatures at these altitudes (~70 K), and the presence of condensation nuclei in the atmosphere (discussed in more details below), Wong *et al.* (2017) and Gao *et al.* (2017) explained this inversion in C_2H_2 and C_2H_4 concentrations by the condensation of these species on ambient solid aerosols. Luspay-Kuti *et al.* (2017) refuted the hypothesis adopted by Wong *et al.* (2017) and Gao *et al.* (2017), because of the saturation vapor densities of C_2 hydrocarbons which are significantly higher than their atmospheric densities. According to Luspay-Kuti *et al.* (2017), the loss of C_2 hydrocarbons essentially comes from heterogeneous processes of aerosol trapping of C_2. More precisely, it involves an irreversible

adsorption of C_2 either by chemical processes or by trapping of the gaseous molecules in the solid material (Kathleen Mandt, Pascal Rannou, personal communication). Finally, Lavvas *et al.* (2020) favor an hypothesis similar to that of Luspay-Kuti *et al.* (2017), with the difference that trapping mechanisms are not irreversible. Desorption processes would then be necessary to explain C_2 profiles (Panayotis Lavvas, Pascal Rannou, personal communication).

One or more other species are also expected in Pluto's atmosphere since its Alice UV spectrum shows still-unknown absorber(s) between 150 and 158 nm (Steffl *et al.*, 2020). In addition, questions remain regarding the atmospheric formation of H_2O, carbon dioxide CO_2, and formaldehyde HCOH (Wong *et al.*, 2017), as well as molecular oxygen O_2 (Kammer *et al.*, 2017).

Moreover, given the presence of aerosols in Pluto's atmosphere (discussed in more details below), an intriguing result is the absence of an ionosphere detection by the REX instrument (Hinson *et al.*, 2018). Pre-encounter models of Pluto's atmosphere expected a peak electron density of $\leq$ 1,300 cm^{-3} at ~700 km of altitude (Bagenal *et al.*, 2016) and a peak integrated electron content of 1.8×10^{11} cm^{-2} (Hinson *et al.*, 2018). The lack of ionosphere detection could be due to the integrated electron content slightly smaller than REX detection threshold (Hinson *et al.*, 2018). Nevertheless, although *New Horizons* did not make a direct measurement of an ionosphere around Pluto, pre-encounter and recent photochemical models concluded on its effective presence, with main cations being $HCNH^+$, $C_2H_5^+$, $C_3H_3^+$ and $C_3H_5^+$ (Krasnopolsky and Cruikshank, 1999; Bagenal *et al.*, 2016; Krasnopolsky, 2020). Moreover, the SWAP instrument revealed the probable presence of CH_4^+ (McComas *et al.*, 2016) and the Alice spectrograph detected emission by N^+ at 108.5 nm (Steffl *et al.*, 2020).

These questions raised by the Pluto *New Horizons* fly-by are investigated in the first part of this manuscript (Chapter III).

I.3.3. Pluto's aerosols

Figure I.14: The aerosols of Pluto backlit by the Sun, observed by the LORRI imager onboard the *New Horizons* spacecraft, while *New Horizons* was leaving the Pluto system. *Credit*: NASA/JHU-APL/SwRI.

Due to the chemical composition of Pluto's atmosphere similar to that of Titan (*i.e.*, a reduced atmosphere rich in N_2 and CH_4), its peculiar temperature profile and the presence of an inflection point in the light curve of a distant star in front of which Pluto passed, the presence of solid aerosols has been debated since the 1990s (Stansberry, Lunine and Tomasko, 1989; Lellouch, 1994; Lara, Ip and Rodrigo, 1997; Krasnopolsky and Cruikshank, 1999). The presence of these aerosols was finally confirmed by the *New Horizons* mission, as evidenced by the bluish haze observed in Figure I.14.

Aerosols were evidenced in Pluto's atmosphere by means of forward-scattering observations and solar occultations by the LORRI, MVIC and Alice instruments. These aerosols, modeled to account for 0.05-0.1 ppm_V of the atmosphere, enshroud Pluto and were detected at least as high as 350 km of altitude above the surface. The solid particles aggregate and superimpose into at least twenty distinct horizontal optically thin haze layers of a few km thick, separated by

~10 km (see Figure I.15) (Stern *et al.*, 2015; Gladstone *et al.*, 2016; Cheng *et al.*, 2017; Young *et al.*, 2018). Such striking layers organization could be explained by gravity waves resulting from orographic forcing (*i.e.*, winds flowing over surface topography) or from the diurnal sublimation of nitrogen ice at the surface (Toigo *et al.*, 2010, 2015; French *et al.*, 2015; Gladstone *et al.*, 2016). Pluto's haze optical depth in the visible was determined to be ~0.013 (Gladstone *et al.*, 2016; Cheng *et al.*, 2017; Hillier *et al.*, 2021). Its global distribution is non-uniform, with a slightly higher abundance near the North Pole (Cheng *et al.*, 2017).

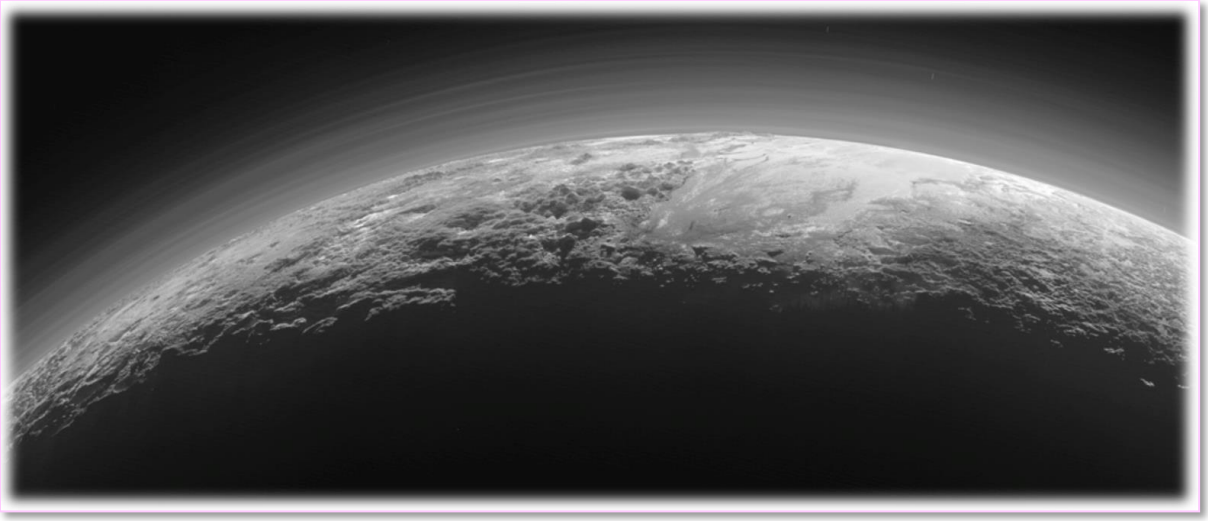

Figure I.15: The aerosols of Pluto, extending at least as high as 350 km of altitude and distributed in about twenty superimposed layers of a few km thick. *Credit*: NASA/JHU-APL/SwRI.

Questions remain regarding the size distribution of Pluto's haze particles since no single solution can satisfy measurements from all instruments onboard *New Horizons*, due to the intrinsic degeneracy of microphysics model inversion for unknown materials. However, the Alice and LORRI instruments gave complementary information on the size of particles at different altitudes. Cheng *et al.* (2017) pointed out the contradiction between haze brightness I/F profiles inferred from the Alice imaging spectrograph in the extreme-UV [52-187 nm] and the LORRI panchromatic imaging instrument in the [350-850 nm] wavelength range. A model of Mie scattering by 0.5 µm spheres reproduces fairly well the phase function of Pluto's haze at peak I/F measured in the visible by LORRI. However, this Mie model gives UV extinction lower by an order of magnitude than that retrieved from Alice solar occultation. On the opposite, results from a model of scattering by aggregates with bulk radius of 0.15 µm composed of several thousands 0.01 µm spherical monomers agree with the measurements made by Alice. They also match with the visible phase function measured by LORRI, but only at higher altitudes in Pluto's atmosphere (Cheng *et al.*, 2017). At higher altitudes, Pluto's haze

is thus thought to be mostly composed of fractal aggregates of 0.15 µm particles made up of 0.01 µm forward-scattering spheres. The haze particles present in the atmosphere from the surface to ~15 km of altitude probably correspond to 0.5 µm spherical particles that got larger by direct condensation of photochemical products onto nuclei (Stern *et al.*, 2015; Gladstone *et al.*, 2016; Cheng *et al.*, 2017; Gao *et al.*, 2017; Young *et al.*, 2018; Lavvas *et al.*, 2020).

Pluto's aerosols are likely formed by a complex photochemistry taking place in the upper atmosphere, from 300 up to 900 km of altitude (see Figure I.12 and Figure I.16) (Stern *et al.*, 2018; Young *et al.*, 2018). This photochemistry is initiated by extreme-ultraviolet (EUV) sunlight and solar Lyman-α photons. EUV radiation breaks the triple bonds of N_2 and CO in the upper atmosphere, while Lyman-α photons – arriving directly from the Sun or scattered by the interplanetary medium – breaks the C–H bonds in CH_4 at lower altitudes (Gladstone, Pryor and Stern, 2015; Gladstone *et al.*, 2016; Grundy *et al.*, 2018; and references therein), with a maximum CH_4 photolysis rate of ~1×10^{-14} $g.cm^{-2}.s^{-1}$ (Gladstone *et al.*, 2016). Although the exact reactive pathways are not well constrained yet, the formation rate of haze particles is limited by the primary photolysis of N_2 and CH_4 (see Figure I.16 showing the primary photodissociation and photoionization rate profiles for N_2 and CH_4 in Pluto's atmosphere). The peak loss rates for N_2 photodissociation and photoionization and CH_4 photoionization occur very high in Pluto's atmosphere, at ~700-800 km of altitude, and at ~500 km of altitude for CH_4 photodissociation (Gladstone and Young, 2019).

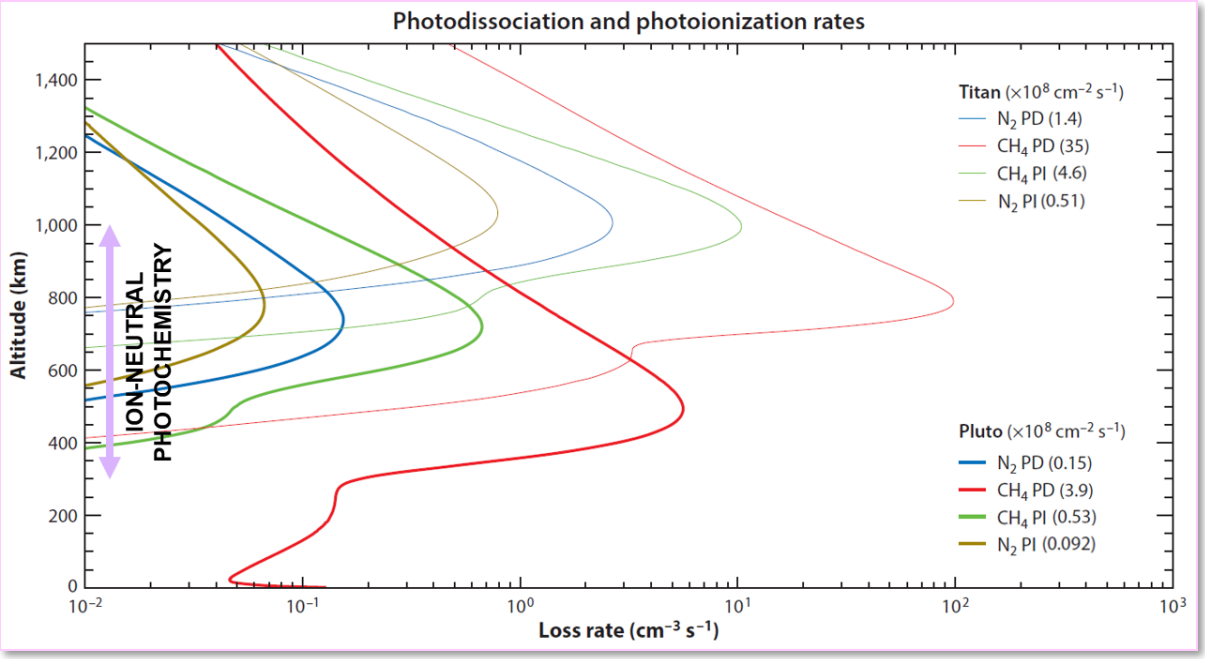

Figure I.16: Estimated primary photodissociation (PD) and photoionization (PI) rate profiles for N_2 and CH_4 in Pluto's atmosphere (*thick lines*) and, for comparison, in Titan's atmosphere (*thin lines*). Regarding Pluto's atmosphere, the primary PD and PI rate profiles were calculated for a solar zenith angle of 60° at the distance from the Sun during the *New Horizons* encounter of 32.91 AU. Column loss rates (referred to the surface) for each process are indicated in parenthesis in the legend as well. *Credit*: The figure is adapted from Gladstone and Young (2019).

It is assumed that Pluto's photochemistry involves neutral molecules formed from the ionization and the dissociation of molecular nitrogen N_2, methane CH_4, and carbon monoxide CO that constitute Pluto's atmosphere (Gladstone *et al.*, 2016; Lellouch *et al.*, 2017; Young *et al.*, 2018). A possible implication of ionic chemistry has also been proposed (*e.g.*, Krasnopolsky and Cruikshank, 1999; Luspay-Kuti *et al.*, 2017; Krasnopolsky, 2020). This chemistry forms complex hydrocarbons, nitriles, and oxygenated molecules. These molecules further polymerize to form the solid aerosols (Gladstone *et al.*, 2016; Wong *et al.*, 2017; Young *et al.*, 2018; Gladstone and Young, 2019; Krasnopolsky, 2020).

The formation of Pluto's aerosols by photochemistry is the topic of the first and second part of this Ph.D. thesis (Chapter III and Chapter IV).

Then, at lower altitudes, between 200 and 400 km where the temperature is ~70 K, the condensation of volatiles onto photochemical aerosols occurs (Luspay-Kuti *et al.*, 2017; Mandt *et al.*, 2017; Wong *et al.*, 2017; Lavvas *et al.*, 2020). Modeling outputs suggest that this condensation involves undersaturated C_2 hydrocarbons – C_2H_2, C_2H_4, C_2H_6 – as well as other photochemical gases such as HCN, CH_2NH, C_3H_4, C_3H_6, CH_3CN, C_4H_2, HC_3N, C_2H_3CN, C_2N_2,

CH_3C_2CN and C_6H_6 (Lara, Ip and Rodrigo, 1997; Krasnopolsky and Cruikshank, 1999; Luspay-Kuti *et al.*, 2017; Gao *et al.*, 2017; Mandt *et al.*, 2017; Wong *et al.*, 2017; Lavvas *et al.*, 2020). This coating incorporated by heterogeneous processes (possibly chemisorption or physisorption) could represent ~30% of the aerosol material at low altitude (Lavvas *et al.*, 2020).

The haze particles have an estimated residence time in the atmosphere of ~90 Earth days (Gladstone *et al.*, 2016), then, the particles (coated or not) deposit at the surface of Pluto and can be subject to further processing, for example through irradiation by photons or charged particles. The haze mass production rate is estimated at $\sim 1 \times 10^{-14}$ $g.cm^{-2}.s^{-1}$, corresponding to 2 $kg.s^{-1}$, and thus 15 m of haze particles deposited on Pluto's surface in 4.5×10^9 Earth years (Gladstone and Young, 2019).

The haze particles scatter the UV sunlight and are suspected to be the dominant factor of extinction at wavelengths greater than ~150 nm, as the extinctions of hydrocarbons or nitriles become less important with increasing wavelength. The haze particles thus contribute to the spectrum of Pluto observed by the Alice instrument (Cheng *et al.*, 2017; Steffl *et al.*, 2020).

Pluto's climate is also affected by the aerosols, that can serve as condensation nuclei (Lavvas *et al.*, 2016; Luspay-Kuti *et al.*, 2017; Gao *et al.*, 2017; Wong *et al.*, 2017; Lavvas *et al.*, 2020) or through direct radiative cooling of the atmosphere by the absorption of solar radiations (Zhang, Strobel and Imanaka, 2017). Pluto's atmosphere temperature, at ~400 km of altitude, is around 30-40 K colder than model predictions for an atmosphere in radiative-conductive equilibrium without haze (Zhu, Strobel and Erwin, 2014; Gladstone *et al.*, 2016; Zhang, Strobel and Imanaka, 2017). This cold upper atmosphere is difficult to explain using only gaseous cooling agents (*e.g.*, Krasnopolsky, 2018), such as HCN (Lellouch *et al.*, 2017) or H_2O molecules from the influx of Kuiper belt dust grains (Strobel and Zhu, 2017). Although gaseous cooling agents are not completely ruled out, Zhang, Strobel and Imanaka (2017) suggested this cooling to be due to the haze particles and their optical properties. Pluto's aerosols are expected to absorb in the UV-Visible and in the far-infrared spectral ranges, which would significantly affect Pluto's atmosphere thermal budget given the surface temperature (and thus, Planck emission function of Pluto), but to be less absorbent in the near- and mid-IR (Zhang, Strobel and Imanaka, 2017; Grundy *et al.*, 2018; and references therein). Haze heating and cooling rates calculated by Zhang, Strobel and Imanaka (2017) appear to be 100 times larger than those of gaseous species. The haze particles thus dominate the thermal balance of Pluto's atmosphere from the surface up to ~700 km of altitude.

The interaction of Pluto's aerosols with solar radiation is partly investigated in the third part of this manuscript (Chapter V).

I.4. Laboratory simulations of planetary atmospheres and objectives of this Ph.D.

Given all these effects mentioned above, the study of the formation processes and the physical and chemical properties of Pluto's aerosols is essential for a better understanding not only of Pluto's atmospheric chemistry, but also of its climate (modulated by interactions between radiation, the constituents of its atmosphere and its aerosols), and of its heterogeneous surface.

In addition to direct observations of Pluto, from the ground or with the instruments onboard the *New Horizons* spacecraft, there are different approaches to study the atmospheric chemistry and the formation of Pluto's aerosols, as well as their physical and chemical properties. For example, through numerical modeling, theoretical mechanisms can be confronted with observations. For my Ph.D. thesis, I used another approach based on experimental laboratory simulation to simulate the atmospheric chemistry of Pluto. This was done using a representative gas mixture and an energy source, to form aerosol analogues, which were then subjected to various physicochemical analyses using state-of-the-art analytical instruments.

These three approaches – observations, modeling, laboratory simulation – are linked, since laboratory experiments provide, for instance, inputs used in numerical models explaining the observations. For example, the optical constants of aerosol analogues are particularly used in numerical modeling, both to understand the radiative transfer in Pluto's atmosphere (*e.g.*, Zhang, Strobel and Imanaka, 2017), and at its surface (*e.g.*, Protopapa *et al.*, 2017, 2020; Grundy *et al.*, 2018). However, due to a lack of both observational and experimental data on these optical properties, the study by Zhang, Strobel and Imanaka (2017) was done using those of Titan aerosol analogues produced on Earth. The modeling studies of Pluto *New Horizons* data across the full [0.4-2.5 µm] wavelength range by Protopapa *et al.* (2020) also used optical constants determined for Titan aerosol analogues by Khare, Sagan, Arakawa *et al.* (1984) and Tran *et al.* (2003). To explain the different colors on Pluto's surface, Grundy *et al.* (2018) used multiple-scattering radiative transfer models with optical constants determined for Titan aerosol analogues by several groups: Khare, Sagan, Arakawa *et al.* (1984), Ramírez *et al.* (2002), Imanaka *et al.* (2004), Vuitton *et al.* (2009), and Sciamma-O'Brien *et al.* (2012), here again given the lack of optical constants for Pluto aerosol analogues.

Protopapa *et al.* (2020) pointed out the lack of optical constants for Pluto aerosol analogues in the Vis-near-IR wavelength range. Additionally, Zhang, Strobel and Imanaka (2017) highlighted that the optical constants determined for Titan aerosol analogues strongly vary with the mode of production and that the optical constants of Pluto's aerosols may be very different from those of Titan aerosol analogues. All these remarks reinforced a clear need by the community for laboratory simulations of aerosol analogues exclusively dedicated to Pluto.

All existing laboratory simulation setups for global simulations of planetary atmospheres are based on the same principle: providing energy to a gas mixture representative of the atmosphere to be studied. This energy induces ionization and dissociation of the gaseous molecules injected in the simulation reactor, forming reactive species. Further reactions occur between these reactive species, potentially ending up in the formation of analogues of planetary aerosols. Different experimental setups exist around the world and have been widely used to study Titan's atmosphere and aerosols for several decades. These experimental devices present a wide variety of experimental parameters, energy sources, *etc*. For more details regarding the different types of experimental setups for the simulation of planetary atmospheres, the reader is referred to *e.g.*, Cable *et al.* (2012), and Coll *et al.* (2013), and more recently to *e.g.*, Sciamma-O'Brien *et al.* (2014, 2017), Sebree *et al.* (2014, 2018), and He *et al.* (2017).

It is widely suggested that the formation of Pluto's aerosols occurs through photochemistry, in a similar way to the processes occurring in Titan's upper atmosphere (Gladstone *et al.*, 2016; Luspay-Kuti *et al.*, 2017; Cheng *et al.*, 2017; Wong *et al.*, 2017; Young *et al.*, 2018; Lavvas *et al.*, 2020). There are nevertheless important differences between Pluto and Titan, despite similarities in terms of atmospheric chemical composition. These differences include their sizes, their distances from the Sun and thus the photon fluxes involved in atmospheric photochemistry, their atmospheric pressures, their thermal structures, but also the proportions of minor atmospheric species, in particular the CO mixing ratio which is more important in the case of Pluto's atmosphere. Due to the lower proportion of methane in Pluto's atmosphere compared to that of Titan, we can for instance expect Pluto's aerosols to present higher nitrogen-to-carbon ratios, and due to a significant amount of CO and an exogenous supply of water by interplanetary dust at a level of 1.5×10^{21} H_2O s^{-1} (or 3.8 $kg.day^{-1}$) (Poppe and Horányi, 2018), oxygenated photoproducts are also expected (*e.g.*, Wong *et al.*, 2017). Due to lower temperatures in Pluto's atmosphere, condensation processes can also take place (Luspay-Kuti *et al.*, 2017; Rannou and West, 2018; Lavvas *et al.*, 2020), affecting the physical and chemical properties of Pluto's aerosols. Finally, due to a lower UV source at the distance of Pluto and

the absence of energetic particles accelerated by the magnetic field of a nearby giant planet, we can expect a lower ionization rate and thus a lower aerosol production efficiency on Pluto.

So far, no experimental studies have focused on the atmospheric chemistry of Pluto and the characterization of Pluto aerosol analogues. However, few studies have focused on the reactivity of a N_2:CH_4:CO gas mixture, but always in the frame of Titan studies and not specifically tailored to study Pluto's atmosphere. Below, I summarize the major results of these few studies, which often served as references for my studies, due to the lack of experimental work on Pluto.

Bernard *et al.* (2003) and Coll *et al.* (2003) analyzed the gaseous products of a N_2:CH_4:CO gas mixture containing 1.99% of methane and 100 ppm of carbon monoxide. These two studies concluded on the presence of O-bearing molecules, containing alcohol, diol, aldehyde and/or ketone chemical groups. Among these oxygenated molecules, the most abundant is C_2H_4O, ethylene oxide isomer, also called oxirane. Tran *et al.* (2008) investigated the impact of adding 0.3% CO in a reactive gas mixture composed of 98% N_2, 1.8% CH_4, 0.2% H_2, and various proportions of C_2H_2, C_2H_4, and HCN. They focused on the effect of CO on the gaseous and solid products resulting from the reactivity of this gas mixture. They identified thirteen O-bearing gaseous molecules, mainly ketones. In the solid products, the oxygenated molecules were essentially composed of aldehyde and saturated and α,β-unsaturated ketone groups. Hörst *et al.* (2012) detected fourteen amino acids and five nucleotide bases in the solid products formed in a N_2:CH_4:CO gas mixture comprising 1.8% CO with 2% or 5% CH_4. Hörst and Tolbert (2014) investigated the effect of CO on the formation and particle size of aerosol analogues produced in N_2:CH_4:CO gas mixtures with 0.1% or 2% CH_4, and CO mixing ratio ranging from 50 ppm to 5%. They concluded that the presence of CO has a dramatic effect on the particle size, number density and aerosol mass loading, which all increase. Fleury *et al.* (2014) investigated the influence of CO on N_2:CH_4 reactivity, with a CH_4 mixing ratio kept constant at 5%, and CO mixing ratios varying from 1% to 4.5%. They focused on both gas phase and solid products. CO affects the composition of the gas phase through the formation of oxygenated compounds: carbon dioxide CO_2 and nitrous oxide N_2O. Fleury *et al.* (2014) also noted that CO affects the production rate of aerosol analogues, which are produced in lower amounts when CO proportion increases. The particle diameter also increases when CO is added to the N_2:CH_4 reactive gas mixture. Finally, the incorporation of oxygen was found to be significant and to depend on the amount of CO introduced in the reactive gas mixture. He *et al.* (2017) conducted a similar study for 5% CH_4, and CO mixing ratio varying from 500 ppm to

5% in N_2:CH_4:CO gas mixtures. They concluded that oxygenated species are formed in the gas phase: CO_2, H_2O, and probably HCNO. Regarding the solid products synthesized by He *et al.* (2017), their density, oxygen content, and degree of unsaturation increase with increasing amount of CO. Lastly, Sebree *et al.* (2018) addressed the question of the presence of prebiotic molecules in aerosol analogues produced in a N_2:CH_4:CO gas mixture containing 5% CH_4 and 5% CO. They additionally reported tentative identification of sixteen molecules of prebiotic interest.

In summary, all these studies showed that CO affects both the composition of the gas phase through the formation of oxygenated molecules, and the morphology and composition of the particles constituting the planetary aerosol analogues. This effect of carbon monoxide will also be discussed throughout this Ph.D. manuscript.

In the context of my Ph.D., I used the PAMPRE experimental setup described in detail in Chapter II, in order to reproduce in the laboratory the atmospheric chemistry of Pluto and to synthesize analogues of Pluto's aerosols and surface materials. To understand the formation of Pluto's aerosols, I used two different and complementary approaches. The first one is a top-bottom study, where I focused on the chemical composition and reactivity of the gas mixture in which Pluto aerosol analogues are formed (see Chapter III). The second one is a bottom-up approach, where both chemical composition (see Chapter IV) and optical properties (see Chapter V) of Pluto aerosol analogues were investigated to infer their formation processes. The evolution of Pluto's aerosols once deposited on the surface was investigated in Chapter VI.

In Chapter III, regarding gas-phase chemistry, I investigated the following questions:

- Which neutral molecules and cations are formed by Pluto-simulated atmospheric chemistry?
- What are the reaction pathways producing these species, and does it include O-bearing molecules?
- Which species are precursors to the formation of Pluto's aerosols?

In Chapter IV, regarding the chemical composition of Pluto aerosol analogues, I investigated the following questions:

- What is the chemical composition of Pluto aerosol analogues?
- Do aerosols formed at different altitudes in Pluto's current atmosphere or during different seasons/epochs of Pluto have different compositions?
- Could Pluto's aerosols have prebiotic implications?

In Chapter V, regarding the optical constants of Pluto aerosol analogues, I investigated the following questions:

- What are the optical constants of Pluto aerosol analogues?
- Are Pluto aerosol analogues made in the laboratory suitable to explain Pluto's surface organic matter and the thermal balance of Pluto's atmosphere observed by *New Horizons*?
- Do aerosols formed at different altitudes in Pluto's current atmosphere or during different seasons/epochs of Pluto have different optical properties?

In Chapter VI, regarding the organic material on Pluto's surface, I investigated the following questions:

- Are Pluto aerosol analogues produced in the laboratory suitable proxies to reproduce observations by *New Horizons* of colored terrains on Pluto?
- What can explain the dark red color on Pluto's surface, in the Cthulhu region?
- How would GCR irradiation affect the properties of surface organics on Pluto?

II. Experimental section

In this chapter are presented the experimental facilities I used during my Ph.D., as well as details about the instruments used for measurement and data processing employed to characterize Pluto-simulated atmosphere and analogues of Pluto's aerosols and surface materials. The PAMPRE experimental setup, located at LATMOS (*Laboratoire Atmosphères, Observations Spatiales*, Guyancourt, France), was used to simulate Pluto's atmospheric chemistry and to synthesize analogues of Pluto's aerosols and surface materials. Experiments performed at GANIL (*Grand Accélérateur National d'Ions Lourds*, Caen, France), using the IGLIAS experimental setup, were intended to simulate the organics ageing due to charged particles at the surface of Pluto, and in particular in the Cthulhu region. At the end of this chapter, a table summarizes the objectives, advantages and drawbacks of the different analytical techniques used during my Ph.D.

II.1. The PAMPRE experimental setup

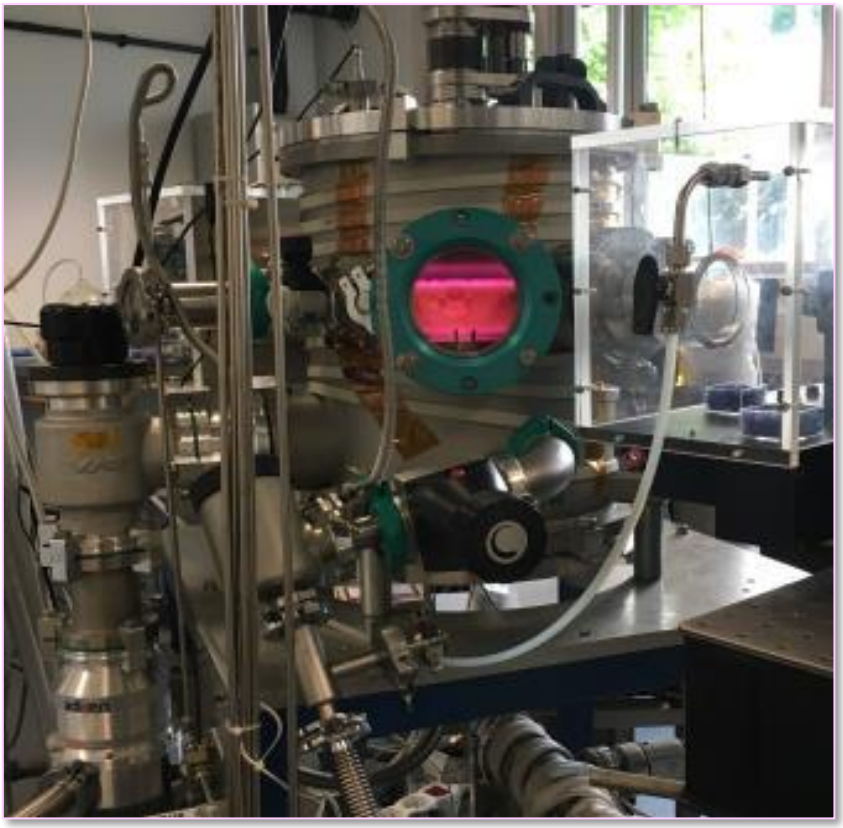

Figure II.1: The PAMPRE experimental setup, located at LATMOS (Guyancourt, France). This plasma reactor is used to simulate Pluto's atmospheric chemistry and to synthesize analogues of Pluto's aerosols and surface materials.

II.1.1. History in brief – From Titan to Pluto

PAMPRE stands for "Production d'Aérosols en Microgravité par Plasma REactif" (French acronym), *i.e.*, "Production of Aerosols in Microgravity by REactive Plasma" (Szopa, Cernogora *et al.*, 2006; Alcouffe *et al.*, 2010). This experimental setup, inspired from a dusty plasma reactor dedicated to the study of microelectronic processes and located at GREMI[5] laboratory (*e.g.*, Bouchoule and Ranson, 1991; Boufendi and Bouchoule, 1994), was developed at *Service d'Aéronomie* (Verrières-le-Buisson, France, ancestor of LATMOS), initially to simulate the chemistry occurring in Titan's atmosphere, and to synthesize analogues of Titan's aerosols, also called "tholins". Note that the term "tholins", from the Ancient Greek word *θολός* (*tholós*) meaning "muddy", was introduced by Carl Sagan and Bishun N. Khare in 1979 to designate a complex organic solid produced from cosmically abundant molecules irradiated by UV photons or spark discharge (Sagan and Khare, 1979). The development of an experimental reactor such as PAMPRE was motivated by the NASA/ESA *Cassini-Huygens* mission exploring the Saturnian system (*e.g.*, Lebreton and Matson, 1992; Matson, 1996; Matson, Spilker and Lebreton, 2003; Spilker, 2019), and especially to help interpret the data acquired by the Aerosol Collector and Pyrolyser (ACP) instrument developed at *Service d'Aéronomie* (Israel *et al.*, 1999, 2003), onboard the *Huygens* probe that landed on Titan's surface (*e.g.*, Lebreton and Matson, 1997).

Due to the versatility of this experimental setup, largely used to study Titan's atmosphere and aerosols (*e.g.*, Szopa, Cernogora *et al.*, 2006; Quirico *et al.*, 2008; Sciamma-O'Brien *et al.*, 2010, 2012; Gautier *et al.*, 2011, 2012, 2014, 2016; Carrasco *et al.*, 2012; Mahjoub *et al.*, 2012, 2014; Fleury *et al.*, 2014; Dubois, Carrasco, Bourgalais, *et al.*, 2019; Dubois *et al.*, 2020), it was expanded to study the atmospheres of the early Earth (Fleury *et al.*, 2015, 2017) and of exoplanets (Gavilan *et al.*, 2017, 2018).

In the context of my Ph.D., I further extended the usage of the PAMPRE experimental setup to simulate the chemistry occurring in Pluto's atmosphere and to produce analogues of Pluto's aerosols and surface materials (Pluto tholins) in the frame of Pluto's fly-by by the *New Horizons* spacecraft.

II.1.2. Technical characteristics

PAMPRE (Szopa, Cernogora *et al.*, 2006; Alcouffe *et al.*, 2010) (Figure II.1) is a Radio-Frequency Capacitively Coupled Plasma (RF CCP) generated in a gas mixture by a 13.56 MHz

[5] GREMI: *Groupe de Recherches sur l'Energétique des Milieux Ionisés* (Orléans, France)

generator (*SAIREM GRP 01KE*) through a match box. PAMPRE is composed of a cylindrical stainless-steel reactor measuring 40 cm in height and 30 cm in diameter, with several apertures for the connection of various analytical instruments (*e.g.*, Quadrupole Mass Spectrometry, Optical Emission Spectroscopy, InfraRed Spectroscopy, *etc.*). A glass window allows a visual monitoring of the plasma (Figure II.1).

The discharge electrons ionize and dissociate the reactive gases introduced into the reactor (see Table II.1 presenting the energies of dissociation and ionization of molecular nitrogen N_2, methane CH_4 and carbon monoxide CO, the main constituents of Pluto's atmosphere (Gladstone and Young, 2019)), producing a plasma rich in neutral molecules, radicals, positive and negative ions, and electrons. The electronic and ionic densities in the plasma are on the order of ppm_V, much lower than the densities of the neutrals, and the pressure is relatively low (~1 mbar). It is therefore a cold plasma out of thermodynamic equilibrium. The temperature of the neutrals and ions is then close to that of the injected gases, *i.e.*, ambient temperature, whereas the highly mobile electrons have higher temperatures (~2 eV, *i.e.*, $\sim 2\times10^4$ K) (Szopa, Cernogora *et al.*, 2006). In this environment, chain reactions occur resulting in the formation of solid particles, analogues of Pluto's aerosols and surface materials, so-called "Pluto tholins".

Table II.1*:* Bond-dissociation and ionization energies of N_2, CH_4 and CO, the main constituents of Pluto's atmosphere. The values are taken from Heays *et al*. (2017).

Energy	**N_2**		**CH_4**		**CO**	
	[eV]	**[nm]**	**[eV]**	**[nm]**	**[eV]**	**[nm]**
Bond-dissociation	9.76	127	4.48	277	11.27	110
Ionization	15.69	79	12.65	98	14.09	88

The plasma discharge can be operated in a continuous regime or in a pulsed mode, depending on the desired study. In the case of the studies presented in the present manuscript, only the continuous regime of the plasma discharge was used.

A scheme of the PAMPRE experimental setup is given in Figure II.2.

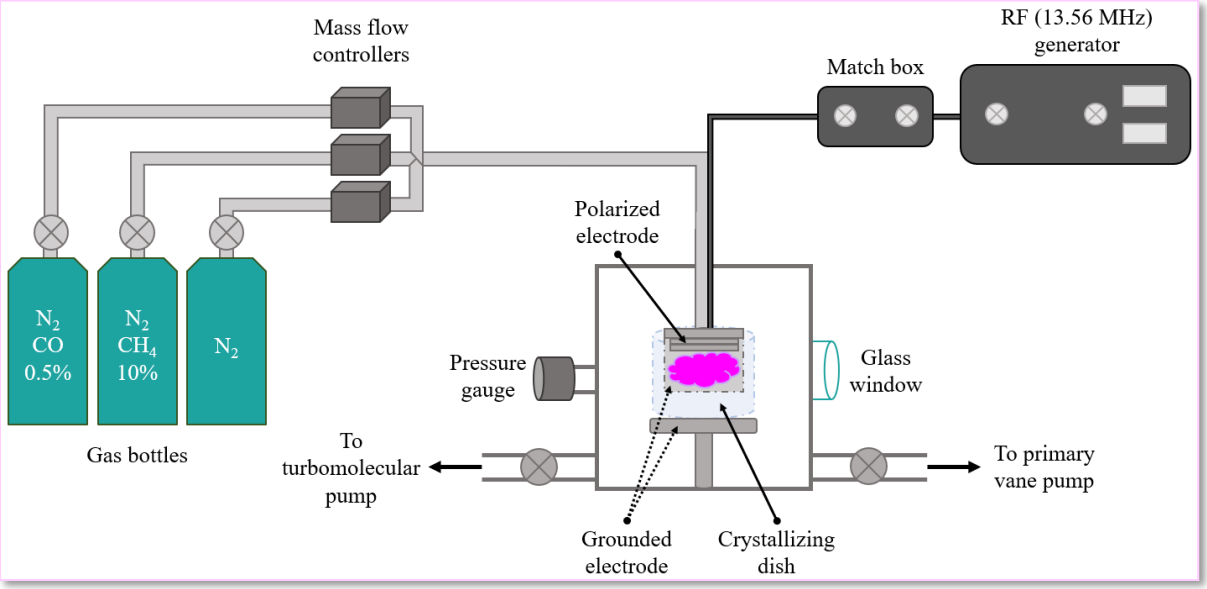

Figure II.2: Scheme of the PAMPRE experimental setup.

In the reactor, there are two capacitively coupled electrodes (Figure II.3). The upper one – the cathode – measures 12.6 cm in diameter. This electrode is polarized and a high voltage is applied. The gas mixture representative of the major components of Pluto's atmosphere is injected into the reactor from the top of the chamber through the cathode, after having undergone a turbulent mixing in the gas injection system. The cathode is equipped with three superimposed grids allowing the gas mixture to be injected as a homogeneous and continuous flow. The central grid whose mesh size is in the order of the Debye length (~0.1 mm) prevents the plasma from returning to the gas injection system. The gas mixture is extracted from the bottom of the chamber by a primary vane pump (*Adixen by Pfeiffer Vacuum Pascal 2015 SD*). The PAMPRE experiments are thus conducted in an open system, like photochemistry occurring in natural atmospheres. An aluminum plate, measuring 16 cm in diameter, acts as the counter-electrode, or anode. This plate is grounded. The inter-electrode distance of 5 to 10 cm is such that, at experimental operating pressure (~1 mbar), the average free path of the electrons is less than 1 cm (Bouchoule and Ranson, 1991), and the electrons, going from one electrode to the other, can induce a cascade of reactions involving the molecules of the reactive gas mixture (Szopa, Cernogora *et al.*, 2006; Alcouffe *et al.*, 2010).

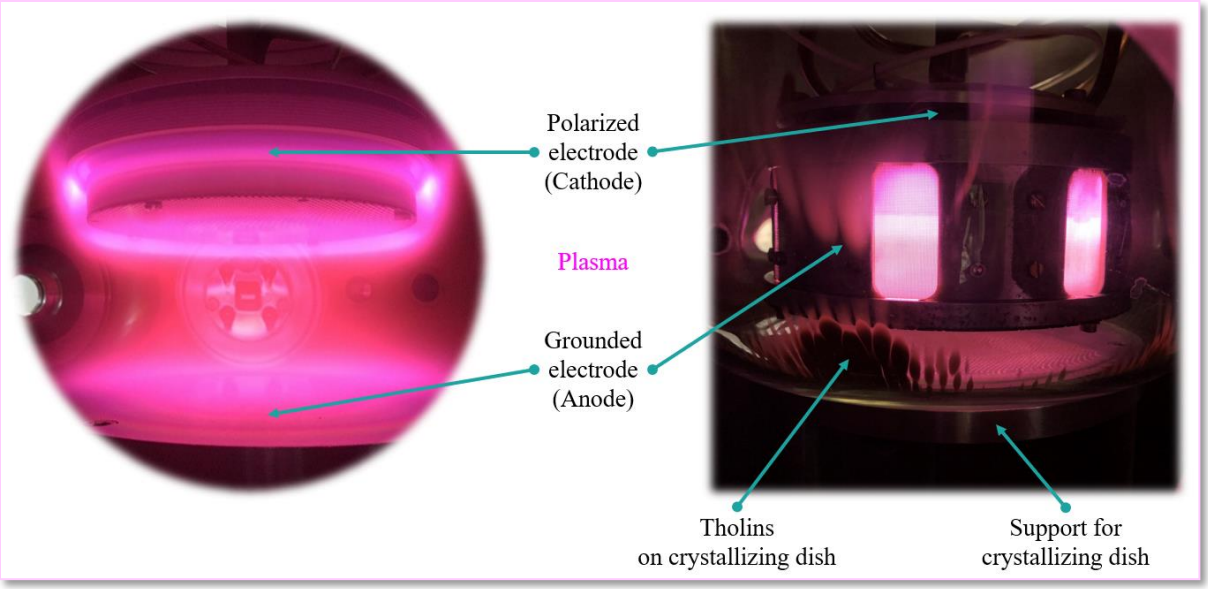

Figure II.3: Capacitively coupled electrodes acting as an energy source for initiating plasma chemistry. The gas mixture representative of the main composition of the atmosphere to be simulated is injected into the reactor through the polarized cathode. *Left*: Without the plasma confining cage, the grounded anode consists of an aluminum plate. This configuration is used to study *in situ* the chemical composition (neutrals, ions) of the plasma. *Right*: With the plasma confining cage acting as the grounded anode. The cage is an aluminum cylinder confining the plasma to facilitate the synthesis of tholins.

For the experiments conducted during my Ph.D., the gas mixture representative of the main composition of Pluto's atmosphere was composed of molecular nitrogen N_2 and methane CH_4 – in variable proportions, to mimic Pluto's atmosphere as observed in 2015 by *New Horizons* at different altitudes, or during different seasons or epochs of Pluto – and 500 ppm of carbon monoxide CO (Bertrand and Forget, 2016; Gladstone *et al.*, 2016; Lellouch *et al.*, 2017; Young *et al.*, 2018; Bertrand *et al.*, 2019). High-purity (> 99.999%) *Air Liquide* gas bottles, with impurities H_2O < 3 ppm, O_2 < 2 ppm and C_xH_y < 0.5 ppm, were connected to the experimental setup (Figure II.2):

- 1 bottle of pure N_2 gas (*ALPHAGAZ™ 2*)
- 1 bottle of pre-mixed N_2:CH_4 gas mixture, with 10% of CH_4 diluted in N_2 (*CRYSTAL* mixture)
- 1 bottle of pre-mixed N_2:CO gas mixture, with 5,000 ppm of CO diluted in N_2 (*CRYSTAL* mixture)

The total flow rate was arbitrarily set at 55 sccm (standard cubic centimeters per minute, 0.66 $g.s^{-1}$), controlled by gas flow controllers (*MKS*, 10 and 100 sccm full scale controllers), resulting in an overall plasma pressure of 0.9 ± 0.1 mbar, at ambient temperature (293 K). Note

that the pressure and temperature are higher in our experiments than in Pluto's upper atmosphere (~10^{-2} µbar and ~65 K at 400 km of altitude and ~10^{-4} µbar and ~65 K at 650 km of altitude (Gladstone and Young, 2019)). However, the most important parameter, the ionization rate, is the same and on the order of ppm_v (Wattieaux *et al.*, 2015). Using similar ionization rate enables a realistic contribution of ions into the whole ion-neutral coupled chemical network and thus better represents Pluto's atmospheric chemistry. As ion-molecule reaction rates are relatively insensitive to low temperatures (Böhme, 2000; Anicich, Wilson and McEwan, 2003; Imanaka and Smith, 2009), the lower temperature in Pluto's upper atmosphere (65 K instead of 293 K in our experiments) is not a first-order issue in our case. Moreover, in this Ph.D., we chose to conduct our experiments at ambient temperature in order to avoid biasing the gas phase composition due to condensation, as pointed out by Mahjoub *et al.* (2014). The higher pressure, for its part, induces shorter mean free path for the molecules, which main implication is faster kinetics in the experiments. This remains true as long as the pressure is low enough to minimize trimolecular reactions (a few mbar), which is the case in all our experiments. As such, pressure is not expected to be a parameter inducing major differences between my experimental simulations and Pluto's atmosphere. Note that although strongly limited, these trimolecular reactions were nevertheless considered in our interpretations.

The radio-frequency discharge, whose power was arbitrarily set at 30 W for the experiments performed during my Ph.D., induces electrons whose energy distribution is similar at first order to the energy distribution of solar photons, with a maximum at ~1-2 eV. However, the tail of the Maxwellian energy distribution of the electrons in the plasma is more populated than the Planck energy distribution of solar photons. This tends to enhance nitrogen inclusion a bit too much in the produced molecules, due to over-dissociation of N_2 (Szopa, Cernogora *et al.*, 2006; Alves *et al.*, 2012). Note that the use of a plasma as a proxy for energy source, although far from being perfect, remains the best option to simulate Pluto's atmospheric chemistry as I did. Indeed, as seen in Table II.1, both N_2 and CO require high energies to be mobilized either through dissociation or through ionization, typically above 10 eV. While photons with these energies are present in the solar spectrum, and thus in Pluto's atmosphere, they are extremely challenging to produce in experimental setups on Earth. This is due to the cut-off of UV wavelengths below ~110 nm by virtually any material that can be used in Vacuum-UltraViolet

(VUV) photon lamp on Earth, and as such, plasma discharge is the main option to initiate nitrogen and oxygen chemistries in Pluto's atmospheric simulations[6].

During my Ph.D., the reactor was used in two operation modes:

- Without the plasma confining cage for *in situ* analysis of the chemical composition (neutrals and cations) of the plasma simulating Pluto's atmosphere (Figure II.3.left)
- With the plasma confining cage for the synthesis of Pluto tholins (Figure II.3.right)

The plasma confining cage is an aluminum cylinder measuring 5 cm in height and 13.6 cm in diameter and containing grid apertures. When this cage is screwed onto the meshed polarized electrode, it then acts as the counter-electrode, and the aluminum plate becomes a support for the crystallizing dish used for collecting the tholins. When the plasma is switched on, the solid particles form in volume, staying in electrostatic levitation between the electrodes, without interactions with the metallic walls. When the spherical particles reach a critical diameter, they are carried away by the gas flow and ejected out of the plasma and they accumulate as a brownish powder on the crystallizing dish walls surrounding the confining cage (Figure II.4.left) (Szopa, Cernogora *et al.*, 2006; Alcouffe *et al.*, 2010). For some specific experiments and analytical measurements (see Chapter V and Chapter VI), Pluto tholins had to be produced also as thin films. For this purpose, substrates of silicon Si, magnesium fluoride MgF_2, zinc selenide ZnSe, or zinc sulfide ZnS were placed at the bottom of the cage. When the plasma is switched on, Pluto tholins form as thin films onto the substrates (Figure II.4.right).

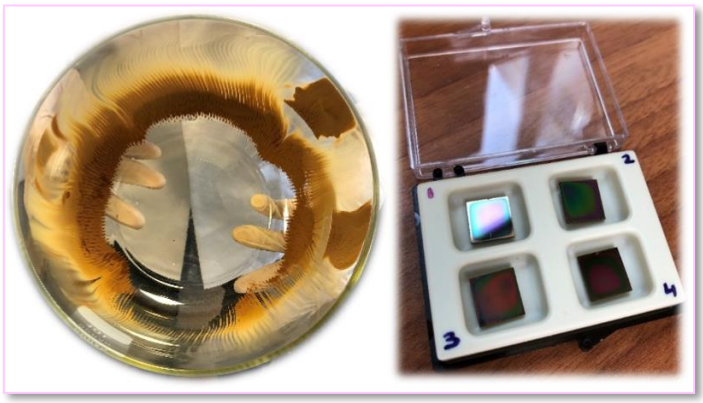

Figure II.4: Pluto tholins synthesized with the PAMPRE experimental setup. *Left*: Pluto tholins produced as brownish solid spherical grains accumulating in the crystallizing dish. *Right*: Pluto tholins formed as thin films onto silicon substrates.

[6] It is also possible to simulate the atmospheric chemistry of Pluto by irradiating a Pluto-type gaseous mixture with VUV synchrotron radiation. Nevertheless, the use of such an energy source requires beam time request, and the beamtime allocated is rarely sufficient on the scale of a Ph.D. thesis.

Pluto tholins, as spherical grains or thin films, are collected at atmospheric pressure. This way of collecting the samples is known to lead to their surface oxidation (about 20 nm from the surface) (*e.g.*, Sciamma-O'Brien *et al.*, 2010; Carrasco *et al.*, 2016). During my Ph.D., I thus had to characterize and consider this surface oxygen contamination factor. A Ph.D. is currently in progress at LATMOS, focusing on developing a way to collect the tholins without exposing them to air, and thus limiting their oxidation.

Note that prior to each series of experiments, to ensure the cleanliness of the reactor, the chamber is cleaned with acetic acid (common vinegar), then with ethanol. This manual cleaning of the reactor interior is followed by baking at ~110 °C to desorb water adsorbed on the reactor walls, as well as a N_2 or O_2 plasma to desorb remaining impurities on the electrodes and the plasma confining cage. The chamber is finally pumped with a turbomolecular pump (*Adixen ATP 80/100*), until reaching a secondary vacuum comprised between 6×10^{-7} and 1.5×10^{-6} mbar.

II.1.3. Summary of selected previous studies involving the PAMPRE experimental setup

As described in Section II.1.1, Titan has been much studied owing to the NASA/ESA *Cassini-Huygens* mission. Pluto has an atmosphere whose chemical composition is close to that of Titan, namely an atmosphere essentially composed of nitrogen and methane, with nevertheless ~500 ppm of carbon monoxide. We can therefore consider Titan as a benchmark to experimentally approach the case of Pluto.

II.1.3.a. Physical and chemical properties of Titan-simulated atmosphere

The electrons of the plasma discharge are sufficiently energetic to dissociate and ionize N_2 and CH_4 continuously injected into the reactor (Pintassilgo, Cernogora and Loureiro, 2001; Szopa, Cernogora *et al.*, 2006). *In situ* measurements performed by Quadrupole Mass Spectrometry (QMS) showed that the first reactions induced by the electrons of the discharge have a slow kinetics. The CH_4 concentration is reduced by more than half and reaches steady state in ~100 seconds (Sciamma-O'Brien *et al.*, 2010; Wattieaux *et al.*, 2015). The dissociation of CH_4 releases atomic hydrogen H in the plasma, and this release follows a linear law with the percentage of injected CH_4 (Carrasco *et al.*, 2012).

For Titan experiments, the main neutral molecule produced, detected by QMS, is hydrogen cyanide HCN, which is one key precursor to the formation of Titan aerosol analogues (Gautier *et al.*, 2011; Carrasco *et al.*, 2012; Wattieaux *et al.*, 2015; Dubois, Carrasco, Petrucciani, *et al.*,

2019). Furthermore, the formation of HCN is enhanced with increasing initial CH_4 concentration (Gautier *et al.*, 2011; Carrasco *et al.*, 2012; Dubois, Carrasco, Petrucciani, *et al.*, 2019), as well as when CO is added to the N_2:CH_4 reactive gas mixture (Fleury *et al.*, 2014). Nevertheless, CO was shown to play an inhibiting role in the formation of Titan's aerosols, by disturbing the CH_4 consumption kinetics (Fleury *et al.*, 2014). *In situ* analyses of the gas phase composition of Titan-simulated atmosphere revealed that N-bearing molecules, such as nitriles, amines and imines favorable to polymerization, play a crucial role in the formation of Titan's aerosols (Gautier *et al.*, 2011, 2012; Carrasco *et al.*, 2012). Numerous neutral molecules up to *m/z* 100 with raw formulae $C_xH_yN_z$ were detected by QMS (Gautier *et al.*, 2011; Carrasco *et al.*, 2012; Dubois, Carrasco, Petrucciani, *et al.*, 2019), as well as various positive and negative ions (Dubois, Carrasco, Bourgalais, *et al.*, 2019; Dubois *et al.*, 2020). In particular, the detection of heteroaromatic molecules in Titan-simulated atmosphere supported the hypothesis of chemical pathways involving Nitrogenous Poly-Aromatic Heterocycles (NPAH) instead of Poly-Aromatic Hydrocarbons (PAH) for the growth of Titan's aerosols (Gautier *et al.*, 2011). In addition, methanimine CH_2=NH and ethanamine CH_3CH=NH (Carrasco *et al.*, 2012), as well as ethylene C_2H_4 (Dubois, Carrasco, Petrucciani, *et al.*, 2019) were suggested to be major precursors to Titan tholin formation. Moreover, C_2 cations[7], such as $HCNH^+$ and $C_2H_5^+$, are thought to play a key role in efficient gas-to-solid conversion, *i.e.*, tholin growth (Dubois *et al.*, 2020). Finally, the detection of N-bearing anions such as CN^-, $CHNN^-$, C_3N^-, C_3HNN^- and $C_2N_3^-$ highlighted the important role of negative ion chemistry in Titan's aerosol growth (Dubois, Carrasco, Bourgalais, *et al.*, 2019). These results are in agreement with observations made on Titan by INMS (Ion and Neutral Mass Spectrometer) (*e.g.*, Waite *et al.*, 2005, 2007; Cravens *et al.*, 2006; Vuitton, Yelle and Anicich, 2006; Vuitton, Yelle and McEwan, 2007) and by CAPS-ELS (Cassini Plasma Spectrometer – Electron Spectrometer) (*e.g.*, Coates *et al.*, 2007; Vuitton *et al.*, 2009), onboard the *Cassini* orbiter (*e.g.*, Waite *et al.*, 2004; Young *et al.*, 2004).

The time required for the formation of Titan tholins is several tens of seconds after turning on the plasma, and this delay depends on the experimental conditions (*e.g.*, plasma pressure, composition of the reactive gas mixture, *etc.*) (Alcouffe *et al.*, 2010). Especially, the efficiency of tholin production depends on the N_2:CH_4 mixing ratio in the reactive gas mixture, with two competitive chemical regimes. The production of Titan tholins in PAMPRE is particularly favored when the initial CH_4 percentage is comprised between 4% and 6%, depending on the

[7] C_w cations correspond to N-bearing organic cations $C_xH_yN_z^+$ with $w = x + z$.

operating plasma pressure (0.9 or 1.7 mbar) (Sciamma-O'Brien *et al.*, 2010). At low CH_4 concentration, the tholin production rate is proportional to the percentage of consumed CH_4. In contrast, the tholin production is inhibited for initial CH_4 percentage significantly higher than 5%, when the atomic H concentration is too high in the reactive plasma (Sciamma-O'Brien *et al.*, 2010; Carrasco *et al.*, 2012). Once formed, the presence of tholins in the plasma affects the physical and chemical properties of the plasma. In particular, free electrons from the plasma discharge attach to the solid particles, rendering tholins electronegative. Therefore, the electron density decreases in the plasma, which is compensated by the increase in the energy of these electrons (Alcouffe *et al.*, 2010; Wattieaux *et al.*, 2015).

II.1.3.b. Physical and chemical properties of Titan aerosol analogues

Electronegative tholins form and are maintained in levitation in the plasma between the two electrodes, the solid particles are therefore spherical in shape. When the grains reach a limit size, they are ejected out of the plasma, the spherical particles therefore have a relatively uniform size distribution (Hadamcik *et al.*, 2009). Scanning Electron Microscopy (SEM) measurements revealed the filamentous growth of the spherical particles, observed on the surface of the particles (Hadamcik *et al.*, 2009). The particle size depends on the experimental conditions, such as N_2:CH_4 mixing ratio in the reactive gas mixture, gas flow rate injected into the reactor, plasma duration, *etc.* (Hadamcik *et al.*, 2009). In particular, the addition of CO in a N_2:CH_4 reactive gas mixture leads to the formation of averagely larger solid particles (Fleury *et al.*, 2014).

The optical constants (*n* and *k* indices) of Titan tholins produced with the PAMPRE experimental setup were determined by spectroscopic ellipsometry (Mahjoub *et al.*, 2012, 2014; Sciamma-O'Brien *et al.*, 2012). These optical constants depend on the N_2:CH_4 mixing ratio in the reactive gas mixture (Mahjoub *et al.*, 2012) and on the synthesis temperature (Mahjoub *et al.*, 2014). *n* index (real part of the complex refractive index) is increased, whereas *k* index (imaginary part of the complex refractive index) is lowered when the initial CH_4 concentration increases. This observation agrees with the color of Titan tholins ranging from dark brown for tholins produced in a N_2:CH_4 = 99%:1% gas mixture to light yellow for tholins produced in a N_2:CH_4 = 90%:10% gas mixture. This result was attributed to the proportion of N-bearing molecules that differ between Titan tholins synthesized with different N_2:CH_4 mixing ratios (Mahjoub *et al.*, 2012). Regarding the effect of synthesis temperature, it was observed that the tholin thin films produced at cryogenic temperature (105 K) are characterized by higher *n*-values and lower *k*-values than thin films produced at ambient temperature (300 K) over the

whole analyzed [350-1,000 nm] wavelength range. This observation was interpreted as different chemical composition of the reactive gas mixture at low temperature, due to condensation effects on the cold walls of the plasma confining cage (Mahjoub *et al.*, 2014).

Fourier-Transform InfraRed (FTIR) analyses performed on Titan tholins showed that tholins produced with a low concentration of CH_4 (1%) are polymer-kind materials containing more amine functional groups (–NH and $–NH_2$) than tholins produced with high methane concentration (10%), whereas tholins produced with a high concentration of CH_4 have a higher contribution of aliphatic carbon (–CH, $–CH_2$ and $–CH_3$) (Gautier *et al.*, 2012). Nitrile –C≡N, isocyanide –N≡C, aromatic and aliphatic –C=C and –C=N functional groups were also detected in the mid-IR (Quirico *et al.*, 2008; Gautier *et al.*, 2012). Absorption bands around 2,900 cm^{-1} (3.4 µm) found in Titan tholin spectrum are in agreement with observations made by VIMS (Visual and Infrared Mapping Spectrometer) instrument onboard *Cassini* orbiter (*e.g.*, Brown *et al.*, 2004). This confirms an aerosol contribution in Titan's atmosphere, which is well reproduced by Titan tholins synthesized in the laboratory (Gautier *et al.*, 2012). In the far-IR, Titan tholin spectrum displays many similarities with observations made by *Cassini*-CIRS (Composite InfraRed Spectrometer) instrument (*e.g.*, Flasar *et al.*, 2004), namely absorption bands at 325 cm^{-1} (30.76 µm), 515 cm^{-1} (19.41 µm), 1,380 cm^{-1} (7.24 µm) and 1,450 cm^{-1} (6.89 µm) (Gautier *et al.*, 2012). An aromatic signature in the [4.1-5.3 µm] spectral range was also identified in tholins synthesized with the PAMPRE experimental setup in N_2:CH_4, N_2:CH_4:C_5H_5N and in N_2:C_5H_5N gas mixtures (Mathé *et al.*, 2018). This aromatic signature is in agreement with the detection of aromatic fragments released by Titan tholins after being submitted to thermal degradation (pyrolysis) and analysis by ThermoGravimetric Analysis-Differential Scanning Calorimetry-Mass Spectrometry (TGA-DSC-MS) (He *et al.*, 2015).

Elemental composition analyses indicated that elemental mass percentages in Titan tholins depend on the N_2:CH_4 mixing ratio in the reactive gas mixture in which the tholins are synthesized. When the initial CH_4 concentration increases, the carbon mass percentage stays roughly constant, whereas the nitrogen mass percentage significantly decreases and the hydrogen mass percentage significantly increases. This result regards Titan tholins as spherical grains (Sciamma-O'Brien *et al.*, 2010; Carrasco *et al.*, 2016). For Titan tholins as thin films, when the initial CH_4 concentration increases, only the N mass percentage decreases, whereas the C and H mass percentages remain constant (Carrasco *et al.*, 2016). A comparative study of the chemical compositions of Titan tholins as solid spherical grains and thin films concluded that these two sorts of samples are chemically different. Thin films are less rich in nitrogen and

hydrogen than solid grains, probably due to efficient etching occurring on the thin films staying in the plasma discharge for 2-3 hours (Carrasco *et al.*, 2016).

High-Resolution Mass Spectrometry (HRMS) measurements were made on both soluble in methanol and insoluble fractions of Titan tholins (*e.g.*, Carrasco *et al.*, 2009; Pernot *et al.*, 2010; Hörst *et al.*, 2012; Gautier *et al.*, 2014, 2016; Maillard *et al.*, 2018). The soluble fraction – which represents up to 35% in mass of the solid samples (Carrasco *et al.*, 2009) – is significantly different from the insoluble fraction – which represents 65% of the global mass sample (Maillard *et al.*, 2018). Mass spectra of both fractions exhibit regularly-spaced peak clusters, suggesting a polymeric nature for the molecules constituting Titan tholins (Carrasco *et al.*, 2009; Pernot *et al.*, 2010; Gautier *et al.*, 2014; Maillard *et al.*, 2018). However, the soluble fraction of Titan tholins is identified as an ideal $(CH_2)_m$-$(HCN)_n$ polymer (Pernot *et al.*, 2010; Gautier *et al.*, 2014), whereas the insoluble fraction is composed of a set of polymers with an average formula $(C_4H_3N_2)_n$ (Maillard *et al.*, 2018). HRMS analyses and Gas Chromatography coupled to Mass Spectrometry (GC-MS) measurements confirmed the presence of amino acids (alanine $C_3H_7NO_2$, glycine $C_2H_5NO_2$ and histidine $C_6H_9N_3O_2$) and nucleotide bases (adenine $C_5H_5N_5$, cytosine $C_4H_5N_3O$, guanine $C_5H_5N_5O$, thymine $C_5H_6N_2O_2$ and uracil $C_4H_4N_2O_2$) in Titan tholins (Hörst *et al.*, 2012).

II.1.3.c. Adapting the PAMPRE experimental setup to the study of Pluto

Relying on these earlier studies for Titan, we were able to develop a robust experimental protocol for the study of Pluto's aerosols, from their formation in the upper atmosphere, to their deposition on the surface, through their interactions with the atmosphere during their sedimentation. In particular:

- Previous studies on Titan performed with the PAMPRE experimental setup helped us to identify the optimal experimental conditions (gas flow rate, pressure, temperature, *etc.*) to be used for the simulation of Pluto's atmospheric chemistry and the synthesis of Pluto aerosol analogues. For instance, in order not to be biased by heterogeneous chemistry due to condensation effects as discussed in Mahjoub *et al.* (2014), we chose to conduct our simulation experiments at ambient temperature.
- Observations made in 2015 by the Alice spectrograph onboard *New Horizons* showed that CH_4 concentration varied from ~0.3% near the surface to 50% at 1,450 km of altitude above the surface (Young *et al.*, 2018). Similarly, Global Circulation Model (GCM) results showed that the mean atmospheric concentration of CH_4 varies from

0.5% to 5% during Pluto's seasons/epochs (Bertrand and Forget, 2016; Bertrand *et al.*, 2019). As said before, previous studies on Titan showed that the CH_4:N_2 mixing ratio has a significant effect on Titan's atmospheric chemistry and on the chemical composition and the optical constants of Titan's aerosols. In the scope of this Ph.D. thesis, to account for the variability in terms of chemical composition in Pluto's atmosphere at different altitudes or at different seasons/epochs, we therefore systematically conducted our studies for at least two different gas mixtures/samples.

The atmosphere of Pluto being similar to that of Titan (N_2 and CH_4 as main components), with nevertheless a greater proportion of CO (~500 ppm), the previous studies on Titan can be used as a reference "without oxygen" to identify and understand the effect of CO on the chemical system N_2:CH_4:CO which constitutes Pluto's atmosphere.

II.1.4. Experiments performed during this Ph.D., using the PAMPRE experimental setup

II.1.4.a. Experimental conditions relative to Chapter III – Investigating the chemical composition of Pluto's atmosphere

In Pluto's atmosphere, the photochemistry takes place between 300 and 900 km of altitude (Stern *et al.*, 2018; Young *et al.*, 2018). In this range of altitude, the CH_4 mixing ratio as observed in 2015 varies from ~0.3% to ~10% (Young *et al.*, 2018), while the CO mixing ratio is constant, around 500 ppm (Lellouch *et al.*, 2017). During this Ph.D., in relation with the detection altitude of Pluto's aerosols (*e.g.*, Gladstone and Young, 2019) and our knowledge of the formation processes of Titan's aerosols at higher altitudes (*e.g.*, Hörst, 2017), we thus chose to simulate the chemistries occurring in Pluto's atmosphere at ~400 km of altitude and between 600 and 700 km of altitude above the surface. The two Pluto gas mixtures injected in the reactor were thus composed of N_2:CH_4:CO = 99%:1%:500ppm (mixture thereafter called A_{400}) or N_2:CH_4:CO = 95%:5%:500ppm (mixture A_{650}) (Lellouch et al., 2017; Young et al., 2018) (Table II.2).

Table II.2: Experimental conditions relative to Chapter III – Investigating the chemical composition of Pluto's atmosphere.

Experimental conditions	**Chapter III**		
Energy deposition	RF CCP 30 W		
Plasma confining cage	No		
Pressure	0.9 ± 0.1 mbar		
Temperature	Ambient temperature		
Composition of the gas mixture injected into the reactor	**N_2**	99%	95%
	CH_4	1%	5%
	CO	500 ppm	500 ppm
Corresponding altitude above the surface on Pluto and acronym	**Altitude**	~400 km	600-700 km
	Acronym of Pluto-simulated atmosphere	A_{400}	A_{650}

II.1.4.b. Experimental conditions relative to Chapter IV – Investigating the chemical composition of Pluto's aerosols

For the study of the chemical composition of Pluto aerosol analogues, solid grains were synthesized. For this purpose, the plasma was run for a week per experimental parameters (*i.e.*,

different CH_4:N_2 mixing ratios to mimic different altitudes in Pluto's current atmosphere or Pluto's atmosphere at different seasons or epochs) (Bertrand and Forget, 2016; Gladstone *et al.*, 2016; Stern, Binzel, *et al.*, 2017; Young *et al.*, 2018; Bertrand *et al.*, 2019). Note that in order to understand the impact of the presence of CO in Pluto's atmosphere, aerosol analogues were also synthesized from a plasma containing 99% of N_2 and 1% of CH_4, but without CO. This type of analogue – equivalent to Titan aerosol analogues – has been studied for decades (*e.g.*, Khare *et al.*, 1984; McDonald *et al.*, 1994; Coll *et al.*, 1999, 2013; Imanaka *et al.*, 2004; Szopa, Cernogora *et al.*, 2006; Sekine *et al.*, 2008; Imanaka and Smith, 2010; Cable *et al.*, 2012; Sciamma-O'Brien, Upton and Salama, 2017) (Table II.3).

Table II.3: Experimental conditions relative to Chapter IV – Investigating the chemical composition of Pluto's aerosols.

Experimental conditions	**Chapter IV**			
Energy deposition	RF CCP 30 W			
Plasma confining cage	Yes			
Pressure	0.9 ± 0.1 mbar			
Temperature	Ambient temperature			
Sample type	Solid grains (solubilized in a methanol:acetonitrile mixture for HRMS measurements only)			
Composition of the gas mixture injected into the reactor	**N_2**	99%	95%	99%
	CH_4	1%	5%	1%
	CO	500 ppm	500 ppm	-
Corresponding altitude above the surface on Pluto and acronym	**Altitude**	~400 km	600-700 km	[Titan-type]
	Acronym of Pluto aerosol analogues	P_{400}	P_{650}	$P_{CO\text{-}free}$

II.1.4.c. Experimental conditions relative to Chapter V – Investigating the optical constants of Pluto's aerosols

For the determination of the optical constants of Pluto aerosol analogues, thin films onto silicon substrates were synthesized from gas mixtures with different N_2:CH_4:CO mixing ratios. For each condition, the plasma was run for 90 minutes, forming films with thicknesses no more than 1 µm to minimize surface roughness and ensure the validity of the spectroscopic ellipsometry technique for the measurements (Fujiwara, 2007; Mahjoub *et al.*, 2012; Sciamma-O'Brien *et al.*, 2012) (Table II.4).

Table II.4: Experimental conditions relative to Chapter V – Investigating the optical constants of Pluto's aerosols.

Experimental conditions	**Chapter V**			
Energy deposition	RF CCP 30 W			
Plasma confining cage	Yes			
Pressure	0.9 ± 0.1 mbar			
Temperature	Ambient temperature			
Sample type	Thin films onto Si substrates			
Composition of the gas mixture injected into the reactor	**N_2**	99.5%	99%	95%
	CH_4	0.5%	1%	5%
	CO	500 ppm	500 ppm	500 ppm
Thickness of the thin film	**Plasma duration: 90 min**	549.8 ± 0.6 nm	540.9 ± 0.2 nm	651.0 ± 0.7 nm
Corresponding altitude above the surface on Pluto and acronym	**Altitude**	< 350 km	~400 km	600-700 km
	Acronym of Pluto aerosol analogues	F_H	F_{400}	F_{650}

II.1.4.d. Experimental conditions relative to Chapter VI – Investigating the organic matter on Pluto's surface

For experiments performed at GANIL, we produced Pluto tholins as thin films with different thicknesses onto different substrates (CaF_2, MgF_2, Si, SiO_2, ZnSe, and ZnS), and as solid grains pressed onto a pre-pressed KBr (potassium bromide) pellet (Table II.5). All these samples were synthesized from a unique N_2:CH_4:CO = 99%:1%:500ppm gas mixture (Table II.6).

More than 30 different samples were synthesized and irradiated during the two irradiation campaigns conducted at GANIL/IRRSUD (see Table II.5), but in Chapter VI, I will only present the results obtained for two samples thereafter named "F_P" (which is a thin film synthesized during 4 hours onto a MgF_2 substrate) and "P_P" (which is Pluto tholins as spherical grains pressed onto a pre-pressed KBr pellet) (Table II.6). This choice is not only for the sake of clarity. Indeed, among all the thin films synthesized at different thicknesses onto different substrates, pre-characterizations made by Eric Quirico with binocular loupe, and UV-Vis and IR spectroscopy showed that the most homogeneous thin films, with the least roughness, and with the best optical quality were those synthesized onto MgF_2 substrate, for plasma duration lower than 8 hours (Eric Quirico, personal communication). In addition, MgF_2 substrates have the advantage that they can be used over a wide spectral range, from 91,000 cm^{-1} (110 nm) to

1,100 cm^{-1} (9 µm). The results presented in Chapter VI, Section VI.2.2 and Section VI.2.4 thus are related to a thin film of Pluto tholins deposited onto a MgF_2 substrate during a 4-hour synthesis time, while the results presented in Section VI.2.1 and Section VI.2.3 are related to a pressed pellet of Pluto tholins, half of whose surface was irradiated (the other half having been hidden by a piece of aluminum).

Table II.5: Samples synthesized for the irradiation campaigns at GANIL/IRRSUD.

Substrate	Synthesis duration
CaF_2	1× 8 hours
	1× 16 hours
	1× 24 hours
MgF_2	1× 10 minutes
	1× 35 minutes
	1× 2 hours
	2× 4 hours
	1× 8 hours
	1× 16 hours
	1× 24 hours
	1× 32 hours
Si	2× 8 hours
	2× 16 hours
	1× 24 hours
SiO_2	1× 8 hours
	1× 16 hours
	1× 24 hours
ZnSe	1× 2 hours
	1× 4 hours
	1× 12 hours
	1× 32 hours
ZnS	1× 8 hours
	1× 16 hours
Pellet of solid grains	9 pellets with different thicknesses (*i.e.*, different [Pluto tholins:KBr] ratios) ~2 weeks for the synthesis of Pluto tholins and the preparation of pellets

Table II.6: Experimental conditions relative to Chapter VI – Investigating the organic matter on Pluto's surface.

Experimental conditions	**Chapter VI**		
Energy deposition	RF CCP 30 W		
Plasma confining cage	Yes		
Pressure	0.9 ± 0.1 mbar		
Temperature	Ambient temperature		
Composition of the gas mixture injected into the reactor	**N_2**	**CH_4**	**CO**
	99%	1%	500 ppm
Sample types and acronym of Pluto aerosol analogues	Thin film onto MgF_2	Solid grains (pressed onto a pre-pressed KBr pellet)	
	F_P	P_P	

II.2. Swift heavy ion irradiation at GANIL

GANIL, the National Large Heavy Ion Accelerator based in Caen (France) (Figure II.5), provides heavy ion beams for a variety of experiments ranging from nuclear and atomic physics to radiobiology, astrophysics and astrochemistry. Using its five cyclotrons, GANIL delivers ion beams whose energies vary from a few keV to several MeV per nucleon (eV/A) (Gales, 2010).

Figure II.5: The GANIL facility based in Caen, France. GANIL is composed of five cyclotrons delivering heavy ion beams whose energies range from a few keV/A to several MeV/A. *Credit*: The picture is from Gales (2010).

To perform an experiment at GANIL, beam time must be requested through a committee-evaluated proposal. During this Ph.D., two proposals were submitted and accepted. I participated in the project P1174 "Organics aging at the surface of Pluto and Charon" whose Principal Investigator (P.I.) was Eric Quirico, and I proposed and will lead the project P1215 "Organics processing by charged particles at the surface of Pluto".

For the project P1174, we used the IRRSUD (*IRRadiation SUD*) beamline (Figure II.6). IRRSUD is a low-energy beamline created in 2004 (Gales, 2010). At IRRSUD, a wide range of stable atomic ions from Carbon (^{12}C) to Uranium (^{238}U) is accelerated at energies from 0.25 to 1 MeV/A. The use of ions with such energies allows to simulate the effects of high-energy Galactic Cosmic Rays (GCR) on a material of interest.

Figure II.6: IRRSUD beamline at GANIL facility. IRRSUD is a low-energy beamline which was used to simulate the effects of high-energy Galactic Cosmic Rays (GCR) on photochemical aerosols deposited on Pluto's surface.

For the project P1215, I requested and was granted beamtime on the ARIBE (*Accélérateur de Recherches sur les Ions de Basse Energie*) beamline (Figure II.7). ARIBE is a very low-energy beamline inaugurated in 2005 (Gales, 2010). At ARIBE, multi-charged ions (*e.g.*, Ar^{17+}, Xe^{30+}) with energies ranging from a few eV to 25 keV per charge (keV/q) are available. Using ions of such energies allows to simulate the effects of low-energy GCR and of Solar Wind (SW) on a material of interest.

Figure II.7: ARIBE beamline at GANIL facility. ARIBE is a very low-energy beamline which will be used to simulate the effects of low-energy GCR and of Solar Wind (SW) on photochemical aerosols deposited on Pluto's surface.

Several *in situ* characterization devices (*e.g.*, CASIMIR, IGLIAS) can be mounted on IRRSUD or ARIBE beamlines.

II.2.1. Ion-matter interaction

An energetic ion penetrating a material interacts both with the nuclei and the electrons of the atoms in the target matter (*e.g.*, Schlutig, 2001; Avasthi and Mehta, 2011; Faure, 2016; Augé, 2017). These interactions result in a dissipation of the kinetic energy of the incident ion. The energy loss per unit path length $\frac{dE}{dx}$ of an ion projectile (expressed in eV.g^{-1}.cm^{-2}) is the sum of three contributions:

$$\frac{dE}{dx} = \frac{dE}{dx}_{nuclear} + \frac{dE}{dx}_{electronic} + \frac{dE}{dx}_{radiation} \quad \text{(Equation II.1)}$$

For projectiles consisting of swift heavy ions, the energy loss in radiative processes, such as bremsstrahlung and Cherenkov radiation, is negligible (Avasthi and Mehta, 2011). Such energy loss processes only occur for electron projectiles or for extremely high ion energies.

Equation II.1 thus becomes:

$$\frac{dE}{dx} = \frac{dE}{dx}_{nuclear} + \frac{dE}{dx}_{electronic} \quad \text{(Equation II.2)}$$

Usually, we refer to the "stopping power" S(E) (expressed in eV.µm^{-1}) which depends on the density ρ (in g.cm^{-3}) of the material:

$$S(E) = -\frac{1}{\rho}\frac{dE}{dx} = S_n(E) + S_e(E) \quad \text{(Equation II.3)}$$

with $S_n(E)$ the nuclear stopping power; and $S_e(E)$ the electronic stopping power. $S_n(E)$ and $S_e(E)$ are expressed in eV.µm^{-1}.

As it penetrates the target condensed matter, the incident ion slows down (decrease of velocity). The incident ion implants itself in the material as soon as its incident energy has been fully transferred and deposited in the matter. The distance where the ion is implanted is called the "penetration depth" or "range" of the particle d*x* (expressed in µm):

$$dx = \int_0^{E_0} \frac{1}{S(E)} dE \quad \text{(Equation II.4)}$$

with E_0 the initial kinetic energy of the incident ion.

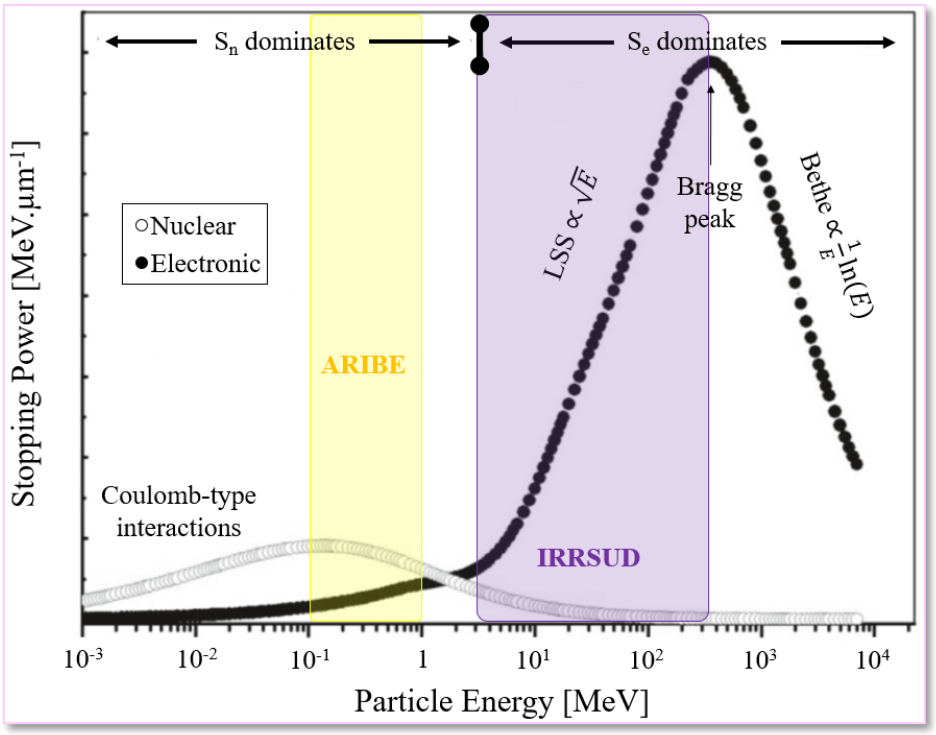

Figure II.8: Nuclear (S_n) and electronic (S_e) stopping powers as a function of incident ion energy. The white dots correspond to S_n, whereas the black dots correspond to S_e. The purple rectangle represents the incident ion energies available on the IRRSUD beamline, whereas the yellow rectangle represents the incident ion energies available on the ARIBE beamline. *Credit*: The figure is adapted from Avasthi and Mehta (2011).

As is the case for any condensed material, the deceleration of an incident ion penetrating Pluto tholins can be described by two quasi-independent processes:

- **S_e**: At high energy (typically above 100 keV), the energy loss mechanism is dominated by inelastic interactions between the incident ion and the electrons of the atoms in Pluto tholins (Figure II.8, black dots). These collisions, involving small energy loss per interaction, cause electronic excitation or ionization of target atoms in Pluto tholins. In Figure II.8, we observe a peak in the electronic stopping power curve, which is referred as Bragg peak. Around this energy, the incident ion is not completely devoid of its electrons; the ion captures electrons from the target matter (*i.e.*, Pluto tholins) and its state of charge decreases. At energies above the Bragg peak, the incident ion is completely devoid of its electrons, S_e is proportional to $\frac{1}{E}\ln(E)$ and is described by the Bethe-Bloch relation (Bethe, 1930; Bloch, 1933). The incident ion goes through various states of charge. When it enters the condensed matter constituting Pluto tholins, the incident ion is devoid of its electrons. By slowing down in Pluto tholins, the incident ion captures the electrons from the target atoms constituting Pluto tholins, until reaching

its equilibrium charge. At energies below the Bragg peak, the incident ion is surrounded by most of its electrons, S_e is proportional to the ion velocity ($\sqrt{E}$) and is described by Lindhard-Scharff-Schiøtt (LSS) theory (Lindhard, Scharff and Schiøtt, 1963). Note that the lower the energy of incident ions is, the more chemical bonds are disrupted. Indeed, during the collision between the low-energy ion and a target atom in Pluto tholins, the electronic clouds of the two members overlap. A rearrangement of the electronic shells takes place during this interaction, resulting in the formation of a quasi-molecule with its own electronic states.

- **S_n**: At low energy (typically below 10 keV), the energy loss mechanism is dominated by a cascade of elastic collisions between the incident ion and the nuclei of the atoms in Pluto tholins (Figure II.8, white dots). These interactions are of Coulomb type, more or less shielded (*e.g.*, Emslie, 1978). These collisions cause the atom nuclei to recoil. If the collision energy is sufficient (above the recoil threshold energy), the displaced nuclei do not return to their original position, leaving spaces called "vacancies" in the initial atomic lattice. After displacement, the nuclei relax by dissipating their energy in the surrounding material constituting Pluto tholins, resulting in strong structural and chemical changes.

S_e and S_n depend on the mass and energy of the incident ion. In particular, both S_e and S_n increase with increasing mass of the incident ion.

The first complete description of the interaction between an incident ion and condensed matter can be found in Lindhard, Scharff and Schiøtt (1963). Since then, computer simulation methods were developed to calculate the motion of ions in a medium. The best known simulation program is SRIM (*Stopping and Range of Ions in Materials*), which was developed by Ziegler, Ziegler and Biersack (2010) and is available on http://www.srim.org/. With SRIM software, nuclear and electronic stopping powers, as well as penetration depth, can be calculated.

As for any condensed matter, the Pluto tholin surface erodes when irradiated by swift heavy ions. Both nuclear and electronic interactions lead to the ejection of atoms/molecules belonging to the layers close to the surface of the tholin material. This effect is called sputtering, characterized by a sputtering yield *Y*:

$$Y = \frac{average\ number\ of\ ejected\ atoms}{number\ of\ incident\ particles} \quad \text{(Equation II.5)}$$

The erosion efficiency strongly depends on the [incident ion/target matter] couple.

As previously said, for experiments performed at GANIL, we produced Pluto tholins as thin films onto different substrates (CaF_2, MgF_2, Si, SiO_2, ZnSe, and ZnS) (see Table II.5 and Figure II.9.left), and as solid grains pressed onto a pre-pressed KBr pellet (see Table II.5 and Figure II.9.right).

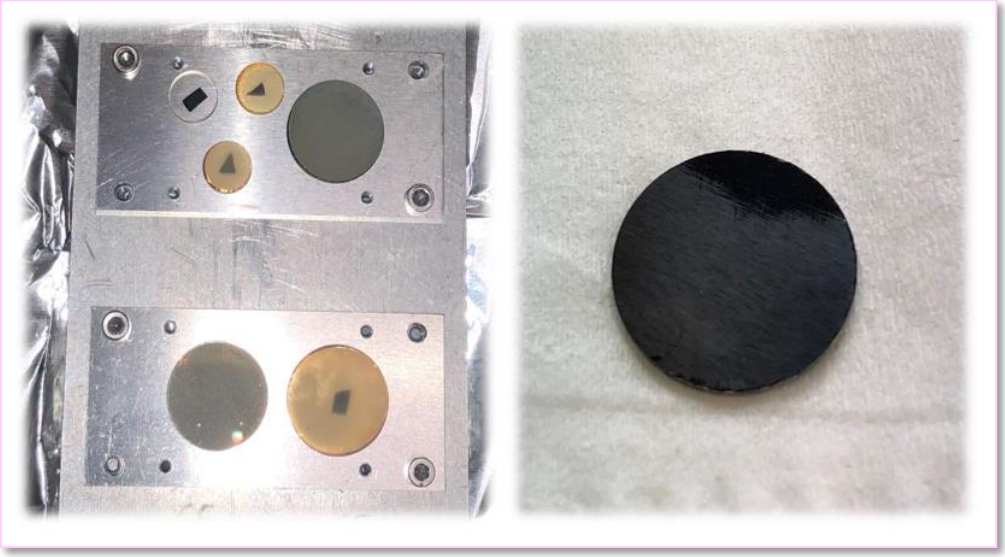

Figure II.9: Pluto tholins synthesized with the PAMPRE experimental setup for experiments at GANIL/IRRSUD. These samples mimic the organics present on Pluto's surface. *Left*: Pluto tholins as thin films onto different substrates (here, MgF_2, ZnS, Si). With this type of samples, only the electronic interactions can be investigated. *Right*: Pluto tholins as solid grains pressed onto a pre-pressed KBr pellet. With this type of samples, both electronic and nuclear interactions can be investigated.

For both samples, the incident ions arrive with high kinetic energies. For Pluto tholins as thin films (Figure II.9.left), as the material is very thin (thickness less than 1 µm), the incident ion cannot decelerate sufficiently to allow nuclear interactions to occur; only the electronic interactions are thus affecting the Pluto tholins. For Pluto tholins as pressed pellets (Figure II.9.right), the sample is a few hundred µm thick, which is sufficient to effectively slow down the incident ion. Electronic interactions are therefore considered close to the sample surface, whereas in the depth of the material, both nuclear and electronic interactions affect the Pluto tholins.

II.2.2. Experiments performed on the IRRSUD beamline

Two sessions of experiments were conducted on the IRRSUD beamline, in April 2019 (5 days, 24/24) and in February 2020 (5 days, 24/24). By irradiating Pluto tholins with Swift Heavy Ions (SHI), these experiments intended to reproduce the effect of Galactic Cosmic Rays on the

chemical composition and optical properties of Pluto's photochemical aerosols that have sedimented on the surface.

Pluto's atmosphere is very thin (Gladstone *et al.*, 2016; Young *et al.*, 2018); the high-energy part of the GCR flux can thus reach the surface. To justify the use of ions available on the IRRSUD beamline, preliminary numerical calculations of the GCR flux density at Pluto's surface were realized, based on the flux density of Webber and Yushak (1983) and stopping powers of the mean atmospheric column density. The calculations were made by Eric Quirico for hydrogen H (Figure II.10.left) and iron Fe (Figure II.10.right) nuclei with SRIM software (Ziegler, Ziegler and Biersack, 2010). H and Fe nuclei are the lightest and the heaviest abundant ions contributing to the deposited dose.

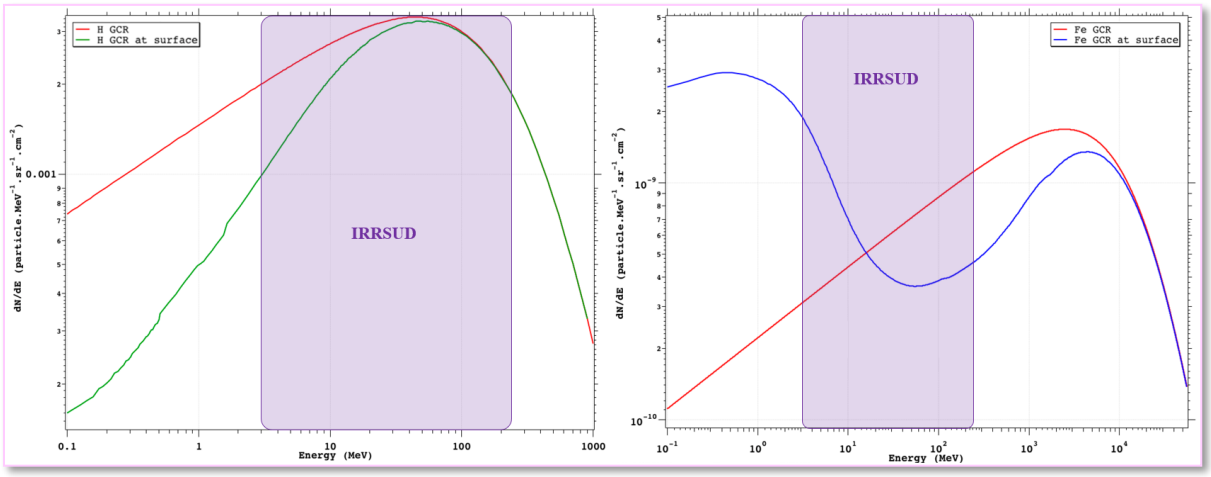

Figure II.10: Numerical calculations of the GCR flux density at Pluto's surface, based on Pluto's present-time atmosphere and the flux density of Webber and Yushak (1983) (red curves). The calculations were made for H nuclei (*left*, green curve) and for Fe nuclei (*right*, blue curve) with SRIM software (Ziegler, Ziegler and Biersack, 2010). The purple rectangle represents the incident ion energies available on the IRRSUD beamline.

The IRRSUD beamline provides stable atomic ions from Carbon (^{12}C) to Uranium (^{238}U) accelerated at energies from 0.25 to 1 MeV/A. Using this beamline, the available incident ion energies [E = nucleon number A × accelerating energy in MeV/A] therefore range from 3 to 238 MeV (purple rectangle in Figure II.10.left and Figure II.10.right). At these energies, numerical calculations show that the GCR flux density reaching Pluto's surface is significant. Indeed, values range from 1×10^{-3} to 3×10^{-3} particle.MeV^{-1}.sr^{-1}.cm^{-2} if considering H nuclei and from 4×10^{-10} to 2×10^{-9} particle.MeV^{-1}.sr^{-1}.cm^{-2} if considering Fe nuclei.

During the first session of experiments (April 2019), Pluto tholins were irradiated at 40 K with ^{58}Ni ions accelerated at 0.58 MeV/A, resulting in an incident ion energy

E = 58 × 0.58 = 33.64 MeV. Considering a density ρ = 1.0 g.cm^{-3} for Pluto tholins (*e.g.*, Hörst and Tolbert, 2013), calculations made with SRIM software resulted in a nuclear stopping power S_n = 17.3 keV.µm^{-1} and in an electronic stopping power S_e = 4,130 keV.µm^{-1}. The implantation depth dx of Ni ions in the Pluto tholin material is approximately 18 µm.

During the second session of experiments (February 2020), Pluto tholins were irradiated at ambient temperature with ^{136}Xe ions accelerated at 0.55 MeV/A, resulting in E = 136 × 0.55 = 74.8 MeV. Considering ρ = 1.0 g.cm^{-3} for Pluto tholins (*e.g.*, Hörst and Tolbert, 2013), SRIM calculations resulted in S_n = 35.9 keV.µm^{-1} and in S_e = 8,140 keV.µm^{-1}. The implantation depth dx of Xe ions in the Pluto tholin material is approximately 28 µm.

For both sessions, the ion flux φ was set between 10^8 and 5×10^9 ions.cm^{-2}.s^{-1}. Different samples were irradiated with different fluences F. Note that the fluence is the product of the ion flux with the irradiation duration dt (see Equation II.6). The fluence F (expressed in cm^{-2}) thus corresponds to the number of ions reaching the sample:

$$F = \varphi \times dt \quad \text{(Equation II.6)}$$

The fluences used for the two samples considered in this Ph.D. thesis, F_P and P_P irradiated with ^{136}Xe ions, are provided in Table II.7:

Table II.7: Fluences deposited on the considered samples F_P and P_P. These samples were irradiated with ^{136}Xe ions accelerated at 0.55 MeV/A, resulting in an incident ion energy E of 74.8 MeV.

Sample	Fluence [cm^{-2}]
F_P	5×10^{10}
	1×10^{11}
	2×10^{11}
	5×10^{11}
	1×10^{12}
	2×10^{12}
	4×10^{12}
P_P	**1×10^{14}**

In the literature, the values of the GCR flux arriving at the surface of Pluto differ greatly, and it is complicated to calculate a single timescale value corresponding to our laboratory irradiation experiments. Indeed, if we rely on Madey, Johnson and Orlando (2002) and Cruikshank *et al.* (2015), the GCR flux deposited at the surface of Pluto would be 6.9×10^9 eV.cm^{-2}.s^{-1}. In the study by Cooper *et al.* (2003) modeling the cosmic ray flux for eV to GeV protons H^+ at 40

AU, for protons of about 75 MeV[8], the corresponding flux would be about 2×10^{-5} ions.cm^{-2}.s^{-1}.sr^{-1}.MeV^{-1}. Finally, in the study by Shen *et al.* (2004) exploring the dose of cosmic rays and UV photons interacting with icy water grains in the outer Solar System, the average energy deposited would be of the order of 6.2×10^{-15} eV.molecule^{-1}.s^{-1}. For our irradiation experiments on F_P and P_P samples (see the final fluences deposited on these samples in Table II.7, in bold), we report in Table II.8 the corresponding timescales at the surface of Pluto, according to the different GCR flux values available in the literature.

Table II.8: Experiments performed at GANIL/IRRSUD and corresponding timescales on Pluto.

Sample	Final fluence [cm^{-2}]	On Pluto [terrestrial year]	Reference used for the GCR flux reaching Pluto's surface
F_P	4×10^{12}	~1,400	Madey, Johnson and Orlando (2002) Cruikshank *et al.* (2015)
		~13.4×10^{6}	Cooper *et al.* (2003)
		~32.3×10^{6}	Shen *et al.* (2004)
P_P	1×10^{14}	~35,000	Madey, Johnson and Orlando (2002) Cruikshank *et al.* (2015)
		~336.1×10^{6}	Cooper *et al.* (2003)
		~811.8×10^{6}	Shen *et al.* (2004)

In Table II.8, we note that depending on the value of the GCR flux used for our calculations, the timescales at the surface of Pluto corresponding to our laboratory irradiation experiments vary greatly, from simple to double to 4 orders of magnitude difference. Keep in mind that these values are based only on estimates on the GCR flux reaching Pluto's surface, and thus only represent the lower limit for actual Pluto's organic material irradiation time equivalence. In order to compare the exact timescales of our irradiation experiments with the one received by the organic material on Pluto's surface, one has to determine the exact deposited doses in both cases. This dose depends not only on the fluence and the stopping power of the incident ion, but also on the material properties, such as the average molar mass, the density, the porosity,

[8] This value of 75 MeV corresponds to the incident energy of the ^{136}Xe ions used during our second irradiation campaign at GANIL/IRRSUD.

etc. Moreover, the GCR flux arriving at the surface of Pluto can be modulated by the presence of Pluto's thin atmosphere, a parameter which is not currently accounted for in the results presented in Table II.8. Finally, Pluto's surface is continuously supplied with haze material, with a mass flux of haze particles to Pluto's surface estimated at 5×10^{-7} kg.m^{-2}.year^{-1} (Grundy *et al.*, 2017, 2018). In the same way, this continuous renewal of organic material on Pluto's surface is not accounted for in the preliminary calculations presented in Table II.8. In summary, precise modeling is required, that goes beyond the scope of the preliminary results presented in Chapter VI.

II.2.3. Experiments planned on the ARIBE beamline

These experiments should have been conducted in 2020 but were postponed due to the Covid-19 pandemic, and are currently planned for end-2021 or beginning-2022. This manuscript thus does not contain results on the low-energy ARIBE beamline.

Experiments are planned on the ARIBE beamline, which provides multi-charged ions with incident ion energies below 1 MeV. The numerical calculations made by Eric Quirico with SRIM software (Ziegler, Ziegler and Biersack, 2010) for H and Fe nuclei (Figure II.11.left and Figure II.11.right, respectively) show that charged particles of low energy (E < 1 MeV) are also significant at Pluto's surface (Figure II.11, yellow rectangle).

The Solar Wind and the low-energy part of the GCR flux can therefore also affect the chemical composition and the optical properties of the organics present on Pluto's surface. With these experiments, we expect significant differences with respect to the experiments performed on the IRRSUD beamline, due to a significant contribution of nuclear deposition.

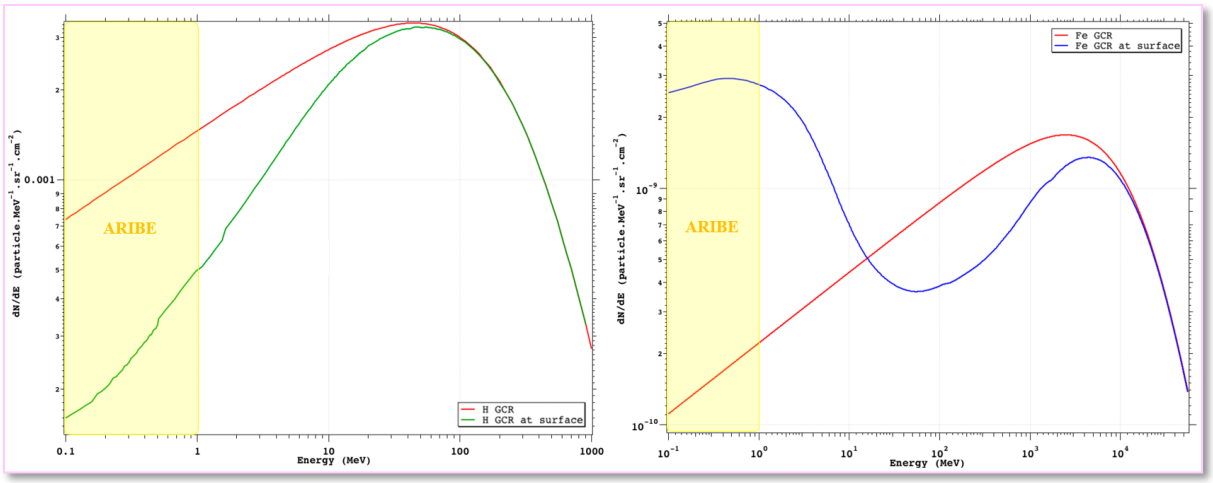

Figure II.11: Numerical calculations of the GCR flux density at Pluto's surface, based on Pluto's present-time atmosphere and the flux density of Webber and Yushak (1983) (red curves). The calculations were made for H nuclei (*left*, green curve) and for Fe nuclei (*right*, blue curve) with SRIM software (Ziegler, Ziegler and Biersack, 2010). The yellow rectangle represents the incident ion energies available on the ARIBE beamline.

II.3. Analytical techniques employed

II.3.1. Analytical techniques relative to Chapter III – Investigating the chemical composition of Pluto's atmosphere

II.3.1.a. Quadrupole Mass Spectrometry

II.3.1.a.*α*. *In situ* analysis of neutral molecules and cations

The neutral and cationic molecules produced in the cold plasma mimicking Pluto's atmospheric chemistry were probed *in situ* at steady state by a *Hiden Analytical EQP 200* Quadrupole Mass Spectrometer (QMS). The analyses were driven by *MASsoft 7* software.

Prior to the analyses, the QMS was properly tuned to detect neutral species and cations with a high sensitivity at parts-per-million (ppm) level[9].

For cation analysis only, the sampling interface of the QMS is placed as close as possible to the plasma (*i.e.*, the "cursor" is at the 230 mm value indicated on the ruler fixed on the QMS bench), without disturbing it (for visualization purpose, see Figure II.12).

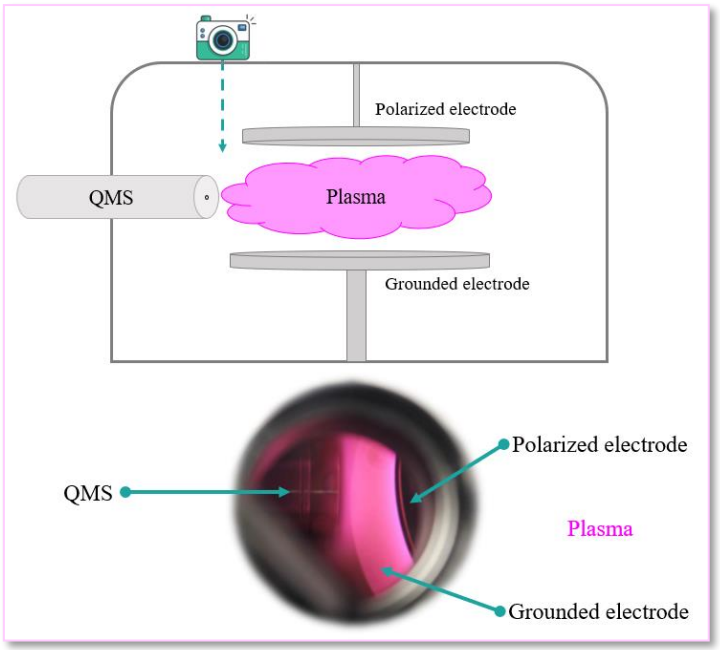

Figure II.12: Visualization of the position of the QMS head for cation analysis. *Top*: Scheme showing the position of the QMS head close to the plasma. *Bottom*: Picture taken through a glass window present on the cover plate of the PAMPRE reactor. We note that the head of the QMS is as close as possible to the plasma diffusing in the reactor between the two electrodes.

[9] See the brochure "EQP Series" from *Hiden Analytical*: https://www.hidenanalytical.com/wp-content/uploads/2018/12/TDS-172-2_EQP-Series-Brochure_Low-Res.pdf

The gaseous molecules pass through an orifice of 100 µm in diameter. The neutral species are ionized in the electron ionization source, the electron energy of which was settled at 70 eV to be able to interpret our mass spectra by comparing them with reference spectra from *National Institute of Standards and Technology* (NIST) *Chemistry WebBook* (more details below). The cations formed in the plasma bypass the ionization source[10]. During the analyses, the pressure in the QMS is maintained at 4.0×10^{-6} mbar, thereby avoiding secondary reactions between the molecules passing through the ion optics of the QMS. The mass analyzer covers a mass range from *m/z* 1 to *m/z* 200 (*m/z*, mass-to-charge ratio), with a resolving power of 1 atomic mass unit (u). The signal is obtained over an integration period (called dwell time) of 2,000 ms. In order to compare the different spectra acquired, the peak intensities were then normalized to the most intense peak in each mass spectrum, typically at *m/z* 28.

The mass spectra of the neutrals (acquired in RGA mode, Residual Gas Analysis) result from the accumulation of 40 scans, while those of the cations (acquired in +SIMS mode, Secondary Ion Mass Spectrometer in positive mode) correspond to the accumulation of 10 scans.

A scheme of the QMS is given in Figure II.13.

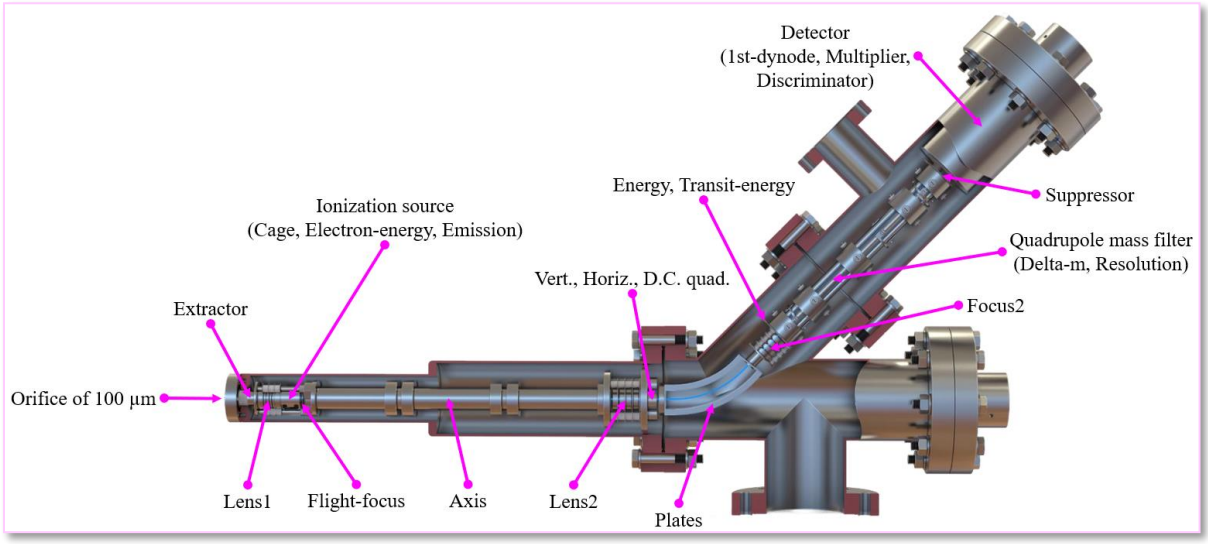

Figure II.13: Scheme of the different parts of *Hiden Analytical EQP 200* Quadrupole Mass Spectrometer. *Credit*: The scheme is adapted from the brochure "EQP Series" from *Hiden Analytical*.

A detailed description of the different parts of the analytical instrument and the operation principles for the neutral and cation detection are reported in Table A1.1 in Appendix A1.

[10] The electron ionization source is turned off during the analysis of positive ions.

Prior to the analyses, PAMPRE (reactor walls, and electrodes) and the sampling orifice of the QMS were cleaned, heated and pumped down to $P_{PAMPRE} \approx 8\times10^{-7}$ mbar and $P_{QMS} < 5\times10^{-9}$ mbar. To ensure the cleanliness of the PAMPRE experimental setup and the QMS, we systematically recorded before each series of experiments a mass spectrum of the QMS isolated on itself and of the PAMPRE reactor at secondary vacuum (see an example in Figure II.14).

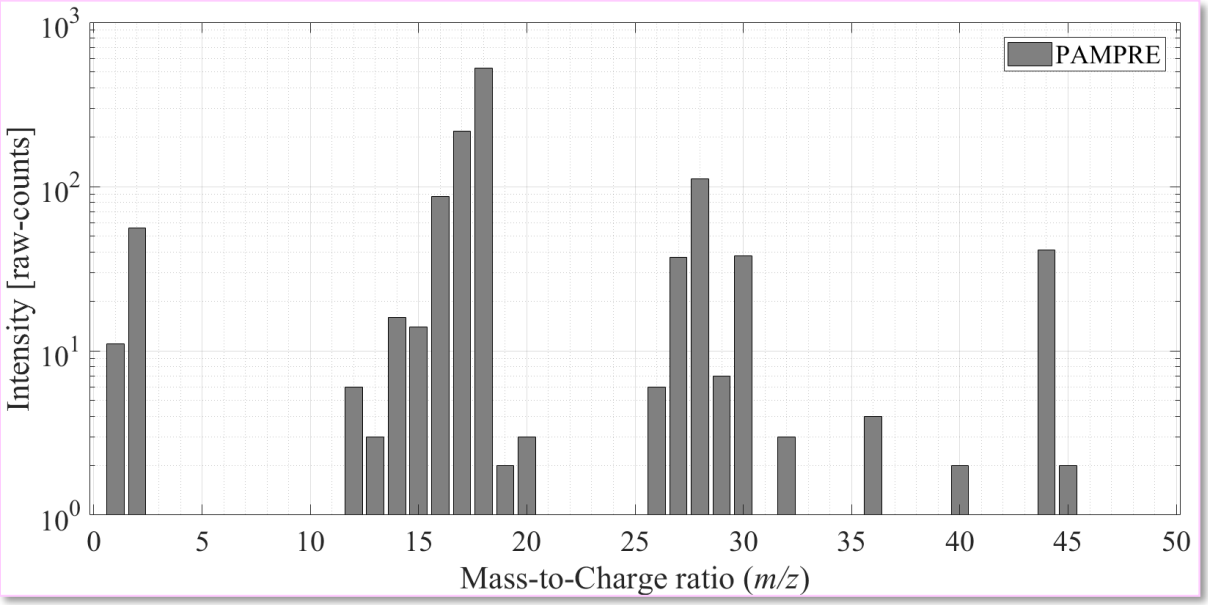

Figure II.14: Blank mass spectrum of the PAMPRE reactor, at $P_{PAMPRE} \approx 8\times10^{-7}$ mbar. This mass spectrum is consistent with residual air (*m/z* 28 and 44) present at low intensity in the QMS and in the PAMPRE reactor, as well as with residual water (*m/z* 18, 17, and 16) adsorbed in the QMS and on the reactor walls.

In Figure II.14, the low-intensity peaks at *m/z* 28 and *m/z* 44 are consistent with residual air (N_2 and CO_2) remaining in the QMS and the PAMPRE reactor, whereas the more intense peaks at *m/z* 18, 17, and 16 correspond to residual water adsorbed on the walls of the chamber of the QMS, and the walls of the PAMPRE reactor.

II.3.1.a.β. Deconvolution of the mass spectra of neutral molecules

The molecules passing through the electron ionization source undergo ionizing dissociation, generating several fragments at different *m/z*. These fragments constitute a specific "fingerprint" for each molecule, called fragmentation pattern. It is thus necessary to decompose the mass spectra in order to retrieve the contribution of all the molecules to a given peak.

The method developed by Gautier *et al.* (2020) is based on the assumption that the measured mass spectrum is a linear combination of the relative concentrations of different contributing

molecules multiplied by their fragmentation patterns. This method uses interior-point least square fitting to retrieve the relative concentrations of the molecules suspected to contribute to the mass spectrum from a fragmentation pattern database. The database containing the molecules to be used by the deconvolution method was populated with the fragmentation patterns provided by the *NIST Chemistry WebBook* (https://webbook.nist.gov/chemistry/). The molecules included in my database were based on observations of Pluto's atmosphere (Gladstone *et al.*, 2016; Lellouch *et al.*, 2017; Young *et al.*, 2018; Steffl *et al.*, 2020), as well as on results of photochemical models (Lara, Ip and Rodrigo, 1997; Krasnopolsky and Cruikshank, 1999; Luspay-Kuti *et al.*, 2017; Wong *et al.*, 2017; Krasnopolsky, 2020). To complete the identification of species contributing to the mass spectra of Pluto-simulated atmospheres, I added in our database other relevant species after testing the suitability of hundreds of molecules. These tested molecules were inspired by species already detected in Titan's atmosphere and/or predicted by Titan photochemical models.

Molecular fragmentation patterns are highly dependent on the geometry of the ionization source within the instrument used for measurements. For a given molecule, the relative intensities of the fragments measured in the laboratory can vary drastically between the reference mass spectra and the actual measured data. These uncertainties are typically in the order of 30% but can be as high as 100% for some fragments/molecules. This induces a major degeneracy in the solving of the linear combination that typically prevents it altogether.

To circumvent this issue, the deconvolution method developed by Gautier *et al.* (2020) uses a Monte-Carlo sampling of the relative intensities in the database fragmentation patterns to generate hundreds of thousands slightly different databases. The mass spectrum is then deconvoluted with every single one of these databases, and statistical analysis allows to retrieve the composition of the gas phase analyzed by the QMS. In this manuscript, I deconvoluted the mass spectra of the neutral molecules in Pluto-simulated atmosphere using this method by adapting the code (developed in *MATLAB*) from Gautier *et al.* (2020) to my dataset and Pluto's atmosphere.

In addition to the deconvolution and to compensate for the higher ionization efficiency of larger molecules, the ionization cross sections of each suspected molecule are ultimately accounted for in order to retrieve the mixing ratios of each contributing molecule.

Regarding the ionization cross sections, for some common species, they were taken from the *NIST Physical Measurement Laboratory*

(https://physics.nist.gov/PhysRefData/Ionization/molTable.html). For the molecules for which the electron-ionization cross section (Q in Å^2) was not provided by *NIST*, we had to calculate it with the semi-empirical formula proposed by Fitch and Sauter (1983) allowing to calculate the electron-ionization cross section of an organic molecule from its atomic composition:

$$Q = 0.082 + \sum_{i=1}^{8} \alpha_i n_i \quad \text{(Equation II.7)}$$

where α_i is a coefficient depending on the type of atom and n_i is the number of atoms for each element constituting the organic molecule of interest. This formula is valid for molecules containing C, H, N, O, Cl, Br, I, and F. The α_i coefficients for C, H, N, and O are respectively: 1.43, 0.73, 1.20, and 1.10 Å^2.

Figure II.15 shows an example of deconvolution result obtained with the method developed by Gautier *et al.* (2020) for the blank mass spectrum of the PAMPRE reactor (shown in Figure II.14).

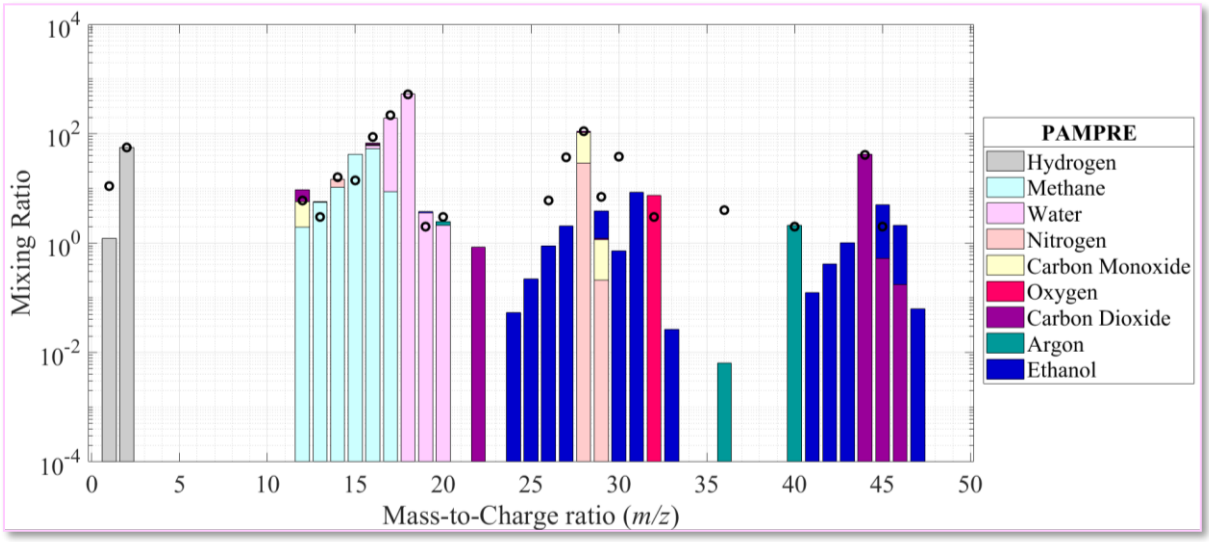

Figure II.15: Example of deconvolution result for the blank mass spectrum of the PAMPRE reactor using the method developed by Gautier *et al.* (2020). The black dots correspond to the experimental mass spectrum shown in Figure II.14, while the colored bars correspond to the calculated contributions of each molecule.

The experimental mass spectrum (black dots in Figure II.15) being globally well reproduced (colored bars in Figure II.15) by the known molecules injected into the PAMPRE reactor (N_2, CH_4, CO) and the common contaminants in QMS, this supports the suitability of the Gautier *et al.* (2020) deconvolution code for the processing of our Pluto data.

II.3.2. Analytical techniques relative to Chapter IV – Investigating the chemical composition of Pluto's aerosols

II.3.2.a. Infrared spectroscopy – Attenuated Total Reflectance

The infrared spectra of Pluto aerosol analogues were acquired using an Attenuated Total Reflectance (ATR) accessory on the *Thermo Scientific Nicolet 6700* spectrometer, driven by *OMNIC* software. The purpose of this analysis is to characterize the chemical functions present in the molecules constituting Pluto aerosol analogues (*e.g.*, Blum and John, 2012).

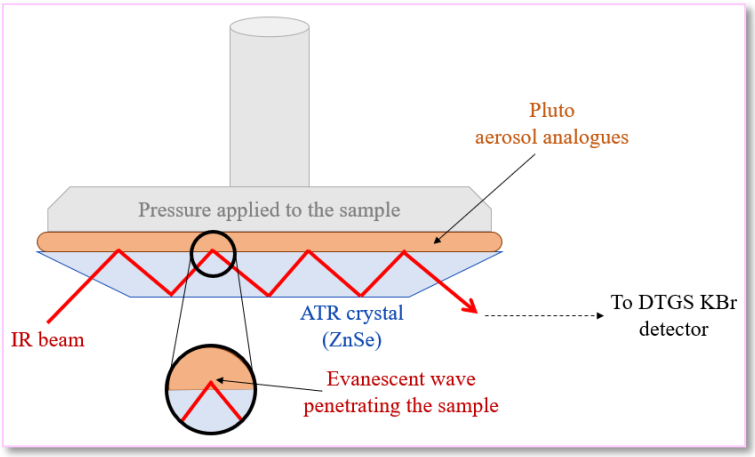

Figure II.16: Scheme presenting the operating principle of the Attenuated Total Reflectance (ATR) technique. *Credit*: The scheme is inspired by Blum and John (2012).

A spatula tip of the aerosol analogues was deposited on a zinc selenide (ZnSe) crystal. Direct contact between the sample and the crystal was facilitated by applying pressure to the sample. An IR beam was pointed onto the crystal at an angle of incidence greater than a critical angle ensuring propagation of the beam in the crystal. Under these conditions, an evanescent wave is generated and passes through the sample for a few micrometers (0.5 to 5 µm). Depending on the chemical functions present in the molecules constituting the aerosol analogues, the evanescent wave is absorbed at different characteristic wavelengths. The resulting altered wave is collected by a DTGS KBr (deuterated-triglycine sulfate, potassium bromide) detector (*e.g.*, Blum and John, 2012) (Figure II.16).

The spectrum presented in Figure IV.2 (see Chapter IV, Section IV.1.2) results from the accumulation of 250 scans, acquired between 500 and 4,000 cm^{-1}, with a resolution of 4 cm^{-1}. Background spectrum was also acquired before the sample analysis, to remove the contribution of ambient atmosphere.

II.3.2.b. High-Resolution Mass Spectrometry – Orbitrap™

II.3.2.b.α. Sample preparation for high-resolution mass spectrometry analysis

To analyze the molecular composition of the aerosol analogues by high-resolution mass spectrometry (Orbitrap™ technique), I dissolved about 1 mg of the samples in 1 mL of a 50/50 %(v/v) methanol/acetonitrile (*Carlo Erba*, UHPLC-MS quality) mixture (MeOH/ACN) in a polypropylene vial at ambient conditions. The choice of the solvent was based on Titan aerosol analogues literature, extracting most of the soluble fraction (Somogyi *et al.*, 2005; Carrasco *et al.*, 2009). The vials were then agitated and centrifuged for a few minute and then, the supernatants were diluted at 0.5 $mg.mL^{-1}$ in order to stabilize the ionization source and to optimize the ionization yield. The sample preparation is schematized in Figure II.17.

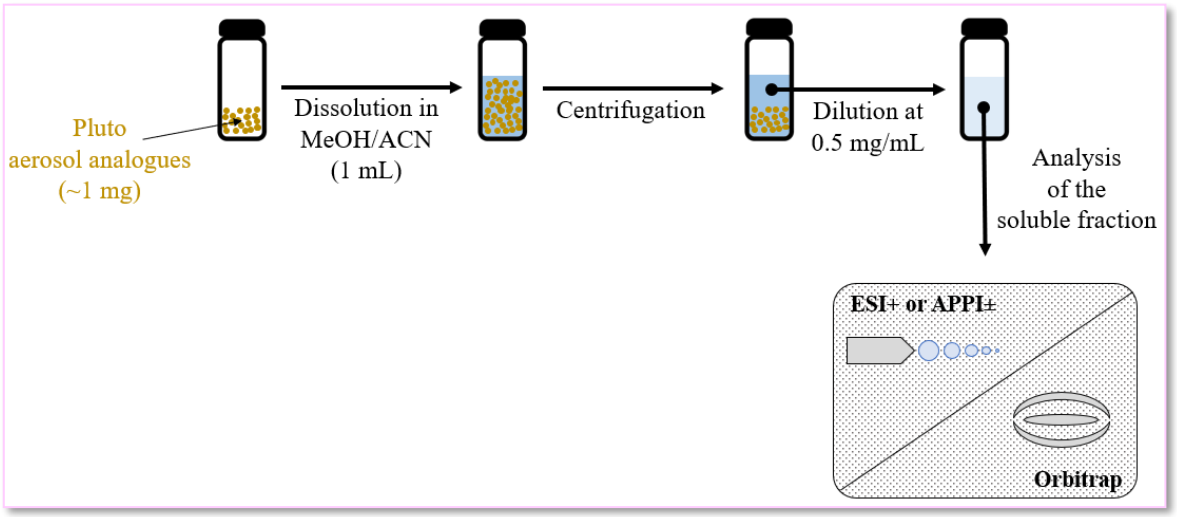

Figure II.17: Sample preparation for High-Resolution Mass Spectrometry (HRMS) analysis.

II.3.2.b.β. High-Resolution Mass Spectrometry – ESI-Orbitrap and APPI-Orbitrap

In order to determine the chemical formulae of the molecules constituting the soluble fraction of Pluto aerosol analogues, I analyzed them by High-Resolution Mass Spectrometry (HRMS). We used the analytical instrument *LTQ Orbitrap™ XL* (*ThermoFisher Scientific*) installed at IPAG (*Institut de Planétologie et d'Astrophysique de Grenoble*, Grenoble, France), a Fourier-Transform mass spectrometer combining two mass analyzers: a Linear Trap Quadrupole (LTQ) and an Orbitrap™ (Makarov *et al.*, 2006; Perry, Cooks and Noll, 2008). A scheme of the analytical instrument can be found in Figure II.18.

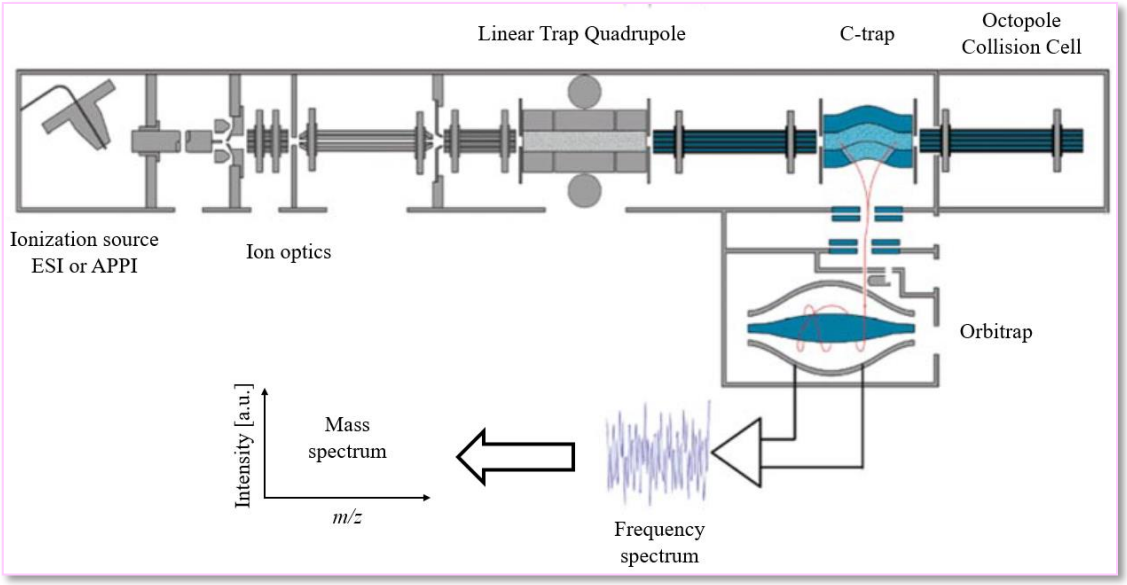

Figure II.18: Scheme of the high-resolution mass spectrometer *LTQ Orbitrap™ XL* (*ThermoFisher Scientific*). *Credit*: The scheme is adapted from Perry, Cooks and Noll (2008).

By applying a potential difference between the four electrodes constituting the quadrupole, the ions belonging to a specific mass range have their trajectories stabilized, and are therefore selected by the LTQ. The stable ion beam is then focused to the C-trap. The C-trap accumulates the ions and focalizes them in an optimal way to the Orbitrap™, which acts as mass analyzer.

Two complementary ionization sources were used: ElectroSpray Ionization (ESI) and Atmospheric Pressure PhotoIonization (APPI). ESI source is suitable for the analysis of polar molecules, whereas APPI source is adapted for the analysis of non-polar molecules (*e.g.*, Cai and Syage, 2006; Hockaday *et al.*, 2009) (Figure II.19).

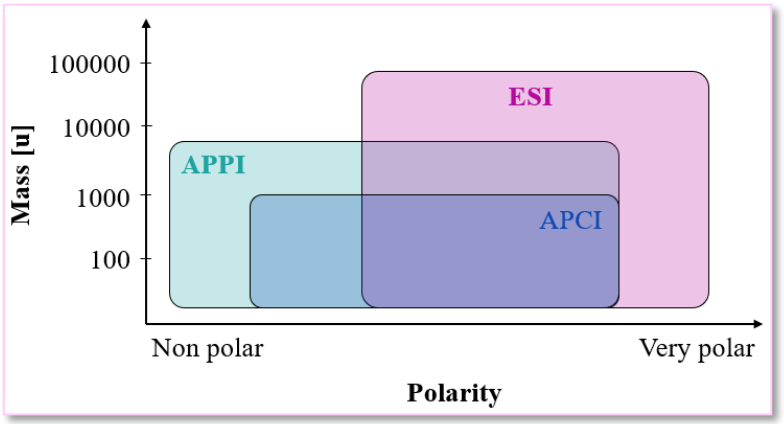

Figure II.19: Complementary ionization sources used with High-Resolution Mass Spectrometry. ESI stands for ElectroSpray Ionization, APPI for Atmospheric Pressure PhotoIonization, and APCI for Atmospheric Pressure Chemical Ionization. During this Ph.D., only ESI and APPI sources were used with Orbitrap™ to analyze Pluto aerosol analogues. *Credit*: The diagram is inspired by Wang (2015).

The first ionization source I used was ElectroSpray Ionization (ESI) in positive mode (ESI+) (*e.g.*, Yamashita and Fenn, 1984; Banks and Whitehouse, 1996). This positive mode of ionization has been widely used for Titan aerosol analogues analysis in the literature (*e.g.*, Sarker *et al.*, 2003; Somogyi *et al.*, 2005, 2012, 2016; Pernot *et al.*, 2010; Vuitton *et al.*, 2010; Gautier *et al.*, 2014, 2016) and, as a "soft" ionization method, gives access to the pristine molecules present in the soluble fractions of interest. The ESI+ source is well adapted to the analysis of samples with high proton affinity such as nitrogen- and oxygen-bearing materials (Rodgers, Schaub and Marshall, 2005). Since, elemental composition analysis of Titan aerosol analogues produced with different proportions of CO has shown that nitrogen and oxygen atoms are substantial components of the samples (Fleury *et al.*, 2014), ESI+ is thus well suited for the analysis of the tholins investigated during my Ph.D., as they were expected to contain both nitrogen and oxygen in significant amounts.

For the analyses, the solution containing the analyte is introduced into the ESI ionization source, at atmospheric pressure, up to a metallic capillary. In this capillary, the sample is subjected to a potential difference and is then ejected out of the capillary in the form of fine charged droplets, thanks to a N_2 gas flow. Under the influence of high temperature and N_2 gas flow, the solvent evaporates from the droplets, which therefore become smaller and smaller, whereas the charge density increases, favoring the charge transfer towards the analyte. Then, by electrostatic repulsion, the positive ions are ejected into the gas phase (Yamashita and Fenn, 1984; Banks and Whitehouse, 1996), and enter into the ion optics *via* a transfer tube. ESI+ is a "soft" ionization method producing mainly mono-charged $[M+H]^+$ (and few multi-charged $[M+nH]^{n+}$) ions by adding protons (H^+) without any substantial fragmentation of the molecules.

The sample was injected into the ESI+ source using a syringe through a PolyEtherEtherKetone (PEEK) capillary (direct infusion) with a fixed flow of 3 $\mu L.min^{-1}$. The capillaries were systematically washed with methanol between each sample analysis. The analyses were run using *Thermo Tune Plus* software, with the following ESI+ source parameters: a spray voltage of 3.5 kV, a sheath gas flow rate of 5 (arbitrary unit), an auxiliary gas flow rate of 0 (arbitrary unit), a sweep gas flow rate of 0 (arbitrary unit), a capillary voltage of 34 V, a capillary temperature of 275 °C and a tube lens voltage of 50 V (Table II.9).

The second ionization source I used was Atmospheric Pressure PhotoIonization (APPI) both in positive and negative modes (APPI+ and APPI–) (*e.g.*, Baim, Eatherton and Hill, 1983; Robb, Covey and Bruins, 2000; Raffaelli and Saba, 2003; Robb and Blades, 2008; Marchi, Rudaz and Veuthey, 2009). This ionization process is based on photoionization using a vacuum-ultraviolet

(VUV) lamp. Usually, a Krypton-filled lamp is used, delivering photons of 10.0 and 10.6 eV, above the ionization energies (IE) of most organic molecules of interest, but below the IE of common solvent (water, acetonitrile, methanol, *etc.*). Just like ESI, APPI is also a "soft" ionization method which does not cause fragmentation of covalent bonds in molecules. In positive mode, APPI+ produces radical molecular cations $M^{\bullet+}$ from compounds with low polarity and low proton affinity, and protonated molecules $[M+H]^+$ from compounds with higher polarity and proton affinity. In negative mode, APPI– produces radical molecular anions $M^{\bullet-}$ and deprotonated molecules $[M–H]^-$ (Raffaelli and Saba, 2003; Robb and Blades, 2008; Marchi, Rudaz and Veuthey, 2009). As a quasi-universal ionization technique (Cai *et al.*, 2005; Robb and Blades, 2008), APPI was introduced to extend the range of ionizable and therefore analyzable molecules. This technique was applied to the analysis of many classes of compounds, including for instance lipids (Cai and Syage, 2006; Roy *et al.*, 2006), hydrophobic peptides (Delobel *et al.*, 2003), PolyAromatic Hydrocarbons (PAH) (Moriwaki *et al.*, 2004; Straube, Dekant and Völkel, 2004; Purcell *et al.*, 2006), aldehydes and ketones (van Leeuwen, Hendriksen and Karst, 2004). In addition, as APPI offers a wider linear dynamic range, a higher sensitivity, and lower detection limits than ESI (Greig *et al.*, 2003; Hakala *et al.*, 2003; Hanold *et al.*, 2004; Straube, Dekant and Völkel, 2004; van Leeuwen, Hendriksen and Karst, 2004; Cai and Syage, 2006; Marchi, Rudaz and Veuthey, 2009), this ionization source is suitable for the analysis of molecules of prebiotic interest potentially present in Pluto aerosol analogues.

The sample was injected into the APPI source using a syringe through a PEEK capillary with a fixed flow of 20 $\mu L.min^{-1}$. The capillaries were systematically washed with MeOH between each sample analysis. The analyses were performed with the following APPI source parameters: a vaporizer temperature of 300 °C, a sheath gas flow rate of 30 (arbitrary unit), an auxiliary gas flow rate of 5 (arbitrary unit), a sweep gas flow rate of 1 (arbitrary unit), a discharge current of 0 µA, a capillary voltage of ± 34 V (depending on positive or negative mode), a capillary temperature of 275 °C and a tube lens voltage of ± 50 V (depending on positive or negative mode) (Table II.9).

For each ionization mode used, in order to increase the signal/noise ratio, each mass spectrum (Figure IV.1, Figure IV.10 and Figure IV.11, in Chapter IV) is the mean of 4 scans and each scan is the sum of 128 microscans (*i.e.*, a cycle of ion residency in the Orbitrap™ cell plus acquisition read-out time). The maximum ion injection time allowed into the Orbitrap™ was 500 ms. This parameter that can be set on the analytical instrument corresponds to the maximum time allowed to reach a target value of 10^6 ions in the Orbitrap™ for each microscan.

The mass spectra were acquired with a resolution $m/\Delta m$ set to 100,000 at m/z 400.

Table II.9 summarizes the parameters implemented in *Thermo Tune Plus* software for the different ionization sources employed with the *LTQ Orbitrap™ XL* instrument.

Table II.9: Parameters implemented in Thermo Tune Plus software for the different ionization sources used with the LTQ Orbitrap™ XL analytical instrument.

	ESI+	**APPI+**	**APPI–**
Ion formed	$[M+H]^+$	$M^{\bullet+}$ and $[M+H]^+$	$M^{\bullet-}$ and $[M-H]^-$
Injection flow [µL.min^{-1}]	3	20	20
Spray voltage [kV]	3.5	-	-
Vaporizer temperature [°C]	-	300	300
Sheath gas flow rate [a.u.]	5	30	30
Auxiliary gas flow rate [a.u.]	0	5	5
Sweep gas flow rate [a.u.]	0	1	1
Discharge current [µA]	-	0	0
Capillary voltage [V]	+34	+34	-34
Capillary temperature [°C]	275	275	275
Tube lens voltage [V]	+50	+50	-50

II.3.2.b.γ. Calibration of the HRMS data and identification of the molecules

Prior to the analyses, the Orbitrap™ was externally calibrated with a mixture of caffeine, MRFA peptide[11] and Ultramark™ 1621[12]. No internal calibration was used. Mass spectra of blanks (solvent only) were also acquired before each analysis of the samples $P_{CO\text{-}free}$, P_{400} and P_{650} with the same procedure as the one used to analyze Pluto aerosol analogues (4 scans of 128 microscans with an ion injection time up to 500 ms). An example of blank mass spectrum is given in Figure II.20. For the analyses performed with the ESI+ source, in order to be sure that the identified molecules belong to Pluto aerosol analogues and not to the blank, we first wanted to remove from the mass spectra the molecules which were also present in the previously acquired blanks. Nevertheless, the fact of having acquired the blanks with an ion injection time up to 500 ms induces a bias by artificially bringing out the molecules which were present in the sample analyzed just before. Indeed, these 500 ms correspond to the maximum injection time

[11] MRFA peptide is a tetrapeptide composed of the following amino acids: Methionine (M), Arginine (R), Phenylalanine (F) and Alanine (A).
[12] Ultramark™ 1621 is a commercial mixture of fluorinated phosphazines.

allowed to the instrument to reach a target value of 10^6 ions in the Orbitrap™. The problem occurs because our Pluto tholins sample is concentrated and the 10^6 ions are reached well before the 500 ms allowed (around 50 ms), whereas for the blank, since there are only few ions, the instrument will effectively inject ions into the Orbitrap™ during 500 ms. Thus, for the same ion/contaminant, the peak in the blank mass spectrum will be 10 times more intense than the peak in the mass spectrum of Pluto tholins. In order not to risk suppressing chemical formulae that could correspond to molecules of prebiotic interest, we therefore decided not to subtract the blanks from the mass spectra of Pluto aerosol analogues acquired with APPI±/Orbitrap but to consider them as source of information for the interpretation of data.

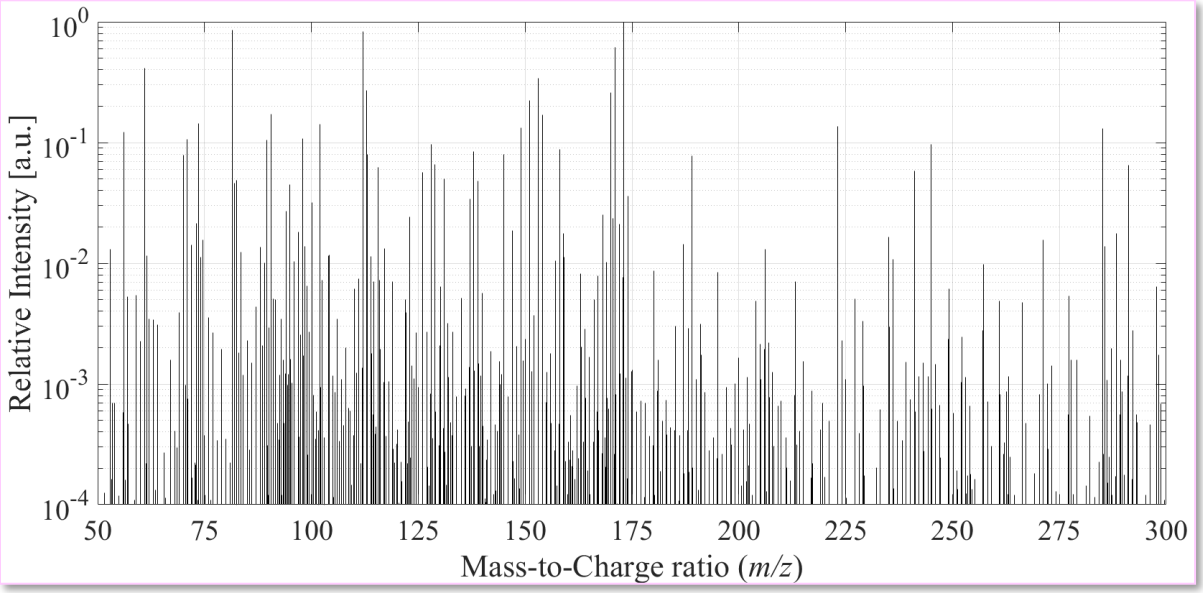

Figure II.20: ESI+/Orbitrap blank mass spectrum of a 50/50 %(v/v) methanol/acetonitrile mixture. This blank was acquired before the analysis of Pluto aerosol analogues P_{400}. The *x*-axis corresponds to the mass-to-charge ratio (*m/z*), while the *y*-axis corresponds to the relative intensity of the peaks, normalized to the most intense peak (*m/z* 173.0783). The small dark peaks are due to an aliasing effect.

Regarding ESI+/Orbitrap data only, the external calibration was not sufficient on a small *m/z* scale, because the lightest calibrator, the caffeine, was at *m/z* 195. Thus, *Attributor*, a software developed at IPAG (Grenoble, France) (Orthous-Daunay *et al.*, 2019), was also used to improve the calibration of the data. We used the masses of molecules known to be present in the $P_{CO\text{-}free}$ sample (Gautier *et al.*, 2014) to refine the calibration curve to correct the mass spectra of Pluto aerosol analogues: $C_3N_2H_5^+$ at *m/z* 69.045 and $C_4N_2H_7^+$ at *m/z* 83.060.

Attributor was also used to attribute the chemical formulae to the molecules constituting the samples analyzed by ESI+/Orbitrap and APPI±/Orbitrap. For the molecule assignment, we excluded the peaks whose intensity was 4 orders of magnitude lower than the most intense peak.

The attribution was based on a combination of *x* carbon, *y* hydrogen, *z* nitrogen and *w* oxygen ($C_xH_yN_zO_w$). The considered isotopes were: ^{12}C, ^{1}H, ^{14}N and ^{16}O. To avoid aberrant formulae, I used some restrictions. The minimum numbers of carbon, hydrogen and nitrogen atoms were set to 1 and there were no maximum numbers, regardless of the ionization source used. For ESI+/Orbitrap analyses only, the minimum number of oxygen atom was set to 0 and the maximum number limited to 3; due to the low proportion of CO injected in the reactor, it is unlikely to form highly-oxygenated molecules. For APPI±/Orbitrap analyses, I restricted the number of O atom to 10, to ensure that chemical formulae that could correspond to molecules of prebiotic interest (monosaccharides can have up to eight oxygen atoms) are not ruled out. Theoretical *m/z* with a deviation more than ± 5 ppm from the measured *m/z* were excluded (according to the instrument specifications in external calibration mode). An additional filter was applied to screen out unrealistic molecules with H/C > 5 and N/C > 3 ratios, which would be molecules with extremely exotic structures and/or C atoms with more than four bonds.

As we estimated that no unequivocal molecular assignment can be made above *m/z* 300 due to the high complexity of the material analyzed (Gautier *et al.*, 2014), I restricted our analysis from *m/z* 50 to *m/z* 300.

II.3.2.c. Elemental composition analysis

In collaboration with LGPM-CentraleSupélec (*Génie des Procédés et Matériaux-CentraleSupélec*, Gif-sur-Yvette, France), an elemental composition analysis of P_{400} and P_{650} samples was performed to determine their carbon, hydrogen, nitrogen and oxygen mass percentages.

The determination of C, H and N was performed using a Flash*Smart*™ elemental analyzer (*ThermoFisher Scientific*) under flash combustion at 930 °C. About 1-2 mg of each sample, with 1 mg of vanadium pentoxide (V_2O_5) for complete combustion, were precisely weighed into a tin container. For the determination of O, the system operated in pyrolysis mode at 1,050 °C. About 1-2 mg of each sample were weighed into a silver container. Then, tin and silver capsules were individually introduced into the combustion reactor via the *Thermo Scientific*™ *MAS Plus Autosampler*. After combustion (C, H and N) and pyrolysis (O), the resulting gases – CO_2, H_2O and N_2 – were transported by a helium flow to a copper-filled layer and then swept through a gas chromatography (GC) column to separate the combustion gases. Finally, they were detected by a Thermal Conductivity Detector (TCD) (Figure II.21).

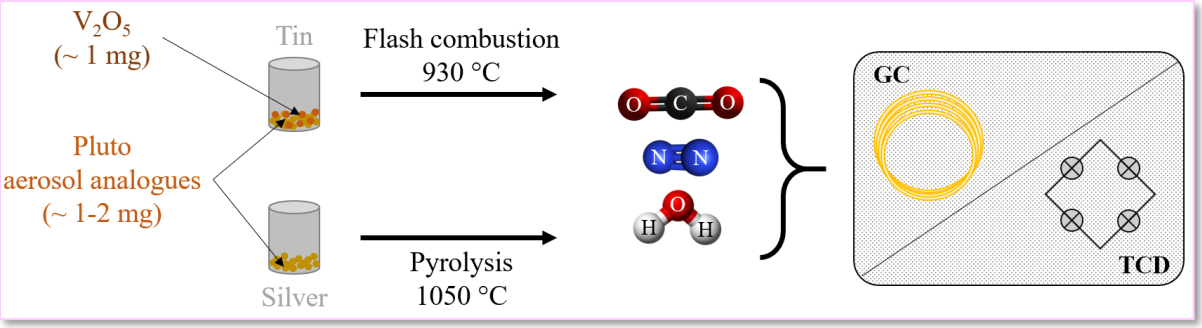

Figure II.21: Scheme presenting the operating principle of the elemental composition analysis of Pluto aerosol analogues.

Two calibration curves have been made: one for C, H and N measurements and one for O measurements. For this purpose, 0.5-5 mg of BBOT (2,5-bis(5-ter-butyl-benzoxazol-2-yl) thiophene**,** $C_{26}H_{26}N_2O_2S$) (*Fisher Scientific*, 99% purity) were analyzed as a standard using K factor as the calibration method.

II.3.2.d. Gas Chromatography coupled to Mass Spectrometry

II.3.2.d.α. Derivatization

Molecules of prebiotic interest, such as amino acids, monosaccharides or nucleotide bases, are difficult to detect with Gas Chromatography coupled to Mass Spectrometry (GC-MS) mainly because of their low volatility. As these molecules are hardly vaporizable, they are not suitable for GC-MS analysis conditions. Indeed, these compounds are composed of polar –NH, –OH, –COOH and –SH groups that can undergo hydrogen bonding and contribute to strong intermolecular attractions, thereby reducing the inherent volatility of the molecules of interest. In addition, these molecules exhibit low volatility even at high temperatures at which they begin to decompose. To overcome their low volatility and to increase the thermal stability of these compounds, chemical derivatization is thus required (Knapp, 1979; Lin *et al.*, 2008; Orata, 2012; Moldoveanu and David, 2019).

About 1 mg of Pluto aerosol analogues was introduced into a quartz DISC (Drop In Sample Chamber) tube. Then, 2.0 µL of derivatizing reagent DMF-DMA (N,N-dimethylformamide dimethyl acetal, $(CH_3)_2NCH(OCH_3)_2$) (*Sigma-Aldrich*, purity ≥ 95%) were added to the sample (Arnaud Buch, personal communication regarding the ratio to be used between the mass of Pluto aerosol analogues and the volume of DMF-DMA). The use of such a reagent is based on literature on the search for organic molecules of prebiotic interest on Mars (Freissinet *et al.*, 2010).

DMF-DMA is a reagent used in organic synthesis in two main categories of reactions, namely alkylation and formylation. As an alkylating agent, the use of DMF-DMA produces methyl esters from carboxylic acids, methyl ethers from phenols, and thioethers from aromatic and heterocyclic thiols. As a formylating agent, DMF-DMA induces the formation of enaminones from active methylene compounds and amidines from amines and amides (Kidjemet, 2002; and references therein). In the special case of amino acids, N,N-dimethylaminomethylene methyl esters are formed (Kataoka and Kijima, 1997; Nollet, 2006; Freissinet *et al.*, 2010) as follows (Figure II.22):

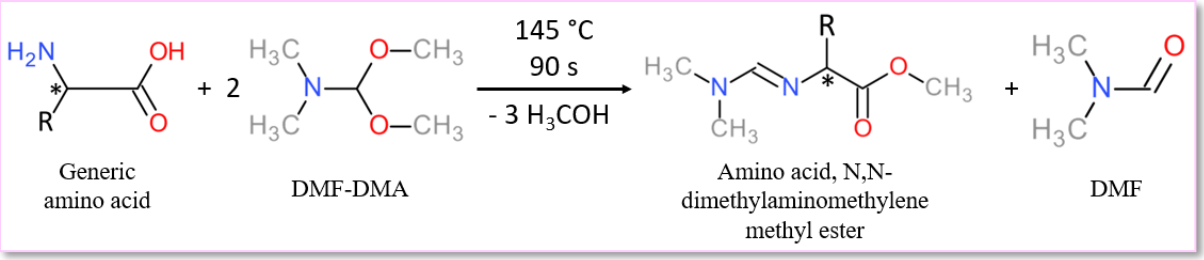

Figure II.22: Derivatization reaction between a generic amino acid and DMF-DMA. The asterisk (*) corresponds to a chiral center; if existing, then it is conserved.

DMF-DMA derivatization is particularly interesting because the derivatization reaction is simple and fast. In addition, DMF-DMA reagent leads to the formation of low-mass derivatives which are suitable for quadrupole mass spectrometry detection (Freissinet *et al.*, 2010).

The quartz DISC tube containing Pluto aerosol analogues mixed with DMF-DMA was then placed in the pyrolizer (*CDS Pyroprobe 6200*) for 90 seconds at 145 °C. The derivatization reaction occurred in one step inside the pyrolizer. The vaporized molecules were then automatically transferred into the GC-MS, through the transfer line, then the injector at 280 and 250 °C, respectively.

II.3.2.d.β. Analysis by GC-MS

GC-MS is an analytical technique combining separation of molecules from a complex mixture by gas chromatography and identification of these molecules by mass spectrometry. A complex mixture is introduced into the instrument, the molecules to be analyzed are vaporized and then carried by an inert carrier gas (mobile phase) through a GC capillary column. The molecules constituting the complex mixture are separated in the chromatographic column according to their affinity with the stationary phase inside the column. The molecules then elute at different times, known as retention time t_R. The column outlet is connected to a mass spectrometer, which acts as detector. In the MS, after the molecules have been ionized and fragmented in the

ionization source and separated by the quadrupole, mass spectra are obtained with molecule-specific fragmentation patterns. By comparing the measured mass spectra with reference spectra in libraries, the structure of the molecules can be identified (*e.g.*, Sparkman, Penton and Kitson, 2011; Poole, 2012; McNair, Miller and Snow, 2019) (Figure II.23).

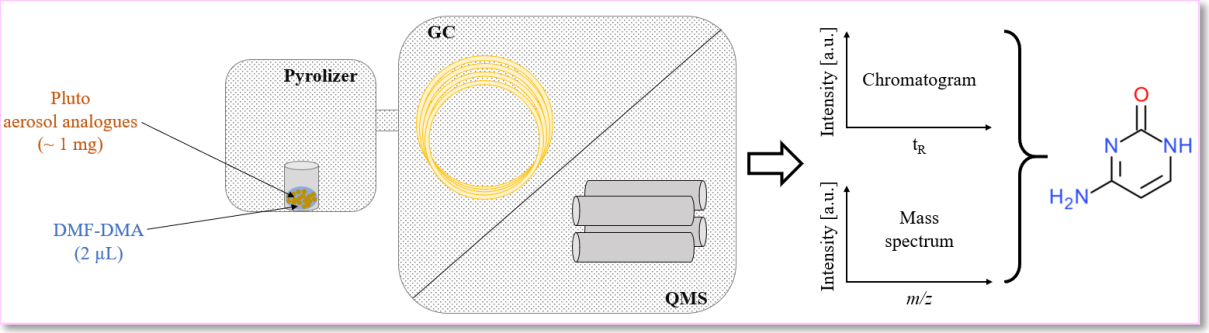

Figure II.23: Scheme presenting the operating principle of the Gas Chromatography coupled to Mass Spectrometry (GC-MS) analysis of Pluto aerosol analogues.

The analysis was performed using a *Thermo Scientific Trace 1300* gas chromatograph coupled with a *Thermo Scientific ISQ QD* single quadrupole mass spectrometer. *Thermo XCalibur* software was used to control data acquisition and to process the data.

The GC capillary column used was Rtx-20 type (*Restek*) with the following characteristics: 30 m length, Crossbond stationary phase composed of 20% diphenyl and 80% dimethyl polysiloxane (mid-polarity phase), 0.25 mm internal diameter (ID), and 0.25 µm film thickness (d_f). This type of fused silica capillary column can be used with temperatures ranging from -20 °C to 320 °C. We chose this type of capillary column, because of its mid-polarity. This stationary phase retains many different compounds, and is therefore perfectly adapted to the analysis of our complex sample. Note that the use of this type of capillary column is planned on the DraMS (Dragonfly Mass Spectrometer) instrument onboard the *Dragonfly* spacecraft, the next mission towards Titan.

Pure helium (*Air Liquide*, *ALPHAGAZ™ 2*, with impurities H_2O < 0.5 ppm, C_xH_y < 0.1 ppm, CO < 0.1 ppm, CO_2 < 0.1 ppm, O_2 < 0.1 ppm, and H_2 < 0.1 ppm) was used as the carrier gas. The following parameters were adopted: split flow of 50.0 $mL.min^{-1}$ and carrier flow of 1.00 $mL.min^{-1}$.

The temperature profile was programmed as follows: initial temperature of 40 °C, linear temperature gradient increasing at 10 $°C.min^{-1}$, final temperature of 300 °C held for 20 min.

Inside the mass spectrometer, the molecules were ionized and fragmented by electron ionization (EI), whose energy was set at 70 eV to allow comparison with reference spectra libraries. The mass analyzer was a quadrupole mass spectrometer.

A blank (DMF-DMA only) was analyzed in a similar way.

II.3.3. Analytical techniques relative to Chapter V – Investigating the optical constants of Pluto's aerosols

II.3.3.a. Theory on spectroscopic ellipsometry

In collaboration with LCP-A2MC (*Laboratoire de Chimie et Physique – Approche Multi-échelle des Milieux Complexes*, Metz, France), Pluto aerosol analogues as thin films were analyzed by spectroscopic ellipsometry. Using this analysis technique, it is possible to determine the thickness of the thin films, as well as their optical constants *n* and *k*, the real and imaginary parts respectively of the complex refractive index.

Spectroscopic ellipsometry measures the change in the polarization state between incident and reflected light on the sample (see *e.g.*, Azzam and Bashara (1977), Tompkins and Irene (2005), and Fujiwara (2007) for complete information on spectroscopic ellipsometry technique). Incident light is linearly polarized, while reflected light is elliptically polarized.

The measured values are the ellipsometric parameters Ψ and Δ, related to the ratio of the Fresnel amplitude reflection coefficients of the sample by fundamental equation:

$$r_p/r_s = \tan\psi\, e^{i\Delta} \quad \text{(Equation II.8)}$$

for p- and s-polarized light[13] with the electric field in the plane of incidence and perpendicular to the plane of incidence, respectively.

Variable Angle Spectroscopic Ellipsometry (VASE) measurements were carried out using a phase-modulated spectroscopic ellipsometer (UVISEL, *Horiba Jobin Yvon*), equipped with a 150 W Xenon light source. Corresponding ellipsometric parameters were obtained through ($I_s(\lambda)$, $I_c(\lambda)$) in the spectral range [270-2,100 nm] with 5 nm steps according an integration time of 1,000 ms, where $I_s = \sin(2\Psi)\sin(\Delta)$ and $I_c = \sin(2\Psi)\cos(\Delta)$, respectively. All measurements were performed for incidence angles between 60 and 75 degrees with 5° steps. By way of comparison, the ellipsometric analyses performed on Titan tholin thin films by

[13] r_p is the reflection coefficient of the sample for a polarization parallel to the plane of incidence ("p" for parallel) and r_s is the reflection coefficient of the sample for a polarization perpendicular to the plane of incidence ("s" for perpendicular, "senkrecht" in German).

Mahjoub *et al.* (2012, 2014) and Sciamma-O'Brien *et al.* (2012) were conducted for a single incidence angle of 70°.

The parameters of the optical model were adjusted by minimizing the Mean Square Error (MSE) defined as:

$$\mathrm{MSE} = \frac{1}{N-1}\sum_{i=1}^{N}\left[\left(I_{s,i}^{calc}(\lambda) - I_{s,i}^{exp}(\lambda)\right)^2 + \left(I_{c,i}^{calc}(\lambda) - I_{c,i}^{exp}(\lambda)\right)^2\right] \qquad \text{(Equation II.9)}$$

where *calc* stands for the calculated and *exp* for the experimental values of (I_s, I_c) and *N* the number of experimental data ($I_s(\lambda)$, $I_c(\lambda)$).

DeltaPsi2® software[14] was used to fit ellipsometric data.

The inversion of ellipsometric data was performed using a model of the sample [Si substrate / Tholin layer / Roughness layer / Air] as schematized in Figure II.24.

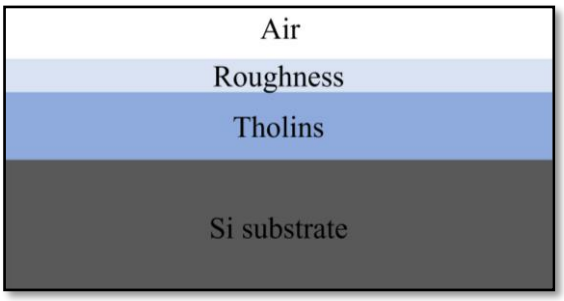

Figure II.24: Scheme of the model of the samples analyzed by spectroscopic ellipsometry.

In this model, the thickness of the roughness layer, the thickness of the tholin layer, and the dielectric function of the tholin layer were unknown, while the roughness layer was modeled by a mixture of 50% air and 50% tholins, according to Bruggeman Effective Medium Approximation (BEMA) (Bruggeman, 1935).

II.3.3.b. Determination of the optical constants of Pluto aerosol analogues with two different inversion methods: modified Tauc-Lorentz and "wavelength-by-wavelength" (λ-by-λ)

Spectroscopic ellipsometry is an indirect technique for determination of the sample physical properties (*i.e.*, thickness and optical constants). Using a model to describe the ellipsometric response of the sample by adjusting specific fit parameters is thus necessary. Basically, the model calculates the reflection coefficients r_p and r_s to retrieve the measured ellipsometric parameters Ψ and Δ. An equation system for each wavelength λ is generated: Ψ = f (n, k, t) and Δ = g (n, k, t), with *n(λ)* and *k(λ)* the real and imaginary parts respectively of the complex

[14] *DeltaPsi2*® software: https://www.horiba.com/en_en/products/detail/action/show/Product/deltapsi2-software-1648/

refractive index, and *t* the thickness of the tholin thin film. The thickness *t* of the thin film and the *n* index are initially determined in a transparent region of the thin film. Then, the fixed *t*-value is used as an input parameter to determine *n* and *k* indices in an absorbing region of the thin film. The inversion method, based on the natures of the analyzed material and the underlying substrate, is used to calculate *n* and *k* indices of the material for each wavelength.

For the study presented in Chapter V, we used sequentially two types of inversion method: modified Tauc-Lorentz dispersion model, and "wavelength-by-wavelength" (λ-by-λ) numerical inversion. Modified Tauc-Lorentz dispersion model is used to extract both thickness and a first estimate of the optical constants *n* and *k* by fitting the thickness values and the Tauc-Lorentz parameters. "λ-by-λ" numerical inversion enables an exact modeling of the optical constants *n* and *k* in spectral ranges where the fit is difficult with dispersion formulas and to check the optical constants results obtained by dispersion formulas (modified Tauc-Lorentz in our work). A "λ-by-λ" fit of the experimental data is performed on the only unknown optical constants *n* and *k* of the thin film without fitting any parameter. To use this numerical inversion method, all parameters of the optical model, such as thicknesses, must be known, which is not the case for tholin material and thus induces much larger uncertainties. This method requires a (even rough) knowledge of the order of magnitude of *n* and *k* indices for initialization. We thus used a two-pronged approach, where the modified Tauc-Lorentz dispersion model is used to determine the initialization parameters of the "λ-by-λ" numerical inversion method, which in return gives us the optical properties with much higher confidence. Therefore, our procedure, based on two sequential modified Tauc-Lorentz and "λ-by-λ" methods, is a good way to determine correctly the optical constants *n* and *k* of the original sample system when the optical responses are not available in the literature. For more details about these two methods, see Keita *et al.* (2010).

II.3.3.b.α. Determination of the thickness and optical constants of Pluto aerosol analogues by a modified Tauc-Lorentz dispersion model

The first model we used is a Tauc-Lorentz dispersion model, based on the Tauc joint density of states and the Lorentz oscillator, which was developed by Jellison and Modine (1996). This dispersion model was developed to better describe the optical properties of semiconductor and amorphous materials. This fitting model is thus adapted for aerosol analogues produced with the PAMPRE experimental setup, as Hadamcik *et al.* (2009) observed these samples with Scanning Electron Microscopy and showed that they present an amorphous structure.

In this model, the imaginary part $\varepsilon_{i,\mathrm{TL}}$ of the complex relative dielectric constant is given by the product of the imaginary part of Tauc's dielectric constant $\varepsilon_{i,\mathrm{T}}$ (Tauc, Grigorovici and Vancu, 1966) with a Lorentzian oscillator $\varepsilon_{i,\mathrm{L}}$:

$$\varepsilon_{i,\mathrm{TL}}(\mathrm{E}) = \varepsilon_{i,\mathrm{T}} \times \varepsilon_{i,\mathrm{L}} = \begin{cases} \frac{1}{\mathrm{E}} \frac{\mathrm{AE_0C(E-E_g)^2}}{(\mathrm{E^2-E_0^2})^2+\mathrm{C^2E^2}} & \text{for } \mathrm{E} > \mathrm{E_g} \\ 0 & \text{for } \mathrm{E} \leq \mathrm{E_g} \end{cases} \qquad \text{(Equation II.10)}$$

where E (in eV) is the photon energy; E_g (in eV) is the optical bandgap energy specifying at which energy the material becomes absorbent; E_0 (in eV) is the energy of the major absorption peak in the UV (the Lorentz peak) ($E_g < E_0$); A is the oscillator amplitude; and C is the broadening term.

The real part $\varepsilon_{r,\mathrm{TL}}$ of the complex relative dielectric constant is derived from the expression of $\varepsilon_{i,\mathrm{TL}}$ (Equation II.10) using the Kramers-Kronig integration (Kronig, 1926; Kramers, 1927):

$$\varepsilon_{r,\mathrm{TL}}(\mathrm{E}) = \varepsilon_{\infty} + \frac{2}{\pi} \cdot \mathrm{P} \cdot \int_{\mathrm{E_g}}^{\infty} \frac{\xi \cdot \varepsilon_{i,\mathrm{TL}}(\xi)}{\xi^2 - \mathrm{E}^2} \mathrm{d}\xi \quad \text{(Equation II.11)}$$

where ε_{∞} is the high-frequency real dielectric constant; and P is the Cauchy principal value.

The optical constants *n* and *k* are then deduced from the real and imaginary parts of the complex relative dielectric constant (Equation II.10 and Equation II.11) by the relation:

$$\varepsilon_{r,\mathrm{TL}} + i \times \varepsilon_{i,\mathrm{TL}} = (n + i \times k)^2 \quad \text{(Equation II.12)}$$

In the standard Tauc-Lorentz model, the imaginary part *k* of the complex refractive index becomes null for energies below the bandgap energy. This is due to the mathematical resolution of Kramers-Kronig equations, but not to the intrinsic material properties. However, this *k* index at wavelengths below the bandgap energy is necessary for numerical models (*e.g.*, radiative transfer, albedo, surface composition, haze vertical profile).

To overcome this problem, we modified the standard Tauc-Lorentz model by adding oscillators characterized by $\varepsilon_{\mathrm{osc}}$:

$$\varepsilon_{\mathrm{osc}} = \frac{\mathrm{f_j} w_{0\mathrm{j}}^2}{w_{0\mathrm{j}}^2 - w^2 + i\gamma_{\mathrm{j}} w} \qquad \text{(Equation II.13)}$$

where $\varepsilon_{\mathrm{osc}}$ is the dielectric function; *w* is the light pulsation; f_j is the oscillator strength of the j^{th} resonator; w_{0j} is the natural pulsation of the j^{th} resonator; and γ_j is the damping rate of the j^{th} resonator (friction coefficient).

Oscillators were added one by one to the model at different wavelengths, until the addition of an additional oscillator had no longer significant improvement in the MSE (Equation II.9). In our work, although the modified Tauc-Lorentz model was adapted for the determination of the thin-films thickness, the addition of oscillators was not adequate to retrieve *k* indices below the bandgap energy (see Figure V.2, in Chapter V, Section V.1).

II.3.3.b.β. Determination of the optical constants of Pluto aerosol analogues by a "λ-by- λ" numerical inversion method

To retrieve *k* indices below the bandgap energy, we thus used another model, only doable after a first estimation of the properties of the tholins using the Tauc-Lorentz approach. Once the thickness of the thin films and the initial couples [n_{270nm}, k_{270nm}] were characterized by the modified Tauc-Lorentz dispersion model (values used as input parameters), we used the "λ-by-λ" numerical inversion method to determine the optical constants of Pluto aerosol analogues.

In the "λ-by-λ" inversion method (also known as "direct data inversion" or "exact numerical inversion"), *n* and *k* indices are calculated for each wavelength by applying mathematical inversion of the Equation II.8 (Fujiwara, 2007). Theoretical ellipsometric parameters are calculated (Ψ_{calc} and Δ_{calc}) and the values are compared to the experimentally measured ellipsometric parameters (Ψ_{exp} and Δ_{exp}). A linear regression algorithm introduces for the initial couple [n_{270nm}, k_{270nm}] the corrections needed to match (Ψ_{calc}, Δ_{calc}) and (Ψ_{exp}, Δ_{exp}). Then, the process is applied iteratively over the whole spectral range (from 270 to 2,100 nm): the values for the couple [n_λ, k_λ] are calculated from the values of the couple [$n_{\lambda-\delta\lambda}$, $k_{\lambda-\delta\lambda}$] with δλ the wavelength step between two measurements (here, 5 nm) (Fujiwara, 2007; Keita *et al.*, 2010; Likhachev, Malkova and Poslavsky, 2015).

The "λ-by-λ" numerical inversion method gives a mathematical solution for [n_λ, k_λ] couples from measured ellipsometric parameters Ψ and Δ, disregarding the *n* and *k* dependency on each other at different wavelengths. For this procedure, other parameters, such as the thickness of the thin film, and the optical properties of the underlying silicon substrate and the overlying roughness layer, need to be accurately known, otherwise it can lead to multiple solutions, unphysical dispersion or discontinuities in the optical constants, generally present at lower energies in the inversion spectrum (Fujiwara, 2007; Keita *et al.*, 2010; Likhachev, Malkova and Poslavsky, 2015).

II.3.4. Analytical techniques relative to Chapter VI – Investigating the organic matter on Pluto's surface

II.3.4.a. The IGLIAS experimental setup mounted on the IRRSUD beamline

IGLIAS ("Irradiation de GLaces d'Intérêt AStrophysique", French acronym for "Irradiation of astrophysical ices") is an experimental setup developed at CIMAP[15] laboratory (Augé *et al.*, 2018). This ensemble of ultra-high vacuum chambers is equipped with various spectroscopic instruments, namely UltraViolet-Visible (UV-Vis) and Fourier-Transform InfraRed (FTIR) spectrometers, as well as a Quadrupole Mass Spectrometer (QMS) (Figure II.25). This device was designed to study the evolution of solid samples of astrophysical interest submitted to swift heavy ion irradiation at ultra-high vacuum and at temperatures ranging from 9 to 300 K (Augé *et al.*, 2018).

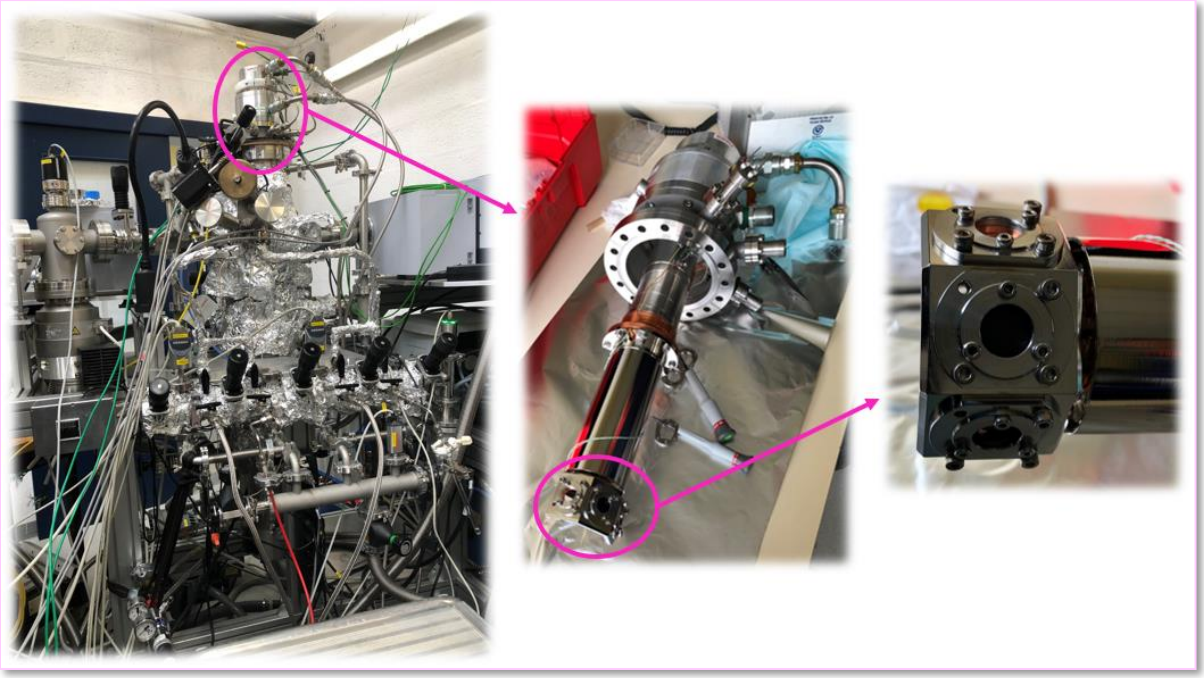

Figure II.25: IGLIAS experimental setup (Augé *et al.*, 2018) mounted on the IRRSUD beamline (*left*), with a zoom on the sample holder (*middle* and *right*).

We used this experimental setup coupled to the IRRSUD beamline to perform heavy ion irradiation on Pluto tholins at ~5.10^{-8} mbar and at 40 K (first session on the IRRSUD beamline) or ambient temperature (second session), and to monitor *in situ* the physical and chemical evolution of our samples, as a function of ion fluence.

[15] CIMAP: *Centre de recherche sur les Ions, les Matériaux et la Photonique* (Caen, France)

A *Perkin Elmer Lambda 650* UV-Vis spectrometer driven by *UV WinLab* software can record spectra in the [200-800 nm] wavelength range. A UV-Vis light beam is guided through an optical fiber to enter the IGLIAS chamber. The UV-Vis light beam then crosses the irradiated sample, before being collected in an integrative sphere to perform the analysis. Note that UV-Vis measurements cannot be performed simultaneously to the irradiation of the sample, because of the configuration of the sample holder (Augé *et al.*, 2018) (for visualization purpose, see Figure II.26). The spectra presented in Chapter VI (see Figure VI.5) were acquired for the F_P sample before irradiation and at different irradiation fluences, between 400 and 800 nm, with a step of 10 nm.

A *Brucker Vertex 70v* FTIR spectrometer driven by *OPUS* software can acquire transmittance spectra from 7,500 to 500 cm^{-1} (1.33 to 20 µm). An IR light beam crosses the irradiated sample and is then focused on a MCT (Mercury Cadmium Telluride) detector cooled with liquid nitrogen. In contrast to UV-Vis measurements, FTIR analysis is performed simultaneously to the sample irradiation. Indeed, the sample holder was designed in such a way that ion irradiation is performed on the sample at normal incidence, whereas the IR transmittance spectra are recorded at 12° of incidence (Augé *et al.*, 2018) (for visualization purpose, see Figure II.26). The spectra presented in Chapter VI (see Figure VI.6) were acquired for the F_P sample before irradiation and at different irradiation fluences, between 4,000 and 1,000 cm^{-1}, with a step of 1.929 cm^{-1}.

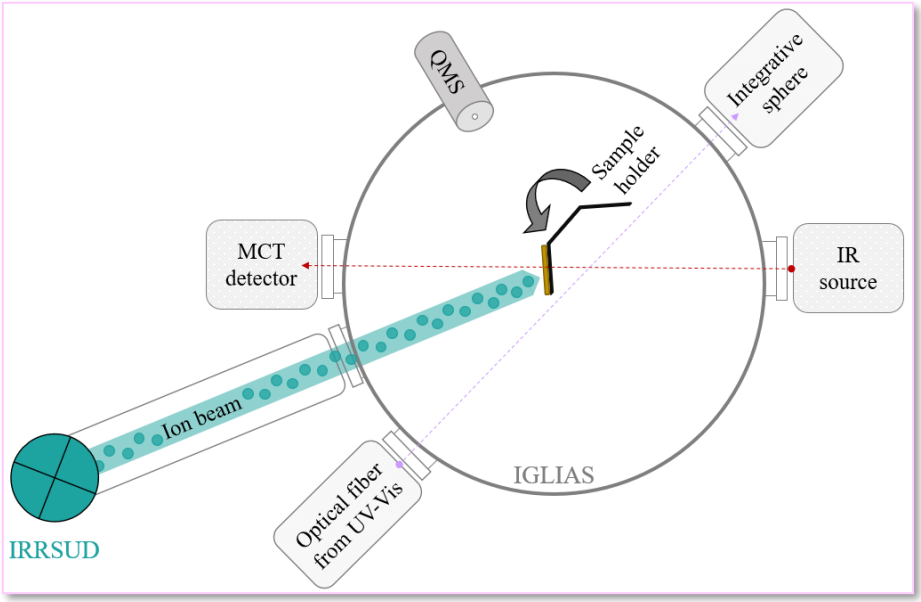

Figure II.26: Top view of IGLIAS experimental setup. FTIR measurements can be performed simultaneously to sample irradiation with an incidence angle of 12°, whereas the sample holder must be rotated after irradiation to allow UV-Vis measurements.

A *Microvision2 MKS104* QMS driven by *Process Eye Professional* software is used to analyze the volatiles released by the sample F_P under ion irradiation, from *m/z* 1 to *m/z* 100, with a resolving power of 1 u. The neutral species are ionized in the electron ionization source, whose electron energy is set at 70 eV.

II.3.4.b. Scanning Electron Microscopy

The evolution of the morphology of Pluto tholins before and after irradiation with swift heavy ions analogues of GCR was analyzed by Scanning Electron Microscopy (SEM). The instrument used was an environment SEM *Quanta 200* from *Field Electron and Ion (FEI) Company* (possible magnification from ×25 to ×20,000), with a Large Field Detector (LFD) installed at LGPM-CentraleSupélec (Gif-sur-Yvette, France). The images were obtained with a high voltage of 15.0 kV and at ~0.71 mbar (0.53 Torr). Since we wanted to perform a further analysis of the chemical composition of the material before and after irradiation, we were not able to metallize our sample, since it is a destructive treatment. As a result, the images were acquired at low vacuum, and their resolution is thus limited.

Scanning Electron Microscopy gives information on the microstructure morphology of sample surfaces. A beam of electrons is sent towards the sample. When the primary electrons strike the sample surface, it causes ionization of target atoms which emit secondary electrons that are attracted to a detector. The detection of secondary electrons allows for the visualization of surface texture and roughness of the analyzed sample (*e.g.*, Zhou *et al.*, 2007) (Figure II.27).

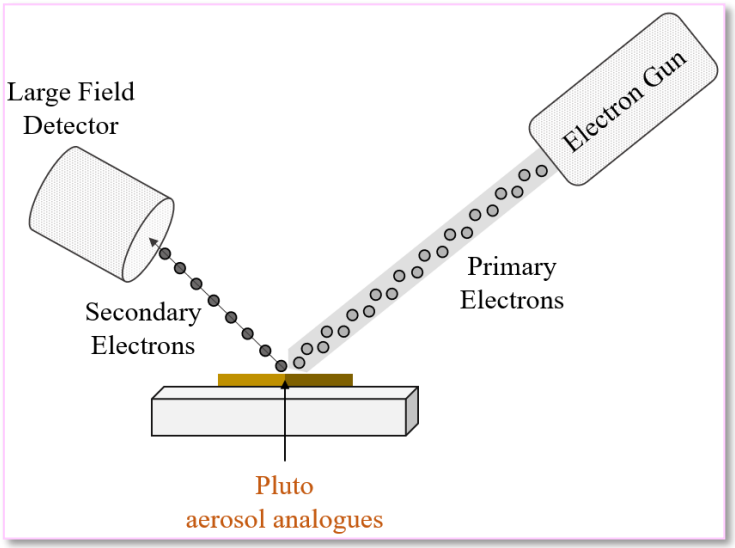

Figure II.27: Scheme presenting the operating principle of Scanning Electron Microscopy (SEM).

II.3.4.c. High-Resolution Mass Spectrometry – Fourier-Transform Ion Cyclotron Resonance

To assess precisely the changes in the molecular composition of Pluto's surface induced by GCR irradiation, I submitted a proposal to the TGE FT-ICR platform (FT-ICR-00288 project accepted after evaluation by a review panel) to study the evolution of the chemical composition of Pluto tholins before and after swift heavy ion irradiation by ultrahigh-resolution mass spectrometry. The choice of this instrumentation was linked to the highly valuable samples, which dictated using a non-destructive ionization method. ESI or APPI/Orbitrap (used in Chapter IV) was thus not an option, and we run these analyses using a Laser Desorption Ionization coupled to a Fourier-Transform Ion Cyclotron Resonance. This also allowed to reach much higher mass resolution. More precisely, we used the *solariX XR* Fourier-Transform Ion Cyclotron Resonance (FT-ICR) mass spectrometer (*Bruker Daltonics*), installed at the COBRA laboratory (*Chimie Organique Bioorganique : Réactivité et Analyse*, Rouen, France). This analytical instrument is equipped with a 12 T superconducting magnet and a Laser Desorption Ionization (LDI) source, consisting of a Nd:YAG (Neodymium-doped Yttrium Aluminum Garnet) laser at 355 nm inside an enclosure at 10^{-3} mbar. A scheme of the analytical instrument is shown in Figure II.28.

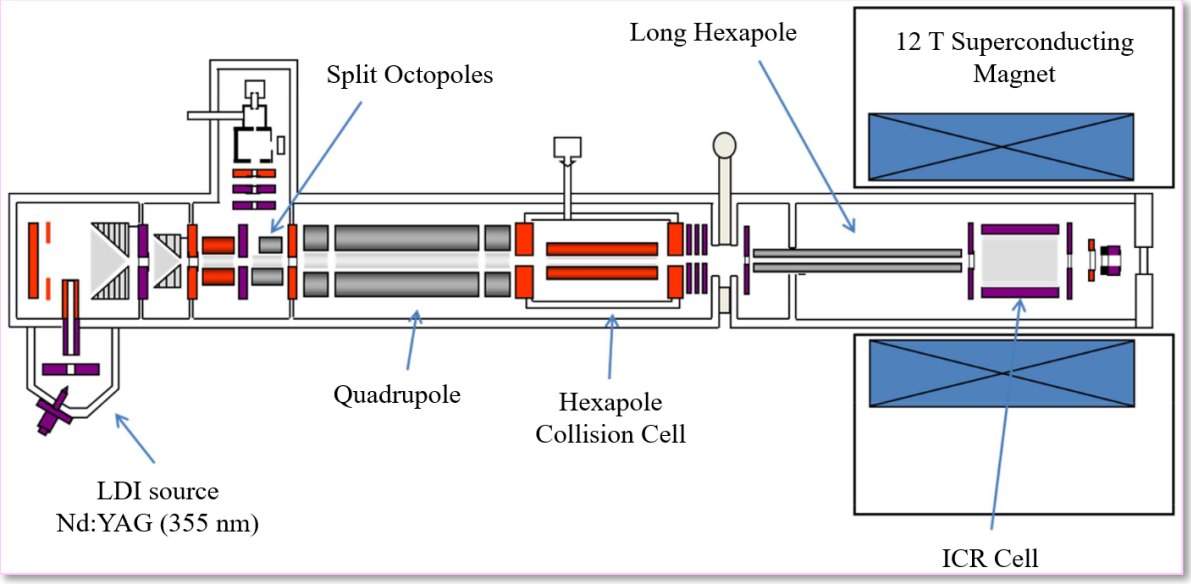

Figure II.28: Scheme of the Fourier-Transform Ion Cyclotron Resonance (FT-ICR) mass spectrometer *solariX XR* (*Bruker Daltonics*). *Credit*: The scheme is adapted from the *Bruker solariX* user guide.

The LDI source was used in positive mode (LDI+). Unlike the ESI and APPI sources presented in Section II.3.2.b.β, which only allowed the analysis of the soluble fraction of Pluto tholins,

the LDI source allowed to analyze the global solid sample without any preparation of the sample (*i.e.*, the sample P_P to be analyzed was just deposited on a conductive plate) (*e.g.*, Barrère *et al.*, 2012). Note that LDI-MS has already been used for the analysis of Titan tholins (*e.g.*, Imanaka *et al.*, 2004; Somogyi *et al.*, 2012; Mahjoub *et al.*, 2016; Gautier *et al.*, 2017; Maillard *et al.*, 2018), because dissociative ionization pathways are minor with this soft mode of ionization, and mass spectra are essentially fragment-free, facilitating the identification of molecules (see Mahjoub *et al.* (2016), for further discussion on the different laser sources available).

After being formed in the ionization source, the ions are transmitted through several electromagnetic lenses (funnels, skimmers, quadrupole) to a collision cell where the ions accumulate before being injected into the ICR cell inside the 12 T superconducting magnet.

In the ICR cell, the ions of mass *m* and charge *z* are subjected to a high magnetic field *B*. Because of the Lorentz force exerted on these ions, they undergo a cyclotron rotation. By measuring the frequency of cyclotron rotation ω, *m/z* ratios can be determined through the cyclotron equation (*e.g.*, Comisarow, 1993; Cho *et al.*, 2015):

$$\omega = \frac{zB}{m} \quad \text{(Equation II.14)}$$

Prior to the analyses, the mass spectrometer was externally calibrated with a solution of sodium trifluoroacetate. Internal calibration was also performed using confident well-known signals, yielding a mass accuracy below 300 ppb in the considered mass range. Mass spectra were recorded in positive mode at 8 million points with a sum of 200 scans, yielding a resolution of 650,000 at *m/z* 400. The following instrumental parameters were set for the LDI+/FT-ICR analysis of both non-irradiated and irradiated area of the sample P_P: plate offset at 100 V, deflector plate at 200 V, laser power at 8% or 8.5% depending on the area considered on the P_P sample, laser shots at 100, frequency of laser shots at 1,000 Hz, funnel 1 at 150 V, and skimmer 1 at 5 V. Note that since the number of desorbed molecules depends on the laser fluence (*e.g.*, Dreisewerd *et al.*, 1995), a comparison between the global intensity of the mass spectra as a function of laser power was conducted. In order to compare the LDI+/FT-ICR mass spectra of the non-irradiated and irradiated areas of the P_P sample, we selected laser powers for which similar global intensities were obtained: in this case, 8% for the non-irradiated part, and 8.5% for the irradiated part.

Molecular attribution was done with a signal/noise ratio of 3. Molecular formulae were obtained using the *SmartFormula* tool from the *Bruker Data Analysis 4.4* software with the following

parameters: molecular formula $C_xH_yN_zO_w$ with no lower limits for C, H, N, and O, no upper limits for C, H, and N, and an upper limit of 4 for O, even and odd electron configuration allowed, and 0.3 ppm error tolerance.

II.3.5. Summary of the complementary analytical techniques used during this Ph.D.

A summary of the different analytical techniques employed during this Ph.D. to characterize Pluto-simulated atmosphere and Pluto tholins can be found in Table II.10. In this table, the objectives of the measurements, as well as the advantages and drawbacks of the analytical techniques employed are reported. In Table II.11, the objectives of the numerical models employed during this Ph.D. are reported.

Table II.10: Analytical techniques employed during this Ph.D.

Analytical technique	Chapter	Objectives	Measured quantity	Advantages	Drawbacks
GAS-PHASE ANALYSIS					
Quadrupole Mass Spectrometry (QMS), with Electron Ionization (EI)	III & VI	Understand Pluto's atmospheric composition and chemistry	Mass-to-Charge ratio (*m/z*) of molecules in the gas phase	• Provides masses of molecules involved in Pluto-simulated atmospheric chemistry • Large mass range (from *m/z* 1 to *m/z* 100 or 200) • High sensitivity (as low as ppm) • Possibility to identify key molecules using a deconvolution code, based on fragmentation patterns • Possibility to detect cations formed *in situ* in PAMPRE dusty plasma, and involved in Pluto-simulated atmospheric chemistry	• No information on the structure of the molecules, only their masses • High rate of degeneracy between different compounds due to low resolution, making most identification difficult • Not a straightforward quantitative analysis
SOLID-PHASE ANALYSIS: CHEMICAL COMPOSITION					
High-Resolution Mass	IV	• Understand Pluto's haze composition	*m/z* of molecules soluble in a	• Provides masses and chemical formulae of	• No information on the structure of the

Spectrometry (HRMS) Orbitrap™ technique, with ElectroSpray Ionization (ESI) or Atmospheric Pressure PhotoIonization (APPI)		• Evaluate the prebiotic implications of Pluto's aerosols	MeOH:ACN mixture	molecules constituting Pluto aerosol analogues • Large mass range (from *m/z* 50 to *m/z* 1,000)	molecules, only their chemical formulae • Information on the soluble fraction of the sample only • Destructive method of analysis
HRMS Fourier-Transform Ion Cyclotron Resonance (FT-ICR) technique, with Laser Desorption Ionization (LDI)	VI	Understand the molecular ageing of Pluto's surface organic matter submitted to GCR irradiation	*m/z* of molecules desorbed by laser ionization	• Extreme mass accuracy • Provides masses and chemical formulae of molecules constituting Pluto tholins • Large mass range (from *m/z* 100 to *m/z* 1,000) • Information on the global sample • Non-destructive method of analysis	• No information on the structure of the molecules, only their chemical formulae
Elemental Composition Analysis	IV	Understand Pluto's atmospheric chemistry and haze composition	Mass percentages of C, H, N, and O elements	• Information on bulk sample • Enhanced sensitivity	• Destructive method of analysis • Limited interpretation
Gas Chromatography coupled to Mass Spectrometry (GC-MS)	IV	Evaluate the prebiotic implications of Pluto's aerosols, by determining the structures of the molecules constituting Pluto aerosol analogues	Retention time and *m/z* of molecules in the gas phase	• Provides information on the structures of the molecules • Information on bulk sample	• Can only detect volatilized and/or derivatized molecules, which is not the case of most of the molecules in Pluto aerosol analogues • Destructive method of analysis
SOLID-PHASE ANALYSIS: MORPHOLOGY					
Scanning Electron	VI	Understand the morphological	Secondary electrons	• Provides visualization of surface texture and	• At low vacuum,

Microscopy (SEM)		ageing of Pluto's surface organic matter submitted to GCR irradiation	emitted by the sample surface	roughness of the analyzed sample • No sample preparation required (*i.e.*, metallization of the sample) at low vacuum	degraded resolution
SOLID-PHASE ANALYSIS: SPECTRAL PROPERTIES					
InfraRed spectroscopy (IR) Attenuated Total Reflectance (ATR) technique	IV	Understand Pluto's atmospheric haze composition	Vibration of chemical bonds	• Provides information on the chemical bonds within the material • Information on bulk sample • No sample preparation required	• Not a quantitative analysis • Sensitivity for a given bond highly dependent on the intensity of the absorption bands. Some bands might not be detectable and band ratios thus do not reflect functional group ratios within the sample • Accuracy of the data strongly dependent on experimental conditions (applied pressure, ambient atmosphere)
Fourier-Transform InfraRed spectroscopy (FTIR)	VI	Understand the compositional ageing of Pluto's surface organic matter submitted to GCR irradiation	Vibration of chemical bonds	• Provides information on the chemical bonds within the material • Information on bulk sample • Real-time measurement (on IGLIAS)	• Sensitive to ambient atmosphere (H_2O, CO_2) • Analysis of solid complex mixture complicated

				• Non-destructive method of analysis	due to overlapping absorption bands • Sensitivity for a given bond highly dependent on the intensity of the absorption bands. Some bands might not be detectable and band ratios thus do not reflect functional group ratios within the sample
UltraViolet-Visible spectroscopy (UV-Vis)	VI	Understand the optical properties ageing of Pluto's surface organic matter submitted to GCR irradiation	Absorbance	• Information on bulk sample • No sample preparation required • Non-destructive method of analysis	• Not a real-time measurement (on IGLIAS)
Spectroscopic Ellipsometry	V	Understand the radiative transfer of Pluto's aerosols by determining the optical constants [*n*, *k*] of Pluto aerosol analogues	Ellipsometric parameters Ψ and Δ	• Most accurate determination of optical constants • No sample preparation required • Non-destructive method of analysis • Enhanced sensitivity	• Need complicated inversion models to determine *n* and *k* indices • *n* and *k* indices strongly dependent on the optical model used to determine them

Table II.11: Numerical modeling employed during this Ph.D.

Numerical modeling	Chapter	Objectives
Deconvolution code based on a Monte-Carlo approach	III	Decomposition of the QMS mass spectra in order to retrieve the molecules formed in Pluto-simulated atmosphere
Attributor	IV	Identification of the molecules constituting Pluto aerosol analogues
Modified Tauc-Lorentz dispersion model	V	Estimation of the initialization parameters (thickness of the thin film, initial *n* and *k* indices)
"Wavelength-by-wavelength" (λ-by-λ) numerical inversion	V	Precise determination of the optical constants *n* and *k* of Pluto aerosol analogues

III. Investigating the chemical composition of Pluto's atmosphere

In this chapter, I present the results regarding the analysis of the gas-phase chemical composition of Pluto-simulated atmospheres. Both neutral molecules and cations were investigated. To account for the variability in terms of chemical composition in Pluto's atmosphere, two N_2:CH_4:CO gas mixtures with different CH_4 concentrations were analyzed: N_2:CH_4:CO = 99%:1%:500ppm, and N_2:CH_4:CO = 95%:5%:500ppm. The results obtained were placed in the context of Pluto and current Pluto photochemical models. The results presented in this chapter will be later submitted for publication.

III.1. Neutral molecular composition of Pluto-simulated atmosphere

Until now, few studies have focused on the reactivity of a N_2:CH_4:CO gas mixture, and always in the frame of Titan studies and not specifically tailored to study Pluto's atmosphere (Bernard *et al.*, 2003; Coll *et al.*, 2003; Tran *et al.*, 2008; Hörst *et al.*, 2012; Fleury *et al.*, 2014; He *et al.*, 2017). In this part of my Ph.D. thesis, I present the analysis of neutral molecules formed in reactive medium relevant to Pluto's atmosphere.

III.1.1. Organic growth in Pluto-simulated atmosphere

To confirm that the studied species are formed in the plasma simulating Pluto's atmospheric chemistry, background mass spectra were acquired before the analysis of Pluto-simulated atmosphere. For the RGA mass spectra only, the backgrounds consisted of acquiring mass spectra in N_2:CH_4:CO gas mixtures (*i.e.*, A_{400} and A_{650} gas mixtures) without applying the radio-frequency discharge (see grey mass spectra in Figure III.1 and Figure III.2).

Figure III.1 and Figure III.2 respectively show *in situ* QMS mass spectra of the neutrals present at steady state in the reactive media simulating Pluto's atmospheric chemistry occurring at ~400 km of altitude above the surface (A_{400}, in turquoise), and between 600 and 700 km of altitude (A_{650}, in lavender color). Although mass spectra were recorded from *m/z* 1 to *m/z* 100, no peak was detected above *m/z* 91 in any of the mass spectra. For comparison purposes, as the absolute intensities measured by QMS are not perfectly reproducible, the peak intensities were normalized to the most intense peak in the mass spectrum, namely *m/z* 28.

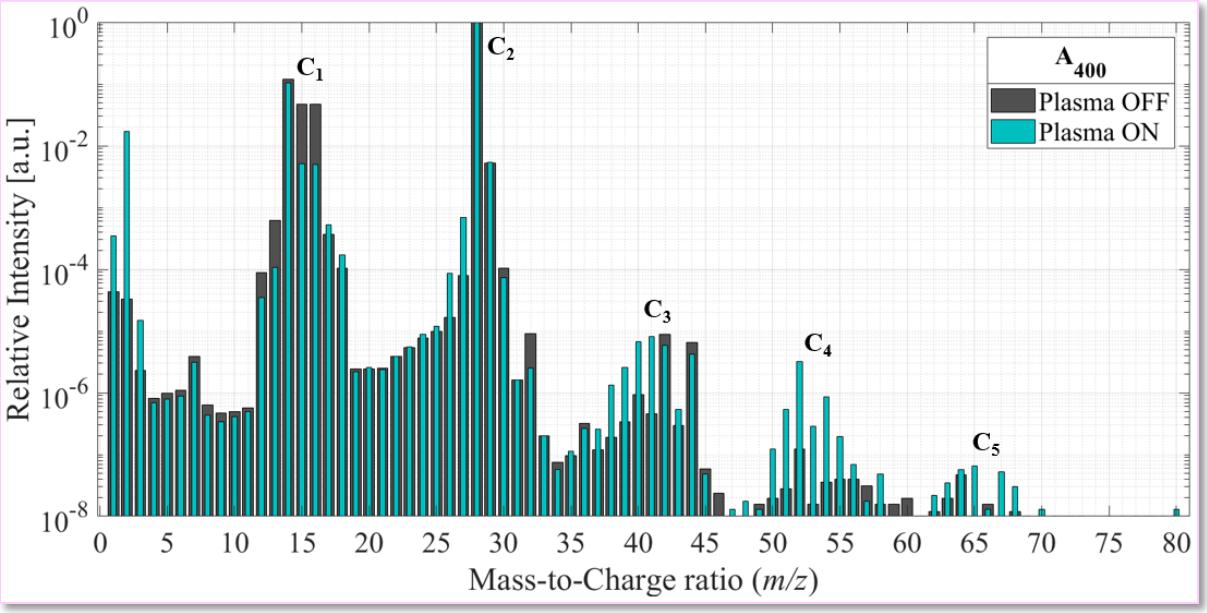

Figure III.1: In turquoise, *in situ* mass spectrum of the neutrals present at steady state in PAMPRE plasma mimicking the photochemistry occurring in Pluto's atmosphere at ~400 km of altitude (A_{400} reactive medium). The grey mass spectrum corresponds to the background acquired in A_{400} gas mixture before ignition of the radio-frequency discharge. Each mass spectrum is the accumulation of 40 scans, acquired with *Hiden Analytical EQP 200* Quadrupole Mass Spectrometer, at $P_{QMS} = 4\times10^{-6}$ mbar. The gas-phase neutral species were ionized in the electron ionization source, with an electron energy settled at 70 eV. The *x*-axis corresponds to the mass-to-charge (*m/z*) ratio, whereas the *y*-axis corresponds to the relative intensity of the peaks, normalized to the most intense peak in the mass spectrum, *m/z* 28.

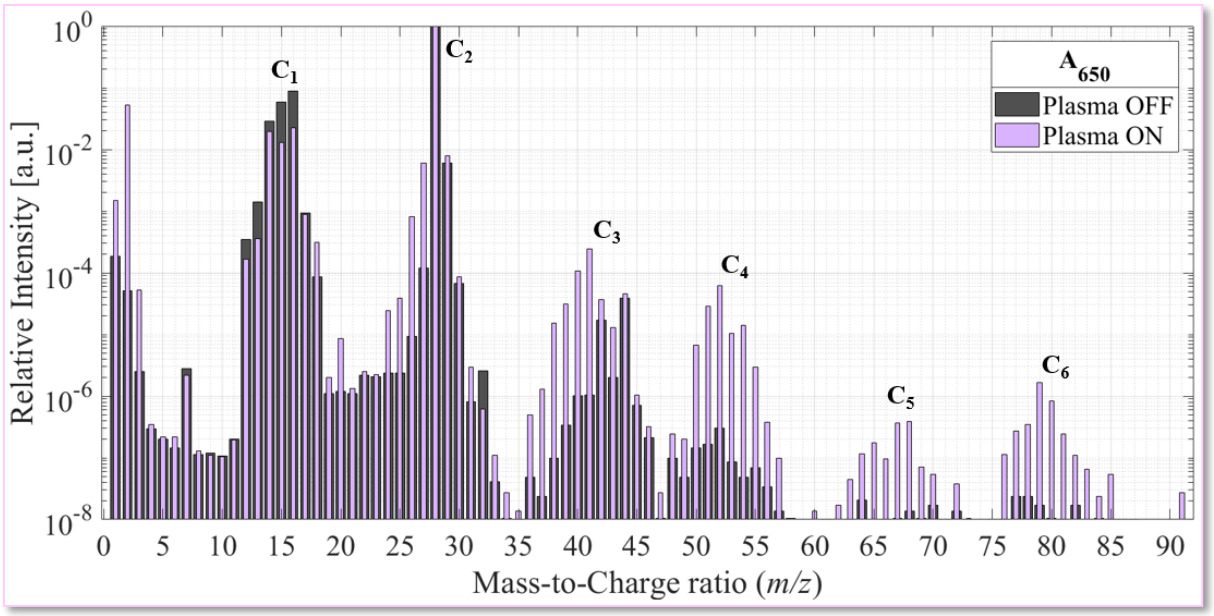

Figure III.2: Same as Figure III.1, but showing in lavender color the neutrals present at steady state in PAMPRE plasma mimicking the photochemistry occurring in Pluto's atmosphere between 600 and 700 km of altitude (A_{650} reactive medium).

In Figure III.1 and Figure III.2, we notice that the background mass spectra in grey are globally representative of the gas mixtures injected into the PAMPRE reactor. Indeed, the most intense peaks correspond to the characteristic fragments of molecular nitrogen N_2, methane CH_4, and carbon monoxide CO. The intense peaks at *m/z* 28, 29, and 30 are attributed to molecular nitrogen N_2^+, $^{14}N^{15}N^+$, and $^{15}N^{15}N^+$, respectively. The peaks at *m/z* 14 and 15 respectively correspond to N^+ and $^{15}N^+$, whereas the peak at *m/z* 7 corresponds to N^{2+}. Some of these peaks (*m/z* 7, 14, 30) are slightly more intense in the A_{400} mixture injected into the PAMPRE reactor (grey mass spectrum in Figure III.1), which is consistent with the A_{400} gas mixture containing more N_2 than the A_{650} mixture, namely 99% *versus* 95%. In contrast, the peaks at *m/z* 16, 15, 14, 13, and 12 characteristic of CH_4 are slightly more intense (except *m/z* 14) in the A_{650} mixture (grey mass spectrum in Figure III.2), in agreement with the higher CH_4-content in this gas mixture compared to the A_{400} mixture, namely 5% *versus* 1%. Note that the peaks at *m/z* 28, 12, and 16 are also characteristic fragments of CO.

The low-intensity inter-cluster peaks (from *m/z* 4 to *m/z* 11, and from *m/z* 19 to *m/z* 23) which are constant (intensity < 10 raw-counts) along the 40 scans constituting the final mass spectra presented here (grey, turquoise and lavender mass spectra) correspond to noise induced by higher pressures ($P_{QMS} = 4\times10^{-6}$ mbar) inside the instrument (*e.g.*, Allodi *et al.*, 2013). In the background mass spectra (in grey, in Figure III.1 and Figure III.2), the peaks at *m/z* > 35 gathering in clusters probably correspond to a persistent deposit of Pluto aerosol analogues on

the electromagnetic lenses of the QMS or to organic molecules formed inside the ionization source. Nevertheless, these signals do not interfere with the analyses of Pluto-simulated atmosphere, since the inter-cluster noise is constant before and after ignition of the radio-frequency discharge. Moreover, the peaks at *m/z* > 35 corresponding to molecules formed in the plasma have much higher intensities than the same peaks in the background mass spectra.

Considering the signals observed in the background mass spectra (grey mass spectra in Figure III.1 and Figure III.2), to confirm that the peaks at *m/z* > 35 are indeed molecules formed by plasma chemistry and not pollution or instrumental noise, we acquired with the same QMS parameterization mass spectra in pure gaseous molecular nitrogen N_2, before and after ignition of the radio-frequency discharge (Figure III.3). To compare spectra with each other, we normalized the intensities of the peaks by that of the most intense peak in the spectra, *i.e.*, *m/z* 28.

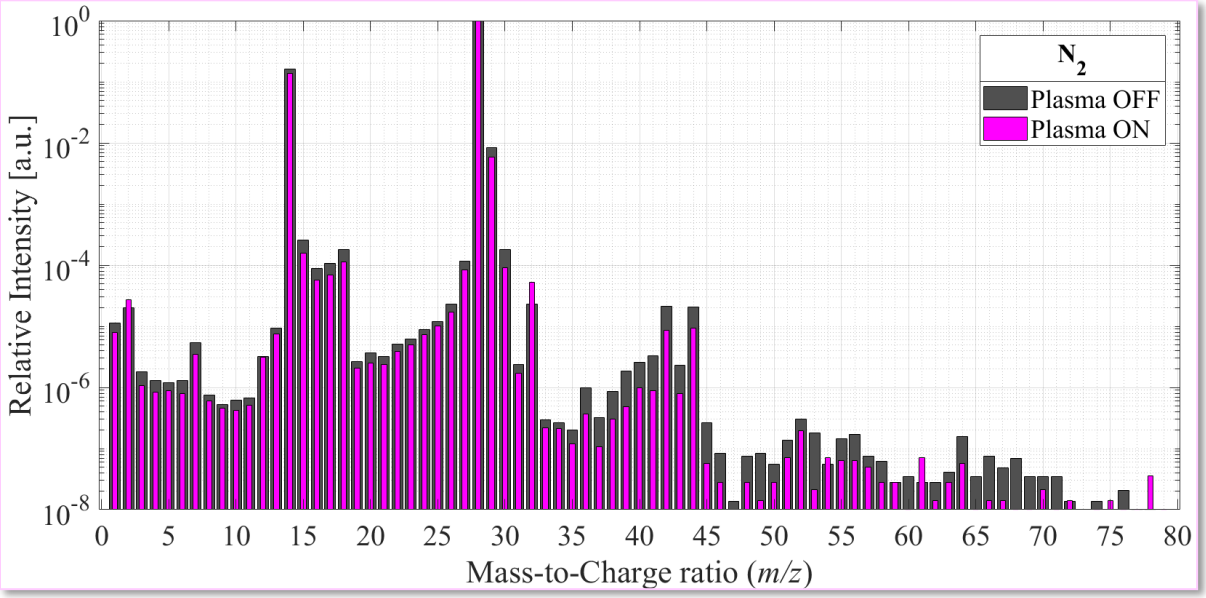

Figure III.3: *In situ* mass spectrum of pure N_2 gas, before (in grey) and after (in pink) ignition of the radio-frequency discharge. Each mass spectrum is the accumulation of 40 scans, acquired at $P_{QMS} = 4\times10^{-6}$ mbar. The peaks were normalized to the most intense peak, *m/z* 28.

By comparing Figure III.1, Figure III.2 and Figure III.3, we can confirm that C_2 to C_6 clusters of peaks observed with significant intensities in the reactive media simulating Pluto's atmospheric chemistry (A_{400} and A_{650} cases, turquoise and lavender mass spectra in Figure III.1 and Figure III.2) are indeed the result of chemical reactions specific to the plasma in presence of a carbon source, mainly thanks to methane, and probably with only a small contribution of carbon monoxide (because of its low abundance, and high bond-dissociation and ionization energies). Indeed, in the absence of these carbon sources (*i.e.*, N_2 plasma), there is logically no

organic growth, no species is significantly produced in a pure N_2 plasma, as evidenced by the absence of peaks with significant intensities in the pink mass spectrum shown in Figure III.3.

Before identifying the molecules formed in Pluto-simulated atmosphere, some general comments can be made on Figure III.1 and Figure III.2. The peaks show a particular aspect already observed in studies on the atmospheric chemistry of Titan, both in observations made by INMS onboard the *Cassini* spacecraft and in laboratory simulations (*e.g.*, Waite *et al.*, 2005; Vuitton, Yelle and Anicich, 2006; Cui *et al.*, 2009; Imanaka and Smith, 2010; Carrasco *et al.*, 2012; Sciamma-O'Brien, Ricketts and Salama, 2014; Hörst *et al.*, 2018; Dubois *et al.*, 2019; Chudják, Kozáková and Krčma, 2021). Indeed, the peaks are grouped in clusters C_α, the index α corresponding to the number of "heavy" atoms included in the molecules. In our case, the "heavy" atoms correspond to carbon C, nitrogen N, and/or oxygen O. Since the raw formulae are of the type $C_xH_yN_zO_w$, the index $\alpha = x + z + w$. Note that this particular aspect is typical of the hydrocarbon chains which constitute the backbone of the molecules in the solid material formed in the gas phase – Pluto aerosol analogues – whose chemical composition is studied in following Chapter IV.

Comparing Figure III.1 and Figure III.2, we find that the mass spectrum of A_{650} lab-simulation has one additional peak cluster (C_6 cluster) compared to the A_{400} simulation, and C_3 to C_5 clusters are overall more intense than for the A_{400} simulation. This was also observed in parametric studies of Titan's atmospheric chemistry (*e.g.*, Gautier *et al.*, 2011; Carrasco *et al.*, 2012; Hörst *et al.*, 2018; Dubois *et al.*, 2019; Chudják, Kozáková and Krčma, 2021). Increasing the initial CH_4 concentration produces heavier, more diverse, and more abundant molecules. In the upper layers of Pluto's atmosphere, where the CH_4 mixing ratio is higher, we can thus expect a richer photochemistry, producing more diverse molecules for ultimate incorporation into Pluto's aerosols.

In Figure III.2 (A_{650} simulation), we notice that the heavier the molecules (*i.e.*, increasing *m/z* ratios), the less abundant they are (*i.e.*, less intense peaks), except for the C_6 cluster which is more intense than the C_5 cluster. This is not due to an instrumental bias, but to the chemical properties of the molecules constituting this C_6 cluster. Indeed, Bourgalais *et al.* (2021) showed the significant formation of aromatics – benzene and toluene – in their laboratory simulation of Titan's atmospheric chemistry. Benzene is a major contributor to the C_6 cluster. The authors showed that because of its stability, the production processes of benzene involving radical pathways are faster than its loss processes. Benzene therefore accumulates, resulting in higher

intensities of the peaks in the C_6 cluster. In the case of Pluto-simulated atmosphere, we can suspect a similar trend.

III.1.2. Identification of neutral molecules in Pluto-simulated atmosphere

III.1.2.a. Based on observations and photochemical models of Pluto's atmosphere

First, in order to identify the molecules contributing to the mass spectra of the A_{400} and A_{650} simulated-atmospheres, we included in our deconvolution database only the species already detected in Pluto's atmosphere (Gladstone *et al.*, 2016; Lellouch *et al.*, 2017; Young *et al.*, 2018; Steffl *et al.*, 2020), as well as species predicted by Pluto photochemical models (Lara, Ip and Rodrigo, 1997; Krasnopolsky and Cruikshank, 1999; Luspay-Kuti *et al.*, 2017; Wong *et al.*, 2017; Krasnopolsky, 2020). These 26 molecules are reported in Table III.1.

Table III.1: Molecules included in the deconvolution database, based on observations and photochemical models of Pluto's atmosphere.

Molecules			
IUPAC name	**Chemical formula**	**Skeletal formula**	**Observations Modeling**
Methane	CH_4	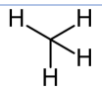	Observations
Ammonia	NH_3	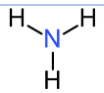	Modeling
Water	H_2O	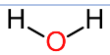	Modeling
Molecular Nitrogen	N_2		Observations
Carbon Monoxide	CO		Observations
Acetylene	C_2H_2	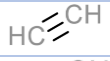	Observations
Ethylene	C_2H_4	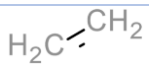	Observations
Ethane	C_2H_6	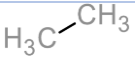	Observations
Hydrogen Cyanide	HCN		Observations
Methylamine	CH_3NH_2	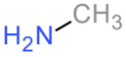	Modeling
Methylacetylene	C_3H_4	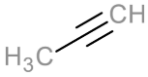	Observations
Propene	C_3H_6	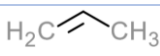	Modeling
Propane	C_3H_8	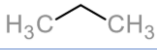	Modeling

Diacetylene	C_4H_2		Modeling
1-Buten-3-yne	C_4H_4	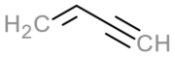	Modeling
1,3-Butadiene	C_4H_6	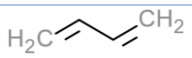	Modeling
Butane	C_4H_{10}	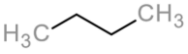	Modeling
Benzene	C_6H_6	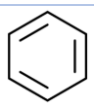	Modeling
Acetonitrile	CH_3CN	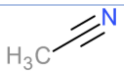	Modeling
Propiolonitrile	HC_3N	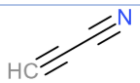	Modeling
2-Propenenitrile	C_3H_3N	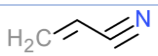	Modeling
Propanenitrile	C_3H_5N	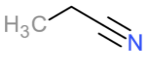	Modeling
Cyanogen	C_2N_2		Modeling
2-Butynedinitrile	C_4N_2	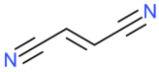	Modeling
Formaldehyde	H_2CO	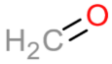	Modeling
Carbon Dioxide	CO_2	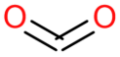	Modeling

For the calculation of the mixing ratios of all the molecules, we did not first apply any constraints. By deconvoluting the global mass spectra without applying any constraints for any of the species, we obtained results regarding C_3, C_4 and C_5 clusters for which the calculated mixing ratios led to theoretical intensities higher than those of the experimental mass spectra. This over-estimation comes from the fitting process of the mass spectra which minimize the global residue, hence favoring the optimization of the highest intensity peaks, *i.e.*, the C_1 and C_2.

Since heavier molecules (C_3, C_4, C_5, and C_6) almost systematically have fragments localized in these C_1 and C_2 clusters, the optimization of the residue tends to over-include them. To overcome this issue, I first deconvoluted each cluster separately without setting any constraints. The results obtained for C_3, C_4, C_5 (and C_6) clusters provide upper limits for them. I have then used these upper limits as constraints for the final deconvolution of the global mass spectrum.

That done, the top 5% of the deconvolution results for the A_{400} and A_{650} mass spectra are given in Figure III.4 and Figure III.5, respectively.

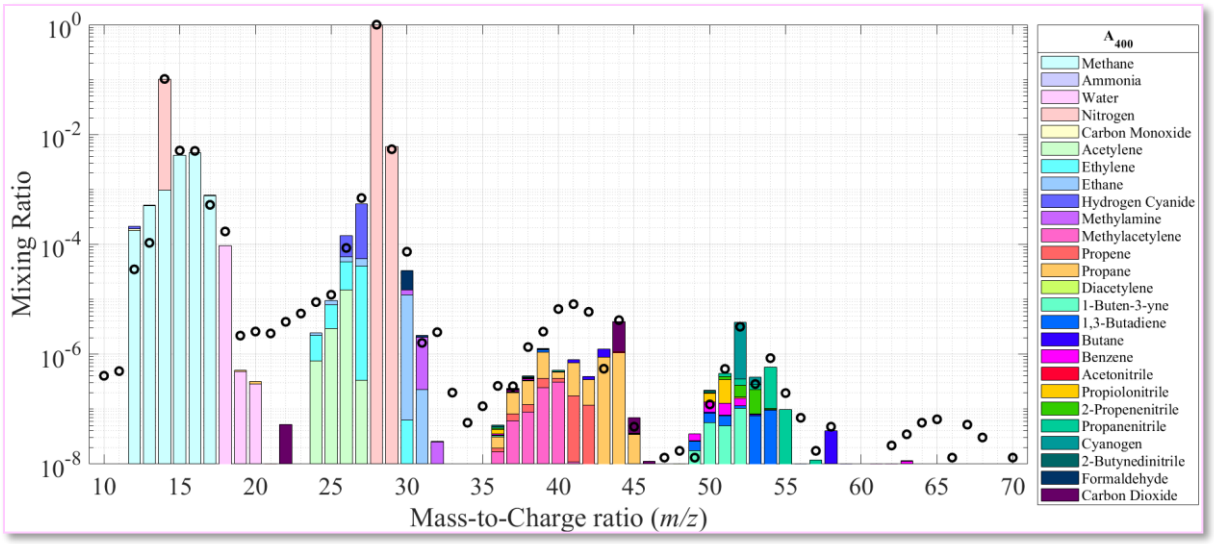

Figure III.4: Top 5% results of the deconvolution of the mass spectrum shown in Figure III.1 (A_{400} simulation) using the method developed by Gautier *et al.* (2020). The black dots correspond to the experimental mass spectrum. The colored bars correspond to the contribution of each molecule calculated by the deconvolution method. The database used for the deconvolution was populated with 26 species already observed in Pluto's atmosphere or predicted by Pluto photochemical models (reported in Table III.1).

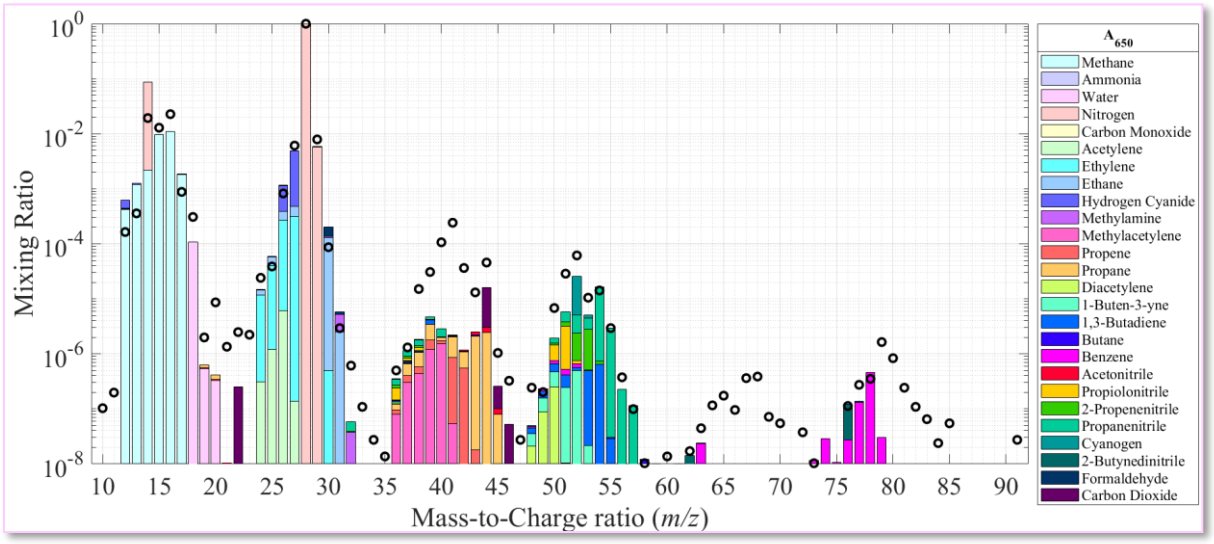

Figure III.5: Same as Figure III.4, but showing the top 5% results of the deconvolution of the mass spectrum shown in Figure III.2 (A_{650} simulation).

In Figure III.4 and Figure III.5, using a database only made up of species already observed in Pluto's atmosphere and/or predicted by Pluto photochemical models, we note that while some species do indeed contribute significantly to the measured mass spectra (*e.g.*, acetylene, ethylene, ethane, hydrogen cyanide, methylamine), other species have such negligible contributions that we can question their actual presence (*e.g.*, ammonia, diacetylene). We also note that with this database consisting of only 26 species, it is clear from Figure III.4 and

Figure III.5 that a certain number of molecules are missing to explain C_5 and C_6 clusters ($m/z > 60$), as well as to complete C_3 and C_4 clusters.

In any case, finding in our deconvolution results the molecules already detected and predicted in Pluto's atmosphere allows us to conclude that, from a qualitative point of view, our A_{400} and A_{650} lab-simulations reproduce fairly well Pluto's atmospheric neutral chemistry. We can therefore hypothesize the presence of molecules not currently predicted by current Pluto photochemical models.

III.1.2.b. Identification of potential new species inferred from laboratory simulations of Pluto's atmosphere and discussion on some selected molecules

As previously stated, our current knowledge of the chemical composition of Pluto's atmosphere (observations and results from photochemical models) is not sufficient to explain our experimental mass spectra as a whole. Therefore, we implemented additional molecules in our database, after sequentially testing more than 100 different molecules. 26 additional potential molecules were found, resulting in a database of 52 species. These 26 additional molecules are reported in Table III.2.

Table III.2: Additional potential molecules included in the deconvolution database, after testing sequentially about 100 different species.

Molecules		
IUPAC name	**Chemical formula**	**Skeletal formula**
Oxygen	O_2	
Hydrazine	N_2H_4	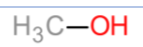
Methyl Alcohol	CH_3OH	
Formic Acid	HCOOH	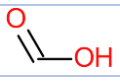
Nitrous Oxide	N_2O	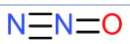
Acetone	C_3H_6O	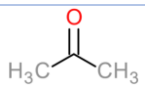
Propanedinitrile	$C_3H_2N_2$	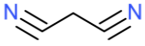
1,3-Cyclopentadiene	C_5H_6	
Cyclopentene	C_5H_8	
Methylacrilonitrile	C_4H_5N	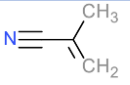

Pyrrole	C_4H_5N	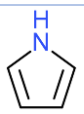
Pyrrolidine	C_4H_9N	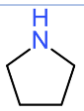
1H-Imidazole	$C_3H_4N_2$	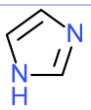
3-Butenenitrile	C_3H_5CN	
1-Butanol	C_4H_9OH	
1,4-Cyclohexadiene	C_6H_8	
1,3,5-Triazine	$C_3H_3N_3$	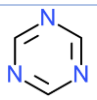
3-Aminopyrazole	$C_3H_5N_3$	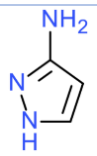
4-Methyl-4H-1,2,4-Triazole	$C_3H_5N_3$	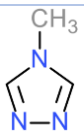
Fumaronitrile	$C_4H_2N_2$	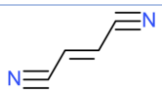
1-Methyl-1H-Imidazole	$C_4H_6N_2$	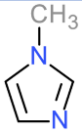
Pyridine	C_5H_5N	
2,4-Pentadienenitrile	C_5H_5N	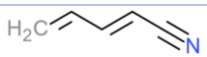
Piperidine	$C_5H_{11}N$	
2-Cyclopenten-1-one	C_5H_6O	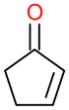
2-Pentenal	C_5H_8O	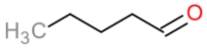

The top 5% of the deconvolution results for the A_{400} and A_{650} mass spectra using this novel database are given in Figure III.6 and Figure III.7, respectively.

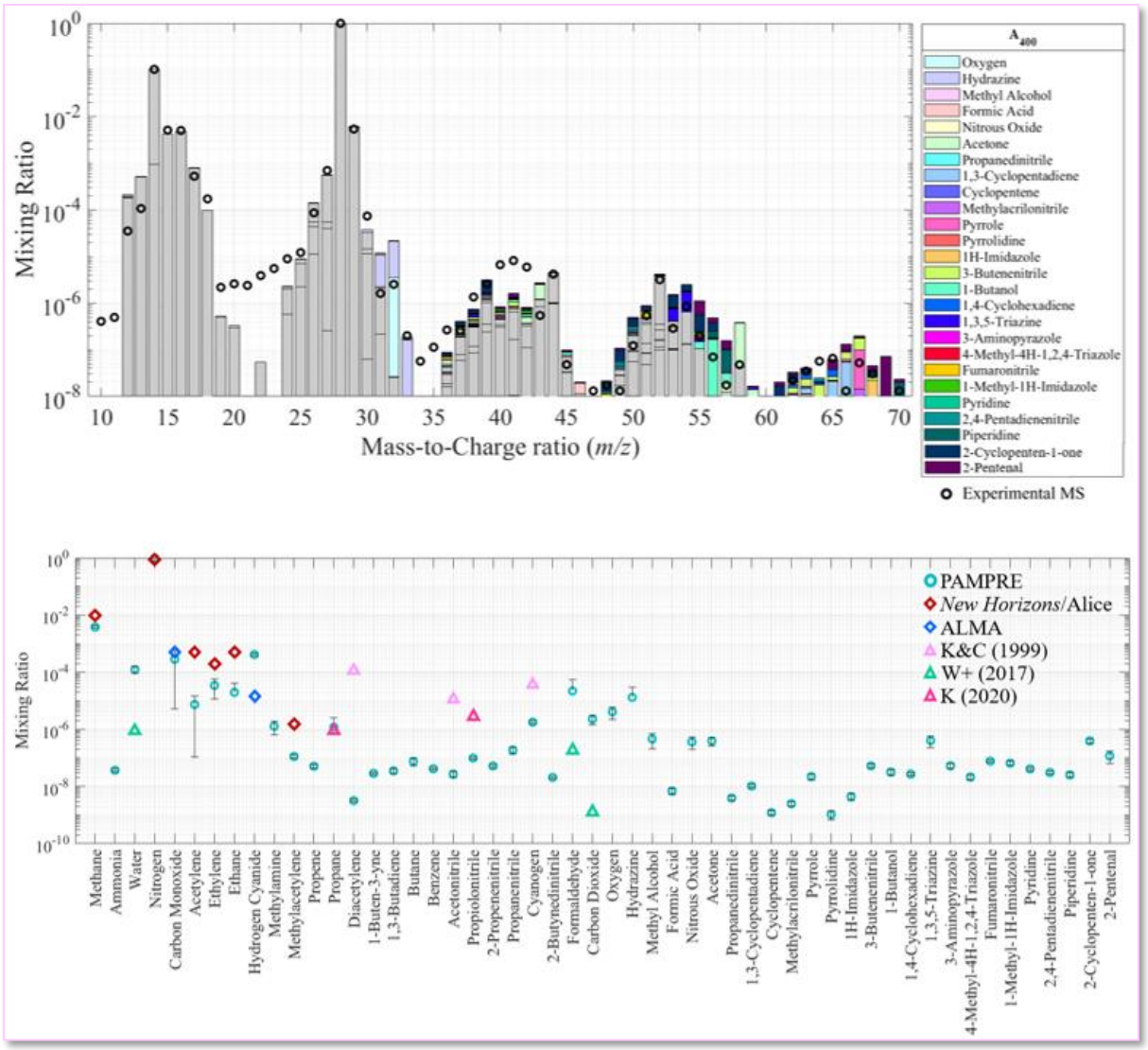

Figure III.6: Top 5% results of the deconvolution of the mass spectrum shown in Figure III.1 (A_{400} simulation) using the method developed by Gautier *et al.* (2020). *Top*: The black dots correspond to the experimental mass spectrum. The colored bars correspond to the contribution of each molecule calculated by the deconvolution method. The database used for the deconvolution was populated with 52 molecules (26 species already observed in Pluto's atmosphere or predicted by Pluto photochemical models in grey, and 26 species found to be suitable in different colors, reported in Table III.2). *Bottom*: The turquoise dots with black error bars correspond to the mixing ratios of the different species contributing to the A_{400} mass spectrum, determined after deconvolution of the mass spectrum. The red and blue diamonds correspond to the mixing ratios of species detected and quantified in Pluto's atmosphere respectively by Young *et al.* (2018) and Steffl *et al.* (2020) using the Alice instrument onboard *New Horizons* and by Lellouch *et al.* (2017) through ALMA observations. The triangles correspond to the mixing ratios of species predicted in Pluto's atmosphere by Pluto photochemical models: "K&C (1999)" for Krasnopolsky and Cruikshank (1999) (in light pink), "W+ (2017)" for Wong *et al.*(2017) (in green), and "K (2020)" for Krasnopolsky (2020) (in dark pink).

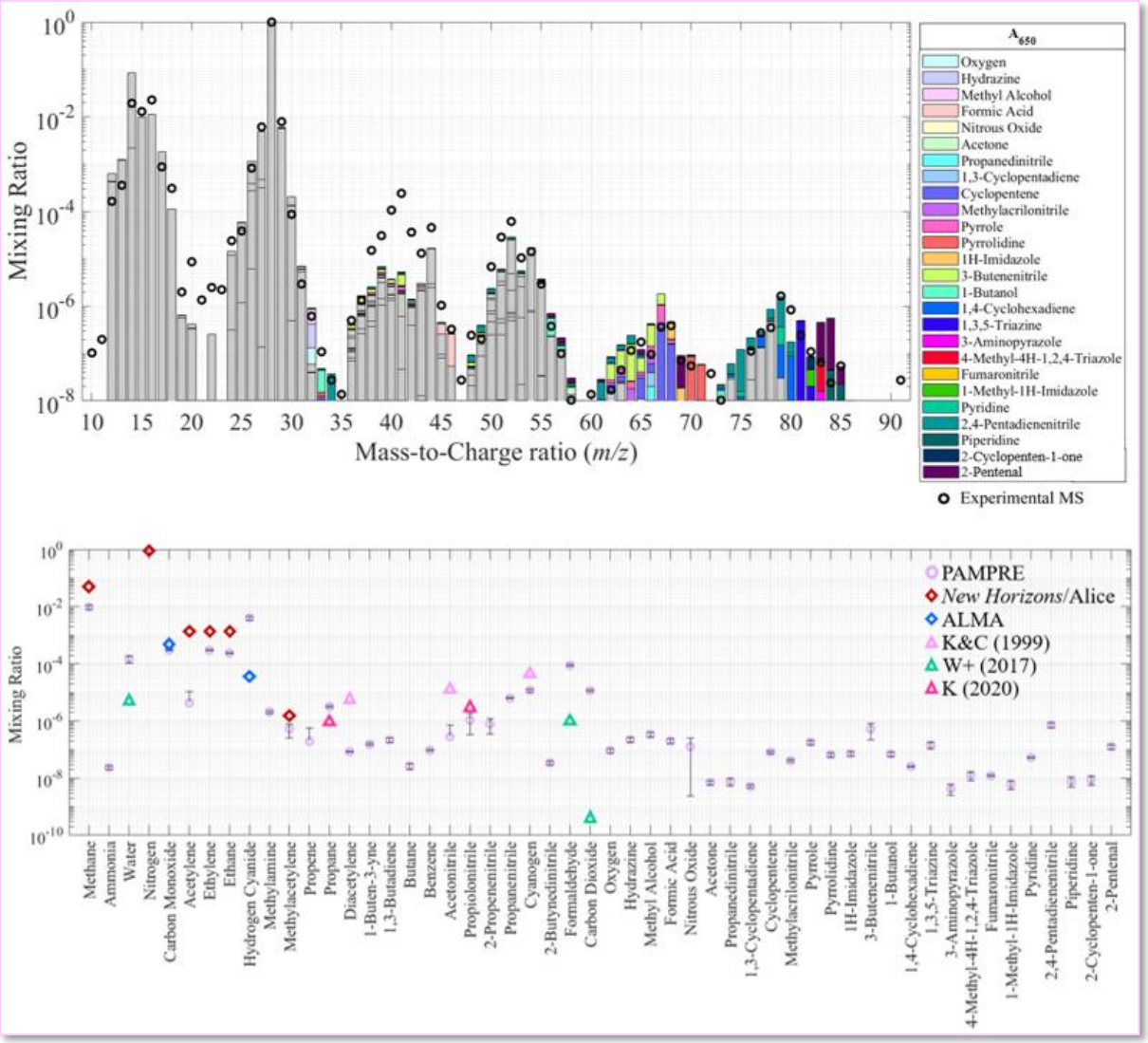

Figure III.7: Same as Figure III.6, but showing the top 5% results of the deconvolution of the mass spectrum shown in Figure III.2 (A_{650} simulation).

Before discussing the results obtained in more details, we can give some general comments on the deconvolution results presented in Figure III.6 and Figure III.7. We note firstly that the C_1, C_2, C_4, C_5, and C_6 clusters are globally well fitted, in contrast to the C_3 cluster, and especially for the A_{650} lab-simulation (Figure III.7.top). This discrepancy suggests that there are species missing from the database to complete the fit of the C_3 cluster. Although more than 100 different molecules were tested (including hydrocarbons, amine and/or nitrile nitrogenous molecules, oxygenated molecules), the current database containing 52 species is not sufficient to fit the C_3 cluster. One or more new molecules therefore remain to be identified, in order to complete the database to better fit the C_3 cluster. Given that the other clusters are globally well-fitted, this suggests that the missing molecule(s) are C_3 molecules that do not fragment much, and therefore do not produce fragments contributing to clusters C_1 and C_2.

Now, we will compare our results regarding C_2 hydrocarbons, hydrogen cyanide HCN, and methylacetylene C_3H_4 with ground-based observations of Pluto's atmosphere (Lellouch *et al.*, 2017) and those made by the Alice instrument onboard *New Horizons* (Young *et al.*, 2018; Steffl *et al.*, 2020) (see the red and blue diamonds in Figure III.6.bottom and Figure III.7.bottom, and Table III.3). Observations made with ALMA (blue diamonds in Figure III.6.bottom and Figure III.7.bottom) quantified a mixing ratio for HCN > 1.5×10^{-5} above 450 km, with a best-determined value of 4×10^{-5} near 800 km of altitude above the surface (Lellouch *et al.*, 2017). Meanwhile, Alice observations (red diamonds in Figure III.6.bottom and Figure III.7.bottom) resulted in the quantification of acetylene C_2H_2, ethylene C_2H_4, and ethane C_2H_6 mixing ratios as a function of altitude, as well as a column-integrated mixing ratio for C_3H_4. Regarding C_2 hydrocarbons at 400 km of altitude in Pluto's atmosphere, C_2H_2 and C_2H_6 have mixing ratios of 5×10^{-4}, whereas C_2H_4 has a mixing ratio of 2×10^{-4}. At 650 km of altitude, the three species have mixing ratios of ~1.5×10^{-3} (Young *et al.*, 2018). Regarding C_3H_4, its mixing ratio was reported at 1.6×10^{-6} (Steffl *et al.*, 2020).

In our A_{400} lab-simulation, QMS measurements and deconvolution of the mass spectrum (Figure III.6.bottom, turquoise dots) resulted in quantified mixing ratios for C_2H_2, C_2H_4, C_2H_6, HCN, and C_3H_4 at about 7.4×10^{-6}, 3.5×10^{-5}, 2.0×10^{-5}, 4.2×10^{-4}, and 1.1×10^{-7}, respectively. For the A_{650} simulation (Figure III.7.bottom, lavender color dots), these mixing ratios are approximately 4.3×10^{-6}, 3.0×10^{-4}, 2.4×10^{-4}, 4.0×10^{-3}, and 5.3×10^{-7}.

Table III.3: Comparison between the mixing ratios of the photoproducts C_2H_2, C_2H_4, C_2H_6, HCN, and C_3H_4 quantified in Pluto's atmosphere (Lellouch *et al.*, 2017; Young *et al.*, 2018; Steffl *et al.*, 2020) and mixing ratios calculated after deconvolution of A_{400} and A_{650} mass spectra.

Photoproducts	On Pluto	In PAMPRE
Mixing ratios at ~400 km of altitude ⇔ A_{400}		
Acetylene (C_2H_2)	5×10^{-4}	7.4×10^{-6}
Ethylene (C_2H_4)	2×10^{-4}	3.5×10^{-5}
Ethane (C_2H_6)	5×10^{-4}	2.0×10^{-5}
Hydrogen Cyanide (HCN)	1.5×10^{-5}	4.2×10^{-4}
Methylacetylene (C_3H_4)	1.6×10^{-6}	1.1×10^{-7}
Mixing ratios at 600-700 km of altitude ⇔ A_{650}		
Acetylene (C_2H_2)	1.5×10^{-3}	4.3×10^{-6}
Ethylene (C_2H_4)	1.5×10^{-3}	3.0×10^{-4}
Ethane (C_2H_6)	1.5×10^{-3}	2.4×10^{-4}
Hydrogen Cyanide (HCN)	4×10^{-5}	4.0×10^{-3}
Methylacetylene (C_3H_4)	1.6×10^{-6}	5.3×10^{-7}

Except for C_2H_2, we notice that the mixing ratios of C_2H_4, C_2H_6, HCN, and C_3H_4 increase globally with increasing initial CH_4 concentration, in agreement with previous laboratory studies of Titan's atmospheric chemistry (Gautier *et al.*, 2011; Carrasco *et al.*, 2012; Hörst, Yoon, *et al.*, 2018; Dubois, Carrasco, Petrucciani, *et al.*, 2019; Chudják, Kozáková and Krčma, 2021).

Regarding the A_{400} simulation, although they are a bit low, the mixing ratios of C_2H_4, C_2H_6 and C_3H_4 are approaching the Alice measurements, whereas this is not the case for C_2H_2 which presents a very low mixing ratio, nor for HCN with a mixing ratio too high compared to the ALMA observations. Regarding the A_{650} simulation, we can again notice that the mixing ratios of C_2H_4, C_2H_6 and C_3H_4 are approaching the Alice observations, whereas the C_2H_2 mixing ratio is much lower than observed at Pluto, and the HCN mixing ratio is much larger.

For both A_{400} and A_{650} lab-simulations, the too large proportion of HCN can be explained by the characteristics of the PAMPRE radio-frequency discharge. As mentioned in Chapter II, Section II.1.2, the energy distribution of the discharge is similar at first order to the energy distribution of solar photons, with a maximum at ~1-2 eV. However, the tail of the energy distribution of the electrons in the plasma is more populated than the energy distribution of solar photons (Szopa, Cernogora *et al.*, 2006; Alves *et al.*, 2012), enhancing the dissociation of N_2, and thus the formation of HCN. Regarding the very low proportion of C_2H_2, either it is an analytical problem, or it could be explained by the active participation of C_2H_2 in the formation of more complex compounds or a lower production of C_2H_2 in the reactive medium in PAMPRE. In the first case, it may be that, in the C_2 cluster, the deconvolution code is struggling to fit C_2H_2 because of the lack of unique peaks. Thus, C_2H_2 is recovering the over- or under-fit errors of the other C_2 molecules. Another explanation could be the transmission function of the QMS, which is not linear[16]. In the latter case, the formation of C_2H_2 would be slower than its consumption, thus not allowing to have a high proportion of this compound at steady state. In conditions relevant to Pluto's atmosphere, the Pluto photochemical model by Krasnopolsky (2020) predicts a significant loss of C_2H_2 through photolysis, reactions with C_2H radicals, and

[16] Because of the way the QMS is tuned, the analytical instrument presents a log-normal transmission curve biasing the recorded mass spectra. More precisely, in order to optimize the signals to detect species as low in abundance as ppm, it was necessary to tune the QMS electromagnetic lenses, and to do so, to set an arbitrary mass. In our case, as N_2 is the major component of our studied gas mixtures, we therefore set our tune on *m/z* 28. Thus, if the detection is particularly optimized for the C_2 and C_1 clusters of peaks, it is not the case for the peaks at *m/z* 1 and 2, nor for the heavier clusters. These clusters (C_3 and more) are less intense than they should be. In the future, it would be useful to calibrate the signals obtained by QMS through complementary experiments, in order to be sure of our quantitative studies. Nevertheless, at the time of writing of this manuscript, these experiments could not be performed, thus we had to proceed differently.

ion reactions; C_2H_2 polymerizes into heavier molecules and ultimately solid aerosols. Meanwhile, the model of Luspay-Kuti *et al.* (2017) calculates a high loss of C_2H_2 through aerosol trapping/irreversible sticking of C_2H_2 on Pluto's aerosols. If it is possible that C_2H_2 actively participates in the formation of heavier molecules in our N_2:CH_4:CO plasma, we cannot conclude on the irreversible sticking of this compound on the aerosol analogues, since this studied process occurs at low temperature, whereas our simulations are conducted at ambient temperature. Finally, Wong, Yung and Gladstone (2015), for their part, suggest a competition between C_2H_2 and HCN formation pathways involving the CH_2 radical; and this hypothesis seems the most likely here. Indeed,

$$CH_2 + CH_2 \rightarrow C_2H_2 + H_2 \qquad \text{(III.1)}$$

is expected to compete with

$$N + CH_2 \rightarrow HCN + H \qquad \text{(III.2)}$$

Given the over-dissociation of N_2 in the PAMPRE plasma discharge compared to Pluto's atmosphere, reaction (III.2) is likely favored over reaction (III.1), thus explaining the large proportion of HCN and the small proportion of C_2H_2 found in our deconvolution results.

In Figure III.6 and Figure III.7, we see that apart from N_2, CH_4, and CO, the main species are: water H_2O, acetylene C_2H_2, ethylene C_2H_4, ethane C_2H_6, hydrogen cyanide HCN, formaldehyde H_2CO, hydrazine N_2H_4, propanenitrile C_3H_5N, cyanogen C_2N_2, and carbon dioxide CO_2.

Although H_2O was detected by He *et al.* (2017) in their CO-enriched Titan-simulated atmosphere, the presence of this species could also be explained by the ambient air and a non-perfect vacuum in the reactor before the experiments. Given the importance of this molecule from an astrobiological point of view, to confirm the formation of H_2O by photochemistry in a N_2:CH_4:CO gas mixture, additional analyses are absolutely necessary, such as experiments conducted with CD_4 and/or $C^{18}O$ isotopic gases. This result will therefore not be discussed further in this manuscript.

The large abundance of C_2 hydrocarbons and HCN in our Pluto-simulated atmosphere is in agreement with the theoretical study of Legrand *et al.* (1998) regarding the kinetics of reactions in N_2:CH_4 plasma. In this study, the authors concluded that the organic growth begins with the dissociation of CH_4 from three possible mechanisms: electron impact, dissociative charge transfer reaction with excited molecular nitrogen N_2^*, or with excited atomic nitrogen N^*. After

several successive two-body reactions, the primary stable products C_2H_2, C_2H_4, C_2H_6, H_2 and HCN are formed and accumulate, and then react to form other hydrocarbons and N-containing species.

Among all the species, we note that the most abundant in our Pluto-simulated atmosphere is HCN. This result agrees with published literature on gas-phase measurements of Titan's atmospheric chemistry simulated in the laboratory either by electric discharge (Sciamma-O'Brien *et al.*, 2010; Gautier *et al.*, 2011; Carrasco *et al.*, 2012; Fleury *et al.*, 2014; Hörst, Yoon, *et al.*, 2018; Dubois, Carrasco, Petrucciani, *et al.*, 2019; Chudják, Kozáková and Krčma, 2021) or UV photons (Imanaka and Smith, 2010; Yoon *et al.*, 2014; Hörst, Yoon, *et al.*, 2018). In the Titan literature, HCN was reported as a key precursor for the formation of aerosols (*e.g.*, Wilson and Atreya, 2003; Imanaka *et al.*, 2004; Lavvas, Coustenis and Vardavas, 2008; Krasnopolsky, 2009; Imanaka and Smith, 2010; Pernot *et al.*, 2010; Sciamma-O'Brien *et al.*, 2010; Gautier *et al.*, 2011; He and Smith, 2013, 2014). Thus, the production and loss processes of HCN in N_2-rich atmospheres have been extensively studied. Different reactions are proposed for the formation of HCN, in a single step or in two steps. The dissociation of N_2 by EUV radiation leads to the formation of excited state $N(^2D)$ and fundamental state $N(^4S)$, playing a crucial role in the formation of HCN (*e.g.*, Lara, Ip and Rodrigo, 1997; Lavvas, Coustenis and Vardavas, 2008). Regarding Pluto's atmosphere, according to Krasnopolsky (2020), the major source of HCN could be the following reactions:

$$N(^4S) + CH_3 \rightarrow H_2CN + H \qquad \text{(III.3)}$$

$$H_2CN + H \rightarrow HCN + H_2 \qquad \text{(III.4)}$$

Another major source of HCN could be the following reactions (*e.g.*, Lavvas, Coustenis and Vardavas, 2008):

$$N(^2D) + CH_4 \rightarrow CH_2NH + H \qquad \text{(III.5)}$$

$$CH_2NH + h\nu \rightarrow HCN + 2\,H \qquad \text{(III.6)}$$

During my Ph.D., I was involved in a study on the importance of HCN in the formation of Titan's aerosols: Perrin, Carrasco, Chatain, Jovanovic *et al.* (2021). An Atmospheric Origin for HCN-Derived Polymers on Titan. *Processes* 9, which could be applicable to Pluto's atmosphere too.

In this study investigating a N_2:CH_4 = 95%:5% reactive gas mixture, we followed by QMS the temporal evolution of CH_4 (at *m/z* 16) and HCN (at *m/z* 27). This monitoring is presented in Figure III.8.

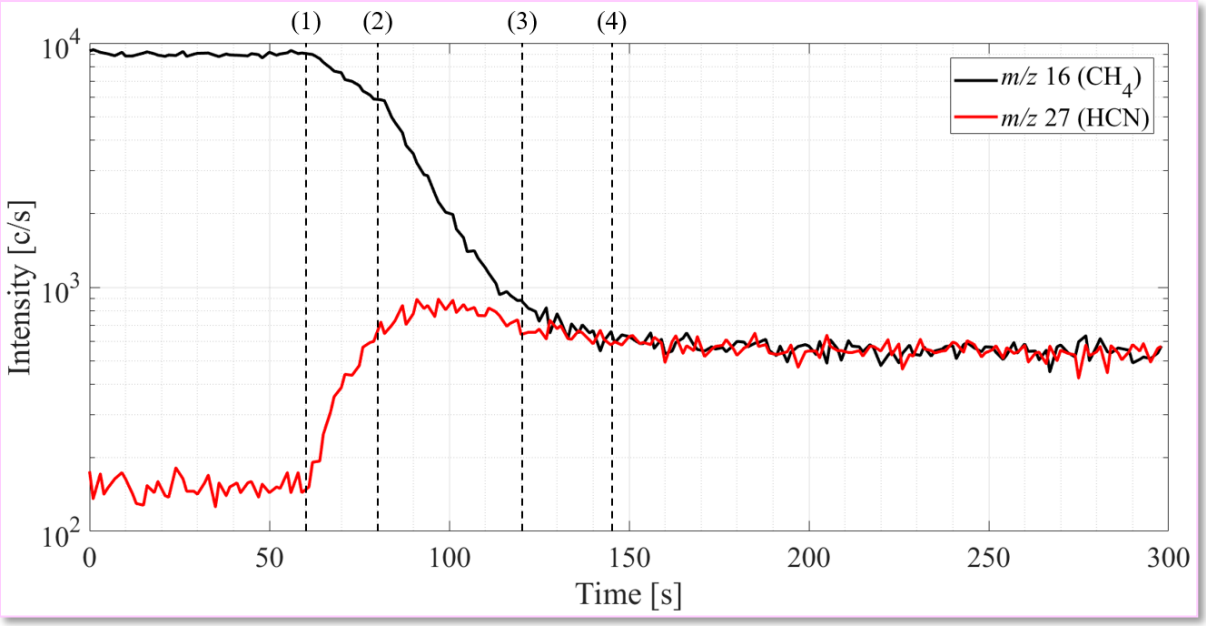

Figure III.8: Monitoring of the temporal evolution of *m/z* 16 (CH_4, in black) and *m/z* 27 (HCN, in red) by QMS, highlighting the importance of HCN in the formation and the growth of Titan's and Pluto's aerosols. The vertical black dashed lines indicate four distinct phases. *Credit*: The figure is adapted from Perrin *et al.* (2021).

In Figure III.8, we observe four phases indicated by the vertical black dashed lines:

- *Phase #1*: The line indicating the beginning of phase #1 (from 60 seconds) corresponds to the ignition of the RF discharge. The electrons of the discharge ionize and dissociate methane CH_4 and molecular nitrogen N_2 (Szopa, Cernogora *et al.*, 2006), the main components of Titan's and Pluto's atmospheres. The ions and radicals formed from N_2 and CH_4 react to form more complex organic molecules, including nitriles, the most abundant of which is HCN. Indeed, we note that the black curve representing the temporal evolution of CH_4 decreases in intensity when the RF discharge is ignited, while the curve corresponding to HCN (in red) increases in intensity. This demonstrates that HCN is a by-product of CH_4 dissociation.
- *Phase #2*: 20 seconds after the ignition of the discharge, we note a change in the slope of the CH_4 curve (*i.e.*, steeper decreasing slope), with a faster consumption of this reagent. This change in slope was recognized by Wattieaux *et al.* (2015) as an indicator of the appearance of the first tholin nanoparticles. In Figure III.9, we can see the

appearance of the solid particles thanks to a green laser beam passing through the PAMPRE reactor. Indeed, before the particles appear, the laser beam is not visible to the naked eye, and when the particles appear, they scatter the light, making the green laser beam visible. Wattieaux *et al.* (2015) showed that the formation of solid particles in the plasma induces an increase in the electron temperature, which results in an acceleration of CH_4 consumption, as evidenced by the steeper decreasing slope of the CH_4 curve. In parallel to this important consumption of CH_4, the formation of HCN slows down. With CH_4 being largely consumed, we would expect HCN to be formed in larger quantities. But here we see that from phase #2, the curve of HCN flattens, suggesting that this compound is consumed quickly after its formation. This correlation between HCN consumption and aerosol appearance shows that HCN is actively involved in aerosol formation and growth. This is consistent with the discussion raised by Sciamma-O'Brien *et al.* (2010) regarding the polymerization of HCN driving the chemical growth of Titan tholins.

- *Phase #3*: From phase #3, we see a second change of slope in the CH_4 curve. The consumption of CH_4 slows down, as well as the formation of HCN. The lower abundance of HCN can be explained either by a decrease in the source (*i.e.*, CH_4 is consumed less), and/or a greater contribution of HCN to aerosol growth.
- *Phase #4*: CH_4 and HCN curves reach a plateau and remain stationary for the whole duration of the tholins synthesis.

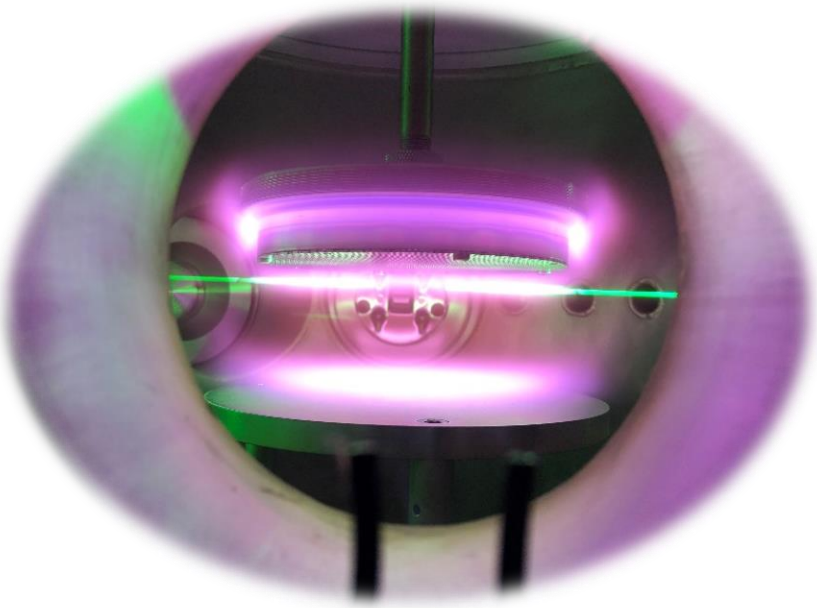

Figure III.9: Appearance of tholins in a Titan-simulated atmosphere, highlighted by a green laser beam (532 nm) passing through the PAMPRE reactor.

In Figure III.6 and Figure III.7, along with HCN, other nitrile compounds are detected in Pluto-simulated atmosphere, both saturated (*e.g.*, acetonitrile, propanenitrile), and unsaturated (*e.g.*, propiolonitrile, 2-propenenitrile). The production and loss pathways for these nitrile compounds are extensively discussed in Loison *et al.* (2015), regarding Titan's atmosphere. In Pluto-simulated atmosphere, and by extension in Pluto's atmosphere, the presence of such a diversity of nitriles, in significant quantities, suggests that the reactivity of these compounds is important in the formation of Pluto's aerosols as well. Moreover, on the early Earth and elsewhere, HCN is a central molecule because of its involvement in prebiotic processes. Hydrogen cyanide is one of the most studied chemical precursors for the formation of biomolecules. Indeed, HCN is recognized as a key ingredient in the abiotic synthesis of nucleobases, α-amino acids, and hydroxy acids (*e.g.*, Saladino *et al.*, 2012; Patel *et al.*, 2015). We will see in Chapter IV that such molecules of prebiotic interest are detected in analogues of Pluto's aerosols, suggesting once again the preponderant role of HCN in the growth mechanisms of Pluto's aerosols.

Regarding oxygenated species, Wong *et al.* (2017) predicted in Pluto's atmosphere the presence of water, carbon dioxide and formaldehyde, along with carbon monoxide. As previously said, we cannot conclude on the formation of H_2O in our Pluto-simulated atmosphere. Nevertheless, our mass spectra deconvolution results suggest the effective presence of H_2CO and CO_2.

For the A_{400} and A_{650} lab-simulations (Figure III.6 and Figure III.7), regarding only the "new" molecules that we propose, these species are reported in Table III.4.

Table III.4: Suggested molecules contributing significantly to the mass spectra of Pluto-simulated atmospheres A_{400} and A_{650}.

Molecule	**Structure**	**Main peaks in mass spectrum (*m/z*)**
Oxygen		32, 16
Hydrazine	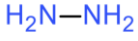	32, 31, 29, 30, 16
Methyl Alcohol	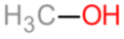	31, 32, 29, 15, 30
Formic Acid	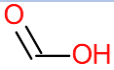	29, 46, 45, 28, 17
Nitrous Oxide	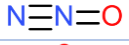	44, 30, 14, 28, 16
Acetone	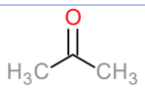	43, 58, 15, 42, 27
Propanedinitrile	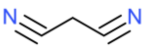	66, 39, 38, 28, 65
1,3-Cyclopentadiene		66, 65, 39, 40, 63

Cyclopentene		67, 68, 39, 53, 41
Methylacrylonitrile	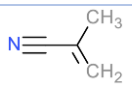	41, 67, 39, 52, 40
Pyrrole	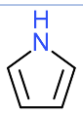	67, 39, 41, 40, 28
Pyrrolidine	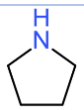	43, 70, 42, 28, 71
1H-Imidazole	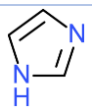	68, 41, 40, 28, 67
3-Butenenitrile	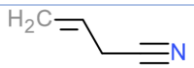	41, 39, 67, 27, 40
1-Butanol		56, 31, 41, 43, 27
1,4-Cyclohexadiene		79, 80, 77, 39, 51
1,3,5-Triazine	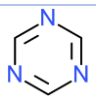	81, 54, 28, 27, 53
3-Aminopyrazole	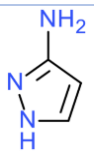	83, 28, 54, 52, 29
4-Methyl-4H-1,2,4-Triazole	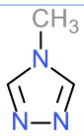	83, 27, 42, 28, 55
Fumaronitrile	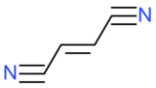	78, 51, 77, 52, 26
1-Methyl-1H-Imidazole	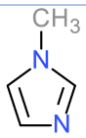	82, 42, 54, 40, 81
Pyridine		79, 52, 51, 50, 78
2,4-Pentadienenitrile	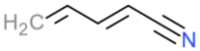	52, 79, 51, 39, 53
Piperidine	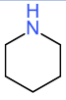	84, 85, 56, 57, 44
2-Cyclopenten-1-one	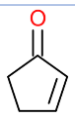	82, 39, 54, 53, 28
2-Pentenal		55, 84, 83, 41, 29

The molecules reported in Table III.4 are particularly interesting in that they differ from the *a priori* of Pluto photochemical models. As we can see, the species which contribute significantly to the mass spectra of the A_{400} and A_{650} simulations are not only hydrocarbons. Although some hydrocarbons, such as 1,3-cyclopentadiene, cyclopentene, and 1,4-cyclohexadiene, are suspected, the majority of species are N-bearing molecules. Indeed, nitriles – methylacrylonitrile, 3-butenenitrile, fumaronitrile, and 2,4-pentadienenitrile – are reported, but also and especially 5- and 6-membered cyclic molecules with one or more intracyclic nitrogen atoms, such as pyrrole, pyrrolidine, 1H-imidazole, 1,3,5-triazine, 3-aminopyrazole, 4-methyl-4H-1,2,4-triazole, 1-methyl-1H-imidazole, pyridine, and piperidine. The predominance of nitrogenous molecules in the gas-phase products of laboratory simulations was already reported in Titan literature (*e.g.*, Coll *et al.*, 1999; Imanaka and Smith, 2010; Gautier *et al.*, 2011; Carrasco *et al.*, 2012; Hörst *et al.*, 2018; Berry *et al.*, 2019; Chudják, Kozáková and Krčma, 2021). The presence in large quantities of gas-phase N-bearing molecules is also consistent with the chemical composition of Pluto aerosol analogues synthesized within Pluto-simulated atmosphere, as will be discussed in next Chapter IV. Moreover, these nitrogenous species are of particular interest, regarding their implications for prebiotic chemistry, as mentioned above for HCN and as discussed in Chapter IV, Section IV.2.

Some O-bearing molecules are also suspected: oxygen, methyl alcohol, formic acid, nitrous oxide, acetone, 1-butanol, 2-cyclopenten-1-one, and 2-pentenal. The oxygenated chemical functions are terminal groups (carboxylic acids, alcohols, carbonyls), as already observed by Bernard *et al.* (2003), Coll *et al.* (2003) and Tran *et al.* (2008). In contrast to N-bearing molecules, the oxygen atoms are not included in an intracyclic way. These oxygenated compounds can participate in the complexification of the molecules constituting Pluto's aerosols. As previously mentioned, HCN is one of the major products formed in Pluto-simulated atmosphere. Here, we conclude to the effective presence of gas-phase products of carbonyl type. Schwartz and Goverde (1982) showed that formaldehyde and simple carbonyl compounds can rapidly react with HCN to produce cyanohydrin compounds, which in turn accelerate the rate of oligomerization of HCN. Therefore, in the final solid products formed in the gas phase – Pluto aerosol analogues –, we can suspect the presence of N- and O-bearing molecules in large quantities.

We note the detection of nitrous oxide. The presence of N_2O is also supported by complementary preliminary QMS analysis performed in a N_2:CO plasma (data not presented here, because the mass spectrum was acquired with a different QMS parameterization). Since

there is little or no hydrogen source in a N_2:CO plasma, the peaks detected at *m/z* 44 and 30 (major fragments of N_2O) supported the formation of this species. N_2O was detected by Fleury *et al.* (2014), who studied the gas-phase composition of a Titan-like atmosphere where CO was added, and by Bourgalais, Carrasco, Vettier, *et al.* (2020) in a Titan-like atmosphere with trace quantity of water as well.

Regarding oxygen O_2, reservations can be expressed about its formation since the peak at *m/z* 32 is not significantly more intense in the "plasma ON" mass spectra compared to the "plasma OFF" mass spectra in Figure III.1 and Figure III.2. From a theoretical point of view, O_2 could be formed by photodissociation of CO_2 (Lu *et al.*, 2014), which is indeed detected in our Pluto-simulated atmospheres A_{400} and A_{650} (Figure III.6 and Figure III.7). However, Lu *et al.* (2014) give a 5 ± 2% yield for the $C(^3P) + O_2(X^3\Sigma_g^-)$ channel in the energy range of 11.7 to 12.2 eV, where the much more abundant competitive CH_4 also absorbs. Thus, the formation of O_2 seems unlikely.

As mentioned above in relation to Figure III.2, the higher intensity of the C_6 cluster compared to the C_5 one was attributed by Bourgalais *et al.* (2021) to the accumulation of benzene C_6H_6. In our Pluto-simulated atmospheres, owing to the deconvolution of the A_{400} and A_{650} mass spectra (Figure III.6 and Figure III.7), we can also conclude on the effective presence of benzene, as well as other stable N-bearing aromatics which can accumulate and contribute to the intense C_6 cluster.

III.1.2.c. Discussion on the formation mechanisms of heterocycles in Pluto-simulated atmosphere

III.1.2.c.α. The case of N-heterocycles

Theoretical studies by Ricca, Bauschlicher and Bakes (2001) and Landera and Mebel (2010) showed that intracyclic N-incorporation mechanisms involve the consecutive additions of HCN/CN and C_2H_2/C_2H – main photoproducts in Pluto's atmosphere (*e.g.*, Gladstone and Young, 2019), and in our Pluto-simulated atmosphere as well (Figure III.6 and Figure III.7) – to benzene C_6H_6, a pure aromatic ring. Then, the presence of a nitrogen atom in the aromatic ring catalyzes the formation of an additional ring, and so forth. The mechanism proposed by Ricca, Bauschlicher and Bakes (2001) and Landera and Mebel (2010) is as follows:

$$C_6H_6 + CN \rightarrow C_6H_5CN + H \qquad \text{(III.7)}$$

$$C_6H_5CN + C_2H \rightarrow C_6H_4(CN)(C_2H) + H \qquad \text{(III.8)}$$

$C_6H_5CN + CN \rightarrow C_6H_4(CN)_2 + H$ (III.9)

$C_6H_4(CN)(C_2H) + C_2H \rightarrow C_{11}H_6N$ (III.10)

$C_6H_4(CN)_2 + C_2H \rightarrow C_6H_4(CN)(NCCCH)$ (III.11)

$C_6H_4(CN)(NCCCH) + C_2H \rightarrow C_{12}H_6N_2$ (III.12)

C_6H_6 is predicted in Pluto's atmosphere (Krasnopolsky, 2020) and was detected in our Pluto-simulated atmospheres A_{400} and especially A_{650} (Figure III.6 and Figure III.7). This aromatic compound was also detected in Titan's atmosphere (Coustenis *et al.*, 2003, 2007; Waite *et al.*, 2007; Cui *et al.*, 2009). Laboratory simulation experiments of Titan's atmospheric chemistry showed that benzene may be an important chemical reactant in the formation of Titan aerosol analogues, even at trace quantities (Trainer *et al.*, 2013; Sciamma-O'Brien, Ricketts and Salama, 2014; Yoon *et al.*, 2014; Gautier *et al.*, 2017; Sciamma-O'Brien, Upton and Salama, 2017). We can thus expect the same for Pluto's aerosols.

In contrast to the theoretical studies by Ricca, Bauschlicher and Bakes (2001) and Landera and Mebel (2010), experiments conducted by Imanaka and Smith (2010) favor the hypothesis of a formation of N-heterocycles in Titan's aerosols through radical chemistry, involving HCCN radicals. Moreover, studies combining experimental and theoretical work suggested that in circumstellar and interstellar environments, N-bearing Polycyclic Aromatic Hydrocarbons (NPAH) are probably formed through sequential gas-phase chemistry mediated by radicals (Parker *et al.*, 2015; Parker and Kaiser, 2017). Other studies otherwise supported that polyaromatic compounds in the interstellar medium grow through ion chemistry (Bera, Lee and Schaefer, 2009; Bera, Head-Gordon and Lee, 2011; Ghesquière, Talbi and Karton, 2014; Yang *et al.*, 2020). Hamid *et al.* (2014) combined experimental and theoretical work to explain the formation of pyrimidine molecules through sequential ion-molecule reactions between HCN and C_2H_2. In Pluto's atmosphere, we can therefore expect that the formation of N-heterocycles is probably a mix of radical reactions, and ion-neutral chemistry (Ricca, Bauschlicher and Bakes, 2001).

III.1.2.c.β. The case of O-heterocycles

Previous numerical models on haze formation on the early Earth showed that atmospheric C/O ratio affects the aerosol formation. For C/O ratio < 1, too many O atoms are present in the reactive mixture and they may terminate hydrocarbon chain polymerization, thereby inhibiting aerosol formation (*e.g.*, Zahnle, 1986; Kasting, 1997; Pavlov *et al.*, 2000, 2001). According to

these models, molecular growth involving oxygen atoms seems to be excluded. However, reservations can be expressed regarding this hypothesis for Pluto's atmospheric chemistry, insofar as a small amount of CO is present in the atmosphere (Lellouch *et al.*, 2017). Moreover, subsequent experimental studies did not support these earlier models, and showed that aerosol formation can occur even for C/O ratios as low as 0.2 (Trainer *et al.*, 2004, 2006; DeWitt *et al.*, 2009).

Despite the absence of O-bearing cycles among the gas-phase products of Pluto-simulated atmosphere – probably because of the difficulty to produce this type of molecules (*e.g.*, Moran and Rodríguez, 2012; Varela and Saá, 2016) and their probable fast consumption in an energetic medium such as the plasma of PAMPRE –, such compounds were nevertheless observed or at least predicted in extraterrestrial environments. Substituted furan and pyran moieties were detected in the insoluble organic matter of carbonaceous chondrites. Such structures were proposed to be formed during the early stages of the Solar System from dehydration of a polyalcohol followed by intramolecular cyclization (Cody *et al.*, 2011). The same structures were also predicted in the interstellar and circumstellar environments. Indeed, UV irradiation of benzene C_6H_6 or naphtalene $C_{10}H_8$ in simple H_2O or H_2O:NH_3 ices resulted in the formation of N- and O-heterocycles (Materese, Nuevo and Sandford, 2015). Moreover, a theoretical study proposed the formation of furan through addition reactions between propadienylidene $:C=C=CH_2$ and formaldehyde H_2CO (Jing *et al.*, 2013).

Such reactions might take place in Pluto's atmosphere, since these precursor species were predicted in Pluto photochemical models (Lara, Ip and Rodrigo, 1997; Krasnopolsky and Cruikshank, 1999). Finally, if such O-heterocycles were indeed formed in Pluto's atmosphere, due to their reactivity, these moieties could serve as active sites for further polymerization (Kroonblawd, Lindsey and Goldman, 2019). As for the formation of NPAH presented above, one could therefore imagine chain reactions resulting in the formation of N- and O-bearing polyaromatic hydrocarbons. We can nevertheless tentatively exclude the formation of pure O-bearing polyaromatic hydrocarbons, due to the low content of oxygen atoms and instead the predominance of nitrogen atoms in Pluto's atmosphere.

III.2. Cations in Pluto-simulated atmosphere

So far, only a few laboratory studies have focused on the study of ions in the ionospheres of Titan and exoplanets (Thissen *et al.*, 2009; Sciamma-O'Brien, Ricketts and Salama, 2014; Berry *et al.*, 2019; Bourgalais *et al.*, 2019; Bourgalais, Carrasco, Changeat, *et al.*, 2020; Dubois

et al., 2020), and none have focused on the ionosphere of Pluto, despite the importance of ion-neutral coupled chemistry in the formation of solid aerosols (McEwan and Anicich, 2007; Waite *et al.*, 2007; Lavvas *et al.*, 2013; Westlake *et al.*, 2014). As already discussed in Titan literature, ion chemistry is suggested as one possible mechanism for nitrogen incorporation into aerosol molecules (Trainer *et al.*, 2006; Vuitton, Yelle and McEwan, 2007; Waite *et al.*, 2007). In particular, in Dubois, Carrasco, Jovanovic *et al.* (2020). Positive ion chemistry in an N_2-CH_4 plasma discharge: Key precursors to the growth of Titan tholins. *Icarus* 338, we investigated the effect of methane concentration on Titan's cations. Regarding Pluto, few current photochemical models deal with the chemistry of cations (and none with the chemistry of anions). To our knowledge, Pluto's atmospheric cations are only studied in the models of Krasnopolsky and Cruikshank (1999) and Krasnopolsky (2020). In his latest model, Krasnopolsky (2020) predicted that the most abundant hydrocarbon cation below 650 km of altitude is $C_9H_{11}^+$ (*m/z* 119), whereas $C_2H_5^+$ (*m/z* 29) dominates above 800 km of altitude. Near the ionospheric peak at ~700-750 km of altitude (Bagenal *et al.*, 2016), $C_3H_5^+$ (*m/z* 41) and $C_5H_5^+$ (*m/z* 65) have comparable densities and dominate. Regarding the nitrile cations, the most prominent are $HCNH^+$ (*m/z* 28), $C_2H_3CNH^+$ (*m/z* 54), and $C_3H_3CNH^+$ (*m/z* 66). Regarding the observations made by *New Horizons*, the SWAP instrument revealed the probable presence of CH_4^+ (*m/z* 16) (McComas *et al.*, 2016) and the Alice spectrograph detected emission by N^+ (*m/z* 14) at 108.5 nm (Steffl *et al.*, 2020).

In this part of my Ph.D. thesis, I therefore investigate the cations formed in reactive media relevant to Pluto's atmosphere.

III.2.1. Identification of cations in Pluto-simulated atmosphere

Figure III.10 shows *in situ* QMS mass spectrum of the cations present at steady state in Pluto-simulated atmosphere A_{400}. The peak intensities were normalized to the most intense peak in the mass spectrum, *i.e.*, *m/z* 28.

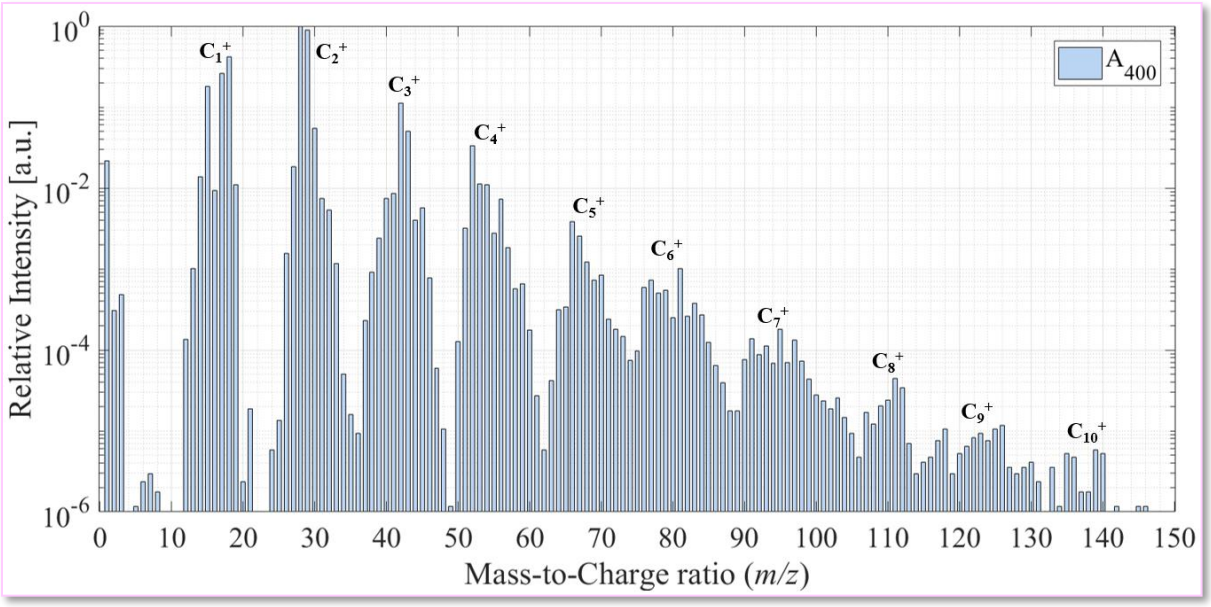

Figure III.10: *In situ* mass spectrum of the cations present at steady state in A_{400} simulation mimicking the photochemistry occurring in Pluto's atmosphere at ~400 km of altitude. The mass spectrum is the accumulation of 10 scans. The cations presented here were formed *in situ* in the plasma, and not in the ionization source of the QMS. The *x*-axis corresponds to the mass-to-charge (*m/z*) ratio, whereas the *y*-axis corresponds to the relative intensity of the peaks, normalized to the most intense peak in the mass spectrum, *m/z* 28.

The mass spectrum shown in Figure III.10 reveals a rich and complex positive ion chemistry, with the production of heavy cations up to *m/z* 150. Attention is drawn to the reader that the detection of cations up to *m/z* 150 but not of neutral molecules does not mean that cations are more abundant than the neutral molecules. All is a question of dynamic range of the QMS which does not allow to detect in RGA directly (without cold trap, for instance) the neutrals beyond the C_6 cluster, because the difference of concentration is too high between the low-abundant heaviest molecules and the major species N_2. Regarding positive ions, their concentration is in the ppm range compared to the neutrals in the plasma (see Chapter II, Section II.1.2). Although the peak at *m/z* 28 seems very intense compared to the C_5^+, C_6^+ (and more) cations, the difference is actually only 2 orders of magnitude, hence the detection of cations as heavy as 150 u.

I have compared the mass spectrum of the cations formed in Pluto-simulated atmosphere with mass spectra published in Dubois, Carrasco, Jovanovic *et al.* (2020) to highlight the influence of CO on N_2:CH_4 reactivity. Figure III.11 shows the comparison between the cations present in the A_{400} reactive medium (in light blue) and those present in a Titan-simulated atmosphere made of 99% of N_2 and 1% of CH_4 (in dark grey, from Dubois *et al.* (2020)). In Dubois,

Carrasco, Jovanovic *et al.* (2020), we studied the positive ions formed in a Titan-like atmospheric chemistry simulated with the PAMPRE experimental setup. In particular, Titan's atmosphere was simulated using different CH_4 mixing ratios.

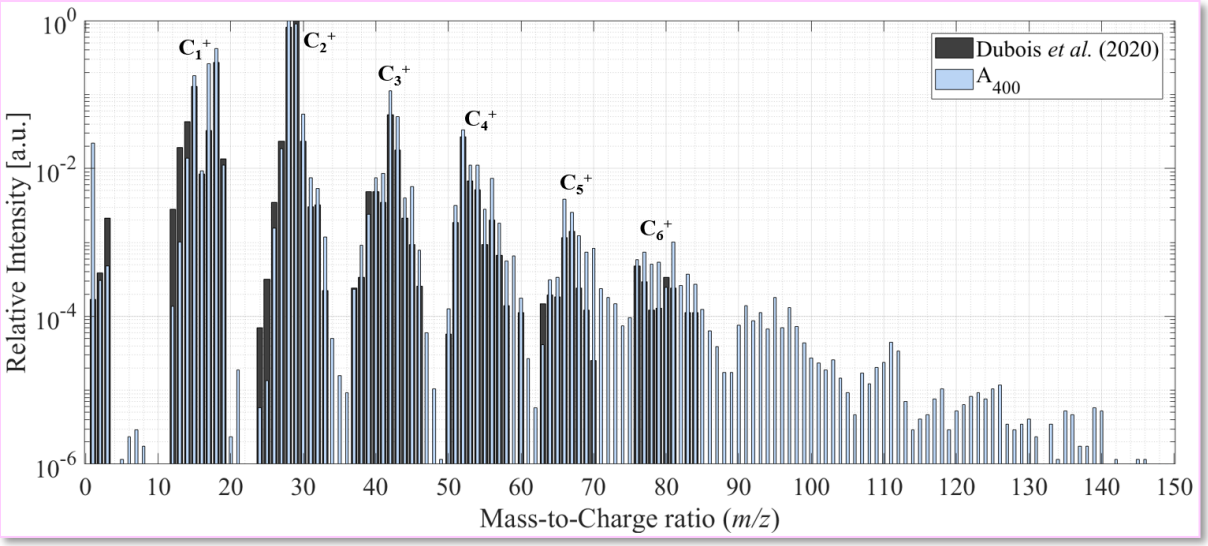

Figure III.11: *In situ* mass spectra of the cations present at steady state in Pluto-simulated atmosphere A_{400} (in light blue) and in Titan-simulated atmosphere composed of 99% of N_2 and 1% of CH_4 (in dark grey). The grey mass spectrum is taken from Dubois, Carrasco, Jovanovic *et al.* (2020).

In Figure III.11, overall, we notice that there is a strong correlation up to ~*m/z* 80 between the cations measured by Dubois *et al.* (2020) for a Titan-simulated ionosphere (in grey) and my simulation of Pluto's atmosphere (in blue). For a detailed discussion and peak attribution of species related to N_2:CH_4 chemistry, we refer the reader to Dubois *et al.* (2020), as our results do not differ significantly. I will focus here on the differences, likely attributed to CO chemistry.

For Pluto, in the C_2^+ cluster, along with N_2^+, $C_2H_4^+$, and $HCNH^+$, CO^+ is an additional contributor to the peak at *m/z* 28, explaining why the peak at *m/z* 28 is more intense in Pluto-simulated atmosphere than in Titan-simulated atmosphere published in Dubois *et al.* (2020). And a likely explanation for the intense peak at *m/z* 29 is a favored formation of HCO^+ in my Pluto simulation A_{400}.This suggests a significant influence of CO in N_2:CH_4 reactivity, of importance for Pluto's atmosphere. In contrast, in the C_3^+ and C_4^+ clusters, as for Titan lab-simulation, the most intense peaks are respectively *m/z* 42 and *m/z* 52.

With increasing *m/z*, and at this mass resolution, the strict identification of the peaks is complex. This was also the case for lab-simulations of Titan's atmospheric chemistry (Dubois *et al.*, 2020), but is even more limiting for Pluto lab-simulations due to the association of nitrogen and

oxygen atoms to the molecular structure that offers a greater possibility of attribution of chemical formulae.

However, in Figure III.11, we notice that the mass spectrum of the cations formed in Pluto-simulated reactive medium (in light blue) presents for each cluster a more populated right wing compared to Dubois *et al.* (2020) (in dark grey). Such right-wing enrichment means that molecules comprised in a cluster are heavier than an "ideal" saturated alkane. This can be induced by species containing a large number of heteroatoms, either nitrogen or oxygen (as both N and O are heavier than C). In Table III.5, we thus suggest possible cations contributing to the right wing of C_1^+ to C_6^+ clusters in A_{400} mass spectrum, based on the *NIST Chemistry WebBook*.

Table III.5: Suggested cations contributing to the right wing of C_1^+ to C_6^+ clusters significantly intense in Pluto-simulated atmosphere A_{400}. The identifications are based on the *NIST Chemistry WebBook*. Delta (Δ) values are also reported. $\Delta = m/z - 14\alpha - 1$, where α corresponds to the cluster number (as in C_α^+).

m/z	**Δ**	**Suggested cations**
19	4	H_3O^+
31	2	HNO^+, CH_3O^+, $C_2H_7^+$ and $N_2H_3^+$
33	4	HO_2^+, H_3NO^+ and CH_5O^+
34	5	$H_2O_2^+$
35	6	$H_3O_2^+$
45	2	CHO_2^+, HN_2O^+, CH_3NO^+, $C_2H_5O^+$, $H_3N_3^+$ and $C_2H_7N^+$
46	3	NO_2^+, $CH_2O_2^+$, $H_2N_2O^+$, CH_4NO^+, $C_2H_6O^+$ and $C_2H_8N^+$
47	4	HNO_2^+, CH_5NO^+, $C_2H_7O^+$ and $C_2H_9N^+$
48	5	O_3^+, C_4^+, $CH_4O_2^+$ and $H_4N_2O^+$
59	2	$CHNO_2^+$, $C_2H_3O_2^+$, $C_2H_5NO^+$, $CH_5N_3^+$, $C_3H_7O^+$ and $C_3H_9N^+$
60	3	CO_3^+, $N_2O_2^+$, C_5^+, $CH_2NO_2^+$, $C_2H_4O_2^+$, $CH_4N_2O^+$, $H_4N_4^+$, $C_2H_6NO^+$, $C_3H_8O^+$ and $C_2H_8N_2^+$
61	4	CHO_3^+, C_5H^+, $CH_3NO_2^+$, $C_2H_5O_2^+$, $C_2H_7NO^+$ and $C_3H_9O^+$
71	0	$C_2HNO_2^+$, $C_3H_5NO^+$, $C_4H_7O^+$, $C_4H_9N^+$ and $C_5H_{11}^+$
72	1	C_6^+, $C_3H_4O_2^+$, $C_4H_8O^+$, $C_3H_8N_2^+$, $C_4H_{10}N^+$ and $C_5H_{12}^+$
73	2	C_6H^+, $C_2H_3NO_2^+$, $H_3N_5^+$, $C_3H_7NO^+$, H_9O_{4+}, $C_4H_9O^+$ and $C_4H_{11}N^+$
74	3	$C_2H_2O_3^+$, C_5N^+, $C_6H_2^+$, $C_3H_6O_2^+$, $C_2H_6N_2O^+$, $C_4H_{10}O^+$ and $C_3H_{10}N_2^+$
83	-2	$C_4H_5NO^+$, $C_3H_5N_3^+$, $C_5H_9N^+$ and $C_6H_{11}^+$
84	-1	$C_2N_2O_2^+$, C_7^+, CN_4O^+, $C_4H_4O_2^+$, $C_3H_4N_2O^+$, $C_2H_4N_4^+$, $C_5H_8O^+$, $C_4H_8N_2^+$ and $C_6H_{12}^+$
85	0	C_7H^+, $C_3H_3NO_2^+$, $C_4H_7NO^+$ and $C_5H_{11}N^+$
86	1	C_6N^+, $C_7H_2^+$, $CH_2N_4O^+$, $C_3H_4NO_2^+$, $C_4H_6O_2^+$, $C_5H_{10}O^+$, $C_4H_{10}N_2^+$ and $C_6H_{14}^+$

87	2	C_6HN^+, $C_3H_5NO_2^+$, $C_4H_9NO^+$, $C_3H_9N_3^+$, $C_5H_{11}O^+$ and $C_5H_{13}N^+$

In Table III.5, we also report delta (Δ) values for the selected *m/z*. The Δ value was defined for cations formed by dissociative ionization by McLafferty and Tureček (1993) and Canagaratna *et al.* (2007) as $\Delta = m/z - 14\alpha + 1$, where α corresponds to the cluster number (as in C_α^+). Since cations in our Pluto simulations are formed mainly by proton attachment, it is therefore necessary to adapt the formula. The Δ values I considered are thus defined as $\Delta = m/z - 14\alpha - 1$. The Δ value indicates the probable type of molecule for each *m/z* considered. Typically, $\Delta = 2$ corresponds to linear saturated hydrocarbons, $\Delta > 2$ corresponds to organic compounds with heteroatoms like nitrogen and/or oxygen, and $\Delta < 2$ corresponds to unsaturated and branched hydrocarbons (Canagaratna *et al.*, 2007).

In view of the Δ values of positive ions reported in Table III.5, we can conclude that the "right wing" of the clusters in the Pluto-simulated mass spectrum shown in Figure III.11 probably indicates a significant amount of oxygenated species. In addition, peaks at *m/z* 31, 33, 34, 35 45, 46, 47, 48, 59, 60, 61, 71, 72, 73, 74, 83, 84, 85, 86, and 87 are either significantly more intense or only detected in the Pluto-simulated atmosphere compared to the Titan-simulated atmosphere. Since the difference between the two simulations lays on the presence of CO, this is also a strong indicator of the possible formation of a large amount of O-bearing cations in Pluto's atmosphere.

In Pluto's atmosphere, the predicted reactions involving CO are the following (Krasnopolsky, 2020):

$$N_2^+ + CO \rightarrow CO^+ + N_2 \qquad \text{(III.13)}$$

$$N^+ + CO \rightarrow CO^+ + N \qquad \text{(III.14)}$$

$$CO^+ + CH_4 \rightarrow CH_4^+ + CO \qquad \text{(III.15)}$$

$$CO^+ + CH_4 \rightarrow HCO^+ + CH_3 \qquad \text{(III.16)}$$

$$CO^+ + HCN \rightarrow HCN^+ + CO \qquad \text{(III.17)}$$

$$CO^+ + H_2 \rightarrow HCO^+ + H \qquad \text{(III.18)}$$

$$HCO^+ + C_2H_2 \rightarrow C_2H_3^+ + CO \qquad \text{(III.19)}$$

$$HCO^+ + C_2H_4 \rightarrow C_2H_5^+ + CO \qquad \text{(III.20)}$$

$HCO^+ + HCN \rightarrow HCNH^+ + CO$ (III.21)

$HCO^+ + e^- \rightarrow CO + H$ (III.22)

These reactions were added to the model of Krasnopolsky (2020) to account for the chemistry of CO. If one strictly follows these few reaction pathways, the incorporation of oxygen atom into heavier molecules and eventually into aerosols seems to be excluded. Nevertheless, our gas-phase analyses of the neutrals presented above highlighted a certain number of oxygenated molecules. Also, as we will see in Chapter IV, analyses of the chemical composition of Pluto aerosol analogues revealed the presence of oxygenated molecules in the solid material. These combined results therefore suggest the existence of more processes involving CO in Pluto's atmosphere, similarly to the chemistry of N_2 at the origin of a large variety of nitrogenous molecules, currently missing from atmospheric models.

III.3. Implications for Pluto

Up until now, no laboratory study has focused on the characterization of neutrals and cations formed in a reactive medium relevant to Pluto's atmosphere. The analyses presented above are the first of their kind. This part of my Ph.D. thesis had two main objectives. Firstly, to understand the chemical processes at the origin of Pluto's aerosols, in order to improve the current Pluto photochemical models. Secondly, to guide future ground-based observations of Pluto, as well as future processing of data acquired by the instruments onboard *New Horizons*.

In Pluto-simulated atmosphere, we were able to detect a large number of neutral molecules that could not be explained by our current knowledge of Pluto's atmospheric composition (*i.e.*, observations and predictions from current photochemical models). Based on the deconvolution of our recorded mass spectra, we were able to predict 26 additional molecules that could participate in Pluto's atmospheric chemistry, and that it would be desirable to implement in future Pluto photochemical models or look for in *New Horizons* data. Among these molecules, we identify a large number of nitrogenous molecules, notably characterized by nitrile functional groups, but also cyclic molecules with intracyclic incorporation of one or more nitrogen atoms. We also identify O-bearing molecules, globally characterized by terminal oxygenated chemical functions.

The detection of a large variety of cations in the Pluto-simulated atmosphere suggests that in a N_2:CH_4:CO reactive medium subjected to solar UV radiation, the formation of ions is possible, and even important in the molecular growth processes at the origin of solid aerosols, as we

pointed out above. Thus, the absence of ionosphere detection by the REX instrument (Hinson *et al.*, 2018) should essentially be explained by a detection threshold of the instrument too high. We can suspect that Pluto's atmosphere may harbor exotic ions, such as Titan's ionosphere (*e.g.*, Anicich and McEwan, 1997; McEwan and Anicich, 2007; Vuitton, Yelle and McEwan, 2007; Vuitton *et al.*, 2019).

Aside from CO, Wong *et al.* (2017) predicted the production of three oxygenated compounds: H_2O, CO_2, and HCOH, specifying "which may later be verified by future observations and data analysis". With our laboratory simulations, we can confirm the formation of CO_2 and HCOH, while we cannot conclude at the moment on the formation of H_2O. Similarly, Kammer *et al.* (2017) questioned the presence of O_2 in Pluto's atmosphere. In view of our results, reservations can be expressed about the formation of O_2, but we would tend to conclude on the negative. Poppe and Horányi (2018) predicted the exogenous delivery of water by interplanetary dust at a level of 1.5×10^{21} H_2O s^{-1} (or 3.8 $kg.day^{-1}$). This exogenous delivery of water can also serve as an additional source of oxygen atoms for incorporation during photochemical reactions in Pluto's atmosphere.

A recent publication by Steffl *et al.* (2020) on the measurements made by *New Horizons*/Alice concluded on the first detection of a C_3 hydrocarbon in Pluto's atmosphere, the methylacetylene $H_3C–C{\equiv}CH$. In their study, the authors examined the absorption cross sections of the following 32 atomic and molecular species: C, CH_3, CH_4O, C_2H, C_2H_5, C_3H_3, C_3H_4 (both allene and methylacetylene isomers), C_3H_6 (both propene and cyclopropane isomers), C_3H_8, C_4H_2, C_4H_4, C_6H_6, CO, CO_2, H, H_2, H_2CO, H_2O, H_2O_2, HCN, HC_3N, HNCO, N, NH_3, O, O_2, O_3, OCS, PH_3, SO, and SO_2. In addition to the positive detection of C_3H_4 by its absorption at 154 nm, an unidentified gas-phase species would be responsible for absorption features at 153 and 157 nm. One of the major differences between the species suspected by Steffl *et al.* (2020) and our results relates to the nature of the molecules. Indeed, if Steffl *et al.* (2020) investigated essentially the presence of hydrocarbons, with some exotic molecules (OCS, PH_3, SO, SO_2), our results tend rather in favor of nitrogenous species (nitriles, N-bearing cycles) and some oxygenated molecules (alcohols, carboxylic acids, carbonyls). In the re-processing of data measured by Alice and future processing of unanalyzed data, we therefore suggest expanding the list of molecules to be considered.

IV. Investigating the chemical composition of Pluto's aerosols

In the first section of this chapter, I present the results regarding the analysis of the chemical composition of Pluto aerosol analogues. This study aimed at characterizing the types of molecules present in Pluto tholins. In particular, I investigated the impact of the presence of atmospheric CO on the chemical composition of Pluto's photochemical aerosols. I also studied the effect induced by the CH_4 mixing ratio, and therefore the altitude of aerosol formation, on the chemical composition of Pluto's aerosols. These results were placed in the context of Pluto and current Pluto photochemical and radiative transfer models. This study was published in *Icarus*: Jovanović, Gautier, […], & Carrasco (2020). Chemical composition of Pluto aerosol analogues. *Icarus* 346, 113774. All results presented in Section IV.1 were published in the mentioned paper. The second section of this chapter (Section IV.2) focuses on preliminary results regarding the search for molecules of prebiotic interest in Pluto aerosol analogues.

IV.1. Study of the chemical composition of Pluto aerosol analogues

IV.1.1. Global aspect of Pluto tholin high-resolution mass spectrum

To characterize the molecular composition of Pluto aerosol analogues, the soluble fraction of the samples was analyzed with a high-resolution mass spectrometer combining an ElectroSpray Ionization source in positive mode (ESI+) and an Orbitrap™ mass analyzer. Figure IV.1 presents as an example a first glance at the mass spectrum of Pluto aerosol analogues P_{400}, from *m/z* 50 to *m/z* 300 (*m/z*, mass-to-charge ratio). Intensity was normalized to the most intense peak in the mass spectrum (*m/z* 127.0725).

A list of molecules identified in Pluto aerosol analogues by the ESI+/Orbitrap technique is given in Appendix A2.

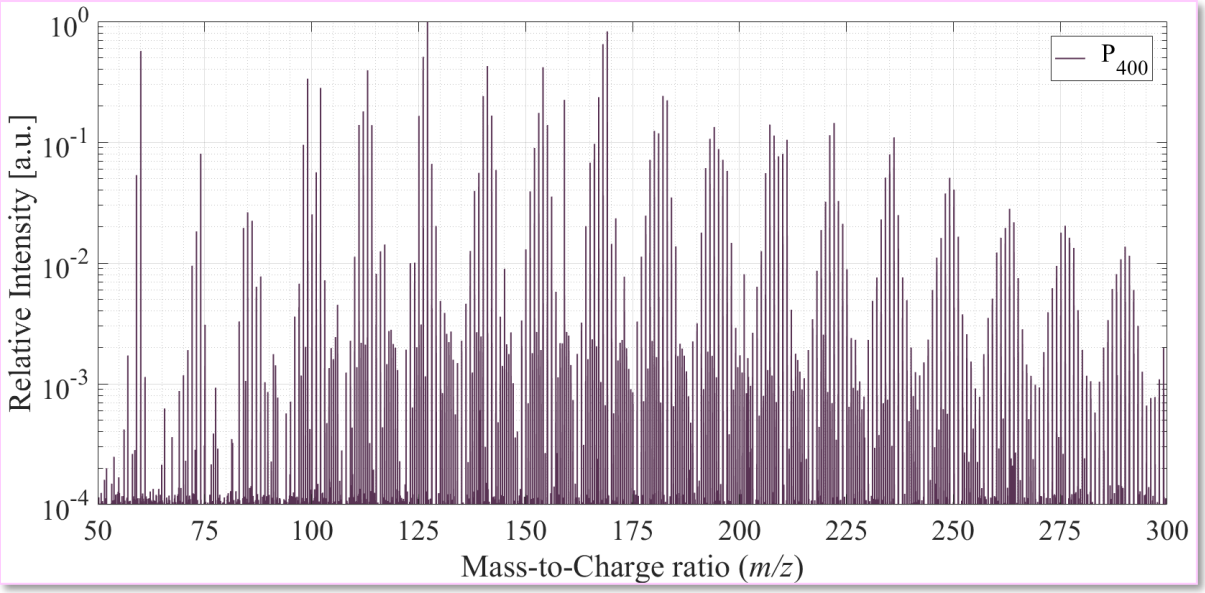

Figure IV.1: ESI+/Orbitrap mass spectrum of the soluble fraction of Pluto aerosol analogues P_{400}. The *x*-axis corresponds to the mass-to-charge ratio (*m/z*), while the *y*-axis corresponds to the relative intensity of the peaks, normalized to the most intense peak (*m/z* 127.0725). The small peaks in dark purple color are due to an aliasing effect.

In the mass spectrum (Figure IV.1), thousands of peaks are seen; hence, the soluble fraction of Pluto aerosol analogues is a complex mixture requiring such a high-resolution and high-precision analysis. Note however that the soluble fraction probably represents only 20 to 35% of the total solid mass of Pluto aerosol analogues (Carrasco *et al.*, 2009).

The peaks are grouped in several periodic clusters similar to those observed in the mass spectrum of Titan tholins, and similar to the mass spectra of Pluto-simulated atmospheres in which Pluto aerosol analogues are produced (see Chapter III). The analogy with Titan tholins suggests that the molecules detected in the soluble fraction of Pluto aerosol analogues are of a random-copolymeric nature, composed at least partially of a repetition of a $(CH_2)_m(HCN)_n$ pattern (Pernot *et al.*, 2010; Gautier *et al.*, 2017; Maillard *et al.*, 2018), consistent with the results presented in Chapter III.

IV.1.2. Importance of N_2 and CO chemistries

IV.1.2.a. N_2 chemistry

From laboratory studies of Titan's atmosphere we have learnt that not only methane, but also nitrogen plays a critical role in the atmospheric chemistry of Titan and in the formation and the growth of the aerosols (*e.g.*, Imanaka *et al.*, 2004; Imanaka and Smith, 2010; Gautier *et al.*, 2011; Carrasco *et al.*, 2012; Trainer *et al.*, 2012; He and Smith, 2013, 2014; Hörst, Yoon, *et al.*,

2018; Dubois *et al.*, 2019). My results emphasize the importance of nitrogen chemistry on Pluto as well. Before getting into the detailed analysis of the molecular composition, this inclusion of nitrogen and oxygen is also visible using infrared spectroscopy (Figure IV.2).

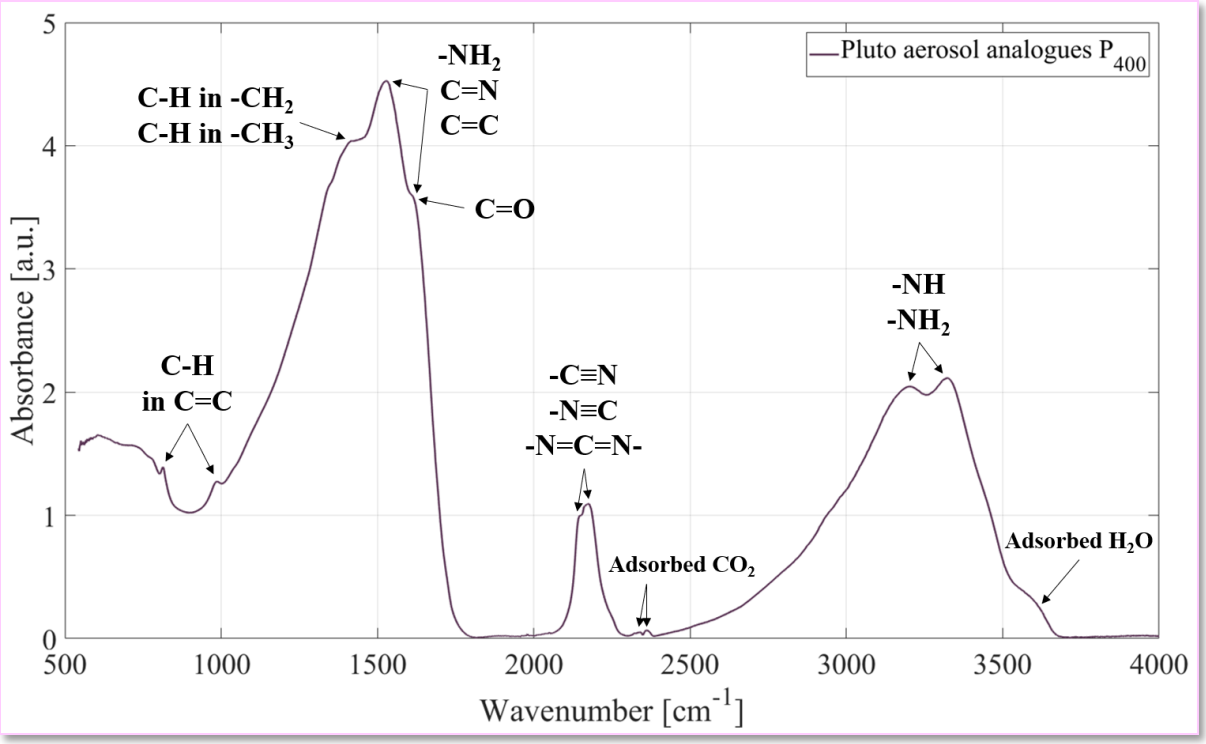

Figure IV.2: Infrared spectrum of Pluto aerosol analogues P_{400}, acquired by the Attenuated Total Reflectance (ATR) technique. At 2,340 and 2,360 cm^{-1}, small absorption bands are attributed to CO_2 adsorbed on the sample, while the shoulder at 3,600 cm^{-1} corresponds to water adsorbed on the analogues as hydroxyl –OH.

Figure IV.2 presents the infrared spectrum of Pluto aerosol analogues P_{400}, obtained by the Attenuated Total Reflectance (ATR) technique. In this spectrum, the importance of N-bearing chemical functions is clearly visible (Imanaka *et al.*, 2004; Socrates, 2004; Gautier *et al.*, 2012). At 1,550 cm^{-1}, a strong absorption band can be attributed to the deformation vibrations of aromatic and aliphatic amines $–NH_2$ and of double bonds C=C and C=N in aromatic and hetero-aromatic cycles. The bands at 2,150 and 2,170 cm^{-1} can be attributed to nitriles –C≡N, isocyanides –N≡C and carbodiimides –N=C=N–. At 3,200 and 3,330 cm^{-1}, there are two strong large bands, characteristic of primary and secondary amines –NH and $–NH_2$ (Table IV.1).

Table IV.1: Mid-IR band assignment of absorption bands found in the infrared spectrum presented in Figure IV.2. The band assignments are based on Imanaka *et al.* (2004), Socrates (2004) and Gautier *et al.* (2012).

Wavenumber [cm^{-1}]	Mid-IR band assignment
800 and 980	Out-of-plane =C–H
1,400	–C–H in aliphatic $–CH_2$ and $–CH_3$
1,550 and 1,650	Aromatic and aliphatic $–NH_2$ Double bonds C=C and C=N in aromatic and hetero-aromatic cycles Carbonyl –C=O
2,160 and 2,170	Nitriles –C≡N, isocyanides –N≡C and carbodiimides –N=C=N–
3,200 and 3,330	Primary and secondary amines –NH and $–NH_2$

According to the IR spectrum (Figure IV.2) and due to the selectivity of the ESI+ source (Rodgers, Schaub and Marshall, 2005), we expect to detect with the Orbitrap a large amount of N-bearing organic molecules in the soluble fraction of P_{400} and P_{650} samples. The presence of oxygenated organic molecules is also expected. In contrast, we do not expect to detect hydrocarbons without heteroatoms, since this kind of molecules was observed to be less abundant in the soluble fraction of similar samples (Derenne *et al.*, 2012; Gautier *et al.*, 2014, 2016; Morisson *et al.*, 2016). In addition, the ESI+ source is not the most adequate to detect them due to their low proton affinity (Molnárné Guricza and Schrader, 2015).

IV.1.2.b. CO chemistry

In order to understand if the presence of CO in Pluto's atmosphere has an impact on the molecular composition of Pluto's aerosols, I compared the intensities of the oxygenated molecules present in the soluble fraction of Pluto aerosol analogues P_{400} and of aerosol analogues produced without CO (Figure IV.3). The intensities of the oxygenated molecules were normalized to the intensity of the most intense peak in the mass spectrum (*m/z* 127.0725 for P_{400} sample and *m/z* 60.0551 for $P_{CO\text{-}free}$ sample, respectively).

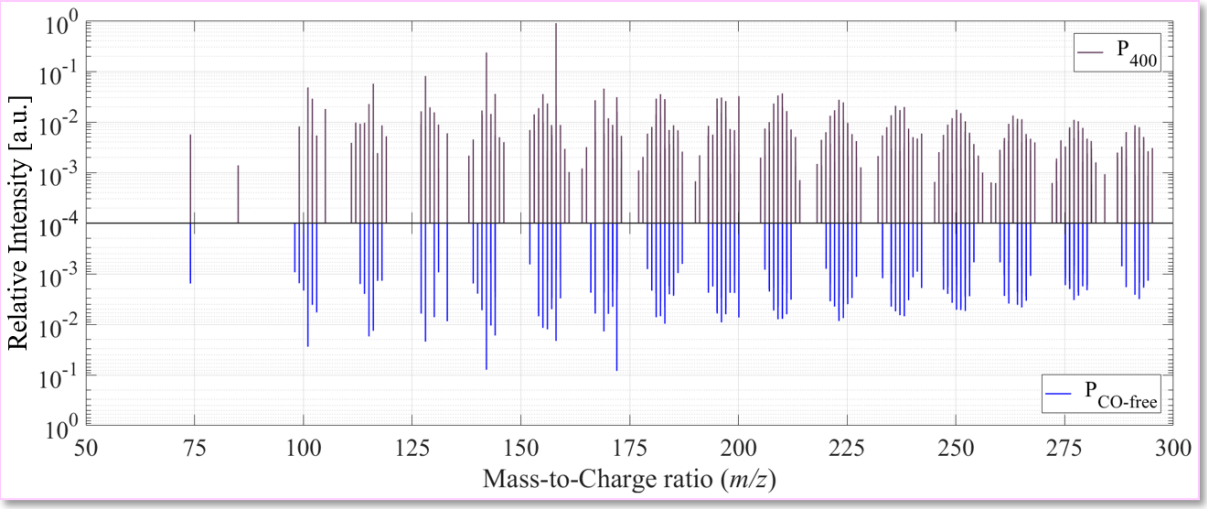

Figure IV.3: Normalized intensities of only the oxygenated molecules present in the soluble fraction of Pluto aerosol analogues P_{400} (in purple) and of aerosol analogues produced without CO ($P_{CO\text{-}free}$, in mirrored axis, in blue). The spectra were acquired with the ESI+/Orbitrap technique. Intensities were normalized to the most intense peak of each mass spectrum (*m/z* 127.0725 for P_{400} sample and *m/z* 60.0551 for $P_{CO\text{-}free}$ sample, respectively).

Upper panel in Figure IV.3 displays in purple the normalized intensities of oxygenated molecules present in the soluble fraction of Pluto aerosol analogues P_{400}. Lower panel (in mirror) shows in blue the normalized intensities of oxygenated molecules present in the soluble fraction of hypothetical Pluto aerosol analogues $P_{CO\text{-}free}$.

Considering the composition of the gas mixture producing the aerosol analogues without CO, oxygenated molecules should not be present. However, in this case, the small proportion of oxygenated molecules are produced by partial oxidation of the surface of the particles during the air exposure when collecting the samples (Fleury *et al.*, 2014; Carrasco *et al.*, 2016).

In Figure IV.3, the oxygenated molecules detected with ESI+/Orbitrap in Pluto aerosol analogues P_{400} appear to be similar to the oxygenated molecules contaminating the aerosol analogues without CO (sample $P_{CO\text{-}free}$). However, when looking at the normalized intensities of these oxygenated molecules, it appears that they are significantly higher in P_{400} analogues than in sample $P_{CO\text{-}free}$, demonstrating an effective reactivity of CO.

The oxygenated molecules are detected at the same *m/z* ratios, within the accuracy of the Orbitrap™, so that the chemical formulae attributions are the same. This means that the reactive pathways leading to their formation for P_{400} in the experiment might be, at least partially, similar to the oxidation pathways affecting $P_{CO\text{-}free}$. The oxygenated molecules present in P_{400} are produced both by reactions within the plasma simulating Pluto's atmospheric chemistry and by

surface oxidation of the particles during the collecting exposed to air. Both processes might involve the same oxidizing agents.

Further experiments would provide information on the oxidizing agents involved in the plasma oxidation pathways, such as the synthesis of Pluto aerosol analogues with $C^{18}O$.

Figure IV.4 shows the molecules present in P_{400} (in purple) and $P_{CO\text{-}free}$ (in blue) samples, between *m/z* 492.20 and *m/z* 493.32 (arbitrary zooming for example purpose). The purple stars point out molecules that are present only in the sample P_{400}. Although the resolution of the analytical instrument is not sufficient above *m/z* 300 to strictly identify molecules, Figure IV.4 demonstrates that CO reactivity impacts the aerosol composition even at large masses.

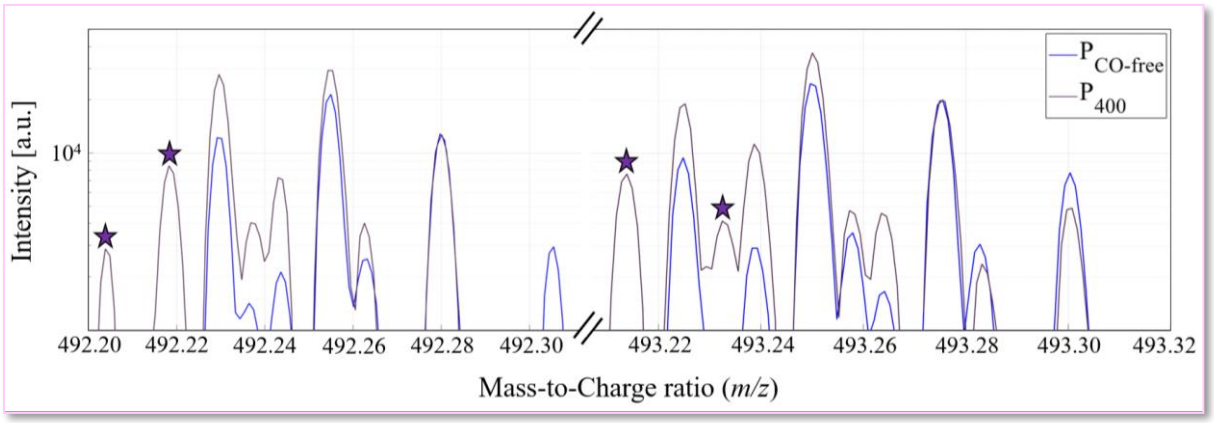

Figure IV.4: Mass spectra of P_{400} (in purple) and $P_{CO\text{-}free}$ (in blue) samples, between *m/z* 492.20 and *m/z* 493.32. The *x*-axis was cropped (//) for a better visualization of the peaks. The purple stars correspond to molecules that are detected only in the analogues P_{400}.

In Figure IV.4, we count 19 peaks. Of these, 14 molecular formulae are common to both P_{400} and $P_{CO\text{-}free}$ samples, 1 formula is present only in the sample $P_{CO\text{-}free}$, while 4 formulae – those pointed out by the purple stars – are present only in the sample P_{400}. We can therefore conclude that the presence of CO in the reactive gas mixture, even in a small proportion (500 ppm), has an impact on the chemistry leading to the formation of aerosols on Pluto, from light gas-phase molecules to large macromolecular polymeric structures incorporated in the aerosols.

IV.1.3. Investigating the effect of the atmospheric composition (and therefore the altitude of aerosol formation) on the chemical composition of Pluto's aerosols

The mixing ratio of CH_4 in Pluto's atmosphere as observed in 2015 by *New Horizons* strongly varies with the altitude (Young *et al.*, 2018). Since previous studies on Titan tholins

demonstrated the impact of methane mixing ratio on their chemical composition (*e.g.*, Gautier *et al.*, 2014), one could expect this parameter to also have an impact on the molecular composition and thus on physical properties of Pluto's aerosols.

As the abundance of CO is nearly constant all along Pluto's atmosphere, the CO/CH_4 ratio varies with the variation of CH_4 mixing ratio, from CO/CH_4 = 0.1 near the surface to CO/CH_4 = 0.001 at around 1,450 km of altitude above the surface. I therefore also studied the distribution of the oxygenated molecules in Pluto aerosol analogues P_{650}.

In Figure IV.5, we compare the normalized intensities of the oxygenated molecules detected with ESI+/Orbitrap in the soluble fraction of P_{400} (upper panel, in purple) and P_{650} (lower panel, in mirror, in red). The intensities of the oxygenated molecules were normalized to the intensity of the most intense peak in the mass spectrum (*m/z* 127.0725 for P_{400} sample and *m/z* 60.0551 for P_{650} sample, respectively).

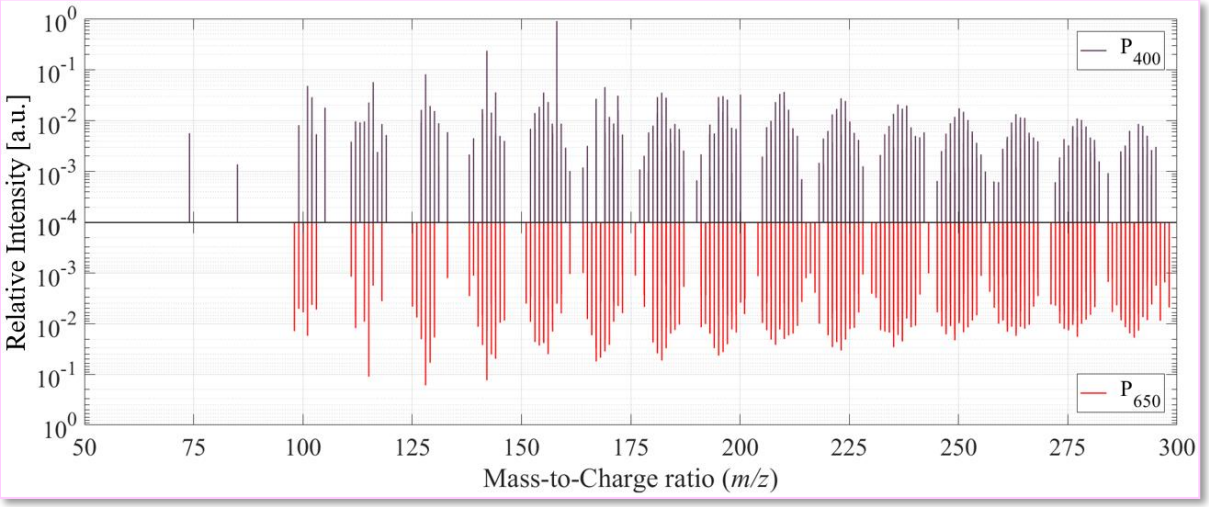

Figure IV.5: Normalized intensities of only the oxygenated molecules present in the soluble fraction of Pluto aerosol analogues P_{400} (in purple) and P_{650} (in mirrored axis, in red). The spectra were acquired with the ESI+/Orbitrap technique. The intensities of the peaks identified as oxygenated molecules were normalized to the most intense peak of each mass spectrum (*m/z* 127.0725 for P_{400} sample and *m/z* 60.0551 for P_{650} sample, respectively).

When looking at the mass spectra on Figure IV.5, it seems that the clusters in P_{650} are shifted towards smaller masses compared to P_{400}, suggesting that the oxygenated molecules in the soluble fraction of P_{650} are different from those constituting the soluble fraction of P_{400}. This could imply that the chemical pathways leading to the formation of oxygenated molecules are quite different in Pluto's aerosols depending on their altitude of formation. Due to the leftward shifting of the clusters, we can suppose that the oxygenated organic molecules detected in the

soluble fraction of the sample P_{650} include less hydrogen atoms than the molecules present in the soluble fraction of P_{400}. Oxygenated organic molecules in P_{650} are therefore more unsaturated. From this observation, we can conclude that the increase in the CH_4 mixing ratio (thus being at higher altitudes on Pluto) leads to an increased formation of unsaturated molecules in the soluble fraction of Pluto aerosol analogues. This conclusion was also made for Titan aerosol analogues produced from N_2:CH_4 gas mixtures with different CH_4 concentrations (Derenne *et al.*, 2012; Gautier *et al.*, 2014). This implies that this effect is likely due to the variation in the CH_4 mixing ratio itself and not to the presence of CO in the reactive gas mixture.

In order to determine the abundances of C, H, N and O atoms in Pluto aerosol analogues, Arnaud Buch performed an elemental composition analysis of P_{400} and P_{650} samples and provided me the results presented in Table IV.2.

Table IV.2: Mass percentages of C, H, N and O elements present in the soluble fraction of Pluto aerosol analogues P_{400} and P_{650}. Given uncertainties correspond to ± 3σ.

Mass percentage (%)	P_{400}	P_{650}
C	42.1 ± 0.2	49.0 ± 0.2
H	3.74 ± 0.06	4.81 ± 0.07
N	45.1 ± 0.2	36.0 ± 0.2
O	1.89 ± 0.03	1.69 ± 0.03

Table IV.2 displays the mass percentages of the elements C, H, N and O present in Pluto aerosol analogues P_{400} and P_{650}. Note for both samples that the sum of the mass percentages does not equal 100%. This is due to uncertainties related to the fact that the measurement of the mass percentage of the element O is not carried out at the same time, nor with the same technique, as the measurement of the mass percentages of the elements C, H and N.

Two observations can be deduced from Table IV.2: (1) sample P_{650} contains more carbon and hydrogen in mass, but less nitrogen than sample P_{400}; (2) sample P_{400} contains more oxygen in mass than sample P_{650}. The first observation can be explained by the fact that the sample P_{650} is synthesized with a higher CH_4 mixing ratio; whereby more C and H atoms and less N atoms are present in the reactive gas mixture. The second one, in agreement with the conclusion of He *et al.* (2017), is due to the fact that the sample P_{400} is produced with a higher CO/CH_4 ratio.

To further visualize the chemical differences between the soluble fraction of the samples P_{400} and P_{650}, we modified conventional van Krevelen [H/C *versus* O/C] diagrams. The van Krevelen diagrams were proposed in 1950 to study the structure and reaction processes of coal

(van Krevelen, 1950, 1984). Since then, this type of representation has been frequently applied on data obtained with high-resolution mass spectrometry (*e.g.*, Kim, Kramer and Hatcher, 2003; Wu, Rodgers and Marshall, 2004; Rodgers, Schaub and Marshall, 2005; Marshall and Rodgers, 2008). More recently, this tool was expanded to the analysis of complex organic mixtures of terrestrial and planetary interests, using [H/C *versus* N/C] axes (*e.g.*, Imanaka and Smith, 2010; Pernot *et al.*, 2010; Tziotis, Hertkorn and Schmitt-Kopplin, 2011; Somogyi *et al.*, 2012; Gautier *et al.*, 2014; Danger *et al.*, 2016).

Figure IV.6 shows the modified van Krevelen diagrams of all the molecules identified in the soluble fraction of the samples P_{400} (left), P_{650} (middle) and $P_{CO\text{-}free}$ (right). The *x*-axis corresponds to Nitrogen-to-Carbon (N/C) ratio and the *y*-axis corresponds to Hydrogen-to-Carbon (H/C) ratio. Each point represents a given molecule constituting the soluble fraction of the sample analyzed by ESI+/Orbitrap. The colors correspond to the number of oxygen atoms included in the molecule. As the oxygen is not supposed to take part to the co-polymeric growth, due to its bivalence and its affinity to labile hydrogen (*e.g.*, Decker and Jenkins, 1985; Ligon *et al.*, 2014), but instead to be randomly included in the molecules, I have chosen to represent the data with the number of oxygen atoms present in the molecules and not with Oxygen-to-Carbon (O/C) ratio.

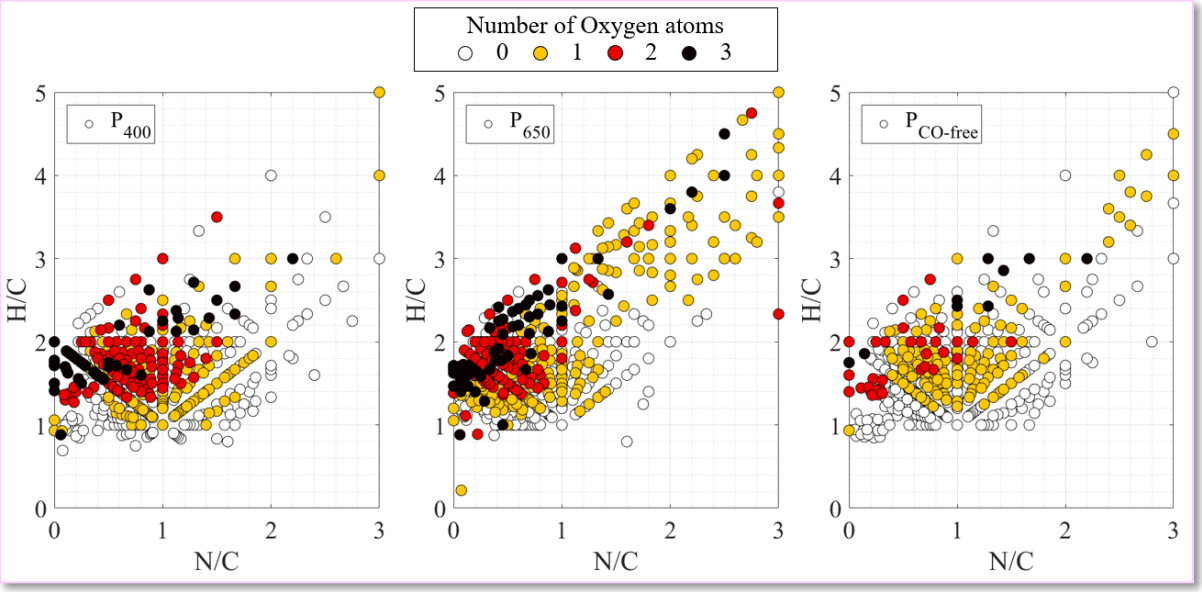

Figure IV.6: Modified van Krevelen diagrams. The samples were analyzed with the ESI+/Orbitrap technique and the molecules were identified with *Attributor* software. Each dot corresponds to a specific molecule characterized by its Hydrogen-to-Carbon (H/C) and Nitrogen-to-Carbon (N/C) ratios. The colors correspond to the number of oxygen atoms included in the molecules: *White* ⇔ Zero O atom; *Yellow* ⇔ One O atom; *Red* ⇔ Two O atoms; *Black* ⇔ Three O atoms. *Left*: P_{400} sample. *Middle*: P_{650} sample. *Right*: $P_{CO\text{-}free}$ sample.

In Figure IV.6.left, Figure IV.6.middle and Figure IV.6.right, we notice that the molecules with one oxygen atom (yellow dots) are scattered all over the distribution for the samples P_{400}, P_{650} and $P_{CO\text{-}free}$. This means that incorporating one atom of oxygen in a molecule does not depend on its nature (light or heavy, low or high H/C and N/C ratios). The second important point is that the oxygenated molecules due to contamination in $P_{CO\text{-}free}$ sample essentially correspond to molecules with one oxygen atom. Therefore, the molecules with two and three oxygen atoms (red and black dots, respectively), that are abundantly detected in the soluble fraction of P_{400} and P_{650} samples, are very likely produced by CO chemistry. These molecules are mainly present in a specific area of the diagrams, characterized by the following elemental ratios: [$1 < H/C < 2.5$ and $0 < N/C < 1$]. The fact that N/C ratio is lower than one suggests that the incorporation of more than one oxygen atom in the molecules constituents of the aerosols is done at the expense of nitrogen incorporation. There may be a competition between N_2 and CO chemistries, as suggested by He *et al.* (2017). The presence of molecules with two or three oxygen atoms at N/C ratio of less than one could also be explained by the incorporation of O atoms into the molecules in the form of carbonyl –C=O or carboxyl –COOH chemical functions. The incorporation of oxygen with carbon into a molecule would therefore necessarily decrease the N/C ratio.

Figure IV.7 presents the modified van Krevelen diagrams of molecules that are exclusively detected in either the P_{400} (left) or P_{650} (right) sample. In Figure IV.7.left and Figure IV.7.right, we can see that the molecules specific to P_{400}, oxygenated or not, are scattered all over the distribution, whereas in the sample P_{650}, the molecules group into two distinct areas, suggesting again different reactive pathways for both samples. The area [$1 < H/C < 2.5$ and $0 < N/C < 1$] is composed of a patchwork of heavier molecules including or not oxygen atoms (white, yellow, red and black dots), while the area [$2 < H/C < 5$ and $1.25 < N/C < 3$] is essentially composed of lighter molecules with one oxygen atom (essentially yellow dots). This reinforces the idea that when the percentage of methane increases, the mixing ratio of molecular nitrogen decreases, while there is likely competition between CO and N_2 chemistries (He *et al.*, 2017). Incorporating more than one oxygen atom into heavier molecules, probably in the form of chemical functions –C=O or –COOH, is done at the expense of N-incorporation.

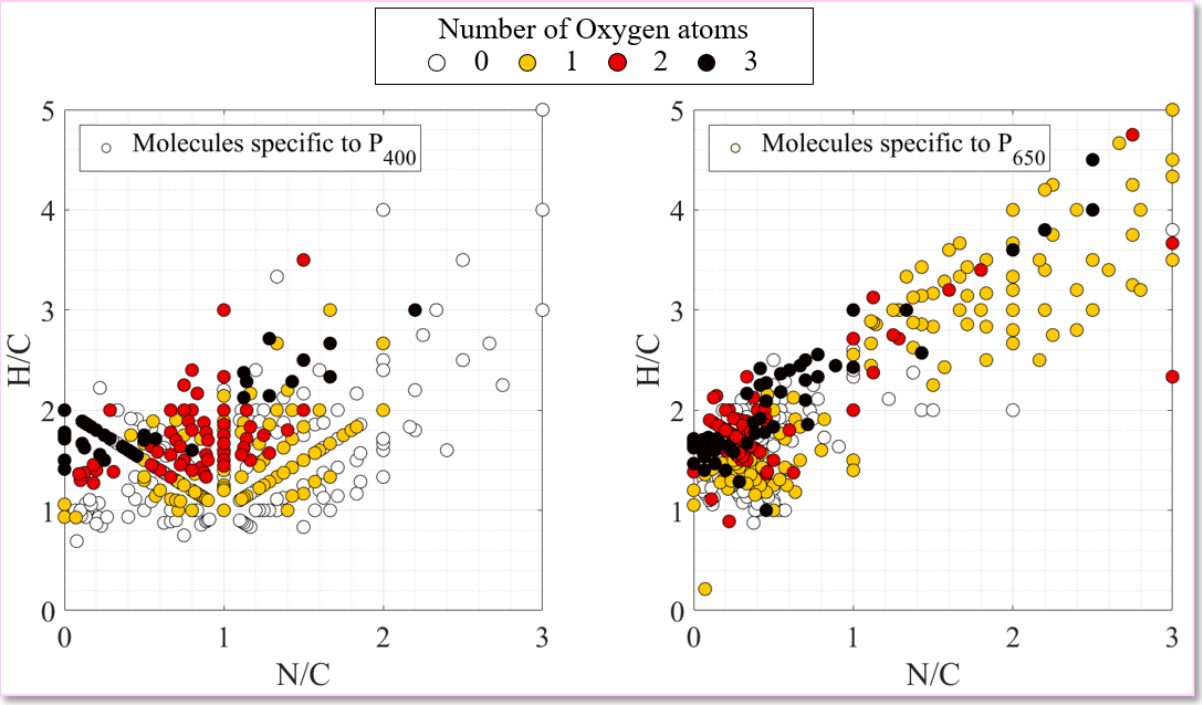

Figure IV.7: Same as Figure IV.6, but showing the molecules exclusively detected in the soluble fraction of P_{400} (*left*) and P_{650} (*right*) samples.

In Gautier *et al.* (2014), a high-resolution mass spectrometry study was carried out on Titan aerosol analogues produced with the PAMPRE experimental setup. This study showed the impact on the molecular composition of Titan aerosol analogues when the methane percentage varies. In particular, there are less molecules formed with N/C < 1 when the percentage of methane increases.

Previous studies also showed that when CH_4 percentage increases, more hydrogen is available in the gas phase leading to the aerosols, and that this hydrogen tends to inhibit the growth of the aerosol analogues (DeWitt *et al.*, 2009; Sciamma-O'Brien *et al.*, 2010). We can exclude this to be the case here since we do not see a depletion of the "N/C < 1" molecules in the P_{650} sample. This suggests that N_2 and CH_4 chemistry is strongly impacted by the presence of CO, even in a small proportion. Hörst and Tolbert (2014) and He *et al.* (2017) also studied the effect of carbon monoxide on planetary atmospheric chemistry and on the formation of aerosol analogues and proposed two hypotheses: (1) in presence of carbon monoxide, oxygen radicals coming from CO react with atomic and molecular hydrogen coming from CH_4 and removes them from the chemical system; (2) in presence of CO, there is more carbon available without increasing the quantity of available hydrogen that inhibits the aerosol growth, resulting in a less reducing environment allowing the production of more unsaturated molecules. According to

our results, the first hypothesis of Hörst and Tolbert (2014) and He *et al.* (2017) may be an explanation to the lack of depletion of the molecules with N/C < 1 when the CH_4 percentage increases. On the contrary, the second hypothesis cannot explain our results. On one hand, the sample P_{650} presents more molecules with higher N/C (and H/C) ratios than P_{400}, meaning that less carbon is incorporated in these molecules. On the other hand, as shown in Figure IV.5, the soluble fraction of P_{650} contains more unsaturated molecules than that of the P_{400} sample, even though the sample P_{650} is produced with a lower CO/CH_4 ratio.

IV.1.4. Discussion on the chemical composition of Pluto's aerosols

Long before the *New Horizons* era, the photochemical models of Pluto's atmosphere scarcely took into consideration N_2 and CO chemistries (Stansberry, Lunine and Tomasko, 1989; Lara, Ip and Rodrigo, 1997; Krasnopolsky and Cruikshank, 1999). It was thought that the formation of the aerosols would be essentially driven by the photolysis of CH_4 by Lyman-α photons. This was also the case on Titan before the *Cassini-Huygens* mission revealed that not only methane, but also molecular nitrogen plays a key role in Titan's atmospheric chemistry and in the formation of N-bearing organic aerosols. In light of this discovery, the latest photochemical models of Pluto's atmosphere compensated this misconception by including the chemistry from N_2, but the question of the CO chemistry still remains unsolved (Luspay-Kuti *et al.*, 2017; Wong *et al.*, 2017). CO serves as a source of oxygen for incorporation in haze particles, leading to the formation of prebiotic molecules in the aerosols. This was pointed out by Hörst *et al.* (2012) who detected amino acids and nucleotide bases in the solid products produced with the PAMPRE experimental setup in a plasma of N_2:CH_4:CO gas mixture. However, even Titan aerosol analogue studies usually do not include CO despite its substantial mixing ratio (47 ± 8 ppm_V) in the hazy atmosphere of Titan (de Kok *et al.*, 2007). Additionally, a few studies on exoplanetary atmospheres have also emphasized the link between the presence of carbon monoxide and haze layers (*e.g.*, Deming *et al.*, 2013; Konopacky *et al.*, 2013; Pont *et al.*, 2013; Barman *et al.*, 2015; He, Hörst, Lewis, Yu, Moses, Kempton, Marley, *et al.*, 2018; He, Hörst, Lewis, Yu, Moses, Kempton, McGuiggan, *et al.*, 2018; Hörst, He, Lewis, *et al.*, 2018).

For Pluto, an endeavor has recently been done by Luspay-Kuti *et al.* (2017) and Krasnopolsky (2020) to incorporate the most important reactions of CO chemistry in their models. Our results obtained by ESI+/Orbitrap, IR-ATR, and elemental composition analysis highlight an important incorporation of both nitrogen and oxygen atoms in the molecules constituting Pluto aerosol analogues and thus active N_2 and CO chemistries influencing the gas phase composition and density. It is thus of prime importance to keep focusing on the effect of CO in Pluto's

atmospheric chemistry and make sure to include extensive oxygen and nitrogen reactive pathways in future Pluto photochemical models.

From our analyses, we conclude that the molecules constituting the soluble fraction of Pluto aerosol analogues are mainly composed of N-bearing organic molecules, with a significant proportion of oxygenated molecules. Unsaturated molecules may also be present in large amount. These heavy, unsaturated N-bearing organic molecules and oxygenated species are likely very reactive and may therefore catalyze and self-sustain the synthesis of other molecules constituting the aerosols. Furthermore, by interacting with molecules in the gas phase, they may also act as cloud condensation nuclei (Kumar, Broekhuizen and Abbatt, 2003; Broekhuizen *et al.*, 2004; Fan *et al.*, 2016; Lavvas *et al.*, 2016; Luspay-Kuti *et al.*, 2017), impacting the climate of Pluto. Seven Pluto clouds candidates were identified by Stern, Kammer, *et al.* (2017) from *New Horizons* image dataset. These clouds could be the result of the condensation of HCN, C_2H_2, C_2H_6, C_2H_4 or CH_4. One interesting question is whether the condensation of clouds on Pluto's aerosols is affected by the proportion of O-bearing molecules in the hazes. The study of the wettability of Pluto aerosol analogues to HCN, C_2H_2, C_2H_6, C_2H_4 or CH_4 may provide answers to this question.

Pluto's atmosphere is around 30-40 K colder than theoretically predicted, at about 400 km of altitude (Zhu, Strobel and Erwin, 2014; Gladstone *et al.*, 2016; Zhang, Strobel and Imanaka, 2017). Because of Pluto's thermal structure, expected to be in radiative-conductive equilibrium, atmospheric gas molecules such as HCN or water vapor are not sufficient to explain Pluto's temperature profile. Zhang, Strobel and Imanaka (2017) proposed that Pluto's haze, rather than its atmospheric gases, could explain Pluto's cold atmosphere. Their study was performed using the optical properties of Titan aerosol analogues, which are oxygen-free. Our results obtained by ESI+/Orbitrap and elemental composition analysis showed a significant incorporation of oxygen atoms in the molecules constituting Pluto aerosol analogues and that this O-incorporation depends on CH_4 mixing ratio. As more oxygen is incorporated, the real and imaginary parts (*n* and *k* indices) of the complex refractive index of haze particles change, resulting in different optical properties that may reduce UV wavelengths from reaching Pluto's surface and influence Pluto's radiative cooling. While Zhang, Strobel and Imanaka (2017) showed a dependency of Pluto's climate to the aerosol-simulated optical constants, Gavilan *et al.* (2017) showed that when the percentage of oxygen increases in organic aerosols, the absorption at longer UV wavelengths is significantly higher. The experimental determination of the optical constants in the UV-Visible of Pluto aerosol analogues is thus of prime importance to further advance our understanding of Pluto's cold atmosphere. This

determination of the optical constants of Pluto aerosol analogues is the topic of Chapter V of this Ph.D. thesis.

IV.2. Search for molecules of prebiotic interest in Pluto aerosol analogues

The presence of organic molecules and liquid water is a *sine qua non* condition for life to appear and persist (Cottin *et al.*, 2017). Liquid water is an important requirement for habitability, because of its exceptional solvent qualities allowing organic chemistry to occur and organic molecules to be stable (Brack, 1993; Mottl *et al.*, 2007; Lammer *et al.*, 2009). On the early Earth, the organic matter could have been of exogenous or endogenous origins. Exogenous origin includes delivery of organic molecules by extraterrestrial objects, such as asteroids, comets, interplanetary dust particles or meteorites, whereas endogenous origin consists in organic synthesis in high-temperature hydrothermal vents or in the atmosphere of the primitive Earth (Chyba and Sagan, 1992; Fleury, 2015; Dalai, Kaddour and Sahai, 2016; Kitadai and Maruyama, 2018).

The hypothesis of abiotic production of organic molecules in the atmosphere was proposed by Alexander I. Oparin and John B. S. Haldane in the 1920s (Oparin, 1924; Haldane, 1929). According to them, the organic synthesis started in the reducing atmosphere of the primitive Earth, under the action of sunlight and lightning. The polymerization then continued in seawater, after the organic compounds had been dissolved and concentrated in the primitive ocean. The concept of "primordial soup" was born.

In the 1950s, to pursue this new theory, Harold C. Urey proposed for the early Earth a reducing atmosphere composed of nitrogen N_2 or ammonia NH_3, methane CH_4, hydrogen H_2 and water H_2O (Urey, 1952), whereas Stanley L. Miller investigated experimentally the reactivity of this gas mixture exposed to an electric discharge (Miller, 1953, 1955, 1957). Proteinogenic and non-proteinogenic amino acids (glycine, sarcosine, alanine, β-alanine, N-methylalanine, α-amino-*n*-butyric acid, α-aminoisobutyric acid, aspartic acid, glutamic acid), as well as other organic molecules of prebiotic interest (glycolic acid, lactic acid, α-hydroxybutyric acid, succinic acid, iminodiacetic acid, iminoacetic-propionic acid, formic acid, acetic acid, propionic acid, urea and N-methyl urea) were identified as products resulting from the reactivity of the simulated atmosphere of the early Earth (Miller, 1953, 1955, 1957; Miller and Urey, 1959).

Subsequently, due to different geochemical constraints (Delano, 2001; Trail, Watson and Tailby, 2011) and modeling studies (Kasting, 1993; Burgisser and Scaillet, 2007), the assumption of the primitive atmospheric composition on Earth changed from highly reducing (N_2/NH_3 + CH_4 + H_2 + H_2O) to redox neutral or slightly oxidizing (N_2 + CO_2 + H_2O). Such an atmospheric composition would be due to the magmatic outgassing of volatiles from Earth's interior. Nevertheless, any robust evidence of the exact composition of the early Earth's atmosphere is still lacking (Chyba, 2005; Tian *et al.*, 2005; Tian, Kasting and Zahnle, 2011).

Miller's experimental setup nonetheless inspired other similar studies for atmospheres assumed to be more oxidizing (*e.g.*, Bar-Nun and Hartman, 1978; Bar-Nun and Chang, 1983; Schlesinger and Miller, 1983; Miyakawa *et al.*, 2002; Civiš *et al.*, 2004; Heinrich, Khare and McKay, 2007; Cleaves *et al.*, 2008; Fleury, 2015; Ferus *et al.*, 2017; Fleury *et al.*, 2017; Hörst, He, Ugelow, *et al.*, 2018).

With its atmosphere rich in N_2 and CH_4, with a small fraction of CO (Gladstone *et al.*, 2016; Lellouch *et al.*, 2017; Young *et al.*, 2018), and due to the presence of a potential subsurface ocean (Nimmo *et al.*, 2016; Kamata *et al.*, 2019; Kimura and Kamata, 2020), Pluto can be considered as a planetary-scale laboratory for the atmospheric synthesis of molecules of prebiotic interest (Cruikshank *et al.*, 2019).

In the solid products formed from a N_2:CH_4 cold plasma enriched with 1.8% CO, Hörst *et al.* (2012) identified five nucleobases (cytosine, uracil, thymine, adenine, and guanine) and fourteen proteinogenic amino acids (glycine, alanine, serine, proline, valine, threonine, isoleucine, leucine, asparagine, glutamine, lysine, histidine, phenylalanine, and arginine). In aerosol analogues formed from an AC cold plasma generated in a N_2:CH_4:CO = 90%:5%:5% gas mixture, Sebree *et al.* (2018) identified seven nucleobases (cytosine, uracil, thymine, adenine, hypoxanthine, guanine, and xanthine), five amino acids (glycine, alanine, sarcosine, β-aminoisobutyric acid, and leucine), and four other organic molecules of prebiotic interest (guanidine, urea, ethanolamine, and glycolic acid). The question of the prebiotic interest of Pluto's aerosols is thus warranted, as discussed in a recent review published by Cruikshank *et al.* (2019) about the implications of Pluto for the prebiotic chemistry.

In the following Section IV.2.1 and Section IV.2.2, I present preliminary results regarding the search for molecules of prebiotic interest in Pluto aerosol analogues.

IV.2.1. Identification by APPI/Orbitrap of molecular formulae potentially corresponding to molecules of prebiotic interest

IV.2.1.a. Comparison between ESI+/Orbitrap and APPI+/Orbitrap analyses

The ESI+/Orbitrap analyses presented in Section IV.1 did not allow the detection of molecules of prebiotic interest in Pluto aerosol analogues. Indeed, only the molecular formula $C_4H_5N_3O$ was identified at *m/z* 111.0433 and could correspond to cytosine nucleobase, the easiest produced nucleobase.

This lack of detection may be due to an incapacity of the ESI+ source to ionize the molecules of prebiotic interest, rather than an absence of these molecules in Pluto aerosol analogues. There are three possible explanations. From a chemical point of view, molecules with low polarity, such as vitamins or certain amino acids, are difficult to ionize and therefore to be detected with the ESI source. From an analytical point of view, ESI is not the most universal of the atmospheric pressure ionization techniques, unlike Atmospheric Pressure PhotoIonization (APPI) source. In addition, even with the high-resolution performance of the Orbitrap™, the molecular attribution by *Attributor* enables only the firm identification of only a fraction (typically around 10%) of the total peaks detected for such a complex mixture as Pluto tholins. APPI is the "softest" of the atmospheric pressure ionization techniques, and the one with the widest linear dynamic range, the highest sensitivity and the lowest detection limit. Moreover, with this source, it is possible to ionize a greater diversity of molecules, thanks to different ionization processes: proton transfer, and charge exchange (Raffaelli and Saba, 2003; Cai and Syage, 2006; Robb and Blades, 2008; Marchi, Rudaz and Veuthey, 2009). Consequently, molecules of prebiotic interest, whether polar or non-polar, are more likely to be ionized by APPI source than by ESI, especially since both positive and negative ionization modes are used. For these reasons, I analyzed Pluto aerosol analogues with APPI, a quasi-universal ionization source, both in positive (APPI+) and negative (APPI–) modes (Cai *et al.*, 2005; Robb and Blades, 2008).

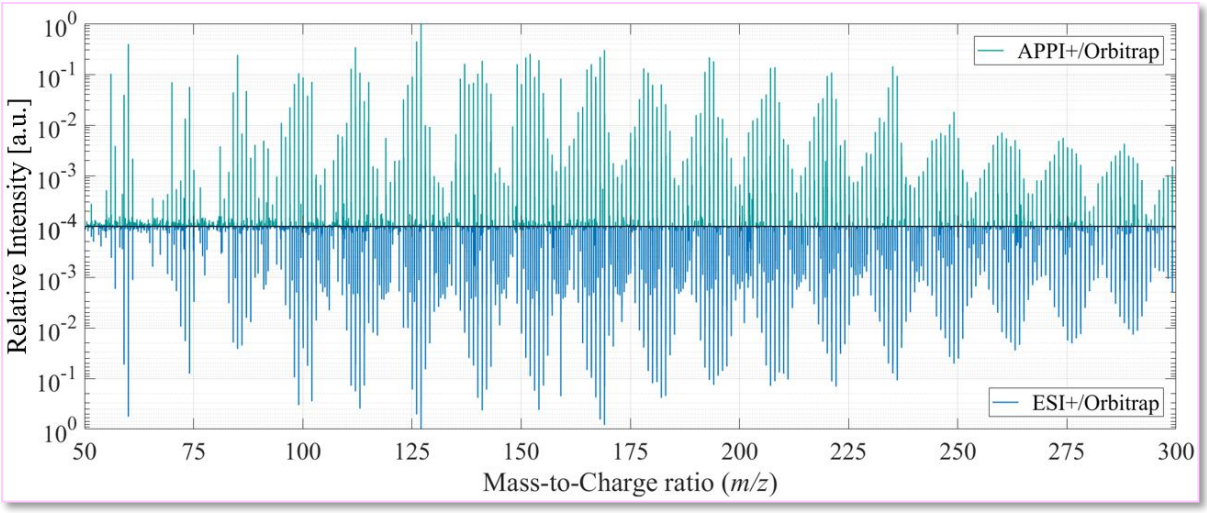

Figure IV.8: Comparison between high-resolution mass spectra of the soluble fraction of Pluto aerosol analogues P_{400} acquired with APPI+/Orbitrap (*upper panel*, in green) and with ESI+/Orbitrap (*lower panel*, in mirrored axis, in blue). The intensities of the peaks were normalized to the most intense peak (*m/z* 127.0725 for both mass spectra).

In Figure IV.8, we notice that the peak clusters characteristic of the polymeric nature of the molecules constituting Pluto aerosol analogues are right-shifted with ESI+/Orbitrap analysis (lower panel, blue mass spectrum). This suggests that the molecules are more hydrogenated (less unsaturated) for a given cluster. This is probably due to the ionization mechanism with the ESI+ source, which ionizes molecules only by protonating them, whereas APPI+ source ionizes molecules either by protonating them or by generating radicals.

For the same sample, here P_{400} analogues, from *m/z* 50 to *m/z* 300, the analysis by APPI+/Orbitrap resulted in the detection of 21,219 peaks, against 27,403 peaks detected with ESI+/Orbitrap (Figure IV.8). Nevertheless, by applying the same data processing with *Attributor* (filtering of electronic noise and interfering radio frequencies, then filtering in intensity to keep only the peaks whose intensities were higher than 0.1% of the most intense peak in the mass spectrum, attribution of the chemical formulae by allowing maximum three oxygen atoms, and finally elimination of the aberrant chemical formulae for which H/C > 5 and/or N/C > 3), we obtained 914 molecules attributed with APPI+/Orbitrap technique (see Figure IV.9, left modified van Krevelen diagram), against 657 molecules attributed with ESI+/Orbitrap (see Figure IV.9, right modified van Krevelen diagram).

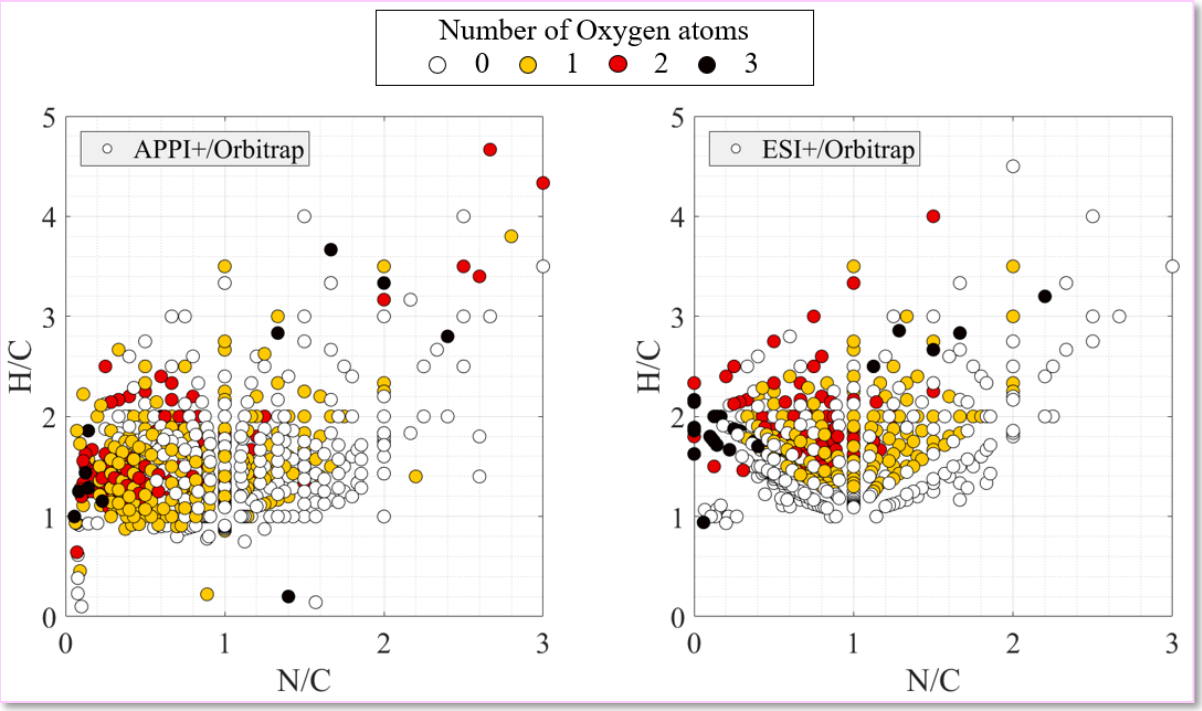

Figure IV.9: Comparison between molecular formulae identified with *Attributor* in the soluble fraction of Pluto aerosol analogues P_{400} analyzed with APPI+/Orbitrap (*left* modified van Krevelen diagram) and with ESI+/Orbitrap (*right* modified van Krevelen diagram).

In Figure IV.9, we note that the distribution of the molecules (dots characterized by their H/C and N/C ratios) is similar between the APPI+/Orbitrap analysis (left diagram) and the ESI+/Orbitrap analysis (right diagram). One of the major differences observed involves a pool of oxygenated molecules (mostly yellow, with some red and black dots) characterized by a N/C ratio lower than 1, and a H/C ratio lower than 2. A comparative statistical analysis concluded that more than 50% of the molecules identified with APPI+/Orbitrap differed from those detected with ESI+/Orbitrap. Among these molecules exclusive to APPI+/Orbitrap analysis, we may be able to identify chemical formulae which may correspond to molecules of prebiotic interest. A list of molecules identified in Pluto aerosol analogues P_{400} and P_{650} by APPI+/Orbitrap and APPI–/Orbitrap techniques is given in Appendix A2.

IV.2.1.b. Focus on molecules of prebiotic interest in P_{400} and P_{650}

In Figure IV.10, we compare the APPI/Orbitrap mass spectra of the soluble fraction of Pluto aerosol analogues P_{400}, acquired in positive mode (upper panel, in purple) and in negative mode (lower panel, in mirror, in lavender color), from *m/z* 50 to *m/z* 300. Intensity was normalized to the most intense peak in each mass spectrum (*m/z* 127.0725 for APPI+/Orbitrap and *m/z* 93.0213 for APPI–/Orbitrap, respectively).

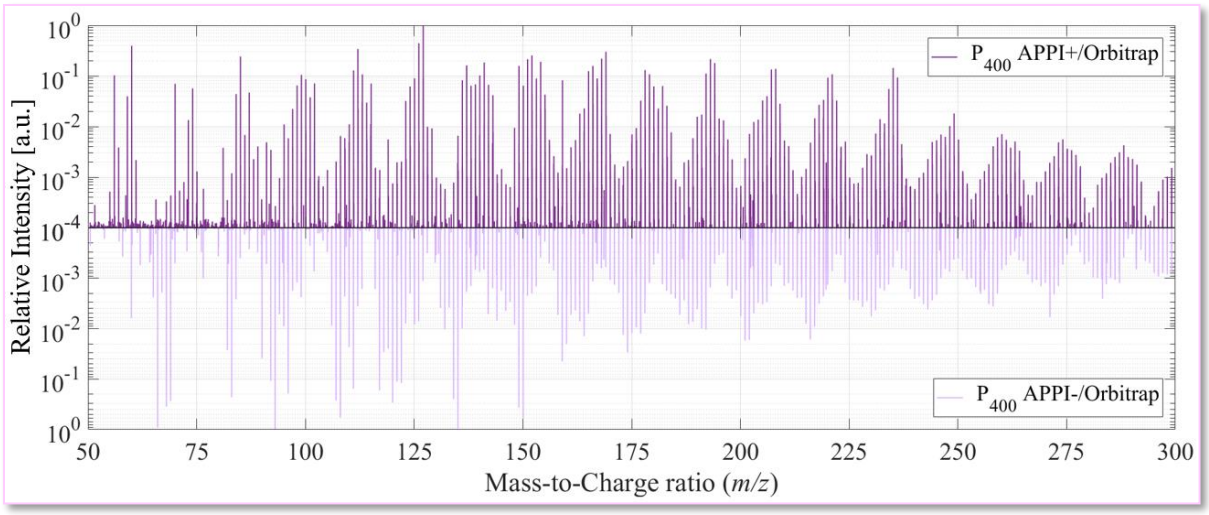

Figure IV.10: APPI/Orbitrap mass spectra of the soluble fraction of Pluto aerosol analogues P_{400}, acquired in positive mode (*upper panel*, in purple) and negative mode (*lower panel*, in mirror, in lavender color). The intensities of the peaks were normalized to the most intense peak of each mass spectrum (*m/z* 127.0725 for APPI+ and *m/z* 93.0213 for APPI–, respectively).

In Figure IV.11, we compare the APPI+/Orbitrap mass spectrum of the soluble fraction of Pluto aerosol analogues P_{650} (upper panel, in red) with the APPI–/Orbitrap mass spectrum of P_{650} (lower panel, in mirror, in pink), from *m/z* 50 to *m/z* 300. Intensity was normalized to the most intense peak in each mass spectrum (*m/z* 60.0553 for APPI+/Orbitrap and *m/z* 121.0525 for APPI–/Orbitrap, respectively).

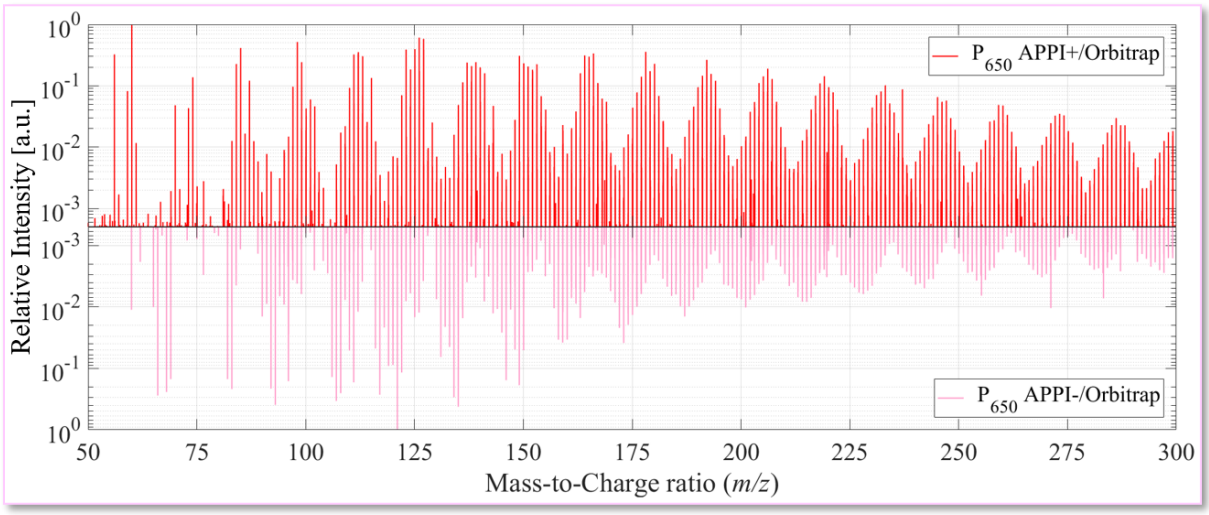

Figure IV.11: APPI/Orbitrap mass spectra of the soluble fraction of Pluto aerosol analogues P_{650}, acquired in positive mode (*upper panel*, in red) and negative mode (*lower panel*, in mirror, in pink). The intensities of the peaks were normalized to the most intense peak of each mass spectrum (*m/z* 60.0553 for APPI+ and *m/z* 121.0525 for APPI–, respectively).

As for ESI+/Orbitrap analysis, data acquired with APPI±/Orbitrap show the characteristic appearance of tholin mass spectra, with regularly-spaced peak clusters. We note, however, that for a given sample (P_{400} in Figure IV.10 and P_{650} in Figure IV.11), the peak clusters detected with APPI– (lower panels) are systematically shifted to the left compared to the peak clusters detected with APPI+ (upper panels). This leftward shifting means that the molecules detected with APPI– are less rich in hydrogen atoms. This is explained by the ionization processes inside the APPI source, which depend on the positive or negative mode used. As a reminder, APPI+ produces radical molecular cations $M^{\bullet+}$ and protonated molecules $[M+H]^+$, whereas APPI– produces radical molecular anions $M^{\bullet-}$ and deprotonated molecules $[M–H]^-$ (Raffaelli and Saba, 2003; Robb and Blades, 2008; Marchi, Rudaz and Veuthey, 2009).

A targeted analysis of the molecules identified in the two samples with APPI+/Orbitrap and APPI–/Orbitrap was conducted. I searched for all chemical formulae that could correspond to molecules of prebiotic interest in radical form $M^{\bullet+}$ or $M^{\bullet-}$, or in (de)protonated form $[M+H]^+$ or $[M–H]^-$. Due to their detection in extraterrestrial objects (*e.g.*, meteorites, comets) or laboratory analogues (*e.g.*, aerosols, interstellar ices), I considered the following types of molecules: nucleobases and derivatives (*e.g.*, Martins *et al.*, 2008; Callahan *et al.*, 2011; Burton, Stern, *et al.*, 2012; Hörst *et al.*, 2012; Sebree *et al.*, 2018; Kawai *et al.*, 2019; Oba *et al.*, 2019; Moran *et al.*, 2020), proteinogenic and non-proteinogenic amino acids (*e.g.*, Neish, Somogyi and Smith, 2010; Burton, Elsila, *et al.*, 2012; Burton, Stern, *et al.*, 2012; Evans *et al.*, 2012; Hörst *et al.*, 2012; Sebree *et al.*, 2018; Moran *et al.*, 2020), monosaccharides (*e.g.*, Meinert *et al.*, 2016; Cooper, Rios and Nuevo, 2018; Furukawa *et al.*, 2019; Moran *et al.*, 2020), fatty acids (*e.g.*, Lowe, Rees and Markham, 1963; Liebman, Pesce-Rodriguez and Matthews, 1995; Matthews, 1995), and vitamins (*e.g.*, Smith *et al.*, 2014). Note that I relied on Lu and Freeland (2006) exhaustive list of non-proteinogenic amino acids to guide the research. In addition, to ensure that chemical formulae that could correspond to molecules of prebiotic interest are not ruled out (for instance, monosaccharides can have up to eight oxygen atoms), I performed a new run of attributions with *Attributor*, but allowing this time up to ten oxygen atoms.

The identified molecules of prebiotic interest are reported in Table IV.3. For a given sample, when the detection was made both in positive and negative modes of ionization, the smaller deviation (Δppm) between the experimental mass *m/z* and the theoretical mass of the chemical formula attributed at the experimental *m/z* is reported.

Table IV.3: Molecular formulae identified in Pluto aerosol analogues P_{400} and P_{650} with APPI+/Orbitrap and APPI–/Orbitrap. These formulae can correspond to molecules of prebiotic interest. Δppm corresponds to the deviation between the mass (*m/z*) experimentally identified and the theoretical mass of the chemical formula attributed at the experimental *m/z*. Note that for a given sample, when the detection was made both in positive and negative modes, only the detection with the smaller deviation Δppm between experimental and theoretical *m/z* is reported.

Proposed potential molecule	Formula	Theoretical mass [u]	Sample			
			P_{400}		P_{650}	
			Experimental mass ± Δppm	Ionized form	Experimental mass ± Δppm	Ionized form
Nucleobases and derivatives						
Cytosine	$C_4H_5N_3O$	111.102	112.051 + 1.714	$[M+H]^+$	112.051 + 0.761	$[M+H]^+$
Thymine	$C_5H_6N_2O_2$	126.113			127.051 + 1.945	$[M+H]^+$
5-Hydroxycytosine	$C_4H_5N_3O_2$	127.101	126.030 – 0.048	$[M–H]^-$	128.046 + 0.457	$[M+H]^+$
Adenine	$C_5H_5N_5$	135.127	136.062 – 0.084	$[M+H]^+$	136.062 – 1.205	$[M+H]^+$
Hypoxanthine	$C_5H_4N_4O$	136.112	136.039 – 1.255	$M^{\bullet-}$		
2,6-Diaminopurine	$C_5H_6N_6$	150.141	151.073 – 0.654	$[M+H]^+$	150.065 – 0.131	$M^{\bullet+}$
Guanine	$C_5H_5N_5O$	151.126	151.049 – 0.496	$M^{\bullet-}$	152.057 + 0.0001	$[M+H]^+$
Queuine	$C_{12}H_{15}N_5O_3$	277.279			276.110 – 1.273	$[M–H]^-$
Proteinogenic Amino Acids and derivatives						
Valine	$C_5H_{11}NO_2$	117.146			118.087 + 1.917	$[M+H]^+$
(Iso)Leucine	$C_6H_{13}NO_2$	131.173			132.102 – 0.869	$[M+H]^+$
Glutamic acid	$C_5H_9NO_4$	147.129	146.045 – 2.930	$[M–H]^-$		
Histidine	$C_6H_9N_3O_2$	155.155	156.077 + 0.989	$[M+H]^+$	156.077 – 0.185	$[M+H]^+$
Phenylalanine	$C_9H_{11}NO_2$	165.189	166.087 + 0.628	$[M+H]^+$	166.0874 – 1.853	$[M+H]^+$
Tryptophan	$C_{11}H_{12}N_2O_2$	204.225	204.090 + 0.770	$M^{\bullet+}$	204.090 + 0.770	$M^{\bullet+}$
3-Hydroxykynurenine	$C_{10}H_{12}N_2O_4$	224.213	223.072 – 0.350	$[M–H]^-$	223.072 – 1.787	$[M–H]^-$
Alanylhistidine	$C_9H_{14}N_4O_3$	226.230			227.114 – 0.308	$[M+H]^+$
N-Acetyltryptophan	$C_{13}H_{14}N_2O_3$	246.260	246.100 + 1.964	$M^{\bullet+}$	246.100 + 0.966	$M^{\bullet-}$
Octopine	$C_9H_{18}N_4O_4$	246.267	245.125 + 1.040	$[M–H]^-$	245.125 – 0.454	$[M–H]^-$
Saccharopine	$C_{11}H_{20}N_2O_6$	276.286	277.140 – 0.514	$[M+H]^+$	276.132 – 0.014	$M^{\bullet-}$
Non-Proteinogenic Amino Acids						
Acetylurea	$C_3H_6N_2O_2$	102.092	103.051 + 2.768	$[M+H]^+$	103.051 + 1.806	$[M+H]^+$
Homoalanine	$C_4H_9NO_2$	103.120			104.071 + 1.275	$[M+H]^+$
β-Cyanoalanine	$C_4H_6N_2O_2$	114.104	115.051 + 1.220	$[M+H]^+$	115.051 + 2.281	$[M+H]^+$
4-Aminobenzoic acid	$C_7H_7NO_2$	137.136	136.040 + 0.878	$[M–H]^-$	136.040 + 1.999	$[M–H]^-$
Triazolylalanine	$C_5H_8N_4O_2$	156.140	157.073 – 0.899	$[M+H]^+$	157.073 – 0.899	$[M+H]^+$
N-Acetylvaline	$C_7H_{13}NO_3$	159.090	159.090 – 2.263	$M^{\bullet+}$		
3-Pyrazinylalanine	$C_7H_9N_3O_2$	167.170			168.077 – 0.262	$[M+H]^+$
Methylhistidine	$C_7H_{11}N_3O_2$	169.184	170.093 – 0.919	$[M+H]^+$	170.093 – 2.175	$[M+H]^+$
Iminoarginine	$C_6H_{12}N_4O_2$	172.190	173.1041 – 0.791	$[M+H]^+$	173.104 – 2.025	$[M+H]^+$
m-Cyano-Phenylglycine	$C_9H_8N_2O_2$	176.175	176.059 + 2.766	$M^{\bullet-}$		
Homophenylalanine	$C_{10}H_{13}NO_2$	179.220			179.095 + 2.774	$M^{\bullet-}$
Lathyrine	$C_7H_{10}N_4O_2$	182.180	183.088 + 1.533	$[M+H]^+$	183.088 – 0.968	$[M+H]^+$
4-Hydroxyarginine	$C_6H_{14}N_4O_3$	190.200			189.099 + 2.637	$[M–H]^-$

m-Acetyl-Phenylglycine	$C_{10}H_{11}NO_3$	193.199			193.074 + 2.187	$M^{\bullet-}$
3-Indazolealanine	$C_{10}H_{11}N_3O_2$	205.210	205.085 + 0.218	$M^{\bullet+}$	205.085 + 1.476	$M^{\bullet-}$
Benzotriazolylalanine	$C_9H_{10}N_4O_2$	206.200	206.080 + 2.330	$M^{\bullet-}$	206.080 – 0.402	$M^{\bullet+}$
Phenylasparagine	$C_{10}H_{12}N_2O_3$	208.214			208.085 + 0.956	$M^{\bullet+}$
p-Nitro-Phenylalanine	$C_9H_{10}N_2O_4$	210.190	209.056 – 2.172	$[M–H]^-$		
3-Methoxytyrosine	$C_{10}H_{13}NO_4$	211.085			210.077 – 2.234	$[M–H]^-$
O-Succinylhomoserine	$C_8H_{13}NO_6$	219.074	218.066 – 0.928	$[M–H]^-$	218.066 – 0.928	$[M–H]^-$
Vanilloylglycine	$C_{10}H_{11}NO_5$	225.200	225.064 – 1.209	$M^{\bullet-}$	224.056 – 2.360	$[M–H]^-$
N'-Formylkynurenine	$C_{11}H_{12}N_2O_4$	236.227			235.072 – 2.280	$[M–H]^-$
Boc-L-Glutamine	$C_{10}H_{18}N_2O_5$	246.122	247.129 – 0.230	$[M+H]^+$	245.114 – 0.402	$[M–H]^-$
Agaritine	$C_{12}H_{17}N_3O_4$	267.285			266.114 + 1.286	$[M–H]^-$
Aspartylhistidine	$C_{10}H_{14}N_4O_5$	270.240	270.096 – 1.633	$M^{\bullet+}$	269.089 – 1.804	$[M–H]^-$
Vitamins						
Pyridoxamine (vit. B_6)	$C_8H_{11}NO_3$	169.178	169.098 + 0.371	$[M+H]^+$	169.098 + 1.544	$[M+H]^+$
Pantothenic acid (vit. B_5)	$C_9H_{17}NO_5$	219.235	219.111 – 1.248	$M^{\bullet-}$	219.111 – 1.380	$M^{\bullet+}$

Considering the two samples (P_{400} and P_{650}) and the two ionization modes (APPI+ and APPI–), I identified molecular formulae that could correspond to 8 nucleobases and derivatives, 11 proteinogenic amino acids and derivatives, 25 non-proteinogenic amino acids, and 2 vitamins. No monosaccharide or fatty acid were identified. The APPI source has therefore enabled the detection of 46 potential molecules of prebiotic interest that were not detected with ESI+/Orbitrap analyses. Note that this result is not biased by allowing *Attributor* to assign up to ten oxygen atoms, since molecules containing up to three oxygens constitute the majority of the molecules reported in Table IV.3.

We can also point out the complementarity of the positive and negative modes of APPI technique, which allow to extend the range of detected molecules. If we take a closer look among the detected molecules, we notice that nucleobases are mostly detected in protonated form $[M+H]^+$, in agreement with the presence in their structure of protonatable secondary or tertiary amines. For some species, in particular 5-hydroxycytosine and queuine, we can explain their detection in deprotonated form $[M–H]^-$ by the presence of one or more deprotonatable hydroxyl functional groups. Regarding the detected amino acids and their derivatives, because of their structure composed of both amino and carboxyl functional groups, both ionization modes (positive and negative) seem possible. It can be expected that the functional groups constituting the side chains of the amino acids, influencing in particular their isoelectric point and thus their classifications, can have an impact on the preferred ionization mode. In particular, glutamic acid is an acid-class amino acid, and acids (proton donors) are theoretically more easily detected in negative ionization mode. Here, we see that glutamic acid is indeed detected in deprotonated form. In contrast, histidine is a basic-class amino acid, and bases (proton

acceptors) are theoretically more easily detected in positive ionization mode. Here, we see that histidine is indeed detected in protonated form. These considerations partially support the hypothesis that the detected species could indeed be molecules of prebiotic interest.

These preliminary results are very promising. Nevertheless, great caution must be taken. These results still require confirmation by other analytical techniques, such as Gas Chromatography coupled to Mass Spectrometry (GC-MS) analysis, High-Performance Liquid Chromatography (HPLC) with concentration addition technique, or other. At this stage, only GC-MS analysis has been performed in order to get structural information of the molecules. Preliminary GC-MS results are briefly discussed below in Section IV.2.2.

IV.2.2. Structural information inferred from GC-MS analysis

High-resolution mass spectrometry analysis only gives access to the chemical formulae of the molecules but not to their structures. However, for a given *m/z* ratio and therefore a given molecular formula, several structures – called isomers – are possible. For instance, in ESI+/Orbitrap and APPI+/Orbitrap data, *Attributor* attributed at *m/z* 112.051 the following molecular formula: $[C_4H_5N_3O+H]^+$ (see Appendix A2). Such a molecular formula can correspond either to cytosine or to 1-[1,2,4]triazol-1-ylethanone. In the first case, the Holy Grail, in the latter case, a molecule with a barbaric name (Figure IV.12).

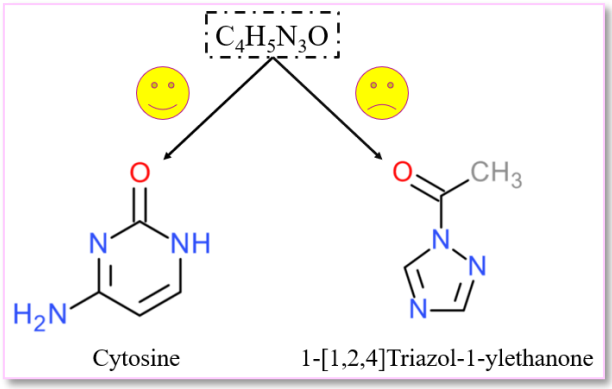

Figure IV.12: The molecular formula $C_4H_5N_3O$ can correspond to two isomers: cytosine and 1-[1,2,4]triazol-1-ylethanone.

To confirm the potential molecules of prebiotic interest that have been identified with APPI±/Orbitrap (Table IV.3), we performed a GC-MS analysis on Pluto aerosol analogues P_{400} derivatized with DMF-DMA (N,N-dimethylformamide dimethyl acetal, $(CH_3)_2NCH(OCH_3)_2$).

IV.2.2.a. Confirmation of certain molecules of prebiotic interest

In Figure IV.13, I compare the chromatogram obtained for P_{400} sample derivatized with DMF-DMA (red plot) with the chromatogram obtained with DMF-DMA alone (blank, in black). The figure is divided into three panels A, B, and C, whose close-ups are given below in order to better highlight the peaks specific to Pluto aerosol analogues.

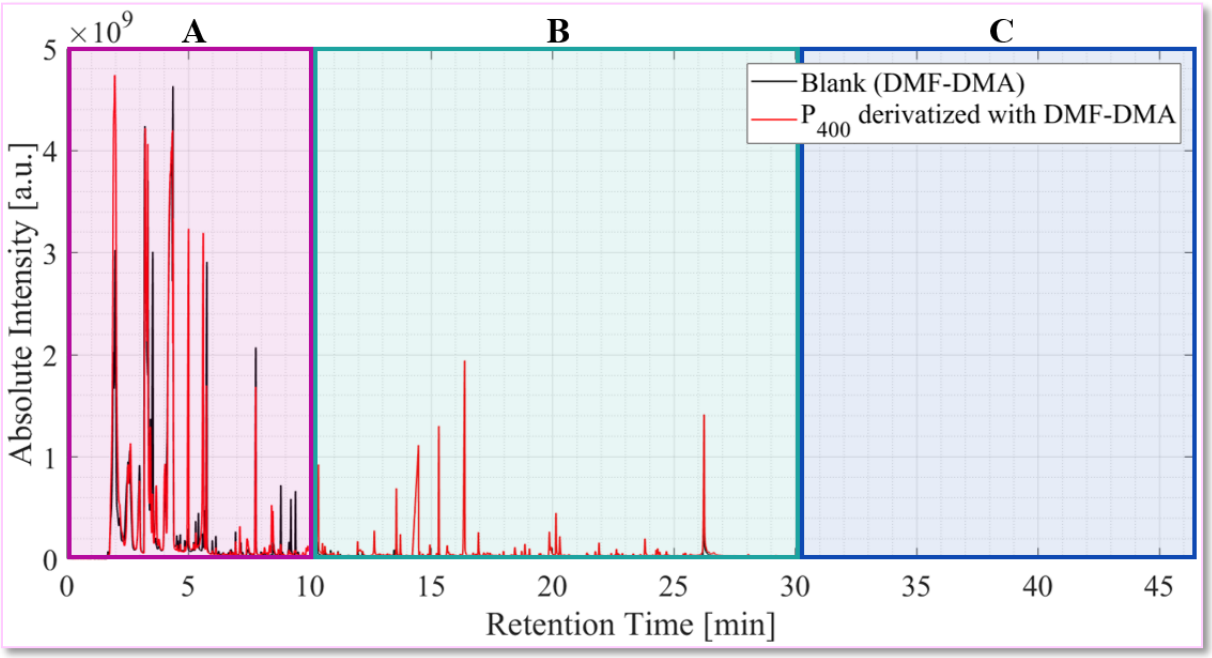

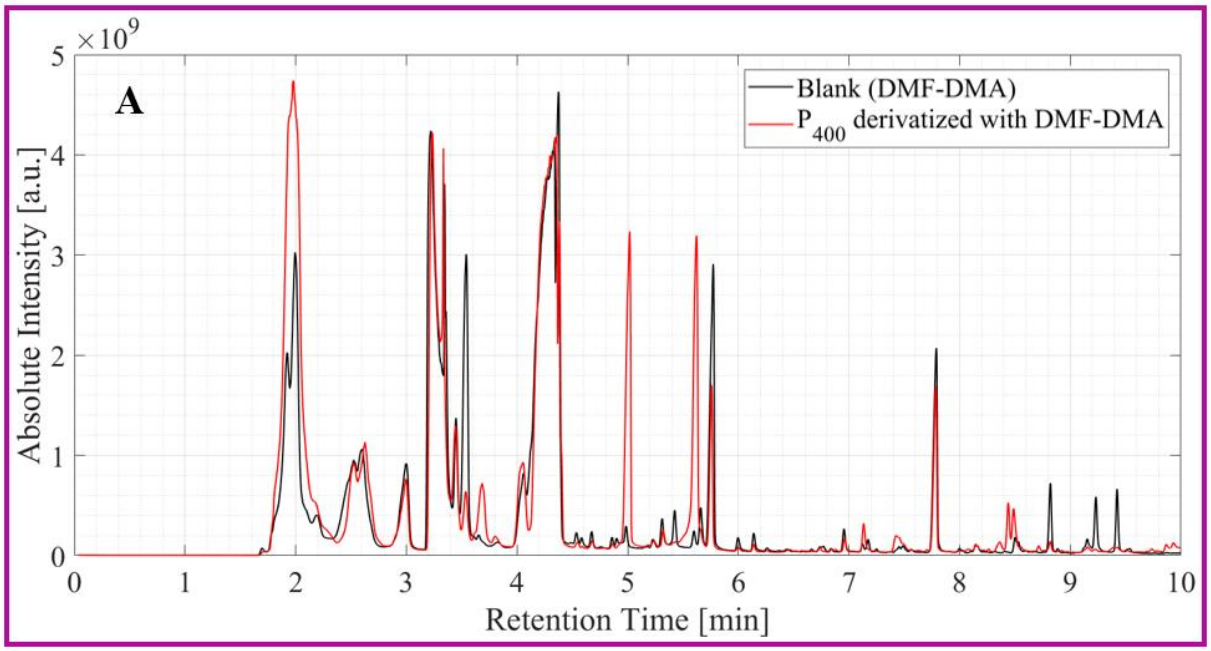

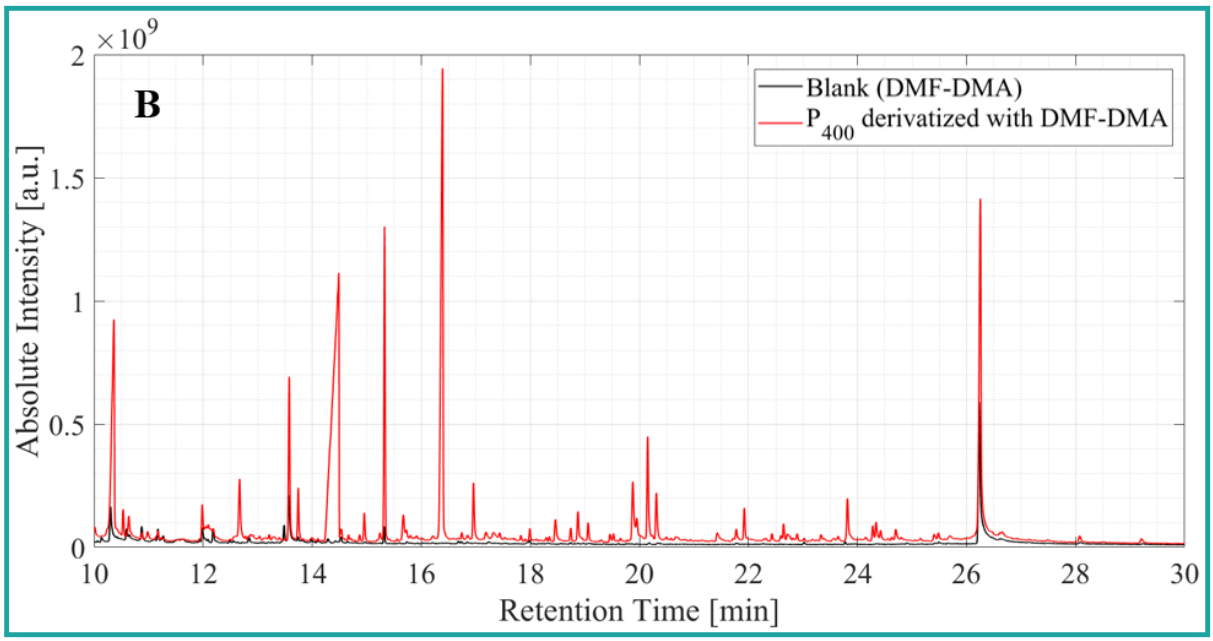

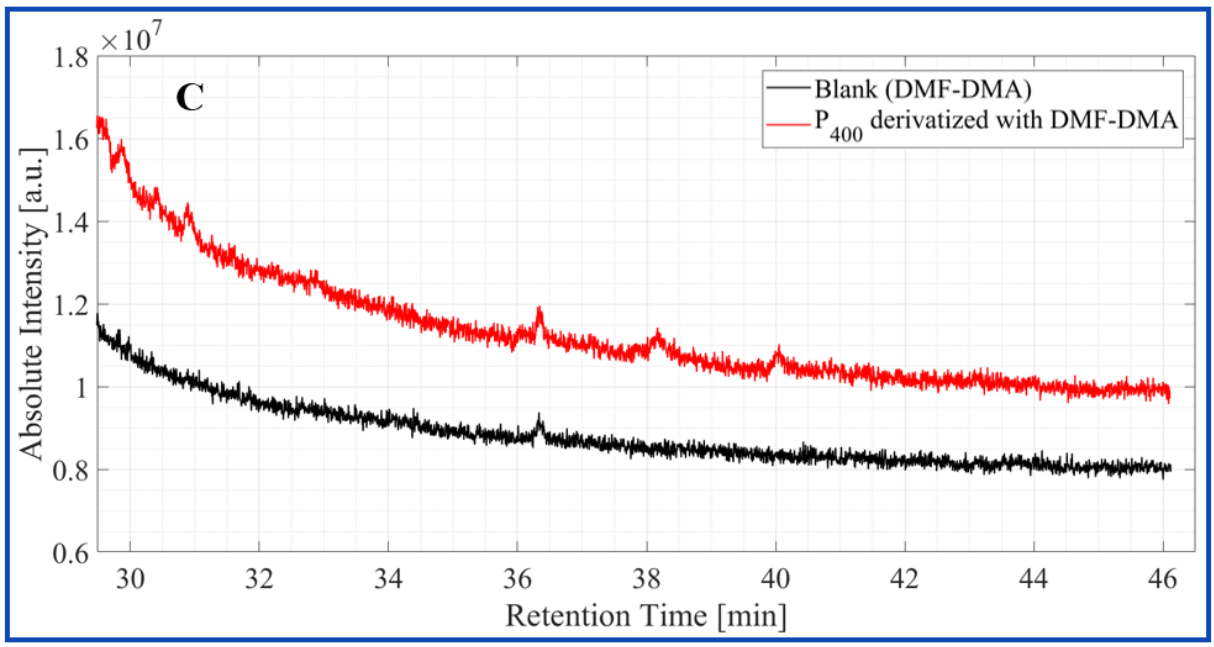

Figure IV.13: GC-MS analysis of Pluto aerosol analogues P_{400} derivatized with DMF-DMA. Comparison of the chromatogram of P_{400} (in red) with that of DMF-DMA alone (in black). The full chromatogram is divided into three panels A, B, and C. The close-ups of these panels are also given. *Panel A*: Retention times from 0 to 10 min. *Panel B*: Retention times from 10 to 30 min. *Panel C*: Retention times from 30 to 46 min.

In Figure IV.13, panel A corresponds to retention times from 0 to 10 min, panel B from 10 to 30 min, and panel C from 30 to 46 min. In panel A, we can see that most of the intense peaks in the P_{400} chromatogram are common to the chromatogram of DMF-DMA. Only the peaks at the following retention times t_R are found significantly and exclusively in P_{400} sample: 3.68, 5.02, and 5.62 min. Other less intense chromatographic peaks are also specific to P_{400} sample.

In panel B, for retention times from 10 to 30 min, most of the intense peaks are specific to P_{400} sample. Only the intense peaks at the following t_R are common to P_{400} sample and DMF-DMA reagent: 10.31, 13.58, and 26.24 min. These peaks were therefore not considered. An attempt was made to identify the intense and small chromatographic peaks that are found only in P_{400} sample. In panel C, only the chromatographic peaks at t_R 29.94, 30.41, 30.95, 38.21, and 40.05 min are exclusively present in P_{400} sample. However, due to the complexity of their mass spectra, the molecules could not be identified.

The identifications of the chromatographic peaks of P_{400} sample are summarized in Table IV.4. Note that the measurements were made twice for the P_{400} sample. The molecules identified are exclusively found in the two replicates and not in DMF-DMA, thus giving confidence that they come from the P_{400} sample and not from the derivatizing reagent.

Table IV.4: Molecules detected by GC-MS in Pluto aerosol analogues P_{400} derivatized with DMF-DMA. Molecules were identified with *Thermo XCalibur Qual Browser* by comparing their mass spectra with reference spectra libraries. Although great care was taken in handling the samples, the molecule in the shaded row is likely to be contamination. The rows written in bold correspond to molecules of prebiotic interest.

t_R in chromatogram [min]	Main peaks in mass spectrum (*m/z*)	Molecule name	Molecular formula	Molecular structure
Panel A				
3.68	83, 42, 58, 84, 43	Dimethylaminoacetonitrile	$C_4H_8N_2$	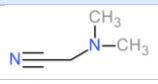
5.02	83, 42, 88, 56, 114	2-(2H-[1,2,4]triazol-3-yl)-ethylamine	$C_4H_8N_4$	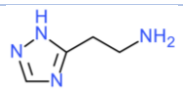
5.62	83, 101, 42, 56, 84	Adipic acid	$C_6H_{10}O_4$	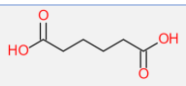
8.18	**44, 88, 45, 42, 72**	**N,N'-Dimethylurea**	**$C_3H_8N_2O$**	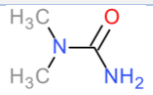
8.36	**110, 42, 28, 55, 69**	**2,4-Diaminopyrimidine**	**$C_4H_6N_4$**	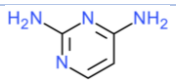
8.49	124, 44, 109, 95, 55	4,5-Dimethyl-2-pyrimidone	$C_6H_8N_2O$	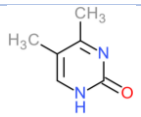
8.71	**44, 111, 71, 42, 40**	**Cytosine-5-carboxylic acid**	**$C_5H_5N_3O_3$**	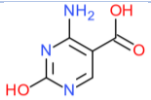
Panel B				
10.53	94, 123, 108, 44, 52	N,N-Dimethyl-2-pyrazinamine	$C_6H_9N_3$	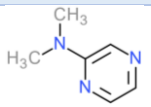

12.67	139, 110, 69, 43, 124	N,N-Dimethyl-1,3,5-triazine-2,4-diamine	$C_5H_9N_5$	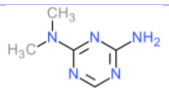
13.04	153, 69, 124, 138, 43	2-Amino-4-methyl-6-dimethylamino-1,3,5-triazine	$C_6H_{11}N_5$	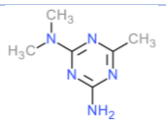
13.39	134, 133, 80, 52, 53	3-Hydroxy-4-methoxycinnamic acid	$C_{10}H_{10}O_4$	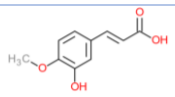
14.49	97, 42, 55, 44, 69	1-Methylpyrazol-4-amine	$C_4H_7N_3$	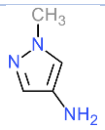
18.46	**44, 124, 83, 42, 53**	**1-Methylhistidine**	**$C_7H_{11}N_3O_2$**	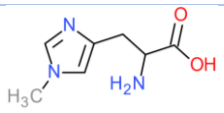
19.06	**99, 44, 178, 42, 57**	**N-Dimethylaminomethylene-alanine**	**$C_6H_{12}N_2O_2$**	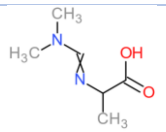
19.88	151, 166, 44, 96, 42	5,6,7,8-Tetrahydro-6-methyl-4(1H)-pteridinone	$C_7H_{10}N_4O$	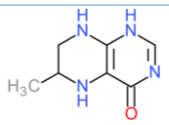
20.15	194, 179, 98, 44, 42	2,5-Dimethyl-3,6-bis(methylamino)-2,5-cyclohexadiene-1,4-dione	$C_{10}H_{14}N_2O_2$	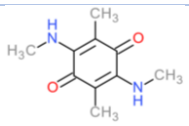
21.33	190, 175, 27, 172, 134	4-Amino-N-ethylphtalimide	$C_{10}H_{10}N_2O_2$	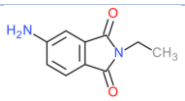

Table IV.4 is the result of a preliminary data processing, as all the very small chromatographic peaks have not been identified yet. For the identification of the molecules, critical thinking was required. When the software compares a given mass spectrum with reference spectra, a score is calculated. The higher the score, the more likely the proposed molecule is. Nevertheless, during data processing, sulphurous, brominated, fluorinated, chlorinated or even phosphorated molecules were proposed as the most likely molecules. In view of the composition of the reactive gas mixture used to synthesize Pluto aerosol analogues, these molecules cannot be formed, and were therefore ruled out automatically. Likewise, certain organic structures could easily be excluded, such as cannabinol proposed as the most likely molecule at t_R 21.72 min, zolpidem at t_R 23.64 min or alprazolam at t_R 24.15 min.

Regarding the molecules of prebiotic interest, we did not strictly identify all the molecules proposed in Table IV.3, only five molecules of prebiotic interest (rows in bold): N,N'-dimethylurea, 2,4-diaminopyrimidine, cytosine-5-carboxylic acid, 1-methylhistidine, and N-

dimethylaminomethylene-alanine. Of these, only 1-methylhistidine was also identified by APPI+/Orbitrap. At this stage, the lack of identification by GC-MS of other molecules from Table IV.3 does not mean that these molecules are absent from Pluto aerosol analogues P_{400}. Indeed, each molecule listed in Table IV.3 represents generally less than 1% of the most intense peak detected with APPI±/Orbitrap. As previously mentioned, all the chromatographic peaks have not been identified yet. Therefore, further in-depth analysis of the GC-MS data, and in particular low-intensity chromatographic peaks, will need to be carried out at a later stage. Other reasons may also explain the lack of identification of all molecules listed in Table IV.3. Some molecules may not be well derivatized, and will therefore be little or not volatilized, and thus difficult to detect with GC-MS. In contrast, by derivatizing molecules, their structures can be greatly modified to the point that they can no longer be automatically identified with *Thermo XCalibur Qual Browser*, if the derivatized molecules are not present in reference spectra libraries. Finally, it is possible that low-concentrated species are co-eluted (*i.e.*, they have the same t_R as a more abundant compound), and are therefore difficult to detect; it could thus be worthwhile to use standards and to make further GC-MS analyses with concentration addition technique.

IV.2.2.b. N-heterocycles and O-bearing terminal functional groups

Another important result relates to the nature of the observed molecular structures. The molecules presented in Table IV.4 seem quite plausible in Pluto aerosol analogues in view of our extensive knowledge of the molecular structure in Titan tholins similarly produced with the PAMPRE experimental setup. Indeed, Carrasco *et al.* (2009) and Gautier *et al.* (2014) highlighted that the incorporation of nitrogen into the molecules is not only in the form of a terminal functional group; nitrogen is essential for molecular growth, hence its incorporation within the molecular structure. Aromatic triazine units were identified as major contributor to Titan tholins molecular structure (Quirico *et al.*, 2008; Derenne *et al.*, 2012; Gautier *et al.*, 2016; Maillard *et al.*, 2020). The same conclusion was drawn for pyrazoles (Gautier *et al.*, 2016; Maillard *et al.*, 2020). N-bearing Poly-Aromatic Heterocycles (NPAH) were thus proposed as key structure governing the growth of Titan's aerosols (Gautier *et al.*, 2016; Mahjoub *et al.*, 2016; Maillard *et al.*, 2020, 2021). Such a structure was finally confirmed by Atomic Force Microscopy (AFM) observations performed by Schulz *et al.* (2021).

In Table IV.4, we also reported triazine- and pyrazole-type structures (N,N-dimethyl-1,3,5-triazine-2,4-diamine; 2-amino-4-methyl-6-dimethylamino-1,3,5-triazine; 1-methylpyrazol-4-amine), as well as pyrazine-type cycles (N,N-dimethyl-2-pyrazinamine). As for Titan's

aerosols, the molecular growth of Pluto aerosol analogues occurs through the incorporation of nitrogen within the structure of the molecules. These results are moreover in agreement with previous HRMS and IR measurements performed, presented in Section IV.1. Our GC-MS analyses therefore also confirm the importance of nitrogen chemistry in the molecular growth of Pluto's aerosols.

The identification of O-bearing molecules, such as 4,5-dimethyl-2-pyrimidone or 5,6,7,8-tetrahydro-6-methyl-4(1H)-pteridinone, also supports the importance of CO chemistry in the formation of Pluto's aerosols, as already discussed in Section IV.1. We note, however, that unlike N-incorporation, the incorporation of oxygen is in the form of a terminal functional group, just as Tran *et al.* (2008) observed in their Titan aerosol analogues. Indeed, we mainly identify molecules substituted with carbonyl, alcohol, ether or carboxylic acid functional groups, but no oxacycles such as furan-, pyran- or pyrone-type structures. In Pluto aerosol analogues, either these compounds are not formed at all, or they could not be detected with GC-MS, probably due to their instability.

In Pluto aerosol analogues, the detection of N-heterocycles and molecules with terminal O-bearing functional groups is in perfect agreement with the gas-phase products detected by QMS in Pluto-simulated atmospheres A_{400} and A_{650} (see Chapter III). Regarding N-heterocycles, formation mechanisms are proposed in Section III.1.2.c, in Chapter III.

Pluto's N-rich photochemical aerosols were proposed as coloring agent on Pluto's surface by Grundy *et al.* (2018) and Protopapa *et al.* (2020). Peeters *et al.* (2005) showed that N-heterocycles rapidly photolyze when exposed to UV irradiation, and their stability decreases with an increasing number of N atoms in the aromatic ring. On Pluto, solar photons, solar wind and galactic cosmic rays are therefore likely to be able to initiate chemistry on the surface of Pluto, involving the sedimented photochemical aerosols and the underlying surface ices. This topic was partially investigated during my Ph.D. and some results are presented in Chapter VI of this manuscript.

V. Investigating the optical constants of Pluto's aerosols

In this chapter, I present the results regarding the characterization of the optical constants of Pluto aerosol analogues. These optical constants are of prime importance to understand the radiative balance of Pluto's atmosphere. In this part of my Ph.D. thesis, I investigated the effect induced by the methane mixing ratio, and therefore the altitude or epoch of aerosol formation, on the optical constants of Pluto's aerosols. I determined Pluto tholins optical constants in collaboration with Laurent Broch and collaborators at University of Lorraine using spectroscopic ellipsometry (see Chapter II, Section II.3.3 for details). The data were then implemented through collaborations with Southwest Research Institute (Silvia Protopapa), NASA-Ames (Tanguy Bertrand) and University of Reims Champagne-Ardenne (Pascal Rannou) in a Pluto surface model developed by Protopapa *et al.* (2020) and in a model of light scattering developed by Rannou *et al.* (1997, 1999) in order to assess the suitability of Pluto aerosol analogues to reproduce the observations by *New Horizons*. This study was published in *Icarus*: Jovanović, Gautier, […] & Carrasco (2021). Optical constants of Pluto aerosol analogues from UV to near-IR. *Icarus* 362, 114398.

V.1. Determination of the optical constants of Pluto tholins from UV to near-IR

Figure V.1 and Figure V.2 respectively display the real and imaginary parts *n* and *k* of the complex refractive index determined for F_H sample with a modified Tauc-Lorentz dispersion model (in turquoise blue) and with a "λ-by-λ" numerical inversion method (in dark blue). The 2σ error bars determined for the "λ-by-λ" inversion method (see Table A3.2 in Appendix A3) were calculated based on the uncertainties of I_s^{exp} and I_c^{exp} at different wavelengths. The uncertainties were then linearly interpolated between two error bars in order to obtain an envelope of uncertainty (in light blue). Note that these error bars are due to the data inversion only and thus do not include all the uncertainties on *n*- and *k*-values. Indeed, the uncertainties on the raw ellipsometric measurements before modeling are known and are modest, given the quality of the setting of the analytical instrument; these uncertainties are therefore not included in the error bars presented. The major source of uncertainties corresponds to the inversion model used, including *e.g.*, the number of fitting parameters and of oscillators used, the problem of presence of local minima during the fit, and in particular the absence of initial values for the

inversion. We can nevertheless expect that the actual uncertainties on the optical constants of Pluto tholins would be slightly higher than those presented here.

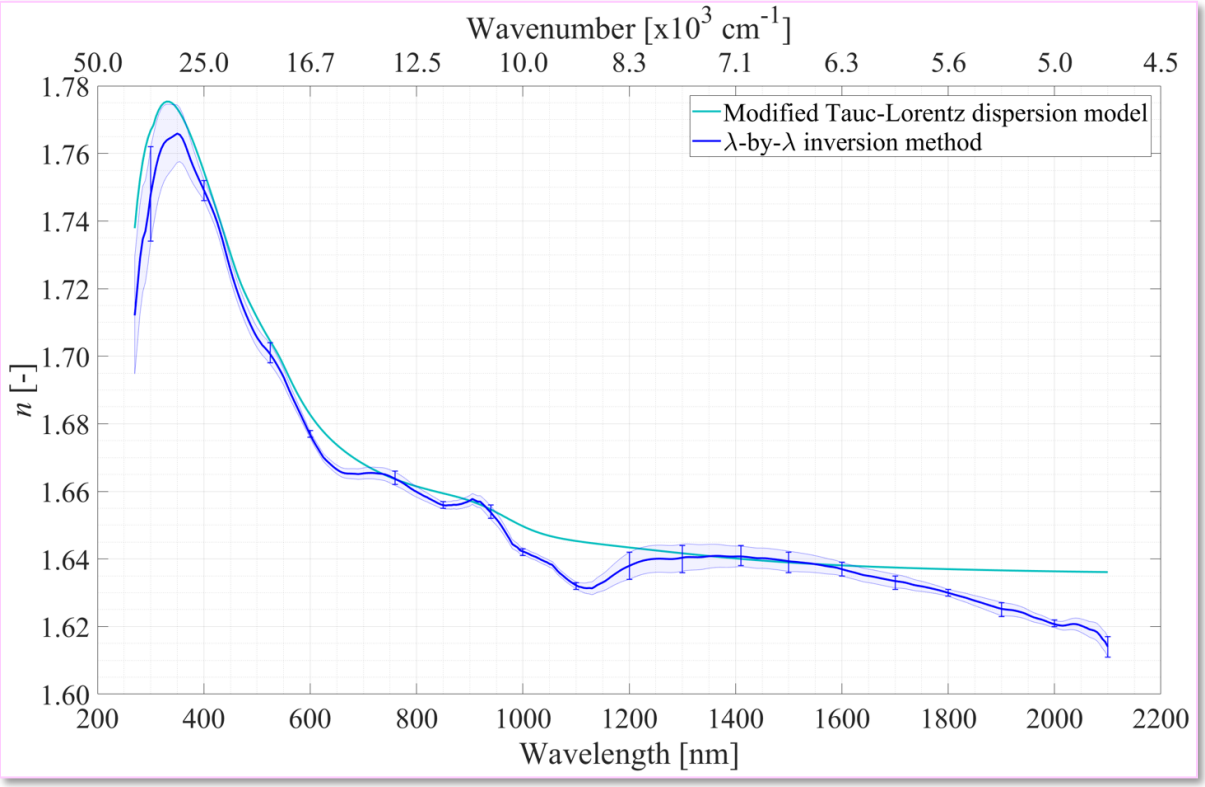

Figure V.1: Real part *n* of the complex refractive index of Pluto aerosol analogues F_H determined by spectroscopic ellipsometry with a modified Tauc-Lorentz dispersion model (in turquoise blue) and with a "λ-by-λ" numerical inversion method (in dark blue). The 2σ error bars were experimentally determined for the "λ-by-λ" inversion method at different wavelengths. The uncertainties were then linearly interpolated between two error bars in order to obtain the envelope of 2σ uncertainty (in light blue).

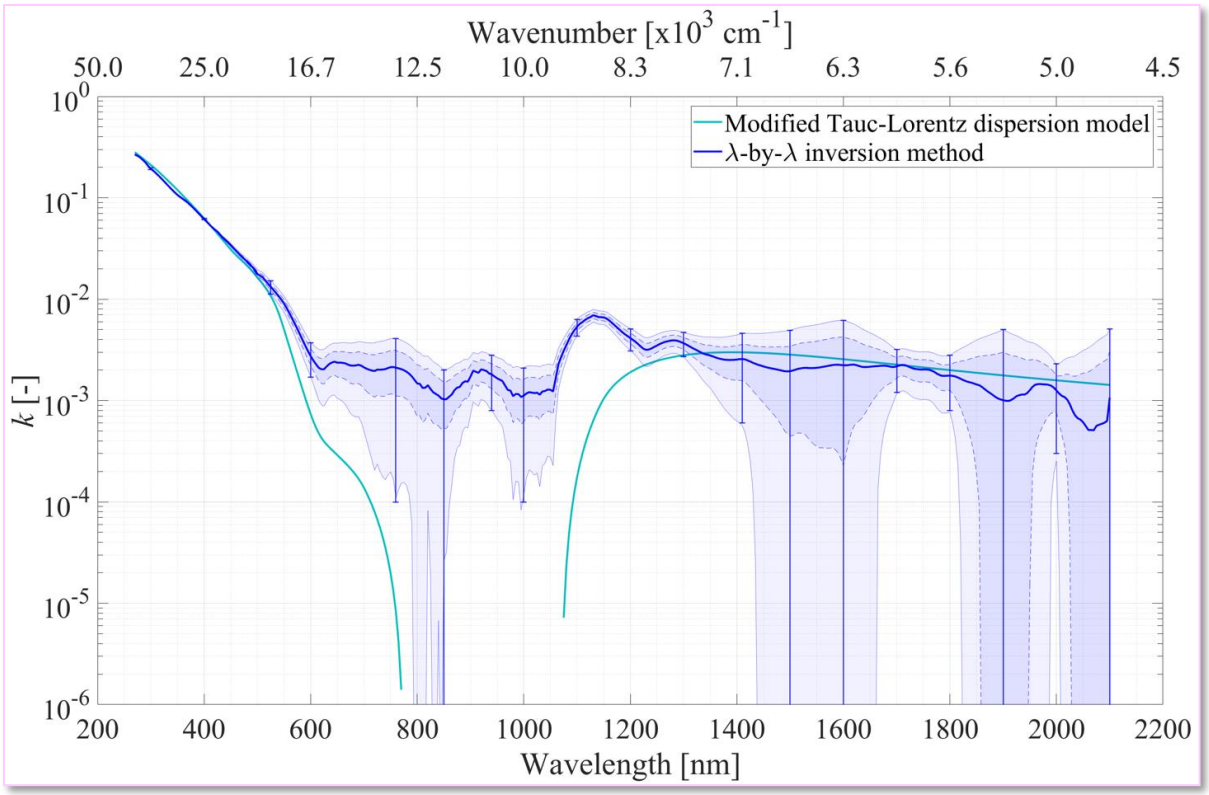

Figure V.2: Same as Figure V.1, but showing the imaginary part *k* of the complex refractive index. The 2σ error bars were experimentally determined for the "λ-by-λ" inversion method at different wavelengths. The uncertainties were then linearly interpolated between two error bars in order to obtain the envelope of 2σ uncertainty (in light blue). The envelope determined by dashed lines corresponds to 1σ uncertainty. Note that the *y*-axis was cropped at 10^{-6}, while the 2σ uncertainties of *k*-values reach 0 in the [800-850], [1,450-1,650] and [1,820-2,100] nm regions.

In Figure V.1, the dark-blue and turquoise-blue curves present the same profile, with a maximal *n*-value of about 1.77 at 325-330 nm and decreasing values of *n* index between 330 and 2,100 nm. In Figure V.2, *k*-values determined with the two models are very similar in the [270-490] and [1,150-2,100] nm regions. The dark-blue and turquoise-blue curves share the same slope, indicating similar values for the bandgap energy (also called "absorption edge", *i.e.*, the wavelength at which there is a sharp increase of the *k* index). The bandgap energy determined with the modified Tauc-Lorentz dispersion model (turquoise-blue curve) is around 575 nm, while it is around 595 nm with the "λ-by-λ" numerical inversion method (dark-blue curve). Beyond the bandgap energy, the behavior of the *k* indices is the same, reaching an asymptotic value of ~2×10^{-3} between 600 and 2,100 nm.

From Figure V.1 and Figure V.2, we can conclude that the choice of the fitting model – modified Tauc-Lorentz or "λ-by-λ" – has no significant impact on the *n* and *k* indices determined for F_H sample in the [270-600] and [1,150-2,100] nm regions. Each method has

advantages and drawbacks (specified in Section II.3.3 in Chapter II). In this work, while the modified Tauc-Lorentz dispersion model was adapted for the determination of the thin-films thickness, it could not manage to determine non-null values for *k* indices between 740 and 1,105 nm. This is due to the software used, which cannot compute *k*-values below 10^{-4}. Therefore, we list in Table A3.1 (found in Appendix A3) the optical constants of Pluto aerosol analogues F_H, F_{400} and F_{650} obtained by spectroscopic ellipsometry and determined with the "λ-by-λ" fitting method from 270 to 2,100 nm with a 5 nm increment. Note that *n* and *k* indices presented in all the following figures and listed in Table A3.1 were smoothed by a moving mean with a step of 15 data points. All the subsequent figures display the smoothed optical constants determined with the "λ-by-λ" numerical inversion method.

V.2. Impact of the altitude (or epoch) of aerosol formation on the optical constants and implications for radiative transfer

F_H, F_{400} and F_{650} samples were produced with N_2:CH_4:CO ratios = 99.5%:0.5%:500ppm, 99%:1%:500ppm, and 95%:5%:500ppm, respectively. As CH_4 mixing ratio in Pluto's atmosphere strongly varies throughout the atmospheric column (Young *et al.*, 2018), the purpose of comparing these three samples is to determine if the altitude of formation of the aerosols in Pluto's atmosphere has an effect on their optical constants.

V.2.1. Effect on real part *n* of the complex refractive index

Figure V.3 shows the real part *n* of the complex refractive index of F_H, F_{400} and F_{650} samples as a function of wavelength. In this figure, the blue curve corresponds to F_H sample, the red curve to F_{400} sample and the green curve to F_{650} sample. The 2σ error bars (see Table A3.2 in Appendix A3) were calculated based on the uncertainties of I_s^{exp} and I_c^{exp} for different wavelengths. The uncertainties were then linearly interpolated between two error bars in order to obtain the envelopes of uncertainty (in light blue, light red and light green).

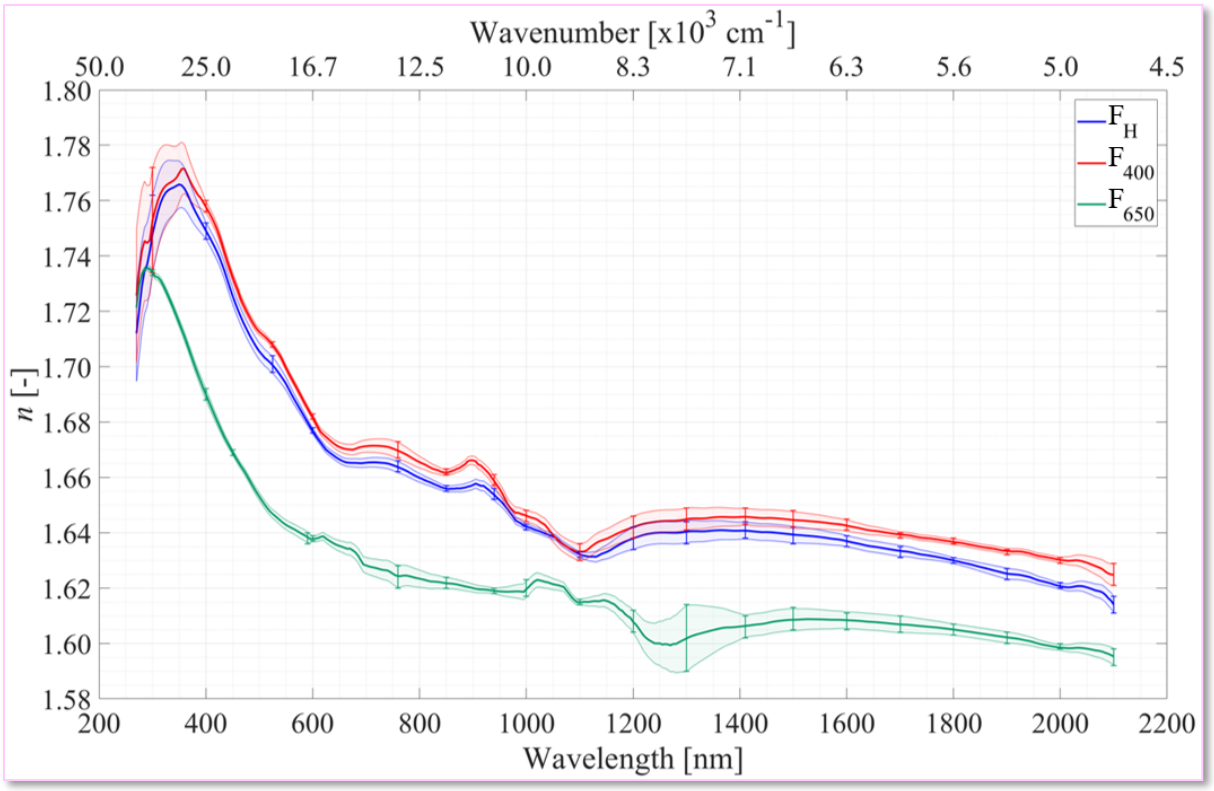

Figure V.3: Real part *n* of the complex refractive index of Pluto tholins determined by spectroscopic ellipsometry with a "λ-by-λ" numerical inversion method. The blue, red and green curves respectively correspond to the samples F_H, F_{400} and F_{650}. The 2σ error bars were experimentally determined for different wavelengths and were then linearly interpolated in-between in order to obtain the envelopes of 2σ uncertainty (in light blue, light red and light green). Note that the small variations observed in the *n*-curves at wavelengths above 600 nm should be considered with caution.

In Figure V.3, we observe that the values of *n* indices of F_H and F_{400} samples are relatively similar, but substantially different from those of F_{650} sample. For F_H and F_{400} samples, *n*-values increase from 1.71-1.73 to ~1.77 between 270 and 330 nm. Then, *n*-values decrease with a steep slope from ~1.77 to around 1.67 between 330 and 650 nm. The slope attenuates between 650 and 1,100 nm. Finally, the *n* indices of F_H and F_{400} reach an asymptotic value of 1.62-1.63 between 1,100 and 2,100 nm. For F_{650} sample, *n* index increases from 1.72 to around 1.74 between 270 and 305 nm, followed by a steep decrease from around 1.74 to 1.64 between 305 and 600 nm. The decreasing slope then attenuates between 600 and 1,200 nm, before *n* index reaches an asymptotic value of 1.60-1.61 between 1,200 and 2,100 nm. In summary, the increase of the CH_4 mixing ratio in the reactive gas mixture producing Pluto tholins leads to a decrease of *n* index over the entire spectral range considered. As well, the maximum of *n*-value is shifted towards shorter wavelengths.

The bell-shaped appearance between 270 and 400 nm, although not observed in the studies of optical constants of Titan aerosol analogues (Brassé *et al.*, 2015), appears to be a consistent trend in Pluto tholins, whatever inversion model – "λ-by-λ" or modified Tauc-Lorentz – is used. In contrast, the small variations observed in the *n*-curves at wavelengths above 600 nm should be considered with caution. Indeed, we cannot totally rule out the fact that these small variations are introduced by the *n* index being a function of wavelength λ (Moise, Flores and Rudich, 2015; Mistrik *et al.*, 2017). Nevertheless, this dependence is especially observed on a large scale: when λ increases, the *n* index increases or decreases monotonically. In addition, in the literature regarding the optical constants of terrestrial aerosols or tholin materials (*e.g.*, Khare, Sagan, Arakawa *et al.*, 1984; Ramírez *et al.*, 2002; Mahjoub *et al.*, 2012; Sciamma-O'Brien *et al.*, 2012; Liu *et al.*, 2015; Cechalova *et al.*, 2019), the *n* indices are often represented as a smooth profile, suggesting that there may be no physical reason to observe fine-scale variations of *n* index.

The overall decreasing trend of *n* indices from UV to near-IR was also observed in the studies of optical constants of Titan tholins, regardless of the production mode (type of energy source, gas pressure, gas temperature, N_2:CH_4 mixing ratios…) or the type of measurement (spectroscopic ellipsometry, spectrophotometry…) (Khare, Sagan, Arakawa *et al.*, 1984; Ramírez *et al.*, 2002; Tran *et al.*, 2003; Imanaka *et al.*, 2004; Mahjoub *et al.*, 2012, 2014; Sciamma-O'Brien *et al.*, 2012; Brassé *et al.*, 2015). In the considered wavelength range, *n* indices of Pluto aerosol analogues vary from around 1.60 to 1.78. These values are similar to the *n*-values determined for Titan aerosol analogues (Brassé *et al.*, 2015). It thus seems that Pluto tholins, produced in gas mixtures composed of N_2, CH_4 and CO, share first-order similar optical properties with Titan tholins. This similarity also extends to the chemical composition, as shown in Section IV.1 of Chapter IV of this Ph.D. thesis.

Such *n*-values agree with the co-polymeric $(CH_2)_w(HCN)_z$ nature of Pluto tholins (described in Chapter IV, Section IV.1.1), and can also correspond to O-bearing organic polymers including polyamides –C(=O)–NH– and polyethers *R*–O–*R'*, as reported by van Krevelen and te Nijenhuis (2009).

We also note in Figure V.3 that the *n* indices are higher for F_H and F_{400} samples compared to the F_{650} one, with a systematic difference of about 0.05 over the entire wavelength range. This difference between F_H/F_{400} and F_{650} is significant and beyond the uncertainties determined for the three samples at different wavelengths. Regarding the effect of CH_4 mixing ratio on *n*-values, our results differ from those of Mahjoub *et al.* (2012). In this study regarding the

influence of CH_4 concentration on the optical constants of Titan aerosol analogues, the higher the CH_4 mixing ratio, the higher the *n*-values. In the case of Pluto tholins, the relation is reversed, suggesting an increasing influence of CO at lower CH_4 concentration.

Aerosols formed in Pluto's lower atmosphere (≤ 400 km of altitude) are thus expected to scatter and polarize the light differently than the aerosols formed at higher altitudes (> 400 km of altitude), due to their different *n* indices (Kolokolova and Jockers, 1997; Kolokolova *et al.*, 1997; Nakayama *et al.*, 2012, 2018; Boucher, 2015), and therefore differently affect the photon flux reaching the lower layers of the atmosphere and the surface.

V.2.2. Effect on imaginary part *k* of the complex refractive index

Figure V.4 shows the imaginary part *k* of the complex refractive index computed for F_H (top panel, blue curve), F_{400} (middle panel, red curve) and F_{650} (bottom panel, green curve) samples as a function of wavelength. The 2σ error bars (see Table A3.2 in Appendix A3) were calculated based on the uncertainties of I_s^{exp} and I_c^{exp} for different wavelengths. The uncertainties were then linearly interpolated in-between in order to obtain the envelopes of uncertainty (in light blue, light red and light green). Dashed envelopes represent the 1σ error bars.

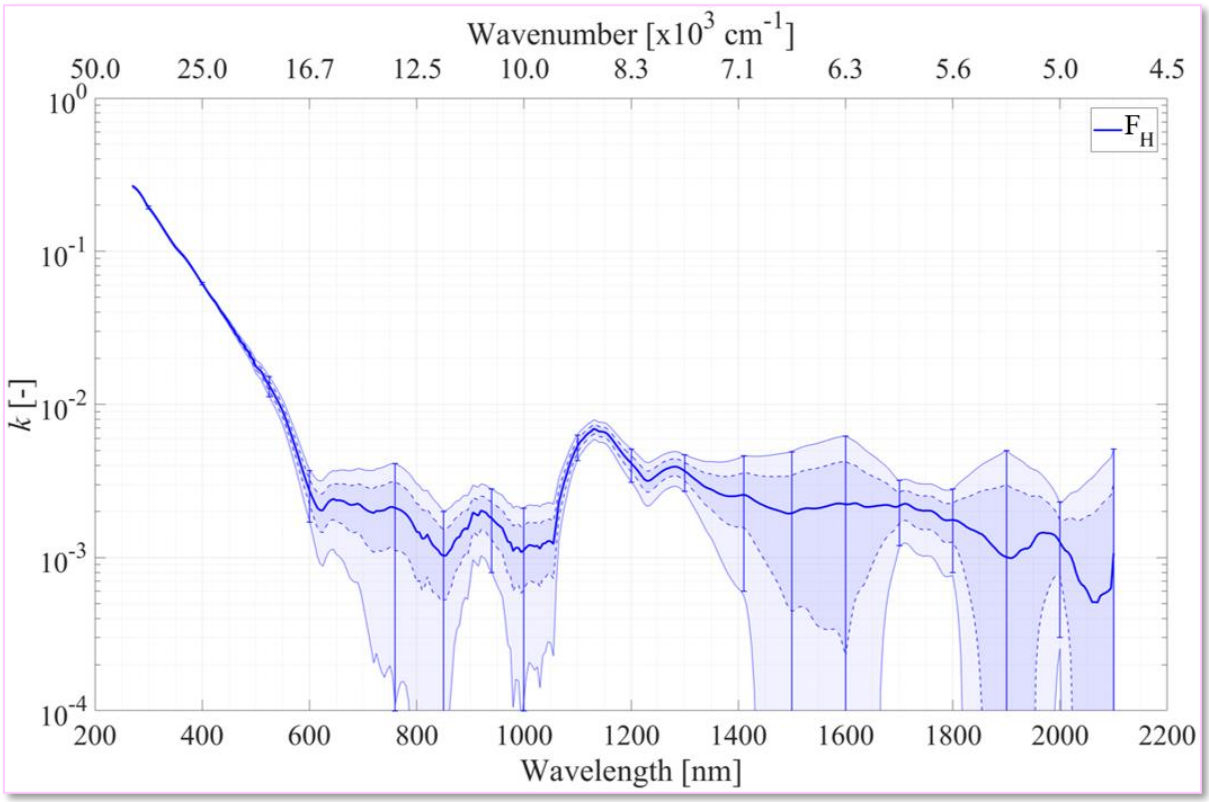

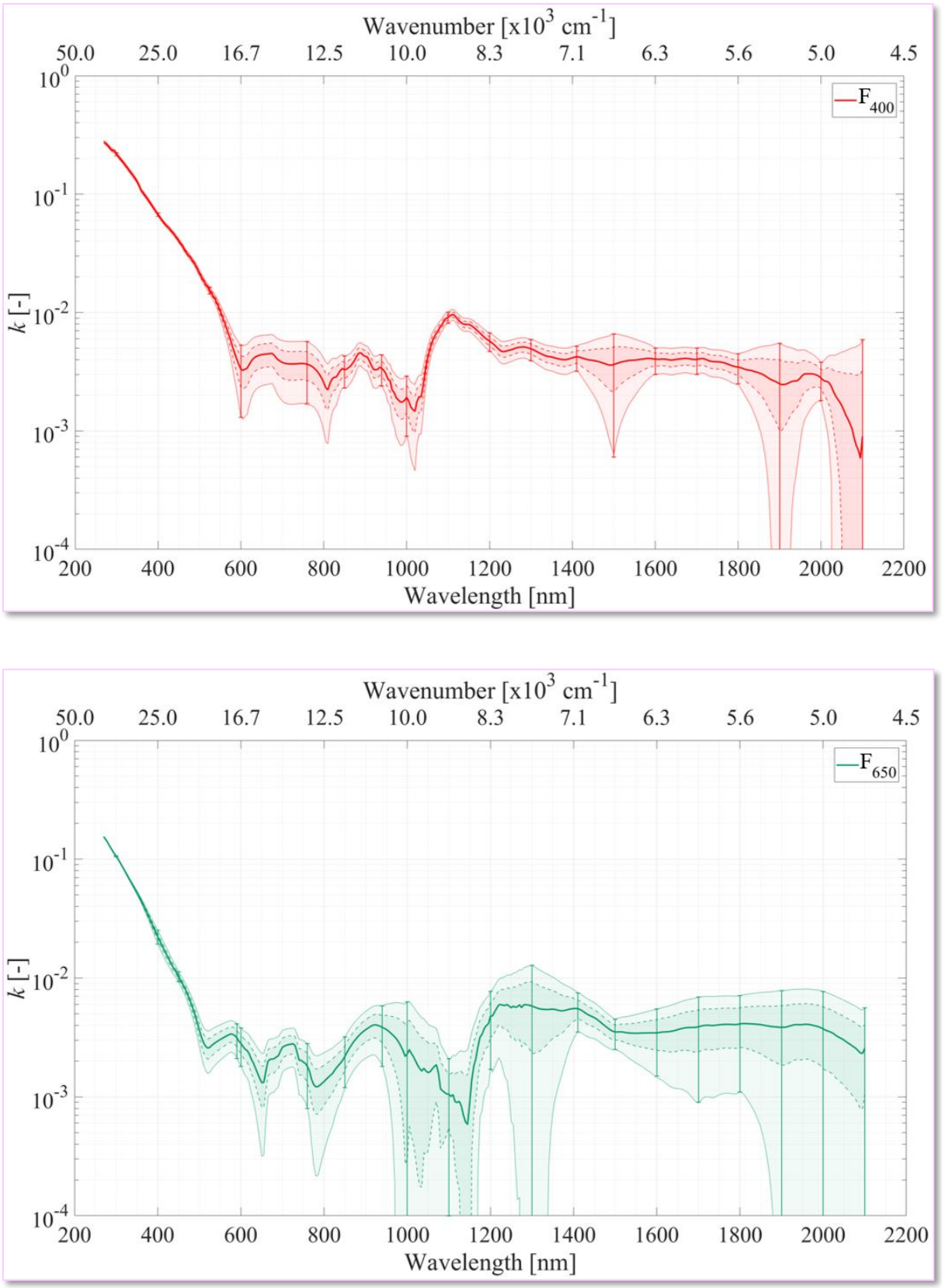

Figure V.4: Imaginary part *k* of the complex refractive index of Pluto tholins determined by spectroscopic ellipsometry with a "λ-by-λ" numerical inversion method. The blue (*top panel*), red (*middle panel*) and green (*bottom panel*) curves respectively correspond to the samples F_H, F_{400} and F_{650}. The 2σ error bars were experimentally determined for different wavelengths and were then linearly

interpolated in-between in order to obtain the envelopes of 2σ uncertainty (in light blue, light red and light green). The envelopes determined by dashed lines correspond to 1σ uncertainty. The *y*-axis was cropped at 10^{-4}. The 2σ uncertainties of *k*-values reach 0 in the [790-850], [1,450-1,650] and [1,820-2,100] nm regions for F_H sample, in the [1,870-1,930] and [2,020-2,100] nm regions for F_{400} sample and in the [980-1,180], [1,270-1,330] and [1,880-2,100] nm regions for F_{650} sample. Note that the large variations observed in the *k*-curves at wavelengths above 600 nm should be considered with caution.

In Figure V.4, we observe that the *k*-values of F_H and F_{400} are significantly higher for wavelengths between 270 and 600 nm than those of F_{650}. From 600 to 2,100 nm, the trend is less clear, because of larger uncertainties on *k*-values. For F_H and F_{400} samples, *k*-values plummet from 2.7×10^{-1} to around 4.5×10^{-3} between 270 and 590 nm. The bandgap energy is estimated to be around 590 nm. For F_{650} sample, the *k* index steeply decreases from 1.5×10^{-1} down to around 2×10^{-3} between 270 and 520 nm. The bandgap energy is estimated at around 520 nm. Due to the large uncertainties on *k*-values determined for the three samples above 600 nm and because this kind of material is weakly absorbent in the near-IR (Brassé *et al.*, 2015), the large variations observed in the *k*-curves should be considered with caution. *k* indices for all samples probably reach an asymptotic value of a few 10^{-3} between 600 and 2,100 nm.

The 2-steps behavior of *k*-values – sharp decrease followed by a plateau – was also observed for Titan aerosol analogues in the considered wavelength range (Khare, Sagan, Arakawa *et al.*, 1984; Ramírez *et al.*, 2002; Tran *et al.*, 2003; Imanaka *et al.*, 2004; Mahjoub *et al.*, 2012, 2014; Sciamma-O'Brien *et al.*, 2012; Brassé *et al.*, 2015).

We do not have a definitive explanation for the variations observed beyond 600 nm in the *k*-curves of the three samples F_H, F_{400} and F_{650}. Nevertheless, assuming that the variations observed are consistent absorption bands (Table V.1): (1) the absorption band around 725 nm observed in F_{650} sample could be ascribed to C–H stretching 4th overtone in $–CH_x$ (x = 1, 2, and 3) and in Aromatic–CH and to O–H stretching 3rd overtone in *R*–OH and in Aromatic–OH; (2) the absorption band between 900 and 950 nm observed in all samples could be attributed to C–H stretching 3rd overtone and to O–H stretching 2nd overtone; (3) the absorption band between 1,100 and 1,150 nm observed in F_H and F_{400} samples could correspond to C–H stretching 2nd overtone and to –C=O stretching 4th overtone; (4) the absorption band between 1,950 and 2,000 nm observed in F_H and F_{400} samples could be in agreement with –C=O stretching 2nd overtone in *R*–(C=O)–*R'*, *R*–(C=O)–O*R'* and in *R*–(C=O)–NH_2 and to N–H combination in *R*–(C=O)–NH_2 and in aromatic amines (Workman and Weyer, 2008; Stenberg *et al.*, 2010; Xiaobo *et al.*, 2010). These overtones are conceivable, given the chemical composition determined for Pluto tholins in Section IV.1 of Chapter IV of this Ph.D. thesis.

Table V.1: Overtone and combination near-IR band assignment of potential absorption bands found in the *k* profiles presented in Figure V.4. The band assignments are based on Workman and Weyer (2008), Stenberg *et al.* (2010), and Xiaobo *et al.* (2010).

Wavelength [nm]	Overtone and combination near-IR band assignment	Present in sample F_x
725	• C–H stretching 4th overtone in $–CH_x$ (x = 1, 2, and 3) and in Aromatic–CH • O–H stretching 3rd overtone in *R*–OH and in Aromatic–OH	F_{650}
900-950	• C–H stretching 3rd overtone in $–CH_x$ (x = 1, 2, and 3) and in Aromatic–CH • O–H stretching 2nd overtone in *R*–OH and in Aromatic–OH	F_H, F_{400}, F_{650}
1,100-1,150	• C–H stretching 2nd overtone in $–CH_x$ (x = 1, 2, and 3) and in Aromatic–CH • –C=O stretching 4th overtone in *R*–(C=O)–*R'*, *R*–(C=O)–O*R'* and in *R*–(C=O)–NH_2	F_H, F_{400}
1,950-2,000	• –C=O stretching 2nd overtone in *R*–(C=O)–*R'*, *R*–(C=O)–O*R'* and in *R*–(C=O)–NH_2 • N–H combination in *R*–(C=O)–NH_2 and in aromatic amines	F_H, F_{400}

From Figure V.4, we can conclude that Pluto aerosol analogues significantly absorb UV and visible radiations, while their absorption is weaker above 600 nm. The strong absorption below 500-600 nm, in the blue-green spectral range, agrees with a brownish color for Pluto tholins. This absorption is likely due to the presence of N- and O-bearing organic molecules with lone pair, such as –NH, $–NH_2$, –NH*R*, *R*–N–*R'*, $–NO_2$, –OH, –COOH, –C=O, *R*–O–*R'* functional groups (Rao, 1975; Imanaka *et al.*, 2004; Mahjoub *et al.*, 2012; Desyaterik *et al.*, 2013; Liu *et al.*, 2015; Moise, Flores and Rudich, 2015). Due to the delocalization of π electrons, fused aromatic rings, N- and O-containing polycyclic aromatic compounds and unsaturated molecules with extensive conjugated multiple bonds also participate to the strong absorption of UV and visible wavelengths (Rao, 1975; D'Amico, Manos and Christensen, 1980; Tran *et al.*, 2003; Imanaka *et al.*, 2004; Zhong *et al.*, 2012; Desyaterik *et al.*, 2013; Lambe *et al.*, 2013; Liu *et al.*, 2015; Moise, Flores and Rudich, 2015). Most of these chemical functions were actually detected in Pluto aerosol analogues, with the presence of unsaturated N- and O-bearing molecules in large amount (see Chapter IV of this Ph.D. thesis).

When CH_4 concentration increases, the bandgap energy shifts towards shorter wavelengths. Therefore, *k* index depends on the CH_4 mixing ratio used to produce the tholins. Indeed, from 270 to around 600 nm, where the uncertainties are low, we can see that F_H and F_{400} samples, produced with a lower CH_4 concentration, present higher *k*-values than F_{650} sample, produced with a higher CH_4 concentration.

This anti-correlation between *k*-values and methane mixing ratio was also detected by Mahjoub *et al.* (2012) in their study about Titan tholins. They attributed this anti-correlation to the proportion of N-bearing molecules: when CH_4 concentration decreases, N-containing molecules increase in proportion and contribute to a higher absorption of UV and visible radiations (Mahjoub *et al.*, 2012, 2014). This conclusion was also proposed by Imanaka *et al.* (2004), when comparing their Titan tholins with Uranus/Neptune tholins from Khare *et al.* (1987) study, produced in CH_4:H_2 gas mixtures. They hypothesized that N-incorporation in Titan tholins could increase *k*-values in the UV-Vis spectral range, in agreement with the laboratory experiments realized by Scattergood and Owen (1977). Indeed, nitrogen promotes unsaturation. In addition, when N_2 content is increased in the reactive gas mixture forming Pluto tholins (case of F_H and F_{400} samples), the formation of sp^2 bonds is favored as hydrogen atoms become scarce to form saturated molecules. In contrast, when the reactive gas mixture contains more CH_4 (case of F_{650} sample), the presence of large amounts of hydrogen promotes the formation of sp^3 bonds, which have no effect on π-π^* electronic transitions in UV and visible wavelength ranges (Ferrari, Rodil and Robertson, 2003; Quirico *et al.*, 2008).

Another explanation to both higher *n*- and *k*-values for F_H and F_{400} could be the higher oxidation of these samples. Indeed, I showed earlier that F_{400} sample (*i.e.*, P_{400}) contains more oxygen in mass than F_{650} (*i.e.*, P_{650}) (Section IV.1.3 in Chapter IV of this thesis). Studies realized on optical properties of terrestrial secondary organic aerosols (Cappa *et al.*, 2011; Nakayama *et al.*, 2012, 2018; Lambe *et al.*, 2013; Moise, Flores and Rudich, 2015) and of oxidized early Earth- and Exoplanets-like aerosols (Gavilan *et al.*, 2017) showed that *n* indices increase when the oxidation level of the aerosols increases. Moreover, the more the aerosols are oxidized, the more they absorb UV and visible radiations.

We can thus expect that aerosols formed at different altitudes in Pluto's atmosphere will differently absorb radiations reaching the atmosphere. In particular, Pluto's aerosols formed at or below 400 km of altitude above the surface, due to their higher N- and O-content, may absorb more efficiently UV and visible wavelengths than aerosols formed above 400 km of altitude.

Besides, as mentioned in the Introduction and Section II.1.4.b of Chapter II, the samples studied here could also be considered as analogues of aerosols produced during different seasons or epochs of Pluto (Bertrand and Forget, 2016; Stern, Binzel, *et al.*, 2017; Bertrand *et al.*, 2019). In Bertrand and Forget (2016), their Pluto General Circulation Model (GCM) predicted a mean CH_4 atmospheric mixing ratio in ~2200 (terrestrial year; northern winter/southern summer on Pluto) about five times higher than that observed in 2015. This is due to the condensation of N_2 onto the surface, which also leads to a decrease in surface pressure as low as 10^{-5}-10^{-6} mbar; the atmosphere being thinner, the methane is less diluted (Bertrand and Forget, 2016; Stern, Binzel, *et al.*, 2017). However, the pressure in the atmosphere would still be sufficient to allow the formation of haze particles (Johnson *et al.*, 2021). Given my results, one could expect different atmospheric methane mixing ratio through time to lead to hazes with different optical properties. In return, this would also modify the effect of Pluto's haze on the whole thermal profile of Pluto and the photon flux reaching the surface.

V.3. New input parameters for Pluto atmospheric and surface models

In this section, I first compare the optical constants determined during my Ph.D. with those from the canonical study by Khare, Sagan, Arakawa *et al.* (1984). Then, I discuss the application of our Pluto tholins optical constants to the modeling of Pluto's surface and atmosphere.

V.3.1. Comparison of my optical constants with those of Titan tholins from the study by Khare *et al.* (1984)

Khare, Sagan, Arakawa *et al.* (1984) did a pioneer work to determine the optical constants *n* and *k* of Titan aerosol analogues from soft X-ray to microwave frequencies. For this purpose, they combined transmittance, specular reflectance, interferometric, Brewster angle and ellipsometric polarization measurements on thin films synthesized on various substrates. Although the large considered wavelength range is valuable, the employed method – combination of different thin films and different measurement techniques, with interpolations – induces major uncertainties. Moreover, Brassé *et al.* (2015) reviewed why Khare *et al.* (1984) optical constants are not representative of Titan's aerosols at different wavelengths.

Even though several other teams have since then determined optical properties of Titan aerosol analogues (Ramírez *et al.*, 2002; Tran *et al.*, 2003; Vuitton, Tran, *et al.*, 2009; Imanaka *et al.*,

2012; Mahjoub *et al.*, 2012, 2014; Sciamma-O'Brien *et al.*, 2012), optical constants from Khare *et al.* (1984) are still widely used by modeling teams to explain atmospheric and surface properties of Titan. This often requires introducing *ad hoc* modifications to them to fit the observations better for Titan (Liang, Yung and Shemansky, 2007; Lavvas, Yelle and Vuitton, 2009; Griffith *et al.*, 2012; Lopes *et al.*, 2016; Seignovert *et al.*, 2017; Brossier *et al.*, 2018; Fan *et al.*, 2019), but also for Pluto (Cheng *et al.*, 2017; Protopapa *et al.*, 2017, 2020; Zhang, Strobel and Imanaka, 2017; Grundy *et al.*, 2018; Young *et al.*, 2018). This is partially due to the lack of optical constants of tholins-like materials covering a wide wavelength range.

Only the data by Khare, Sagan, Arakawa *et al.* (1984) and Tran *et al.* (2003) for Titan tholins cover the same wavelength range as the Pluto optical constants determined in this part of my Ph.D. thesis, and therefore are used for comparison purposes. In Figure V.5 and Figure V.6, we respectively compare the *n* index and the *k* index of Pluto aerosol analogues F_{400} (red asterisks) to Khare *et al.* (1984) data (black asterisks), from 270 to 2,100 nm. Note that Titan tholins from Khare *et al.* (1984) were produced in a reactive gas mixture composed of 90% of N_2 and 10% of CH_4.

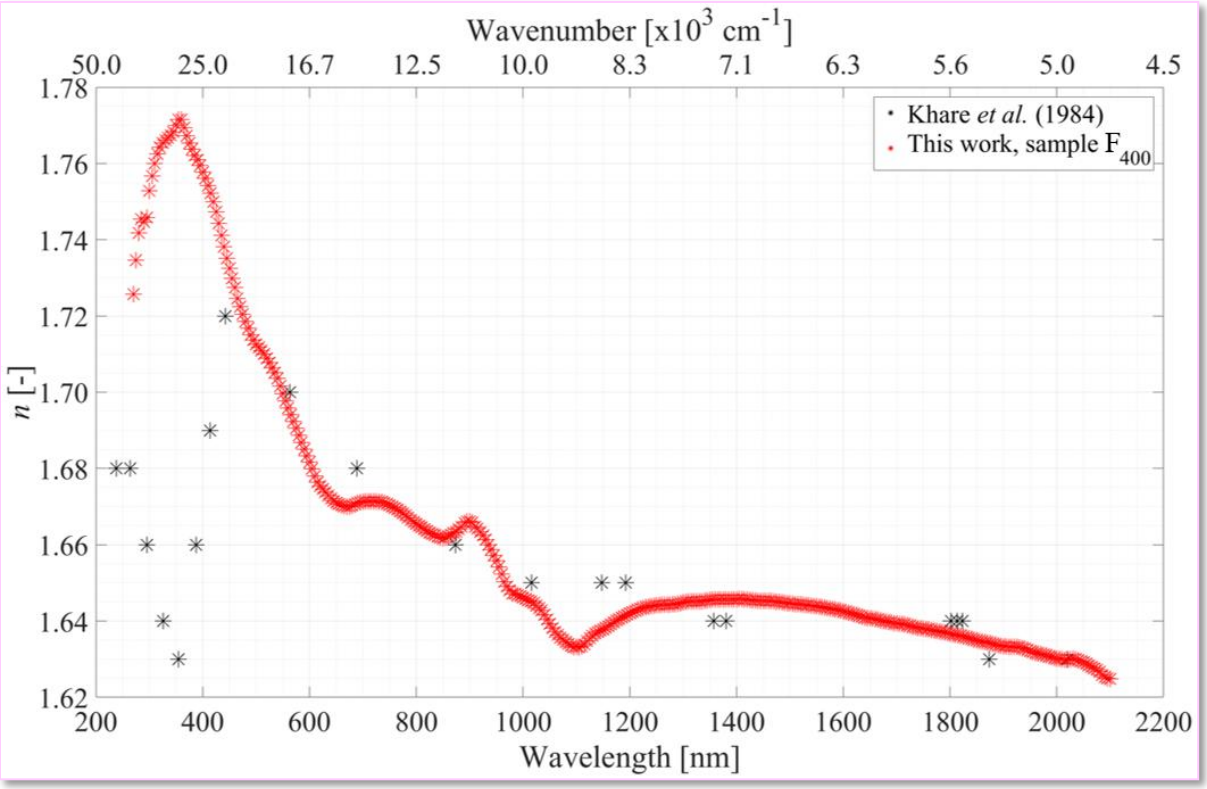

Figure V.5: Comparison between the real part *n* of the complex refractive index of our Pluto tholins F_{400} (red asterisks) and Titan tholins from Khare, Sagan, Arakawa *et al.* (1984) study (black asterisks).

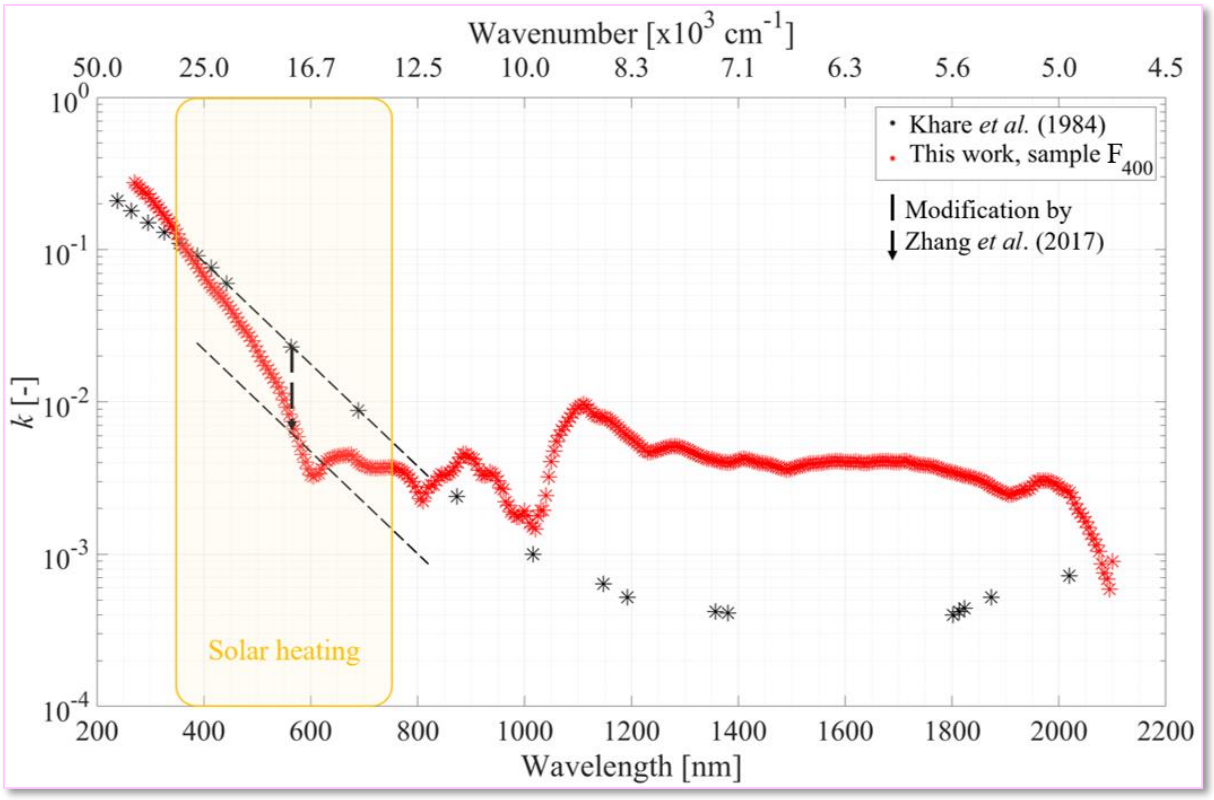

Figure V.6: Comparison between the imaginary part *k* of the complex refractive index of our Pluto tholins F_{400} (red asterisks) and Titan tholins from Khare, Sagan, Arakawa *et al.* (1984) study (black asterisks). The black dashed arrow indicates the modification implemented by Zhang, Strobel and Imanaka (2017) to the *k*-values from Khare *et al.* (1984) in the region where solar heating dominates (represented by the yellow rectangle) in order to adjust Pluto's thermal balance.

In Figure V.5, we observe that the *n* index of Pluto tholins F_{400} is similar to that of Khare *et al.* (1984) Titan tholins from 450 to 2,100 nm. Below 450 nm, the behavior is reversed. While *n*-value reaches a maximum near 330 nm for F_{400}, Khare *et al.* (1984) data present a minimum *n*-value near 350 nm. We do not have a definitive explanation for this – rather unphysical – behavior of Khare *et al.* (1984) *n* index. As no other organic polymeric material evidences such behavior (*e.g.*, van Krevelen and te Nijenhuis, 2009), it seems rather plausible that this dip could be due to technical difficulties rather than material properties. For example, it could have been induced by the low sampling rate of Khare *et al.* (1984) measurements combined with the interpolation they had to use to extend the range; or by a poor definition of the optical properties of the substrates used for the synthesis of the tholin thin films and the data inversion; or by the light source and/or detector used for the measurements being at the limit of their range.

Regarding the *k* indices (Figure V.6), the bandgap energy of Khare *et al.* (1984) tholins is shifted towards longer wavelengths (around 1,200 nm) compared to F_{400} sample (around 590 nm). *k*-values of F_{400} are higher than those of Khare *et al.* (1984) below 380 nm and in the near-IR

(> 900 nm). These higher values can be explained by higher N- and O-content of Pluto aerosol analogues F_{400} (Imanaka *et al.*, 2004; Quirico *et al.*, 2008; Cappa *et al.*, 2011; Mahjoub *et al.*, 2012; Nakayama *et al.*, 2012, 2018; Lambe *et al.*, 2013; Gavilan *et al.*, 2017; Jovanović *et al.*, 2020). From 380 to around 800 nm, *k*-values of F_{400} are lower than those of Khare *et al.* (1984), due to the shifted bandgap energy which is caused by higher *k*-values in the UV and a steeper slope in the UV-Vis for our F_{400} sample.

Even though *k*-values of F_{400} sample are one order of magnitude higher than those of Khare *et al.* (1984) between 1,000 and 2,000 nm, they are constant and do not present the anomalous sharp increase beyond 1,800 nm presented by the Khare *et al.* (1984) *k*-values. The fact that our *k*-values are one order of magnitude higher in the near-IR is consistent with published literature on Titan's aerosols. For example, Lavvas, Yelle and Griffith (2010) and Larson *et al.* (2015) reported that the actual optical properties of Titan's aerosols should be about an order of magnitude larger in the near-IR compared to the optical constants from Khare *et al.* (1984).

V.3.2. Application of my optical constants to Pluto's surface modeling

Recently, Protopapa *et al.* (2020) studied the coloring materials across Pluto's surface. To support the conclusion developed by Grundy *et al.* (2018), Pluto's photochemical aerosols were considered as potential surface coloring agent. Thus, in their model, they implemented the *k* indices determined for Titan tholins by Khare, Sagan, Arakawa *et al.* (1984) and Tran *et al.* (2003). Nevertheless, in order to fit their models to spectra acquired in the regions of Cthulhu Macula and Lowell Regio by the imagers MVIC and LEISA constituting the Ralph instrument (Reuter *et al.*, 2008), some modifications of *k* indices determined by Khare *et al.* (1984) were necessary. Specifically, Protopapa *et al.* (2020): first applied no change to the *n* index of Khare *et al.* (1984); secondly decreased the *k*-value of Khare *et al.* (1984) at 690 nm by ~55% to match the observations of Pluto in the *RED* filter between 540 and 700 nm (note that Protopapa *et al.* (2020) preserved the original sampling of Khare *et al.* (1984) explaining why the *k*-value was modified at 690 nm); and thirdly assumed *k* index to be constant between 1.8 and 2.2 µm, given that the increase displayed by the *k*-values of Khare *et al.* (1984) beyond 1.8 µm was not consistent with the observations.

Figure V.7 was adapted from Protopapa *et al.* (2020) by Silvia Protopapa. It displays the imaginary part *k* of the complex refractive index (right *y*-axis) of our F_{400} sample (red curve, with an envelope of uncertainties represented in salmon pink), compared to those of the Titan

tholins from the studies by Khare *et al.* (1984) (orange triangles) and Tran *et al.* (2003) (blue dots). Additionally, the set of *k* indices determined by Protopapa *et al.* (2020) (black squares) that best fits the MVIC and LEISA *New Horizons* measurements acquired in the regions of Cthulhu Macula and Lowell Regio are shown, as well as the MVIC transmission filters (left *y*-axis). See Protopapa *et al.* (2020) for details about the modeling of MVIC and LEISA spectra.

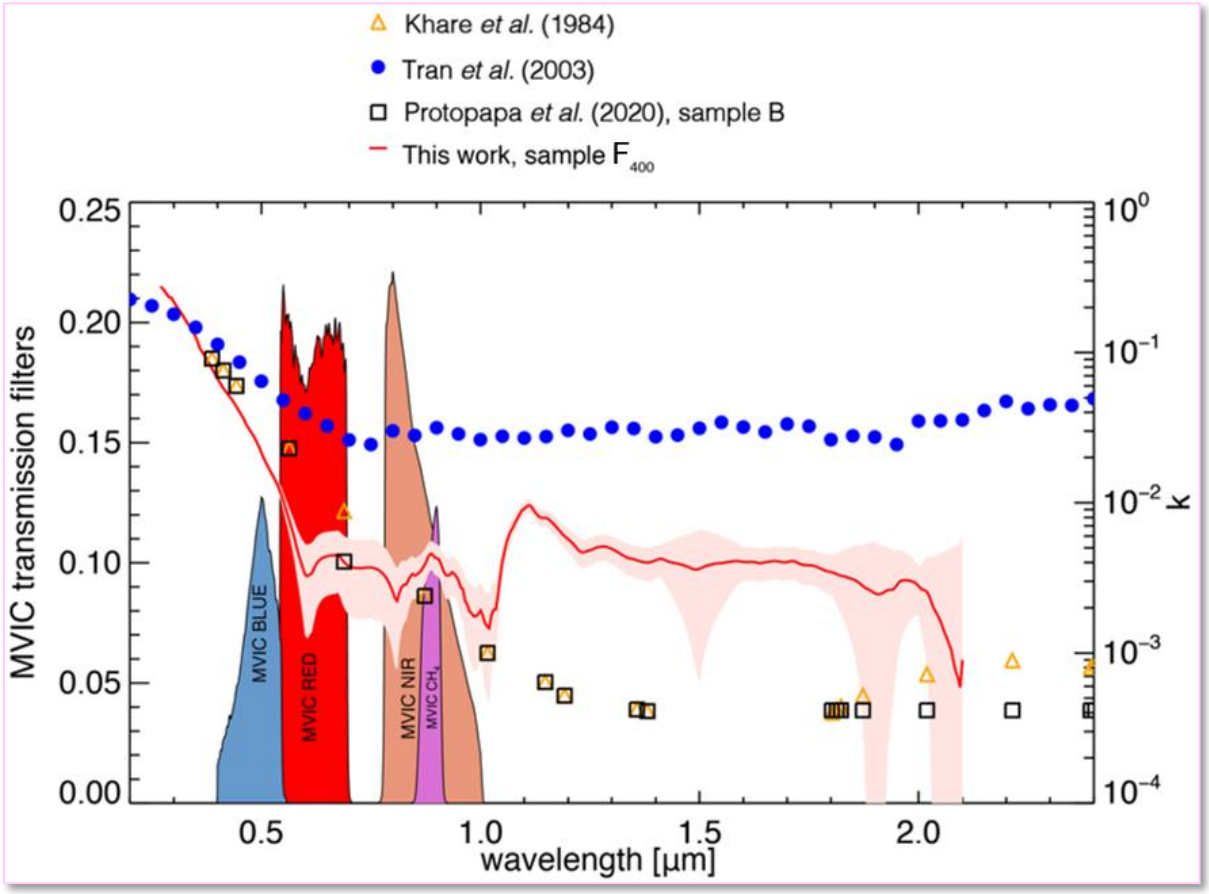

Figure V.7: Figure adapted from Protopapa *et al.* (2020). Imaginary part *k* of the complex refractive index (right *y*-axis) is represented as a function of wavelength. The red curve with the salmon-pink envelope corresponds to the *k* index of our sample F_{400}. The orange triangles correspond to the *k* index determined by Khare, Sagan, Arakawa *et al.* (1984), while the blue dots are from the study by Tran *et al.* (2003). The black squares are the *k*-values determined by Protopapa *et al.* (2020) that best fit the MVIC and LEISA data. The MVIC transmission filters (left *y*-axis) are shown for reference. See Protopapa *et al.* (2020) for details about the modeling.

Protopapa *et al.* (2020) recognized that the *k*-values of Titan tholins by Khare *et al.* (1984) present a sharp increase beyond 1.8 µm (see Figure V.7, orange triangles), inconsistent with the Pluto *New Horizons* data. Therefore, Protopapa *et al.* (2020) modified the *k*-values determined by Khare *et al.* (1984) beyond 1.8 µm, assuming them to be constant with wavelengths up to 2.4 µm and equal to the mean value computed between 1.35 and 1.45 µm (see Figure V.7, sample B from Protopapa et al. (2020)). This is consistent with the trend exhibited by Pluto

tholins F_{400}. Indeed, as noted above, while the *k*-values of F_{400} sample are one order of magnitude higher than those of Khare *et al.* (1984) between 1.0 and 2.0 µm, they are constant with wavelengths and do not display the sharp increase beyond 1.8 µm presented by the Khare *et al.* (1984) *k*-values.

In Figure V.7, we observe that the change to the Khare *et al.* (1984) data implemented at 690 nm by Protopapa *et al.* (2020) (black squares) to match the Pluto *New Horizons* observations is consistent with the *k*-curve of our Pluto tholins F_{400} (red curve, with the salmon-pink envelope). Also, sample B from Protopapa *et al.* (2020) shares the same slope in the UV-Vis as our F_{400} sample and is in agreement, within the uncertainties, with our data between 0.8 and 1.0 µm.

These considerations support the suitability of our optical constants to reproduce Pluto compositional observations at least in the UV and visible spectral ranges. Nevertheless, from 1.1 to 1.8 µm, our *k*-values are obviously larger by an order of magnitude with respect to the *k*-values adopted to reproduce Pluto *New Horizons* data by Protopapa *et al.* (2020). This difference of one order of magnitude might be explained by different concentrations of organic material. Indeed, the determination of the optical constants was made on pure tholins, whereas on the surface of Pluto, it is possible that the organic material is mixed with ices, thus decreasing the *k*-values. An in-depth modeling analysis of the Pluto *New Horizons* observations using as inputs our Pluto tholins optical constants throughout the full wavelength range, from 0.4 to 2.5 µm, is therefore required to confirm that Pluto's coloration and composition can be attributed to the photochemical aerosols that I reproduced in the laboratory. Another possible explanation could be the ageing of aerosols deposited at the surface of Pluto by subsequent irradiation by solar photons, solar wind and/or galactic cosmic rays.

V.3.3. Application of my optical constants to Pluto's atmosphere modeling

In order to evaluate the effect of our Pluto tholins optical constants on aerosol properties, and to compare with those of Titan, I display the extinction coefficient Q_{ext} (Figure V.8), the single-scattering albedo ω (Figure V.9), and the absorption coefficient Q_{abs} (Figure V.10) calculated by Tanguy Bertrand and Pascal Rannou for a spherical particle of 10 nm according to Mie theory (formalized in Bohren and Huffman (1983)) and for a fractal aggregate of 3,375 spheres (Rannou *et al.*, 1997, 1999).

These parameters are key in the atmospheric radiative transfer (Bohren and Huffman, 1983). Q_{ext} is the ratio of the extinction cross section (σ_{ext}) and the geometric projection of the particle (σ_{geo}). It characterizes the extinction, *i.e.*, the absorption and scattering of radiation by aerosols. ω represents the fraction of scattered radiation, while $(1 - \omega)$ represents the fraction of absorbed radiation. ω is equal to 0 for a perfect absorber and equal to 1 for a perfect scatterer. These two coefficients control the amount of energy absorption by aerosols at solar wavelengths through $Q_{abs} = (1 - \omega) \times Q_{ext}$ and the emission in thermal infrared $Q_{emi} = Q_{abs} = (1 - \omega) \times Q_{ext}$. They participate to the thermal balance of Pluto's atmosphere, as demonstrated by Zhang, Strobel and Imanaka (2017).

At first glance, the scattering of haze at Pluto's limb in the forward direction indicates particles having radii in the range 0.1-0.5 µm (Stern *et al.*, 2015; Gladstone *et al.*, 2016). Further detailed analyses and arguments from microphysical models (Cheng *et al.*, 2017; Gao *et al.*, 2017; Zhang, Strobel and Imanaka, 2017) yielded a better result with fractal aggregates of small grains. In these studies, a fractal dimension $D_f = 2$ was assumed, the morphology of the haze particles is thus more like that of snowflakes instead of solid spheres. The study by Cheng *et al.* (2017) showed that spherical monomers should have ~10 nm radius (R_m) and aggregates should have a "bulk radius" (or "volume equivalent radius") of about R_b = 0.15 µm, corresponding to $\mathcal{N} = (R_b/R_m)^3 \approx$ 3,375 monomers per aggregate. Such a fractal structure globally satisfies, although not perfectly, the main requirements to explain Pluto *New Horizons* observations (Cheng *et al.*, 2017). This aerosol structure was also used by Zhang, Strobel and Imanaka (2017) to study Pluto's thermal balance. Note, however, that in the study by Gao *et al.* (2017), the particle size distributions of their model are displayed as a function of the "effective radius" R_f. Since their aerosols grow up to R_f = 0.15 µm, with a fractal dimension $D_f = 2$, the corresponding aggregates appear much smaller ($\mathcal{N}$ = 225) than those considered by Cheng *et al.* (2017), Zhang, Strobel and Imanaka (2017) and Lavvas *et al.* (2020) ($\mathcal{N}$ = 3,375). The most probable reason for this difference stands in that Cheng *et al.* (2017) and Lavvas *et al.* (2020) matched data from *New Horizons* containing information about the aerosol size, with observations made at different phase angles, while Gao *et al.* (2017) used data that are not sensitive to the aerosol size. Since aerosols are produced from growth mechanisms, they are expected to start as small spherical particles at high altitudes and continuously get larger by coagulation (direct gas-particle interactions) while sedimenting (Cheng *et al.*, 2017; Gao *et al.*, 2017; Zhang, Strobel and Imanaka, 2017). Thus, both the properties of small spherical monomers and fractal aggregates are interesting.

In Figure V.8 and Figure V.9, I compare, for several sets of optical constants, the parameters Q_{ext} and ω computed for spherical monomers of 10 nm radius, distributed with a log-normal distribution and an effective variance ν of 0.03 (dotted lines), and for fractal aggregates of 3,375 monomers of 10 nm radius (plain lines). We used the optical constants determined during my Ph.D. (F_H, F_{400} and F_{650}, in blue, red and green respectively), optical constants determined for Titan tholins by Khare *et al.* (1984) (in black) and for Titan's aerosols from observations by Rannou *et al.* (2010) and Vinatier *et al.* (2012) (in pink).

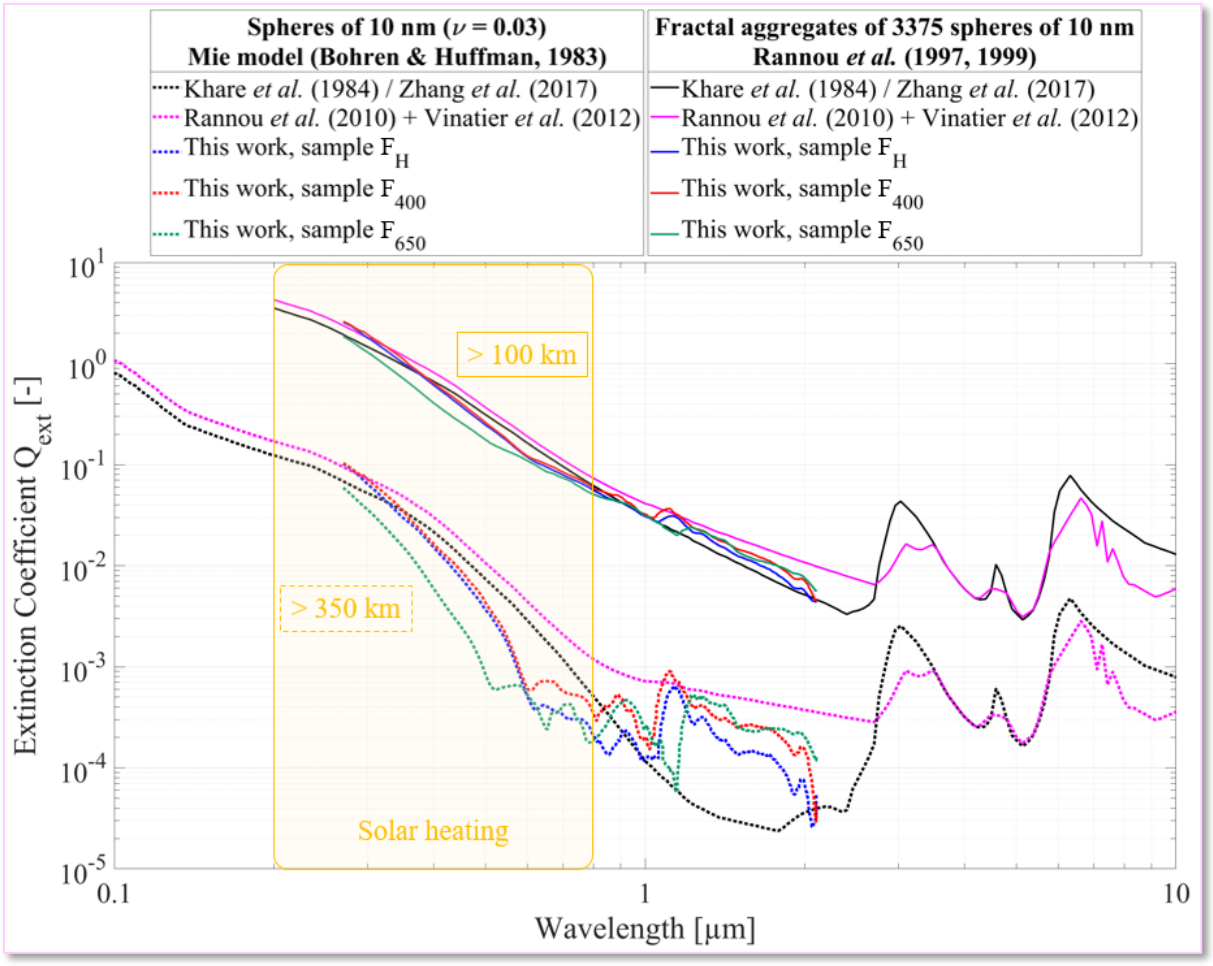

Figure V.8: Extinction coefficients Q_{ext} determined for spherical monomers of 10 nm radius (log-normal distribution, with effective variance ν = 0.03) with a Mie model formalized in Bohren and Huffman (1983) (dotted curves) and for fractal aggregates of 3,375 monomers of 10 nm radius with the model developed by Rannou *et al.* (1997, 1999) (plain curves). The black curves were generated with the optical constants determined by Khare *et al.* (1984) for Titan tholins. Note that these Khare *et al.* (1984) optical constants were adopted in Zhang, Strobel and Imanaka (2017) study. The pink curves were generated with the optical constants determined by Rannou *et al.* (2010) and Vinatier *et al.* (2012) for Titan's aerosols. The blue, red and green curves were generated with the optical constants determined respectively for my samples F_H, F_{400} and F_{650}. The yellow rectangle indicates the region where solar heating dominates. The dotted curves (spherical monomers) give information on the radiative transfer in the upper layers of Pluto's atmosphere (> 350 km of altitude), while the plain curves (fractal

aggregates) give information on the radiative transfer in Pluto's lower atmosphere (between 100 and 300 km of altitude).

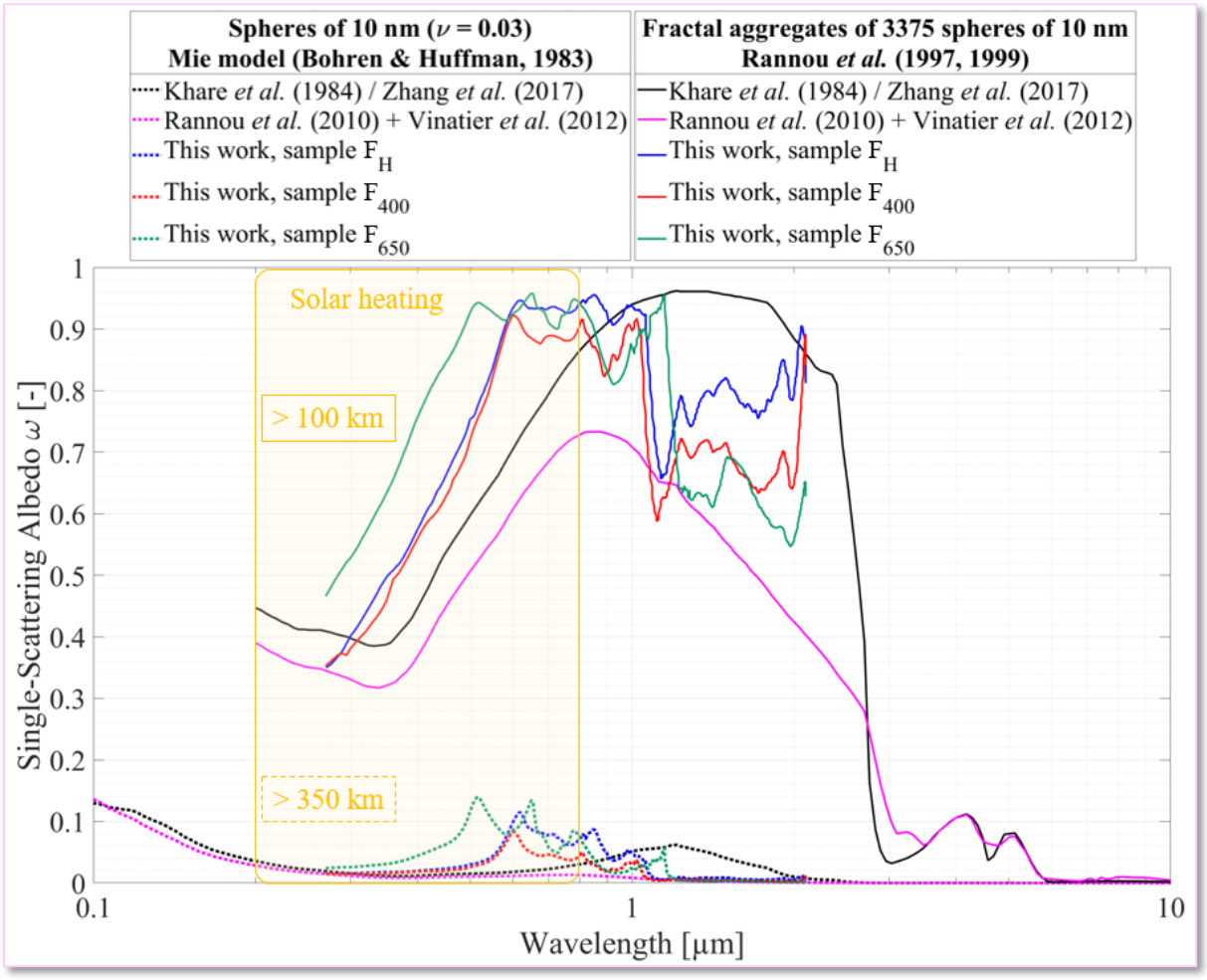

Figure V.9: Same as Figure V.8, but showing the single-scattering albedo ω.

In Figure V.8, we remark that the extinction coefficients Q_{ext} for spherical particles or fractal aggregates computed with tholins relevant for Pluto have a steepest spectral slope at visible wavelengths (broadly from 0.2 to 0.8 µm, where most Pluto New Horizons photometrical data were taken, and where solar heating occurs) than those computed with optical constants relevant for Titan's aerosols.

In Figure V.9, considering single spheres or fractal aggregates, we see that the single-scattering albedo ω is significantly higher in the UV and visible spectral ranges with the optical constants of Pluto tholins than with Titan optical constants. In the near-IR, ω of Pluto tholins are lower than that of Khare *et al.* (1984) Titan tholins. This suggests that Pluto's haze could absorb less in the UV-Vis wavelength range than Titan's haze.

However, to really assess the absorption efficiency of each type of particles, one has to compare the absorption coefficients $Q_{abs} = (1 - \omega) \times Q_{ext}$ (displayed in Figure V.10).

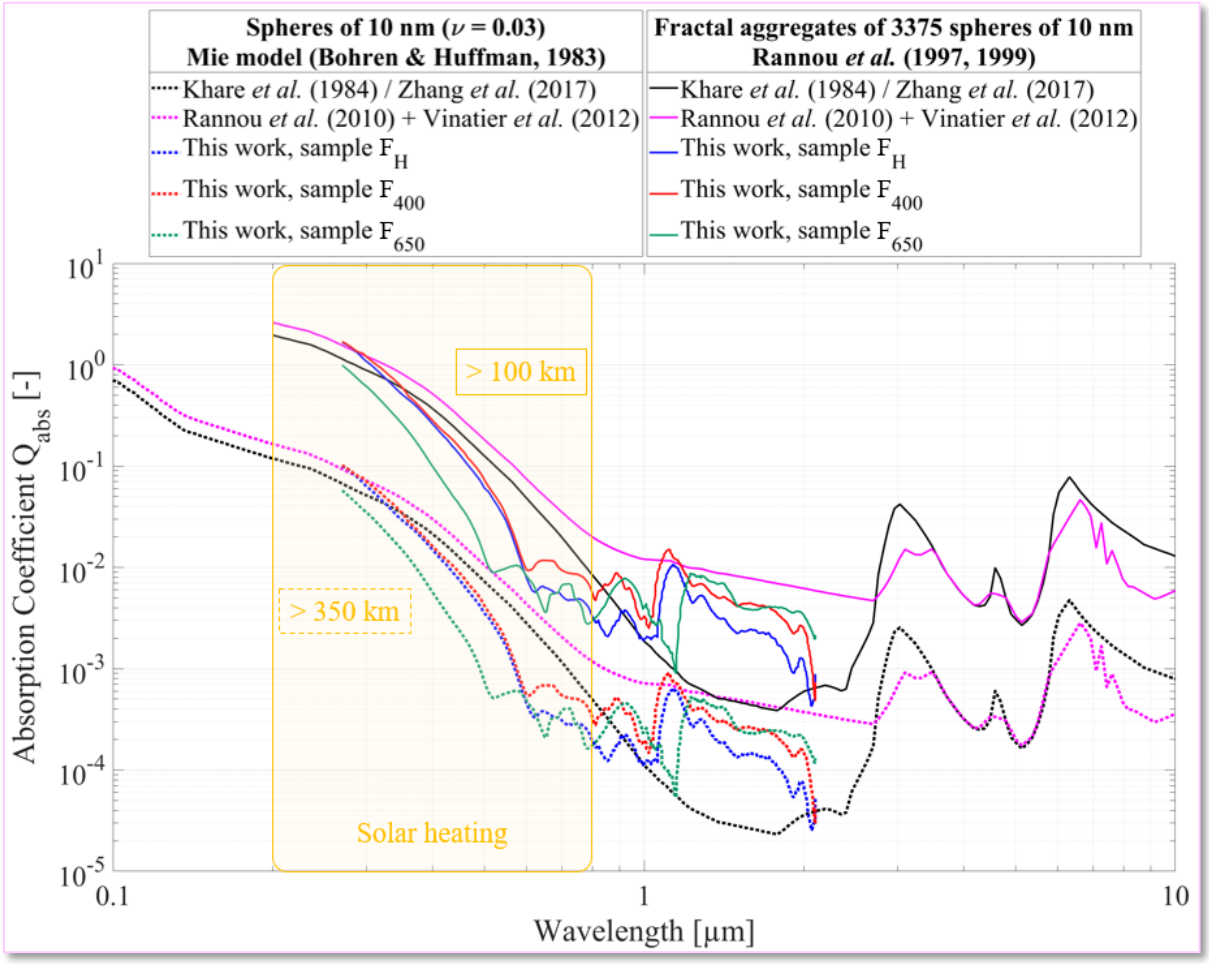

Figure V.10: Same as Figure V.8, but showing the absorption coefficients Q_{abs}.

The absorption coefficients Q_{abs} (Figure V.10) computed with Pluto tholins optical constants are about equal to those computed with Titan optical constants at 0.3 µm. Nevertheless, they drop much faster with wavelengths and are lower by a factor 3 to 10 at wavelengths larger than ~0.4-0.5 µm. This is true for small spherical particles and fractal aggregates.

Beyond 1 µm, the marked structures of Pluto tholins set the extinction coefficients Q_{ext} (Figure V.8) between those obtained with optical constants of Khare *et al.* (1984) and Rannou *et al.* (2010), but this has less consequence on data analysis or on the thermal balance. On the other hand, the scattering efficiency $Q_{sca} = \omega \times Q_{ext}$ (Figure V.11), the phase functions and the asymmetry parameters (Figure V.12) are not modified at all by optical constants.

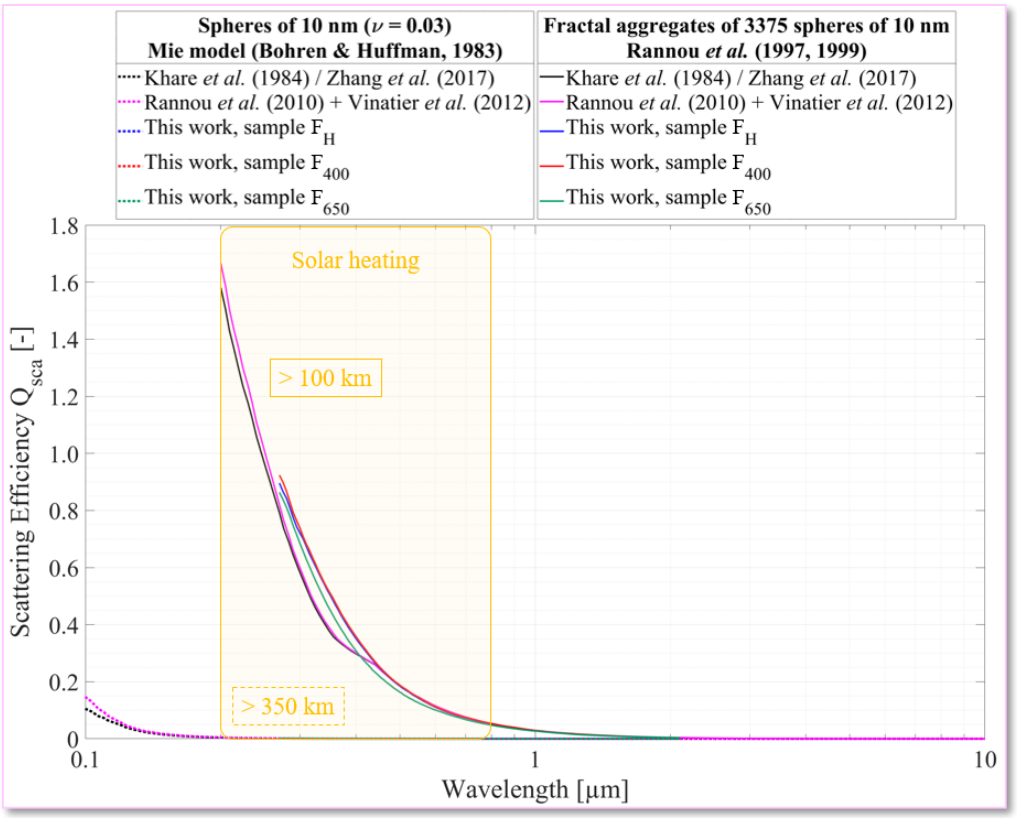

Figure V.11: Same as Figure V.8, but showing the scattering efficiency Q_{sca}.

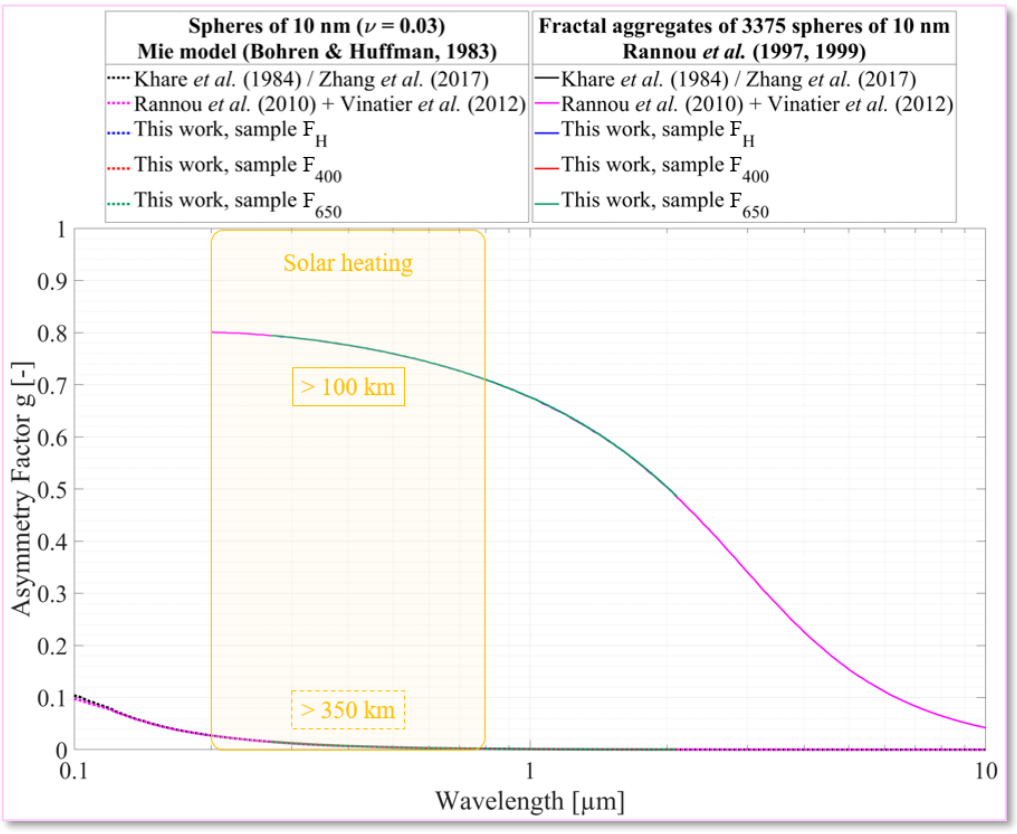

Figure V.12: Same as Figure V.8, but showing the asymmetry factor g.

This has an important consequence: using other optical constants than those already used to analyze scattering photometry at Pluto's limb (*e.g.*, Stern *et al.*, 2015; Gladstone *et al.*, 2016; Cheng *et al.*, 2017; Gao *et al.*, 2017) would not change the result about aerosol size and vertical profile. Nevertheless, optical constants of Pluto tholins determined during my Ph.D. deeply modify the link between the scattering properties and the absorption properties, compared to Titan tholins. That is, for the same scattering efficiency (Figure V.11), Pluto tholins absorb about 5 to 10 times less than Titan tholins at 0.5 µm (effective wavelength of solar input).

To adjust Pluto's thermal balance, Zhang, Strobel and Imanaka (2017) used the optical constants from Khare *et al.* (1984), and had to decrease significantly (up to a factor 4) the absorption efficiency of aerosols in the visible wavelength range (see Figure V.6, black dashed arrow), to increase it in thermal IR and grossly keep the same extinction properties to match Alice UV spectrometer (Stern *et al.*, 2008) retrieval for the haze extinction (*e.g.*, Stern *et al.*, 2015). Here, we see that low absorption is a natural outcome of Pluto tholins produced during my Ph.D. with chemical conditions representative of Pluto's atmosphere, and could therefore help explaining the peculiar temperature profile measured in Pluto's atmosphere.

VI. Investigating the organic matter on Pluto's surface

This chapter is part of a large collaboration with IPAG (Marie Fayolle, Eric Quirico, Bernard Schmitt, Basile Augé, Olivier Poch, Véronique Vuitton), GANIL (Philippe Boduch, Hermann Rothard), and members of the *New Horizons* team. This work is still in progress, but already yielded very interesting data and I present in this chapter preliminary results on the most promising ones.

First, I discuss the characterization of the suitability of Pluto tholins to reproduce Pluto's equatorial dark region, named Cthulhu (Fayolle, Quirico, Schmitt, Jovanovic, Gautier, Carrasco, *et al.* (2021). Testing tholins as analogues of the dark reddish material covering Pluto's Cthulhu region. *Icarus* 367). Second, I present results from Pluto tholins swift heavy ion (SHI) irradiation campaign at GANIL/IRRSUD in order to understand the effect of Galactic Cosmic Ray (GCR) irradiation on Pluto's aerosols deposited at Pluto's surface.

VI.1. Pluto tholins as analogues of Pluto's surface material

Grundy *et al.* (2018) and Protopapa *et al.* (2020) studied the coloring materials across Pluto's surface. They proposed that photochemical aerosols sedimented and covered Pluto's surface, explaining in particular, but not only, the dark reddish equatorial region named Cthulhu. To support this hypothesis, I synthesized solid-grain Pluto aerosol analogues (P_{400} and P_{650} types) with the PAMPRE experimental setup, and Marie Fayolle performed laboratory measurements and modeling on them. The objective of this study was to test the suitability of our Pluto tholins to reproduce *New Horizons* reflectance spectra of Cthulhu region, collected both in the visible and the near-IR spectral ranges by the MVIC and LEISA instruments.

In brief, we investigated the spectrophotometric properties of Pluto tholins, by measuring their reflectance with a spectro-gonio-radiometer developed at IPAG, the Spectro-photometer with cHanging Angles for Detection Of Weak Signals (SHADOWS) (Potin *et al.*, 2018). Measurements were conducted under different incidence angles (0°, 30° and 60°) and emergence angles varying from -70° to 70° with a step of 10°. The optical constants and reflectance properties were determined for the P_{400} and P_{650} samples. In addition to the reflectance measurements, the Hapke model (Hapke, 1981, 2012) – one of the most complete theoretical models currently available to simulate planetary surface reflectance – was used to

simulate the reflectance spectra of Pluto's surface, at the Cthulhu region, using the previously determined optical and reflectance properties. Thanks to the Hapke model, the single scattering albedo and the phase function of Pluto tholins P_{400} and P_{650} were retrieved.

The *New Horizons* spectra acquired by the MVIC and LEISA instruments were then compared to laboratory reflectance measurements of P_{400} and P_{650} tholins, at identical illumination and observation geometries to prevent any bias in the photometric level caused by different measurement geometries. This comparison is shown in Figure VI.1. Regarding the *New Horizons* spectra, precisely two regions were considered at the eastern periphery of the Cthulhu region: a H_2O-poor region (158.8°E, 2.6°S) and a H_2O-rich region (152.9°E, 13.8°S). Indeed, Schmitt *et al.* (2017) highlighted a gradient in H_2O concentration from the center to the periphery of the Cthulhu region.

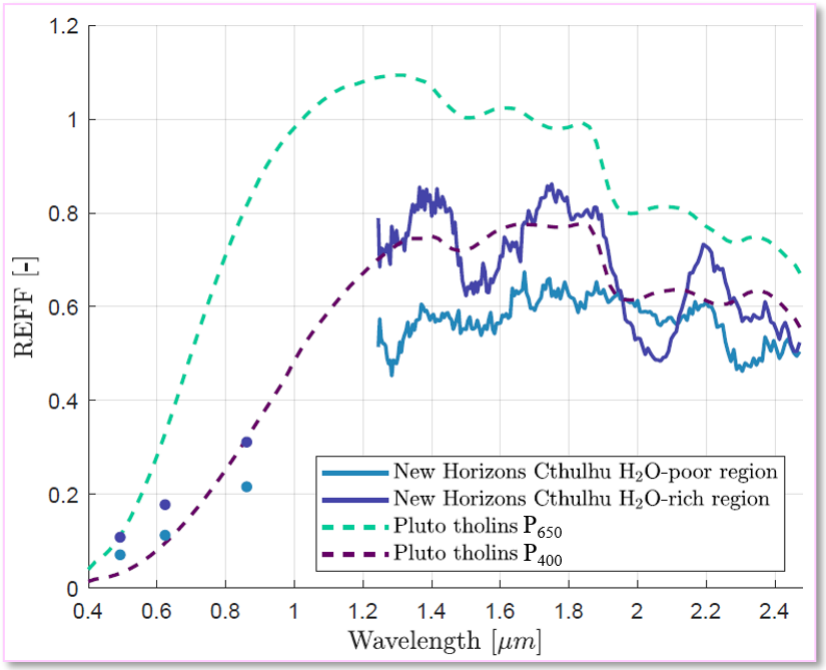

Figure VI.1: Direct comparison between *New Horizons* reflectance spectra and laboratory measurements of Pluto tholins P_{400} (dashed purple curve) and P_{650} (dashed green curve). The light-blue dots and curve respectively correspond to *New Horizons* MVIC and LEISA spectra collected over the H_2O-poor eastern periphery of the Cthulhu region. The dark-blue dots (MVIC) and curve (LEISA) correspond to spectra acquired over an H_2O-rich region at Cthulhu. *Credit*: The figure is adapted from Fayolle *et al.* (2021).

From reconstructed reflectance spectra and direct comparison with *New Horizons* data (Figure VI.1), we concluded that the Pluto tholins we investigated (non-irradiated solid grains) reproduce the photometric level in the near-IR fairly well, but the red visible slope of Pluto tholins does not match with that of Pluto's surface. Moreover, Pluto tholins present absorption

bands that are not found in *New Horizons* spectra. As such, pure Pluto tholins seem unlikely to be the sole explanation for Cthulhu's surface color. One or several additional phenomena may be considered to explain the discrepancies:

- Contamination of the soil by interplanetary dust, bringing dark material to the surface.
- High porosity of the dark terrains at Cthulhu region.
- Galactic Cosmic Ray (GCR) irradiation, which may explain the darkening of surface-deposited organic material (Grundy *et al.*, 2018; Protopapa *et al.*, 2020), and the attenuation of absorption bands, by promoting dehydrogenation reactions, unsaturated bond formation, cross linking, chain scission and disorder (Balanzat, Betz and Bouffard, 1995; Betz, 1998; Moroz *et al.*, 2004; Ngono-Ravache, 2015), or could induce formation and complexification of organics directly in the surface ices (Andronico *et al.*, 1987; Moroz *et al.*, 2004; Cruikshank *et al.*, 2015).

Regarding the first hypothesis, to completely attenuate the absorption bands of the surface organic material, a large amount of interplanetary dust would be necessary. This would lead to a severe drop in the reflectance level, inconsistent with the high reflectance level of the Cthulhu region observed in the near-IR by the LEISA instrument (Fayolle *et al.*, 2021).

For the second one, high porosity could be achieved through cycles of sublimation/condensation of surface volatiles. This could attenuate the combination/overtone bands in the near-IR (Poch *et al.*, 2016). However, N_2 and CH_4 sublimation cycles do not appear to involve Cthulhu region, due to the absence of N_2 ice on Cthulhu region, because N_2 is too volatile to subsist in these hot and low-albedo terrains, and due to the absence of spectral evidence of CH_4 ice in the reddest terrains of Cthulhu (Schmitt *et al.*, 2017; Bertrand *et al.*, 2018, 2019, 2020).

Regarding the third hypothesis, as GCR irradiation is expected to induce dehydrogenation in polymeric material such as Pluto tholins (Balanzat, Betz and Bouffard, 1995; Betz, 1998; Moroz *et al.*, 2004; Ngono-Ravache, 2015), I first made a comparison between MVIC and LEISA data with optical properties of more unsaturated Pluto tholins than the one used in Fayolle *et al.* (2021). As a reminder, in Fayolle *et al.* (2021), the samples were tholins as spherical grains, whose residence time in the plasma is of the order of a few minutes (Hadamcik *et al.*, 2009). On the other hand, samples on which I determined optical constants in Chapter V were thin films deposited on silicon substrates which remained 90 minutes in the plasma (samples F_H, F_{400} and F_{650}). Carrasco *et al.* (2016) compared the chemical composition of Titan aerosol

analogues synthesized under the same experimental conditions as spherical grains and thin films. The authors concluded that the thin films were significantly less rich in N and H compared to the spherical grains, relating indeed to a dehydrogenation process.

The optical constants determined in Chapter V were thus implemented in the Hapke model used by Marie Fayolle, and the simulated reflectance spectra compared to the *New Horizons* MVIC and LEISA spectra. This comparison between the H_2O-poor and H_2O-rich areas of the Cthulhu region and the reflectance spectra simulated from the optical constants of Pluto tholins F_H, F_{400} and F_{650} is shown in Figure VI.2.top and Figure VI.2.bottom, respectively.

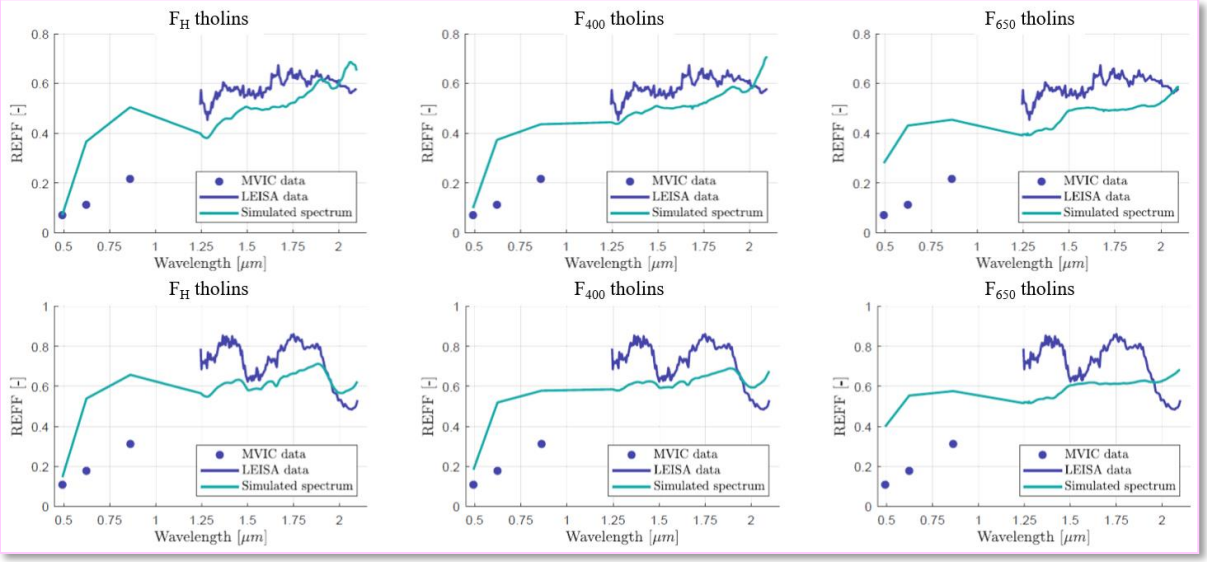

Figure VI.2: Direct comparison between *New Horizons* MVIC and LEISA reflectance spectra (blue dots and curve) collected over H_2O-poor (*top*) and H_2O-rich (*bottom*) areas of Cthulhu region and reflectance spectra simulated from the optical constants of Pluto tholins (green curves) F_H (*left*), F_{400} (*middle*), and F_{650} (*right*) determined in Chapter V.

In Figure VI.2, with the optical constants determined in Chapter V, although the slope in the visible seems to be problematic and deteriorates the overall fit, we nevertheless note the absence of the strong absorption bands around 1.5, 1.7 and 2.0 µm, which are present in the laboratory reflectance spectra of Pluto tholins shown in Figure VI.1. Thus, the presence of dehydrogenated aerosols on the surface of Pluto could help explain the featureless spectra collected over Cthulhu region.

As GCRs are expected to induce such dehydrogenation of organic material at Pluto's surface, we performed Swift Heavy Ion (SHI) irradiation on Pluto tholins at GANIL/IRRSUD to simulate this effect and test further this hypothesis.

VI.2. Irradiations at GANIL/IRRSUD

From Figure VI.1 presented above, we deduced that the spectra of Pluto tholins P_{400} better reproduce the near-IR photometric level of Pluto's surface, we therefore chose to synthesize only P_{400}-type samples for our swift heavy ion irradiation campaigns at GANIL whose results are presented in this section.

As mentioned in Chapter II, although many samples were irradiated, only preliminary results obtained with two samples will be presented here. As a reminder, the F_P sample is a thin film of Pluto tholins deposited on a MgF_2 substrate during a 4-hour plasma duration. Since this sample was sequentially irradiated with 75 MeV ^{136}Xe to a final fluence of 4×10^{12} cm^{-2} in the IGLIAS chamber, UV-Vis and IR spectroscopic monitoring, as well as QMS analysis of the released volatiles could be performed *in situ* and will be presented below. The P_P sample is a pellet of powdery Pluto tholins pressed onto a pre-pressed pellet of KBr. An aluminum piece was used to hide half of the pellet surface. Only one half of the pellet was thus irradiated in one shot outside the IGLIAS chamber with 75 MeV ^{136}Xe ions at a fluence of 1×10^{14} cm^{-2}. For this sample, we thus do not have *in situ* monitoring during irradiation. This sample was analyzed *ex situ* by SEM and FT-ICR to characterize the morphological and molecular evolution of Pluto tholins before and after SHI irradiation.

VI.2.1. Evolution of morphology of Pluto tholins

Half of the P_P sample was irradiated in order to be able to compare the chemical composition of Pluto tholins before and after swift heavy ion irradiation. This is a convenient method to understand irradiation effect on the sample without having any bias due to the consideration of slightly different samples. Figure VI.3 is a picture of the P_P sample before and after SHI irradiation.

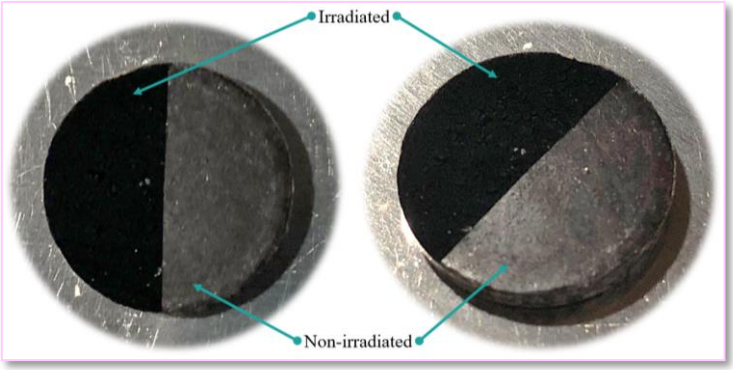

Figure VI.3: Picture of Pluto tholins P_P before (right half) and after (left half) swift heavy ion irradiation (75 MeV ^{136}Xe) at a fluence of 1×10^{14} cm^{-2}.

The right part of the P_P sample was hidden by an aluminum cover, while the left part was irradiated with 75 MeV ^{136}Xe ions at a fluence of 1×10^{14} cm^{-2}. With the naked eye, we notice a macroscopic modification of Pluto tholins. Indeed, the non-irradiated part, which seems lighter in color, is quite smooth due to the pellet compression, while the irradiated part, which seems darker, closely resembles velvet. From a microscopic point of view, we can therefore expect differences due to the irradiation of the material by the swift heavy ions analogous to GCR.

SEM images of the half-irradiated sample P_P are shown in Figure VI.4.

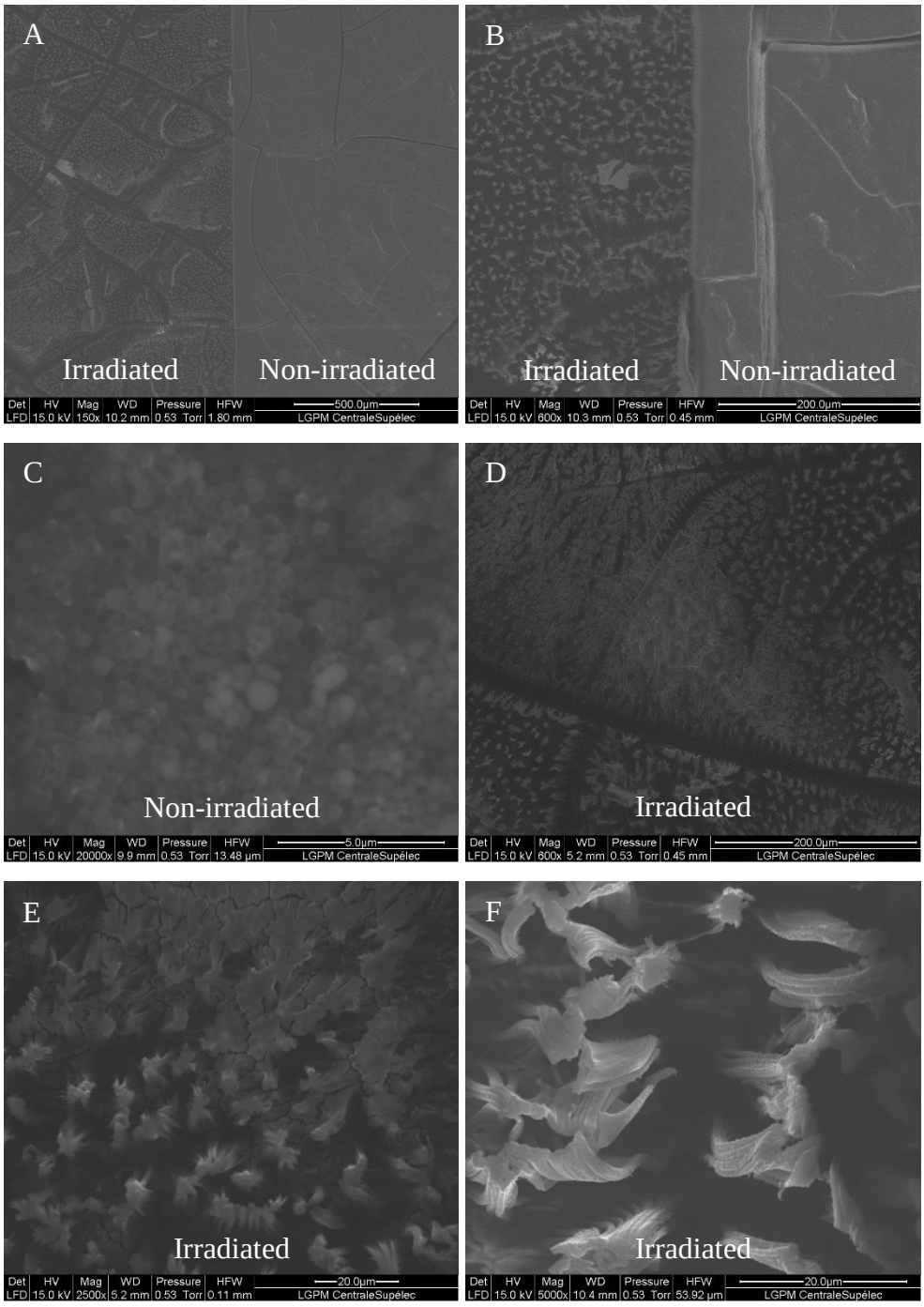

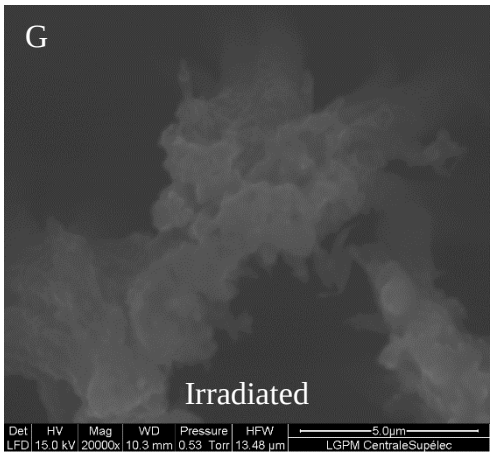

Figure VI.4: SEM images of the sample P_P half of whose surface was irradiated by swift heavy ions analogous to GCR (75 MeV ^{136}Xe), at a fluence of 1×10^{14} cm^{-2}. The images were acquired with a high voltage of 15.0 kV at low vacuum (~0.71 mbar), with an environment SEM *Quanta 200* from *Field Electron and Ion Company*, equipped with a Large Field Detector. *Magnifications*: **(A)** ×150, **(B)** ×600, **(C)** ×20,000, **(D)** ×600, **(E)** ×2,500, **(F)** ×5,000, and **(G)** ×20,000.

At low magnification (×150, Figure VI.4.A) and at higher magnification (×600, Figure VI.4.B), we see a surface difference between the non-irradiated part (on the right) and the irradiated part (on the left) of the P_P sample. The non-irradiated part is smoother (despite some cracks due to the pellet compression), while the irradiated part is much more cracked.

When we magnify the non-irradiated part of the P_P sample (×20,000, Figure VI.4.C), we recognize the characteristic appearance of powdery tholins, as observed by Hadamcik *et al.* (2009) regarding Titan tholins or by Fayolle *et al.* (2021) regarding Pluto tholins.

In Figure VI.4 D to Figure VI.4.G, we increasingly magnify the irradiated part of the P_P sample (×600, ×2,500, ×5,000, and ×20,000, respectively). In Figure VI.4.D (×600), we see linear cracks surely initially due to the pellet compression, and with the irradiation by swift heavy ions it seems that the cracks are spread out. This is supported by Figure VI.4.A where it can be seen that the linear cracks run between the non-irradiated and the irradiated part of the P_P sample. Nevertheless, in the irradiated part, the cracks are widened. Lighter clumps are also observed in this Figure VI.4.D. In Figure VI.4.E (×2,500), we magnify on a clear clump, and we observe a kind of agglomerate and a filamentous aspect. In Figure VI.4.F (×5,000), we magnify a crack edge, and we see a very peculiar filamentous aspect, for which we do not have an explanation at this time.

In Figure VI.4.G (×20,000), we magnify a bright area observed in Figure VI.4.D, and we see that the initially separated spherical particles (see Figure VI.4.C, Pluton tholins before SHI

irradiation) agglomerate into aggregates, while around the aggregates, the material appears eroded.

In summary, SHI irradiation leads to a micro-structural change of Pluto tholins affecting also the macro-morphological aspect observed with the naked eye.

In studies related to SHI irradiation of materials of astrophysical interest, a compaction effect was noted, leading to a loss of porosity of initially porous amorphous or crystalline ices and organic polymers (*e.g.*, Moroz *et al.*, 2004; Pilling *et al.*, 2010; Dartois *et al.*, 2013, 2015; Mejía *et al.*, 2015; Rothard *et al.*, 2017; Ada Bibang *et al.*, 2019). In all cases – ice and refractory organic material – SHI irradiation, and thus sputtering by ions, is considered as a major source of material erosion (Strazzulla and Johnson, 1991). In our case, we find that SHI irradiation of Pluto tholins leads to heterogeneous zones by sputtering, with compact aggregates surrounded by eroded zones, devoid of tholins. This indicates that GCR irradiation could directly affect the porosity of the organic material in the Cthulhu region, in addition to porosity induced by sublimation of the surface ices (Poch *et al.*, 2016).

VI.2.2. Evolution of spectral properties of Pluto tholins

VI.2.2.a. In the visible spectral range

The evolution of the visible spectrum before and during irradiation of F_P Pluto tholins with 75 MeV ^{136}Xe ions was followed. The spectra acquired *in situ* sequentially after irradiations at different known fluences are shown in Figure VI.5. The dashed grey curve corresponds to the F_P tholins before irradiation, while the purple cameo (from lighter to darker) corresponds to increasing deposited fluences “F”.

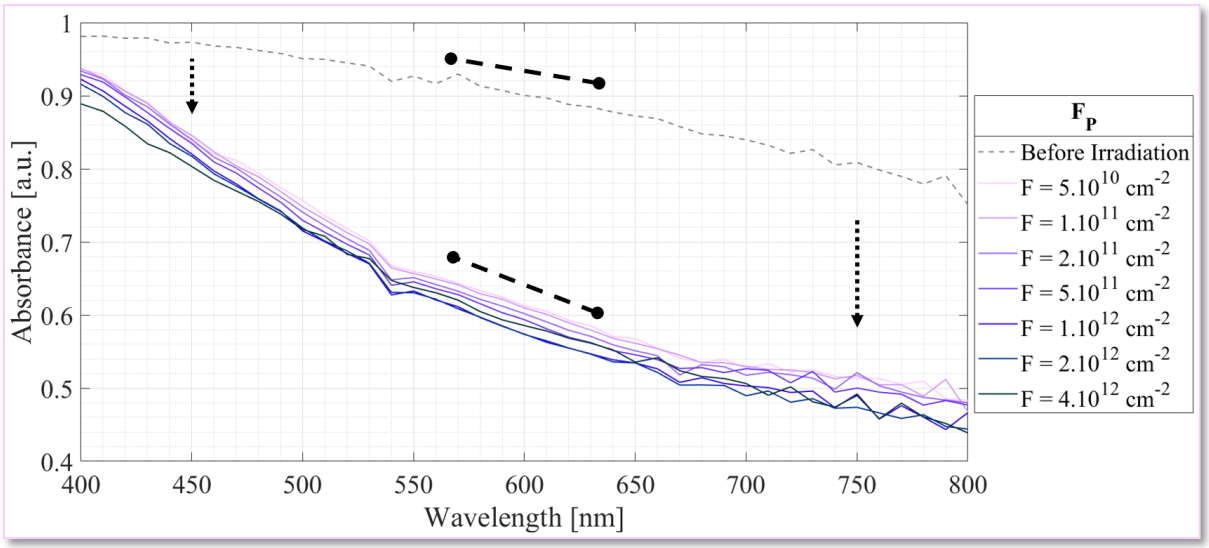

Figure VI.5: *In situ* monitoring of the spectrum in the visible spectral range of Pluto tholins F_P before (dashed grey curve) and after sequential irradiations with increasing fluences "F" (purple cameo curves) by 75 MeV ^{136}Xe swift heavy ions. The bold black dashed lines are indicative to the average slopes in the [570-630] nm region. The visible spectra were acquired with a *Perkin Elmer Lambda 650* UV-Vis spectrometer.

In Figure VI.5, we see that before SHI irradiation (dashed grey curve) Pluto tholins show a continuum of absorption in the visible wavelength range, between 400 and 800 nm, and in particular a greater absorption in the short wavelengths (400-500 nm). This absorption is in agreement with our knowledge of the material whose chemical composition and optical constants were characterized in Chapter IV and Chapter V. More specifically, the strong absorption in the blue wavelength range agrees with a yellowish thin film.

The more the material is irradiated, the more the absorbance decreases over the entire spectral range [400-800 nm] considered. In particular, we note that the first dose of SHI irradiation has a drastic effect on the absorbance: depending on the wavelength, the absorbance is divided by up to 1.5. The following irradiation doses have a lesser effect on the absorbance, although this physical parameter decreases globally.

We also note a change in the shape and slope of the Pluto tholins absorbance spectra between 400 and 800 nm (see the bold black dashed lines). Indeed, the absorbance spectrum of Pluto tholins before irradiation is rather convex and the average slope is not very important, with an absorbance varying from 0.98 at 400 nm to 0.75 at 800 nm. The absorbance spectra of Pluto tholins after SHI irradiation are on the contrary rather concave, and the average slopes are more important, with, for instance for Pluto tholins irradiated at F = 4×10^{12} cm^{-2}, an absorbance varying from 0.89 at 400 nm to 0.44 at 800 nm. Assuming that the spectra presented in

Figure VI.5 are only due to the absorption properties of Pluto tholins, and not to scattering, we can therefore hypothesize that irradiation of Pluto tholins with swift heavy ions analogous to GCR leads to the reddening of the material. This hypothesis, although requiring additional supporting measurements, is in agreement with previous works on irradiations of ices and organic polymers of astrophysical interest, which showed reddening of irradiated materials (Andronico *et al.*, 1987; Jones, Kaiser and Strazzulla, 2014; Rothard *et al.*, 2017; Faure *et al.*, 2021). Nevertheless, it should be noted that these previous studies showed that at higher doses of irradiation, the spectra collected are then flattened and the materials considered present a low albedo (Andronico *et al.*, 1987; Strazzulla *et al.*, 2003; Moroz *et al.*, 2004).

However, it should be pointed out that it is complicated to compare our visible data with the literature, as very little UV-Vis monitoring of irradiated ices or organic polymers of astrophysical interest has been published so far, in contrast to IR monitoring, as highlighted by Hendrix, Domingue and Noll (2013), Jones, Kaiser and Strazzulla (2014) and Rothard *et al.* (2017). This is explained by the fact that the most intense molecular bands are found in the near-IR and mid-IR spectral ranges, while the spectral fingerprints at shorter wavelengths are elusive in solid state.

VI.2.2.b. In the mid-infrared spectral range

The evolution of the mid-infrared spectrum before and during irradiation of the F_P Pluto tholins with 75 MeV ^{136}Xe ions was also monitored. The spectra acquired *in situ* sequentially after irradiations at different known fluences are shown in Figure VI.6. As for Figure VI.5, the dashed grey curve corresponds to the F_P tholins before irradiation, while the purple cameo (from lighter to darker) corresponds to increasing deposited fluences.

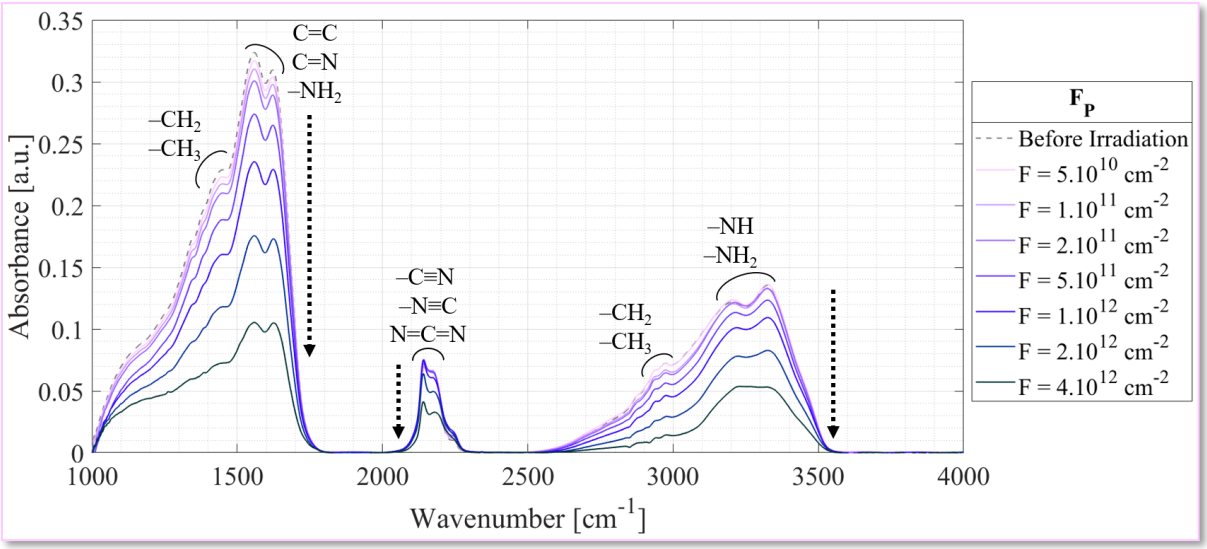

Figure VI.6: *In situ* monitoring of the spectrum in the mid-infrared spectral range of Pluto tholins F_P before (dashed grey curve) and after sequential irradiations with increasing fluences "F" (purple cameo curves) by 75 MeV ^{136}Xe swift heavy ions. The infrared spectra were acquired with a *Bruker Vertex 70v* FTIR spectrometer.

In Figure VI.6, if we look in detail at the absorption bands, we find that the massif consisting of the two peaks around 1,558 and 1,622 cm^{-1}, characteristic of the C=N, C=C and –NH_2 functional groups (Imanaka *et al.*, 2004; Socrates, 2004), seems to be constant, despite an overall decrease in intensity, up to an irradiation fluence of 2×10^{11} cm^{-2}. Indeed, the ratio $\frac{I_{1622}}{I_{1558}}$ is about 0.95 before irradiation and until SHI irradiation at a fluence of 2×10^{11} cm^{-2}. This ratio is then equal to 0.96 for an irradiation at a fluence of 5×10^{11} cm^{-2} and reaches a value of 1 after SHI irradiation at a fluence 4×10^{12} cm^{-2}. In addition to an overall decrease in the intensity of the absorption bands, we thus observe a change in the shape of the massif, with a more pronounced effect of SHI irradiation on the band at 1,558 cm^{-1}. Regarding the ridge observed at about 1,445 cm^{-1} assigned to C–H bonds in –CH_2 and –CH_3, we note that the absorption band in question keeps the same shape, despite a decrease in intensity with increasing SHI irradiation.

The region between 2,100 and 2,200 cm^{-1} shows an important variability of the speciation of nitrile, isocyanide and carbodiimide functional groups (Imanaka *et al.*, 2004; Socrates, 2004). Indeed, we notice the growth of the band at ~2,142 cm^{-1} to the detriment of that at ~2,179 cm^{-1} from the first irradiation doses. This suggests the isomerization of nitriles –C≡N (~2,179 cm^{-1}) to isocyanides –N≡C (~2,142 cm^{-1}), or their transformation to carbodiimides N=C=N (~2,142 cm^{-1}). This effect is observed until the final SHI irradiation at a fluence of 4×10^{12} cm^{-2}, when the ratio $\frac{I_{2179}}{I_{2142}}$ is 0.7, while before irradiation this ratio was 0.95.

The massif extending between 2,600 and 3,500 cm^{-1} is characterized by two small absorption bands at around 2,939 and 2,974 cm^{-1} characteristic of $–CH_2$ and $–CH_3$ respectively, and two large bands at around 3,199 and 3,323 cm^{-1} attributed to –NH and $–NH_2$ respectively (Imanaka *et al.*, 2004; Socrates, 2004). This massif follows globally the same trend as the one between 1,000 and 1,700 cm^{-1}. Indeed, the absorption bands at 2,939 and 2,974 cm^{-1} only undergo a decrease in intensity, without change of shape until final irradiation at a fluence of 4×10^{12} cm^{-2}, while the absorption bands at 3,199 and 3,323 cm^{-1} also undergo a change in shape with a more pronounced effect of SHI irradiation on the band at 3,323 cm^{-1}.

During SHI irradiation of Pluto tholins, two processes can take place: sputtering and radiolysis (*e.g.*, Strazzulla, 2011; Rothard *et al.*, 2017; Ada Bibang *et al.*, 2019). The sputtering corresponds to the erosion of the material following both nuclear and electronic interactions with the swift heavy ions which will eject atoms/molecules from the surface layers of the studied Pluto tholins. The erosion efficiency is strongly dependent on the [incident ion/Pluto tholins] couple. The swift heavy ions can also induce radiolysis of pre-existing molecules. These molecules fragment and form radicals, which can then react chemically to form new daughter molecules. The total number of new molecules produced is roughly proportional to the deposited energy density (*e.g.*, Strazzulla, 2011; Rothard *et al.*, 2017; Ada Bibang *et al.*, 2019). If there was only a sputtering effect, all the mid-IR bands observed in Figure VI.6 would decrease in intensity in the same way with increasing irradiation fluences. On the contrary, if there is radiolysis, we should observe mid-IR band intensities decreasing differently according to the radioresistance of the functional groups considered.

Ices of astrophysical interest analogous to interstellar ices or planetary/satellite/comet surfaces have been widely studied. In the published studies, the authors were interested in simple ices of N_2, CH_4, NH_3, H_2O, CO, CO_2, CH_3OH, *etc.*, or binary or ternary mixtures of these compounds. When these ices are irradiated by swift heavy ions, new complex organic molecules are formed, affecting the recorded IR spectra (*e.g.*, de Barros *et al.*, 2011; Allodi *et al.*, 2013; Bordalo *et al.*, 2013; Augé *et al.*, 2016; Rothard *et al.*, 2017; Vasconcelos *et al.*, 2017; Ada Bibang *et al.*, 2019; Mejía *et al.*, 2020).

In view of our results (Figure VI.6), we can therefore conclude that organic tholins have a substantially different behavior than ices when subjected to SHI irradiation. Indeed, we did not observe with Pluto tholins the formation of new molecules impacting the recorded IR spectra by the appearance of new features. On the contrary, we observed an overall decrease in the intensity of all characteristic absorption bands of Pluto tholins with increasing deposited

fluences, suggesting an overall destruction of the organic material of interest. This result is in agreement with published literature on SHI-irradiated organic polymers (Balanzat, Betz and Bouffard, 1995; Ngono-Ravache, 2015). Nevertheless, since the intensity ratios $\frac{I_{1622}}{I_{1558}}$, $\frac{I_{2179}}{I_{2142}}$, and $\frac{I_{3199}}{I_{3323}}$ evolve differently with increasing irradiation fluences, we can suspect a radiolysis effect that may be at the origin of new daughter molecules. However, we do not expect these new molecules to be drastically different from those constituting Pluto tholins, since new absorption bands do not appear in the mid-IR spectrum of SHI-irradiated Pluto tholins.

These IR analyses bring us clues regarding the contribution of photochemical aerosols as a coloring agent on the surface of Pluto. Indeed, we saw previously (Section VI.1) that Pluto tholins synthesized in the laboratory reproduce fairly well the photometric level in the near-IR, nevertheless they present absorption bands at about 1.5, 1.75, 2.0 and 2.3 µm not present in the *New Horizons* spectra (Fayolle *et al.*, 2021). The 1.5 µm band is related to the first overtone of stretching mode of N–H bond. The 1.75 µm band corresponds to the first overtone of stretching mode of C–H bond. The 2.0 µm band is assigned to combination of N–H bending and stretching modes. Finally, the 2.3 µm band corresponds to combination of C–H stretching and bending modes, as well as to the first overtone of stretching mode of –C≡N bond (Workman, 1996; Xiaobo *et al.*, 2010; Fayolle *et al.*, 2021). As we discussed in Chapter IV and reminded above, the bands in the mid-IR spectral range characteristic of Pluto tholins correspond among others to C–H, N–H, and –C≡N bonds. Given the attenuation of these fundamental molecular vibrations in the mid-IR following SHI irradiation, we can therefore expect that the corresponding near-IR signatures will also be attenuated.

Therefore, although further analysis is needed (in particular, updated reflectance measurements on irradiated Pluto tholins and comparison with *New Horizons* data, and investigation of the kinetics of the IR spectra evolution), the preliminary data presented here suggest that GCR irradiation of photochemical aerosols deposited on Pluto's surface could explain the differences in absorption bands observed between the spectra of Pluto's surface and freshly-synthesized aerosol analogues.

VI.2.3. Evolution of molecular composition of Pluto tholins

The sample P_P was half-irradiated with 75 MeV ^{136}Xe ions at a fluence of 1×10^{14} cm^{-2}. The molecular composition of Pluto tholins before and after SHI irradiation was analyzed by LDI+/FT-ICR. The high-resolution mass spectra are shown in Figure VI.7. The black mass

spectrum (upper panel) corresponds to P_P sample before irradiation, whereas the red mass spectrum (lower panel, in mirror) corresponds to P_P sample after SHI irradiation.

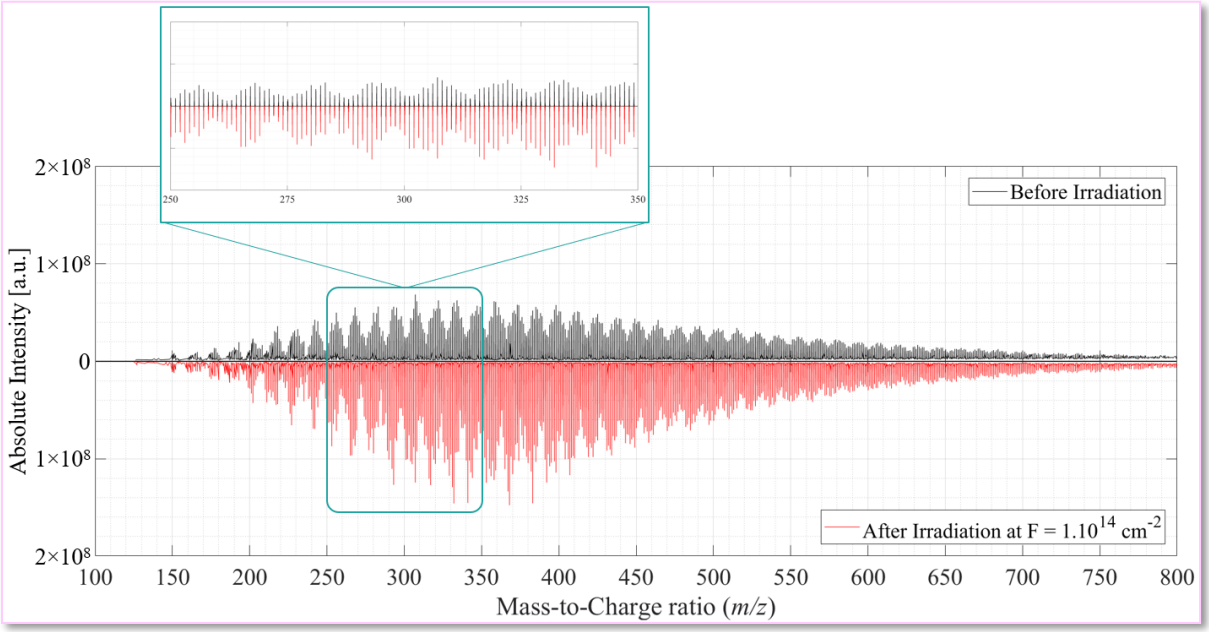

Figure VI.7: LDI+/FT-ICR mass spectra of Pluto tholins P_P before (*upper panel*, in black) and after (*lower panel*, in mirror, in red) irradiation with 75 MeV ^{136}Xe swift heavy ions at a fluence of 1×10^{14} cm^{-2}. The *x*-axis corresponds to the mass-to-charge ratio (*m/z*), while the *y*-axis corresponds to the absolute intensity of the peaks. The mass spectra were acquired with a *solariX XR* FT-ICR mass spectrometer. The turquoise rectangle corresponds to a close-up of the high-resolution mass spectrum between *m/z* 250 and *m/z* 350.

The mass spectra in Figure VI.7 show the characteristic pattern of Pluto aerosol analogues, as discussed in Chapter IV. In contrast to the ESI+/Orbitrap and APPI±/Orbitrap mass spectra (presented in Chapter IV) which only involved the soluble fraction of Pluto aerosol analogues, *i.e.*, only 20-35% of the total solid material (Carrasco *et al.*, 2009), the mass spectra presented here, acquired by LDI+/FT-ICR, involve the total fraction of Pluto tholins (see *e.g.*, Maillard *et al.* (2018) for a comparison of the soluble, insoluble and total fractions of Titan tholins).

At first sight, we note that at equivalent laser power, the peaks in the mass spectrum of Pluto tholins after irradiation are globally more intense than the peaks in the mass spectrum before irradiation and the clusters in the “after irradiation” high-resolution mass spectrum are shifted to the left (see the close-up in Figure VI.7). Assuming that these differences are not due to different detection efficiency, these two observations could be consistent with the formation of new molecules and these daughter molecules are more unsaturated than the parent molecules. The assignment of molecular formulae resulted in the identification of 7,363 molecules in the

P_P sample before SHI irradiation and 11,384 molecules in the P_P sample after irradiation with 75 MeV ^{136}Xe ions at a fluence of 1×10^{14} cm^{-2}.

Between the P_P sample before irradiation and the P_P sample after irradiation, there are 4,021 more molecular formulae. Nevertheless, if we look at all the molecular formulae in detail, it appears that 2,590 formulae are specific to the pre-irradiation P_P sample and are not found in the post-irradiation P_P sample, while 6,611 chemical formulae are specific to the post-irradiation P_P sample. This suggests that during SHI irradiation, some parent molecules are completely degraded, split off in favor of a larger number of daughter molecules in the sample after irradiation. This scission of polymeric organic molecules during SHI irradiation is notably discussed in Venkatesan (1985) and in Betz (1998).

Thanks to the identification of molecular formulae, we were able to plot modified van Krevelen diagrams (van Krevelen, 1950, 1984), in order to compare more easily the P_P sample before and after SHI irradiation. In Figure VI.8, these modified van Krevelen diagrams [H/C *versus* N/C] are shown. The color bar corresponds to the intensity of the molecules.

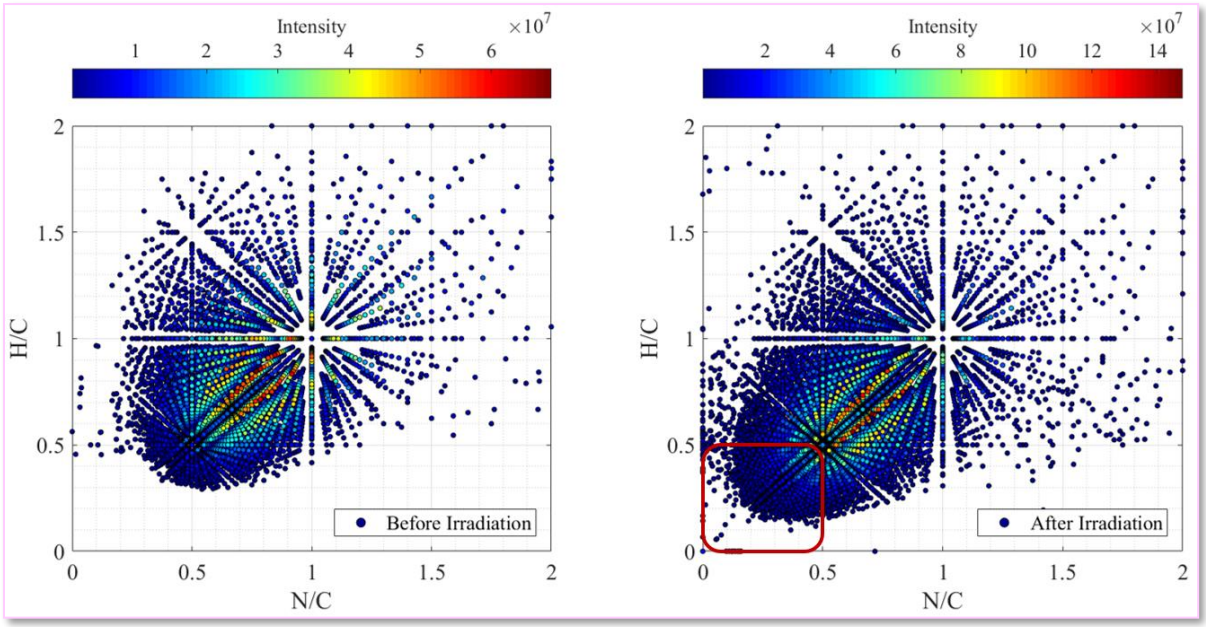

Figure VI.8: Modified van Krevelen diagrams. The sample P_P was analyzed with the LDI+/FT-ICR technique and the molecules were identified with the *SmartFormula* tool from the *Bruker Data Analysis 4.4* software. Each dot corresponds to a specific molecule characterized by its Hydrogen-to-Carbon (H/C) and Nitrogen-to-Carbon (N/C) ratios. The color bar corresponds to the intensity of the molecules. *Left*: Before SHI irradiation. *Right*: After irradiation with 75 MeV ^{136}Xe swift heavy ions at a fluence of 1×10^{14} cm^{-2}. The red square indicates the new molecules characterized by H/C and N/C ratios lower than 0.5, formed after SHI irradiation.

In Figure VI.8, comparing the van Krevelen diagrams before (left) and after (right) SHI irradiation, we note among other findings the appearance of many molecules characterized by H/C and N/C ratios below 0.5, and low intensities (intensity < 3×10^7 a.u.) (see the red square in Figure VI.8.right). Note that the formation of molecules with low H/C ratio is expected for an organic material submitted to irradiation by swift heavy ions (Lanzerotti, Brown and Marcantonio, 1987; Johnson, 1989). These new molecules with low H/C ratio suggest the dehydrogenation of molecules and thus the formation of unsaturated molecules of PAH- and NPAH-types (Poly-Aromatic Hydrocarbons, and N-bearing Poly-Aromatic Hydrocarbons) in Pluto tholins submitted to SHI irradiation.

This hypothesis of dehydrogenation of the molecules and the formation of molecules of PAH- and NPAH-types is supported by the results presented in Figure VI.9. Indeed, thanks to the identification of the molecular formulae, we were also able to calculate the Double Bond Equivalent (DBE) of each $C_xH_yN_zO_w$ molecule, by using the following formula:

$$\mathrm{DBE} = \mathrm{C} + 1 - \frac{\mathrm{H}}{2} + \frac{\mathrm{N}}{2} \quad \text{(Equation VI.1)}$$

with C, H, and N the numbers of Carbon, Hydrogen and Nitrogen atoms in the molecule, respectively. The DBE gives an idea of the level of unsaturation of the molecules.

In Figure VI.9, we show the DBE (*y*-axis) as a function of the number of Carbon atoms (#C, *x*-axis). As in Figure VI.8, the color bar corresponds to the intensity of the molecules. We also plotted in red dashed line the theoretical DBE expected for a polymer only composed of PAH.

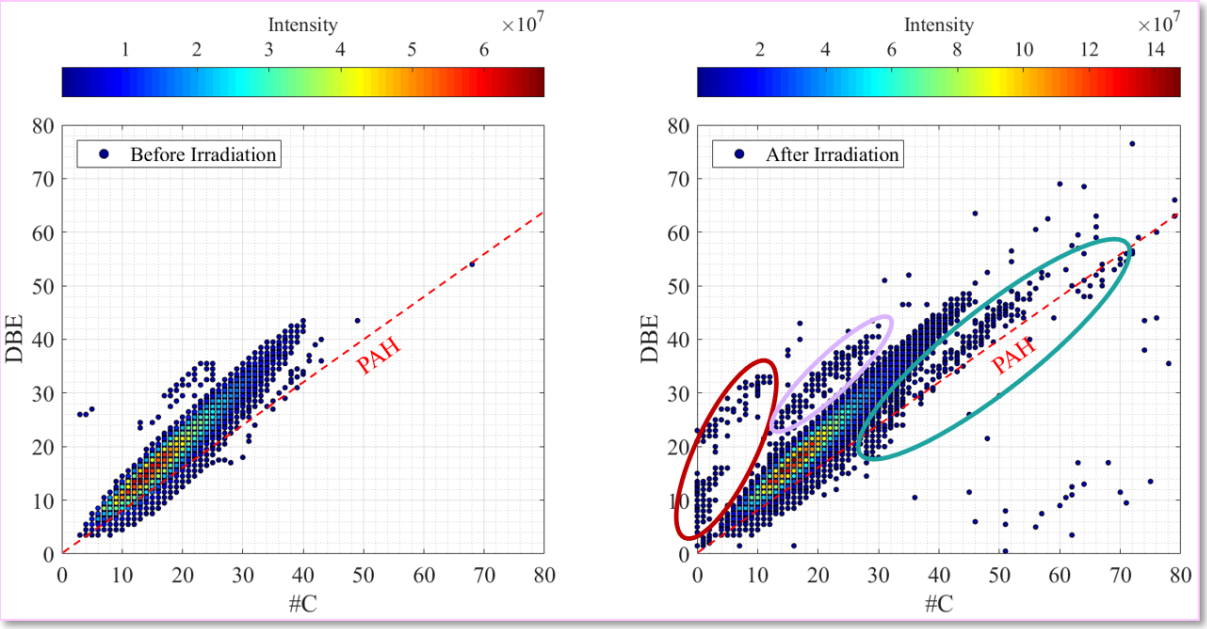

Figure VI.9: Double Bond Equivalent (DBE) as a function of number of C atoms (#C) present in the molecules. The DBE gives an idea of the unsaturation level of the molecules. The color bar corresponds to the intensity of the molecules. The red dashed line corresponds to the theoretical DBE expected for a polymer purely composed of Poly-Aromatic Hydrocarbons (PAH). *Left*: Before SHI irradiation. *Right*: After irradiation with 75 MeV ^{136}Xe swift heavy ions at a fluence of 1×10^{14} cm^{-2}. The red, lavender color and turquoise circles indicate new molecules formed after SHI irradiation.

In Figure VI.9, looking first only at the DBE diagram before SHI irradiation (left), we note that the constituent molecules of the total fraction of Pluto tholins are overall highly unsaturated, as we discussed for the soluble fraction in Chapter IV. Moreover, these molecules do not correspond to pure PAHs since the average slope that characterizes the molecules of Pluto tholins is different from the red dashed line characteristic of pure PAH polymers. This result agrees with the results presented in Chapter IV, as well as with studies on Titan tholins. In this case, the fact that the distribution of molecules constituting Pluto tholins is above the red dashed line suggests a polymer bearing N atoms (*e.g.*, Pernot *et al.*, 2010; Gautier *et al.*, 2016; Mahjoub *et al.*, 2016; Maillard *et al.*, 2020, 2021).

Now comparing the DBE plots before (left) and after (right) irradiation, we note after SHI irradiation the appearance of a pool of new, highly unsaturated light molecules (#C < 12, red circle in Figure VI.9.right) and medium to heavy molecules (28 < #C < 70, turquoise circle in Figure VI.9.right) whose distribution is quite close to the line of pure PAHs (red dashed line), as well as an enrichment of the distribution of medium molecules (12 < #C < 30, circle in lavender color in Figure VI.9.right) lying above the main distribution of Pluto tholins molecules. These molecules, of low intensities (intensity < 2×10^7 a.u.), do not represent the

major part of the P_P sample, and because of the absence of particular functional groups (*i.e.*, we remain on molecules relatively close in terms of composition), this explains the absence of new features in the IR spectra presented in Section VI.2.2.b. Note that the pool of very unsaturated light molecules, the molecules whose distribution is above the main distribution, as well as the molecules whose distribution is close to the line of pure PAHs correspond essentially to molecules very rich in nitrogen (see Figure VI.10.left) and/or in oxygen (see Figure VI.10.right).

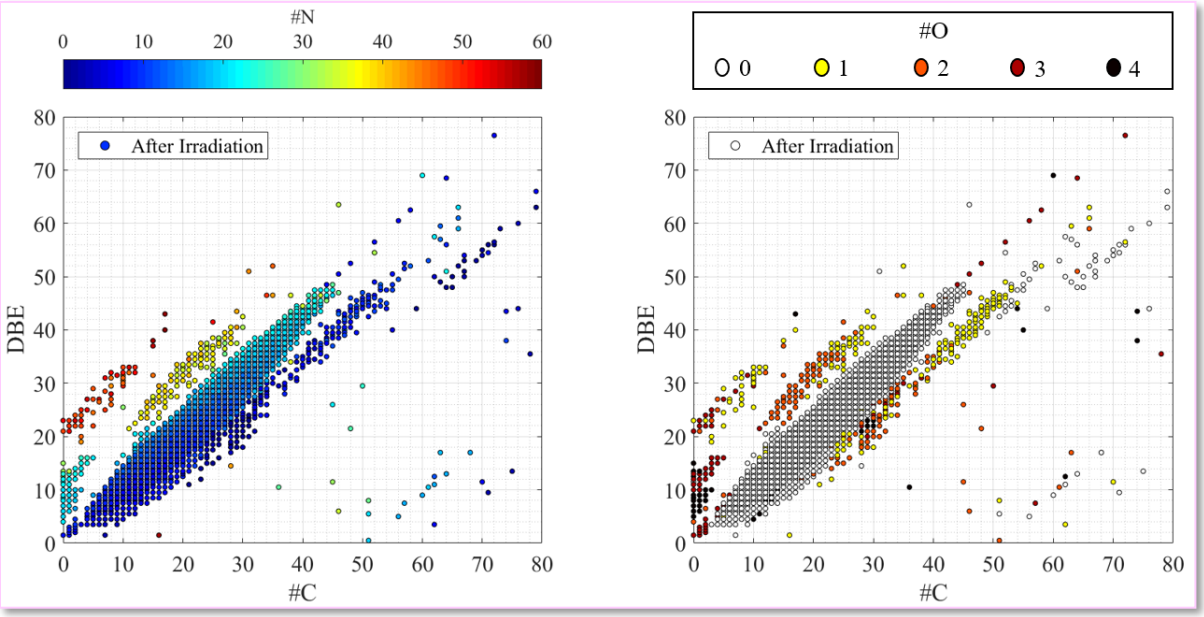

Figure VI.10: DBE as a function of number of C atoms present in the molecules constituting the P_P sample after SHI irradiation. *Left*: The color bar corresponds to the number of N atoms (#N) present in the molecules. *Right*: The colors correspond to the number of O atoms (#O) present in the molecules.

All these observations are consistent with the hypothesis of the dehydrogenation of the organic matter submitted to SHI irradiation, and thus the formation of unsaturated molecules. This is in agreement with the studies on SHI-irradiated organic polymers, where dehydrogenation of molecules is one of the major effects observed (Balanzat, Betz and Bouffard, 1995; Betz, 1998; Moroz *et al.*, 2004). Regarding the formation of PAH, SHI-irradiation experiments on graphite grains confirmed the formation of this type of molecules (Starukhina and Shkuratov, 1995). In our case, in view of our results, we can therefore suggest that not only PAH and NPAH, but also O-bearing Poly-Aromatic Hydrocarbons (OPAH) are formed in Pluto tholins submitted to swift heavy ion irradiation.

In order to confirm and understand the pathways of dehydrogenation in Pluto tholins, it will be necessary to go further in the data mining on these measurements. It will be of particular interest

to have a detailed look on the possible correlation in the evolution under swift heavy ion irradiation of different chemical families (for example, depending on the number of heteroatoms, chemical functions, *etc.*).

VI.2.4. Volatiles released by Pluto tholins under swift heavy ion irradiation

Swift heavy ion irradiation leads to the outgassing of gas-phase molecules from the surface of the irradiated solid material (*e.g.*, Ada Bibang *et al.*, 2019). In this part of this Ph.D. thesis, I will discuss as an example the preliminary results on the irradiation of the F_P sample with 75 MeV ^{136}Xe ions inside the IGLIAS experimental setup, for which I monitored by QMS the volatiles released continuously from the Pluto tholins. Although mass spectra were recorded from *m/z* 1 to *m/z* 100, no peak was significantly detected above *m/z* 53 in the mass spectra presented in Figure VI.11. For comparison purposes, the peak intensities were normalized to the most intense peak in the mass spectrum, namely *m/z* 18.

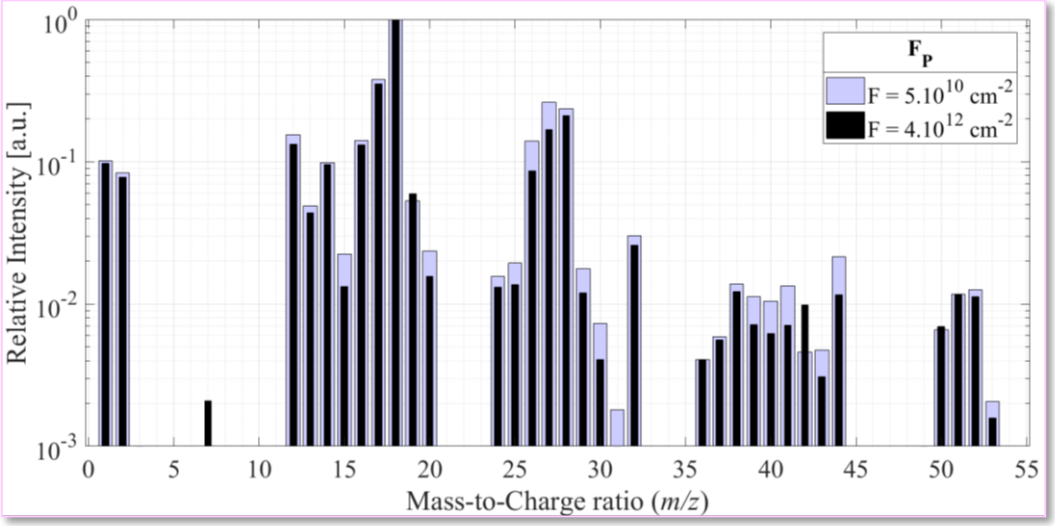

Figure VI.11: *In situ* mass spectrum of the gas-phase volatiles released by Pluto tholins F_P submitted to irradiation with 75 MeV ^{136}Xe swift heavy ions at different fluences: 5×10^{10} cm^{-2} (in lavender color) and 4×10^{12} cm^{-2} (in black). The mass spectra were acquired with a *Microvision2 MKS104* quadrupole mass spectrometer. The gas-phase neutral species were ionized in the electron ionization source, with an electron energy settled at 70 eV. The *x*-axis corresponds to the mass-to-charge (*m/z*) ratio, whereas the *y*-axis corresponds to the relative intensity of the peaks, normalized to the most intense peak in the mass spectrum, *m/z* 18.

In Figure VI.11, we note that whatever the irradiation fluence, the same peaks are observed in the mass spectra. A higher deposited fluence on the Pluto tholins does not release new species.

In the subsequent discussion, we will only focus on the mass spectrum corresponding to SHI irradiation of the F_P sample at a fluence of 5×10^{10} cm^{-2}.

During my Ph.D., I supervised César Feniou, a graduate student who processed the QMS data acquired during the two irradiation campaigns at GANIL/IRRSUD. During his 4-month internship, we used the mass spectra deconvolution code developed by Gautier *et al.* (2020) (used also in Chapter III) to interpret the mass spectra of the volatiles released by Pluto tholins under SHI irradiation. The preliminary results of the deconvolution are presented in Figure VI.12.

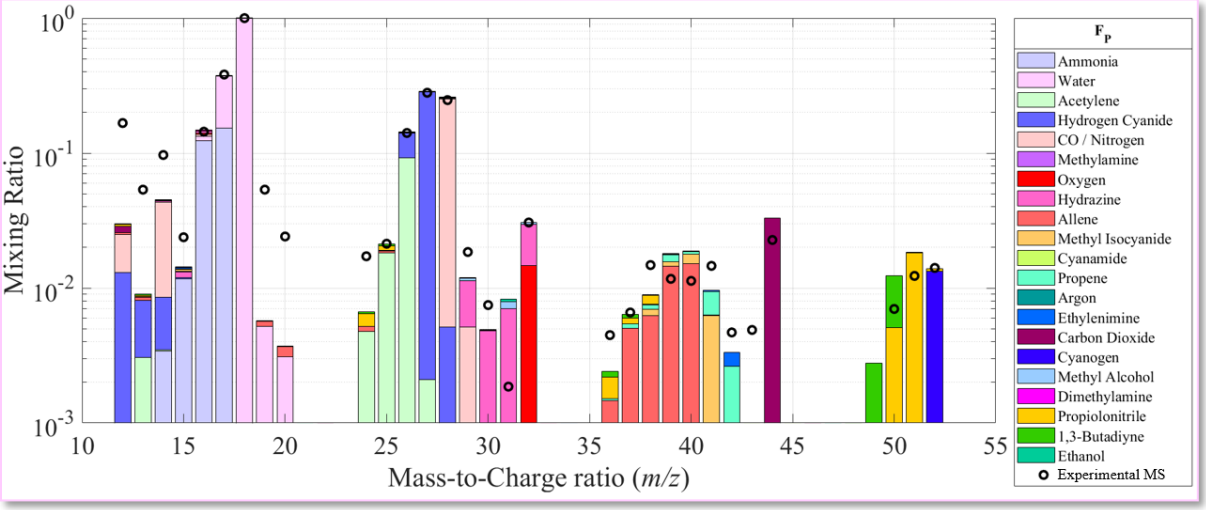

Figure VI.12: Preliminary results of the deconvolution of the mass spectrum in lavender color shown in Figure VI.11 (F = 5×10^{10} cm^{-2}). The black dots correspond to the experimental mass spectrum, whereas the colored bars correspond to the contribution of each molecule calculated by the deconvolution method developed by Gautier *et al.* (2020).

Apart from the ammonia which seems to be released by Pluto tholins even without being irradiated[17], and apart from the methyl alcohol coming from a leak[18], we note that no organic molecules are detected among the volatiles when Pluto tholins are not irradiated (see Figure A4.1 in Appendix A4).

The gas-phase molecules released following chain scission of the macromolecule backbone will depend on the chemical composition and structure of the irradiated solid matter and in particular

[17] A peculiar odor emanates from Pluto tholins when they are handled in the open air, and this odor could be partly explained by the release of ammonia.
[18] During the second irradiation campaign at GANIL/IRRSUD, we also conducted an experiment of methyl alcohol ice condensation followed by the irradiation of this ice, in order to understand the different types of organic matter that can be found on the surface of the Trans-Neptunian Objects (TNOs), and it turns out that the valve isolating the test tube containing the gas-phase methanol was leaking.

on the side chains of the polymer (Chapiro, 1988; Betz, 1998; Picq, Ramillon and Balanzat, 1998). Therefore, the analysis of the released gas-phase molecules gives an idea of how the irradiated materials were synthesized. For instance, SHI irradiation of organic polymers, such as polyethylene or polybutene, releases H_2, as well as the hydrocarbons CH_4, C_2H_2, C_2H_4, and C_2H_6, and hydrocarbons containing up to six carbon atoms (Chapiro, 1988; Betz, 1998; Picq, Ramillon and Balanzat, 1998), while polymers containing O heteroatoms release CO and CO_2 (Venkatesan, 1985; Chapiro, 1988; Betz, 1998). In our case, in addition to the planetological interest (*i.e.*, feeding the atmosphere with potentially new exotic molecules), the analysis of the released volatiles will also give us an idea of how Pluto tholins were synthesized and possibly confirm the hypotheses raised in Chapter III.

The release of ammonia from Pluto tholins, either as a result of SHI irradiation or even in the absence of irradiation, is in agreement with the high proportion of –NH and $–NH_2$ amine functional groups observed in the IR spectra of Pluto tholins presented in Chapter IV and above in Section VI.2.2.b.

Among the identified molecules, we report the outgassing of unsaturated hydrocarbons (acetylene, allene, propene, 1,3-butadiyne), as well as nitriles and isocyanides (hydrogen cyanide, methyl isocyanide, cyanamide, cyanogen, propiolonitrile), when Pluto tholins are subjected to SHI irradiation. Among the unsaturated molecules detected, the most abundant are C_2H_2 and HCN. The release of gas-phase nitriles is in perfect agreement with the hypothesis raised in Chapter III regarding the formation of Pluto tholins by polymerization of nitrile-type molecules and HCN incorporation in Pluto tholins.

We also note the release of molecules bearing an isocyanide functional group (methyl isocyanide) as well as a carbodiimide chemical function (cyanamide). These molecules are consistent with the isomerization of nitrile functional groups into isocyanides, and their transformation into carbodiimide functional groups suggested in Section VI.2.2.b from the monitoring of IR spectra of Pluto tholins subjected to SHI irradiation.

Regarding the released oxygenated molecules, O_2 and CO_2 were already present in the mass spectrum before SHI irradiation (residual air in the IGLIAS experimental setup, see Figure A4.1 in Appendix A4). As mentioned before, the methyl alcohol would probably come from the leakage of the valve isolating the test tube containing the gas-phase methanol for methanol condensation experiments and SHI irradiation of methanol ice. We can therefore wonder about the ethanol detected: is it released by Pluto tholins under SHI irradiation, or does it come from

the irradiation of the methanol from the leak? Given the persistent doubt about this molecule, this result will not be discussed further in the manuscript.

At the surface of Pluto, these molecules released following GCR irradiation of photochemical aerosols deposited on the surface of Pluto could either redeposit at the surface or accumulate in the atmosphere and thus serve as reagents for the formation of new photochemical aerosols. Based on the second hypothesis, it is interesting to compare the species released during the SHI irradiation of Pluto tholins with the results obtained in Chapter III (*i.e.*, the molecules formed in the gas phase of Pluto-simulated atmosphere), and thus predict if new molecules could feed the atmosphere of Pluto. This comparison is given in Table VI.1.

Table VI.1: Comparison between the molecules formed in Pluto-simulated atmosphere and the molecules released from Pluto tholins submitted to SHI irradiation. "Yes" means that the molecule is present, while "No" indicates the absence of the molecule in the studied environment. When there is a doubt about the presence of a species in the studied environment, we indicate "?".

Molecules	Gas phase of Pluto-simulated atmosphere	Released from Pluto tholins under SHI irradiation
Methane	Yes	No
Ammonia	?	?
Water	?	?
Molecular nitrogen	Yes	?
Carbon monoxide	Yes	?
Acetylene	Yes	Yes
Ethylene	Yes	No
Ethane	Yes	No
Hydrogen cyanide	Yes	Yes
Methylamine	Yes	Yes
Methylacetylene	Yes	No
Propene	Yes	Yes
Propane	Yes	No
Diacetylene	Yes	No
1-Buten-3-yne	Yes	No
1,3-Butadiene	Yes	No
Butane	Yes	No
Benzene	Yes	No
Acetonitrile	Yes	No
Propiolonitrile	Yes	Yes
2-Propenenitrile	Yes	No
Propanenitrile	Yes	No
Cyanogen	Yes	Yes

2-Butynedinitrile	Yes	No
Formaldehyde	Yes	No
Carbon dioxide	Yes	?
Oxygen	?	?
Hydrazine	Yes	Yes
Methyl alcohol	Yes	?
Formic acid	Yes	No
Nitrous oxide	Yes	No
Acetone	Yes	No
Propanedinitrile	Yes	No
1,3-Cyclopentadiene	Yes	No
Cyclopentene	Yes	No
Methylacrylonitrile	Yes	No
Pyrrole	Yes	No
Pyrrolidine	Yes	No
1H-Imidazole	Yes	No
3-Butenenitrile	Yes	No
1-Butanol	Yes	No
1,4-Cyclohexadiene	Yes	No
1,3,5-Triazine	Yes	No
3-Aminopyrazole	Yes	No
4-Methyl-4H-1,2,4-triazole	Yes	No
Fumaronitrile	Yes	No
1-Methyl-1H-imidazole	Yes	No
Pyridine	Yes	No
2,4-Pentadienenitrile	Yes	No
Piperidine	Yes	No
2-Cyclopenten-1-one	Yes	No
2-Pentenal	Yes	No
Allene	No	Yes
Methyl isocyanide	No	Yes
Cyanamide	No	Yes
Ethylenimine	No	Yes
Dimethylamine	No	Yes
1,3-Butadiyne	No	Yes
Ethanol	No	?

From Table VI.1, we note that SHI irradiation of Pluto tholins allows the release of 6 or even 7 new species not identified in Pluto-simulated atmosphere (molecules indicated in bold). These molecules are: allene, methyl isocyanide, cyanamide, ethylenimine, dimethylamine, 1,3-butadiyne, and perhaps ethanol. It will be interesting in the future to assess whether this

outgassing is large enough so that surface sources should be considered for these molecules in future Pluto atmospheric models.

In the future, it will be also interesting to investigate the velocity of these predicted ejecta at the surface of Pluto, in order to have an idea if this phenomenon could have implication at Pluto's planetary scale. With the presence of Pluto's tenuous atmosphere, it is likely that these velocities are not sufficient for atmospheric escape, and the molecules released by GCR irradiation of photochemical aerosols deposited at the surface could be retained in the atmosphere and serve as reagents for the formation of new photochemical aerosols, or redeposited at the surface.

VII. Conclusion and Perspectives

VII.1. Summary of results

During my Ph.D., I used an experimental approach to study the aerosols of Pluto, from their formation in the upper atmosphere to their ageing at the surface, through their interactions with the atmosphere. More precisely, I used the PAMPRE experimental setup (LATMOS, Guyancourt, France) to simulate Pluto's atmospheric chemistry and to synthesize analogues of Pluto's aerosols and surface materials (called Pluto tholins). Swift heavy ion (SHI) irradiation experiments were performed at GANIL (Caen, France), on the IRRSUD beamline, using the IGLIAS experimental setup, to simulate the ageing due to charged particles, such as galactic cosmic rays (GCR), of the organic matter present on the surface of Pluto, and in particular in the Cthulhu region. The reader will find below a summary of the different results obtained.

In the first part of my Ph.D. thesis (Chapter III: Investigating the chemical composition of Pluto's atmosphere), using the PAMPRE experimental setup, I reproduced Pluto's atmospheric chemistry leading to the formation of aerosols. Two gas mixtures with different N_2:CH_4:CO proportions were investigated, to account for the variability in terms of chemical composition at different altitudes in Pluto's atmosphere as observed in 2015 during *New Horizons* fly-by. The A_{400} gas mixture (N_2:CH_4:CO = 99%:1%:500ppm) is representative of the main components present in Pluto's atmosphere at ~400 km of altitude, whereas the A_{650} gas mixture (N_2:CH_4:CO = 95%:5%:500ppm) mimics Pluto's atmosphere between 600 and 700 km of altitude. To study the chemical composition of Pluto-simulated atmosphere, I used a quadrupole mass spectrometer (QMS). Both neutral molecules and cations formed *in situ* in Pluto-simulated atmospheres were analyzed, to provide an insight into the diversity of molecules formed by photochemistry in Pluto's atmosphere and assess the precursor species and reaction pathways at the origin of Pluto's aerosols. To identify the neutral species formed in Pluto-simulated atmospheres, the recorded mass spectra of reactive media were deconvoluted using a Monte-Carlo approach. The cations formed in Pluto-simulated atmosphere A_{400} were compared to those formed in a Titan-simulated atmosphere studied by Dubois, Carrasco, Jovanovic *et al.* (2020), in order to assess the effect of CO on N_2:CH_4 positive ion chemistry.

The QMS results regarding the neutral molecules formed in Pluto-simulated atmospheres showed the significant formation of nitrogenous and/or oxygenated molecules, up to *m/z* 91. The N-bearing compounds detected correspond to molecules with amine –NH and $–NH_2$, or

nitrile –C≡N functional groups. We also detected N-heterocycles, such as triazine-, pyrazole- and pyrrole-type structures. The O-bearing compounds essentially correspond to molecules with a terminal oxygenated functional group, including alcohols –OH, carboxylic acids –COOH, and carbonyls –C=O.

My Pluto lab-simulations confirmed the formation of gas-phase CO_2 and H_2CO predicted by Wong *et al.* (2017). Nevertheless, I can conclude neither on the formation of H_2O predicted by Wong *et al.* (2017), nor on the formation of O_2 questioned by Kammer *et al.* (2017).

Regarding the cations formed in Pluto-simulated atmospheres, I concluded on the production of a wide variety of positive ions, up to *m/z* 150, despite the absence of detection of an ionosphere around Pluto (Hinson *et al.*, 2018). Among these cations, we count not only organic nitrogenous ions, but also oxygenated ones.

A strong dependency of neutral and ion chemistry to the CH_4 mixing ratio was found. This dependency is notably expressed by a more pronounced formation of heavier molecules with increasing CH_4 concentration.

The combined analysis of neutrals and cations formed in Pluto-simulated atmospheres highlighted the importance of ion-molecule chain reactions in the formation mechanisms of increasingly heavy species and the final formation of solid aerosols. Among the different mechanisms proposed to explain the molecular growth and the formation of aerosols in the atmosphere of Titan, the hypothesis that I privilege in the case of Pluto, in view of my results, relate to the molecular growth through the co-polymerization of nitriles, and incorporation of hydrogen cyanide HCN into the molecules. Such highly unsaturated and N-rich structures produced, by constituting the backbone of the macromolecules at the origin of the solid material, are suspected to be responsible for a strong absorption of radiations, in particular in the UV wavelength range (Rao, 1975), as discussed in the third part of my Ph.D. thesis (Chapter V).

These QMS analyses of Pluto-simulated atmospheres highlighted also the incompleteness of current Pluto photochemical models, and thus the need to include in future models extensive reaction pathways of nitrogen chemistry, with a particular focus on nitriles, as well as more extensive reaction pathways including CO chemistry.

In the second part of my Ph.D. thesis (Chapter IV: Investigating the chemical composition of Pluto's aerosols), I synthesized Pluto aerosol analogues as solid spherical grains,

using the PAMPRE experimental setup, from gas mixtures with different N_2:CH_4:CO proportions, in order to mimic aerosols formed at different altitudes in Pluto's atmosphere as observed in 2015. The sample P_{400} is expected to be representative of aerosols that form at ~400 km of altitude in Pluto's atmosphere. The sample P_{650} is an analogue of aerosols that form between 600 and 700 km of altitude. To determine the chemical composition of these analogues of Pluto's aerosols, I performed infrared spectroscopy and elemental composition analyses on them. The samples were also analyzed using high-resolution mass spectrometry (HRMS), with the ESI+/Orbitrap and APPI±/Orbitrap techniques. In order to get structural information of the molecules constituting Pluto aerosol analogues, and evaluate the prebiotic implications of Pluto's aerosols, the sample P_{400} was also analyzed by gas chromatography coupled to mass spectrometry (GC-MS), after derivatization with DMF-DMA, an alkylating and formylating reagent increasing the volatility and thermal stability of the molecules to be analyzed.

The elemental composition analyses showed a substantial incorporation of nitrogen atoms in Pluto aerosol analogues. Nitrogen accounts for about 36 and 45% in mass of Pluto aerosol analogues P_{650} and P_{400}, respectively. Thanks to the mid-IR diagnosis, I concluded that the N-bearing chemical functions essentially correspond to primary and secondary amines $–NH_2$ and –NH, C=N double bonds in aromatic and hetero-aromatic cycles, nitriles –C≡N, isocyanides –N≡C and carbodiimides –N=C=N–. Pluto aerosol analogues are also very rich in N-heterocycles, such as triazine-, pyrazole- and pyrazine-type structures, which were detected by GC-MS. Such N-heterocycles were also identified by QMS among the gas-phase molecules produced in the Pluto-simulated atmospheres investigated in the first part of my Ph.D. thesis (Chapter III).

The elemental composition analyses showed also a significant proportion of O-bearing molecules, formed by chemistry of CO, with about 1.9 and 1.7% of oxygen in mass in samples P_{400} and P_{650}, respectively. As such, Pluto tholins differ from Titan tholins by the incorporation of oxygen atoms in the molecules constituting the solid material, through CO chemistry. Thanks to GC-MS analysis, I concluded that the O-bearing chemical functions essentially correspond to carbonyl –C=O, alcohol –OH, ether *R*–O–*R'*, and carboxyl –COOH terminal functional groups. However, no O-heterocycles, such as furan-, pyran- or pyrone-type structures, were detected.

I noticed an impact of methane percentage – and thus the altitude of aerosol formation on Pluto – on the chemical composition of the aerosols. This strongly affects the nitrogen and

oxygen contents of the hazes. In particular, I showed that aerosols produced at low altitude (P_{400}) contain more nitrogen and oxygen than aerosols produced at high altitude (P_{650}).

When combining all my results obtained by HRMS, IR spectroscopy, elemental composition analysis, and GC-MS, I conclude that N_2 and CO chemistries are important in the formation and the growth of Pluto's aerosols. As previously stated, Pluto aerosol analogues are rich in unsaturated N- and/or O-bearing organic molecules. These species are likely reactive and they may therefore facilitate the formation of other molecules constituting the aerosols. My results here also strongly emphasize the need to include extensive nitrogen and oxygen reactive pathways in future Pluto photochemical models.

Some of the results of this study can be found in an article published in *Icarus*: Jovanović *et al.* (2020).

In the third part of my Ph.D. thesis (Chapter V: Investigating the optical constants of Pluto's aerosols), I determined the optical constants (*n* and *k* indices, the real and imaginary parts of the complex refractive index) of Pluto tholins deposited as thin films onto silicon substrates, and studied the effect of these properties on Pluto's atmosphere and surface. Three types of analogues were produced from gas mixtures with different N_2:CH_4:CO proportions, in order to mimic aerosols formed at different altitudes in Pluto's current atmosphere. In addition to F_{400} and F_{650} samples, I also produced a sample in a reactive N_2:CH_4:CO = 99.5%:0.5%:500ppm gas mixture. This sample called F_H is expected to be representative of aerosols formed below 350 km of altitude above the surface. These three gas mixtures differing in their CH_4 mixing ratio can also be considered as analogues of Pluto's atmosphere at different seasons or epochs. The optical constants of Pluto tholins were determined from UV to near-IR by spectroscopic ellipsometry, with two inversion methods, modified Tauc-Lorentz dispersion model and "wavelength-by-wavelength" numerical inversion.

The characterization of *n* and *k* indices showed a strong absorption of UV and visible radiations by Pluto tholins, attributed to their N-bearing and O-bearing organic molecules, which were detected and discussed in the second part of my Ph.D. thesis (Chapter IV). The absorption in the near-IR spectral range by Pluto tholins was found to be more moderate, with *k* indices of a few 10^{-3}.

I noticed a dependency of *n* and *k* indices to the CH_4 mixing ratio, and thus to the altitude of aerosol formation in Pluto's atmosphere. The N- and O-content in Pluto low-altitude aerosols

being enhanced (as discussed in the second part of my Ph.D. thesis (Chapter IV)), it leads to an increase of both *n*- and *k*-values. This dependency of the optical constants to the CH_4 mixing ratio has also implications for the seasonal and past epochal radiative transfer of Pluto.

The comparison of my Pluto data with the optical constants determined for Titan tholins by Khare *et al.* (1984) showed that Pluto tholins present globally similar *n*-values to those of Titan. However, differences were observed regarding the *k* indices. In particular, *k*-values of Pluto tholins are one order of magnitude higher than those of Titan in the near-IR. In the UV spectral range, *k* indices of Pluto tholins are also higher, which is probably due to the reactivity of nitrogen and carbon monoxide in the gas mixture producing Pluto's aerosols.

The optical properties of tholins depend on their chemical composition, and particularly on the N- and O-content. As Pluto tholins are compositionally different from Titan tholins (as discussed in the second part of my Ph.D. thesis (Chapter IV)), I proposed the optical constants determined during my Ph.D. thesis as new input parameters from 270 to 2,100 nm to model Pluto's atmosphere and surface properties.

My optical constants of Pluto tholins were used by Silvia Protopapa as input parameters in a Pluto surface model. The modeling results concluded on the suitability of these optical constants to reproduce Pluto compositional observations by MVIC and LEISA, at least in the UV-Vis spectral ranges. Moreover, these optical constants were also implemented by Tanguy Bertrand and Pascal Rannou in a model of light scattering. These results concluded that Pluto tholins absorb 5 to 10 times less than Titan tholins at 500 nm. This lower absorption is consistent with Alice observations of Pluto's haze.

All the results of this study can be found in an article published in *Icarus*: Jovanović *et al.* (2021).

Finally, in the fourth part of my Ph.D. thesis (Chapter VI: Investigating the organic matter on Pluto's surface), I first discussed the characterization of the suitability of Pluto tholins to reproduce Pluto's dark equatorial region, named Cthulhu, and second, I investigated the effect of GCR irradiation on the organic matter on Pluto's surface.

I was involved in a study aiming to explain the origin and composition of Pluto's Cthulhu region: Fayolle, Quirico, Schmitt, Jovanovic *et al.* (2021). In this study, laboratory reflectance measurements were performed to test the suitability of my Pluto tholins P_{400} and P_{650} to reproduce *New Horizons* reflectance spectra of Cthulhu region, collected both in the visible and

the near-IR spectral ranges by the MVIC and LEISA instruments. From reconstructed reflectance spectra and direct comparison with *New Horizons* data, we concluded that Pluto tholins, and in particular the P_{400} sample, reproduce the photometric level in the near-IR fairly well, but the red visible slope of Pluto tholins does not match with that of Pluto's surface. In addition, freshly-synthesized Pluto tholins are characterized by strong absorption bands that are not found in *New Horizons* spectra. To explain these discrepancies, we proposed several hypotheses, the two most likely being high porosity of the dark terrains at Cthulhu region, and galactic cosmic ray (GCR) irradiation of surface-deposited organic material.

To support the hypothesis of GCR irradiation on Pluto's surface, I synthesized Pluto tholins as spherical solid grains (P_P sample) and as thin films (F_P sample). These Pluto tholins were subjected to irradiation by 75 MeV ^{136}Xe swift heavy ions at GANIL/IRRSUD and several *in situ* and *ex situ* measurements were performed. Such energetic ions mimic the high-energy part of the GCR flux reaching Pluto's surface. *Ex situ* analysis by scanning electron microscopy (SEM) was performed to study the morphological evolution of Pluto tholins submitted to swift heavy ion irradiation. *In situ* spectroscopy analyses in the visible and the mid-IR spectral ranges were conducted to investigate the evolution of the optical properties and chemical composition of Pluto tholins under swift heavy ion irradiation. *Ex situ* Fourier-transform ion cyclotron resonance (FT-ICR) analyses were carried out to better understand the evolution of the fine molecular composition of Pluto tholins after swift heavy ion irradiation. Finally, *in situ* measurements by QMS provided an insight of the volatiles released by Pluto tholins under swift heavy ion irradiation.

SEM observations highlighted a micro-structural change of Pluto tholins P_P submitted to swift heavy ion irradiation, affecting the macro-morphological aspect observed with the naked eye. Due to sputtering effect, irradiated Pluto tholins present heterogeneous zones, with compact aggregates surrounded by zones devoid of tholins. I suggested that GCR irradiation could affect the porosity of the organic material deposited on the surface, in the Cthulhu region.

In the visible wavelength range, spectroscopy measurements showed that swift heavy ion irradiation leads to a decrease in the absorbance of Pluto tholins F_P, and a likely reddening of the material. Regarding the mid-IR spectral range, we noticed after swift heavy ion irradiation an overall decrease in the intensity of all fundamental characteristic absorption bands of Pluto tholins, thereby probably affecting the near-IR overtones as well. This decrease is due both to sputtering and radiolysis effects. These observations – decrease of absorbance in the visible, reddening of the material, and decrease of absorption bands in the mid-IR – favor the hypothesis

that the irradiation of the organic matter on the surface of Pluto by GCR could explain the differences between the featureless spectra of Pluto's surface and the reflectance spectra of freshly-synthesized Pluto tholins.

The formation of new molecules after swift heavy ion irradiation of Pluto tholins P_P was pointed out by FT-ICR analyses. These daughter molecules are characterized by H/C and N/C ratios lower than 0.5, and the calculation of their Double Bond Equivalent values is consistent with unsaturated poly-aromatic and N-bearing poly-aromatic hydrocarbons. These molecules were also found to be rich in O atoms, suggesting the formation of O-bearing poly-aromatic hydrocarbons under swift heavy ion irradiation.

QMS analysis revealed that Pluto tholins submitted to swift heavy ion irradiation release gas-phase molecules up to *m/z* 52, including unsaturated hydrocarbons, and molecules bearing nitrile, isocyanide or carbodiimide functional groups. Among the unsaturated molecules released, the most abundant are acetylene C_2H_2 and hydrogen cyanide HCN. These results suggest that GCR irradiation could eject additional molecules from Pluto's surface, and those molecules could be retained in Pluto's atmosphere and participate in the formation of more complex photochemical aerosols.

VII.2. Perspectives

This first laboratory study described in this Ph.D. manuscript opens new research perspectives on Pluto's atmosphere and aerosols.

Regarding the study about the chemical composition of Pluto-simulated atmosphere and the understanding of Pluto's atmospheric chemistry, to confirm the species predicted from the deconvolution of the neutral mass spectra, it would be essential to conduct complementary experiments, such as gas chromatography measurements. In this Ph.D. thesis, I showed the importance of positive ions in Pluto's atmospheric chemistry. Given the major role of negative ions in the formation of Titan's aerosols (Coates *et al.*, 2007; Vuitton, Lavvas, *et al.*, 2009; Dubois, Carrasco, Bourgalais, *et al.*, 2019), it would be important to analyze the anions formed in Pluto-simulated atmosphere to understand their role in Pluto's atmosphere as well.

Regarding the study about the chemical composition of Pluto aerosol analogues, in order to better distinguish the incorporation of oxygen atoms in Pluto tholins due to CO chemistry from external contamination, it would be desirable to synthesize samples in a N_2:CH_4:$C^{18}O$ reactive medium. To confirm the position of oxygen atoms inside the molecular structure, affecting the

chemical and physical properties of Pluto's hazes, it would be important to further refine my GC-MS analyses by comparing with standards.

Pluto's aerosols, by interacting with gas-phase molecules in the atmosphere, can have a strong impact on Pluto's climate, acting as condensation nuclei (Luspay-Kuti *et al.*, 2017; Stern, Kammer, *et al.*, 2017; Lavvas *et al.*, 2020) or affecting the atmosphere radiative balance (Zhu, Strobel and Erwin, 2014; Zhang, Strobel and Imanaka, 2017). During my Ph.D., all my studies focused on Pluto's aerosols formed by photochemistry. However, as mentioned in Introduction, additional processes may affect aerosols in Pluto's atmosphere due to condensation on photochemical nuclei (Luspay-Kuti *et al.*, 2017; Lavvas *et al.*, 2020). Such condensation of gaseous molecules, resulting in coated photochemical aerosols would occur on preexisting Pluto's aerosols formed by photochemistry, requiring to know their properties as well, as studied in the third part of my Ph.D. thesis (Chapter V). The differences observed between my data and the *New Horizons* observations could originate, at least partially, from this contribution of coated aerosols. By analogy with the C_4H_2 ice studied in Lavvas *et al.* (2020) presenting lower *n*- and *k*-values than those determined for our Pluto tholins in the common wavelength range [270-1,000 nm], we can suppose that if gaseous molecules condense or adsorb on Pluto's photochemical aerosols, their optical constants *n* and *k* could be slightly lowered. Assessing the exact effect on the optical constants of [tholins/ices] mixture will be of prime importance for further studies of Pluto's atmosphere and surface, and require in-depth modeling and experimental investigation. Future studies of interest should also include the characterization of optical properties of Pluto aerosol analogues in the far-IR to better understand how Pluto's aerosols participate in radiative cooling of the atmosphere.

Regarding the study about the organics processing at the surface of Pluto, as mentioned in Chapter II, experiments are planned on the ARIBE beamline in order to evaluate the effect of the solar wind and the low-energy part of the GCR flux irradiating Pluto's surface. These experiments will probably provide significant different results, since the contribution of nuclear interactions will be more important. In the same way, it would be interesting to irradiate Pluto tholins with VUV photons or electrons and compare the results obtained with those presented in the fourth part of my Ph.D. thesis (Chapter VI).

The work presented in this manuscript represents the first experimental attempt to study Pluto's atmospheric chemistry and haze formation. Given the necessarily limited number of experimental parameters explored during my Ph.D., it would be important to continue to explore Pluto's complexity by extending the experimental parameter space (experimental

setups, experimental conditions such as varying the pressure, the temperature, or energy source, …).

Pluto and Triton share several similar characteristics, namely comparable sizes, densities, distances from Sun. The dwarf planet and the largest Neptune's satellite are small, ice-covered worlds surrounded by thin atmospheres (McKinnon and Kirk, 2014; Strobel and Zhu, 2017; Zalucha and Cook, 2019). The atmospheres surrounding these two planetary bodies share similar chemical compositions: atmospheres essentially composed of N_2, CH_4, and CO (Broadfoot *et al.*, 1989; Tyler *et al.*, 1989; Lellouch *et al.*, 2010, 2017; Young *et al.*, 2018), Extended haze was also observed on Triton. Photochemical and condensation processes were proposed to explain its presence (Smith *et al.*, 1989). Since Triton's atmosphere contains at most 0.1% of CH_4 (Lellouch *et al.*, 2010), different CO/CH_4 ratios characterize Triton's and Pluto's atmospheres. Therefore, it would be interesting to extend my approach developed on Pluto's case to the study of Triton.

List of publications related to this Ph.D. thesis

Peer-reviewed publications

❶ Dubois, D., Carrasco, N., **Jovanovic, L.**, Vettier, L., Gautier, T., & Westlake, J. (2020). Positive ion chemistry in an N_2-CH_4 plasma discharge: Key precursors to the growth of Titan tholins. *Icarus*, *338*, 113437. https://doi.org/10.1016/j.icarus.2019.113437

❷ Bourgalais, J., Carrasco, N., Changeat, Q., Venot, O., **Jovanović, L.**, Pernot, P., Tennyson, J., Chubb, K. L., Yurchenko, S. N., & Tinetti, G. (2020). Ions in the Thermosphere of Exoplanets: Observable Constraints Revealed by Innovative Laboratory Experiments. *The Astrophysical Journal*, *895*. https://doi.org/10.3847/1538-4357/ab8e2d

❸ **Jovanović, L.**, Gautier, T., Vuitton, V., Wolters, C., Bourgalais, J., Buch, A., Orthous-Daunay, F.-R., Vettier, L., Flandinet, L., & Carrasco, N. (2020). Chemical composition of Pluto aerosol analogues. *Icarus*, *346*, 113774. https://doi.org/10.1016/j.icarus.2020.113774

❹ **Jovanović, L.**, Gautier, T., Broch, L., Fayolle, M., Quirico, E., Protopapa, S., Bertrand, T., Johann, L., En Naciri, A., & Carrasco, N. (2021). Optical constants of Pluto aerosol analogues from UV to near-IR. *Icarus*, *362*, 114398. https://doi.org/10.1016/j.icarus.2021.114398

❺ Phan, V. T. H., Quirico, E., Beck, P., Le Brech, Y., **Jovanovic, L.**, Le Guillou, C., Bernard, S., Bonal, L., Carrasco, N., Gautier, T., & Raya, J. (2021). Infrared spectroscopy quantification of functional carbon groups in kerogens and coals: A calibration procedure. *Spectrochimica Acta A*, *259*, 119853. https://doi.org/10.1016/j.saa.2021.119853

❻ Fayolle, M., Quirico, E., Schmitt, B., **Jovanovic, L.**, Gautier, T., Carrasco, N., Grundy, W., Vuitton, V., Poch, O., Gabasova, L., Protopapa, S., & Young, L. (2021). Testing tholins as analogues of the dark reddish material covering the Cthulhu region. *Icarus*, *367*, 114574. https://doi.org/10.1016/j.icarus.2021.114574

❼ Perrin, Z., Carrasco, N., Chatain, A., **Jovanovic, L.**, Vettier, L., Ruscassier, N., & Cernogora, G. (2021). An atmospheric origin for HCN-derived polymers on Titan. *Processes*, *9(6)*, 965. https://doi.org/10.3390/pr9060965

Appendix A1: Detailed description of the different parts of the *Hiden Analytical EQP 200* Quadrupole Mass Spectrometer (QMS)

Table A1.1: Table summarizing the function of each of the QMS components.

Ion trajectory through the different components of the QMS	Function
Extractor (sampling orifice)	In +SIMS mode only, *Extractor* is used to attract the ions formed *in situ* in the plasma, by generating an electric field between the sample and the QMS inlet. Note that in RGA mode, the neutrals enter the QMS by diffusion, bypassing the extractor.
Lens1 (transfer lens)	In +SIMS mode only, *Lens1* is used to refocus the ion beam formed *in situ* in the plasma from the sampling orifice to the output of the ionization source. It allows the cations formed *in situ* in the plasma to bypass the ionization source.
Ionization source ❋ **Cage** ❋ **Electron-energy** ❋ **Emission**	The *Ionization source* is used in RGA mode only. - A filament emits electrons at 70 eV (*Electron-energy* arbitrary value), which ionize and fragment neutrals/radicals. - The *Cage* value (2.9 V recommended) is the potential energy at which the ions are formed. - The *Emission* value (500.0 µA for our analyses) corresponds to the filament current produced by thermionic emission.
Flight-focus	*Flight-focus* is a long focal-length lens allowing the transport of the ion beam from the ionization source to the energy filter.
Lens2 (transfer ion optics)	*Lens2* allows an efficient transfer of the ion beam, by linking the ionization source to the energy filter.
Energy filter ❋ **Axis** ❋ **D.C. quad.** ❋ **Vert. & Horiz.** ❋ **Plates**	*Energy filter* at 45° to the sampling part of the QMS, controlled by Axis, D.C. quad, Vert, Horiz, and Plates. ❋ When the ions leave the ionization source, they are accelerated through the energy filter with a kinetic energy defined by *Axis* (recommended value of -40.0 V for RGA and +SIMS modes). ❋ *D.C. quad.* optimizes the ion trajectory by correcting the astigmatism of the ion beam (*i.e.*, the fact that all the ions in the beam do not converge at the same point). ❋ *Vert.* and *Horiz.* control the alignment of the ion beam before entering the energy filter. ❋ *Plates* is used to set the potential of 2 plates, one being positive and the other negative. These plates allow the energy filtering. The value of Plates is defined in relation to that of Axis via the ratio: $\text{Plates} = \frac{-\text{Axis}}{5.498}$ (recommended value of +7.27 V for RGA and +SIMS modes).
Focus2 (decelerating/focus lens)	*Focus2* reduces the kinetic energy of the ions and focuses the ion beam towards the Quadrupole (mass filter). The ions with a stable trajectory through the energy filter are able to pass through the mass filter, with an energy defined by *Transit-energy* (recommended value of +3.0 V for RGA and +SIMS modes).
Energy	*Energy* defines the energy of the ions that can be filtered and analyzed in mass.

Quadrupole mass filter ❋ **Delta-m** ❋ **Resolution** ❋ **Suppressor**	The main filter is driven by RF (Radio-Frequency) and DC (Direct Current) voltages, whereas the pre- and post-filters are driven by RF voltage only. The mass resolution is controlled by Delta-m and Resolution. ❋ *Delta-m* controls the peak width, especially at low *m/z*. ❋ *Resolution* controls the peak width, especially at high *m/z*. ❋ In RGA and +SIMS modes, *Suppressor* prevents electrons from entering the detector.
Detector ❋ **1st-dynode** ❋ **Multiplier** ❋ **Discriminator**	*Detector* is an electron multiplier off-axis to the ion trajectory, located behind the 45° bend. It is controlled by 1st-dynode, Multiplier, and Discriminator. ❋ *1st-dynode* controls the potential at the front of the detector. This potential (recommended value of -3500 V for RGA and +SIMS analyses) allows to convert ions into electrons. ❋ Multiplier controls the potential across the detector. This potential accelerates the electrons in the detector. ❋ *Discriminator* sets an amplitude threshold at which a pulse is counted (recommended value of -10% for RGA and +SIMS modes).

Appendix A2: Chemical composition of Pluto aerosol analogues inferred from HRMS (Orbitrap technique)

List of molecules detected with ESI+/Orbitrap and identified with *Attributor* software in the soluble fraction of samples P_{400} and P_{650}

Molecules common to P_{400} and P_{650}

85.0640	C3H7N3
86.0592	C2H6N4
86.0844	C4H10N2
87.0796	C3H9N3
95.0483	C4H5N3
96.0436	C3H4N4
98.0844	C5H10N2
99.0433	C3H5N3O
99.0796	C4H9N3
100.0749	C3H8N4
100.1000	C5H12N2
101.0589	C3H7N3O
101.0953	C4H11N3
102.0429	C3H6N2O2
102.0542	C2H6N4O
103.0746	C3H9N3O
107.0483	C5H5N3
108.0687	C6H8N2
111.0433	C4H5N3O
112.0385	C3H4N4O
112.0637	C5H8N2O
113.0701	C3H7N5
113.0953	C5H11N3
114.0542	C3H6N4O
114.0905	C4H10N4
114.1157	C6H14N2
115.0746	C4H9N3O
115.0858	C3H9N5
115.1109	C5H13N3
116.0586	C4H8N2O2
118.0742	C4H10N2O2
121.0640	C6H7N3
122.0592	C5H6N4
122.0844	C7H10N2
127.0746	C5H9N3O
127.1109	C6H13N3
128.0698	C4H8N4O
128.0950	C6H12N2O
128.1062	C5H12N4
128.1313	C7H16N2
129.0902	C5H11N3O
129.1014	C4H11N5
130.0855	C4H10N4O
133.0640	C7H7N3
133.0851	C4H11N3O2
134.0592	C6H6N4
135.0796	C7H9N3
136.1000	C8H12N2
138.0654	C4H6N6
138.0905	C6H10N4
138.1157	C8H14N2
139.0494	C4H5N5O
139.1109	C7H13N3
141.0651	C4H7N5O
141.0763	C3H7N7
141.0902	C6H11N3O
141.1266	C7H15N3
142.0855	C5H10N4O
142.1106	C7H14N2O
142.1218	C6H14N4
143.0807	C4H9N5O
143.1059	C6H13N3O
144.0899	C6H12N2O2
144.1011	C5H12N4O
147.0796	C8H9N3
148.0749	C7H8N4
149.0701	C6H7N5
149.0953	C8H11N3
151.0606	C4H5N7
152.0698	C6H8N4O
152.1313	C9H16N2
153.0902	C7H11N3O
153.1266	C8H15N3
154.0855	C6H10N4O
154.1106	C8H14N2O
154.1218	C7H14N4
154.1470	C9H18N2
155.0807	C5H9N5O
155.0919	C4H9N7
155.1059	C7H13N3O
155.1171	C6H13N5
155.1422	C8H17N3
156.0647	C5H8N4O2
156.1011	C6H12N4O
156.1263	C8H16N2O
157.0851	C6H11N3O2
157.0964	C5H11N5O
157.1215	C7H15N3O
158.1168	C6H14N4O
159.1008	C6H13N3O2
161.0701	C7H7N5
161.0800	C5H11N3O3
162.0654	C6H6N6
162.0905	C8H10N4
163.1109	C9H13N3
165.0763	C5H7N7
165.1266	C9H15N3
167.0807	C6H9N5O
167.1059	C8H13N3O
167.1422	C9H17N3
169.0851	C7H11N3O2
169.0964	C6H11N5O
169.1076	C5H11N7
169.1215	C8H15N3O
169.1327	C7H15N5
169.1579	C9H19N3
170.1168	C7H14N4O
171.0756	C5H9N5O2
171.1008	C7H13N3O2
171.1120	C6H13N5O
171.1372	C8H17N3O
172.1212	C8H16N2O2
173.0913	C5H11N5O2
173.1164	C7H15N3O2
175.0858	C8H9N5
176.0559	C5H4N8
177.1266	C10H15N3
180.0872	C5H8N8
180.1011	C8H12N4O
180.1375	C9H16N4
180.1626	C11H20N2
181.0712	C5H7N7O
181.0964	C7H11N5O
181.1076	C6H11N7
181.1215	C9H15N3O
181.1327	C8H15N5
181.1579	C10H19N3
182.0804	C7H10N4O2
182.0916	C6H10N6O
182.1028	C5H10N8
182.1168	C8H14N4O
182.1280	C7H14N6

182.1531	C9H18N4	197.1277	C8H15N5O	221.1025	C8H11N7O
183.0756	C6H9N5O2	197.1389	C7H15N7	221.1137	C7H11N9
183.0981	C4H9N9	198.1117	C8H14N4O2	221.1277	C10H15N5O
183.1120	C7H13N5O	198.1481	C9H18N4O	221.1389	C9H15N7
183.1232	C6H13N7	199.1069	C7H13N5O2	221.1640	C11H19N5
183.1372	C9H17N3O	199.1208	C10H17NO3	222.0978	C7H10N8O
183.1484	C8H17N5	200.1273	C8H16N4O2	222.1090	C6H10N10
184.0960	C7H12N4O2	202.0967	C9H10N6	222.1341	C8H14N8
184.1324	C8H16N4O	203.0919	C8H9N7	222.1481	C11H18N4O
185.0913	C6H11N5O2	203.1171	C10H13N5	223.1069	C9H13N5O2
185.1164	C8H15N3O2	204.0872	C7H8N8	223.1182	C8H13N7O
185.1277	C7H15N5O	204.1375	C11H16N4	223.1294	C7H13N9
186.0753	C6H10N4O3	205.0964	C9H11N5O	223.1433	C10H17N5O
186.1117	C7H14N4O2	206.1531	C11H18N4	223.1545	C9H17N7
187.0858	C9H9N5	207.0869	C7H9N7O	224.1134	C7H12N8O
188.0810	C8H8N6	207.1120	C9H13N5O	224.1246	C6H12N10
189.0763	C7H7N7	207.1484	C10H17N5	224.1386	C9H16N6O
189.1014	C9H11N5	208.1185	C7H12N8	224.1498	C8H16N8
190.1218	C10H14N4	208.1324	C10H16N4O	224.1749	C10H20N6
191.0807	C8H9N5O	208.1436	C9H16N6	225.1226	C9H15N5O2
191.0919	C7H9N7	208.1688	C11H20N4	225.1338	C8H15N7O
191.1422	C11H17N3	209.1025	C7H11N7O	225.1590	C10H19N5O
192.0872	C6H8N8	209.1137	C6H11N9	226.1291	C7H14N8O
192.1375	C10H16N4	209.1389	C8H15N7	226.1430	C10H18N4O2
193.0712	C6H7N7O	209.1640	C10H19N5	227.1382	C9H17N5O2
193.0824	C5H7N9	210.0978	C6H10N8O	229.1076	C10H11N7
193.0964	C8H11N5O	210.1090	C5H10N10	230.1028	C9H10N8
193.1400	C3H15N9O	210.1117	C9H14N4O2	231.0981	C8H9N9
193.1579	C11H19N3	210.1341	C7H14N8	231.1484	C12H17N5
194.1028	C6H10N8	210.1481	C10H18N4O	232.1185	C9H12N8
194.1168	C9H14N4O	210.1593	C9H18N6	233.1025	C9H11N7O
194.1531	C10H18N4	211.1069	C8H13N5O2	233.1137	C8H11N9
195.0869	C6H9N7O	211.1182	C7H13N7O	233.1389	C10H15N7
195.0981	C5H9N9	211.1545	C8H17N7	233.1640	C12H19N5
195.1120	C8H13N5O	212.1273	C9H16N4O2	234.1090	C7H10N10
195.1232	C7H13N7	213.1226	C8H15N5O2	234.1593	C11H18N6
195.1372	C10H17N3O	214.0967	C10H10N6	235.1182	C9H13N7O
195.1484	C9H17N5	215.0919	C9H9N7	235.1433	C11H17N5O
195.1735	C11H21N3	215.1171	C11H13N5	235.1545	C10H17N7
196.1185	C6H12N8	216.0872	C8H8N8	235.1797	C12H21N5
196.1324	C9H16N4O	216.1123	C10H12N6	236.1134	C8H12N8O
196.1436	C8H16N6	217.1076	C9H11N7	236.1246	C7H12N10
196.1688	C10H20N4	217.1327	C11H15N5	236.1273	C11H16N4O2
197.0913	C7H11N5O2	218.1028	C8H10N8	236.1498	C9H16N8
197.1025	C6H11N7O	218.1531	C12H18N4	237.1087	C7H11N9O
197.1137	C5H11N9	220.1185	C8H12N8	237.1226	C10H15N5O2

237.1338	C9H15N7O	255.1232	C12H13N7	274.1654	C12H18N8
237.1450	C8H15N9	256.1185	C11H12N8	274.1906	C14H22N6
237.1590	C11H19N5O	256.1436	C13H16N6	275.1355	C9H13N11
237.1702	C10H19N7	257.1137	C10H11N9	275.1495	C12H17N7O
238.1291	C8H14N8O	257.1389	C12H15N7	275.1607	C11H17N9
238.1654	C9H18N8	258.1593	C13H18N6	275.1858	C13H21N7
239.1382	C10H17N5O2	259.1294	C10H13N9	276.1308	C8H12N12
239.1495	C9H17N7O	259.1393	C8H17N7O3	276.1447	C11H16N8O
240.1447	C8H16N8O	259.1545	C12H17N7	276.1559	C10H16N10
241.1076	C11H11N7	260.1134	C10H12N8O	276.1811	C12H20N8
242.1028	C10H10N8	260.1498	C11H16N8	277.1400	C10H15N9O
243.1232	C11H13N7	261.1199	C8H11N11	277.1512	C9H15N11
243.1484	C13H17N5	261.1338	C11H15N7O	277.1651	C12H19N7O
244.1185	C10H12N8	261.1450	C10H15N9	277.2015	C13H23N7
245.1137	C9H11N9	261.1702	C12H19N7	278.1604	C11H18N8O
245.1640	C13H19N5	262.1403	C9H14N10	278.1716	C10H18N10
246.1090	C8H10N10	262.1654	C11H18N8	278.1967	C12H22N8
246.1341	C10H14N8	262.1906	C13H22N6	279.1444	C11H17N7O2
247.1182	C10H13N7O	263.1243	C9H13N9O	279.1808	C12H21N7O
247.1294	C9H13N9	263.1355	C8H13N11	279.1920	C11H21N9
247.1797	C13H21N5	263.1495	C11H17N7O	280.1760	C11H20N8O
248.1134	C9H12N8O	263.1607	C10H17N9	281.1052	C17H15NO3
248.1246	C8H12N10	263.1706	C8H21N7O3	281.1600	C11H19N7O2
248.1498	C10H16N8	263.1858	C12H21N7	281.1713	C10H19N9O
248.1570	C4H16N12O	264.1447	C10H16N8O	282.1341	C13H14N8
249.1087	C8H11N9O	264.1559	C9H16N10	283.1294	C12H13N9
249.1338	C10H15N7O	264.1811	C11H20N8	284.1246	C11H12N10
249.1450	C9H15N9	265.1287	C10H15N7O2	284.1498	C13H16N8
249.1590	C12H19N5O	265.1400	C9H15N9O	284.2212	C14H28N4O2
249.1702	C11H19N7	265.1651	C11H19N7O	285.1450	C12H15N9
249.1953	C13H23N5	265.1763	C10H19N9	286.1403	C11H14N10
250.1291	C9H14N8O	266.1604	C10H18N8O	287.1355	C10H13N11
250.1403	C8H14N10	269.1389	C13H15N7	287.1607	C12H17N9
250.1654	C10H18N8	270.1341	C12H14N8	287.1858	C14H21N7
251.1131	C9H13N7O2	271.1294	C11H13N9	288.1559	C11H16N10
251.1243	C8H13N9O	271.1545	C13H17N7	288.1811	C13H20N8
251.1382	C11H17N5O2	272.1246	C10H12N10	289.1512	C10H15N11
251.1495	C10H17N7O	272.1498	C12H16N8	289.1651	C13H19N7O
251.1607	C9H17N9	272.1749	C14H20N6	289.1763	C12H19N9
251.1858	C11H21N7	273.1199	C9H11N11	291.1444	C12H17N7O2
252.1447	C9H16N8O	273.1450	C11H15N9	291.1556	C11H17N9O
252.1699	C11H20N6O	273.1523	C5H15N13O	291.1668	C10H17N11
252.1811	C10H20N8	273.1702	C13H19N7	291.1808	C13H21N7O
253.1287	C9H15N7O2	274.1291	C11H14N8O	291.1920	C12H21N9
253.1539	C11H19N5O2	274.1403	C10H14N10	292.1760	C12H20N8O
254.1491	C10H18N6O2	274.1502	C8H18N8O3	292.1872	C11H20N10

293.1713	C11H19N9O
297.1450	C13H15N9
298.1403	C12H14N10
298.1654	C14H18N8

Molecules exclusively present in P_{400}

56.0374	C2H4N2
58.0531	C2H6N2
68.0374	C3H4N2
69.0327	C2H3N3
71.0483	C2H5N3
74.0480	C2H6N2O
83.0483	C3H5N3
84.0436	C2H4N4
85.0276	C2H3N3O
88.0749	C2H8N4
93.0327	C4H3N3
98.0592	C3H6N4
99.0545	C2H5N5
101.0701	C2H7N5
102.0905	C3H10N4
105.0538	C2H7N3O2
108.0436	C4H4N4
109.0388	C3H3N5
110.0844	C6H10N2
111.0796	C5H9N3
112.1000	C6H12N2
113.0589	C4H7N3O
114.0654	C2H6N6
116.0698	C3H8N4O
116.0810	C2H8N6
117.0538	C3H7N3O2
118.0967	C2H10N6
119.0695	C3H9N3O2
123.0545	C4H5N5
124.0497	C3H4N6
124.1000	C7H12N2
125.0953	C6H11N3
127.0494	C3H5N5O
128.0810	C3H8N6
131.0695	C4H9N3O2
131.0807	C3H9N5O
136.0749	C6H8N4
137.0701	C5H7N5
137.0953	C7H11N3
138.0542	C5H6N4O
139.0858	C5H9N5
141.0538	C5H7N3O2
141.1014	C5H11N5
142.0967	C4H10N6
143.0919	C3H9N7
144.0760	C3H8N6O
144.0786	C7H12O3
145.0739	C6H11NO3
146.0943	C7H14O3
150.0654	C5H6N6
150.0905	C7H10N4
151.0858	C6H9N5
151.1109	C8H13N3
152.0810	C5H8N6
152.1062	C7H12N4
153.0651	C5H7N5O
153.0763	C4H7N7
153.0790	C8H11NO2
153.1014	C6H11N5
154.0603	C4H6N6O
154.0967	C5H10N6
156.0786	C8H12O3
156.0872	C3H8N8
156.1123	C5H12N6
156.1626	C9H20N2
157.0600	C4H7N5O2
158.0804	C5H10N4O2
158.0916	C4H10N6O
158.0943	C8H14O3
158.1055	C7H14N2O2
159.0895	C7H13NO3
160.0749	C8H8N4
160.0960	C5H12N4O2
163.0606	C5H5N7
163.0858	C7H9N5
164.0698	C7H8N4O
164.0810	C6H8N6
164.1062	C8H12N4
165.0651	C6H7N5O
165.1014	C7H11N5
169.0712	C4H7N7O
170.1028	C4H10N8
171.0895	C8H13NO3
172.0596	C5H8N4O3
172.0709	C4H8N6O2
172.0848	C7H12N2O3
172.0960	C6H12N4O2
172.1099	C9H16O3
173.0701	C8H7N5
173.1052	C8H15NO3
174.0654	C7H6N6
174.0905	C9H10N4
175.0606	C6H5N7
176.0810	C7H8N6
176.1062	C9H12N4
177.0651	C7H7N5O
177.0763	C6H7N7
177.1014	C8H11N5
178.0603	C6H6N6O
178.0715	C5H6N8
178.0967	C7H10N6
178.1218	C9H14N4
179.0556	C5H5N7O
179.0735	C13H9N
179.0807	C7H9N5O
179.0919	C6H9N7
179.0946	C10H13NO2
179.1171	C8H13N5
179.1422	C10H17N3
180.1123	C7H12N6
182.1055	C9H14N2O2
183.0869	C5H9N7O
184.0821	C4H8N8O
184.0848	C8H12N2O3
184.1000	C12H12N2
184.1185	C5H12N8
185.1025	C5H11N7O
185.1052	C9H15NO3
185.1137	C4H11N9
186.1004	C8H14N2O3
187.1069	C6H13N5O2
187.1208	C9H17NO3
188.1062	C10H12N4
190.0715	C6H6N8
190.1106	C11H14N2O
191.1171	C9H13N5
192.1123	C8H12N6
193.1076	C7H11N7
193.1103	C11H15NO2
193.1327	C9H15N5
194.1055	C10H14N2O2

194.1280	C8H14N6	217.0824	C7H7N9	236.0995	C5H8N12
196.0821	C5H8N8O	218.0777	C6H6N10	236.1022	C9H12N6O2
196.1073	C7H12N6O	218.0916	C9H10N6O	236.1749	C11H20N6
198.0865	C6H10N6O2	218.1280	C10H14N6	237.0974	C8H11N7O2
198.0978	C5H10N8O	219.0869	C8H9N7O	237.1199	C6H11N11
198.1004	C9H14N2O3	219.0981	C7H9N9	237.1953	C12H23N5
198.1090	C4H10N10	219.1120	C10H13N5O	238.1039	C6H10N10O
199.0818	C5H9N7O2	219.1232	C9H13N7	238.1178	C9H14N6O2
199.0957	C8H13N3O3	219.1484	C11H17N5	238.1358	C17H18O
199.1182	C6H13N7O	220.0821	C7H8N8O	239.1243	C7H13N9O
200.0810	C9H8N6	220.0933	C6H8N10	239.1355	C6H13N11
200.0909	C7H12N4O3	220.1073	C9H12N6O	239.1607	C8H17N9
200.1022	C6H12N6O2	220.1436	C10H16N6	240.1083	C7H12N8O2
202.0715	C7H6N8	221.0774	C6H7N9O	240.1222	C10H16N4O3
203.0668	C6H5N9	222.1157	C15H14N2	240.1335	C9H16N6O2
204.1123	C9H12N6	222.1229	C9H14N6O	241.1287	C8H15N7O2
205.0824	C6H7N9	223.0930	C6H9N9O	242.1240	C7H14N8O2
205.1327	C10H15N5	223.1042	C5H9N11	243.0981	C9H9N9
206.0916	C8H10N6O	223.1109	C14H13N3	244.0933	C8H8N10
206.1028	C7H10N8	223.1797	C11H21N5	244.1436	C12H16N6
206.1055	C11H14N2O2	224.1022	C8H12N6O2	245.0886	C7H7N11
207.0981	C6H9N9	224.1313	C15H16N2	245.1025	C10H11N7O
207.1232	C8H13N7	225.0974	C7H11N7O2	245.1389	C11H15N7
208.0821	C6H8N8O	225.1087	C6H11N9O	246.0978	C9H10N8O
208.0933	C5H8N10	225.1199	C5H11N11	246.1593	C12H18N6
208.1073	C8H12N6O	225.1266	C14H15N3	247.0930	C8H9N9O
208.1212	C11H16N2O2	225.1450	C7H15N9	247.1042	C7H9N11
209.0953	C13H11N3	227.0919	C10H9N7	247.1545	C11H17N7
209.1204	C15H15N	227.1131	C7H13N7O2	248.0883	C7H8N10O
209.1277	C9H15N5O	228.0872	C9H8N8	248.1386	C11H16N6O
210.0865	C7H10N6O2	228.1123	C11H12N6	248.1749	C12H20N6
210.1045	C15H14O	228.1335	C8H16N6O2	249.1199	C7H11N11
210.1157	C14H14N2	229.0824	C8H7N9	250.1039	C7H10N10O
210.1229	C8H14N6O	230.1280	C11H14N6	250.1151	C6H10N12
211.0818	C6H9N7O2	231.1232	C10H13N7	250.1218	C15H14N4
211.0930	C5H9N9O	232.0933	C7H8N10	250.1542	C11H18N6O
211.0997	C14H13NO	232.1073	C10H12N6O	250.1906	C12H22N6
211.1042	C4H9N11	232.1436	C11H16N6	251.1355	C7H13N11
211.1294	C6H13N9	233.0886	C6H7N11	251.1746	C12H21N5O
211.1433	C9H17N5O	234.0978	C8H10N8O	252.1083	C8H12N8O2
212.1134	C6H12N8O	234.1341	C9H14N8	252.1196	C7H12N10O
212.1246	C5H12N10	235.0930	C7H9N9O	252.1308	C6H12N12
213.0974	C6H11N7O2	235.1042	C6H9N11	252.1559	C8H16N10
213.1338	C7H15N7O	235.1109	C15H13N3	253.1036	C7H11N9O2
214.1066	C8H14N4O3	235.1294	C8H13N9	253.1148	C6H11N11O
214.1317	C10H18N2O3	236.0883	C6H8N10O	253.1400	C8H15N9O

253.1651	C10H19N7O
254.1240	C8H14N8O2
254.1352	C7H14N10O
254.1379	C11H18N4O3
255.0981	C10H9N9
255.1331	C10H17N5O3
255.1444	C9H17N7O2
256.0933	C9H8N10
256.1396	C8H16N8O2
258.0978	C10H10N8O
258.1090	C9H10N10
258.1341	C11H14N8
259.1042	C8H9N11
260.0995	C7H8N12
260.1345	C7H16N8O3
260.1386	C12H16N6O
260.1749	C13H20N6
261.1087	C9H11N9O
261.1298	C6H15N9O3
262.1039	C8H10N10O
262.1151	C7H10N12
262.1291	C10H14N8O
262.1430	C13H18N4O2
262.1542	C12H18N6O
263.0992	C7H9N11O
264.1083	C9H12N8O2
264.1196	C8H12N10O
264.1308	C7H12N12
264.1335	C11H16N6O2
264.1699	C12H20N6O
265.1148	C7H11N11O
265.1260	C6H11N13
265.1512	C8H15N11
266.1240	C9H14N8O2
266.1352	C8H14N10O
266.1464	C7H14N12
266.1491	C11H18N6O2
266.1716	C9H18N10
267.1192	C8H13N9O2
267.1331	C11H17N5O3
267.1444	C10H17N7O2
267.1556	C9H17N9O
267.1668	C8H17N11
268.1185	C12H12N8
268.1396	C9H16N8O2
269.1137	C11H11N9
270.1090	C10H10N10
271.1042	C9H9N11
272.1134	C11H12N8O
273.1087	C10H11N9O
273.1298	C7H15N9O3
274.1039	C9H10N10O
274.1151	C8H10N12
274.1250	C6H14N10O3
274.1470	C19H18N2
275.1104	C7H9N13
276.1196	C9H12N10O
276.1407	C6H16N10O3
276.1725	C17H24O3
277.1148	C8H11N11O
277.1260	C7H11N13
277.1359	C5H15N11O3
277.1579	C18H19N3
277.1611	C7H19N9O3
278.1240	C10H14N8O2
278.1280	C15H14N6
278.1352	C9H14N10O
278.1464	C8H14N12
279.1192	C9H13N9O2
279.1305	C8H13N11O
279.1417	C7H13N13
279.1556	C10H17N9O
279.1668	C9H17N11
280.1396	C10H16N8O2
280.1509	C9H16N10O
281.1349	C9H15N9O2
281.1488	C12H19N5O3
282.1090	C11H10N10
282.1553	C10H18N8O2
283.1042	C10H9N11
284.2100	C15H28N2O3
285.1199	C10H11N11
286.1151	C9H10N12
286.1654	C13H18N8
287.1104	C8H9N13
287.1243	C11H13N9O
287.1454	C8H17N9O3
288.1196	C10H12N10O
288.1308	C9H12N12
288.1407	C7H16N10O3
288.1447	C12H16N8O
288.1626	C20H20N2
289.1148	C9H11N11O
289.1260	C8H11N13
289.1400	C11H15N9O
289.1611	C8H19N9O3
291.1305	C9H13N11O
291.1417	C8H13N13
291.1735	C19H21N3
292.1369	C7H12N14
292.1396	C11H16N8O2
292.1509	C10H16N10O
292.1621	C9H16N12
293.1349	C10H15N9O2
293.1461	C9H15N11O
293.1573	C8H15N13
293.1600	C12H19N7O2
293.1825	C10H19N11
294.1301	C9H14N10O2
294.1553	C11H18N8O2
294.1665	C10H18N10O
295.1505	C10H17N9O2
296.1246	C12H12N10
296.1498	C14H16N8
297.1199	C11H11N11
298.1151	C10H10N12

Molecules exclusively present in P_{650}

82.0531	C4H6N2
94.0531	C5H6N2
98.0480	C4H6N2O
100.0637	C4H8N2O
120.0687	C7H8N2
125.0589	C5H7N3O
126.0542	C4H6N4O
126.0793	C6H10N2O
126.1157	C7H14N2
129.1266	C6H15N3
130.0742	C5H10N2O2
134.0844	C8H10N2
138.0793	C7H10N2O
140.0698	C5H8N4O
140.0950	C7H12N2O
140.1313	C8H16N2
143.0695	C5H9N3O2
143.1171	C5H13N5
144.0647	C4H8N4O2

145.1103	C7H15NO2	194.1783	C12H22N2	213.1365	C11H19NO3
146.1055	C6H14N2O2	196.0960	C8H12N4O2	213.1477	C10H19N3O2
148.1000	C9H12N2	196.1212	C10H16N2O2	214.1218	C12H14N4
150.1157	C9H14N2	197.1164	C9H15N3O2	214.1430	C9H18N4O2
151.0746	C7H9N3O	197.1528	C10H19N3O	215.1018	C7H13N5O3
152.0950	C8H12N2O	197.1640	C9H19N5	216.1196	C4H12N10O
156.0899	C7H12N2O2	198.1368	C10H18N2O2	216.1375	C12H16N4
156.1375	C7H16N4	198.1593	C8H18N6	217.1400	C5H15N9O
157.1103	C8H15NO2	199.1321	C9H17N3O2	217.1467	C14H19NO
159.1259	C8H17NO2	199.1361	C14H17N	217.1579	C13H19N3
161.0953	C9H11N3	199.1433	C8H17N5O	218.1352	C4H14N10O
162.1157	C10H14N2	200.1062	C11H12N4	220.1324	C11H16N4O
164.0909	C4H12N4O3	200.1525	C10H20N2O2	220.1396	C5H16N8O2
164.1313	C10H16N2	201.0215	C14H3NO	220.1509	C4H16N10O
165.0902	C8H11N3O	201.0723	C3H7N9O2	220.1688	C12H20N4
166.0855	C7H10N4O	201.1014	C10H11N5	220.1760	C6H20N8O
166.1470	C10H18N2	201.1087	C4H11N9O	221.1528	C12H19N3O
167.1171	C7H13N5	201.1113	C8H15N3O3	221.1892	C13H23N3
168.0872	C4H8N8	201.1266	C12H15N3	222.1665	C4H18N10O
168.1011	C7H12N4O	202.1218	C11H14N4	222.1844	C12H22N4
168.1263	C9H16N2O	203.1422	C12H17N3	223.1321	C11H17N3O2
168.1375	C8H16N4	204.1011	C10H12N4O	223.1685	C12H21N3O
170.1280	C6H14N6	205.1036	C3H11N9O2	223.2048	C13H25N3
170.1531	C8H18N4	205.1215	C11H15N3O	224.1273	C10H16N4O2
175.1109	C10H13N3	205.1400	C4H15N9O	224.1637	C11H20N4O
176.0586	C9H8N2O2	205.1579	C12H19N3	224.2001	C12H24N4
176.0698	C8H8N4O	206.1168	C10H14N4O	225.1477	C11H19N3O2
178.0855	C8H10N4O	206.1307	C13H18O2	225.1517	C16H19N
178.1291	C3H14N8O	206.1604	C5H18N8O	225.1702	C9H19N7
178.1470	C11H18N2	206.1783	C13H22N2	225.1953	C11H23N5
182.1783	C11H22N2	207.1372	C11H17N3O	226.1218	C13H14N4
183.1008	C8H13N3O2	207.1556	C4H17N9O	226.1569	C13H22O3
183.1735	C10H21N3	207.1735	C12H21N3	226.1681	C12H22N2O2
185.1204	C13H15N	208.1939	C13H24N2	227.1171	C12H13N5
185.1416	C10H19NO2	209.0913	C8H11N5O2	227.1634	C11H21N3O2
186.0905	C10H10N4	209.1164	C10H15N3O2	227.1674	C16H21N
186.1368	C9H18N2O2	209.1528	C11H19N3O	228.1222	C9H16N4O3
187.1109	C11H13N3	209.1892	C12H23N3	228.1375	C13H16N4
187.1321	C8H17N3O2	210.1368	C11H18N2O2	229.1327	C12H15N5
189.1266	C11H15N3	210.1844	C11H22N4	229.1579	C14H19N3
191.1059	C10H13N3O	211.1321	C10H17N3O2	230.1352	C5H14N10O
191.1243	C3H13N9O	211.1797	C10H21N5	230.1531	C13H18N4
192.1011	C9H12N4O	212.1412	C12H20O3	231.1120	C11H13N5O
192.1447	C4H16N8O	212.1525	C11H20N2O2	231.1305	C4H13N11O
192.1626	C12H20N2	212.1637	C10H20N4O	231.1556	C6H17N9O
193.1215	C10H15N3O	213.1014	C11H11N5	231.1735	C14H21N3

232.1324	C12H16N4O	246.1665	C6H18N10O	259.1797	C14H21N5
232.1509	C5H16N10O	246.1844	C14H22N4	259.2048	C16H25N3
232.1688	C13H20N4	247.1393	C7H17N7O3	260.1570	C5H16N12O
232.1760	C7H20N8O	247.1433	C12H17N5O	260.1637	C14H20N4O
233.1277	C11H15N5O	247.1618	C5H17N11O	260.1822	C7H20N10O
233.1461	C4H15N11O	247.1685	C14H21N3O	260.2001	C15H24N4
233.1600	C7H19N7O2	247.1869	C7H21N9O	261.0862	C11H11N5O3
233.1713	C6H19N9O	247.2048	C15H25N3	261.1590	C13H19N5O
233.1892	C14H23N3	248.1637	C13H20N4O	261.1662	C7H19N9O2
234.1481	C12H18N4O	248.1822	C6H20N10O	261.1774	C6H19N11O
234.1665	C5H18N10O	249.1226	C11H15N5O2	261.1953	C14H23N5
235.1505	C5H17N9O2	249.2205	C15H27N3	261.2026	C8H23N9O
235.1618	C4H17N11O	250.1430	C12H18N4O2	261.2205	C16H27N3
235.1685	C13H21N3O	250.1470	C17H18N2	262.1753	C9H22N6O3
235.2048	C14H25N3	250.1502	C6H18N8O3	262.1794	C14H22N4O
236.1637	C12H20N4O	250.1569	C15H22O3	262.1978	C7H22N10O
236.1822	C5H20N10O	250.1727	C4H18N12O	262.2157	C15H26N4
236.2001	C13H24N4	250.1794	C13H22N4O	263.1521	C15H21NO3
237.1477	C12H19N3O2	250.1978	C6H22N10O	263.1746	C13H21N5O
237.1774	C4H19N11O	250.2157	C14H26N4	263.1931	C6H21N11O
237.2205	C14H27N3	251.1634	C13H21N3O2	263.2110	C14H25N5
238.1403	C7H14N10	251.1931	C5H21N11O	263.2182	C8H25N9O
238.1470	C16H18N2	251.1998	C14H25N3O	263.2361	C16H29N3
238.1794	C12H22N4O	252.1407	C4H16N10O3	264.1514	C19H20O
238.1906	C11H22N6	252.1586	C12H20N4O2	264.1586	C13H20N4O2
238.2157	C13H26N4	252.1883	C4H20N12O	264.1883	C5H20N12O
239.1171	C13H13N5	252.2062	C12H24N6	264.1950	C14H24N4O
239.1634	C12H21N3O2	253.1426	C12H19N3O3	264.2135	C7H24N10O
239.1674	C17H21N	253.1678	C14H23NO3	264.2314	C15H28N4
239.1746	C11H21N5O	253.1723	C4H19N11O2	265.1539	C12H19N5O2
239.1858	C10H21N7	253.1790	C13H23N3O2	265.1678	C15H23NO3
240.1123	C12H12N6	253.1903	C12H23N5O	265.1723	C5H19N11O2
240.1474	C12H20N2O3	254.1563	C4H18N10O3	265.1790	C14H23N3O2
240.1586	C11H20N4O2	254.1630	C13H22N2O3	265.2015	C12H23N7
240.1725	C14H24O3	254.1743	C12H22N4O2	266.1563	C5H18N10O3
240.1838	C13H24N2O2	255.1484	C14H17N5	266.1743	C13H22N4O2
241.1327	C13H15N5	255.1695	C11H21N5O2	266.1783	C18H22N2
241.1790	C12H23N3O2	257.1277	C13H15N5O	266.1882	C16H26O3
242.1531	C14H18N4	257.1461	C6H15N11O	266.1967	C11H22N8
243.1372	C14H17N3O	257.1640	C14H19N5	266.2219	C13H26N6
244.1688	C14H20N4	258.1414	C5H14N12O	266.2470	C15H30N4
245.1277	C12H15N5O	258.1665	C7H18N10O	267.1232	C13H13N7
245.1461	C5H15N11O	258.1844	C15H22N4	267.1484	C15H17N5
245.1892	C15H23N3	259.1182	C11H13N7O	267.1583	C13H21N3O3
246.1414	C4H14N12O	259.1433	C13H17N5O	267.1808	C11H21N7O
246.1481	C13H18N4O	259.1618	C6H17N11O	267.1834	C15H25NO3

267.1947	C14H25N3O2	279.1834	C16H25NO3	289.2266	C16H27N5
268.1436	C14H16N6	279.2131	C8H25N9O2	290.1280	C16H14N6
268.1535	C12H20N4O3	279.2171	C13H25N7	290.1352	C10H14N10O
268.1787	C14H24N2O3	279.2423	C15H29N5	290.1379	C14H18N4O3
268.1899	C13H24N4O2	280.1436	C15H16N6	290.1491	C13H18N6O2
269.1825	C8H19N11	280.1621	C8H16N12	290.1563	C7H18N10O3
270.1593	C14H18N6	280.1787	C15H24N2O3	290.1604	C12H18N8O
271.1618	C7H17N11O	280.1827	C20H24O	290.1716	C11H18N10
271.1685	C16H21N3O	280.1899	C14H24N4O2	290.1783	C20H22N2
272.1570	C6H16N12O	280.2375	C14H28N6	290.1815	C9H22N8O3
272.1682	C5H16N14	281.1389	C14H15N7	290.1855	C14H22N6O
272.1889	C17H24N2O	281.1640	C16H19N5	290.1927	C8H22N10O2
272.2001	C16H24N4	281.1672	C5H19N11O3	290.1967	C13H22N8
273.1338	C12H15N7O	281.1739	C14H23N3O3	290.2040	C7H22N12O
273.1590	C14H19N5O	281.1825	C9H19N11	290.2066	C11H26N6O3
273.1662	C8H19N9O2	281.1852	C13H23N5O2	290.2107	C16H26N4O
273.1801	C11H23N5O3	281.1991	C16H27NO3	290.2219	C15H26N6
273.1841	C16H23N3O	281.2103	C15H27N3O2	290.2291	C9H26N10O
273.1953	C15H23N5	282.1593	C15H18N6	290.2470	C17H30N4
273.2026	C9H23N9O	283.1545	C14H17N7	291.1583	C15H21N3O3
274.1727	C6H18N12O	284.2185	C10H24N10	291.1992	C6H21N13O
274.1794	C15H22N4O	284.2252	C19H28N2	291.2019	C10H25N7O3
274.1978	C8H22N10O	284.2325	C13H28N6O	291.2059	C15H25N5O
274.2005	C12H26N4O3	285.1523	C6H15N13O	291.2171	C14H25N7
274.2157	C16H26N4	285.1590	C15H19N5O	291.2244	C8H25N11O
275.1679	C5H17N13O	285.1801	C12H23N5O3	291.2270	C12H29N5O3
275.1706	C9H21N7O3	286.1906	C15H22N6	291.2423	C16H29N5
275.1746	C14H21N5O	286.1978	C9H22N10O	292.1945	C5H20N14O
275.1957	C11H25N5O3	287.1495	C13H17N7O	292.2124	C13H24N8
275.2110	C15H25N5	287.1706	C10H21N7O3	292.2196	C7H24N12O
275.2361	C17H29N3	287.1931	C8H21N11O	292.2375	C15H28N6
276.1883	C6H20N12O	287.1998	C17H25N3O	293.1852	C14H23N5O2
276.1910	C10H24N6O3	287.2110	C16H25N5	293.1964	C13H23N7O
276.1950	C15H24N4O	288.1632	C5H16N14O	293.1991	C17H27NO3
276.2062	C14H24N6	288.1699	C14H20N6O	293.2076	C12H23N9
276.2135	C8H24N10O	288.1883	C7H20N12O	293.2216	C15H27N5O
276.2314	C16H28N4	288.1910	C11H24N6O3	293.2328	C14H27N7
277.1763	C11H19N9	288.1950	C16H24N4O	294.1341	C14H14N8
277.1862	C9H23N7O3	288.2062	C15H24N6	294.1844	C18H22N4
277.1903	C14H23N5O	288.2135	C9H24N10O	294.1917	C12H22N8O
277.2087	C7H23N11O	288.2314	C17H28N4	294.1943	C16H26N2O3
277.2266	C15H27N5	289.1862	C10H23N7O3	294.2056	C15H26N4O2
278.1630	C15H22N2O3	289.1948	C5H19N15	295.1545	C15H17N7
278.1743	C14H22N4O2	289.2015	C14H23N7	295.1869	C11H21N9O
278.2040	C6H22N12O	289.2087	C8H23N11O	295.2008	C14H25N5O2
278.2219	C14H26N6	289.2114	C12H27N5O3	295.2048	C19H25N3

295.2147	C17H29NO3
296.1525	C18H20N2O2
296.1961	C13H24N6O2
297.1702	C15H19N7
297.1801	C13H23N5O3
297.1841	C18H23N3O
298.1727	C8H18N12O
298.1753	C12H22N6O3
298.1794	C17H22N4O

List of molecules detected with APPI+/Orbitrap and identified with *Attributor* software in the soluble fraction of samples P_{400} and P_{650}

Molecules common to P_{400} and P_{650}

56.0500	C3H6N
71.0609	C3H7N2
74.0606	C3H8NO
74.0718	C2H8N3
75.0558	C2H7N2O
83.0609	C4H7N2
84.0562	C3H6N3
85.0766	C4H9N2
86.0718	C3H8N3
87.0922	C4H11N2
88.0762	C4H10NO
88.0875	C3H10N3
96.0562	C4H6N3
97.0766	C5H9N2
98.0592	C3H6N4
98.0718	C4H8N3
99.0558	C4H7N2O
99.0671	C3H7N4
99.0922	C5H11N2
100.0511	C3H6N3O
100.0623	C2H6N5
100.0762	C5H10NO
100.0875	C4H10N3
101.0827	C3H9N4
101.1079	C5H13N2
102.0667	C3H8N3O
102.0780	C2H8N5
102.1031	C4H12N3
103.0508	C3H7N2O2
104.0712	C4H10NO2
108.0562	C5H6N3
108.0813	C7H10N
109.0766	C6H9N2
110.0718	C5H8N3
111.0558	C5H7N2O
111.0671	C4H7N4
111.0684	C6H9NO
111.0922	C6H11N2
112.0511	C4H6N3O
112.0623	C3H6N5
112.0749	C4H8N4
112.0875	C5H10N3
113.0715	C5H9N2O
113.0827	C4H9N4
113.1079	C6H13N2
114.0667	C4H8N3O
114.0780	C3H8N5
114.1031	C5H12N3
115.0508	C4H7N2O2
115.0620	C3H7N4O
115.0732	C2H7N6
115.0871	C5H11N2O
115.0984	C4H11N4
116.0824	C4H10N3O
116.0936	C3H10N5
117.0664	C4H9N2O2
117.0776	C3H9N4O
120.0562	C6H6N3
122.0718	C6H8N3
123.0671	C5H7N4
123.0922	C7H11N2
124.0511	C5H6N3O
124.0623	C4H6N5
124.0749	C5H8N4
124.0875	C6H10N3
125.0701	C4H7N5
125.0827	C5H9N4
125.0841	C7H11NO
125.1079	C7H13N2
126.0667	C5H8N3O
126.0780	C4H8N5
126.1031	C6H12N3
128.0460	C4H6N3O2
128.0572	C3H6N5O
128.0698	C4H8N4O
128.0824	C5H10N3O
128.0936	C4H10N5
128.1188	C6H14N3
129.0776	C4H9N4O
129.1028	C6H13N2O
129.1140	C5H13N4
130.0617	C4H8N3O2
130.0980	C5H12N3O
131.0821	C5H11N2O2
131.0933	C4H11N4O
132.0813	C9H10N
134.0718	C7H8N3
135.0109	C10HN
135.0671	C6H7N4
136.0623	C5H6N5
136.0875	C7H10N3
137.0589	C6H7N3O
137.0827	C6H9N4
138.0667	C6H8N3O
138.0780	C5H8N5
138.1031	C7H12N3
139.0620	C5H7N4O
139.0732	C4H7N6
139.0858	C5H9N5
139.0984	C6H11N4
139.1235	C8H15N2
140.0572	C4H6N5O
140.0824	C6H10N3O
140.0936	C5H10N5
140.1188	C7H14N3
141.0776	C5H9N4O
141.0889	C4H9N6
141.0902	C6H11N3O
141.1028	C7H13N2O
141.1140	C6H13N4
141.1392	C8H17N2
142.0617	C5H8N3O2
142.0729	C4H8N5O
142.0841	C3H8N7
142.0980	C6H12N3O
142.1093	C5H12N5
142.1344	C7H16N3
143.0569	C4H7N4O2
143.0681	C3H7N6O
143.0933	C5H11N4O
143.1045	C4H11N6
143.1297	C6H15N4
144.0773	C5H10N3O2
144.1137	C6H14N3O
145.0977	C6H13N2O2
146.0930	C5H12N3O2
147.0671	C7H7N4

148.0623	C6H6N5	162.0780	C7H8N5	173.1039	C6H13N4O2
148.0762	C9H10NO	162.0793	C9H10N2O	174.0780	C8H8N5
148.0875	C8H10N3	163.0620	C7H7N4O	175.0732	C7H7N6
149.0701	C6H7N5	163.0732	C6H7N6	175.0984	C9H11N4
149.0827	C7H9N4	163.0984	C8H11N4	176.0685	C6H6N7
150.0654	C5H6N6	164.0572	C6H6N5O	176.0936	C8H10N5
150.0780	C6H8N5	164.0685	C5H6N7	176.1188	C10H14N3
150.1031	C8H12N3	164.0936	C7H10N5	177.0889	C7H9N6
151.0620	C6H7N4O	164.0950	C9H12N2O	177.0902	C9H11N3O
151.0732	C5H7N6	164.1188	C9H14N3	177.1140	C9H13N4
151.0984	C7H11N4	165.0776	C7H9N4O	178.0729	C7H8N5O
152.0572	C5H6N5O	165.0889	C6H9N6	178.0841	C6H8N7
152.0685	C4H6N7	165.1140	C8H13N4	178.1093	C8H12N5
152.0698	C6H8N4O	166.0729	C6H8N5O	179.0681	C6H7N6O
152.0824	C7H10N3O	166.0841	C5H8N7	179.0794	C5H7N8
152.0936	C6H10N5	166.0980	C8H12N3O	179.0933	C8H11N4O
152.1188	C8H14N3	166.1093	C7H12N5	179.1045	C7H11N6
153.0776	C6H9N4O	166.1344	C9H16N3	179.1297	C9H15N4
153.0889	C5H9N6	167.0371	C11H5NO	180.0634	C5H6N7O
153.0902	C7H11N3O	167.0681	C5H7N6O	180.0885	C7H10N5O
153.1140	C7H13N4	167.0794	C4H7N8	180.0998	C6H10N7
154.0617	C6H8N3O2	167.0933	C7H11N4O	180.1249	C8H14N5
154.0729	C5H8N5O	167.1045	C6H11N6	181.0726	C7H9N4O2
154.0841	C4H8N7	167.1059	C8H13N3O	181.0838	C6H9N6O
154.0980	C7H12N3O	167.1297	C8H15N4	181.0950	C5H9N8
154.1093	C6H12N5	168.0885	C6H10N5O	181.1089	C8H13N4O
154.1344	C8H16N3	168.0998	C5H10N7	181.1202	C7H13N6
155.0569	C5H7N4O2	168.1011	C7H12N4O	181.1453	C9H17N4
155.0681	C4H7N6O	168.1137	C8H14N3O	182.0678	C6H8N5O2
155.0933	C6H11N4O	168.1249	C7H14N5	182.0790	C5H8N7O
155.1045	C5H11N6	168.1501	C9H18N3	182.1042	C7H12N5O
155.1297	C7H15N4	169.0726	C6H9N4O2	182.1154	C6H12N7
156.0773	C6H10N3O2	169.0838	C5H9N6O	182.1406	C8H16N5
156.0885	C5H10N5O	169.0950	C4H9N8	183.0882	C7H11N4O2
156.0998	C4H10N7	169.0977	C8H13N2O2	183.0994	C6H11N6O
156.1137	C7H14N3O	169.1089	C7H13N4O	183.1107	C5H11N8
156.1249	C6H14N5	169.1202	C6H13N6	183.1246	C8H15N4O
157.0726	C5H9N4O2	169.1453	C8H17N4	183.1358	C7H15N6
157.1089	C6H13N4O	170.0678	C5H8N5O2	184.0835	C6H10N5O2
157.1202	C5H13N6	170.0790	C4H8N7O	184.0947	C5H10N7O
158.0678	C4H8N5O2	170.0930	C7H12N3O2	184.1198	C7H14N5O
158.0930	C6H12N3O2	170.1042	C6H12N5O	184.1311	C6H14N7
158.1545	C9H20NO	170.1154	C5H12N7	185.1039	C7H13N4O2
159.0882	C5H11N4O2	171.0882	C6H11N4O2	185.1151	C6H13N6O
159.1134	C7H15N2O2	171.0994	C5H11N6O	186.0780	C9H8N5
160.0623	C7H6N5	171.1246	C7H15N4O	186.0991	C6H12N5O2
160.0722	C5H10N3O3	171.1497	C9H19N2O	187.0732	C8H7N6
161.0827	C8H9N4	172.0835	C5H10N5O2	188.0685	C7H6N7

188.0936	C9H10N5	203.0794	C7H7N8	217.0950	C8H9N8
189.0889	C8H9N6	203.1045	C9H11N6	217.1202	C10H13N6
189.1140	C10H13N4	204.0746	C6H6N9	218.0790	C8H8N7O
190.0841	C7H8N7	204.0998	C8H10N7	218.0903	C7H8N9
190.1093	C9H12N5	204.1249	C10H14N5	218.1154	C9H12N7
191.0794	C6H7N8	205.0838	C8H9N6O	218.1406	C11H16N5
191.1045	C8H11N6	205.0950	C7H9N8	219.0855	C6H7N10
191.1297	C10H15N4	205.1202	C9H13N6	219.0994	C9H11N6O
192.0885	C8H10N5O	206.0790	C7H8N7O	219.1107	C8H11N8
192.0998	C7H10N7	206.0903	C6H8N9	219.1358	C10H15N6
192.1249	C9H14N5	206.1042	C9H12N5O	221.0787	C8H9N6O2
193.0838	C7H9N6O	206.1154	C8H12N7	221.0899	C7H9N8O
193.0950	C6H9N8	206.1406	C10H16N5	221.1012	C6H9N10
193.1089	C9H13N4O	207.0994	C8H11N6O	221.1052	C12H15NO3
193.1202	C8H13N6	207.1107	C7H11N8	221.1151	C9H13N6O
193.1453	C10H17N4	207.1192	C3H13N9O2	221.1263	C8H13N8
194.0678	C7H8N5O2	207.1246	C10H15N4O	221.1515	C10H17N6
194.0790	C6H8N7O	207.1358	C9H15N6	222.0991	C9H12N5O2
194.0903	C5H8N9	208.0947	C7H10N7O	222.1103	C8H12N7O
194.0930	C9H12N3O2	208.1059	C6H10N9	222.1216	C7H12N9
194.1042	C8H12N5O	208.1198	C9H14N5O	222.1243	C11H16N3O2
194.1154	C7H12N7	208.1311	C8H14N7	222.1355	C10H16N5O
194.1240	C3H14N8O2	208.1562	C10H18N5	222.1467	C9H16N7
194.1406	C9H16N5	209.0787	C7H9N6O2	223.0633	C14H9NO2
195.0994	C7H11N6O	209.0899	C6H9N8O	223.0943	C8H11N6O2
195.1107	C6H11N8	209.1012	C5H9N10	223.1056	C7H11N8O
195.1246	C9H15N4O	209.1151	C8H13N6O	223.1168	C6H11N10
195.1358	C8H15N6	209.1263	C7H13N8	223.1307	C9H15N6O
195.1610	C10H19N4	209.1515	C9H17N6	223.1671	C10H19N6
196.0835	C7H10N5O2	210.0991	C8H12N5O2	224.1260	C8H14N7O
196.0947	C6H10N7O	210.1103	C7H12N7O	224.1624	C9H18N7
196.1059	C5H10N9	210.1216	C6H12N9	224.2014	C14H26NO
196.1198	C8H14N5O	210.1355	C9H16N5O	225.1464	C9H17N6O
196.1311	C7H14N7	210.1467	C8H16N7	225.1576	C8H17N8
196.1562	C9H18N5	211.0943	C7H11N6O2	226.0841	C10H8N7
197.0787	C6H9N6O2	211.1056	C6H11N8O	228.0998	C10H10N7
197.1039	C8H13N4O2	211.1168	C5H11N10	229.0950	C9H9N8
197.1151	C7H13N6O	211.1307	C8H15N6O	230.1154	C10H12N7
197.1263	C6H13N8	211.1420	C7H15N8	231.1107	C9H11N8
197.1515	C8H17N6	212.0896	C6H10N7O2	231.1358	C11H15N6
198.0991	C7H12N5O2	212.1148	C8H14N5O2	232.1059	C8H10N9
198.1103	C6H12N7O	212.1260	C7H14N7O	232.1311	C10H14N7
198.1355	C8H16N5O	213.0889	C10H9N6	232.1562	C12H18N5
200.0936	C10H10N5	214.1093	C11H12N5	233.0899	C8H9N8O
200.1148	C7H14N5O2	215.1045	C10H11N6	233.1012	C7H9N10
201.0889	C9H9N6	216.0998	C9H10N7	233.1151	C10H13N6O
202.0841	C8H8N7	216.1249	C11H14N5	233.1263	C9H13N8
202.1093	C10H12N5	217.0838	C9H9N6O	233.1528	C13H19N3O

234.1103	C9H12N7O	250.1780	C11H20N7	272.1372	C11H14N9
234.1216	C8H12N9	250.1794	C13H22N4O	272.1386	C13H16N6O
234.1467	C10H16N7	251.1382	C11H17N5O2	273.1212	C11H13N8O
235.1056	C8H11N8O	251.1481	C8H15N10	273.1325	C10H13N10
235.1168	C7H11N10	251.1733	C10H19N8	273.1338	C12H15N7O
235.1307	C10H15N6O	254.1168	C14H14N4O	273.1590	C14H19N5O
235.1420	C9H15N8	255.1107	C11H11N8	273.1886	C6H19N13
235.1671	C11H19N6	255.1120	C13H13N5O	273.1900	C8H21N10O
236.1008	C7H10N9O	256.1059	C10H10N9	274.1277	C9H12N11
236.1121	C6H10N11	256.1073	C12H12N6O	274.1291	C11H14N8O
236.1260	C9H14N7O	256.1311	C12H14N7	274.1416	C12H16N7O
236.1386	C10H16N6O	256.1324	C14H16N4O	274.1529	C11H16N9
236.1624	C10H18N7	257.1277	C13H15N5O	274.1542	C13H18N6O
237.1100	C9H13N6O2	258.1103	C11H12N7O	276.1335	C12H16N6O2
237.1212	C8H13N8O	258.1216	C10H12N9	276.1434	C9H14N11
237.1576	C9H17N8	258.1481	C14H18N4O	276.1699	C13H20N6O
238.0352	C9H2N8O	259.1056	C10H11N8O	277.1539	C13H19N5O2
238.0801	C6H8N9O2	259.1168	C9H11N10	277.1638	C10H17N10
238.1416	C9H16N7O	259.1182	C11H13N7O	277.1651	C12H19N7O
238.1430	C11H18N4O2	259.1433	C13H17N5O	277.1889	C12H21N8
238.1529	C8H16N9	260.1134	C10H12N8O	277.1903	C14H23N5O
239.0416	C7HN11	260.1386	C12H16N6O	278.1491	C12H18N6O2
241.0964	C12H11N5O	260.1637	C14H20N4O	278.1842	C11H20N9
242.1154	C11H12N7	261.1113	C13H15N3O3	278.1855	C13H22N6O
243.1358	C12H15N6	261.1212	C10H13N8O	282.1216	C12H12N9
244.1073	C11H12N6O	261.1325	C9H13N10	282.1229	C14H14N6O
244.1324	C13H16N4O	261.1338	C11H15N7O	283.1420	C13H15N8
245.1012	C8H9N10	261.1590	C13H19N5O	283.1433	C15H17N5O
245.1025	C10H11N7O	262.1430	C13H18N4O2	284.1372	C12H14N9
245.1277	C12H15N5O	262.1542	C12H18N6O	284.1386	C14H16N6O
245.1528	C14H19N3O	262.1780	C12H20N7	285.1325	C11H13N10
246.1103	C10H12N7O	262.1794	C14H22N4O	285.1338	C13H15N7O
246.1467	C11H16N7	263.1382	C12H17N5O2	285.1590	C15H19N5O
247.1168	C8H11N10	263.1481	C9H15N10	286.1529	C12H16N9
247.1307	C11H15N6O	263.1733	C11H19N8	286.1542	C14H18N6O
247.1433	C12H17N5O	263.1746	C13H21N5O	287.1481	C11H15N10
247.1685	C14H21N3O	264.1335	C11H16N6O2	287.1495	C13H17N7O
248.1386	C11H16N6O	264.1685	C10H18N9	287.1733	C13H19N8
249.1212	C9H13N8O	264.1699	C12H20N6O	288.1321	C11H14N9O
249.1226	C11H15N5O2	268.1059	C11H10N9	288.1335	C13H16N6O2
249.1338	C10H15N7O	269.1263	C12H13N8	288.1434	C10H14N11
249.1576	C10H17N8	269.1277	C14H15N5O	288.1447	C12H16N8O
249.1828	C12H21N6	270.1216	C11H12N9	288.1685	C12H18N9
250.1066	C11H14N4O3	270.1229	C13H14N6O	288.1699	C14H20N6O
250.1178	C10H14N6O2	271.1168	C10H11N10	289.1512	C10H15N11
250.1277	C7H12N11	271.1182	C12H13N7O	289.1638	C11H17N10
250.1430	C12H18N4O2	271.1420	C12H15N8	289.1651	C13H19N7O
250.1529	C9H16N9	271.1433	C14H17N5O	289.1903	C15H23N5O

290.1491	C13H18N6O2
290.1590	C10H16N11
290.1842	C12H20N9
290.1855	C14H22N6O
296.1287	C18H18NO3
296.1386	C15H16N6O
297.1325	C12H13N10
297.1338	C14H15N7O
298.1529	C13H16N9
298.1542	C15H18N6O
299.1481	C12H15N10
299.1495	C14H17N7O
299.1733	C14H19N8

Molecules exclusively present in P_{400}

59.0609	C2H7N2
72.0562	C2H6N3
73.0766	C3H9N2
86.0480	C3H6N2O
87.0671	C2H7N4
99.0545	C2H5N5
102.0793	C4H10N2O
103.0620	C2H7N4O
112.0637	C5H8N2O
113.0589	C4H7N3O
114.0793	C5H10N2O
126.0654	C3H6N6
126.0793	C6H10N2O
128.0712	C6H10NO2
129.0889	C3H9N6
138.0542	C5H6N4O
140.0810	C4H8N6
140.0950	C7H12N2O
142.0742	C6H10N2O2
149.0841	C9H11NO
149.0953	C8H11N3
150.0793	C8H10N2O
151.0606	C4H5N7
151.0746	C7H9N3O
152.0712	C8H10NO2
152.0950	C8H12N2O
153.0651	C5H7N5O
154.0742	C7H10N2O2
154.0855	C6H10N4O
154.0868	C8H12NO2
155.0807	C5H9N5O
155.0946	C8H13NO2
157.0838	C4H9N6O
157.0950	C3H9N8
159.0895	C7H13NO3
161.0589	C8H7N3O
163.0746	C8H9N3O
164.0810	C6H8N6
165.0763	C5H7N7
165.0862	C3H11N5O3
165.0902	C8H11N3O
166.0855	C7H10N4O
166.0868	C9H12NO2
167.0807	C6H9N5O
168.1025	C9H14NO2
169.0851	C7H11N3O2
169.0891	C12H11N
169.0964	C6H11N5O
170.0916	C5H10N6O
173.0265	C13H3N
175.0422	C13H5N
177.0763	C6H7N7
178.0657	C13H8N
178.0814	C3H10N6O3
178.0855	C8H10N4O
178.0868	C10H12NO2
179.0821	C9H11N2O2
180.0760	C6H8N6O
180.1011	C8H12N4O
181.0977	C9H13N2O2
181.1467	C11H19NO
182.0903	C4H8N9
183.0630	C5H7N6O2
183.1008	C8H13N3O2
183.1120	C7H13N5O
184.1059	C4H10N9
184.1324	C8H16N4O
185.0787	C5H9N6O2
185.0899	C4H9N8O
191.0681	C7H7N6O
191.0919	C7H9N7
192.0746	C5H6N9
192.0872	C6H8N8
192.1025	C11H14NO2
193.0977	C10H13N2O2
195.0630	C6H7N6O2
195.0743	C5H7N8O
195.0869	C6H9N7O
197.0899	C5H9N8O
198.1216	C5H12N9
199.0943	C6H11N6O2
199.1056	C5H11N8O
199.1069	C7H13N5O2
203.0807	C9H9N5O
204.0634	C7H6N7O
204.1011	C10H12N4O
206.1028	C7H10N8
206.1168	C10H14N4O
207.0141	C5HN7O3
207.0684	C14H9NO
207.0743	C6H7N8O
207.0981	C6H9N9
207.1120	C9H13N5O
208.0933	C5H8N10
208.1126	C15H14N
208.1212	C11H16N2O2
208.1324	C10H16N4O
209.1079	C14H13N2
209.1277	C9H15N5O
214.0841	C9H8N7
214.1304	C8H16N5O2
215.0794	C8H7N8
217.0824	C7H7N9
218.0930	C11H12N3O2
219.0743	C7H7N8O
219.0981	C7H9N9
219.1134	C12H15N2O2
220.0947	C8H10N7O
220.1059	C7H10N9
220.1198	C10H14N5O
220.1311	C9H14N7
220.1562	C11H18N5
221.1290	C12H17N2O2
222.0852	C6H8N9O
222.0978	C7H10N8O
223.1420	C8H15N8
224.0896	C7H10N7O2
224.1008	C6H10N9O
224.1386	C9H16N6O
225.1087	C6H11N9O
225.1212	C7H13N8O
225.1325	C6H13N10
226.1052	C7H12N7O2
226.1165	C6H12N9O
227.0794	C9H7N8
228.0746	C8H6N9
229.1202	C11H13N6
230.0903	C8H8N9

231.0855	C7H7N10	247.1182	C10H13N7O	261.1073	C7H9N12
232.0960	C11H12N4O2	247.1195	C12H15N4O2	261.1087	C9H11N9O
232.1086	C12H14N3O2	247.1420	C10H15N8	261.1226	C12H15N5O2
233.1515	C11H17N6	247.1671	C12H19N6	261.1576	C11H17N8
234.0852	C7H8N9O	248.1008	C8H10N9O	262.1151	C7H10N12
234.0964	C6H8N11	248.1022	C10H12N6O2	262.1178	C11H14N6O2
234.0978	C8H10N8O	248.1121	C7H10N11	262.1277	C8H12N11
234.1243	C12H16N3O2	248.1246	C8H12N10	262.1291	C10H14N8O
234.1301	C4H14N10O2	248.1273	C12H16N4O2	262.1317	C14H18N2O3
234.1341	C9H14N8	248.1399	C13H18N3O2	262.1403	C9H14N10
235.0943	C9H11N6O2	248.1624	C11H18N7	262.1529	C10H16N9
235.1069	C10H13N5O2	249.0947	C5H7N13	263.1117	C8H11N10O
236.0896	C8H10N7O2	249.0974	C9H11N7O2	263.1131	C10H13N7O2
236.0909	C10H12N4O3	249.1352	C12H17N4O2	263.1230	C7H11N12
236.1188	C15H14N3	249.1424	C6H17N8O3	263.1243	C9H13N9O
236.1399	C12H18N3O2	250.1039	C7H10N10O	263.1355	C8H13N11
237.0835	C5H7N11O	250.1165	C8H12N9O	263.1495	C11H17N7O
237.0961	C6H9N10O	250.1291	C9H14N8O	264.1308	C7H12N12
237.1087	C7H11N9O	250.1416	C10H16N7O	264.1434	C8H14N11
237.1154	C16H15NO	250.1542	C11H18N6O	264.1447	C10H16N8O
237.1325	C7H13N10	251.1005	C8H11N8O2	264.1559	C9H16N10
237.1338	C9H15N7O	251.1104	C5H9N13	265.1148	C7H11N11O
237.1464	C10H17N6O	251.1131	C9H13N7O2	265.1260	C6H11N13
238.1052	C8H12N7O2	251.1230	C6H11N12	265.1287	C10H15N7O2
238.1151	C5H10N12	251.1369	C9H15N8O	265.1512	C8H15N11
238.1165	C7H12N9O	251.1495	C10H17N7O	265.1539	C12H19N5O2
238.1542	C10H18N6O	251.1746	C12H21N5O	265.1638	C9H17N10
239.1256	C9H15N6O2	252.1209	C9H14N7O2	265.1651	C11H19N7O
239.1369	C8H15N8O	252.1308	C6H12N12	266.1464	C7H14N12
240.0998	C11H10N7	252.1335	C10H16N6O2	266.1590	C8H16N11
240.1209	C8H14N7O2	252.1685	C9H18N9	268.1073	C13H12N6O
241.0950	C10H9N8	252.1699	C11H20N6O	269.1012	C10H9N10
242.0903	C9H8N9	254.0903	C10H8N9	269.1025	C12H11N7O
242.1168	C13H14N4O	257.1012	C9H9N10	270.0978	C11H10N8O
243.0855	C8H7N10	257.1025	C11H11N7O	270.1467	C13H16N7
243.0869	C10H9N7O	257.1263	C11H13N8	272.1121	C9H10N11
243.1107	C10H11N8	258.0964	C8H8N11	272.1134	C11H12N8O
243.1372	C14H17N3O	258.1229	C12H14N6O	272.1624	C13H18N7
244.1059	C9H10N9	258.1467	C12H16N7	273.1073	C8H9N12
244.1311	C11H14N7	259.1069	C12H13N5O2	273.1087	C10H11N9O
245.0886	C7H7N11	259.1420	C11H15N8	273.1226	C13H15N5O2
245.1263	C10H13N8	260.0995	C7H8N12	273.1576	C12H17N8
245.1515	C12H17N6	260.1022	C11H12N6O2	274.1151	C8H10N12
246.0838	C6H6N12	260.1121	C8H10N11	274.1178	C12H14N6O2
246.0964	C7H8N11	260.1246	C9H12N10	274.1780	C13H20N7
246.1216	C9H12N9	260.1372	C10H14N9	275.1104	C7H9N13
246.1481	C13H18N4O	260.1624	C12H18N7	275.1131	C11H13N7O2
247.1042	C7H9N11	261.0961	C8H9N10O	275.1230	C8H11N12

275.1243	C10H13N9O
275.1355	C9H13N11
275.1382	C13H17N5O2
275.1481	C10H15N10
275.1495	C12H17N7O
275.1733	C12H19N8
275.1746	C14H21N5O
276.1182	C7H10N13
276.1308	C8H12N12
276.1447	C11H16N8O
276.1559	C10H16N10
276.1685	C11H18N9
277.1260	C7H11N13
277.1287	C11H15N7O2
277.1386	C8H13N12
277.1400	C10H15N9O
277.1512	C9H15N11
278.1127	C11H14N6O3
278.1226	C8H12N11O
278.1240	C10H14N8O2
278.1339	C7H12N13
278.1352	C9H14N10O
278.1464	C8H14N12
278.1590	C9H16N11
278.1604	C11H18N8O
283.1168	C11H11N10
283.1182	C13H13N7O
284.1121	C10H10N11
284.1134	C12H12N8O
285.1073	C9H9N12
285.1087	C11H11N9O
285.1576	C13H17N8
286.1277	C10H12N11
286.1291	C12H14N8O
287.1104	C8H9N13
287.1230	C9H11N12
287.1243	C11H13N9O
288.1182	C8H10N13
288.1196	C10H12N10O
289.1260	C8H11N13
289.1287	C12H15N7O2
289.1386	C9H13N12
289.1400	C11H15N9O
289.1889	C13H21N8
290.1213	C7H10N14
290.1312	C5H14N12O3
290.1352	C10H14N10O
290.1464	C9H14N12
290.1604	C12H18N8O
291.1417	C8H13N13
291.1444	C12H17N7O2
291.1543	C9H15N12
291.1556	C11H17N9O
291.1628	C5H17N13O2
291.1709	C16H23N2O3
291.1754	C6H19N12O2
291.1794	C11H19N10
291.1808	C13H21N7O
291.1866	C5H19N14O
291.2046	C13H23N8
292.1369	C7H12N14
292.1509	C10H16N10O
292.1621	C9H16N12
292.1747	C10H18N11
292.1760	C12H20N8O
296.1121	C11H10N11
298.1277	C11H12N11
298.1291	C13H14N8O
299.1230	C10H11N12
299.1243	C12H13N9O

Molecules exclusively present in P_{650}

84.0813	C5H10N
85.0528	C4H7NO
95.0609	C5H7N2
96.0813	C6H10N
98.0606	C5H8NO
99.0684	C5H9NO
101.0715	C4H9N2O
107.0609	C6H7N2
110.0606	C6H8NO
110.0970	C7H12N
111.0796	C5H9N3
113.0841	C6H11NO
114.0919	C6H12NO
115.1235	C6H15N2
116.1188	C5H14N3
118.0868	C5H12NO2
121.0766	C7H9N2
122.0970	C8H12N
123.0684	C7H9NO
123.0796	C6H9N3
125.0715	C6H9N2O
127.0508	C5H7N2O2
127.0620	C4H7N4O
127.0732	C3H7N6
127.0871	C6H11N2O
127.0984	C5H11N4
127.0997	C7H13NO
127.1235	C7H15N2
132.0562	C7H6N3
132.1025	C6H14NO2
133.0766	C8H9N2
135.0796	C7H9N3
135.0922	C8H11N2
136.0511	C6H6N3O
137.0715	C7H9N2O
137.1079	C8H13N2
138.0905	C6H10N4
139.0871	C7H11N2O
140.0460	C5H6N3O2
141.0664	C6H9N2O2
143.0821	C6H11N2O2
143.0946	C7H13NO2
143.1184	C7H15N2O
143.1310	C8H17NO
145.0726	C4H9N4O2
146.0718	C8H8N3
147.0922	C9H11N2
148.0511	C7H6N3O
148.0749	C7H8N4
149.0800	C4H11N3O3
149.1079	C9H13N2
150.0667	C7H8N3O
150.0865	C2H10N6O2
151.0871	C8H11N2O
151.1235	C9H15N2
153.1028	C8H13N2O
153.1154	C9H15NO
153.1392	C9H17N2
154.1106	C8H14N2O
155.0821	C7H11N2O2
155.1059	C7H13N3O
155.1184	C8H15N2O
155.1548	C9H19N2
156.0522	C4H6N5O2
156.1501	C8H18N3
157.1341	C8H17N2O
157.1453	C7H17N4
158.0718	C9H8N3
158.1293	C7H16N3O
159.0671	C8H7N4
160.0875	C9H10N3

161.0715	C9H9N2O	178.1344	C10H16N3	194.0691	C9H10N2O3
161.0953	C9H11N3	179.1059	C9H13N3O	194.1293	C10H16N3O
161.1079	C10H13N2	179.1131	C3H13N7O2	194.1657	C11H20N3
162.0667	C8H8N3O	179.1548	C11H19N2	195.0882	C8H11N4O2
162.0865	C3H10N6O2	180.1137	C9H14N3O	196.1086	C9H14N3O2
162.0905	C8H10N4	180.1501	C10H18N3	196.1450	C10H18N3O
162.1031	C9H12N3	181.1341	C10H17N2O	196.1814	C11H22N3
163.0858	C7H9N5	181.1705	C11H21N2	197.1402	C9H17N4O
163.0997	C10H13NO	182.0930	C8H12N3O2	197.1766	C10H21N4
163.1069	C4H13N5O2	182.1293	C9H16N3O	198.0780	C10H8N5
163.1235	C10H15N2	182.1657	C10H20N3	198.1031	C12H12N3
164.0824	C8H10N3O	183.1610	C9H19N4	198.1243	C9H16N3O2
164.1022	C3H12N6O2	184.0875	C11H10N3	198.1606	C10H20N3O
164.1062	C8H12N4	184.1086	C8H14N3O2	199.0732	C9H7N6
165.1028	C9H13N2O	184.1450	C9H18N3O	199.0831	C7H11N4O3
165.1392	C10H17N2	184.1562	C8H18N5	199.0984	C11H11N4
166.1106	C9H14N2O	185.0827	C10H9N4	199.1195	C8H15N4O2
167.1184	C9H15N2O	185.0841	C12H11NO	199.1307	C7H15N6O
167.1310	C10H17NO	185.1402	C8H17N4O	200.1188	C12H14N3
167.1548	C10H19N2	186.1031	C11H12N3	200.1399	C9H18N3O2
168.0773	C7H10N3O2	186.1243	C8H16N3O2	201.0776	C10H9N4O
169.1341	C9H17N2O	187.0858	C9H9N5	201.1014	C10H11N5
170.1293	C8H16N3O	187.0984	C10H11N4	201.1140	C11H13N4
170.1406	C7H16N5	187.1235	C12H15N2	202.0729	C9H8N5O
170.1657	C9H20N3	188.0810	C8H8N6	202.0927	C4H10N8O2
171.0671	C9H7N4	188.0824	C10H10N3O	202.0980	C11H12N3O
171.1134	C8H15N2O2	188.1188	C11H14N3	202.1192	C8H16N3O3
172.0623	C8H6N5	189.0776	C9H9N4O	202.1344	C12H16N3
172.0875	C10H10N3	189.0974	C4H11N7O2	203.0933	C10H11N4O
172.1086	C7H14N3O2	189.1392	C12H17N2	203.1131	C5H13N7O2
173.0827	C9H9N4	190.0729	C8H8N5O	203.1297	C11H15N4
173.1079	C11H13N2	190.0927	C3H10N8O2	203.1548	C13H19N2
173.1290	C8H17N2O2	190.0980	C10H12N3O	204.0885	C9H10N5O
174.1031	C10H12N3	190.1178	C5H14N6O2	204.1083	C4H12N8O2
175.0620	C8H7N4O	190.1344	C11H16N3	204.1137	C11H14N3O
175.1235	C11H15N2	191.0933	C9H11N4O	204.1335	C6H16N6O2
176.0810	C7H8N6	191.1131	C4H13N7O2	204.1501	C12H18N3
176.0824	C9H10N3O	191.1171	C9H13N5	205.1036	C3H11N9O2
176.1022	C4H12N6O2	191.1382	C6H17N5O2	205.1089	C10H13N4O
177.0776	C8H9N4O	191.1548	C12H19N2	205.1287	C5H15N7O2
177.0974	C3H11N7O2	192.1083	C3H12N8O2	205.1453	C11H17N4
177.1014	C8H11N5	192.1123	C8H12N6	206.1240	C4H14N8O2
177.1154	C11H15NO	192.1137	C10H14N3O	206.1293	C11H16N3O
177.1226	C5H15N5O2	192.1335	C5H16N6O2	206.1491	C6H18N6O2
177.1392	C11H17N2	192.1501	C11H18N3	206.1657	C12H20N3
178.0980	C9H12N3O	193.1287	C4H15N7O2	207.0882	C9H11N4O2
178.1106	C10H14N2O	193.1341	C11H17N2O	207.1444	C5H17N7O2
178.1178	C4H14N6O2	193.1705	C12H21N2	207.1610	C11H19N4

207.1682	C5H19N8O	221.1587	C4H17N10O	231.0994	C10H11N6O
208.0835	C8H10N5O2	221.1600	C6H19N7O2	231.1120	C11H13N5O
208.1158	C4H14N7O3	221.1766	C12H21N4	231.1232	C10H13N7
208.1396	C4H16N8O2	222.1606	C12H20N3O	231.1246	C12H15N4O
208.1450	C11H18N3O	222.1719	C11H20N5	231.1259	C14H17NO2
208.1634	C4H18N9O	222.1791	C5H20N9O	231.1444	C7H17N7O2
208.1814	C12H22N3	222.1970	C13H24N3	231.1623	C15H21NO
209.1039	C9H13N4O2	223.1195	C10H15N4O2	232.0947	C9H10N7O
209.1349	C3H15N9O2	223.1321	C11H17N3O2	232.1073	C10H12N6O
209.1402	C10H17N4O	223.1433	C10H17N5O	232.1198	C11H14N5O
209.1766	C11H21N4	223.1505	C4H17N9O2	232.1338	C14H18NO2
210.1229	C8H14N6O	223.1559	C11H19N4O	232.1383	C4H14N11O
210.1606	C11H20N3O	223.1743	C4H19N10O	232.1450	C13H18N3O
210.1719	C10H20N5	223.1923	C12H23N4	232.1634	C6H18N9O
210.1970	C12H24N3	224.0936	C12H10N5	232.1648	C8H20N6O2
211.0746	C12H9N3O	224.1148	C9H14N5O2	232.1814	C14H22N3
211.0984	C12H11N4	224.1372	C7H14N9	233.1349	C5H15N9O2
211.1195	C9H15N4O2	224.1399	C11H18N3O2	233.1402	C12H17N4O
211.1433	C9H17N5O	224.1511	C10H18N5O	233.1600	C7H19N7O2
211.1559	C10H19N4O	224.1875	C11H22N5	233.1766	C13H21N4
211.1671	C9H19N6	225.0889	C11H9N6	234.0991	C10H12N5O2
211.1936	C13H25NO	225.1100	C8H13N6O2	234.1229	C10H14N6O
212.0936	C11H10N5	225.1140	C13H13N4	234.1368	C13H18N2O2
212.1188	C13H14N3	225.1365	C12H19NO3	234.1553	C6H18N8O2
212.1399	C10H18N3O2	225.1715	C11H21N4O	234.1606	C13H20N3O
212.1511	C9H18N5O	225.1729	C13H23NO2	234.1719	C12H20N5
213.0902	C12H11N3O	225.1828	C10H21N6	234.1791	C6H20N9O
213.1140	C12H13N4	226.1093	C12H12N5	234.1804	C8H22N6O2
214.0855	C11H10N4O	226.1304	C9H16N5O2	234.1970	C14H24N3
214.1344	C13H16N3	226.1556	C11H20N3O2	235.0957	C11H13N3O3
215.1297	C12H15N4	226.1668	C10H20N5O	235.1182	C9H13N7O
216.0885	C10H10N5O	227.0933	C12H11N4O	235.1505	C5H17N9O2
216.0899	C12H12N2O2	227.1045	C11H11N6	235.1559	C12H19N4O
216.1501	C13H18N3	227.1297	C13H15N4	235.1743	C5H19N10O
217.1103	C13H15NO2	228.1263	C14H16N2O	235.1757	C7H21N7O2
217.1287	C6H15N7O2	228.1501	C14H18N3	235.1923	C13H23N4
217.1453	C12H17N4	229.1103	C14H15NO2	236.1148	C10H14N5O2
218.1055	C12H14N2O2	229.1215	C13H15N3O	236.1161	C12H16N2O3
218.1240	C5H14N8O2	229.1287	C7H15N7O2	236.1372	C8H14N9
218.1293	C12H16N3O	229.1467	C15H19NO	236.1511	C11H18N5O
218.1491	C7H18N6O2	230.0916	C10H10N6O	236.1709	C6H20N8O2
218.1657	C13H20N3	230.1042	C11H12N5O	236.1763	C13H22N3O
219.1192	C4H13N9O2	230.1055	C13H14N2O2	236.1875	C12H22N5
219.1259	C13H17NO2	230.1226	C4H12N11O	236.2127	C14H26N3
219.1444	C6H17N7O2	230.1280	C11H14N6	237.1352	C11H17N4O2
219.1610	C12H19N4	230.1406	C12H16N5	237.1365	C13H19NO3
221.1349	C4H15N9O2	230.1478	C6H16N9O	237.1477	C12H19N3O2
221.1402	C11H17N4O	230.1657	C14H20N3	237.1715	C12H21N4O

237.1729	C14H23NO2
237.1828	C11H21N6
237.2079	C13H25N4
237.2093	C15H27NO
238.0814	C8H10N6O3
238.0841	C11H8N7
238.1093	C13H12N5
238.1106	C15H14N2O
238.1304	C10H16N5O2
238.1556	C12H20N3O2
238.1668	C11H20N5O
238.1681	C13H22N2O2
238.1780	C10H20N7
238.2032	C12H24N5
239.0767	C7H9N7O3
239.1045	C12H11N6
239.1059	C14H13N3O
239.1270	C11H17N3O3
239.1297	C14H15N4
239.1508	C11H19N4O2
239.1620	C10H19N6O
239.1634	C12H21N3O2
239.1998	C13H25N3O
240.1011	C13H12N4O
240.1249	C13H14N5
240.1461	C10H18N5O2
241.1202	C12H13N6
241.1453	C14H17N4
242.1406	C13H16N5
242.1657	C15H20N3
243.0994	C11H11N6O
243.1008	C13H13N3O2
243.1120	C12H13N5O
243.1259	C15H17NO2
243.1444	C8H17N7O2
243.1610	C14H19N4
243.1623	C16H21NO
244.0960	C12H12N4O2
244.1198	C12H14N5O
244.1396	C7H16N8O2
244.1562	C13H18N5
244.1634	C7H18N9O
244.1814	C15H22N3
245.0899	C9H9N8O
245.1151	C11H13N6O
245.1164	C13H15N3O2
245.1290	C14H17N2O2
245.1335	C4H13N12O
245.1402	C13H17N4O
245.1587	C6H17N10O
245.1614	C10H21N4O3
245.1766	C14H21N4
246.1117	C12H14N4O2
246.1229	C11H14N6O
246.1243	C13H16N3O2
246.1301	C5H14N10O2
246.1355	C12H16N5O
246.1494	C15H20NO2
246.1539	C5H16N11O
246.1553	C7H18N8O2
246.1719	C13H20N5
246.1818	C11H24N3O3
246.1970	C15H24N3
247.1056	C9H11N8O
247.1492	C4H15N12O
247.1505	C6H17N9O2
247.1559	C13H19N4O
247.1572	C15H21NO2
247.1743	C6H19N10O
247.1757	C8H21N7O2
247.1923	C14H23N4
248.1148	C11H14N5O2
248.1260	C10H14N7O
248.1458	C5H16N10O2
248.1511	C12H18N5O
248.1637	C13H20N4O
248.1696	C5H18N11O
248.1723	C9H22N5O3
248.1763	C14H22N3O
248.1889	C15H24N2O
248.1947	C7H22N9O
248.2127	C15H26N3
249.1100	C10H13N6O2
249.1113	C12H15N3O3
249.1325	C8H13N10
249.1365	C14H19NO3
249.1477	C13H19N3O2
249.1662	C6H19N9O2
249.1675	C8H21N6O3

List of molecules detected with APPI-/Orbitrap and identified with *Attributor* software in the soluble fraction of samples P_{400} and P_{650}

Molecules common to P_{400} and P_{650}

107.0371	C6H5NO
117.0215	C7H3NO
120.0562	C6H6N3
121.0514	C5H5N4
121.0528	C7H7NO
122.0354	C5H4N3O
122.0467	C4H4N5
123.0671	C5H7N4
124.0511	C5H6N3O
124.0623	C4H6N5
125.0463	C4H5N4O
125.0576	C3H5N6
126.0304	C4H4N3O2
130.0405	C7H4N3
131.0371	C8H5NO
133.0514	C6H5N4
133.0528	C8H7NO
134.0354	C6H4N3O
134.0467	C5H4N5
134.0480	C7H6N2O
136.0511	C6H6N3O
136.0623	C5H6N5
137.0463	C5H5N4O
138.0304	C5H4N3O2
144.0324	C8H4N2O
145.0514	C7H5N4
146.0467	C6H4N5
147.0433	C7H5N3O
147.0671	C7H7N4
148.0623	C6H6N5
151.0382	C6H5N3O2
151.0620	C6H7N4O
151.0732	C5H7N6
151.0746	C7H9N3O
152.0572	C5H6N5O
153.0413	C5H5N4O2
153.0525	C4H5N6O
156.0324	C9H4N2O
157.0514	C8H5N4
157.0528	C10H7NO
158.0467	C7H4N5
159.0320	C9H5NO2
159.0671	C8H7N4
160.0273	C8H4N2O2
160.0385	C7H4N4O
160.0623	C7H6N5
161.0463	C7H5N4O
161.0477	C9H7NO2

161.0576	C6H5N6	180.0535	C8H8N2O3	201.0525	C8H5N6O
161.0589	C8H7N3O	182.0467	C9H4N5	201.0538	C10H7N3O2
162.0416	C6H4N5O	183.0433	C10H5N3O	201.0651	C9H7N5O
162.0780	C7H8N5	184.0623	C9H6N5	201.0902	C11H11N3O
163.0269	C8H5NO3	184.0637	C11H8N2O	204.0522	C8H6N5O2
163.0382	C7H5N3O2	185.0589	C10H7N3O	204.0647	C9H8N4O2
163.0620	C7H7N4O	186.0402	C6H2N8	204.0872	C7H8N8
163.0732	C6H7N6	186.0429	C10H6N2O2	204.0998	C8H10N7
164.0572	C6H6N5O	186.0528	C7H4N7	204.1011	C10H12N4O
164.0586	C8H8N2O2	186.0542	C9H6N4O	205.0851	C10H11N3O2
164.0685	C5H6N7	186.0780	C9H8N5	205.0950	C7H9N8
164.0936	C7H10N5	186.0793	C11H10N2O	206.0665	C6H6N8O
164.0950	C9H12N2O	187.0732	C8H7N6	206.0777	C5H6N10
165.0413	C6H5N4O2	188.0572	C8H6N5O	206.0804	C9H10N4O2
165.0525	C5H5N6O	188.0586	C10H8N2O2	206.1168	C10H14N4O
165.0538	C7H7N3O2	188.0685	C7H6N7	209.0589	C12H7N3O
165.0637	C4H5N8	188.0698	C9H8N4O	210.0542	C11H6N4O
166.0167	C10H2N2O	188.0936	C9H10N5	211.0732	C10H7N6
166.0729	C6H8N5O	189.0525	C7H5N6O	211.0746	C12H9N3O
167.0569	C6H7N4O2	189.0538	C9H7N3O2	212.0685	C9H6N7
167.0582	C8H9NO3	189.0637	C6H5N8	212.0698	C11H8N4O
168.0324	C10H4N2O	189.0889	C8H9N6	213.0651	C10H7N5O
170.0467	C8H4N5	189.0902	C10H11N3O	213.0889	C10H9N6
171.0433	C9H5N3O	190.0742	C10H10N2O2	213.0902	C12H11N3O
172.0623	C8H6N5	190.0841	C7H8N7	214.0855	C11H10N4O
172.0637	C10H8N2O	190.0855	C9H10N4O	215.0668	C7H5N9
173.0477	C10H7NO2	191.0695	C9H9N3O2	215.0807	C10H9N5O
173.0576	C7H5N6	191.0794	C6H7N8	215.1045	C10H11N6
174.0416	C7H4N5O	191.0807	C8H9N5O	215.1059	C12H13N3O
174.0429	C9H6N2O2	191.1045	C8H11N6	216.0620	C6H4N10
174.0528	C6H4N7	191.1059	C10H13N3O	216.0647	C10H8N4O2
174.0542	C8H6N4O	192.0522	C7H6N5O2	216.0746	C7H6N9
174.0780	C8H8N5	192.0647	C8H8N4O2	216.0760	C9H8N6O
175.0382	C8H5N3O2	192.0746	C5H6N9	216.0998	C9H10N7
175.0494	C7H5N5O	192.0760	C7H8N6O	216.1011	C11H12N4O
175.0732	C7H7N6	192.0998	C7H10N7	217.0824	C7H7N9
175.0746	C9H9N3O	192.1011	C9H12N4O	217.0950	C8H9N8
176.0572	C7H6N5O	193.0487	C8H7N3O3	217.0964	C10H11N5O
176.0685	C6H6N7	193.0851	C9H11N3O2	217.1202	C10H13N6
176.0936	C8H10N5	196.0623	C10H6N5	218.0777	C6H6N10
178.0365	C6H4N5O2	197.0576	C9H5N6	218.0804	C10H10N4O2
178.0477	C5H4N7O	197.0589	C11H7N3O	218.1168	C11H14N4O
178.0491	C7H6N4O2	198.0542	C10H6N4O	219.0617	C6H5N9O
178.0729	C7H8N5O	198.0780	C10H8N5	219.0644	C10H9N3O3
178.0742	C9H10N2O2	199.0746	C11H9N3O	219.0729	C5H5N11
178.0841	C6H8N7	200.0586	C11H8N2O2	219.0981	C7H9N9
178.0855	C8H10N4O	200.0685	C8H6N7	219.1008	C11H13N3O2
179.0695	C8H9N3O2	200.0698	C10H8N4O	224.0698	C12H8N4O

225.0651	C11H7N5O
226.0841	C10H8N7
226.0855	C12H10N4O
227.0668	C8H5N9
227.0807	C11H9N5O
228.0760	C10H8N6O
228.1011	C12H12N4O
229.0824	C8H7N9
229.0964	C11H11N5O
230.0777	C7H6N10
230.0804	C11H10N4O2
230.0916	C10H10N6O
230.1154	C10H12N7
230.1168	C12H14N4O
231.0729	C6H5N11
231.1120	C11H13N5O
232.0933	C7H8N10
232.0960	C11H12N4O2
233.0774	C7H7N9O
233.0886	C6H7N11
233.1528	C13H19N3O
238.0855	C13H10N4O
239.0807	C12H9N5O
240.0620	C8H4N10
240.0760	C11H8N6O
240.1011	C13H12N4O
241.0964	C12H11N5O
242.0777	C8H6N10
242.0804	C12H10N4O2
242.0916	C11H10N6O
243.0729	C7H5N11
243.0756	C11H9N5O2
243.0981	C9H9N9
243.1120	C12H13N5O
244.0933	C8H8N10
244.0960	C12H12N4O2
244.1073	C11H12N6O
245.0886	C7H7N11
245.0913	C11H11N5O2
245.1277	C12H15N5O
246.1090	C8H10N10
251.0807	C13H9N5O
253.0964	C13H11N5O
254.0916	C12H10N6O
254.1168	C14H14N4O
255.0869	C11H9N7O
255.1080	C8H13N7O3
255.1120	C13H13N5O
255.1947	C13H25N3O2
256.0933	C9H8N10
256.0960	C13H12N4O2
256.1073	C12H12N6O
257.0886	C8H7N11
257.0913	C12H11N5O2
257.0985	C6H11N9O3
257.1025	C11H11N7O
257.1277	C13H15N5O
258.1229	C12H14N6O
259.1042	C8H9N11
265.0923	C9H11N7O3
266.0876	C8H10N8O3
266.0916	C13H10N6O
267.1080	C9H13N7O3
268.1032	C8H12N8O3
268.1073	C13H12N6O
269.0886	C9H7N11
269.1025	C12H11N7O
269.1236	C9H15N7O3
270.1189	C8H14N8O3
271.1042	C9H9N11
271.1069	C13H13N5O2
271.1182	C12H13N7O
271.1743	C8H19N10O
272.1134	C11H12N8O
272.1345	C8H16N8O3
272.1386	C13H16N6O
272.1749	C14H20N6
273.1199	C9H11N11
280.1073	C14H12N6O
281.1236	C10H15N7O3
282.1189	C9H14N8O3
282.1229	C14H14N6O
283.1141	C8H13N9O3
284.1345	C9H16N8O3
284.1386	C14H16N6O
285.1298	C8H15N9O3
287.1692	C8H19N10O2
294.1189	C10H14N8O3
296.1134	C13H12N8O
296.1345	C10H16N8O3

Molecules exclusively present in P_{400}

82.0405	C3H4N3
83.0371	C4H5NO
110.0467	C3H4N5
118.0405	C6H4N3
120.0324	C6H4N2O
121.0164	C6H3NO2
122.0480	C6H6N2O
126.0416	C3H4N5O
132.0324	C7H4N2O
133.0164	C7H3NO2
133.0276	C6H3N3O
134.0116	C6H2N2O2
136.0273	C6H4N2O2
136.0385	C5H4N4O
136.0399	C7H6NO2
136.0637	C7H8N2O
137.0576	C4H5N6
138.0416	C4H4N5O
138.0429	C6H6N2O2
138.0780	C5H8N5
140.0572	C4H6N5O
141.0215	C9H3NO
141.0413	C4H5N4O2
145.0528	C9H7NO
147.0320	C8H5NO2
147.0684	C9H9NO
148.0273	C7H4N2O2
148.0385	C6H4N4O
151.0058	C10HNO
151.0269	C7H5NO3
151.0494	C5H5N5O
151.0508	C7H7N2O2
151.0633	C8H9NO2
152.0586	C7H8N2O2
152.0685	C4H6N7
153.0426	C7H7NO3
154.0365	C4H4N5O2
157.0276	C8H3N3O
158.0229	C7H2N4O
158.0480	C9H6N2O
159.0433	C8H5N3O
159.0684	C10H9NO
160.0637	C9H8N2O
161.0225	C7H3N3O2
162.0429	C8H6N2O2
162.0528	C5H4N7
162.0793	C9H10N2O
163.0633	C9H9NO2
164.0698	C7H8N4O
165.0889	C6H9N6
165.0902	C8H11N3O

166.0365	C5H4N5O2	187.0494	C8H5N5O	205.0964	C9H11N5O
166.0378	C7H6N2O3	187.0746	C10H9N3O	206.0678	C8H8N5O2
166.0491	C6H6N4O2	188.0334	C8H4N4O2	206.0916	C8H10N6O
166.0742	C8H10N2O2	188.0658	C4H8N6O3	206.1154	C8H12N7
166.0841	C5H8N7	188.0712	C11H10NO2	207.0617	C5H5N9O
166.0855	C7H10N4O	189.0610	C3H7N7O3	207.0644	C9H9N3O3
167.0007	C10HNO2	189.0664	C10H9N2O2	207.0729	C4H5N11
167.0668	C3H5N9	190.0464	C4H2N10	207.0756	C8H9N5O2
167.0681	C5H7N6O	190.0491	C8H6N4O2	207.0855	C5H7N10
167.0794	C4H7N8	190.0590	C5H4N9	207.0869	C7H9N7O
167.0807	C6H9N5O	190.0603	C7H6N6O	207.0981	C6H9N9
168.0508	C3H4N8O	190.0715	C6H6N8	207.1107	C7H11N8
168.0535	C7H8N2O3	191.0668	C5H5N9	208.0570	C4H4N10O
168.0634	C4H6N7O	191.0821	C10H11N2O2	208.0596	C8H8N4O3
169.0276	C9H3N3O	192.0620	C4H4N10	208.0933	C5H8N10
170.0480	C10H6N2O	192.0872	C6H8N8	211.0494	C10H5N5O
172.0385	C8H4N4O	193.0461	C4H3N9O	213.0511	C7H3N9
173.0549	C4H7N5O3	193.0600	C7H7N5O2	214.0464	C6H2N10
173.0589	C9H7N3O	193.0766	C13H9N2	214.0491	C10H6N4O2
174.0501	C3H6N6O3	193.0824	C5H7N9	214.0590	C7H4N9
174.0555	C10H8NO2	193.0950	C6H9N8	214.0603	C9H6N6O
174.0793	C10H10N2O	193.0964	C8H11N5O	214.0729	C10H8N5O
175.0355	C4HN9	194.0777	C4H6N10	215.0794	C8H7N8
175.0606	C6H5N7	194.0804	C8H10N4O2	216.0773	C11H10N3O2
175.0633	C10H9NO2	195.0433	C11H5N3O	216.0845	C5H10N7O3
176.0334	C7H4N4O2	195.0630	C6H7N6O2	217.0461	C6H3N9O
176.0586	C9H8N2O2	195.0644	C8H9N3O3	217.0487	C10H7N3O3
176.0950	C10H12N2O	199.0494	C9H5N5O	217.0573	C5H3N11
178.0378	C8H6N2O3	200.0447	C8H4N6O	217.0600	C9H7N5O2
178.0657	C13H8N	200.0559	C7H4N8	217.0712	C8H7N7O
179.0331	C7H5N3O3	201.0610	C4H7N7O3	217.0766	C15H9N2
179.0668	C4H5N9	203.0416	C4HN11	218.0413	C5H2N10O
179.0794	C5H7N8	203.0443	C8H5N5O2	218.0525	C4H2N12
179.0807	C7H9N5O	203.0556	C7H5N7O	218.0552	C8H6N6O2
180.0508	C4H4N8O	203.0609	C14H7N2	218.0718	C14H8N3
180.0634	C5H6N7O	203.0668	C6H5N9	218.0916	C9H10N6O
180.0647	C7H8N4O2	203.0695	C10H9N3O2	218.1154	C9H12N7
180.1011	C8H12N4O	203.0807	C9H9N5O	219.0756	C9H9N5O2
181.0461	C3H3N9O	203.1045	C9H11N6	219.0855	C6H7N10
181.0474	C5H5N6O2	203.1059	C11H13N3O	219.0869	C8H9N7O
182.0678	C6H8N5O2	204.0620	C5H4N10	219.1120	C10H13N5O
182.0691	C8H10N2O3	204.0746	C6H6N9	221.0522	C4H3N11O
183.0518	C6H7N4O3	204.0760	C8H8N6O	221.0774	C6H7N9O
184.0385	C9H4N4O	205.0461	C5H3N9O	221.0886	C5H7N11
186.0501	C4H6N6O3	205.0487	C9H7N3O3	221.0913	C9H11N5O2
186.0555	C11H8NO2	205.0573	C4H3N11	221.1025	C8H11N7O
187.0355	C5HN9	205.0600	C8H7N5O2	222.0528	C10H4N7
187.0382	C9H5N3O2	205.0824	C6H7N9	222.0739	C7H8N7O2

225.0723	C5H7N9O2	244.0821	C9H8N8O	258.0937	C5H10N10O3
226.0590	C8H4N9	245.0522	C6H3N11O	258.0978	C10H10N8O
226.0603	C10H6N6O	245.0634	C5H3N13	258.1189	C7H14N8O3
227.0416	C6HN11	245.0661	C9H7N7O2	259.0679	C7H5N11O
227.0556	C9H5N7O	245.1025	C10H11N7O	259.0705	C11H9N5O3
228.0620	C7H4N10	245.1236	C7H15N7O3	259.0791	C6H5N13
229.0573	C6H3N11	246.0726	C7H6N10O	259.0890	C4H9N11O3
229.0600	C10H7N5O2	246.0753	C11H10N4O3	259.0930	C9H9N9O
229.0712	C9H7N7O	246.0838	C6H6N12	259.1069	C12H13N5O2
229.1202	C11H13N6	246.0865	C10H10N6O2	259.1141	C6H13N9O3
231.0756	C10H9N5O2	246.0937	C4H10N10O3	259.1182	C11H13N7O
231.0869	C9H9N7O	246.0978	C9H10N8O	260.0770	C9H8N8O2
232.0570	C6H4N10O	246.1189	C6H14N8O3	260.0995	C7H8N12
232.0682	C5H4N12	246.1229	C11H14N6O	260.1022	C11H12N6O2
232.0709	C9H8N6O2	247.0679	C6H5N11O	260.1094	C5H12N10O3
232.0821	C8H8N8O	247.0791	C5H5N13	260.1134	C10H12N8O
232.1073	C10H12N6O	247.0818	C9H9N7O2	260.1345	C7H16N8O3
233.0522	C5H3N11O	247.1042	C7H9N11	260.1386	C12H16N6O
233.0800	C11H11N3O3	247.1069	C11H13N5O2	261.0947	C6H7N13
233.0913	C10H11N5O2	247.1141	C5H13N9O3	261.0974	C10H11N7O2
233.1025	C9H11N7O	247.1182	C10H13N7O	261.1046	C4H11N11O3
233.1277	C11H15N5O	248.0883	C7H8N10O	262.0788	C6H6N12O
234.0726	C6H6N10O	248.0995	C6H8N12	262.1151	C7H10N12
234.0753	C10H10N4O3	248.1022	C10H12N6O2	263.0767	C9H9N7O3
234.0838	C5H6N12	248.1094	C4H12N10O3	264.0719	C8H8N8O3
234.0865	C9H10N6O2	249.0610	C8H7N7O3	265.0672	C7H7N9O3
234.0978	C8H10N8O	249.0651	C13H7N5O	267.0729	C9H5N11
234.1090	C7H10N10	249.0835	C6H7N11O	267.0828	C7H9N9O3
234.1229	C10H14N6O	249.0947	C5H7N13	267.0869	C12H9N7O
235.0679	C5H5N11O	249.0974	C9H11N7O2	268.0682	C8H4N12
235.0818	C8H9N7O2	252.0719	C7H8N8O3	268.0781	C6H8N10O3
235.1042	C6H9N11	252.0760	C12H8N6O	268.0821	C11H8N8O
236.0658	C8H8N6O3	252.0998	C12H10N7	269.0733	C5H7N11O3
237.0610	C7H7N7O3	253.0712	C11H7N7O	269.0985	C7H11N9O3
237.0651	C12H7N5O	253.0923	C8H11N7O3	270.0838	C8H6N12
238.0590	C9H4N9	254.1154	C12H12N7	270.0865	C12H10N6O2
240.0647	C12H8N4O2	255.0729	C8H5N11	270.0937	C6H10N10O3
240.0719	C6H8N8O3	255.0756	C12H9N5O2	270.0978	C11H10N8O
241.0573	C7H3N11	255.0828	C6H9N9O3	270.1229	C13H14N6O
241.0600	C11H7N5O2	256.0682	C7H4N12	271.0791	C7H5N13
241.0672	C5H7N9O3	256.0709	C11H8N6O2	271.0818	C11H9N7O2
241.0712	C10H7N7O	256.0781	C5H8N10O3	271.0890	C5H9N11O3
242.0665	C9H6N8O	256.0821	C10H8N8O	271.0930	C10H9N9O
242.0876	C6H10N8O3	256.1032	C7H12N8O3	271.1141	C7H13N9O3
242.1154	C11H12N7	257.1236	C8H15N7O3	271.1393	C9H17N7O3
243.0869	C10H9N7O	258.0726	C8H6N10O	272.0995	C8H8N12
244.0570	C7H4N10O	258.0838	C7H6N12	272.1022	C12H12N6O2
244.0682	C6H4N12	258.0865	C11H10N6O2	272.1094	C6H12N10O3

273.0947	C7H7N13
273.0974	C11H11N7O2
273.1046	C5H11N11O3
273.1087	C10H11N9O
273.1298	C7H15N9O3
273.1338	C12H15N7O
274.0774	C5H4N15
274.0900	C6H6N14
274.0999	C4H10N12O3
274.1039	C9H10N10O
274.1151	C8H10N12
274.1178	C12H14N6O2
274.1250	C6H14N10O3
274.1291	C11H14N8O
275.1104	C7H9N13
275.1131	C11H13N7O2
275.1203	C5H13N11O3
278.0876	C9H10N8O3
278.0916	C14H10N6O
279.0828	C8H9N9O3
279.0869	C13H9N7O
280.0781	C7H8N10O3
280.1032	C9H12N8O3
281.0985	C8H11N9O3
281.1025	C13H11N7O
282.0838	C9H6N12
282.0937	C7H10N10O3
282.0978	C12H10N8O
283.0791	C8H5N13
283.0890	C6H9N11O3
283.0930	C11H9N9O
283.1182	C13H13N7O
284.0995	C9H8N12
284.1094	C7H12N10O3
284.1134	C12H12N8O
285.0723	C10H7N9O2
285.0822	C7H5N14
285.0947	C8H7N13
285.0988	C14H13N4O3
285.1046	C6H11N11O3
285.1087	C11H11N9O
285.1338	C13H15N7O
286.0900	C7H6N14
286.0999	C5H10N12O3
286.1039	C10H10N10O
286.1151	C9H10N12
286.1178	C13H14N6O2
286.1250	C7H14N10O3
286.1291	C12H14N8O
287.1104	C8H9N13
287.1131	C12H13N7O2
287.1203	C6H13N11O3
287.1256	C13H15N6O2
287.1454	C8H17N9O3
288.1056	C7H8N14
288.1407	C7H16N10O3
292.1032	C10H12N8O3
293.0985	C9H11N9O3
294.0937	C8H10N10O3
294.0978	C13H10N8O
295.0890	C7H9N11O3
295.1141	C9H13N9O3
295.1182	C14H13N7O
296.0995	C10H8N12
296.1094	C8H12N10O3
297.0947	C9H7N13
297.1046	C7H11N11O3
297.1087	C12H11N9O
297.1298	C9H15N9O3
297.1338	C14H15N7O
298.0999	C6H10N12O3
298.1052	C13H12N7O2
298.1250	C8H14N10O3
298.1291	C13H14N8O
299.1104	C9H9N13
299.1203	C7H13N11O3
299.1243	C12H13N9O
299.1454	C9H17N9O3

Molecules exclusively present in P_{650}

93.0215	C5H3NO
96.0562	C4H6N3
110.0354	C4H4N3O
111.0671	C4H7N4
120.0449	C7H6NO
122.0718	C6H8N3
132.0562	C7H6N3
134.0718	C7H8N3
135.0320	C7H5NO2
135.0433	C6H5N3O
135.0671	C6H7N4
135.0684	C8H9NO
139.0269	C6H5NO3
139.0620	C5H7N4O
140.0460	C5H6N3O2
142.0405	C8H4N3
144.0562	C8H6N3
146.0354	C7H4N3O
146.0480	C8H6N2O
146.0718	C8H8N3
148.0511	C7H6N3O
149.0463	C6H5N4O
149.0576	C5H5N6
149.0589	C7H7N3O
149.0827	C7H9N4
150.0304	C6H4N3O2
150.0416	C5H4N5O
150.0528	C4H4N7
150.0667	C7H8N3O
150.0780	C6H8N5
152.0460	C6H6N3O2
155.0371	C10H5NO
156.0562	C9H6N3
158.0718	C9H8N3
160.0511	C8H6N3O
161.0827	C8H9N4
163.0243	C4HN7O
163.0984	C8H11N4
165.0215	C11H3NO
165.0651	C6H7N5O
165.0776	C7H9N4O
167.0371	C11H5NO
169.0514	C9H5N4
170.0354	C9H4N3O
171.0320	C10H5NO2
171.0671	C9H7N4
172.0511	C9H6N3O
173.0463	C8H5N4O
173.0827	C9H9N4
174.0667	C9H8N3O
175.0620	C8H7N4O
175.0984	C9H11N4
175.0997	C11H13NO
176.0824	C9H10N3O
177.0413	C7H5N4O2
177.0525	C6H5N6O
177.0637	C5H5N8
177.0776	C8H9N4O
177.0889	C7H9N6
177.1154	C11H15NO
178.0617	C8H8N3O2
178.1093	C8H12N5
178.1106	C10H14N2O

179.0569	C7H7N4O2	199.0633	C12H9NO2	215.1297	C12H15N4
179.0582	C9H9NO3	199.0732	C9H7N6	216.0508	C7H4N8O
179.0681	C6H7N6O	199.0984	C11H11N4	216.0535	C11H8N2O3
181.0514	C10H5N4	199.0997	C13H13NO	216.0872	C8H8N8
181.0528	C12H7NO	200.0572	C9H6N5O	216.0899	C12H12N2O2
182.0480	C11H6N2O	200.0936	C10H10N5	216.1263	C13H16N2O
183.0671	C10H7N4	200.0950	C12H12N2O	217.0851	C11H11N3O2
183.0684	C12H9NO	201.0399	C7H3N7O	217.1076	C9H11N7
185.0463	C9H5N4O	201.0637	C7H5N8	217.1215	C12H15N3O
185.0477	C11H7NO2	201.0763	C8H7N7	218.0665	C7H6N8O
185.0576	C8H5N6	201.0790	C12H11NO2	218.0903	C7H8N9
185.0827	C10H9N4	201.0889	C9H9N6	218.1028	C8H10N8
185.0841	C12H11NO	201.1140	C11H13N4	218.1055	C12H14N2O2
187.0620	C9H7N4O	201.1154	C13H15NO	219.1107	C8H11N8
187.0633	C11H9NO2	204.0535	C10H8N2O3	219.1358	C10H15N6
187.0984	C10H11N4	204.0634	C7H6N7O	222.0780	C12H8N5
187.0997	C12H13NO	204.0899	C11H12N2O2	222.0793	C14H10N2O
189.0651	C8H7N5O	204.1249	C10H14N5	223.0732	C11H7N6
189.0776	C9H9N4O	204.1263	C12H16N2O	223.0746	C13H9N3O
189.0790	C11H11NO2	205.0712	C7H7N7O	224.0936	C12H10N5
189.1154	C12H15NO	205.0726	C9H9N4O2	224.0950	C14H12N2O
190.0167	C12H2N2O	205.0838	C8H9N6O	225.0525	C10H5N6O
190.0729	C8H8N5O	205.1202	C9H13N6	225.0637	C9H5N8
190.1093	C9H12N5	205.1215	C11H15N3O	225.0889	C11H9N6
190.1106	C11H14N2O	206.0691	C10H10N2O3	225.0902	C13H11N3O
191.0569	C8H7N4O2	206.0903	C6H8N9	226.0715	C9H6N8
191.0582	C10H9NO3	206.1028	C7H10N8	226.0742	C13H10N2O2
191.0681	C7H7N6O	206.1055	C11H14N2O2	226.1093	C12H12N5
191.0933	C9H11N4O	208.0623	C11H6N5	226.1106	C14H14N2O
191.0946	C11H13NO2	209.0576	C10H5N6	227.0695	C12H9N3O2
192.0535	C9H8N2O3	210.0528	C9H4N7	227.1059	C13H13N3O
192.0634	C6H6N7O	210.0793	C13H10N2O	228.0634	C9H6N7O
192.0885	C8H10N5O	211.0984	C12H11N4	228.0647	C11H8N4O2
192.0899	C10H12N2O2	211.0997	C14H13NO	228.0746	C8H6N9
193.0474	C6H5N6O2	212.0559	C8H4N8	228.0872	C9H8N8
193.0739	C10H11NO3	212.0936	C11H10N5	228.0899	C13H12N2O2
193.0838	C7H9N6O	212.0950	C13H12N2O	228.0998	C10H10N7
194.0480	C12H6N2O	213.0538	C11H7N3O2	228.1249	C12H14N5
194.0691	C9H10N2O3	213.0637	C8H5N8	228.1263	C14H16N2O
195.0671	C11H7N4	213.0763	C9H7N7	229.0851	C12H11N3O2
195.0684	C13H9NO	213.1140	C12H13N4	229.1076	C10H11N7
196.0637	C12H8N2O	214.0715	C8H6N8	229.1215	C13H15N3O
197.0827	C11H9N4	214.0742	C12H10N2O2	230.1028	C9H10N8
197.0841	C13H11NO	214.0841	C9H8N7	230.1055	C13H14N2O2
198.0429	C11H6N2O2	214.1093	C11H12N5	230.1419	C14H18N2O
198.0528	C8H4N7	214.1106	C13H14N2O	231.0855	C7H7N10
198.0793	C12H10N2O	215.0695	C11H9N3O2	231.0981	C8H9N9
199.0606	C8H5N7	215.0919	C9H9N7	231.1008	C12H13N3O2

231.1358	C11H15N6	255.1372	C15H17N3O	279.1372	C17H17N3O
231.1372	C13H17N3O	256.1185	C11H12N8	280.1284	C11H16N6O3
232.1311	C10H14N7	256.1212	C15H16N2O2	281.1515	C15H17N6
232.1324	C12H16N4O	256.1324	C14H16N4O	281.1528	C17H19N3O
233.1137	C8H11N9	257.1137	C10H11N9	282.1090	C11H10N10
233.1164	C12H15N3O2	257.1164	C14H15N3O2	282.1440	C11H18N6O3
236.0685	C11H6N7	257.1488	C10H19N5O3	282.1481	C16H18N4O
236.0698	C13H8N4O	257.1528	C15H19N3O	283.1294	C12H13N9
236.0936	C13H10N5	258.1090	C9H10N10	283.1393	C10H17N7O3
237.0902	C14H11N3O	258.1117	C13H14N4O2	283.1644	C12H21N5O3
238.1093	C13H12N5	258.1341	C11H14N8	283.1685	C17H21N3O
238.1106	C15H14N2O	258.1481	C14H18N4O	284.1246	C11H12N10
239.1059	C14H13N3O	259.1294	C10H13N9	284.1597	C11H20N6O3
240.0872	C10H8N8	259.1321	C14H17N3O2	284.1637	C16H20N4O
240.0899	C14H12N2O2	259.1393	C8H17N7O3	285.1199	C10H11N11
240.1263	C15H16N2O	259.1433	C13H17N5O	285.1450	C12H15N9
241.0824	C9H7N9	260.1246	C9H12N10	285.1549	C10H19N7O3
241.0851	C13H11N3O2	263.1045	C14H11N6	285.1590	C15H19N5O
241.1215	C14H15N3O	264.0998	C13H10N7	286.1403	C11H14N10
242.1028	C10H10N8	264.1011	C15H12N4O	287.1355	C10H13N11
242.1168	C13H14N4O	265.0964	C14H11N5O	292.1284	C12H16N6O3
243.0855	C8H7N10	265.1175	C11H15N5O3	292.1324	C17H16N4O
243.1008	C13H13N3O2	266.1127	C10H14N6O3	293.1236	C11H15N7O3
243.1372	C14H17N3O	267.1120	C14H13N5O	293.1277	C16H15N5O
244.1185	C10H12N8	267.1331	C11H17N5O3	294.1440	C12H18N6O3
244.1212	C14H16N2O2	267.1372	C16H17N3O	295.1168	C12H11N10
244.1324	C13H16N4O	268.1324	C15H16N4O	295.1393	C11H17N7O3
245.0774	C8H7N9O	269.1012	C10H9N10	295.1433	C16H17N5O
245.1137	C9H11N9	269.1137	C11H11N9	295.1644	C13H21N5O3
245.1164	C13H15N3O2	269.1164	C15H15N3O2	296.1246	C12H12N10
245.1263	C10H13N8	269.1277	C14H15N5O	296.1386	C15H16N6O
245.1528	C14H19N3O	269.1488	C11H19N5O3	296.1597	C12H20N6O3
246.1117	C12H14N4O2	269.1528	C16H19N3O	297.1199	C11H11N11
249.0889	C13H9N6	270.1090	C10H10N10	297.1576	C14H17N8
249.0902	C15H11N3O	270.1117	C14H14N4O2	298.1403	C12H14N10
250.0841	C12H8N7	270.1440	C10H18N6O3	298.1502	C10H18N8O3
250.0855	C14H10N4O	270.1481	C15H18N4O	298.1753	C12H22N6O3
251.1059	C15H13N3O	271.1294	C11H13N9	298.1794	C17H22N4O
252.1011	C14H12N4O	271.1420	C12H15N8	299.1355	C11H13N11
252.1263	C16H16N2O	271.1433	C14H17N5O	299.1706	C11H21N7O3
253.0824	C10H7N9	272.1246	C10H12N10		
253.1215	C15H15N3O	272.1273	C14H16N4O2		
254.0777	C9H6N10	272.1597	C10H20N6O3		
254.0804	C13H10N4O2	273.1450	C11H15N9		
254.1379	C11H18N4O3	278.1154	C14H12N7		
254.1419	C16H18N2O	278.1168	C16H14N4O		
255.0981	C10H9N9	279.1080	C10H13N7O3		
255.1008	C14H13N3O2	279.1331	C12H17N5O3		

Appendix A3: Optical constants of Pluto aerosol analogues from UV to near-IR, characterized with spectroscopic ellipsometry and "λ-by-λ" numerical inversion method

Table A3.1: Optical constants of Pluto aerosol analogues determined from 270 to 2100 nm with spectroscopic ellipsometry and "λ-by-λ" numerical inversion method. *n* and *k* indices presented in this table were smoothed by a moving mean with a step of 15 data points. Regarding the "Reliability" column, 1 stands for very reliable *n*- and *k*-values, 2 stands for moderately reliable values, and 3 stands for *n*- and *k*-values to be considered with caution.

[nm]	[cm^{-1}]	F_H			F_{400}			F_{650}		
		n	***k***	**Reliability**	***n***	***k***	**Reliability**	***n***	***k***	**Reliability**
270	37037	1.712	2.67E-01	1	1.726	2.75E-01	1	1.721	1.54E-01	1
275	36364	1.720	2.60E-01	1	1.735	2.66E-01	1	1.729	1.46E-01	1
280	35714	1.729	2.49E-01	1	1.742	2.55E-01	1	1.733	1.37E-01	1
285	35088	1.735	2.36E-01	1	1.745	2.42E-01	1	1.735	1.28E-01	1
290	34483	1.737	2.22E-01	1	1.745	2.33E-01	1	1.736	1.20E-01	1
295	33898	1.742	2.06E-01	1	1.746	2.31E-01	1	1.735	1.12E-01	1
300	33333	1.748	1.93E-01	1	1.753	2.17E-01	1	1.734	1.06E-01	1
305	32787	1.752	1.84E-01	1	1.757	2.06E-01	1	1.733	9.96E-02	1
310	32258	1.756	1.74E-01	1	1.760	1.96E-01	1	1.732	9.29E-02	1
315	31746	1.759	1.64E-01	1	1.763	1.87E-01	1	1.731	8.65E-02	1
320	31250	1.761	1.54E-01	1	1.764	1.78E-01	1	1.729	8.06E-02	1
325	30769	1.763	1.45E-01	1	1.765	1.68E-01	1	1.727	7.49E-02	1
330	30303	1.764	1.36E-01	1	1.766	1.59E-01	1	1.725	6.97E-02	1
335	29851	1.764	1.28E-01	1	1.767	1.51E-01	1	1.723	6.48E-02	1
340	29412	1.765	1.20E-01	1	1.767	1.43E-01	1	1.721	6.04E-02	1
345	28986	1.765	1.13E-01	1	1.768	1.35E-01	1	1.718	5.63E-02	1
350	28571	1.766	1.07E-01	1	1.770	1.27E-01	1	1.716	5.23E-02	1
355	28169	1.765	1.02E-01	1	1.772	1.17E-01	1	1.713	4.86E-02	1
360	27778	1.764	9.76E-02	1	1.771	1.06E-01	1	1.711	4.50E-02	1

365	27397	1.763	9.33E-02	1	1.769	1.01E-01	1	1.708	4.14E-02	1
370	27027	1.760	8.88E-02	1	1.767	9.59E-02	1	1.705	3.80E-02	1
375	26667	1.758	8.40E-02	1	1.765	9.05E-02	1	1.703	3.49E-02	1
380	26316	1.756	7.91E-02	1	1.764	8.54E-02	1	1.700	3.20E-02	1
385	25974	1.754	7.44E-02	1	1.762	8.04E-02	1	1.697	2.92E-02	1
390	25641	1.753	6.99E-02	1	1.761	7.56E-02	1	1.695	2.66E-02	1
395	25316	1.751	6.56E-02	1	1.759	7.12E-02	1	1.692	2.43E-02	1
400	25000	1.749	6.16E-02	1	1.758	6.71E-02	1	1.690	2.23E-02	1
405	24691	1.747	5.79E-02	1	1.756	6.33E-02	1	1.688	2.05E-02	1
410	24390	1.746	5.44E-02	1	1.754	5.98E-02	1	1.685	1.89E-02	1
415	24096	1.744	5.13E-02	1	1.752	5.68E-02	1	1.683	1.74E-02	1
420	23810	1.742	4.86E-02	1	1.750	5.43E-02	1	1.681	1.60E-02	1
425	23529	1.740	4.63E-02	1	1.747	5.20E-02	1	1.679	1.48E-02	1
430	23256	1.737	4.33E-02	1	1.744	4.98E-02	1	1.676	1.37E-02	1
435	22989	1.734	4.05E-02	1	1.741	4.75E-02	1	1.674	1.27E-02	1
440	22727	1.731	3.84E-02	1	1.738	4.51E-02	1	1.673	1.18E-02	1
445	22472	1.728	3.62E-02	1	1.735	4.27E-02	1	1.671	1.11E-02	1
450	22222	1.726	3.41E-02	1	1.732	4.03E-02	1	1.669	1.03E-02	1
455	21978	1.723	3.20E-02	1	1.730	3.81E-02	1	1.667	9.57E-03	1
460	21739	1.720	3.00E-02	1	1.727	3.60E-02	1	1.666	8.89E-03	1
465	21505	1.718	2.82E-02	1	1.725	3.33E-02	1	1.664	8.24E-03	1
470	21277	1.716	2.65E-02	1	1.722	3.16E-02	1	1.663	7.52E-03	1
475	21053	1.714	2.50E-02	1	1.720	3.00E-02	1	1.661	6.83E-03	1
480	20833	1.712	2.36E-02	1	1.719	2.85E-02	1	1.660	6.16E-03	1
485	20619	1.710	2.23E-02	1	1.717	2.69E-02	1	1.658	5.50E-03	1
490	20408	1.709	2.09E-02	1	1.715	2.52E-02	1	1.656	4.85E-03	1
495	20202	1.707	1.94E-02	1	1.714	2.34E-02	1	1.655	4.23E-03	1
500	20000	1.706	1.77E-02	1	1.713	2.15E-02	1	1.653	3.65E-03	1
505	19802	1.704	1.71E-02	1	1.712	1.99E-02	1	1.652	3.19E-03	1
510	19608	1.703	1.64E-02	1	1.711	1.85E-02	1	1.650	2.86E-03	1

515	19417	1.702	1.52E-02	1	1.710	1.74E-02	1	1.649	2.66E-03	1
520	19231	1.702	1.42E-02	1	1.709	1.63E-02	1	1.648	2.57E-03	1
525	19048	1.701	1.32E-02	1	1.708	1.54E-02	1	1.647	2.61E-03	1
530	18868	1.699	1.24E-02	1	1.706	1.44E-02	1	1.646	2.71E-03	1
535	18692	1.698	1.15E-02	1	1.705	1.35E-02	1	1.645	2.80E-03	1
540	18519	1.697	1.07E-02	1	1.704	1.25E-02	1	1.644	2.88E-03	1
545	18349	1.695	9.86E-03	1	1.702	1.14E-02	1	1.644	2.95E-03	1
550	18182	1.694	9.07E-03	1	1.700	1.03E-02	1	1.643	3.03E-03	1
555	18018	1.692	8.16E-03	1	1.698	9.25E-03	1	1.642	3.10E-03	1
560	17857	1.690	7.29E-03	1	1.696	8.30E-03	1	1.642	3.18E-03	1
565	17699	1.688	6.49E-03	1	1.694	7.43E-03	1	1.641	3.24E-03	1
570	17544	1.687	5.75E-03	1	1.692	6.62E-03	1	1.641	3.31E-03	1
575	17391	1.685	5.08E-03	1	1.691	5.89E-03	1	1.640	3.37E-03	1
580	17241	1.683	4.47E-03	1	1.689	5.11E-03	1	1.640	3.36E-03	1
585	17094	1.682	3.93E-03	1	1.687	4.53E-03	1	1.639	3.29E-03	1
590	16949	1.680	3.46E-03	1	1.685	4.04E-03	1	1.638	3.14E-03	1
595	16807	1.678	3.07E-03	1	1.683	3.63E-03	1	1.638	2.95E-03	1
600	16667	1.677	2.74E-03	1	1.682	3.31E-03	1	1.638	2.81E-03	1
605	16529	1.675	2.49E-03	1	1.680	3.25E-03	1	1.638	2.66E-03	1
610	16393	1.674	2.28E-03	1	1.678	3.32E-03	1	1.638	2.52E-03	1
615	16260	1.673	2.11E-03	1	1.676	3.38E-03	1	1.639	2.45E-03	1
620	16129	1.671	2.04E-03	1	1.675	3.63E-03	1	1.639	2.30E-03	1
625	16000	1.670	2.03E-03	1	1.675	3.89E-03	1	1.638	2.08E-03	1
630	15873	1.669	2.17E-03	1	1.674	4.08E-03	1	1.637	1.93E-03	1
635	15748	1.668	2.29E-03	1	1.673	4.21E-03	1	1.637	1.75E-03	1
640	15625	1.668	2.37E-03	1	1.672	4.30E-03	1	1.636	1.58E-03	1
645	15504	1.667	2.42E-03	1	1.672	4.36E-03	1	1.636	1.44E-03	1
650	15385	1.666	2.36E-03	1	1.671	4.40E-03	1	1.635	1.32E-03	1
655	15267	1.666	2.37E-03	1	1.671	4.43E-03	1	1.635	1.32E-03	1
660	15152	1.666	2.35E-03	1	1.670	4.45E-03	1	1.635	1.64E-03	1

665	15038	1.665	2.32E-03	1	1.670	4.47E-03	1	1.634	1.99E-03	1
670	14925	1.665	2.26E-03	1	1.670	4.49E-03	1	1.634	2.07E-03	1
675	14815	1.665	2.21E-03	1	1.670	4.52E-03	1	1.634	2.08E-03	1
680	14706	1.665	2.21E-03	1	1.670	4.37E-03	1	1.633	2.10E-03	1
685	14599	1.665	2.22E-03	1	1.671	4.14E-03	1	1.632	2.16E-03	1
690	14493	1.665	2.25E-03	1	1.671	3.98E-03	1	1.630	2.21E-03	1
695	14388	1.665	2.20E-03	1	1.671	3.87E-03	1	1.629	2.43E-03	1
700	14286	1.665	2.12E-03	1	1.671	3.79E-03	1	1.628	2.62E-03	1
705	14184	1.665	2.06E-03	3	1.671	3.74E-03	2	1.628	2.67E-03	2
710	14085	1.665	2.01E-03	3	1.671	3.70E-03	2	1.628	2.72E-03	2
715	13986	1.665	1.98E-03	3	1.671	3.68E-03	2	1.627	2.75E-03	2
720	13889	1.665	1.95E-03	3	1.671	3.68E-03	2	1.627	2.77E-03	2
725	13793	1.665	2.02E-03	3	1.671	3.67E-03	2	1.627	2.79E-03	2
730	13699	1.665	2.01E-03	3	1.671	3.68E-03	2	1.627	2.72E-03	2
735	13605	1.665	2.02E-03	3	1.671	3.69E-03	2	1.626	2.37E-03	2
740	13514	1.665	2.04E-03	3	1.671	3.70E-03	2	1.626	2.04E-03	2
745	13423	1.665	2.09E-03	3	1.671	3.71E-03	2	1.626	2.03E-03	2
750	13333	1.664	2.13E-03	3	1.670	3.71E-03	2	1.625	1.96E-03	2
755	13245	1.664	2.14E-03	3	1.670	3.69E-03	2	1.625	1.91E-03	2
760	13158	1.664	2.11E-03	3	1.670	3.65E-03	2	1.624	1.80E-03	2
765	13072	1.663	2.08E-03	3	1.669	3.60E-03	2	1.624	1.64E-03	2
770	12987	1.663	2.04E-03	3	1.669	3.53E-03	2	1.625	1.40E-03	2
775	12903	1.662	1.99E-03	3	1.668	3.43E-03	2	1.625	1.27E-03	2
780	12821	1.662	1.92E-03	3	1.668	3.31E-03	2	1.624	1.22E-03	2
785	12739	1.661	1.84E-03	3	1.667	3.16E-03	2	1.624	1.22E-03	2
790	12658	1.661	1.73E-03	3	1.667	2.98E-03	2	1.624	1.25E-03	2
795	12579	1.660	1.60E-03	3	1.666	2.78E-03	2	1.624	1.30E-03	2
800	12500	1.660	1.47E-03	3	1.666	2.55E-03	2	1.623	1.35E-03	2
805	12422	1.659	1.46E-03	3	1.665	2.31E-03	2	1.623	1.40E-03	2
810	12346	1.659	1.33E-03	3	1.665	2.22E-03	2	1.623	1.46E-03	2

815	12270	1.659	1.34E-03	3	1.664	2.52E-03	2	1.623	1.51E-03	2
820	12195	1.658	1.42E-03	3	1.664	2.74E-03	2	1.622	1.57E-03	2
825	12121	1.658	1.30E-03	3	1.663	2.84E-03	2	1.622	1.67E-03	2
830	12048	1.657	1.21E-03	3	1.663	2.85E-03	2	1.622	1.76E-03	2
835	11976	1.657	1.16E-03	3	1.663	3.03E-03	2	1.622	1.85E-03	2
840	11905	1.657	1.12E-03	3	1.662	3.24E-03	2	1.622	1.93E-03	2
845	11834	1.656	1.05E-03	3	1.662	3.36E-03	2	1.622	2.04E-03	2
850	11765	1.656	1.03E-03	3	1.662	3.28E-03	2	1.622	2.19E-03	2
855	11696	1.656	1.03E-03	3	1.662	3.32E-03	2	1.622	2.36E-03	2
860	11628	1.656	1.09E-03	3	1.662	3.43E-03	2	1.622	2.54E-03	2
865	11561	1.656	1.15E-03	3	1.663	3.54E-03	2	1.621	2.70E-03	2
870	11494	1.656	1.27E-03	3	1.663	3.75E-03	2	1.621	2.87E-03	2
875	11429	1.656	1.34E-03	3	1.663	3.97E-03	2	1.621	3.02E-03	2
880	11364	1.656	1.36E-03	3	1.664	4.33E-03	2	1.621	3.17E-03	2
885	11299	1.656	1.49E-03	3	1.665	4.55E-03	2	1.621	3.31E-03	2
890	11236	1.657	1.55E-03	3	1.666	4.55E-03	2	1.620	3.44E-03	2
895	11173	1.657	1.53E-03	3	1.666	4.35E-03	2	1.620	3.56E-03	2
900	11111	1.657	1.72E-03	3	1.666	4.26E-03	2	1.620	3.67E-03	2
905	11050	1.658	1.97E-03	3	1.666	4.21E-03	2	1.620	3.77E-03	3
910	10989	1.657	1.92E-03	3	1.665	3.90E-03	2	1.620	3.88E-03	3
915	10929	1.657	1.88E-03	3	1.664	3.56E-03	2	1.620	3.97E-03	3
920	10870	1.657	2.03E-03	3	1.663	3.31E-03	2	1.619	4.03E-03	3
925	10811	1.656	2.00E-03	3	1.662	3.28E-03	2	1.619	4.03E-03	3
930	10753	1.655	1.95E-03	3	1.661	3.30E-03	2	1.619	3.98E-03	3
935	10695	1.654	1.85E-03	3	1.660	3.45E-03	2	1.619	3.92E-03	3
940	10638	1.654	1.81E-03	3	1.659	3.37E-03	2	1.619	3.84E-03	3
945	10582	1.653	1.73E-03	3	1.657	3.23E-03	2	1.619	3.77E-03	3
950	10526	1.652	1.66E-03	3	1.656	3.04E-03	2	1.619	3.68E-03	3
955	10471	1.651	1.61E-03	3	1.654	2.73E-03	2	1.619	3.58E-03	3
960	10417	1.650	1.55E-03	3	1.652	2.66E-03	2	1.619	3.44E-03	3

965	10363	1.648	1.40E-03	3	1.650	2.22E-03	2	1.619	3.32E-03	3
970	10309	1.647	1.27E-03	3	1.649	2.10E-03	2	1.619	3.19E-03	3
975	10256	1.646	1.25E-03	3	1.648	1.90E-03	2	1.619	3.04E-03	3
980	10204	1.644	1.11E-03	3	1.647	1.83E-03	2	1.619	2.86E-03	3
985	10152	1.644	1.16E-03	3	1.647	1.75E-03	2	1.619	2.66E-03	3
990	10101	1.643	1.16E-03	3	1.647	1.76E-03	2	1.619	2.43E-03	3
995	10050	1.642	1.08E-03	3	1.647	1.81E-03	2	1.619	2.19E-03	3
1000	10000	1.642	1.12E-03	3	1.646	1.92E-03	2	1.620	2.30E-03	3
1005	9950	1.642	1.17E-03	3	1.646	1.79E-03	2	1.621	2.49E-03	3
1010	9901	1.642	1.21E-03	3	1.645	1.59E-03	2	1.622	2.31E-03	3
1015	9852	1.641	1.20E-03	3	1.645	1.51E-03	2	1.622	2.17E-03	3
1020	9804	1.641	1.18E-03	3	1.645	1.46E-03	2	1.623	2.00E-03	3
1025	9756	1.641	1.19E-03	3	1.644	1.77E-03	2	1.623	1.84E-03	3
1030	9709	1.640	1.14E-03	3	1.643	1.94E-03	2	1.623	1.73E-03	3
1035	9662	1.640	1.23E-03	3	1.643	1.94E-03	2	1.622	1.65E-03	3
1040	9615	1.639	1.24E-03	3	1.642	2.43E-03	2	1.622	1.74E-03	3
1045	9569	1.639	1.28E-03	3	1.640	3.21E-03	2	1.622	1.65E-03	3
1050	9524	1.639	1.28E-03	3	1.639	4.05E-03	2	1.621	1.60E-03	3
1055	9479	1.638	1.23E-03	3	1.638	4.74E-03	2	1.621	1.63E-03	3
1060	9434	1.637	1.66E-03	3	1.637	5.47E-03	2	1.621	1.72E-03	3
1065	9390	1.636	2.27E-03	3	1.636	6.05E-03	2	1.621	1.80E-03	3
1070	9346	1.636	2.67E-03	3	1.636	6.53E-03	2	1.620	1.86E-03	3
1075	9302	1.635	3.09E-03	3	1.635	6.92E-03	2	1.619	1.59E-03	3
1080	9259	1.634	3.52E-03	3	1.634	7.46E-03	2	1.618	1.17E-03	3
1085	9217	1.634	4.02E-03	3	1.634	7.89E-03	2	1.617	1.12E-03	3
1090	9174	1.633	4.50E-03	3	1.634	8.44E-03	2	1.616	1.09E-03	3
1095	9132	1.633	4.94E-03	3	1.633	8.92E-03	2	1.615	1.06E-03	3
1100	9091	1.632	5.34E-03	3	1.633	9.10E-03	2	1.615	1.05E-03	3
1105	9050	1.632	5.70E-03	2	1.633	9.41E-03	2	1.615	1.01E-03	3
1110	9009	1.632	5.93E-03	2	1.633	9.61E-03	2	1.615	1.04E-03	3

1115	8969	1.631	6.23E-03	2	1.634	9.51E-03	2	1.615	9.10E-04	3
1120	8929	1.631	6.48E-03	2	1.635	9.03E-03	2	1.615	8.97E-04	3
1125	8889	1.631	6.65E-03	2	1.636	8.62E-03	2	1.615	9.17E-04	3
1130	8850	1.631	6.93E-03	2	1.636	8.28E-03	2	1.615	8.37E-04	3
1135	8811	1.632	6.83E-03	2	1.637	8.03E-03	2	1.615	7.02E-04	3
1140	8772	1.632	6.66E-03	2	1.637	7.93E-03	2	1.615	6.16E-04	3
1145	8734	1.633	6.64E-03	2	1.637	7.93E-03	2	1.616	5.87E-04	3
1150	8696	1.633	6.61E-03	2	1.638	7.92E-03	2	1.615	8.82E-04	3
1155	8658	1.633	6.45E-03	2	1.638	7.79E-03	2	1.615	1.38E-03	3
1160	8621	1.634	6.18E-03	2	1.639	7.57E-03	2	1.615	1.81E-03	3
1165	8584	1.635	5.87E-03	2	1.639	7.31E-03	2	1.614	2.10E-03	3
1170	8547	1.635	5.56E-03	2	1.640	7.06E-03	2	1.613	2.65E-03	3
1175	8511	1.636	5.26E-03	2	1.640	6.80E-03	2	1.612	3.18E-03	3
1180	8475	1.636	4.98E-03	2	1.641	6.54E-03	2	1.612	3.36E-03	3
1185	8439	1.637	4.72E-03	2	1.641	6.29E-03	2	1.611	3.75E-03	3
1190	8403	1.637	4.50E-03	2	1.641	6.07E-03	2	1.610	3.97E-03	3
1195	8368	1.638	4.32E-03	2	1.642	5.89E-03	2	1.609	4.12E-03	3
1200	8333	1.638	4.13E-03	2	1.642	5.74E-03	1	1.608	4.75E-03	3
1205	8299	1.638	3.96E-03	2	1.642	5.56E-03	1	1.607	4.81E-03	3
1210	8264	1.639	3.79E-03	2	1.643	5.39E-03	1	1.606	5.18E-03	3
1215	8230	1.639	3.59E-03	2	1.643	5.18E-03	1	1.604	5.56E-03	3
1220	8197	1.639	3.40E-03	2	1.643	4.98E-03	1	1.603	5.94E-03	3
1225	8163	1.639	3.23E-03	2	1.643	4.79E-03	1	1.602	5.98E-03	3
1230	8130	1.640	3.16E-03	2	1.644	4.69E-03	1	1.601	5.90E-03	3
1235	8097	1.640	3.19E-03	2	1.644	4.68E-03	1	1.601	5.87E-03	3
1240	8065	1.640	3.27E-03	2	1.644	4.72E-03	1	1.600	5.98E-03	3
1245	8032	1.640	3.38E-03	2	1.644	4.78E-03	1	1.600	5.80E-03	3
1250	8000	1.640	3.49E-03	2	1.644	4.83E-03	1	1.600	5.62E-03	3
1255	7968	1.640	3.60E-03	2	1.644	4.88E-03	1	1.600	5.78E-03	3
1260	7937	1.640	3.70E-03	2	1.644	4.96E-03	1	1.600	5.68E-03	3

1265	7905	1.640	3.79E-03	2	1.644	5.03E-03	1	1.600	5.74E-03	3
1270	7874	1.640	3.84E-03	2	1.644	5.07E-03	1	1.599	5.94E-03	3
1275	7843	1.640	3.89E-03	2	1.644	5.10E-03	1	1.600	5.63E-03	3
1280	7813	1.640	3.92E-03	2	1.644	5.12E-03	1	1.600	5.95E-03	3
1285	7782	1.640	3.91E-03	2	1.644	5.11E-03	1	1.600	5.96E-03	3
1290	7752	1.640	3.86E-03	2	1.645	5.07E-03	1	1.601	5.93E-03	3
1295	7722	1.640	3.77E-03	2	1.645	4.99E-03	1	1.601	5.88E-03	3
1300	7692	1.640	3.67E-03	2	1.645	4.93E-03	1	1.602	5.80E-03	3
1305	7663	1.641	3.57E-03	2	1.645	4.85E-03	1	1.602	5.71E-03	2
1310	7634	1.641	3.45E-03	2	1.645	4.76E-03	1	1.603	5.63E-03	2
1315	7605	1.641	3.33E-03	2	1.645	4.65E-03	1	1.603	5.54E-03	2
1320	7576	1.641	3.23E-03	2	1.645	4.56E-03	1	1.603	5.49E-03	2
1325	7547	1.641	3.13E-03	2	1.645	4.47E-03	1	1.604	5.46E-03	2
1330	7519	1.641	3.03E-03	2	1.645	4.39E-03	1	1.604	5.44E-03	2
1335	7491	1.641	2.94E-03	2	1.645	4.31E-03	1	1.604	5.43E-03	2
1340	7463	1.641	2.87E-03	2	1.645	4.26E-03	1	1.604	5.44E-03	2
1345	7435	1.641	2.82E-03	2	1.645	4.23E-03	1	1.605	5.46E-03	2
1350	7407	1.641	2.78E-03	2	1.646	4.21E-03	1	1.605	5.47E-03	2
1355	7380	1.641	2.72E-03	2	1.646	4.16E-03	1	1.605	5.44E-03	2
1360	7353	1.641	2.66E-03	2	1.646	4.11E-03	1	1.605	5.39E-03	2
1365	7326	1.641	2.61E-03	2	1.646	4.07E-03	1	1.606	5.33E-03	2
1370	7299	1.641	2.57E-03	2	1.646	4.04E-03	1	1.606	5.30E-03	2
1375	7273	1.641	2.54E-03	2	1.646	4.01E-03	1	1.606	5.30E-03	2
1380	7246	1.641	2.52E-03	2	1.646	4.00E-03	1	1.606	5.35E-03	2
1385	7220	1.641	2.51E-03	2	1.646	4.00E-03	1	1.606	5.41E-03	2
1390	7194	1.641	2.51E-03	2	1.646	4.04E-03	1	1.606	5.46E-03	2
1395	7168	1.641	2.52E-03	2	1.646	4.08E-03	1	1.606	5.51E-03	2
1400	7143	1.641	2.54E-03	3	1.646	4.14E-03	1	1.606	5.53E-03	2
1405	7117	1.641	2.56E-03	3	1.646	4.19E-03	1	1.606	5.54E-03	2
1410	7092	1.641	2.56E-03	3	1.646	4.23E-03	1	1.606	5.52E-03	2

1415	7067	1.641	2.55E-03	3	1.646	4.21E-03	1	1.606	5.44E-03	2
1420	7042	1.641	2.49E-03	3	1.646	4.17E-03	1	1.607	5.32E-03	2
1425	7018	1.641	2.43E-03	3	1.646	4.10E-03	1	1.607	5.17E-03	2
1430	6993	1.640	2.36E-03	3	1.645	4.05E-03	1	1.607	5.03E-03	2
1435	6969	1.640	2.30E-03	3	1.645	4.01E-03	1	1.607	4.91E-03	2
1440	6944	1.640	2.25E-03	3	1.645	3.98E-03	1	1.607	4.81E-03	2
1445	6920	1.640	2.21E-03	3	1.645	3.96E-03	1	1.607	4.73E-03	2
1450	6897	1.640	2.17E-03	3	1.645	3.93E-03	1	1.607	4.64E-03	2
1455	6873	1.640	2.13E-03	3	1.645	3.90E-03	1	1.608	4.52E-03	2
1460	6849	1.640	2.10E-03	3	1.645	3.87E-03	1	1.608	4.38E-03	2
1465	6826	1.640	2.07E-03	3	1.645	3.83E-03	1	1.608	4.24E-03	2
1470	6803	1.640	2.05E-03	3	1.645	3.78E-03	1	1.608	4.10E-03	2
1475	6780	1.640	2.02E-03	3	1.645	3.73E-03	1	1.608	3.97E-03	2
1480	6757	1.640	2.00E-03	3	1.645	3.68E-03	1	1.608	3.84E-03	2
1485	6734	1.640	1.97E-03	3	1.645	3.62E-03	1	1.608	3.73E-03	2
1490	6711	1.640	1.94E-03	3	1.645	3.60E-03	1	1.608	3.63E-03	2
1495	6689	1.639	1.94E-03	3	1.645	3.60E-03	1	1.609	3.56E-03	2
1500	6667	1.639	1.95E-03	3	1.645	3.64E-03	1	1.609	3.52E-03	2
1505	6645	1.639	1.98E-03	3	1.645	3.69E-03	1	1.609	3.51E-03	2
1510	6623	1.639	2.01E-03	3	1.644	3.74E-03	1	1.609	3.52E-03	2
1515	6601	1.639	2.05E-03	3	1.644	3.80E-03	1	1.609	3.52E-03	2
1520	6579	1.639	2.08E-03	3	1.644	3.83E-03	1	1.609	3.50E-03	2
1525	6557	1.639	2.10E-03	3	1.644	3.87E-03	1	1.609	3.47E-03	2
1530	6536	1.639	2.10E-03	3	1.644	3.90E-03	1	1.609	3.45E-03	2
1535	6515	1.639	2.09E-03	3	1.644	3.93E-03	1	1.609	3.44E-03	2
1540	6494	1.639	2.09E-03	3	1.644	3.94E-03	1	1.609	3.43E-03	2
1545	6472	1.639	2.09E-03	3	1.644	3.95E-03	1	1.609	3.43E-03	2
1550	6452	1.638	2.10E-03	3	1.644	3.96E-03	1	1.609	3.43E-03	2
1555	6431	1.638	2.12E-03	3	1.644	3.98E-03	1	1.609	3.43E-03	2
1560	6410	1.638	2.14E-03	3	1.644	4.00E-03	1	1.609	3.44E-03	2

1565	6390	1.638	2.16E-03	3	1.644	4.03E-03	1	1.609	3.44E-03	2
1570	6369	1.638	2.19E-03	3	1.643	4.05E-03	1	1.609	3.44E-03	2
1575	6349	1.638	2.21E-03	3	1.643	4.07E-03	1	1.609	3.44E-03	2
1580	6329	1.638	2.24E-03	3	1.643	4.09E-03	1	1.609	3.45E-03	2
1585	6309	1.638	2.25E-03	3	1.643	4.09E-03	1	1.609	3.46E-03	2
1590	6289	1.637	2.25E-03	3	1.643	4.08E-03	1	1.609	3.45E-03	2
1595	6270	1.637	2.24E-03	3	1.643	4.05E-03	1	1.608	3.45E-03	2
1600	6250	1.637	2.23E-03	3	1.643	4.04E-03	1	1.608	3.45E-03	2
1605	6231	1.637	2.23E-03	3	1.642	4.03E-03	1	1.608	3.47E-03	2
1610	6211	1.637	2.24E-03	3	1.642	4.03E-03	1	1.608	3.49E-03	2
1615	6192	1.636	2.26E-03	3	1.642	4.04E-03	1	1.608	3.51E-03	2
1620	6173	1.636	2.26E-03	3	1.642	4.04E-03	1	1.608	3.52E-03	2
1625	6154	1.636	2.23E-03	3	1.642	4.03E-03	1	1.608	3.53E-03	2
1630	6135	1.636	2.18E-03	3	1.641	4.00E-03	1	1.608	3.54E-03	2
1635	6116	1.635	2.15E-03	3	1.641	3.97E-03	1	1.608	3.56E-03	2
1640	6098	1.635	2.14E-03	3	1.641	3.96E-03	1	1.608	3.59E-03	2
1645	6079	1.635	2.14E-03	3	1.641	3.99E-03	1	1.608	3.63E-03	2
1650	6061	1.635	2.15E-03	3	1.641	4.01E-03	1	1.608	3.67E-03	2
1655	6042	1.635	2.17E-03	3	1.641	4.04E-03	1	1.608	3.72E-03	2
1660	6024	1.635	2.18E-03	3	1.641	4.05E-03	1	1.608	3.76E-03	2
1665	6006	1.635	2.19E-03	3	1.640	4.08E-03	1	1.608	3.79E-03	2
1670	5988	1.634	2.20E-03	3	1.640	4.09E-03	1	1.607	3.82E-03	2
1675	5970	1.634	2.21E-03	3	1.640	4.09E-03	1	1.607	3.83E-03	2
1680	5952	1.634	2.20E-03	3	1.640	4.07E-03	1	1.607	3.83E-03	2
1685	5935	1.634	2.18E-03	3	1.640	4.05E-03	1	1.607	3.84E-03	2
1690	5917	1.634	2.15E-03	3	1.640	4.02E-03	1	1.607	3.84E-03	2
1695	5900	1.634	2.14E-03	3	1.639	4.01E-03	1	1.607	3.85E-03	2
1700	5882	1.633	2.17E-03	3	1.639	4.02E-03	1	1.607	3.88E-03	2
1705	5865	1.633	2.22E-03	3	1.639	4.05E-03	1	1.607	3.93E-03	2
1710	5848	1.633	2.25E-03	3	1.639	4.08E-03	1	1.607	3.96E-03	2

1715	5831	1.633	2.23E-03	3	1.639	4.08E-03	1	1.607	3.99E-03	2
1720	5814	1.633	2.19E-03	3	1.639	4.04E-03	1	1.607	4.01E-03	2
1725	5797	1.633	2.13E-03	3	1.639	3.97E-03	1	1.607	4.00E-03	2
1730	5780	1.633	2.08E-03	3	1.639	3.90E-03	1	1.606	3.99E-03	2
1735	5764	1.632	2.05E-03	3	1.638	3.87E-03	1	1.606	3.98E-03	2
1740	5747	1.632	2.04E-03	3	1.638	3.85E-03	1	1.606	4.00E-03	2
1745	5731	1.632	2.02E-03	3	1.638	3.85E-03	1	1.606	4.02E-03	2
1750	5714	1.632	2.03E-03	3	1.638	3.83E-03	1	1.606	4.04E-03	2
1755	5698	1.632	2.02E-03	3	1.638	3.83E-03	1	1.606	4.05E-03	2
1760	5682	1.632	2.02E-03	3	1.638	3.80E-03	1	1.606	4.07E-03	2
1765	5666	1.631	1.98E-03	3	1.638	3.77E-03	1	1.606	4.07E-03	2
1770	5650	1.631	1.92E-03	3	1.638	3.72E-03	1	1.606	4.08E-03	2
1775	5634	1.631	1.85E-03	3	1.637	3.66E-03	1	1.606	4.07E-03	2
1780	5618	1.631	1.79E-03	3	1.637	3.61E-03	1	1.606	4.07E-03	2
1785	5602	1.631	1.75E-03	3	1.637	3.55E-03	1	1.605	4.05E-03	2
1790	5587	1.630	1.75E-03	3	1.637	3.51E-03	1	1.605	4.06E-03	2
1795	5571	1.630	1.76E-03	3	1.637	3.48E-03	1	1.605	4.07E-03	2
1800	5556	1.630	1.76E-03	2	1.637	3.46E-03	1	1.605	4.11E-03	2
1805	5540	1.630	1.75E-03	2	1.637	3.43E-03	1	1.605	4.13E-03	2
1810	5525	1.630	1.73E-03	2	1.636	3.38E-03	1	1.605	4.14E-03	2
1815	5510	1.629	1.68E-03	2	1.636	3.33E-03	1	1.605	4.13E-03	2
1820	5495	1.629	1.64E-03	2	1.636	3.29E-03	1	1.604	4.12E-03	2
1825	5479	1.629	1.59E-03	2	1.636	3.26E-03	1	1.604	4.11E-03	2
1830	5464	1.629	1.55E-03	2	1.636	3.24E-03	1	1.604	4.11E-03	2
1835	5450	1.628	1.52E-03	2	1.636	3.21E-03	1	1.604	4.09E-03	2
1840	5435	1.628	1.50E-03	2	1.635	3.16E-03	1	1.604	4.08E-03	2
1845	5420	1.628	1.47E-03	2	1.635	3.13E-03	1	1.604	4.07E-03	2
1850	5405	1.628	1.44E-03	2	1.635	3.09E-03	1	1.604	4.05E-03	2
1855	5391	1.627	1.42E-03	2	1.635	3.05E-03	1	1.603	4.02E-03	2
1860	5376	1.627	1.36E-03	2	1.635	2.99E-03	1	1.603	3.99E-03	2

1865	5362	1.627	1.30E-03	2	1.635	2.92E-03	1	1.603	3.96E-03	2
1870	5348	1.627	1.24E-03	2	1.634	2.84E-03	1	1.603	3.94E-03	2
1875	5333	1.626	1.19E-03	2	1.634	2.76E-03	1	1.603	3.91E-03	2
1880	5319	1.626	1.14E-03	2	1.634	2.70E-03	1	1.603	3.89E-03	2
1885	5305	1.626	1.09E-03	2	1.634	2.65E-03	1	1.603	3.88E-03	2
1890	5291	1.626	1.05E-03	2	1.634	2.61E-03	1	1.602	3.87E-03	2
1895	5277	1.625	1.02E-03	2	1.633	2.55E-03	1	1.602	3.85E-03	2
1900	5263	1.625	1.01E-03	2	1.633	2.50E-03	3	1.602	3.85E-03	3
1905	5249	1.625	9.95E-04	2	1.633	2.46E-03	3	1.602	3.85E-03	3
1910	5236	1.625	9.91E-04	2	1.633	2.46E-03	3	1.602	3.86E-03	3
1915	5222	1.625	1.01E-03	2	1.633	2.48E-03	3	1.602	3.90E-03	3
1920	5208	1.625	1.05E-03	2	1.633	2.52E-03	3	1.602	3.95E-03	3
1925	5195	1.625	1.10E-03	2	1.633	2.58E-03	3	1.602	4.00E-03	3
1930	5181	1.625	1.13E-03	2	1.633	2.62E-03	3	1.601	4.03E-03	3
1935	5168	1.624	1.15E-03	2	1.633	2.64E-03	3	1.601	4.05E-03	3
1940	5155	1.624	1.14E-03	2	1.633	2.63E-03	3	1.601	4.05E-03	3
1945	5141	1.624	1.18E-03	2	1.632	2.69E-03	3	1.601	4.05E-03	3
1950	5128	1.623	1.27E-03	2	1.632	2.81E-03	3	1.600	4.05E-03	3
1955	5115	1.623	1.36E-03	2	1.632	2.95E-03	3	1.600	4.07E-03	3
1960	5102	1.623	1.43E-03	2	1.632	3.03E-03	3	1.600	4.08E-03	3
1965	5089	1.623	1.45E-03	2	1.631	3.04E-03	3	1.600	4.07E-03	3
1970	5076	1.622	1.45E-03	2	1.631	3.04E-03	3	1.599	4.04E-03	3
1975	5063	1.622	1.44E-03	2	1.631	3.04E-03	3	1.599	4.00E-03	3
1980	5051	1.622	1.44E-03	2	1.631	3.03E-03	3	1.599	3.96E-03	3
1985	5038	1.622	1.43E-03	2	1.631	2.99E-03	3	1.599	3.92E-03	3
1990	5025	1.621	1.40E-03	2	1.631	2.96E-03	3	1.599	3.87E-03	3
1995	5013	1.621	1.34E-03	2	1.630	2.89E-03	3	1.599	3.81E-03	3
2000	5000	1.621	1.25E-03	2	1.630	2.79E-03	3	1.599	3.73E-03	3
2005	4988	1.620	1.17E-03	2	1.630	2.68E-03	3	1.598	3.65E-03	3
2010	4975	1.620	1.11E-03	2	1.630	2.63E-03	3	1.598	3.58E-03	3

2015	4963	1.620	1.08E-03	2	1.630	2.61E-03	3	1.598	3.54E-03	3
2020	4950	1.620	1.02E-03	2	1.630	2.53E-03	3	1.598	3.48E-03	3
2025	4938	1.620	9.20E-04	2	1.630	2.37E-03	3	1.598	3.41E-03	3
2030	4926	1.621	7.96E-04	2	1.630	2.14E-03	3	1.598	3.30E-03	3
2035	4914	1.621	7.12E-04	2	1.630	1.97E-03	3	1.598	3.21E-03	3
2040	4902	1.621	6.68E-04	2	1.630	1.86E-03	3	1.598	3.14E-03	3
2045	4890	1.621	6.48E-04	2	1.629	1.75E-03	3	1.598	3.08E-03	3
2050	4878	1.620	6.10E-04	2	1.629	1.63E-03	3	1.598	3.00E-03	3
2055	4866	1.620	5.59E-04	2	1.629	1.49E-03	3	1.598	2.92E-03	3
2060	4854	1.620	5.11E-04	2	1.628	1.35E-03	3	1.598	2.83E-03	3
2065	4843	1.619	5.12E-04	2	1.628	1.25E-03	3	1.598	2.77E-03	3
2070	4831	1.619	5.09E-04	2	1.628	1.14E-03	3	1.597	2.68E-03	3
2075	4819	1.619	5.61E-04	2	1.627	1.04E-03	3	1.597	2.62E-03	3
2080	4808	1.618	5.77E-04	2	1.627	8.67E-04	3	1.597	2.53E-03	3
2085	4796	1.617	5.89E-04	2	1.626	7.53E-04	3	1.597	2.43E-03	3
2090	4785	1.616	6.03E-04	2	1.625	6.85E-04	3	1.596	2.33E-03	3
2095	4773	1.615	6.30E-04	2	1.625	5.90E-04	3	1.596	2.33E-03	3
2100	4762	1.614	1.07E-03	2	1.625	8.97E-04	3	1.595	2.56E-03	3

Table A3.2: 2σ uncertainties calculated for *n*- and *k*-values determined with "λ-by-λ" numerical inversion method. The error bars were calculated based on the uncertainties of I_s^{exp} and I_c^{exp} at different wavelengths. Note that these error bars do not include all the uncertainties on *n*- and *k*-values, but only the major source of uncertainties, which is the inversion model used. To obtain an envelope of uncertainty, linear interpolation between two error bars was realized.

2σ Uncertainties	F_H				F_{400}				F_{650}			
[nm]	***n***		***k***		***n***		***k***		***n***		***k***	
	Δ*n* (±)	**Δ*n*/*n***	**Δ*k* (±)**	**Δ*k*/*k***	**Δ*n* (±)**	**Δ*n*/*n***	**Δ*k* (±)**	**Δ*k*/*k***	**Δ*n* (±)**	**Δ*n*/*n***	**Δ*k* (±)**	**Δ*k*/*k***
300	0.014	0.8%	0.004	2%	0.019	1.1%	0.007	3.2%	0.001	0.1%	0.001	1%
400	0.003	0.2%	0.001	2%	0.002	0.1%	0.002	3%	0.002	0.1%	0.003	14%
450									0.001	0.1%	0.001	10%
525	0.003	0.2%	0.002	15%	0.001	0.1%	0.001	7%				
590									0.002	0.1%	0.001	32%
600	0.001	0.1%	0.001	37%	0.001	0.1%	0.002	60%	0.001	0.1%	0.001	36%
760	0.002	0.1%	0.002	95%	0.003	0.2%	0.002	55%	0.004	0.2%	0.001	55%
850	0.001	0.1%	0.001	97%	0.001	0.1%	0.001	31%	0.002	0.1%	0.001	46%
940	0.002	0.1%	0.001	55%	0.002	0.1%	0.001	30%	0.001	0.1%	0.002	52%
1000	0.001	0.1%	0.001	90%	0.002	0.1%	0.001	52%	0.003	0.2%	0.004	174%
1100	0.001	0.1%	0.001	19%	0.003	0.2%	0.001	10%	0.001	0.1%	0.001	95%
1200	0.004	0.2%	0.001	24%	0.004	0.2%	0.001	17%	0.004	0.2%	0.003	63%
1300	0.004	0.2%	0.001	27%	0.004	0.2%	0.001	20%	0.012	0.7%	0.007	121%
1410	0.003	0.2%	0.002	78%	0.003	0.2%	0.001	24%	0.004	0.2%	0.002	36%
1500	0.003	0.2%	0.003	154%	0.003	0.2%	0.003	82%	0.004	0.2%	0.001	28%
1600	0.002	0.1%	0.004	180%	0.002	0.1%	0.001	25%	0.003	0.2%	0.002	58%
1700	0.002	0.1%	0.001	46%	0.001	0.1%	0.001	25%	0.003	0.2%	0.003	77%
1800	0.001	0.1%	0.001	57%	0.001	0.1%	0.001	29%	0.002	0.1%	0.003	73%
1900	0.002	0.1%	0.004	398%	0.001	0.1%	0.003	120%	0.002	0.1%	0.004	104%
2000	0.001	0.1%	0.001	80%	0.001	0.1%	0.001	36%	0.001	0.1%	0.004	107%
2100	0.003	0.2%	0.004	375%	0.004	0.2%	0.005	557%	0.003	0.2%	0.003	117%

Appendix A4: Deconvolution of the IGLIAS background mass spectrum

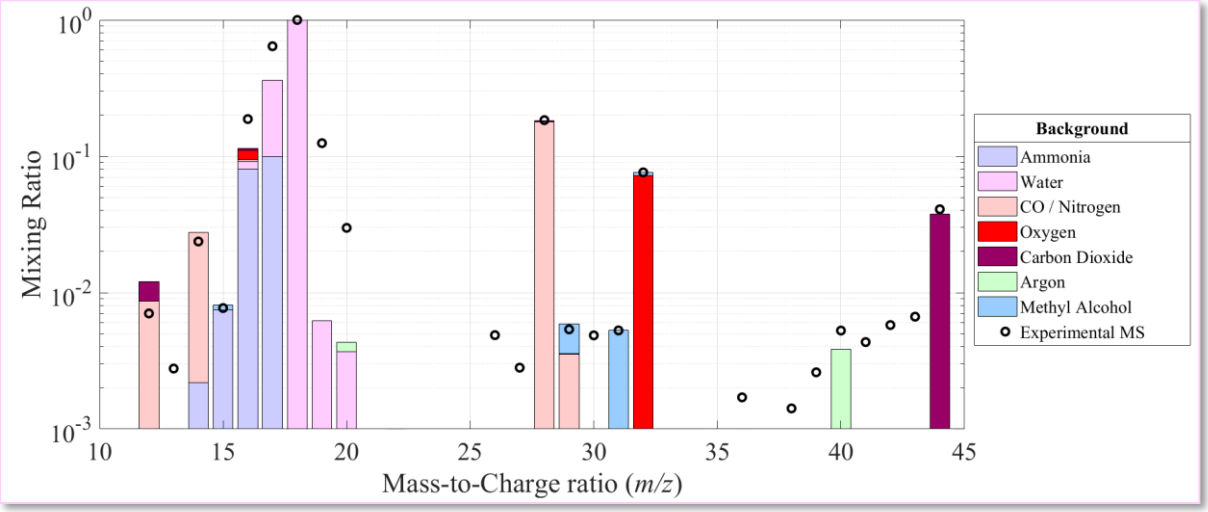

Figure A4.1: Preliminary results of the deconvolution of the blank mass spectrum (*i.e.*, before irradiation of Pluto tholins F_P). The black dots correspond to the experimental mass spectrum, whereas the colored bars correspond to the contribution of each molecule calculated by the deconvolution method developed by Gautier *et al.* (2020).

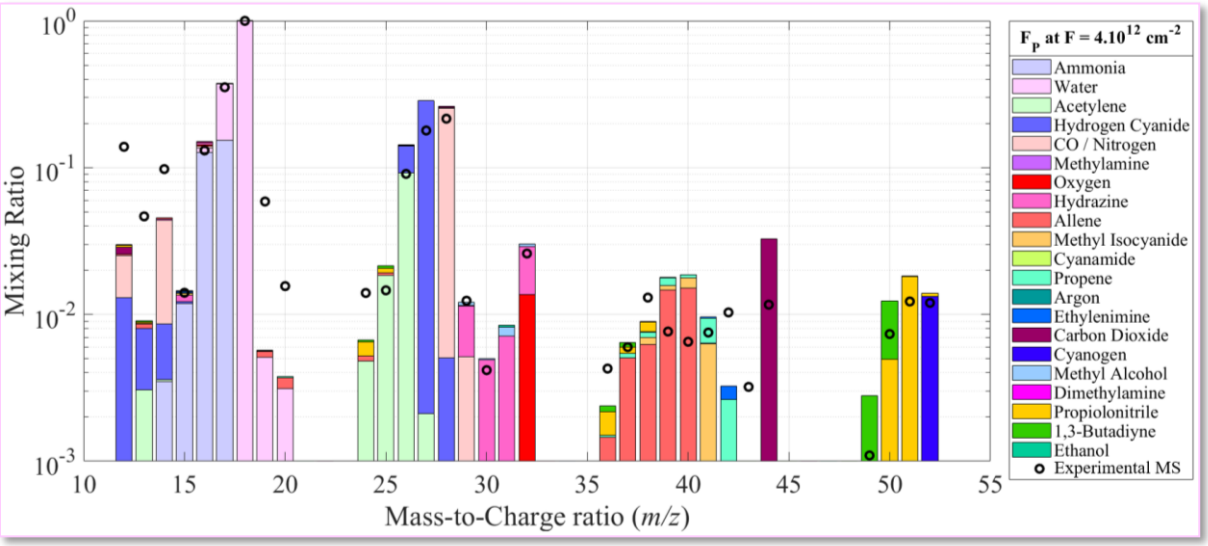

Figure A4.2: Preliminary results of the deconvolution of the mass spectrum in black color shown in Figure VI.11 ($F = 4\times10^{12}$ cm^{-2}). The black dots correspond to the experimental mass spectrum, whereas the colored bars correspond to the contribution of each molecule calculated by the deconvolution method developed by Gautier *et al.* (2020).

Table of illustrations (Figures and Tables)

Figures

Tables

References

Ada Bibang, P. C. J. *et al.* (2019) 'Ion radiation in icy space environments: Synthesis and radioresistance of complex organic molecules', *Low Temperature Physics*. AIP Publishing LLC, 45(692–700), pp. 590–597. doi: 10.1063/1.5103250.

Alcouffe, G. *et al.* (2010) 'Capacitively coupled plasma used to simulate Titan's atmospheric chemistry', *Plasma Sources Science and Technology*, 19(1), p. 15008. doi: 10.1088/0963-0252/19/1/015008.

Allodi, M. A. *et al.* (2013) 'Complementary and Emerging Techniques for Astrophysical Ices Processed in the Laboratory', *Space Science Reviews*, 180(1–4), pp. 101–175. doi: 10.1007/s11214-013-0020-8.

Alves, L. L. *et al.* (2012) 'Capacitively coupled radio-frequency discharges in nitrogen at low pressures', *Plasma Sources Science and Technology*, 21(4), p. 45008. doi: 10.1088/0963-0252/21/4/045008.

Amato, E. and Blasi, P. (2018) 'Cosmic ray transport in the Galaxy: A review', *Advances in Space Research*, 62(10), pp. 2731–2749. doi: 10.1016/j.asr.2017.04.019.

Andersson, L. E. and Fix, J. D. (1973) 'Pluto: New Photometry and a Determination of the Axis of Rotation', *Icarus*, 20, pp. 279–283.

Andronico, G. *et al.* (1987) 'Optical evolution of laboratory-produced organics: Applications to Phoebe, Iapetus, outer belt asteroids and cometary nuclei', *Astronomy and Astrophysics*, 184, pp. 333–336.

Anicich, V. G. and McEwan, M. J. (1997) 'Ion-molecule chemistry in Titan's ionosphere', *Planetary and Space Science*, 45(8), pp. 897–921. doi: https://doi.org/10.1016/S0032-0633(97)00053-6.

Anicich, V. G., Wilson, P. and McEwan, M. J. (2003) 'Termolecular ion-molecule reactions in Titan's atmosphere. IV. A search made at up to 1 micron in pure hydrocarbons', *Journal of the American Society for Mass Spectrometry*, 14(8), pp. 900–915. doi: 10.1016/S1044-0305(03)00218-6.

Arakawa, S., Hyodo, R. and Genda, H. (2019) 'Early formation of moons around large trans-Neptunian objects via giant impacts', *Nature Astronomy*. Springer US, 3(9), pp. 802–807. doi: 10.1038/s41550-019-0797-9.

Augé, B. *et al.* (2016) 'Irradiation of nitrogen-rich ices by swift heavy ions: Clues for the formation of ultracarbonaceous micrometeorites', *Astronomy and Astrophysics*, 592(A99), pp. 1–9. doi: 10.1051/0004-6361/201527650.

Augé, B. (2017) *Effets du rayonnement cosmique galactique sur les petits corps glacés du système solaire externe : Indices pour la formation de la matière organique des micrométéorites antarctiques ultracarbonées*. Université de Caen Normandie.

Augé, B. *et al.* (2018) 'IGLIAS: A new experimental set-up for low temperature irradiation studies at large irradiation facilities', *Review of Scientific Instruments*. American Institute of Physics, 89(7), p. 75105. doi: 10.1063/1.5028056.

Avasthi, D. K. and Mehta, G. K. (2011) *Swift Heavy Ions for Materials Engineering and Nanostructuring, Springer Series in Materials Science*.

Azzam, R. M. A. and Bashara, N. M. (1977) *Ellipsometry and Polarized Light*, *Ellipsometry and Polarized Light*. North-Holland Publishing Company.

Bagenal, F. *et al.* (2016) 'Pluto's interaction with its space environment: Solar wind, energetic particles, and dust', *Science*, 351(6279), p. aad9045. doi: 10.1126/science.aad9045.

Baim, M. A., Eatherton, R. L. and Hill, H. H. (1983) 'Ion Mobility Detector for Gas Chromatography with a Direct Photoionization Source', *Analytical Chemistry*, 55(11), pp. 1761–1766. doi:

10.1021/ac00261a026.

Balanzat, E., Betz, N. and Bouffard, S. (1995) 'Swift heavy ion modification of polymers', *Nuclear Instruments and Methods in Physics Research Section B: Beam Interactions with Materials and Atoms*, 105, pp. 46–54.

Banks, J. F. and Whitehouse, C. M. (1996) 'Electrospray Ionization Mass Spectrometry', *Methods in Enzymology*, 270, pp. 486–519. doi: 10.1016/s0076-6879(96)70023-x.

Bar-Nun, A. and Chang, S. (1983) 'Photochemical Reactions of Water and Carbon Monoxide in Earth's Primitive Atmosphere', *Journal of Geophysical Research*, 88(C11), pp. 6662–6672.

Bar-Nun, A. and Hartman, H. (1978) 'Synthesis of organic compounds from carbon monoxide and water by UV photolysis', *Origins of Life*, 9(2), pp. 93–101. doi: 10.1007/BF00931407.

Barman, T. S. *et al.* (2015) 'Simultaneous Detection of Water, Methane and Carbon Monoxide in the Atmosphere of Exoplanet HR 8799 b', *The Astrophysical Journal*, 804(1), p. 61. doi: 10.1088/0004-637x/804/1/61.

Barr, A. C. and Collins, G. C. (2015) 'Tectonic activity on Pluto after the Charon-forming impact', *Icarus*, 246, pp. 146–155. doi: https://doi.org/10.1016/j.icarus.2014.03.042.

Barrère, C. *et al.* (2012) 'Solvent-based and solvent-free characterization of low solubility and low molecular weight polyamides by mass spectrometry: a complementary approach', *Rapid Communications in Mass Spectrometry*, 26, pp. 1347–1354. doi: 10.1002/rcm.6231.

de Barros, A. L. F. *et al.* (2011) 'Radiolysis of frozen methanol by heavy cosmic ray and energetic solar particle analogues', *Monthly Notices of the Royal Astronomical Society*, 418(2), pp. 1363–1374. doi: 10.1111/j.1365-2966.2011.19587.x.

Benner, C. D., Fink, U. and Cromwell, R. H. (1978) 'Image tube spectra of pluto and triton from 6800 to 9000 Å', *Icarus*, 36(1), pp. 82–91. doi: https://doi.org/10.1016/0019-1035(78)90075-1.

Bera, P. P., Head-Gordon, M. and Lee, T. J. (2011) 'Initiating molecular growth in the interstellar medium via dimeric complexes of observed ions and molecules', *Astronomy and Astrophysics*, 535(A74), pp. 1–12. doi: 10.1051/0004-6361/201117103.

Bera, P. P., Lee, T. J. and Schaefer, H. F. (2009) 'Are isomers of the vinyl cyanide ion missing links for interstellar pyrimidine formation?', *Journal of Applied Physics*, 131(7), p. 074303. doi: 10.1063/1.3206298.

Bernard, J.-M. *et al.* (2003) 'Experimental simulation of Titan's atmosphere: Detection of ammonia and ethylene oxide', *Planetary and Space Science*, 51(14), pp. 1003–1011. doi: https://doi.org/10.1016/j.pss.2003.05.009.

Berry, J. L. *et al.* (2019) 'Chemical Composition of Gas-Phase Positive Ions during Laboratory Simulations of Titan's Haze Formation', *ACS Earth and Space Chemistry*, 3(2), pp. 202–211. doi: 10.1021/acsearthspacechem.8b00139.

Berry, J. L. *et al.* (2019) 'The Influence of Gas-phase Chemistry on Organic Haze Formation', *The Astrophysical Journal*. IOP Publishing, 885(1), p. L6. doi: 10.3847/2041-8213/ab4b5b.

Bertrand, T. *et al.* (2018) 'The nitrogen cycles on Pluto over seasonal and astronomical timescales', *Icarus*, 309, pp. 277–296. doi: https://doi.org/10.1016/j.icarus.2018.03.012.

Bertrand, T. *et al.* (2019) 'The CH4 cycles on Pluto over seasonal and astronomical timescales', *Icarus*, 329, pp. 148–165. doi: https://doi.org/10.1016/j.icarus.2019.02.007.

Bertrand, T. *et al.* (2020) 'Equatorial mountains on Pluto are covered by methane frosts resulting from a unique atmospheric process', *Nature Communications*, 11(1), pp. 1–7. doi: 10.1038/s41467-020-18845-3.

Bertrand, T. and Forget, F. (2016) 'Observed glacier and volatile distribution on Pluto from atmosphere–topography processes', *Nature*, 540, p. 86. Available at: https://doi.org/10.1038/nature19337.

Bethe, H. (1930) 'Zur Theorie des Durchgangs schneller Korpuskularstrahlen durch Materie', *Annalen der Physik*. John Wiley & Sons, Ltd, 397(3), pp. 325–400. doi: https://doi.org/10.1002/andp.19303970303.

Betz, N. (1998) 'Chemical Modifications Induced In Swift Heavy Ion Irradiated Polymers', *SPIE Conference on Materials Modification by Ion Irradiation*, 3413, pp. 16–26.

Bierson, C. J., Nimmo, F. and McKinnon, W. B. (2018) 'Implications of the observed Pluto–Charon density contrast', *Icarus*. Elsevier Inc., 309, pp. 207–219. doi: 10.1016/j.icarus.2018.03.007.

Binzel, R. P. (1989) 'Pluto-Charon Mutual Events', *Geophysical Research Letters*, 16(11), pp. 1205–1208.

Binzel, R. P. *et al.* (2017) 'Climate zones on Pluto and Charon', *Icarus*, 287, pp. 30–36. doi: https://doi.org/10.1016/j.icarus.2016.07.023.

Blasi, P. (2013) *The origin of galactic cosmic rays*, *Astronomy and Astrophysics Review*. doi: 10.1007/s00159-013-0070-7.

Bloch, F. (1933) 'Zur Bremsung rasch bewegter Teilchen beim Durchgang durch Materie', *Annalen der Physik*. John Wiley & Sons, Ltd, 408(3), pp. 285–320. doi: https://doi.org/10.1002/andp.19334080303.

Blum, M. M. and John, H. (2012) 'Historical perspective and modern applications of Attenuated Total Reflectance - Fourier Transform Infrared Spectroscopy (ATR-FTIR)', *Drug Testing and Analysis*, 4(3–4), pp. 298–302. doi: 10.1002/dta.374.

Böhme, D. K. (2000) 'Experimental studies of positive ion chemistry with flow-tube mass spectrometry: birth, evolution, and achievements in the 20th century', *International Journal of Mass Spectrometry*, 200(1), pp. 97–136. doi: https://doi.org/10.1016/S1387-3806(00)00299-2.

Bohren, C. F. and Huffman, D. R. (1983) *Absorption and Scattering of Light by Small Particles*. John Wiley & Sons.

Bordalo, V. *et al.* (2013) 'Chemical Processing of Pure Ammonia and Ammonia-Water Ices Induced by Heavy Ions', *The Astrophysical Journal*, 774(105), pp. 1–13. doi: 10.1088/0004-637X/774/2/105.

Boucher, O. (2015) 'Atmospheric Aerosols - Properties and Climate Impacts', in. Springer Netherlands. doi: 10.1007/978-94-017-9649-1_2.

Bouchoule, A. and Ranson, P. (1991) 'Study of volume and surface processes in low pressure radio frequency plasma reactors by pulsed excitation methods. I. Hydrogen–argon plasma', *Journal of Vacuum Science & Technology A*, 9(2), pp. 317–326. doi: 10.1116/1.577508.

Boufendi, L. and Bouchoule, A. (1994) 'Particle nucleation and growth in a low-pressure argon-silane discharge', *Plasma Sources Science and Technology*, 3(3), pp. 262–267. doi: 10.1088/0963-0252/3/3/004.

Bourgalais, J. *et al.* (2019) 'Low-Pressure EUV Photochemical Experiments: Insight on the Ion Chemistry Occurring in Titan's Atmosphere', *Journal of Geophysical Research: Space Physics*, 124(11), pp. 9214–9228. doi: 10.1029/2019JA026953.

Bourgalais, J., Carrasco, N., Changeat, Q., *et al.* (2020) 'Ions in the Thermosphere of Exoplanets: Observable Constraints Revealed by Innovative Laboratory Experiments', *The Astrophysical Journal*, 895(77), pp. 1–13. doi: 10.3847/1538-4357/ab8e2d.

Bourgalais, J., Carrasco, N., Vettier, L., *et al.* (2020) 'On an EUV Atmospheric Simulation Chamber to Study the Photochemical Processes of Titan's Atmosphere', *Scientific Reports*, 10(1), p. 10009. doi: 10.1038/s41598-020-66950-6.

Bourgalais, J. *et al.* (2021) 'Aromatic Formation Promoted by Ion-Driven Radical Pathways in EUV Photochemical Experiments Simulating Titan's Atmospheric Chemistry', *The Journal of Physical Chemistry A*, 125, pp. 3159–3168. doi: 10.1021/acs.jpca.1c00324.

Brack, A. (1993) 'Liquid water and the origin of life', *Origins of life and evolution of the biosphere*, 23(1), pp. 3–10. doi: 10.1007/BF01581985.

Brassé, C. *et al.* (2015) 'Optical constants of Titan aerosols and their tholins analogs: Experimental results and modeling/observational data', *Planetary and Space Science*, 109–110, pp. 159–174. doi: https://doi.org/10.1016/j.pss.2015.02.012.

Broadfoot, A. L. *et al.* (1989) 'Ultraviolet Spectrometer Observations of Neptune and Triton', *Science*, 246(4936), pp. 1459 LP – 1466. doi: 10.1126/science.246.4936.1459.

Broekhuizen, K. E. *et al.* (2004) 'Formation of cloud condensation nuclei by oxidative processing: Unsaturated fatty acids', *Journal of Geophysical Research: Atmospheres*, 109(D24). doi: 10.1029/2004JD005298.

Bromley, B. C. and Kenyon, S. J. (2020) 'A Pluto–Charon Concerto: An Impact on Charon as the Origin of the Small Satellites', *The Astronomical Journal*, 160(2), p. 85. doi: 10.3847/1538-3881/ab9e6c.

Brossier, J. F. *et al.* (2018) 'Geological Evolution of Titan's Equatorial Regions: Possible Nature and Origin of the Dune Material', *Journal of Geophysical Research: Planets*, 123(5), pp. 1089–1112. doi: 10.1029/2017JE005399.

Brown, M. E. and Schaller, E. L. (2005) 'S/2005 (2003 UB_313) 1', *International Astronomical Union*, 8610.

Brown, R. H. *et al.* (2004) 'The Cassini Visual and Infrared Mapping Spectrometer (VIMS) Investigation', in Russell, C. T. (ed.) *The Cassini-Huygens Mission*, p. 111. doi: 10.1007/1-4020-3874-7_3.

Brozović, M. *et al.* (2015) 'The orbits and masses of satellites of Pluto', *Icarus*, 246, pp. 317–329. doi: https://doi.org/10.1016/j.icarus.2014.03.015.

Bruggeman, D. A. G. (1935) 'Berechnung verschiedener physikalischer Konstanten von heterogenen Substanzen. I. Dielektrizitätskonstanten und Leitfähigkeiten der Mischkörper aus isotropen Substanzen', *Annalen der Physik*, 416(7), pp. 636–664. doi: 10.1002/andp.19354160705.

Buie, M. W. *et al.* (2010) 'Pluto and Charon with the Hubble Space Telescope. II. Resolving Changes on Pluto's Surface and a Map for Charon', *The Astronomical JournalAstronomical Journal*, 139(3), pp. 1128–1143. doi: 10.1088/0004-6256/139/3/1128.

Buie, M. W., Tholen, D. J. and Grundy, W. M. (2012) 'The Orbit of Charon is Circular', *The Astronomical Journal*, 144(15), p. 19. doi: 10.1088/0004-6256/144/1/15.

Burgisser, A. and Scaillet, B. (2007) 'Redox evolution of a degassing magma rising to the surface', *Nature*, 445(7124), pp. 194–197. doi: 10.1038/nature05509.

Burton, A. S., Elsila, J. E., *et al.* (2012) 'A propensity for n-omega-amino acids in thermally altered Antarctic meteorites', *Meteoritics & Planetary Science*, 47(3), pp. 374–386. doi: 10.1111/j.1945-5100.2012.01341.x.

Burton, A. S., Stern, J. C., *et al.* (2012) 'Understanding prebiotic chemistry through the analysis of extraterrestrial amino acids and nucelobases in meteorites', *Chemical Society Reviews*, 41, pp. 5459–5472. doi: 10.1039/c2cs35109a.

Cable, M. L. *et al.* (2012) 'Titan Tholins: Simulating Titan Organic Chemistry in the Cassini-Huygens Era', *Chemical Reviews*, 112(3), pp. 1882–1909. doi: 10.1021/cr200221x.

Cai, S.-S. and Syage, J. A. (2006) 'Comparison of Atmospheric Pressure Photoionization, Atmospheric

Pressure Chemical Ionization, and Electrospray Ionization Mass Spectrometry for Analysis of Lipids', *Analytical Chemistry*, 78(4), pp. 1191–1199. doi: 10.1021/ac0515834.

Cai, Y. *et al.* (2005) 'Advantages of atmospheric pressure photoionization mass spectrometry in support of drug discovery', *Rapid Communications in Mass Spectrometry*, 19(12), pp. 1717–1724. doi: 10.1002/rcm.1981.

Callahan, M. P. *et al.* (2011) 'Carbonaceous meteorites contain a wide range of extraterrestrial nucleobases', *Proceedings of the National Academy of Sciences*, 108(34), pp. 13995–13998. doi: 10.1073/pnas.1106493108.

Canagaratna, M. R. *et al.* (2007) 'Chemical and Microphysical Characterization of Ambient Aerosols with the Aerodyne Aerosol Mass Spectrometer', *Mass Spectrometry Reviews*, 26, pp. 185–222. doi: 10.1002/mas.

Canup, R. M. (2005) 'A Giant Impact Origin of Pluto-Charon', *Science*, 307, pp. 546–550.

Canup, R. M. (2011) 'On a Giant Impact Origin of Charon, Nix, and Hydra', *The Astronomical JournalAstronomical Journal*, 141(35), p. 9. doi: 10.1088/0004-6256/141/2/35.

Canup, R. M., Kratter, K. M. and Neveu, M. (2021) 'On the Origin of the Pluto System', in *The Pluto System After New Horizons*.

Cappa, C. D. *et al.* (2011) 'Variations in organic aerosol optical and hygroscopic properties upon heterogeneous OH oxidation', *Journal of Geophysical Research: Atmospheres*, 116(D15). doi: 10.1029/2011JD015918.

Carrasco, N. *et al.* (2009) 'Chemical Characterization of Titan's Tholins: Solubility, Morphology and Molecular Structure Revisited', *The Journal of Physical Chemistry A*, 113(42), pp. 11195–11203. doi: 10.1021/jp904735q.

Carrasco, N. *et al.* (2012) 'Volatile products controlling Titan's tholins production', *Icarus*, 219(1), pp. 230–240. doi: https://doi.org/10.1016/j.icarus.2012.02.034.

Carrasco, N. *et al.* (2016) 'Laboratory analogues simulating Titan's atmospheric aerosols: Compared chemical compositions of grains and thin films', *Planetary and Space Science*, 128, pp. 52–57. doi: https://doi.org/10.1016/j.pss.2016.05.006.

Cechalova, B. *et al.* (2019) 'Optical Properties of Oxidized Plasma-Polymerized Organosilicones and Their Correlation with Mechanical and Chemical Parameters', *Materials*. doi: 10.3390/ma12030539.

Chapiro, A. (1988) 'Chemical Modifications in Irradiated Polymers', *Nuclear Instruments and Methods in Physics Research, B*, 32(1–4), pp. 111–114. doi: 10.1016/0168-583X(88)90191-7.

Cheng, A. F. *et al.* (2008) 'Long-Range Reconnaissance Imager on New Horizons', *Space Science Reviews*, 140(1), pp. 189–215. doi: 10.1007/s11214-007-9271-6.

Cheng, A. F. *et al.* (2017) 'Haze in Pluto's atmosphere', *Icarus*, 290, pp. 112–133. doi: https://doi.org/10.1016/j.icarus.2017.02.024.

Cho, Y. *et al.* (2015) 'Developments in FT-ICR MS Instrumentation, Ionization Techniques, and Data Interpretation Methods for Petroleomics', *Mass Spectrometry Reviews*, 34, pp. 248–263. doi: 10.1021/ef201312m.

Christy, J. W. and Harrington, R. S. (1978) 'The Satellite of Pluto', *The Astronomical Journal*, 83(8), pp. 1005–1008.

Christy, J. W. and Harrington, R. S. (1980) 'The Discovery and Orbit of Charon', *Icarus*, 44(1), pp. 38–40. doi: 10.1016/0019-1035(80)90051-2.

Chudják, S., Kozáková, Z. and Krčma, F. (2021) 'Study of Chemical Processes Initiated by Electrical

Discharge in Titan-Related Atmosphere at Laboratory Temperature and Pressure', *ACS Earth and Space Chemistry*, 5(3), pp. 535–543. doi: 10.1021/acsearthspacechem.0c00308.

Chyba, C. F. (2005) 'Rethinking Earth's Early Atmosphere', *Science*, 308(5724), pp. 962–963. doi: 10.1126/science.1113157.

Chyba, C. and Sagan, C. (1992) 'Endogenous production, exogenous delivery and impact-shock synthesis of organic molecules: An inventory for the origins of life', *Nature*, 355(6356), pp. 125–132. doi: 10.1038/355125a0.

Civiš, S. *et al.* (2004) 'Amino acid formation induced by high-power laser in CO2/CO-N2-H2O gas mixtures', *Chemical Physics Letters*, 386(1–3), pp. 169–173. doi: 10.1016/j.cplett.2004.01.034.

Cleaves, H. J. *et al.* (2008) 'A Reassessment of Prebiotic Organic Synthesis in Neutral Planetary Atmospheres', *Origins of Life and Evolution of Biospheres*, 38(2), pp. 105–115. doi: 10.1007/s11084-007-9120-3.

Coates, A. J. *et al.* (2007) 'Discovery of heavy negative ions in Titan's ionosphere', *Geophysical Research Letters*. John Wiley & Sons, Ltd, 34(22). doi: https://doi.org/10.1029/2007GL030978.

Cody, G. D. *et al.* (2011) 'Establishing a molecular relationship between chondritic and cometary organic solids', *Proceedings of the National Academy of Sciences of the United States of America*, 108(48), pp. 19171–19176. doi: 10.1073/pnas.1015913108.

Coll, P. *et al.* (1999) 'Experimental laboratory simulation of Titan's atmosphere: aerosols and gas phase', *Planetary and Space Science*, 47(10), pp. 1331–1340. doi: https://doi.org/10.1016/S0032-0633(99)00054-9.

Coll, P. *et al.* (2003) 'Oxirane: An Exotic Oxygenated Organic Compound On Titan?', *The Astrophysical Journal*, 598(2003), pp. 700–703.

Coll, P. *et al.* (2013) 'Can laboratory tholins mimic the chemistry producing Titan's aerosols? A review in light of ACP experimental results', *Planetary and Space Science*, 77, pp. 91–103. doi: https://doi.org/10.1016/j.pss.2012.07.006.

Comisarow, M. B. (1993) 'Fundamental aspects of FT-ICR and applications to chemistry', *Hyperfine Interactions*, 81, pp. 171–178.

Cook, J. C. *et al.* (2019) 'The distribution of H2O, CH3OH, and hydrocarbon-ices on Pluto: Analysis of New Horizons spectral images', *Icarus*, 331, pp. 148–169. doi: 10.1016/j.icarus.2018.09.012.

Cooper, G., Rios, A. C. and Nuevo, M. (2018) 'Monosaccharides and Their Derivatives in Carbonaceous Meteorites: A Scenario for Their Synthesis and Onset of Enantiomeric Excesses', *Life*, 8(3), p. 36. doi: 10.3390/life8030036.

Cooper, J. F. *et al.* (2003) 'Proton Irradiation of Centaur, Kuiper Belt, and Oort Cloud Objects at Plasma to Cosmic Ray Energy', *Earth, Moon and Planets*, 92(1–4), pp. 261–277. doi: 10.1023/B:MOON.0000031944.41883.80.

Cottin, H. *et al.* (2017) 'Astrobiology and the Possibility of Life on Earth and Elsewhere…', *Space Science Reviews*, 209(1), pp. 1–42. doi: 10.1007/s11214-015-0196-1.

Coustenis, A. *et al.* (2003) 'Titan's atmosphere from ISO mid-infrared spectroscopy', *Icarus*, 161(2), pp. 383–403. doi: 10.1016/S0019-1035(02)00028-3.

Coustenis, A. *et al.* (2007) 'The composition of Titan's stratosphere from Cassini/CIRS mid-infrared spectra', *Icarus*, 189(1), pp. 35–62. doi: 10.1016/j.icarus.2006.12.022.

Cravens, T. E. *et al.* (2006) 'Composition of Titan's ionosphere', *Geophysical Research Letters*. John Wiley & Sons, Ltd, 33(7). doi: https://doi.org/10.1029/2005GL025575.

Cruikshank, D. P. *et al.* (1997) 'The Surfaces of Pluto and Charon', in *Pluto and Charon*, pp. 221–268.

Cruikshank, D. P. *et al.* (2015) 'The surface compositions of Pluto and Charon', *Icarus*, 246, pp. 82–92. doi: https://doi.org/10.1016/j.icarus.2014.05.023.

Cruikshank, D. P. *et al.* (2019) 'Prebiotic Chemistry of Pluto', *Astrobiology*, 19(7), pp. 831–848. doi: 10.1089/ast.2018.1927.

Cruikshank, D. P. *et al.* (2021) 'Cryovolcanic flooding in Viking Terra on Pluto', *Icarus*. Elsevier Inc., 356(November 2019), p. 113786. doi: 10.1016/j.icarus.2020.113786.

Cruikshank, D. P., Pilcher, C. B. and Morrison, D. (1976) 'Pluto: Evidence for Methane Frost', *Science*, 194(4268), pp. 835–837. doi: 10.1126/science.194.4268.935.

Cui, J. *et al.* (2009) 'Analysis of Titan's neutral upper atmosphere from Cassini Ion Neutral Mass Spectrometer measurements', *Icarus*. Elsevier Inc., 200(2), pp. 581–615. doi: 10.1016/j.icarus.2008.12.005.

D'Amico, K. L., Manos, C. and Christensen, R. L. (1980) 'Electronic energy levels in a homologous series of unsubstituted linear polyenes', *Journal of the American Chemical Society*, 102(6), pp. 1777–1782. doi: 10.1021/ja00526a003.

Dalai, P., Kaddour, H. and Sahai, N. (2016) 'Incubating Life: Prebiotic Sources of Organics for the Origin of Life', *Elements*, 12(6), pp. 401–406. doi: 10.2113/gselements.12.6.401.

Danger, G. *et al.* (2016) 'Insight into the molecular composition of laboratory organic residues produced from interstellar/pre-cometary ice analogues using very high resolution mass spectrometry', *Geochimica et Cosmochimica Acta*, 189, pp. 184–196. doi: https://doi.org/10.1016/j.gca.2016.06.014.

Dartois, E. *et al.* (2013) 'Swift heavy ion irradiation of water ice from MeV to GeV energies: Approaching true cosmic ray compaction', *Astronomy & Astrophysics*, 557(A97), pp. 1–8.

Dartois, E. *et al.* (2015) 'Swift heavy ion modifications of astrophysical water ice', *Nuclear Instruments and Methods in Physics Research B*, 365, pp. 472–476. doi: 10.1016/j.nimb.2015.08.053.

Decker, C. and Jenkins, A. D. (1985) 'Kinetic approach of oxygen inhibition in ultraviolet- and laser-induced polymerizations', *Macromolecules*, 18, pp. 1241–1244. doi: 10.1021/ma00148a034.

Delano, J. W. (2001) 'Redox History of the Earth's Interior since 3900 Ma: Implications for Prebiotic Molecules', *Origins of Life and Evolution of the Biosphere*, 31(4–5), pp. 311–341. doi: 10.1023/A:1011895600380.

Delobel, A. *et al.* (2003) 'Characterization of Hydrophobic Peptides by Atmospheric Pressure Photoionization-Mass Spectrometry and Tandem Mass Spectrometry', *Analytical Chemistry*, 75(21), pp. 5961–5968. doi: 10.1021/ac034532k.

DeMeo, F. E. *et al.* (2010) 'A search for ethane on Pluto and Triton', *Icarus*, 208(1), pp. 412–424. doi: https://doi.org/10.1016/j.icarus.2010.01.014.

Deming, D. *et al.* (2013) 'Infrared Transmission Spectroscopy of the Exoplanets HD 209458b and XO-1b using the Wide Field Camera-3 on the Hubble Space Telescope', *Astrophysical Journal*, 774(2), p. 17. doi: DOI:101088/0004-637X/774/2/95.

Derenne, S. *et al.* (2012) 'New insights into the structure and chemistry of Titan's tholins via 13C and 15N solid state nuclear magnetic resonance spectroscopy', *Icarus*, 221(2), pp. 844–853. doi: https://doi.org/10.1016/j.icarus.2012.03.003.

Desch, S. J. *et al.* (2009) 'Thermal evolution of Kuiper belt objects, with implications for cryovolcanism', *Icarus*. Elsevier Inc., 202(2), pp. 694–714. doi: 10.1016/j.icarus.2009.03.009.

Desch, S. J. (2015) 'Density of Charon formed from a disk generated by the impact of partially

differentiated bodies', *Icarus*, 246, pp. 37–47. doi: https://doi.org/10.1016/j.icarus.2014.07.034.

Desyaterik, Y. *et al.* (2013) 'Speciation of "brown" carbon in cloud water impacted by agricultural biomass burning in eastern China', *Journal of Geophysical Research: Atmospheres*, 118(13), pp. 7389–7399. doi: 10.1002/jgrd.50561.

DeWitt, H. L. *et al.* (2009) 'Reduction in Haze Formation Rate on Prebiotic Earth in the Presence of Hydrogen', *Astrobiology*, 9(5), pp. 447–453. doi: 10.1089/ast.2008.0289.

Dias-Oliveira, A. *et al.* (2015) 'Pluto's Atmosphere from Stellar Occultations in 2012 and 2013', *The Astrophysical Journal*, 811(53), p. 20. doi: 10.1088/0004-637X/811/1/53.

Doressoundiram, A. and Lellouch, E. (2008) 'Pluton : 80 ans d'exploration à distance', in *Aux confins du système solaire*. Belin, pp. 22–65.

Douté, S. *et al.* (1999) 'Evidence for Methane Segregation at the Surface of Pluto', *Icarus*, 142(2), pp. 421–444. doi: 10.1006/icar.1999.6226.

Dreisewerd, K. *et al.* (1995) 'Influence of the laser intensity and spot size on the desorption of molecules and ions in matrix-assisted laser desorption/ionization with a uniform beam profile', *International Journal of Mass Spectrometry and Ion Processes*, 141, pp. 127–148.

Dubois, D., Carrasco, N., Petrucciani, M., *et al.* (2019) 'In situ investigation of neutrals involved in the formation of Titan tholins', *Icarus*, 317, pp. 182–196. doi: https://doi.org/10.1016/j.icarus.2018.07.006.

Dubois, D., Carrasco, N., Bourgalais, J., *et al.* (2019) 'Nitrogen-containing Anions and Tholin Growth in Titan's Ionosphere: Implications for Cassini CAPS-ELS Observations', *The Astrophysical Journal*. American Astronomical Society, 872(2), p. L31. doi: 10.3847/2041-8213/ab05e5.

Dubois, D. *et al.* (2020) 'Positive ion chemistry in an N2-CH4 plasma discharge: Key precursors to the growth of Titan tholins', *Icarus*, 338, p. 113437. doi: https://doi.org/10.1016/j.icarus.2019.113437.

Earle, A. M. *et al.* (2017) 'Long-term surface temperature modeling of Pluto', *Icarus*, 287, pp. 37–46. doi: https://doi.org/10.1016/j.icarus.2016.09.036.

Earle, A. M. and Binzel, R. P. (2015) 'Pluto's insolation history: Latitudinal variations and effects on atmospheric pressure', *Icarus*. Elsevier Inc., 250, pp. 405–412. doi: 10.1016/j.icarus.2014.12.028.

Elkins-Tanton, L. T. (2011) 'Pluto and the Kuiper Belt', in *Uranus, Neptune, Pluto, and the Outer Solar System*, pp. 107–172.

Elliot, J. L. (1979) 'Stellar Occultation Studies of the Solar System', *Annual Review of Astronomy and Astrophysics*, 17, pp. 445–475. Available at: www.annualreviews.org.

Elliot, J. L. *et al.* (1989) 'Pluto's atmosphere', *Icarus*, 77(1), pp. 148–170. doi: https://doi.org/10.1016/0019-1035(89)90014-6.

Elliot, J. L. *et al.* (2007) 'Changes in Pluto's Atmosphere: 1988-2006', *The Astronomical Journal*, 134(1), pp. 1–13. doi: 10.1086/517998.

Elliot, J. L. and Olkin, C. B. (1996) 'Probing Planetary Atmospheres With Stellar Occultations', *Annual Review of Earth and Planetary Sciences*, 24, pp. 89–123. doi: 10.1146/annurev.earth.24.1.89.

Emslie, A. G. (1978) 'The collisional interaction of a beam of charged particles with a hydrogen target of arbitrary ionization level.', *The Astrophysical Journal*, 224, pp. 241–246. doi: 10.1086/156371.

Evans, A. C. *et al.* (2012) 'Chirality, photochemistry and the detection of amino acids in interstellar ice analogues and comets', *Chemical Society Reviews*, 41, pp. 5447–5458. doi: 10.1039/c2cs35051c.

Fan, J. *et al.* (2016) 'Review of Aerosol-Cloud Interactions: Mechanisms, Significance, and Challenges', *Journal of the Atmospheric Sciences*, 73(11), pp. 4221–4252. doi: 10.1175/JAS-D-16-0037.1.

Fan, S. *et al.* (2019) 'Retrieval of Chemical Abundances in Titan's Upper Atmosphere From Cassini UVIS Observations With Pointing Motion', *Earth and Space Science*, 6(7), pp. 1057–1066. doi: 10.1029/2018EA000477.

Faure, M. (2016) *Évolution des glaces et des composés organiques interstellaires et cométaires : Étude expérimentale et analyse des données VIRTIS/ROSETTA*. Université Grenoble Alpes.

Faure, M. *et al.* (2021) 'A radiolytic origin of organic matter in primitive chondrites and trans-neptunian objects? New clues from ion irradiation experiments', *Icarus*. Elsevier Inc., 364, p. 114462. doi: 10.1016/j.icarus.2021.114462.

Fayolle, M. *et al.* (2021) 'Testing tholins as analogues of the dark reddish material covering Pluto's Cthulhu region', *Icarus*.

Ferrari, A. C., Rodil, S. E. and Robertson, J. (2003) 'Interpretation of infrared and Raman spectra of amorphous carbon nitrides', *Physical Review B - Condensed Matter and Materials Physics*, 67(15), p. 155306. doi: 10.1103/PhysRevB.67.155306.

Ferus, M. *et al.* (2017) 'Formation of nucleobases in a Miller-Urey reducing atmosphere', *Proceedings of the National Academy of Sciences of the United States of America*, 114(17), pp. 4306–4311. doi: 10.1073/pnas.1700010114.

Fitch, W. L. and Sauter, A. D. (1983) 'Calculation of Relative Electron Impact Total Ionization Cross Sections for Organic Molecules', *Analytical Chemistry*, 55(6), pp. 832–835. doi: 10.1021/ac00257a006.

Flasar, F. M. *et al.* (2004) 'Exploring the Saturn System in the Thermal Infrared: The Composite Infrared Spectrometer', in Russell, C. T. (ed.) *The Cassini-Huygens Mission: Orbiter Remote Sensing Investigations*. Dordrecht: Springer Netherlands, pp. 169–297. doi: 10.1007/1-4020-3874-7_4.

Fleury, B. *et al.* (2014) 'Influence of CO on Titan atmospheric reactivity', *Icarus*, 238, pp. 221–229. doi: https://doi.org/10.1016/j.icarus.2014.05.027.

Fleury, B. (2015) *The upper atmosphere of the early Earth , a source of prebiotic organic compounds*. Université Paris-Saclay.

Fleury, B. *et al.* (2015) 'Water formation in the upper atmosphere of the Early Earth', *The Astrophysical Journal*. American Astronomical Society, 807(2), p. L29. doi: 10.1088/2041-8205/807/2/l29.

Fleury, B. *et al.* (2017) 'Organic chemistry in a CO2 rich early Earth atmosphere', *Earth and Planetary Science Letters*, 479, pp. 34–42. doi: https://doi.org/10.1016/j.epsl.2017.09.026.

Forget, F. *et al.* (2017) 'A post-New Horizons global climate model of Pluto including the N2, CH4 and CO cycles', *Icarus*, 287, pp. 54–71. doi: https://doi.org/10.1016/j.icarus.2016.11.038.

Freissinet, C. *et al.* (2010) 'Search for evidence of life in space: Analysis of enantiomeric organic molecules by N,N-dimethylformamide dimethylacetal derivative dependant Gas Chromatography-Mass Spectrometry', *Journal of Chromatography A*, 1217(5), pp. 731–740. doi: 10.1016/j.chroma.2009.11.009.

French, R. G. *et al.* (2015) 'Seasonal variations in Pluto's atmospheric tides', *Icarus*, 246, pp. 247–267. doi: https://doi.org/10.1016/j.icarus.2014.05.017.

Fujiwara, H. (2007) *Spectroscopic Ellipsometry: Principles and Applications*. John Wiley, *Spectroscopic Ellipsometry: Principles and Applications*. John Wiley.

Furukawa, Y. *et al.* (2019) 'Extraterrestrial ribose and other sugars in primitive meteorites', *Proceedings of the National Academy of Sciences*, 116(49), pp. 24440–24445. doi: 10.1073/pnas.1907169116.

Gales, S. (2010) 'The GANIL facility', *Scholarpedia*, 5(7), p. 9670. doi: 10.4249/scholarpedia.9670.

Gao, P. *et al.* (2017) 'Constraints on the microphysics of Pluto's photochemical haze from New

Horizons observations', *Icarus*, 287, pp. 116–123. doi: https://doi.org/10.1016/j.icarus.2016.09.030.

Gautier, T. *et al.* (2011) 'Nitrile gas chemistry in Titan's atmosphere', *Icarus*, 213(2), pp. 625–635. doi: https://doi.org/10.1016/j.icarus.2011.04.005.

Gautier, T. *et al.* (2012) 'Mid- and far-infrared absorption spectroscopy of Titan's aerosols analogues', *Icarus*, 221(1), pp. 320–327. doi: https://doi.org/10.1016/j.icarus.2012.07.025.

Gautier, T. *et al.* (2014) 'Nitrogen incorporation in Titan's tholins inferred by high resolution orbitrap mass spectrometry and gas chromatography–mass spectrometry', *Earth and Planetary Science Letters*, 404, pp. 33–42. doi: https://doi.org/10.1016/j.epsl.2014.07.011.

Gautier, T. *et al.* (2016) 'Development of HPLC-Orbitrap method for identification of N-bearing molecules in complex organic material relevant to planetary environments', *Icarus*, 275, pp. 259–266. doi: https://doi.org/10.1016/j.icarus.2016.03.007.

Gautier, T. *et al.* (2017) 'Influence of trace aromatics on the chemical growth mechanisms of Titan aerosol analogues', *Planetary and Space Science*, 140, pp. 27–34. doi: https://doi.org/10.1016/j.pss.2017.03.012.

Gautier, T. *et al.* (2020) 'Decomposition of electron ionization mass spectra for space application using a Monte-Carlo approach', *Rapid Communications in Mass Spectrometry*, 34(8), p. e8684. doi: 10.1002/rcm.8684.

Gavilan, L. *et al.* (2017) 'Organic Aerosols in the Presence of CO2 in the Early Earth and Exoplanets: UV–Vis Refractive Indices of Oxidized Tholins', *The Astrophysical Journal*, 848(1), p. L5. doi: 10.3847/2041-8213/aa8cc4.

Gavilan, L. *et al.* (2018) 'Organic Aerosols in Anoxic and Oxic Atmospheres of Earth-like Exoplanets: VUV-MIR Spectroscopy of CHON Tholins', *The Astrophysical Journal*. American Astronomical Society, 861(2), p. 110. doi: 10.3847/1538-4357/aac8df.

Ghesquière, P., Talbi, D. and Karton, A. (2014) 'The reaction of the benzene cation with acetylenes for the growth of PAHs in the interstellar medium', *Chemical Physics Letters*, 595–596, pp. 13–19. doi: 10.1016/j.cplett.2014.01.040.

Gladstone, G. R. *et al.* (2016) 'The atmosphere of Pluto as observed by New Horizons', *Science*, 351(6279). Available at: http://science.sciencemag.org/content/351/6279/aad8866.abstract.

Gladstone, G. R., Pryor, W. R. and Stern, S. A. (2015) 'Lyα@Pluto', *Icarus*, 246, pp. 279–284. doi: https://doi.org/10.1016/j.icarus.2014.04.016.

Gladstone, G. R. and Young, L. A. (2019) 'New Horizons Observations of the Atmosphere of Pluto', *Annual Review of Earth and Planetary Sciences*, 47(1), pp. 119–140. doi: 10.1146/annurev-earth-053018-060128.

Golitsyn, G. S. (1975) 'A possible atmosphere on Pluto', *Soviet Astronomy Letters*, 1, pp. 38–42.

Greig, M. J. *et al.* (2003) 'Fourier transform ion cyclotron resonance mass spectrometry using atmospheric pressure photoionization for high-resolution analyses of corticosteroids', *Rapid Communications in Mass Spectrometry*, 17(24), pp. 2763–2768. doi: 10.1002/rcm.1257.

Grenier, I. A., Black, J. H. and Strong, A. W. (2015) 'The Nine Lives of Cosmic Rays in Galaxies', *Annual Review of Astronomy and Astrophysics*, 53(1), pp. 199–246. doi: 10.1146/annurev-astro-082214-122457.

Griffith, C. A. *et al.* (2012) 'Radiative transfer analyses of Titan's tropical atmosphere', *Icarus*, 218(2), pp. 975–988. doi: https://doi.org/10.1016/j.icarus.2011.11.034.

Grundy, W. M. *et al.* (2013) 'Near-infrared spectral monitoring of Pluto's ices: Spatial distribution and secular evolution', *Icarus*, 223(2), pp. 710–721. doi: 10.1016/j.icarus.2013.01.019.

Grundy, W. M. *et al.* (2014) 'Near-infrared spectral monitoring of Pluto's ices II: Recent decline of CO and N2 ice absorptions', *Icarus*. Elsevier Inc., 235, pp. 220–224. doi: 10.1016/j.icarus.2014.02.025.

Grundy, W. M. *et al.* (2016) 'Surface compositions across Pluto and Charon', *Science*, 351(6279). Available at: http://science.sciencemag.org/content/351/6279/aad9189.abstract.

Grundy, W. M. *et al.* (2017) 'Haze and Cosmic Ray Influences on Pluto's Compositional Environments', in *Lunar and Planetary Science XLVIII*, p. 2165.

Grundy, W. M. *et al.* (2018) 'Pluto's haze as a surface material', *Icarus*, 314, pp. 232–245. doi: https://doi.org/10.1016/j.icarus.2018.05.019.

Grundy, W. M. and Buie, M. W. (2001) 'Distribution and Evolution of CH4, N2, and CO Ices on Pluto's Surface: 1995 to 1998', *Icarus*, 153(2), pp. 248–263. doi: 10.1006/icar.2001.6684.

Grundy, W. M., Buie, M. W. and Spencer, J. R. (2002) 'Spectroscopy of Pluto and Triton at 3–4 Microns: Possible Evidence for Wide Distribution of Nonvolatile Solids', *The Astronomical Journal*, 124(4), pp. 2273–2278. doi: 10.1086/342933.

Guo, Y. and Farquhar, R. W. (2008) 'New Horizons Mission Design', *Space Science Reviews*, 140(1), pp. 49–74. doi: 10.1007/s11214-007-9242-y.

Hadamcik, E. *et al.* (2009) 'Laboratory light-scattering measurements with Titan's aerosols analogues produced by a dusty plasma', *Planetary and Space Science*, 57(13), pp. 1631–1641. doi: https://doi.org/10.1016/j.pss.2009.06.013.

Hakala, K. S. *et al.* (2003) 'Development of LC/MS/MS Methods for Cocktail Dosed Caco-2 Samples Using Atmospheric Pressure Photoionization and Electrospray Ionization', *Analytical Chemistry*, 75(21), pp. 5969–5977. doi: 10.1021/ac034679b.

Haldane, J. B. S. (1929) 'Origin of life', *Rationalist Annual*, 148, pp. 3–10.

Hamid, A. M. *et al.* (2014) 'Evidence for the Formation of Pyrimidine Cations from the Sequential Reactions of Hydrogen Cyanide with the Acetylene Radical Cation', *Journal of Physical Chemistry Letters*, 5(19), pp. 3392–3398. doi: 10.1021/jz501648q.

Hanold, K. A. *et al.* (2004) 'Atmospheric pressure photoionization. 1. General properties for LC/MS', *Analytical Chemistry*, 76(10), pp. 2842–2851. doi: 10.1021/ac035442i.

Hapke, B. (1981) 'Bidirectional Reflectance Spectroscopy', *Journal of Geophysical Research*, 86(B4), pp. 3039–3054. doi: http://dx.doi.org/10.1029/JB086iB04p03039; doi:10.1029/JB086iB04p03039.

Hapke, B. (2012) *Theory of reflectance and emittance spectroscopy*. New York: Cambridge University Press.

Hart, M. H. (1974) 'A possible atmosphere for Pluto', *Icarus*, 21(3), pp. 242–247. doi: https://doi.org/10.1016/0019-1035(74)90039-6.

He, C. *et al.* (2017) 'Carbon Monoxide Affecting Planetary Atmospheric Chemistry', *The Astrophysical Journal*, 841(2), p. L31. doi: 10.3847/2041-8213/aa74cc.

He, C., Hörst, S. M., Lewis, N. K., Yu, X., Moses, J. I., Kempton, E. M.-R., McGuiggan, P., *et al.* (2018) 'Laboratory Simulations of Haze Formation in the Atmospheres of Super-Earths and Mini-Neptunes: Particle Color and Size Distribution', *The Astrophysical Journal*, 856(1), p. L3. doi: 10.3847/2041-8213/aab42b.

He, C., Hörst, S. M., Lewis, N. K., Yu, X., Moses, J. I., Kempton, E. M.-R., Marley, M. S., *et al.* (2018) 'Photochemical Haze Formation in the Atmospheres of Super-Earths and Mini-Neptunes', *The Astronomical Journal*, 156(1), p. 38. doi: 10.3847/1538-3881/aac883.

He, C. and Smith, M. A. (2013) 'Identification of nitrogenous organic species in Titan aerosols analogs:

Nitrogen fixation routes in early atmospheres', *Icarus*, 226(1), pp. 33–40. doi: https://doi.org/10.1016/j.icarus.2013.05.013.

He, C. and Smith, M. A. (2014) 'Identification of nitrogenous organic species in Titan aerosols analogs: Implication for prebiotic chemistry on Titan and early Earth', *Icarus*, 238, pp. 86–92. doi: https://doi.org/10.1016/j.icarus.2014.05.012.

He, J. *et al.* (2015) 'Thermal degradation of organics for pyrolysis in space: Titan's atmospheric aerosol case study', *Icarus*, 248, pp. 205–212. doi: https://doi.org/10.1016/j.icarus.2014.10.010.

Heays, A. N., Bosman, A. D. and van Dishoeck, E. F. (2017) 'Photodissociation and photoionisation of atoms and molecules of astrophysical interest', *Astronomy & Astrophysics*, 602, p. A105. Available at: https://doi.org/10.1051/0004-6361/201628742.

Heinrich, M. N., Khare, B. N. and McKay, C. P. (2007) 'Prebiotic organic synthesis in early Earth and Mars atmospheres: Laboratory experiments with quantitative determination of products formed in a cold plasma flow reactor', *Icarus*, 191(2), pp. 765–778. doi: 10.1016/j.icarus.2007.05.017.

Hendrix, A. R., Domingue, D. L. and Noll, K. S. (2013) 'Ultraviolet Properties of Planetary Ices', in Gudipati, M. S. and Castillo-Rogez, J. (eds) *The Science of Solar System Ices*. New York: Springer, pp. 73–105. doi: 10.1007/978-1-4614-3076-6.

Hillier, J. H. *et al.* (2021) 'Characteristics of Pluto's Haze and Surface from an Analytic Radiative Transfer Model', *The Planetary Science Journal*. IOP Publishing, 2(11), p. 12. doi: 10.3847/psj/abbdaf.

Hinson, D. P. *et al.* (2017) 'Radio occultation measurements of Pluto's neutral atmosphere with New Horizons', *Icarus*, 290, pp. 96–111. doi: https://doi.org/10.1016/j.icarus.2017.02.031.

Hinson, D. P. *et al.* (2018) 'An upper limit on Pluto's ionosphere from radio occultation measurements with New Horizons', *Icarus*, 307, pp. 17–24. doi: https://doi.org/10.1016/j.icarus.2018.02.011.

Hockaday, W. C. *et al.* (2009) 'Electrospray and photoionization mass spectrometry for the characterization of organic matter in natural waters: A qualitative assessment', *Limnology and Oceanography: Methods*, 7(1), pp. 81–95. doi: 10.4319/lom.2009.7.81.

Holler, B. J. *et al.* (2014) 'Evidence for longitudinal variability of ethane ice on the surface of pluto', *Icarus*. Elsevier Inc., 243, pp. 104–110. doi: 10.1016/j.icarus.2014.09.013.

Horányi, M. *et al.* (2008) 'The Student Dust Counter on the New Horizons Mission', *Space Science Reviews*, 140(1), pp. 387–402. doi: 10.1007/s11214-007-9250-y.

Hörst, S. M. *et al.* (2012) 'Formation of Amino Acids and Nucleotide Bases in a Titan Atmosphere Simulation Experiment', *Astrobiology*, 12(9), pp. 809–817. doi: 10.1089/ast.2011.0623.

Hörst, S. M. (2017) 'Titan's atmosphere and climate', *Journal of Geophysical Research: Planets*, 122(3), pp. 432–482. doi: 10.1002/2016JE005240.

Hörst, S. M., He, C., Ugelow, M. S., *et al.* (2018) 'Exploring the Atmosphere of Neoproterozoic Earth: The Effect of O2 on Haze Formation and Composition', *The Astrophysical Journal*. IOP Publishing, 858(2), p. 119. doi: 10.3847/1538-4357/aabd7d.

Hörst, S. M., He, C., Lewis, N. K., *et al.* (2018) 'Haze production rates in super-Earth and mini-Neptune atmosphere experiments', *Nature Astronomy*, 2(4), pp. 303–306. doi: 10.1038/s41550-018-0397-0.

Hörst, S. M., Yoon, Y. H., *et al.* (2018) 'Laboratory investigations of Titan haze formation: In situ measurement of gas and particle composition', *Icarus*, 301, pp. 136–151. doi: https://doi.org/10.1016/j.icarus.2017.09.039.

Hörst, S. M. and Tolbert, M. A. (2013) 'In situ Measurements of the Size and Density of Titan Aerosol Analogs', *The Astrophysical Journal*. American Astronomical Society, 770(1), p. L10. doi: 10.1088/2041-8205/770/1/l10.

Hörst, S. M. and Tolbert, M. A. (2014) 'The Effect of Carbon Monoxide on Planetary Haze Formation', *The Astrophysical Journal*, 781(1), p. 53. doi: 10.1088/0004-637x/781/1/53.

Howard, A. D., Moore, J. M., White, O. L., *et al.* (2017) 'Pluto: Pits and mantles on uplands north and east of Sputnik Planitia', *Icarus*. Elsevier Inc., 293, pp. 218–230. doi: 10.1016/j.icarus.2017.02.027.

Howard, A. D., Moore, J. M., Umurhan, O. M., *et al.* (2017) 'Present and past glaciation on Pluto', *Icarus*, 287, pp. 287–300. doi: https://doi.org/10.1016/j.icarus.2016.07.006.

Hubbard, W. B. *et al.* (1988) 'Occultation evidence for an atmosphere on Pluto', *Nature*, 336, p. 452. Available at: http://dx.doi.org/10.1038/336452a0.

Imanaka, H. *et al.* (2004) 'Laboratory experiments of Titan tholin formed in cold plasma at various pressures: Implications for nitrogen-containing polycyclic aromatic compounds in Titan haze', *Icarus*, 168(2), pp. 344–366. doi: https://doi.org/10.1016/j.icarus.2003.12.014.

Imanaka, H. *et al.* (2012) 'Optical constants of Titan tholins at mid-infrared wavelengths (2.5–25μm) and the possible chemical nature of Titan's haze particles', *Icarus*, 218(1), pp. 247–261. doi: https://doi.org/10.1016/j.icarus.2011.11.018.

Imanaka, H. and Smith, M. A. (2009) 'EUV Photochemical Production of Unsaturated Hydrocarbons: Implications to EUV Photochemistry in Titan and Jovian Planets', *The Journal of Physical Chemistry A*, 113(42), pp. 11187–11194. doi: 10.1021/jp9041952.

Imanaka, H. and Smith, M. A. (2010) 'Formation of nitrogenated organic aerosols in the Titan upper atmosphere', *Proceedings of the National Academy of Sciences of the United States of America*, 107(28), pp. 12423–12428. doi: 10.1073/pnas.0913353107.

International Astronomical Union (2006) '(134340) Pluto, (136199) Eris, and (136199) Eris I (Dysnomia)', *International Astronomical Union*, 8747.

Israel, G. *et al.* (1999) 'The Cassini-Huygens ACP experiment and exobiological implications', *Advances in Space Research*, 23(2), pp. 319–331. doi: https://doi.org/10.1016/S0273-1177(99)00053-8.

Israel, G. *et al.* (2003) 'Huygens Probe Aerosol Collector Pyrolyser Experiment', in Russell, C. T. (ed.) *The Cassini-Huygens Mission: Overview, Objectives and Huygens Instrumentarium Volume 1*. Dordrecht: Springer Netherlands, pp. 433–468. doi: 10.1007/978-94-017-3251-2_12.

Jellison, G. E. J. and Modine, F. A. (1996) 'Parameterization of the optical functions of amorphous materials in the interband region', *Applied Physics Letters*, 69(3), pp. 371–373. doi: 10.1063/1.118064.

Jing, Y. *et al.* (2013) 'Theoretical Study on the Addition Reaction Mechanism Between Propadienylidene and Formaldehyde: An Alternative Approach to the Formation of Furan', *Revue Roumaine de Chimie*, 58(9–10), pp. 799–807. doi: 10.2298/JSC191217026W.

Johnson, B. C. *et al.* (2016) 'Formation of the Sputnik Planum basin and the thickness of Pluto's subsurface ocean', *Geophysical Research Letters*, 43(19), pp. 10068–10077. doi: 10.1002/2016GL070694.

Johnson, P. E. *et al.* (2021) 'Modeling Pluto's minimum pressure: Implications for haze production', *Icarus*, 356, p. 114070. doi: https://doi.org/10.1016/j.icarus.2020.114070.

Johnson, R. E. (1989) 'Effect of Irradiation on the Surface of Pluto', *Geophysical Research Letters*, 16(11), pp. 1233–1236.

Jones, B. M., Kaiser, R. I. and Strazzulla, G. (2014) 'UV-Vis, Infrared, and Mass Spectroscopy of Electron Irradiated Frozen Oxygen and Carbon Dioxide Mixtures with Water', *The Astrophysical Journal*, 781(85), pp. 1–11. doi: 10.1088/0004-637X/781/2/85.

Jovanović, L. *et al.* (2020) 'Chemical composition of Pluto aerosol analogues', *Icarus*, 346, p. 113774.

doi: https://doi.org/10.1016/j.icarus.2020.113774.

Jovanović, L. *et al.* (2021) 'Optical constants of Pluto aerosol analogues from UV to near-IR', *Icarus*, p. 114398. doi: https://doi.org/10.1016/j.icarus.2021.114398.

Kamata, S. *et al.* (2019) 'Pluto's ocean is capped and insulated by gas hydrates', *Nature Geoscience*, 12(6), pp. 407–410. doi: 10.1038/s41561-019-0369-8.

Kammer, J. A. *et al.* (2017) 'New Horizons Upper Limits on O2 in Pluto's Present Day Atmosphere', *The Astronomical Journal*, 154(2), p. 55. doi: 10.3847/1538-3881/aa78a7.

Kasting, J. F. (1993) 'Earth's Early Atmosphere', *Science*, 259, pp. 920–926. Available at: http://www.jstor.org/stable/1698323.

Kasting, J. F. (1997) 'Warming Early Earth and Mars', *Science*, 276(5316), pp. 1213–1215. doi: 10.1126/science.276.5316.1213.

Kataoka, H. and Kijima, K. (1997) 'Analysis of heterocyclic amines as their N-dimethylaminomethylene derivatives by gas chromatography with nitrogen-phosphorus selective detection', *Journal of Chromatography A*, 767, pp. 187–194. doi: 10.1002/jssc.200600208.

Kawai, J. *et al.* (2019) 'Nucleic acid bases in Titan tholins and possible genetic systems in the Titan liquidosphere', *Life Sciences in Space Research*. Elsevier, 20, pp. 20–29. doi: 10.1016/j.lssr.2018.11.002.

Keita, A.-S. *et al.* (2010) 'Spectroscopic ellipsometry investigation of the optical properties of nanostructured Si/SiNx films', *Journal of Applied Physics*, 107(9), p. 93516. doi: 10.1063/1.3331551.

Kenyon, S. J. and Bromley, B. C. (2014) 'The Formation of Pluto's Low-Mass Satellites', *The Astronomical Journal*, 147(8), p. 17. doi: 10.1088/0004-6256/147/1/8.

Khare, B. N., Sagan, C., Arakawa, E. T., *et al.* (1984) 'Optical constants of organic tholins produced in a simulated Titanian atmosphere: From soft X-ray to microwave frequencies', *Icarus*, 60(1), pp. 127–137. doi: https://doi.org/10.1016/0019-1035(84)90142-8.

Khare, B. N., Sagan, C., Thompson, W. R., *et al.* (1984) 'The organic aerosols of Titan', *Advances in Space Research*, 4(12), pp. 59–68. doi: https://doi.org/10.1016/0273-1177(84)90545-3.

Khare, B. N. *et al.* (1987) 'Solid hydrocarbon aerosols produced in simulated Uranian and Neptunian stratospheres', *Journal of Geophysical Research: Space Physics*, 92(A13), pp. 15067–15082. doi: 10.1029/JA092iA13p15067.

Kidjemet, D. (2002) 'N,N-Dimethylformamide Dimethyl Acetal', *Synlett*, (10), pp. 1741–1742.

Kim, S., Kramer, R. W. and Hatcher, P. G. (2003) 'Graphical Method for Analysis of Ultrahigh-Resolution Broadband Mass Spectra of Natural Organic Matter, the Van Krevelen Diagram', *Analytical Chemistry*, 75(20), pp. 5336–5344. doi: 10.1021/ac034415p.

Kimura, J. and Kamata, S. (2020) 'Stability of the subsurface ocean of Pluto', *Planetary and Space Science*. Elsevier Ltd, 181, p. 104828. doi: 10.1016/j.pss.2019.104828.

Kitadai, N. and Maruyama, S. (2018) 'Origins of building blocks of life: A review', *Geoscience Frontiers*. Elsevier, 9(4), pp. 1117–1153. doi: 10.1016/j.gsf.2017.07.007.

Knapp, D. R. (1979) *Handbook of Analytical Derivatization Reactions*. Wiley-Interscience.

de Kok, R. *et al.* (2007) 'Oxygen compounds in Titan's stratosphere as observed by Cassini CIRS', *Icarus*, 186(2), pp. 354–363. doi: https://doi.org/10.1016/j.icarus.2006.09.016.

Kolokolova, L. *et al.* (1997) 'Properties of Cometary Dust from Color and Polarization', *Icarus*, 126(2), pp. 351–361. doi: https://doi.org/10.1006/icar.1996.5660.

Kolokolova, L. and Jockers, K. (1997) ‘Composition of cometary dust from polarization spectra’, *Planetary and Space Science*, 45(12), pp. 1543–1550. doi: https://doi.org/10.1016/S0032-0633(97)00099-8.

Konopacky, Q. M. *et al.* (2013) ‘Detection of Carbon Monoxide and Water Absorption Lines in an Exoplanet Atmosphere’, *Science*, 339(6126), pp. 1398–1401. doi: 10.1126/science.1232003.

Kramers, H. A. (1927) ‘La diffusion de la lumière par les atomes’, in *Atti. Cong. Intern. Fisica (Transactions of Volta Centenary Congress) Como 2*, pp. 545–557.

Krasnopolsky, V. A. (2009) ‘A photochemical model of Titan’s atmosphere and ionosphere’, *Icarus*, 201(1), pp. 226–256. doi: https://doi.org/10.1016/j.icarus.2008.12.038.

Krasnopolsky, V. A. (2018) ‘Some problems in interpretation of the New Horizons observations of Pluto’s atmosphere’, *Icarus*, 301, pp. 152–154. doi: https://doi.org/10.1016/j.icarus.2017.08.021.

Krasnopolsky, V. A. (2020) ‘A photochemical model of Pluto’s atmosphere and ionosphere’, *Icarus*, 335, p. 113374. doi: https://doi.org/10.1016/j.icarus.2019.07.008.

Krasnopolsky, V. A. and Cruikshank, D. P. (1999) ‘Photochemistry of Pluto’s atmosphere and ionosphere near perihelion’, *Journal of Geophysical Research: Planets*, 104(E9), pp. 21979–21996. doi: 10.1029/1999JE001038.

van Krevelen, D. W. (1950) ‘Graphical-statistical method for the study of structure and reaction processes of coal’, *Fuel*, 29, pp. 269–284.

van Krevelen, D. W. (1984) ‘Organic Geochemistry: Old and New’, *Organic Geochemistry*, 6, pp. 1–10. doi: https://doi.org/10.1016/0146-6380(84)90021-4.

van Krevelen, D. W. and te Nijenhuis, K. (2009) ‘Chapter 10: Optical Properties’, in *Properties of Polymers - Fourth edition*, pp. 287–320. doi: https://doi.org/10.1016/B978-0-444-82877-4.50017-2.

Kronig, R. de L. (1926) ‘On the Theory of Dispersion of X-Rays’, *Journal of the Optical Society of America*, 12(6), pp. 547–557. doi: 10.1364/JOSA.12.000547.

Kroonblawd, M. P., Lindsey, R. K. and Goldman, N. (2019) ‘Synthesis of functionalized nitrogen-containing polycyclic aromatic hydrocarbons and other prebiotic compounds in impacting glycine solutions’, *Chemical Science*. Royal Society of Chemistry, 10(24), pp. 6091–6098. doi: 10.1039/c9sc00155g.

Kumar, P. P., Broekhuizen, K. E. and Abbatt, J. P. D. (2003) ‘Organic acids as cloud condensation nuclei: Laboratory studies of highly soluble and insoluble species’, *Atmospheric Chemistry and Physics*, 3(3), pp. 509–520. doi: 10.5194/acp-3-509-2003.

Lambe, A. T. *et al.* (2013) ‘Relationship between Oxidation Level and Optical Properties of Secondary Organic Aerosol’, *Environmental Science & Technology*, 47(12), pp. 6349–6357. doi: 10.1021/es401043j.

Lammer, H. *et al.* (2009) ‘What makes a planet habitable?’, *The Astronomy and Astrophysics Review*, 17(2), pp. 181–249. doi: 10.1007/s00159-009-0019-z.

Landera, A. and Mebel, A. M. (2010) ‘Mechanisms of formation of nitrogen-containing polycyclic aromatic compounds in low-temperature environments of planetary atmospheres: A theoretical study’, *Faraday Discussions*, 147, pp. 479–494. doi: 10.1039/c003475d.

Lanzerotti, L. J., Brown, W. L. and Marcantonio, K. J. (1987) ‘Experimental Study of Erosion of Methane Ice by Energetic Ions and Some Considerations for Astrophysics’, *The Astrophysical Journal*, 313, pp. 910–919. doi: 10.1086/165031.

Lara, L. M., Ip, W. and Rodrigo, R. (1997) ‘Photochemical Models of Pluto’s Atmosphere’, *Icarus*, 130(1), pp. 16–35. doi: https://doi.org/10.1006/icar.1997.5798.

Larson, E. J. L. *et al.* (2015) 'Microphysical modeling of Titan's detached haze layer in a 3D GCM', *Icarus*, 254, pp. 122–134. doi: https://doi.org/10.1016/j.icarus.2015.03.010.

Lauer, T. R. *et al.* (2018) 'The New Horizons and Hubble Space Telescope search for rings, dust, and debris in the Pluto-Charon system', *Icarus*. Elsevier Inc., 301, pp. 155–172. doi: 10.1016/j.icarus.2017.09.033.

Lavvas, P. *et al.* (2013) 'Aerosol growth in Titan's ionosphere', *Proceedings of the National Academy of Sciences of the United States of America*, 110(8), pp. 2729–2734. doi: 10.1073/pnas.1217059110.

Lavvas, P. *et al.* (2016) 'Photochemical aerosol formation in planetary atmospheres: A comparison between Pluto and Titan', in *AAS/Division for Planetary Sciences Meeting Abstracts #48*, p. 224.06. Available at: https://ui.adsabs.harvard.edu/abs/2016DPS....4822406L.

Lavvas, P. *et al.* (2020) 'A major ice component in Pluto's haze', *Nature Astronomy*. doi: 10.1038/s41550-020-01270-3.

Lavvas, P., Coustenis, A. and Vardavas, I. M. (2008) 'Coupling photochemistry with haze formation in Titan's atmosphere, Part II: Results and validation with Cassini/Huygens data', *Planetary and Space Science*, 56(1), pp. 67–99. doi: https://doi.org/10.1016/j.pss.2007.05.027.

Lavvas, P., Yelle, R. V. and Griffith, C. A. (2010) 'Titan's vertical aerosol structure at the Huygens landing site: Constraints on particle size, density, charge, and refractive index', *Icarus*, 210(2), pp. 832–842. doi: https://doi.org/10.1016/j.icarus.2010.07.025.

Lavvas, P., Yelle, R. V. and Vuitton, V. (2009) 'The detached haze layer in Titan's mesosphere', *Icarus*, 201(2), pp. 626–633. doi: https://doi.org/10.1016/j.icarus.2009.01.004.

Lebreton, J.-P. and Matson, D. L. (1992) 'An overview of the Cassini mission', *Nuovo Cimento C Geophysics Space Physics C*, 15C(6), pp. 1137–1147. doi: 10.1007/BF02506708.

Lebreton, J.-P. and Matson, D. L. (1997) 'The Huygens Probe: Science, Payload and Mission Overview', *Huygens: Science, Payload and Mission*, 1177, pp. 5–24.

van Leeuwen, S. M., Hendriksen, L. and Karst, U. (2004) 'Determination of aldehydes and ketones using derivatization with 2,4-dinitrophenylhydrazine and liquid chromatography-atmospheric pressure photoionization-mass spectrometry', *Journal of Chromatography A*, 1058(1–2), pp. 107–112. doi: 10.1016/j.chroma.2004.08.149.

Legrand, J.-C. *et al.* (1998) 'Kinetics of reactions in CH4/N2 afterglow plasma : A simplified model', *Vacuum*, 50(3–4), pp. 491–495. doi: 10.1016/S0042-207X(98)00085-2.

Lellouch, E. (1994) 'The Thermal Structure of Pluto's Atmosphere: Clear vs. Hazy Models', *Icarus*, 108(2), pp. 255–264. doi: https://doi.org/10.1006/icar.1994.1060.

Lellouch, E. *et al.* (2009) 'Pluto's lower atmosphere structure and methane abundance from high-resolution spectroscopy and stellar occultations', *Astronomy and Astrophysics*, 495(3), pp. 17–21. doi: 10.1051/0004-6361/200911633.

Lellouch, E. *et al.* (2010) 'Detection of CO in Triton's atmosphere and the nature of surface-atmosphere interactions', *Astronomy & Astrophysics*, 512, p. L8. Available at: https://doi.org/10.1051/0004-6361/201014339.

Lellouch, E. *et al.* (2011) 'High resolution spectroscopy of Pluto's atmosphere: Detection of the 2.3 μm CH4 bands and evidence for carbon monoxide', *Astronomy and Astrophysics*, 530(4), p. 4. doi: 10.1051/0004-6361/201116954.

Lellouch, E. *et al.* (2015) 'Exploring the spatial, temporal, and vertical distribution of methane in Pluto's atmosphere', *Icarus*, 246, pp. 268–278. doi: https://doi.org/10.1016/j.icarus.2014.03.027.

Lellouch, E. *et al.* (2017) 'Detection of CO and HCN in Pluto's atmosphere with ALMA', *Icarus*, 286,

pp. 289–307. doi: https://doi.org/10.1016/j.icarus.2016.10.013.

Leonard, F. C. (1930) 'The New Planet Pluto', *Leaflet of the Astronomical Society of the Pacific*, 1, pp. 121–124.

Lewis, J. S. (1971) 'Satellites of the Outer Planets: Their Physical and Chemical Nature', *Icarus*, 15(2), pp. 174–185. doi: 10.1016/0019-1035(71)90072-8.

Liang, M.-C., Yung, Y. L. and Shemansky, D. E. (2007) 'Photolytically Generated Aerosols in the Mesosphere and Thermosphere of Titan', *The Astrophysical Journal*, 661(2), pp. L199–L202. doi: 10.1086/518785.

Liebman, S. A., Pesce-Rodriguez, R. A. and Matthews, C. N. (1995) 'Organic Analysis of Hydrogen Cyanide Polymers: Prebiotic and Extraterrestrial Chemistry', *Advances in Space Research*, 15(3), pp. 71–80.

Ligon, S. C. *et al.* (2014) 'Strategies to Reduce Oxygen Inhibition in Photoinduced Polymerization', *Chemical Reviews*, 114(1), pp. 557–589. doi: 10.1021/cr3005197.

Likhachev, D. V., Malkova, N. and Poslavsky, L. (2015) 'Modified Tauc-Lorentz dispersion model leading to a more accurate representation of absorption features below the bandgap', *Thin Solid Films*, 589, pp. 844–851. doi: https://doi.org/10.1016/j.tsf.2015.07.035.

Lin, D. L. *et al.* (2008) 'Chemical derivatization for the analysis of drugs by GC-MS - A conceptual review', *Journal of Food and Drug Analysis*, 16(1), pp. 1–10. doi: 10.38212/2224-6614.2373.

Lindhard, J., Scharff, M. and Schiøtt, H. E. (1963) 'Range Concepts and Heavy Ion Ranges (Notes on Atomic Collisions, II)', *Matematisk-fysiske Meddelelser udgivet af Det Kongelige Danske Videnskabernes Selskab*, 33(14), p. 42 p. Available at: http://www.sdu.dk/media/bibpdf/Bind 30-39%5CBind%5Cmfm-33-14.pdf%5Cnhttp://catalog.hathitrust.org/Record/009643906%5Cnhttp://hdl.handle.net/2027/uc1.l0065861890.

Liu, P. F. *et al.* (2015) 'Ultraviolet and visible complex refractive indices of secondary organic material produced by photooxidation of the aromatic compounds toluene and m-xylene', *Atmospheric Chemistry & Physics*, 15, pp. 1435–1446. doi: 10.5194/acp-15-1435-2015.

Loison, J.-C. *et al.* (2015) 'The neutral photochemistry of nitriles, amines and imines in the atmosphere of Titan', *Icarus*, 247, pp. 218–247. doi: https://doi.org/10.1016/j.icarus.2014.09.039.

Lopes, R. M. C. *et al.* (2016) 'Nature, distribution, and origin of Titan's Undifferentiated Plains', *Icarus*, 270, pp. 162–182. doi: https://doi.org/10.1016/j.icarus.2015.11.034.

Lowe, C. U., Rees, M. W. and Markham, R. (1963) 'Synthesis of Complex Organic Compounds from Simple Precursors: Formation of Amino-Acids, Amino-Acid Polymers, Fatty ACids and Purines from Ammonium Cyanide', *Nature*, 199(4890), pp. 219–222.

Lu, Y. and Freeland, S. (2006) 'Testing the Potential for Computational Chemistry to Quantify Biophysical Properties of the Non-Proteinaceous Amino Acids', *Astrobiology*, 6(4), pp. 606–624.

Lu, Z. *et al.* (2014) 'Evidence for direct molecular oxygen production in CO2 photodissociation', *Science*, 346(6205), pp. 61 LP – 64. doi: 10.1126/science.1257156.

Luspay-Kuti, A. *et al.* (2017) 'Photochemistry on Pluto: Part I. Hydrocarbons and aerosols', *Monthly Notices of the Royal Astronomical Society*, 472(1), pp. 104–117. doi: 10.1093/mnras/stx1362.

Madey, T. E., Johnson, R. E. and Orlando, T. M. (2002) 'Far-out surface science: Radiation-induced surface processes in the Solar System', *Surface Science*, 500(1–3), pp. 838–858. doi: 10.1016/S0039-6028(01)01556-4.

Mahjoub, A. *et al.* (2012) 'Influence of methane concentration on the optical indices of Titan's aerosols

analogues', *Icarus*, 221(2), pp. 670–677. doi: https://doi.org/10.1016/j.icarus.2012.08.015.

Mahjoub, A. *et al.* (2014) 'Effect of the Synthesis Temperature on the Optical Indices of Organic Materials Produced by N2–CH4 RF Plasma', *Plasma Processes and Polymers*, 11(5), pp. 409–417. doi: 10.1002/ppap.201300150.

Mahjoub, A. *et al.* (2016) 'Characterization of aromaticity in analogues of Titan's atmospheric aerosols with two-step laser desorption ionization mass spectrometry', *Planetary and Space Science*. Elsevier, 131, pp. 1–13. doi: 10.1016/j.pss.2016.05.003.

Maillard, J. *et al.* (2018) 'Comparison of soluble and insoluble organic matter in analogues of Titan's aerosols', *Earth and Planetary Science Letters*, 495, pp. 185–191. doi: https://doi.org/10.1016/j.epsl.2018.05.014.

Maillard, J. *et al.* (2020) 'Structural elucidation of soluble organic matter: Application to Titan's haze', *Icarus*, 340(113627), pp. 1–7. doi: 10.1016/j.icarus.2020.113627.

Maillard, J. *et al.* (2021) 'Suggested plausible structures for Titan's haze analogs using tandem mass spectrometry', *Icarus*. Elsevier Inc., 358(114181), pp. 1–8. doi: 10.1016/j.icarus.2020.114181.

Makarov, A. *et al.* (2006) 'Performance Evaluation of a Hybrid Linear Ion Trap/Orbitrap Mass Spectrometer', *Analytical Chemistry*, 78(7), pp. 2113–2120. doi: 10.1021/ac0518811.

Mandt, K. E. *et al.* (2017) 'Photochemistry on Pluto: Part II. HCN and nitrogen isotope fractionation', *Monthly Notices of the Royal Astronomical Society*, 472(1), pp. 118–128. doi: 10.1093/mnras/stx1587.

Marchi, I., Rudaz, S. and Veuthey, J.-L. (2009) 'Atmospheric pressure photoionization for coupling liquid-chromatography to mass spectrometry: A review', *Talanta*, 78(1), pp. 1–18. doi: 10.1016/j.talanta.2008.11.031.

Marshall, A. G. and Rodgers, R. P. (2008) 'Petroleomics: Chemistry of the underworld', *Proceedings of the National Academy of Sciences*, 105(47), pp. 18090–18095. doi: 10.1073/pnas.0805069105.

Martin, C. R. and Binzel, R. P. (2021) 'Ammonia-water freezing as a mechanism for recent cryovolcanism on Pluto', *Icarus*. Elsevier Inc., 356(March 2020), p. 113763. doi: 10.1016/j.icarus.2020.113763.

Martins, Z. *et al.* (2008) 'Extraterrestrial nucleobases in the Murchison meteorite', *Earth and Planetary Science Letters*, 270, pp. 130–136. doi: 10.1016/j.epsl.2008.03.026.

Materese, C. K. *et al.* (2014) 'Ice Chemistry on Outer Solar System bodies: Carboxylic Acids, Nitriles, and Urea Detected in Refractory Residues Produced From the UV Photolysis of N2:CH4:CO-containing Ices', *The Astrophysical Journal*, 788(111), p. 11. doi: 10.1088/0004-637X/788/2/111.

Materese, C. K. *et al.* (2015) 'Ice Chemistry on Outer Solar System Bodies: Electron Radiolysis of N2-, CH4-, and CO-containing Ices', *The Astrophysical Journal*. IOP Publishing, 812(150), p. 9. doi: 10.1088/0004-637X/812/2/150.

Materese, C. K., Nuevo, M. and Sandford, S. A. (2015) 'N- and O-Heterocycles Produced from the Irradiation of Benzene and Naphthalene in H2O/NH3-containing Ices', *The Astrophysical JournalAstrophysical Journal*, 800(116), p. 8. doi: 10.1088/0004-637X/800/2/116.

Mathé, C. *et al.* (2018) 'Detection Opportunity for Aromatic Signature in Titan's Aerosols in the 4.1–5.3 μm Range', *The Astrophysical Journal*. American Astronomical Society, 861(2), p. L25. doi: 10.3847/2041-8213/aacf88.

Matson, D. L. (1996) 'Cassini/Huygens mission to the Saturnian system', in *SPIE'S 1996 International Symposium on Optical Science, Engineering, and Instrumentation*. doi: 10.1117/12.253423.

Matson, D. L., Spilker, L. J. and Lebreton, J.-P. (2003) 'The Cassini/Huygens Mission to the Saturnian System', in Russell, C. T. (ed.) *The Cassini-Huygens Mission: Overview, Objectives and Huygens*

Instrumentarium Volume 1. Dordrecht: Springer Netherlands, pp. 1–58. doi: 10.1007/978-94-017-3251-2_1.

Matthews, C. N. (1995) 'Hydrogen cyanide polymers: From laboratory to space', *Planetary and Space Science*, 43(10–11), pp. 1365–1370.

McComas, D. J. *et al.* (2008) 'The Solar Wind Around Pluto (SWAP) Instrument Aboard New Horizons', *Space Science Reviews*, 140(1), pp. 261–313. doi: 10.1007/s11214-007-9205-3.

McComas, D. J. *et al.* (2016) 'Pluto's interaction with the solar wind', *Journal of Geophysical Research: Space Physics*, 121(5), pp. 4232–4246. doi: 10.1002/2016JA022599.

McDonald, G. D. *et al.* (1994) 'Chemical Investigation of Titan and Triton Tholins', *Icarus*, 108(1), pp. 137–145. doi: https://doi.org/10.1006/icar.1994.1046.

McEwan, M. J. and Anicich, V. G. (2007) 'Titan's Ion Chemistry: A Laboratory Perspective', *Mass Spectrometry Reviews*, 26(2), pp. 281–319. doi: 10.1002/mas.20117.

McKinnon, W. B. (1989) 'On the Origin of the Pluto-Charon Binary', *The Astrophysical Journal*, 344, pp. 41–44.

McKinnon, W. B. *et al.* (2016) 'Convection in a volatile nitrogen-ice-rich layer drives Pluto's geological vigour', *Nature*, 534, p. 82. Available at: https://doi.org/10.1038/nature18289.

McKinnon, W. B. *et al.* (2017) 'Origin of the Pluto–Charon system: Constraints from the New Horizons flyby', *Icarus*, 287, pp. 2–11. doi: https://doi.org/10.1016/j.icarus.2016.11.019.

McKinnon, W. B. *et al.* (2021) 'Formation, Composition, and History of the Pluto System: A Post-New Horizons Synthesis', in *The Pluto System After New Horizons*. doi: 10.2458/azu_uapress_9780816540945-ch022.

McKinnon, W. B. and Kirk, R. L. (2014) 'Chapter 40 - Triton', in Spohn, T., Breuer, D., and Johnson, T. V. B. T.-E. of the S. S. (Third E. (eds) *Encyclopedia of the Solar System (Third Edition)*. Elsevier, pp. 861–881. doi: https://doi.org/10.1016/B978-0-12-415845-0.00040-2.

McLafferty, F. W. and Tureček, F. (1993) *Interpretation of Mass Spectra*.

McNair, H. M., Miller, J. M. and Snow, N. H. (2019) *Basic Gas Chromatography*. John Wiley.

McNutt, R. L. *et al.* (2008) 'The Pluto Energetic Particle Spectrometer Science Investigation (PEPSSI) on the New Horizons Mission', *Space Science Reviews*, 140(1), pp. 315–385. doi: 10.1007/s11214-008-9436-y.

Meinert, C. *et al.* (2016) 'Ribose and related sugars from ultraviolet irradiation of interstellar ice analogs', *Science*, 352(6282), pp. 208–212. doi: 10.1126/science.aad8137.

Mejía, C. *et al.* (2015) 'Compaction of porous ices rich in water by swift heavy ions', *Icarus*, 250, pp. 222–229. doi: 10.1016/j.icarus.2014.12.002.

Mejía, C. *et al.* (2020) 'Radiolysis of Ices by Cosmic-Rays: CH4 and H2O Ices Mixtures Irradiated by 40 MeV 58Ni11+ Ions', *The Astrophysical Journal*. IOP Publishing, 894(132), pp. 1–22. doi: 10.3847/1538-4357/ab8935.

Merlin, F. *et al.* (2010) 'Chemical and physical properties of the variegated Pluto and Charon surfaces', *Icarus*. Elsevier Inc., 210(2), pp. 930–943. doi: 10.1016/j.icarus.2010.07.028.

Miller, S. L. (1953) 'A Production of Amino Acids Under Possible Primitive Earth Conditions', *Science*, 117(5), pp. 528–529.

Miller, S. L. (1955) 'Production of Some Organic Compounds under Possible Primitive Earth Conditions', *Journal of the American Chemical Society*, 77(9), pp. 2351–2361. doi: 10.1039/j3970000x001.

Miller, S. L. (1957) ‘The Mechanism of Synthesis of Amino Acids by Electric Discharged’, *Biochimica et Biophysica Acta*, 23, pp. 480–489.

Miller, S. L. and Urey, H. C. (1959) ‘Organic Compound Synthesis on the Primitive Earth’, *Science*, 130(3370), pp. 245–251. Available at: http://www.jstor.org/stable/1757918.

Mistrik, J. *et al.* (2017) ‘Optical Properties of Electronic Materials: Fundamentals and Characterization’, in. Springer International Publishing. doi: 10.1007/978-3-319-48933-9_3.

Miyakawa, S. *et al.* (2002) ‘Prebiotic synthesis from CO atmospheres: Implications for the origins of life’, *Proceedings of the National Academy of Sciences*, 99(23), pp. 14628 LP – 14631. doi: 10.1073/pnas.192568299.

Moise, T., Flores, J. M. and Rudich, Y. (2015) ‘Optical Properties of Secondary Organic Aerosols and Their Changes by Chemical Processes’, *Chemical Reviews*, 115(10), pp. 4400–4439. doi: 10.1021/cr5005259.

Moldoveanu, S. C. and David, V. (2019) ‘Derivatization Methods in GC and GC/MS’, in *Gas Chromatography: Derivatization, Sample Preparation, Application*, pp. 9–42. doi: 10.5772/intechopen.81954.

Molnárné Guricza, L. and Schrader, W. (2015) ‘Electrospray ionization for determination of non-polar polyaromatic hydrocarbons and polyaromatic heterocycles in heavy crude oil asphaltenes’, *Journal of Mass Spectrometry*, 50(3), pp. 549–557. doi: 10.1002/jms.3561.

Moore, J. M. *et al.* (2016) ‘The geology of Pluto and Charon through the eyes of New Horizons’, *Science*, 351(6279).

Moore, J. M. *et al.* (2017) ‘Sublimation as a landform-shaping process on Pluto’, *Icarus*, 287, pp. 320–333. doi: https://doi.org/10.1016/j.icarus.2016.08.025.

Moore, J. M. *et al.* (2018) ‘Bladed Terrain on Pluto: Possible origins and evolution’, *Icarus*. Elsevier Inc., 300, pp. 129–144. doi: 10.1016/j.icarus.2017.08.031.

Moores, J. E. *et al.* (2017) ‘Penitentes as the origin of the bladed terrain of Tartarus Dorsa on Pluto’, *Nature*. Nature Publishing Group, 541(7636), pp. 188–190. doi: 10.1038/nature20779.

Moran, S. E. *et al.* (2020) ‘Chemistry of Temperate Super-Earth and Mini-Neptune Atmospheric Hazes from Laboratory Experiments’, *The Planetary Science Journal*, 1(1), pp. 1–17. doi: https://doi.org/10.3847/PSJ/ab8eae.

Moran, W. J. and Rodríguez, A. (2012) ‘Metal-catalyzed Furan Synthesis. A Review’, *Organic Preparations and Procedures International*, 44(2), pp. 103–130. doi: 10.1080/00304948.2012.657558.

Morisson, M. *et al.* (2016) ‘Titan’s organic aerosols: Molecular composition and structure of laboratory analogues inferred from pyrolysis gas chromatography mass spectrometry analysis’, *Icarus*, 277, pp. 442–454. doi: https://doi.org/10.1016/j.icarus.2016.05.038.

Moriwaki, H. *et al.* (2004) ‘Determination of Polycyclic Aromatic Hydrocarbons in Sediment by Liquid Chromatography-Atmospheric Pressure Photoionization-Mass Spectrometry’, *Analytical Sciences*, 20(2), pp. 375–377. doi: 10.2116/analsci.20.375.

Moroz, L. V. *et al.* (2004) ‘Optical alteration of complex organics induced by ion irradiation: 1. Laboratory experiments suggest unusual space weathering trend’, *Icarus*, 170, pp. 214–228. doi: 10.1016/j.icarus.2004.02.003.

Mottl, M. J. *et al.* (2007) ‘Water and astrobiology’, *Chemie der Erde*, 67(4), pp. 253–282. doi: 10.1016/j.chemer.2007.09.002.

Nakayama, T. *et al.* (2012) ‘Wavelength Dependence of Refractive Index of Secondary Organic Aerosols Generated during the Ozonolysis and Photooxidation of α-Pinene’, *SOLA*, 8, pp. 119–123. doi:

10.2151/sola.2012-030.

Nakayama, T. *et al.* (2018) 'Effect of Oxidation Process on Complex Refractive Index of Secondary Organic Aerosol Generated from Isoprene', *Environmental Science & Technology*, 52(5), pp. 2566–2574. doi: 10.1021/acs.est.7b05852.

Neish, C. D., Somogyi, Á. and Smith, M. A. (2010) 'Titan's Primordial Soup: Formation of Amino Acids via Low-Temperature Hydrolysis of Tholins', *Astrobiology*, 10(3), pp. 337–347.

Neufeld, M. J. (2016) 'The difficult birth of NASA's Pluto mission', *Physics Today*, 69(4), pp. 40–47. doi: 10.1063/PT.3.3138.

Ngono-Ravache, Y. (2015) 'Spectroscopic study of chemical modifications induced by swift heavy ions on polymers: The contribution of the CIRIL Platform and the CIMAP Laboratory', *Journal of Physics: Conference Series*, 629(012006), pp. 1–13. doi: 10.1088/1742-6596/629/1/012006.

Nimmo, F. *et al.* (2016) 'Reorientation of Sputnik Planitia implies a subsurface ocean on Pluto', *Nature*. Nature Publishing Group, 540(7631), pp. 94–96. doi: 10.1038/nature20148.

Nimmo, F. *et al.* (2017) 'Mean radius and shape of Pluto and Charon from New Horizons images', *Icarus*, 287, pp. 12–29. doi: https://doi.org/10.1016/j.icarus.2016.06.027.

Nollet, L. M. L. (2006) *Chromatographic Analysis of the Environment*. CRC Press. doi: 10.2134/jeq1976.00472425000500020025x.

Oba, Y. *et al.* (2019) 'Nucleobase synthesis in interstellar ices', *Nature Communications*, 10(4413), pp. 1–8. doi: 10.1038/s41467-019-12404-1.

Oparin, A. I. (1924) 'Proiskhozhdenie zhizny (The origin of life)', in Bernal, J. D. (ed.) *The origin of life*. London.

Orata, F. (2012) 'Derivatization Reactions and Reagents for Gas Chromatography Analysis', in *Advanced Gas Chromatography - Progress in Agricultural, Biomedical and Industrial Applications*, pp. 83–108. doi: 10.5772/33098.

Orthous-Daunay, F.-R. *et al.* (2019) 'Ultraviolet-photon fingerprints on chondritic large organic molecules', *Geochemical Journal*, 53(1), pp. 21–32.

Owen, T. C. *et al.* (1993) 'Surface Ices and the Atmospheric Composition of Pluto', *Science*, 261(5122), pp. 745 LP – 748. Available at: http://science.sciencemag.org/content/261/5122/745.abstract.

Parker, D. S. N. *et al.* (2015) 'Gas Phase Synthesis of (Iso)Quinoline and its Role in the Formation of Nucleobases in the Interstellar Medium', *The Astrophysical Journal*. IOP Publishing, 803(2), p. 53. doi: 10.1088/0004-637X/803/2/53.

Parker, D. S. N. and Kaiser, R. I. (2017) 'On the formation of nitrogen-substituted polycyclic aromatic hydrocarbons (NPAHs) in circumstellar and interstellar environments', *Chemical Society Reviews*. Royal Society of Chemistry, 46(2), pp. 452–463. doi: 10.1039/c6cs00714g.

Patel, B. H. *et al.* (2015) 'Common origins of RNA, protein and lipid precursors in a cyanosulfidic protometabolism', *Nature Chemistry*, 7(4), pp. 301–307. doi: 10.1038/nchem.2202.

Pavlov, A. A. *et al.* (2000) 'Greenhouse warming by CH4 in the atmosphere of early Earth', *Journal of Geophysical Research*, 105(E5), pp. 11981–11990.

Pavlov, A. A. *et al.* (2001) 'Organic haze in Earth's early atmosphere: Source of low-13C Late Archean kerogens?', *Geology*, 29(11), pp. 1003–1006. doi: 10.1130/0091-7613(2001)029<1003:OHIESE>2.0.CO;2.

Peeters, Z. *et al.* (2005) 'Formation and photostability of N-heterocycles in space - I. The effect of nitrogen on the photostability of small aromatic molecules', *Astronomy and Astrophysics*, 433(2), pp.

583–590. doi: 10.1051/0004-6361:20042443.

Pernot, P. *et al.* (2010) 'Tholinomics - Chemical Analysis of Nitrogen-Rich Polymers', *Analytical Chemistry*, 82(4), pp. 1371–1380. doi: 10.1021/ac902458q.

Perrin, Z. *et al.* (2021) 'An atmospheric origin for HCN-derived polymers on Titan', *Processes*, 9.

Perry, R. H., Cooks, R. G. and Noll, R. J. (2008) 'Orbitrap mass spectrometry: Instrumentation, ion motion and applications', *Mass Spectrometry Reviews*, 27(6), pp. 661–699. doi: 10.1002/mas.20186.

Picq, V., Ramillon, J. M. and Balanzat, E. (1998) 'Swift heavy ions on polymers: Hydrocarbon gas release', *Nuclear Instruments and Methods in Physics Research, Section B: Beam Interactions with Materials and Atoms*, 146(1–4), pp. 496–503. doi: 10.1016/S0168-583X(98)00497-2.

Pilling, S. *et al.* (2010) 'Radiolysis of ammonia-containing ices by energetic, heavy, and highly charged ions inside dense astrophysical environments', *Astronomy & Astrophysics*, 509(A87), pp. 1–10.

Pintassilgo, C. D., Cernogora, G. and Loureiro, J. (2001) 'Spectroscopy study and modelling of an afterglow created by a low-pressure pulsed discharge in N2-CH4', *Plasma Sources Science and Technology*. IOP Publishing, 10(2), pp. 147–161. doi: 10.1088/0963-0252/10/2/304.

Poch, O. *et al.* (2016) 'Sublimation of water ice mixed with silicates and tholins: Evolution of surface texture and reflectance spectra, with implications for comets', *Icarus*. Elsevier Inc., 267, pp. 154–173. doi: 10.1016/j.icarus.2015.12.017.

Pont, F. J. *et al.* (2013) 'The prevalence of dust on the exoplanet HD 189733b from Hubble and Spitzer observations', *Monthly Notices of the Royal Astronomical Society*, 432(4), pp. 2917–2944. doi: 10.1093/mnras/stt651.

Poole, C. F. (2012) *Gas Chromatography, Gas Chromatography*. doi: 10.1016/C2010-0-66721-6.

Poppe, A. R. and Horányi, M. (2018) 'Interplanetary dust delivery of water to the atmospheres of Pluto and Triton', *Astronomy & Astrophysics*, 617(5), pp. 1–6.

Potin, S. *et al.* (2018) 'SHADOWS: A spectro-gonio radiometer for bidirectional reflectance studies of dark meteorites and terrestrial analogues. Design, calibrations and performances on challenging surfaces', *Applied Optics*, 57(28), pp. 8279–8296. doi: 10.1364/ao.57.008279.

Protopapa, S. *et al.* (2008) 'Surface characterization of Pluto and Charon by L and M band spectra', *Astronomy and Astrophysics*, 490(1), pp. 365–375. doi: 10.1051/0004-6361:200809994.

Protopapa, S. *et al.* (2017) 'Pluto's global surface composition through pixel-by-pixel Hapke modeling of New Horizons Ralph/LEISA data', *Icarus*, 287, pp. 218–228. doi: https://doi.org/10.1016/j.icarus.2016.11.028.

Protopapa, S. *et al.* (2020) 'Disk-resolved Photometric Properties of Pluto and the Coloring Materials across its Surface', *The Astronomical Journal*, 159(2), p. 74. doi: 10.3847/1538-3881/ab5e82.

Purcell, J. M. *et al.* (2006) 'Atmospheric pressure photoionization fourier transform ion cyclotron resonance mass spectrometry for complex mixture analysis', *Analytical Chemistry*, 78(16), pp. 5906–5912. doi: 10.1021/ac060754h.

Quirico, E. *et al.* (2008) 'New experimental constraints on the composition and structure of tholins', *Icarus*, 198(1), pp. 218–231. doi: https://doi.org/10.1016/j.icarus.2008.07.012.

Raffaelli, A. and Saba, A. (2003) 'Atmospheric Pressure Photoionization Mass Spectrometry', *Mass Spectrometry Reviews*, 22(5), pp. 318–331. doi: 10.1002/mas.10060.

Ramírez, S. I. *et al.* (2002) 'Complex Refractive Index of Titan's Aerosol Analogues in the 200–900 nm Domain', *Icarus*, 156(2), pp. 515–529. doi: https://doi.org/10.1006/icar.2001.6783.

Rannou, P. *et al.* (1997) 'A new interpretation of scattered light measurements at Titan's limb', *Journal*

of Geophysical Research: Planets, 102(E5), pp. 10997–11013. doi: 10.1029/97JE00719.

Rannou, P. *et al.* (1999) 'Semi-empirical model of absorption and scattering by isotropic fractal aggregates of spheres', *Planetary and Space Science*, 47(3), pp. 385–396. doi: https://doi.org/10.1016/S0032-0633(99)00007-0.

Rannou, P. *et al.* (2010) 'Titan haze distribution and optical properties retrieved from recent observations', *Icarus*, 208(2), pp. 850–867. doi: https://doi.org/10.1016/j.icarus.2010.03.016.

Rannou, P. and West, R. A. (2018) 'Supersaturation on Pluto and elsewhere', *Icarus*, 312, pp. 36–44. doi: https://doi.org/10.1016/j.icarus.2018.04.025.

Rao, C. N. R. (1975) 'Ultra-violet and visible spectroscopy'. Butterworth.

Reuter, D. C. *et al.* (2008) 'Ralph: A Visible/Infrared Imager for the New Horizons Pluto/Kuiper Belt Mission', *Space Science Reviews*, 140(1), pp. 129–154. doi: 10.1007/s11214-008-9375-7.

Ricca, A., Bauschlicher, C. W. and Bakes, E. L. O. (2001) 'A Computational Study of the Mechanisms for the Incorporation of a Nitrogen Atom into Polycyclic Aromatic Hydrocarbons in the Titan Haze', *Icarus*, 154(2), pp. 516–521. doi: 10.1006/icar.2001.6694.

Robb, D. B. and Blades, M. W. (2008) 'State-of-the-art in atmospheric pressure photoionization for LC/MS', *Analytica Chimica Acta*, 627(1), pp. 34–49. doi: 10.1016/j.aca.2008.05.077.

Robb, D. B., Covey, T. R. and Bruins, A. P. (2000) 'Atmospheric Pressure Photoionization: An Ionization Method for Liquid Chromatography-Mass Spectrometry', *Analytical Chemistry*, 72(15), pp. 3653–3659. doi: 10.1021/ac0001636.

Robbins, S. J. *et al.* (2017) 'Craters of the Pluto-Charon system', *Icarus*, 287, pp. 187–206. doi: https://doi.org/10.1016/j.icarus.2016.09.027.

Rodgers, R. P., Schaub, T. M. and Marshall, A. G. (2005) 'Petroleomics: MS Returns to Its Roots', *Analytical Chemistry*, 77(1), pp. 20–27. doi: 10.1021/ac053302y.

Rothard, H. *et al.* (2017) 'Modification of ices by cosmic rays and solar wind', *Journal of Physics B: Atomic, Molecular and Optical Physics*. IOP Publishing, 50(062001), pp. 1–23.

Roy, S. *et al.* (2006) 'Liquid chromatography on porous graphitic carbon with atmospheric pressure photoionization mass spectrometry and tandem mass spectrometry for the analysis of glycosphingolipids', *Journal of Chromatography A*, 1117(2), pp. 154–162. doi: 10.1016/j.chroma.2006.03.083.

Sagan, C. and Khare, B. N. (1979) 'Tholins: organic chemistry of interstellar grains and gas', *Nature*, 277(5692), pp. 102–107. doi: 10.1038/277102a0.

Saladino, R. *et al.* (2012) 'Formamide and the origin of life', *Physics of Life Reviews*, 9(1), pp. 84–104. doi: 10.1016/j.plrev.2011.12.002.

Sarker, N. *et al.* (2003) 'Titan Aerosol Analogues: Analysis of the Nonvolatile Tholins', *Astrobiology*, 3(4), pp. 719–726. doi: 10.1089/153110703322736042.

Scattergood, T. and Owen, T. (1977) 'On the sources of ultraviolet absorption in spectra of Titan and the outer planets', *Icarus*, 30(4), pp. 780–788. doi: https://doi.org/10.1016/0019-1035(77)90095-1.

Schlesinger, G. and Miller, S. L. (1983) 'Prebiotic synthesis in atmospheres containing CH4, CO, and CO2', *Journal of Molecular Evolution*, 19(5), pp. 383–390. doi: 10.1007/bf02101643.

Schlutig, S. (2001) *Contribution à l'étude de la pulvérisation et de l'endommagement du dioxyde d'uranium par les ions lourds rapides*. Université de Caen Basse-Normandie.

Schmitt, B. *et al.* (2017) 'Physical state and distribution of materials at the surface of Pluto from New Horizons LEISA imaging spectrometer', *Icarus*, 287, pp. 229–260. doi:

https://doi.org/10.1016/j.icarus.2016.12.025.

Schulz, F. *et al.* (2021) 'Imaging Titan's Organic Haze at Atomic Scale', *The Astrophysical Journal*. IOP Publishing, 908(1), p. L13. doi: 10.3847/2041-8213/abd93e.

Schwartz, A. W. and Goverde, M. (1982) 'Acceleration of HCN Oligomerization by Formaldehyde and Related Compounds: Implications for Prebiotic Syntheses', *Journal of Molecular Evolution*, 18(5), pp. 351–353.

Sciamma-O'Brien, E. *et al.* (2010) 'Titan's atmosphere: An optimal gas mixture for aerosol production?', *Icarus*, 209(2), pp. 704–714. doi: https://doi.org/10.1016/j.icarus.2010.04.009.

Sciamma-O'Brien, E. *et al.* (2012) 'Optical constants from 370 nm to 900 nm of Titan tholins produced in a low pressure RF plasma discharge', *Icarus*, 218(1), pp. 356–363. doi: https://doi.org/10.1016/j.icarus.2011.12.014.

Sciamma-O'Brien, E., Ricketts, C. L. and Salama, F. (2014) 'The Titan Haze Simulation experiment on COSmIC: Probing Titan's atmospheric chemistry at low temperature', *Icarus*, 243, pp. 325–336. doi: 10.1016/j.icarus.2014.08.004.

Sciamma-O'Brien, E., Upton, K. T. and Salama, F. (2017) 'The Titan Haze Simulation (THS) experiment on COSmIC. Part II. Ex-situ analysis of aerosols produced at low temperature', *Icarus*, 289, pp. 214–226. doi: https://doi.org/10.1016/j.icarus.2017.02.004.

Sebree, J. A. *et al.* (2014) 'Titan aerosol analog absorption features produced from aromatics in the far infrared', *Icarus*. Elsevier Inc., 236, pp. 146–152. doi: 10.1016/j.icarus.2014.03.039.

Sebree, J. A. *et al.* (2018) 'Detection of Prebiotic Molecules in Plasma and Photochemical Aerosol Analogs Using GC/MS/MS Techniques', *The Astrophysical Journal*, 865(2), p. 133. doi: 10.3847/1538-4357/aadba1.

Sebree, J. A., Wayson, J. M. and Lopez, J. R. (2018) 'Variation in photon flux during extended photochemical aerosol experiments: Implications for atmospheric laboratory simulations', *Journal of Photochemistry and Photobiology A: Chemistry*, 360, pp. 1–5. doi: https://doi.org/10.1016/j.jphotochem.2018.04.023.

Seignovert, B. *et al.* (2017) 'Aerosols optical properties in Titan's detached haze layer before the equinox', *Icarus*, 292, pp. 13–21. doi: https://doi.org/10.1016/j.icarus.2017.03.026.

Sekine, Y. *et al.* (2008) 'The role of organic haze in Titan's atmospheric chemistry: II. Effect of heterogeneous reaction to the hydrogen budget and chemical composition of the atmosphere', *Icarus*, 194(1), pp. 201–211. doi: https://doi.org/10.1016/j.icarus.2007.08.030.

Sekine, Y. *et al.* (2017) 'The Charon-forming giant impact as a source of Pluto's dark equatorial regions', *Nature Astronomy*, 1(0031), pp. 1–6. doi: 10.1038/s41550-016-0031.

Shen, C. J. *et al.* (2004) 'Cosmic ray induced explosive chemical desorption in dense clouds', *Astronomy & Astrophysics*, 415(1), pp. 203–215. doi: 10.1051/0004-6361:20031669.

Showalter, M. R. *et al.* (2011) 'New Satellite of (134340) Pluto: S/2011 (134340) 1', *International Astronomical Union*, 2769(1), p. 1.

Showalter, M. R. *et al.* (2012) 'New Satellite of (134340) Pluto: S/2012 (134340) 1', *International Astronomical Union*, 9253(1), p. 1.

Showalter, M. R. and Hamilton, D. P. (2015) 'Resonant interactions and chaotic rotation of Pluto's small moons', *Nature*, 522, pp. 45–58. doi: 10.1038/nature14469.

Sicardy, B. *et al.* (2003) 'Large changes in Pluto's atmosphere as revealed by recent stellar occultations', *Nature*, 424, pp. 168–170. doi: 10.1038/nature01762.1.

Sicardy, B. *et al.* (2016) 'Pluto's Atmosphere from the 2015 June 29 Ground-Based Stellar Occultation at the Time of the New Horizons Flyby', *The Astrophysical Journal Letters*, 819(L38), p. 8. doi: 10.3847/2041-8205/819/2/l38.

Singer, K. N. *et al.* (2021) 'Impact Craters on Pluto and Charon and Terrain Age Estimates', in *The Pluto System After New Horizons*.

Smith, B. A. *et al.* (1989) 'Voyager 2 at Neptune: Imaging Science Results', *Science*, 246(4936), pp. 1422 LP – 1449. doi: 10.1126/science.246.4936.1422.

Smith, K. E. *et al.* (2014) 'Investigation of pyridine carboxylic acids in CM2 carbonaceous chondrites: Potential precursor molecules for ancient coenzymes', *Geochimica et Cosmochimica Acta*. Elsevier Ltd, 136, pp. 1–12. doi: 10.1016/j.gca.2014.04.001.

Socrates, G. (2004) *Infrared and Raman Characteristic Group Frequencies: Tables and Charts*. John Wiley & Sons, Ltd. doi: 10.1016/0003-2670(94)80274-2.

Somogyi, Á. *et al.* (2005) 'Organic environments on Saturn's moon, Titan: Simulating chemical reactions and analyzing products by FT-ICR and ion-trap mass spectrometry', *Journal of the American Society for Mass Spectrometry*, 16(6), pp. 850–859. doi: 10.1016/j.jasms.2005.01.027.

Somogyi, Á. *et al.* (2012) 'Chemical ionization in the atmosphere? A model study on negatively charged "exotic" ions generated from Titan's tholins by ultrahigh resolution MS and MS/MS', *International Journal of Mass Spectrometry*, 316–318, pp. 157–163. doi: https://doi.org/10.1016/j.ijms.2012.02.026.

Somogyi, Á. *et al.* (2016) 'The Role of Ultrahigh Resolution Fourier Transform Mass Spectrometry (FT-MS) in Astrobiology-Related Research: Analysis of Meteorites and Tholins', *International Journal of Molecular Sciences*. doi: 10.3390/ijms17040439.

Sparkman, O. D., Penton, Z. E. and Kitson, F. G. (2011) *Gas Chromatography and Mass Spectrometry: A practical guide*.

Spilker, L. J. (2019) 'Cassini-Huygens' exploration of the Saturn system: 13 years of discovery', *Science*. American Association for the Advancement of Science, 364(6445), pp. 1046–1051. doi: 10.1126/science.aat3760.

Standish, E. M. J. (1993) 'Planet X: No Dynamical Evidence in the Optical Observations', *The Astronomical Journal*, 105(5), pp. 2000–2006.

Stansberry, J. A., Lunine, J. I. and Tomasko, M. G. (1989) 'Upper limits on possible photochemical hazes on Pluto', *Geophysical Research Letters*, 16(11), pp. 1221–1224. doi: 10.1029/GL016i011p01221.

Starukhina, L. V. and Shkuratov, Y. G. (1995) 'A Model for Ion Bombardment-Induced Organic Synthesis on Carbon-Bearing Surfaces in Cosmic Space', *Icarus*, 113, pp. 442–449.

Steffl, A. J. *et al.* (2006) 'New Constraints on Additional Satellites of the Pluto System', *The Astronomical Journal*, 132(2), pp. 614–619. doi: 10.1086/505424.

Steffl, A. J. *et al.* (2020) 'Pluto's Ultraviolet Spectrum, Surface Reflectance, and Airglow Emissions', *Astrophysical Journal*.

Steffl, A. J. and Stern, S. A. (2007) 'First Constraints on Rings in the Pluto System', *The Astronomical Journal*, 133(4), pp. 1485–1489. doi: 10.1086/511770.

Stenberg, B. *et al.* (2010) 'Chapter Five - Visible and Near Infrared Spectroscopy in Soil Science', in Sparks, D. L. B. T.-A. in A. (ed.) *Advances in Agronomy*. Academic Press, pp. 163–215. doi: https://doi.org/10.1016/S0065-2113(10)07005-7.

Stern, A. S. and Mitton, J. (1998) *Pluto and Charon*. John Wiley & Sons.

Stern, S. A. (1989) ‘Pluto: Comments on Crustal Composition, Evidence for Global Differentiation’, *Icarus*, 81(1), pp. 14–23. doi: 10.1016/0019-1035(89)90121-8.

Stern, S. A. (1992) ‘The Pluto-Charon System’, *Annual Review of Astronomy and Astrophysics*, 30, pp. 185–233.

Stern, S. A. (1993) ‘The Pluto Reconnaissance Flyby Mission’, *Eos, Transactions, American Geophysical Union*, 74(7), pp. 73–78. doi: 10.1029/93EO00257.

Stern, S. A. *et al.* (2008) ‘ALICE: The Ultraviolet Imaging Spectrograph Aboard the New Horizons Pluto-Kuiper Belt Mission’, *Space Science Reviews*, 140(1), p. 155. doi: 10.1007/s11214-008-9407-3.

Stern, S. A. (2008) ‘The New Horizons Pluto Kuiper Belt Mission: An Overview with Historical Context’, *Space Science Reviews*, 140(1), pp. 3–21. doi: 10.1007/s11214-007-9295-y.

Stern, S. A. (2014) ‘Pluto’, in *Encyclopedia of the Solar System*, pp. 909–924. doi: 10.5860/choice.44-5979.

Stern, S. A. *et al.* (2015) ‘The Pluto system: Initial results from its exploration by New Horizons’, *Science*, 350(6258). Available at: http://science.sciencemag.org/content/350/6258/aad1815.abstract.

Stern, S. A., Kammer, J. A., *et al.* (2017) ‘Evidence for Possible Clouds in Pluto’s Present-day Atmosphere’, *The Astronomical Journal*, 154(2), p. 43. doi: 10.3847/1538-3881/aa78ec.

Stern, S. A., Binzel, R. P., *et al.* (2017) ‘Past epochs of significantly higher pressure atmospheres on Pluto’, *Icarus*, 287, pp. 47–53. doi: https://doi.org/10.1016/j.icarus.2016.11.022.

Stern, S. A. *et al.* (2018) ‘The Pluto System After New Horizons’, *Annual Review of Astronomy and Astrophysics*, 56(1), pp. 357–392. doi: 10.1146/annurev-astro-081817-051935.

Straube, E. A., Dekant, W. and Völkel, W. (2004) ‘Comparison of Electrospray Ionization, Atmospheric Pressure Chemical Ionization, and Atmospheric Pressure Photoionization for the Analysis of Dinitropyrene and Aminonitropyrene LC-MS/MS’, *Journal of the American Society for Mass Spectrometry*, 15(12), pp. 1853–1862. doi: 10.1016/j.jasms.2004.08.017.

Strazzulla, G. *et al.* (2003) ‘Ion irradiation of TNOs: from the fluxes measured in space to the laboratory experiments’, *Comptes Rendus Physique*, 4, pp. 791–801. doi: 10.1016/j.crhy.2003.10.009.

Strazzulla, G. (2011) ‘Cosmic ion bombardment of the icy moons of Jupiter’, *Nuclear Instruments and Methods in Physics Research, Section B: Beam Interactions with Materials and Atoms*. Elsevier B.V., 269(9), pp. 842–851. doi: 10.1016/j.nimb.2010.11.093.

Strazzulla, G. and Johnson, R. E. (1991) ‘Irradiation Effects on Comets and Cometary Debris’, in Newburn, R. L. J. (ed.) *Comets in the Post-Halley Era*, pp. 243–275.

Strobel, D. F. and Zhu, X. (2017) ‘Comparative planetary nitrogen atmospheres: Density and thermal structures of Pluto and Triton’, *Icarus*, 291, pp. 55–64. doi: https://doi.org/10.1016/j.icarus.2017.03.013.

Szopa, C. *et al.* (2006) ‘PAMPRE: A dusty plasma experiment for Titan’s tholins production and study’, *Planetary and Space Science*, 54(4), pp. 394–404. doi: https://doi.org/10.1016/j.pss.2005.12.012.

Tauc, J., Grigorovici, R. and Vancu, A. (1966) ‘Optical Properties and Electronic Structure of Amorphous Germanium’, *Physica Status Solidi (b)*, 15(2), pp. 627–637. doi: 10.1002/pssb.19660150224.

Telfer, M. W. *et al.* (2018) ‘Dunes on Pluto’, *Science*, 360(6392), pp. 992–997. doi: 10.1126/science.aao2975.

Thissen, R. *et al.* (2009) ‘Laboratory Studies of Molecular Growth in the Titan Ionosphere’, *Journal of Physical Chemistry A*, 113(42), pp. 11211–11220. doi: 10.1021/jp9050353.

Tian, F. *et al.* (2005) ‘A Hydrogen-rich Early Earth Atmosphere’, *Science*, 308(5724), pp. 1014–1017.

doi: 10.1126/science.1106983.

Tian, F., Kasting, J. F. and Zahnle, K. J. (2011) 'Revisiting HCN formation in Earth's early atmosphere', *Earth and Planetary Science Letters*. Elsevier B.V., 308(3–4), pp. 417–423. doi: 10.1016/j.epsl.2011.06.011.

Toigo, A. D. *et al.* (2010) 'Thermal tides on Pluto', *Icarus*. Elsevier Inc., 208(1), pp. 402–411. doi: 10.1016/j.icarus.2010.01.027.

Toigo, A. D. *et al.* (2015) 'General circulation models of the dynamics of Pluto's volatile transport on the eve of the New Horizons encounter', *Icarus*. Elsevier Inc., 254, pp. 306–323. doi: 10.1016/j.icarus.2015.03.034.

Tompkins, H. G. and Irene, E. A. (2005) *Handbook of Ellipsometry*. William Andrew Publishing.

Trail, D., Watson, E. B. and Tailby, N. D. (2011) 'The oxidation state of Hadean magmas and implications for early Earth's atmosphere', *Nature*. Nature Publishing Group, 480(7375), pp. 79–82. doi: 10.1038/nature10655.

Trainer, M. G. *et al.* (2004) 'Haze Aerosols in the Atmosphere of Early Earth: Manna from Heaven', *Astrobiology*, 4(4), pp. 409–419.

Trainer, M. G. *et al.* (2006) 'Organic haze on Titan and the early Earth', *Proceedings of the National Academy of Sciences of the United States of America*, 103(48), pp. 18035–18042. doi: 10.1073/pnas.0608561103.

Trainer, M. G. *et al.* (2012) 'Nitrogen Incorporation in CH4-N2 Photochemical Aerosol Produced by Far Ultraviolet Irradiation', *Astrobiology*, 12(4), pp. 315–326. doi: 10.1089/ast.2011.0754.

Trainer, M. G. *et al.* (2013) 'The Influence of Benzene as a Trace Reactant in Titan Aerosol Analogs', *Astrophysical Journal Letters*, 766(1). doi: 10.1088/2041-8205/766/1/L4.

Tran, B. N. *et al.* (2003) 'Simulation of Titan haze formation using a photochemical flow reactor: The optical constants of the polymer', *Icarus*, 165(2), pp. 379–390. doi: https://doi.org/10.1016/S0019-1035(03)00209-4.

Tran, B. N. *et al.* (2008) 'Titan's atmospheric chemistry: Photolysis of gas mixtures containing hydrogen cyanide and carbon monoxide at 185 and 254 nm', *Icarus*, 193(1), pp. 224–232. doi: 10.1016/j.icarus.2007.09.010.

Trowbridge, A. J. *et al.* (2016) 'Vigorous convection as the explanation for Pluto's polygonal terrain', *Nature*, 534, p. 79. Available at: https://doi.org/10.1038/nature18016.

Tyler, G. L. *et al.* (1989) 'Voyager Radio Science Observations of Neptune and Triton', *Science*, 246(4936), pp. 1466 LP – 1473. doi: 10.1126/science.246.4936.1466.

Tyler, G. L. *et al.* (2008) 'The New Horizons Radio Science Experiment (REX)', *Space Science Reviews*, 140(1), pp. 217–259. doi: 10.1007/s11214-007-9302-3.

Tziotis, D., Hertkorn, N. and Schmitt-Kopplin, P. (2011) 'Kendrick-Analogous Network Visualisation of Ion Cyclotron Resonance Fourier Transform Mass Spectra: Improved Options for the Assignment of Elemental Compositions and the Classification of Organic Molecular Complexity', *European Journal of Mass Spectrometry*, 17(4), pp. 415–421. doi: 10.1255/ejms.1135.

Urey, H. C. (1952) 'On the Early Chemical History of the Earth and the Origin of Life', *Proceedings of the National Academy of Sciences*, 38(4), pp. 351–363. doi: 10.1073/pnas.38.4.351.

Varela, J. A. and Saá, C. (2016) 'Metal-Catalyzed Cyclizations to Pyran and Oxazine Derivatives', *Synthesis*, 48(20), pp. 3470–3478. doi: 10.1055/s-0035-1562466.

Vasconcelos, F. de A. *et al.* (2017) 'Energetic Processing of N2:CH4 Ices Employing X-Rays and Swift

Ions: Implications for Icy Bodies in the Outer Solar System', *The Astrophysical Journal*, 850(174), pp. 1–15. doi: https://doi.org/10.3847/1538-4357/aa965f.

Venkatesan, T. (1985) 'High Energy Ion Beam Modification of Polymer Films', *Nuclear Instruments and Methods in Physics Research - B7/8 Implantation in Polymers, Insulators, Ceramics*, pp. 461–467.

Vilella, K. and Deschamps, F. (2017) 'Thermal convection as a possible mechanism for the origin of polygonal structures on Pluto's surface', *Journal of Geophysical Research: Planets*, 122(5), pp. 1056–1076. doi: 10.1002/2016JE005215.

Vinatier, S. *et al.* (2012) 'Optical constants of Titan's stratospheric aerosols in the 70-1500 cm-1 spectral range constrained by Cassini/CIRS observations', *Icarus*, 219(1), pp. 5–12. doi: https://doi.org/10.1016/j.icarus.2012.02.009.

Vuitton, V., Tran, B. N., *et al.* (2009) 'Determination of the complex refractive indices of Titan haze analogs using photothermal deflection spectroscopy', *Icarus*, 203(2), pp. 663–671. doi: https://doi.org/10.1016/j.icarus.2009.04.016.

Vuitton, V., Lavvas, P., *et al.* (2009) 'Negative ion chemistry in Titan's upper atmosphere', *Planetary and Space Science*, 57(13), pp. 1558–1572. doi: https://doi.org/10.1016/j.pss.2009.04.004.

Vuitton, V. *et al.* (2010) 'Very high resolution mass spectrometry of HCN polymers and tholins', *Faraday Discussions*, 147, pp. 495–508. doi: 10.1039/C003758C.

Vuitton, V. *et al.* (2019) 'Simulating the density of organic species in the atmosphere of Titan with a coupled ion-neutral photochemical model', *Icarus*, 324, pp. 120–197. doi: https://doi.org/10.1016/j.icarus.2018.06.013.

Vuitton, V., Yelle, R. V. and Anicich, V. G. (2006) 'The Nitrogen Chemistry of Titan's Upper Atmosphere Revealed', *The Astrophysical Journal*, 647(2), pp. L175–L178. doi: 10.1086/507467.

Vuitton, V., Yelle, R. V. and McEwan, M. J. (2007) 'Ion chemistry and N-containing molecules in Titan's upper atmosphere', *Icarus*, 191(2), pp. 722–742. doi: https://doi.org/10.1016/j.icarus.2007.06.023.

Waite, J. H. *et al.* (2004) 'The Cassini ion and neutral mass spectrometer (INMS) investigation', *Space Science Reviews*. Springer, 114(1–4), pp. 113–231.

Waite, J. H. *et al.* (2005) 'Ion Neutral Mass Spectrometer Results from the First Flyby of Titan', *Science*. American Association for the Advancement of Science, 308(5724), pp. 982–986. doi: 10.1126/science.1110652.

Waite, J. H. *et al.* (2007) 'The Process of Tholin Formation in Titan's Upper Atmosphere', *Science*. American Association for the Advancement of Science, 316(5826), pp. 870–875. doi: 10.1126/science.1139727.

Wang, C. (2015) 'The Ionization Technology of LC-MS, Advantages of APPI on Detection of PPCPs and Hormones', *Austin Chromatography*, 2(2), pp. 1032 (1–3).

Wattieaux, G. *et al.* (2015) 'Transient phenomena during dust formation in a N2–CH4 capacitively coupled plasma', *Plasma Sources Science and Technology*, 24(1), p. 15028. doi: 10.1088/0963-0252/24/1/015028.

Weaver, H. A. *et al.* (2006) 'Discovery of two new satellites of Pluto', *Nature*, 439(7079), pp. 943–945. doi: 10.1038/nature04547.

Weaver, H. A. and Stern, S. A. (2008) 'New Horizons: NASA's Pluto-Kuiper Belt Mission', *The Solar System Beyond Neptune*, p. 557. Available at: http://adsabs.harvard.edu/cgi-bin/nph-data_query?bibcode=2008ssbn.book..557W&link_type=ABSTRACT%5Cnpapers://fedb1a86-f693-4042-a040-86e952d868c2/Paper/p7055.

Webber, W. R. and Yushak, S. M. (1983) ‘A measurement of the energy spectra and relative abundance of the cosmic-ray H and He isotopes over a broad energy range’, *The Astrophysical Journal*, 275, p. 391. doi: 10.1086/161541.

Westlake, J. H. *et al.* (2014) ‘The role of ion-molecule reactions in the growth of heavy ions in Titan’s ionosphere’, *Journal of Geophysical Research : Space Physics*, 119, pp. 5951–5963. doi: 10.1002/2015JA021094.Received.

White, O. L. *et al.* (2017) ‘Geological mapping of Sputnik Planitia on Pluto’, *Icarus*, 287, pp. 261–286. doi: https://doi.org/10.1016/j.icarus.2017.01.011.

Wilson, E. H. and Atreya, S. K. (2003) ‘Chemical sources of haze formation in Titan’s atmosphere’, *Planetary and Space Science*, 51(14–15), pp. 1017–1033. doi: 10.1016/j.pss.2003.06.003.

Wong, M. L. *et al.* (2017) ‘The photochemistry of Pluto’s atmosphere as illuminated by New Horizons’, *Icarus*, 287, pp. 110–115. doi: https://doi.org/10.1016/j.icarus.2016.09.028.

Wong, M. L., Yung, Y. L. and Gladstone, G. R. (2015) ‘Pluto’s implications for a Snowball Titan’, *Icarus*, 246, pp. 192–196. doi: https://doi.org/10.1016/j.icarus.2014.05.019.

Workman, J. J. (1996) ‘Interpretive Spectroscopy for Near Infrared’, *Applied Spectroscopy Reviews*, 31(3), pp. 251–320. doi: 10.1080/05704929608000571.

Workman, J. and Weyer, L. (2008) *Practical Guide to Interpretive Near-Infrared Spectroscopy*. doi: 10.1080/00344080080030105.

Wu, Z., Rodgers, R. P. and Marshall, A. G. (2004) ‘Two- and Three-Dimensional van Krevelen Diagrams: A Graphical Analysis Complementary to the Kendrick Mass Plot for Sorting Elemental Compositions of Complex Organic Mixtures Based on Ultrahigh-Resolution Broadband Fourier Transform Ion Cyclotron Resonance’, *Analytical Chemistry*, 76(9), pp. 2511–2516. doi: 10.1021/ac0355449.

Xiaobo, Z. *et al.* (2010) ‘Variables selection methods in near-infrared spectroscopy’, *Analytica Chimica Acta*, 667(1), pp. 14–32. doi: https://doi.org/10.1016/j.aca.2010.03.048.

Yamashita, M. and Fenn, J. B. (1984) ‘Electrospray ion source. Another variation on the free-jet theme’, *The Journal of Physical Chemistry*, 88(20), pp. 4451–4459. doi: 10.1021/j150664a002.

Yang, Y. *et al.* (2020) ‘Laboratory formation and photochemistry of covalently bonded polycyclic aromatic nitrogen heterocycle (PANH) clusters in the gas phase’, *Monthly Notices of the Royal Astronomical Society*. Oxford University Press, 498(1), pp. 1–11. doi: 10.1093/mnras/staa2212.

Yoon, Y. H. *et al.* (2014) ‘The role of benzene photolysis in Titan haze formation’, *Icarus*. Elsevier Inc., 233, pp. 233–241. doi: 10.1016/j.icarus.2014.02.006.

Young, D. T. *et al.* (2004) ‘Cassini Plasma Spectrometer Investigation’, in Russell, C. T. (ed.) *The Cassini-Huygens Mission: Orbiter In Situ Investigations Volume 2*. Dordrecht: Springer Netherlands, pp. 1–112. doi: 10.1007/978-1-4020-2774-1_1.

Young, L. A. *et al.* (1997) ‘Detection of Gaseous Methane on Pluto’, *Icarus*, 127(1), pp. 258–262. doi: 10.1006/icar.1997.5709.

Young, L. A. *et al.* (2008) ‘New Horizons: Anticipated Scientific Investigations at the Pluto System’, *Space Science Reviews*, 140(1), pp. 93–127. doi: 10.1007/s11214-008-9462-9.

Young, L. A. *et al.* (2018) ‘Structure and composition of Pluto’s atmosphere from the New Horizons solar ultraviolet occultation’, *Icarus*, 300, pp. 174–199. doi: https://doi.org/10.1016/j.icarus.2017.09.006.

Zahnle, K. J. (1986) ‘Photochemistry of Methane and the Formation of Hydrocyanic Acid (HCN) in the Earth’s Early Atmosphere.’, *Journal of Geophysical Research*, 91(D2), pp. 2819–2834. doi:

10.1029/JD091iD02p02819.

Zalucha, A. M. and Cook, J. C. (2019) 'The Structure and Dynamics of the Atmospheres of Pluto and Triton', in *Oxford Research Encyclopedia of Planetary Science*. Oxford University Press. doi: 10.1093/acrefore/9780190647926.013.113.

Zhang, X., Strobel, D. F. and Imanaka, H. (2017) 'Haze heats Pluto's atmosphere yet explains its cold temperature', *Nature*, 551, p. 352. Available at: https://doi.org/10.1038/nature24465.

Zhong, M. *et al.* (2012) 'The SOA formation model combined with semiempirical quantum chemistry for predicting UV-Vis absorption of secondary organic aerosols', *Physical Chemistry Chemical Physics*, 14(25), pp. 9058–9066. doi: 10.1039/C2CP23906J.

Zhou, W. *et al.* (2007) 'Fundamentals of Scanning Electron Microscopy', in *Scanning Microscopy for Nanotechnology: Techniques and Applications*, pp. 1–40. doi: 10.1007/978-0-387-39620-0_1.

Zhu, X., Strobel, D. F. and Erwin, J. T. (2014) 'The density and thermal structure of Pluto's atmosphere and associated escape processes and rates', *Icarus*, 228, pp. 301–314. doi: https://doi.org/10.1016/j.icarus.2013.10.011.

Ziegler, J. F., Ziegler, M. D. and Biersack, J. P. (2010) 'SRIM – The stopping and range of ions in matter (2010)', *Nuclear Instruments and Methods in Physics Research Section B: Beam Interactions with Materials and Atoms*, 268(11), pp. 1818–1823. doi: https://doi.org/10.1016/j.nimb.2010.02.091.

université PARIS-SACLAY

ÉCOLE DOCTORALE
Sciences mécaniques et énergétiques, matériaux et géosciences (SMEMAG)

Titre : Étude Expérimentale de l'Atmosphère et des Aérosols de Pluton

Mots clés : Pluton, Simulation expérimentale, Atmosphère, Aérosols, Matière organique

Résumé : Le 14 Juillet 2015, la sonde *New Horizons* de la NASA a survolé Pluton, révélant une atmosphère et une surface complexes observées nulle part ailleurs dans le Système Solaire. La surface de Pluton est composée de glaces de diazote N_2, de méthane CH_4, et de monoxyde de carbone CO. Au cours de l'orbite elliptique de Pluton, ces glaces subissent un cycle de sublimation/condensation à l'origine d'une atmosphère ténue (~11 µbar à la surface). Cette atmosphère est majoritairement composée de N_2 et CH_4, avec ~500 ppm de CO. Soumise au rayonnement ultraviolet extrême et aux photons Lyman-α, elle est le siège de la production d'aérosols photochimiques, des particules solides en suspension dans l'atmosphère. Les processus exacts de formation de ces aérosols ne sont toutefois pas encore bien définis. Ces particules solides, dont la composition chimique et les propriétés optiques sont inconnues, sont observées jusqu'à plus de 350 km d'altitude dans l'atmosphère de Pluton.

Des modèles numériques ont montré que la présence de ces aérosols dans l'atmosphère pouvait avoir un impact sur la chimie atmosphérique et le climat de Pluton. De plus, il a été suggéré que ces aérosols sédimentent et constituent une source de matière organique à la surface de Pluton.

Dans le cadre de ma thèse, j'ai utilisé une approche expérimentale afin d'étudier les aérosols de Pluton, de leur formation dans la haute atmosphère à leur devenir en surface, en passant par leurs interactions avec l'atmosphère. La formation des aérosols de Pluton par photochimie et leur composition chimique sont les sujets de la première et de la deuxième partie de cette thèse de Doctorat. L'interaction des aérosols de Pluton avec le rayonnement solaire et la contribution des aérosols photochimiques en tant qu'agent colorant à la surface de Pluton sont les sujets de la troisième et de la quatrième partie de cette thèse de Doctorat.

Title: Experimental Study of Pluto's Atmosphere and Aerosols

Keywords: Pluto, Experimental simulation, Atmosphere, Aerosols, Organic matter

Abstract: On July 14th, 2015, the NASA's *New Horizons* spacecraft flew by Pluto, revealing a complex atmosphere and surface seen nowhere else in the Solar System. Pluto's surface ices are composed of molecular nitrogen N_2, methane CH_4, and carbon monoxide CO. During Pluto's elliptical orbit, these ices undergo a sublimation/condensation cycle resulting in a tenuous atmosphere (~11 µbar at the surface). This atmosphere is mostly composed of N_2 and CH_4, with ~500 ppm of CO. Subjected to extreme ultraviolet radiation and Lyman-α photons, it is the place of photochemical aerosol production, aerosols being solid particles in suspension in the atmosphere. The exact processes of formation of these aerosols are however not well constrained yet. These solid particles, whose chemical composition and optical properties are unknown, are observed up to more than 350 km of altitude in the atmosphere of Pluto.

Numerical models have shown that the presence of these aerosols in the atmosphere could have an impact on the atmospheric chemistry and climate of Pluto. Moreover, it has been suggested that these aerosols sediment and constitute a source of organic matter on the surface of Pluto.

During my Ph.D., I used an experimental approach to study the aerosols of Pluto, from their formation in the upper atmosphere to their evolution on the surface, through their interactions with the atmosphere. The formation of Pluto's aerosols by photochemistry and their chemical composition are the subjects of the first and second part of this Ph.D. thesis. The interaction of Pluto's aerosols with solar radiation and the contribution of photochemical aerosols as a coloring agent on the surface of Pluto are the subjects of the third and fourth part of this Ph.D. thesis.

Maison du doctorat de l'Université Paris-Saclay
2ème étage aile ouest, Ecole normale supérieure Paris-Saclay
4 avenue des Sciences,
91190 Gif sur Yvette, France